CMS Draft Analysis Note

The content of this note is intended for CMS internal use and distribution only

2021/05/10
Archive Hash: 058f599
Archive Date: 2021/05/10

Run-II monojet / mono-V analysis (common AN)

Andreas Albert[1], Alp Akpinar[1], Sridhara Dasu[3], Zeynep Demiragli[1], Guillelmo Gomez-Ceballos[2], Yalcin Guler[4], Emine Gurpinar[4], Evan Koenig[3], Dmytro Kovalskyi[2], Shuichi Kunori[5], Kamal Lamichhane[5], Sungwon Lee[5], Benedikt Maier[2], Abhishikth Mallampalli[3], Samila Muthmuni[5], Christoph Paus[2], Varun Sharma[3], Bayram Tali[4], Zhangqier Wang[2], Andrew Witbeck[5], Siqi Yuan[1], Greg Landsberg[6], Chang-Seong Moon[7], and Sunil Dogra[7]

[1] Boston University (US)
[2] MIT (US)
[3] University of Wisconsin - Madison (US)
[4] Cukurova University (Turkey)
[5] Texas Tech (US)
[6] Brown University (US)
[7] Kyungpook National University (Republic of Korea)

Abstract

A search for new physics using events containing an imbalance in transverse momentum and one or more energetic jets arising from initial-state radiation or the hadronic decay of W or Z bosons is presented. A data sample of proton-proton collisions at $\sqrt{s} = 13$ TeV, collected with the CMS detector at the LHC and corresponding to an integrated luminosity of 101 fb^{-1}, is used. The results are interpreted in terms of invisible decays of the Higgs boson, as well as the dark matter production cross section in simplified models with vector, axial-vector, scalar, or pseudoscalar mediators. In addition, the results are interpreted in terms of leptoquark production. Finally, stringent limits are set on the fundamental Planck scale in the Arkani-Hamed, Dimopoulos, and Dvali model with large extra spatial dimensions.

Known open issues

- Leptoquarks: For the highest mass point (leptoquark mass of 2 TeV) we are adding a signal parameter point at $\lambda = 2$ to stabilize the interpolation (which is currently an extrapolation due to the missing sample point). We expect this to reduce the apparent difference between observed and expected limit in this case.

Analysis / documentation change log

Changes in version 23 (May 10th, 2021)

- DMsimp spin-1: Added interpolation for near-diagonal and offshell region.
- Fixed a problem where the MC stat uncertainties for MC-driven backgrounds were not set correctly in combine.
- Fixed a problem where an artifically large electron ID uncertainty was applied to dielectron events.
- Split the statistical and systematic part of the eletron ID uncertainty in the fit (two nuisances per year instead of one).
- Added clarifications in response to ARC comments.
- Added high-level summary of fit behavior and terminology (sec. 6.3.1).

Changes in version 21 (April 13th, 2021)

- Added final limit setup with template replacement for 2016.
- Added DMsimp spin-1 coupling limits to main results chapter.

Changes in version 19 (April 1st, 2021)

- Added fully unblinded analysis results.

Changes in version 17 (March 29th, 2021)

- Fixed a latex issue that made the impact plots not show up in the compiled documemt.

Changes in version 16 (March 27th, 2021)

- Increased electron and photon uncertainties relative to previous, aggressive values.
- Remove stitching correction for photons introduced in previous version.
- Added full fit results with CR+1/5 SR partial unblinding. Note that the sensitivity results have only been updated accordingly for the H(inv) interpretation.

Changes in version 14 (March 5th, 2021)

- Switch to NLO DY,Z,W samples.
- Added JER correction.
- Added photon scale uncertainty.
- Added in-situ stitching correction for photons.
- Add cut on $\Delta\phi(\mathrm{PF}, \mathrm{Tk})$.

Changes in version 14 (February 8th, 2021)

- Added t-channel DM interpretation.
- Improved mistag SF uncertainty treatment.
- Added stat uncertainty nuisances for MC-driven backgrounds.
- Added goodness-of-fit study.

Changes in version 12 (October 8th, 2020)

- Replaced LO Gjets with NLO samples.
- Updated DMsimp spin-0 interpretation with 2017/18 central production samples (no more rescaling of 2016 templates).
- Added appendix about DMsimp spin-1 coupling limits.
- Added DMsimp spin-1 direct detection plots.

Changes in version 11 (September 14th, 2020)

- Added DMsimp spin-1 mono-V signal and updated interpretation accordingly.
- Updated H(inv) interpretation with higher-stat signal samples for gluon-fusion production.
- Added description of higher-order corrections and uncertainties for diboson processes.
- Added appendix detailing the improvement in data/MC agreement obtained via NLO photon samples.
- Added appendix detailing studies on the dielectron agreement.

Changes in version 9 (August 6th, 2020)

- Added ADD interpretation (including combination with 2016).
- Updated spin-1 DMsimp interpretation: Now using 2017+2018 monojet samples. Added combination with 2016. 2017/18 mono-V samples still missing, will be added as soon as available, not expected to change the result appreciably.

Changes in version 8 (July 24th, 2020)

- Removed use of JER corrections for jets and $p_{\mathrm{T}}^{\mathrm{miss}}$ (JME discourages the correction with $p_{\mathrm{T}}^{\mathrm{miss}}$ at the moment.)
- Updated to new EGamma-approved electron ID SFs.
- Finalized lepton veto uncertainties.
- Update theory + PDF uncertainties on transfer factors.
- Added V(qq)γ MC to mono-V photon CR.
- Updated synchronization appendix.

Changes in version 7 (June 23rd, 2020)

- Added data-driven QCD estimate.
- Added DMsimp interpretations (vector, scalar, pseudoscalar) based on rescaled 2016 signal templates and 2017+2018 BG estimates.
- Added leptoquark interpretation.
- Added table of signal sample production status.

Changes in version 5 (May 29th, 2020)

- Performed and documented partial unblinding of 20% of the 2017, 18 data sets.
- Updated HEM veto strategy: Now using ”dynamic veto”, see appendix for details.
- Updated to new photon ID SF, which has been approved by EGamma.
- Documented new studies on various uncertainties (prefiring, b tagging, lepton vetos, PDF)
- Updated photon k factor.

Changes in version 3 (April 24th, 2020)

- Added updated prefiring uncertainties
- Added updated tau and muon veto corrections + uncertainties
- Updated DeepAK8 tagging scale factors following new release from JMAR
- Various smaller items in reply to comments, collected here

Note to the reader

In this version of the documentation, data / MC comparison plots in the main body of the document...

1. ...for the **monojet** category are obtained from the **BU framework based on NanoAOD**.
2. ...for the **mono-V** category are obtained from the **BU framework based on NanoAOD**.

Contents

1 Introduction

Several astrophysical observations [1–3] provide compelling evidence for the existence of dark matter (DM), a type of matter not accounted for in the standard model (SM). To date only gravitational interactions of DM have been observed and it remains unknown if DM has a particle origin and could interact with ordinary matter via SM processes. However, many theoretical models have been proposed in which DM and SM particles interact with sufficient strength that DM may be directly produced with observable rates in high energy collisions at the CERN LHC. While the DM particles would remain undetected, they may recoil with large transverse momentum (p_{T}) against other detectable particles resulting in an overall visible p_{T} imbalance in a collision event. This type of event topology is rarely produced in SM processes and therefore enables a highly sensitive search for DM. Similar event topologies are predicted by other extensions of the SM, such as the Arkani-Hamed, Dimopoulos, and Dvali (ADD) model [4–8] of large extra spatial dimensions (EDs).

This paper describes a search for new physics resulting in final states with one or more energetic jets and an imbalance in p_{T} due to undetected particles. The jets are the result of the fragmentation and hadronization of quarks or gluons, which may be produced directly in the hard scattering process as initial-state radiation or as the decay products of a vector boson V (W or Z). These final states are commonly referred to as “monojet” and “mono-V”. Several searches have been performed at the LHC using the monojet and mono-V channels [9–15]. This analysis makes use of a data sample of proton-proton (pp) collisions at $\sqrt{s} = 13\,\mathrm{TeV}$ collected with the CMS detector at the LHC, corresponding to an integrated luminosity of 101.3 fb^{-1}. This sample is approximately three times larger than the one used in Ref. [16]. The analysis strategy is similar to that of previous CMS searches, and simultaneously employs event categories to target both the monojet and mono-V final states. In an improvement compared to previous searches, in this paper revised theoretical predictions and uncertainties for $\gamma +$ jets, $\mathrm{Z} +$ jets, and $\mathrm{W} +$ jets processes based on recommendations of Ref. [17] are used.

2 Data and MC simulation samples

The analysis described in this note is performed using data collected in 2017 and 2018 by CMS at 13 TeV and corresponds to an integrated luminosity of 41.5 and 59.7 fb^{-1} respectively. The MC simulation samples for the background processes have been produced in the `Fall17` and `Autumn18` campaigns. Further details are given in the following sub-sections.

2.1 Data samples

The data sets listed in Tab. 1 are used to select events in the signal and the control regions.

Table 1: List of data sets used to select events in the signal and control regions. The datasets are used in both the MiniAOD and NanoAOD tiers. The NanoAOD datasets are from the `Nano1June2019` campaign, otherwise known as `v5`. For the 2017 data, the `31Mar2018` reconstruction is used for all periods. For 2018 data, the `17Sep2018` reconstruction is used for runs A to C, and the `22Jan2019` reconstruction is used for run D.

Year	Data set name	Events selected for
both	/MET/Run201*/*AOD	Signal , single muon, double muon control regions
2017	/SingleElectron/Run2017*/*AOD	Single electron, double electron control regions
	/SinglePhoton/Run2017*/*AOD	Single electron and photon control regions
2018	/EGamma/Run2018*/*AOD	Single electron, double electron control, single photon control regions

Events for the signal regions are collected using a set of dedicated triggers designed to select events with large $p_{\mathrm{T}}^{\mathrm{miss}}$ and large $H_{\mathrm{T}}^{\mathrm{miss}}$ based on the online particle flow (PF) algorithm. In these dedicated trigger algorithms, identified PF muons are removed from the event before the $p_{\mathrm{T}}^{\mathrm{miss}}$ and the $H_{\mathrm{T}}^{\mathrm{miss}}$ objects are calculated. With this definition, the signal trigger paths can also be used to select single and double muon events for the W and Z control regions, respectively. During 2017 data-taking, it was observed that the default configuration of $p_{\mathrm{T}}^{\mathrm{miss}}$ triggers suffered from high noise rates, which were mitigated by switching to a nominally identical trigger with an additional requirement of $H_T > 60$ GeV as both the L1 and HLT level, which is trivially fulfilled for all events of interest to this analysis. For 2018, the noise rate problem was addressed in the reconstruction and this additional trigger is not strictly necessary. However, it still profits from a lower $p_{\mathrm{T}}^{\mathrm{miss}}$ threshold at L1, which improves the offline turn-on behavior, and is therefore used consistently in both years.

Electron events for the W and Z regions are selected using the unprescaled single electron trigger with the lowest available p_{T} threshold in each year. To ensure optimal trigger efficiency also for high-p_{T} electrons, the low-threshold trigger is used in combination with a higher threshold single electron trigger that has less stringent requirements on the electron isolation, as well as a wider range of L1 seeds, as well as a single photon trigger [18], which makes the triggering procedure more robust with respect to failures of track reconstruction at the HLT level. The same photon trigger is used to select events for the photon control region.

The full list of triggers used, along with the L1 seeds and the associated primary data sets are shown in Table 2.

2.2 Background simulation samples

Simulation data sets for the background processes are listed in Table 33 and 4. These following physics processes considered:

Table 2: HLT paths and the associated L1 seeds used in the analysis for the 2017 and 2018 data sets.

Year	HLT path	L1 seed	Primary data set
2017	HLT_PFMETNoMu120_PFMHTNoMu120_IDTight	`L1_ETMHF70`	MET
	HLT_PFMETNoMu120_PFMHTNoMu120_IDTight_PFHT60	`L1_ETMHF80_HTT60er`	
	HLT_Ele35_WPTight_Gsf	`L1_SingleEG24`	SingleElectron
	HLT_Ele115_CaloIdVT_GsfTrkIdT	`L1_SingleEG30`	
		`L1_SingleJet170`	
		`L1_SingleTau100er2p1`	
	HLT_Photon200	`L1_SingleEG30`	SinglePhoton
		`L1_SingleJet170`	
		`L1_SingleTau100er2p1`	
2018	HLT_PFMETNoMu120_PFMHTNoMu120_IDTight	`L1_ETMHF100`	MET
		`L1_ETM150`	
	HLT_PFMETNoMu120_PFMHTNoMu120_IDTight_PFHT60	`L1_ETMHF90_HTT60er`	
	HLT_Ele32_WPTight_Gsf	`L1_SingleIsoEG24er2p1`	EGamma
		`L1_SingleEG26er2p5`	
		`L1_SingleEG60`	
	HLT_Ele115_CaloIdVT_GsfTrkIdT	`L1_SingleEG34er2p5`	
		`L1_SingleJet160er2p5`	
		`L1_SingleJet180`	
		`L1_SingleTau120er2p1`	
		`L1_SingleEG60`	
	HLT_Photon200	`L1_SingleEG34er2p5`	
		`L1_SingleJet160er2p5`	
		`L1_SingleJet180`	
		`L1_SingleTau120er2p1`	
		`L1_SingleEG60`	

$\mathrm{Z}(\nu\nu) + \mathrm{jets}$: This process yields the largest irreducible background in the analysis. Simulated samples for this background have been produced at next-to-leading order (NLO) in QCD using the aMC@NLO generator in several bins of the boson momentum.

$\mathrm{W} + \mathrm{jets}$: The second largest source of background in this analysis. The contribution of this background can be reduced by rejecting events with charged lepton candidates (electron/muon/tau). However, this process becomes irreducible in the case where the charged leptons are outside of the detector acceptance. next-to-leading order (NLO) in QCD using the aMC@NLO generator in several bins of the boson momentum.

$\mathrm{Z}(\ell\ell) + \mathrm{jets}$: As in the case of $\mathrm{W} \rightarrow \ell\nu$, the contribution of this background is reduced by rejecting events with charged leptons. Signal-like events are produced in the case where the charged leptons from the Z boson decay are not reconstructed. Similarly to the $\mathrm{W} + \mathrm{jets}$ case, . next-to-leading order (NLO) in QCD using the aMC@NLO generator in several bins of the boson momentum.

Top: Top-quark decays (both $\mathrm{t\bar{t}}$ and single top) also contribute background events to this analysis. In these processes, the W boson produced in a top-quark decay further decays leptonically, which produces genuine $p_{\mathrm{T}}^{\mathrm{miss}}$ in the event. Next-to-leading order (NLO) $\mathrm{t\bar{t}}$ simulation samples have been produced with the aMC@NLO generator. Single-top events have been generated with the Powheg generator at NLO.

Dibosons: Decays of diboson pairs (WW, WZ, ZZ) also constitute background processes. Typically, one of the bosons decays leptonically ($\mathrm{W} \rightarrow \ell\nu$,$\mathrm{Z} \rightarrow \nu\nu$) while the other boson decays hadronically, thus producing jets and $p_{\mathrm{T}}^{\mathrm{miss}}$ in the final state. Simulated samples for WW, WZ and ZZ production have been generated at LO with Pythia 8.

QCD Multijet: QCD multijet events typically do not have large genuine $p_{\mathrm{T}}^{\mathrm{miss}}$. However, given the large cross section with which these events are produced, even a small fraction of events with jet mismeasurement results in a non-zero contribution of this process as background in the analysis. Simulated QCD samples have been generated at LO in QCD using the MadGraph generator in several bins of H_{T}.

The MC samples produced using MADGRAPH5_aMC@NLO, and POWHEG generators are interfaced with PYTHIA using the CP5 tune [19] for the fragmentation, hadronization, and underlying event description. In the case of the MADGRAPH5_aMC@NLO samples, jets from the matrix element calculations are matched to the parton shower description following the MLM [20] (FxFx [21]) prescription to match jets from matrix element calculations and parton shower description for LO (NLO) samples. The NNPDF 3.1 NNLO [22] parton distribution functions (PDFs) are used in all generated samples. The propagation of all final-state particles through the CMS detector is simulated with the GEANT 4 software [23]. The simulated events include the effects of pileup, with the multiplicity of reconstructed primary vertices matching that in data. The average number of pileup interactions per proton bunch crossing is found to be 32 for both the 2017 and 2018 data samples used in this analysis (assuming a total inelastic proton-proton cross-section of 69.2 mb).

Data set name	Cross section (pb)	Order in QCD
W1JetsToLNu_LHEWpT_100-150_TuneCP5_13TeV-amcnloFXFX-pythia8 (2017)	284.06	NLO
W1JetsToLNu_LHEWpT_150-250_TuneCP5_13TeV-amcnloFXFX-pythia8 (2017)	71.71	NLO
W1JetsToLNu_LHEWpT_250-400_TuneCP5_13TeV-amcnloFXFX-pythia8 (2017)	8.06	NLO
W1JetsToLNu_LHEWpT_400-inf_TuneCP5_13TeV-amcnloFXFX-pythia8 (2017)	0.89	NLO
W2JetsToLNu_LHEWpT_100-150_TuneCP5_13TeV-amcnloFXFX-pythia8 (2017)	281.63	NLO
W2JetsToLNu_LHEWpT_150-250_TuneCP5_13TeV-amcnloFXFX-pythia8 (2017)	108.59	NLO
W2JetsToLNu_LHEWpT_250-400_TuneCP5_13TeV-amcnloFXFX-pythia8 (2017)	18.03	NLO
W2JetsToLNu_LHEWpT_400-inf_TuneCP5_13TeV-amcnloFXFX-pythia8 (2017)	3	NLO
WJetsToLNu_Pt-50To100_TuneCP5_13TeV-amcatnloFXFX-pythia8 (2018)	3569	NLO
WJetsToLNu_Pt-100To250_TuneCP5_13TeV-amcatnloFXFX-pythia8 (2018)	769.8	NLO
WJetsToLNu_Pt-250To400_TuneCP5_13TeV-amcatnloFXFX-pythia8 (2018)	27.62	NLO
WJetsToLNu_Pt-400To600_TuneCP5_13TeV-amcatnloFXFX-pythia8 (2018)	3.591	NLO
WJetsToLNu_Pt-600ToInf_TuneCP5_13TeV-amcatnloFXFX-pythia8 (2018)	0.549	NLO
Z1JetsToNuNu_M-50_LHEZpT_50-150_TuneCP5_13TeV-amcnloFXFX-pythia8	598.9	NLO
Z1JetsToNuNu_M-50_LHEZpT_150-250_TuneCP5_13TeV-amcnloFXFX-pythia8	18.04	NLO
Z1JetsToNuNu_M-50_LHEZpT_250-400_TuneCP5_13TeV-amcnloFXFX-pythia8	2.051	NLO
Z1JetsToNuNu_M-50_LHEZpT_400-inf_TuneCP5_13TeV-amcnloFXFX-pythia8	0.2251	NLO
Z2JetsToNuNu_M-50_LHEZpT_50-150_TuneCP5_13TeV-amcnloFXFX-pythia8	326.3	NLO
Z2JetsToNuNu_M-50_LHEZpT_150-250_TuneCP5_13TeV-amcnloFXFX-pythia8	29.6	NLO
Z2JetsToNuNu_M-50_LHEZpT_250-400_TuneCP5_13TeV-amcnloFXFX-pythia8	5.174	NLO
Z2JetsToNuNU_M-50_LHEZpT_400-inf_TuneCP5_13TeV-amcnloFXFX-pythia8	0.8472	NLO
DY1JetsToLL_M-50_LHEZpT_50-150_TuneCP5_13TeV-amcnloFXFX-pythia8	315.1	NLO
DY1JetsToLL_M-50_LHEZpT_150-250_TuneCP5_13TeV-amcnloFXFX-pythia8	9.5	NLO
DY1JetsToLL_M-50_LHEZpT_250-400_TuneCP5_13TeV-amcnloFXFX-pythia8	1.097	NLO
DY1JetsToLL_M-50_LHEZpT_400-inf_TuneCP5_13TeV-amcnloFXFX-pythia8	0.1207	NLO
DY2JetsToLL_M-50_LHEZpT_50-150_TuneCP5_13TeV-amcnloFXFX-pythia8	169	NLO
DY2JetsToLL_M-50_LHEZpT_150-250_TuneCP5_13TeV-amcnloFXFX-pythia8	15.73	NLO
DY2JetsToLL_M-50_LHEZpT_250-400_TuneCP5_13TeV-amcnloFXFX-pythia8	2.74	NLO
DY2JetsToLL_M-50_LHEZpT_400-inf_TuneCP5_13TeV-amcnloFXFX-pythia8	0.4492	NLO
GJets_1j_Gpt-50To100_5f_NLO-amcatnlo	14165.0	NLO
GJets_1j_Gpt-100To250_5f_NLO-amcatnlo	1183.0	NLO
GJets_1j_Gpt-250To400_5f_NLO-amcatnlo	26.09	NLO
GJets_1j_Gpt-400To650_5f_NLO-amcatnlo	3.148e	NLO
GJets_1j_Gpt-650ToInf_5f_NLO-amcatnlo	0.2887	NLO

Table 3: Simulated datasets for the modelling of single electroweak boson backgrounds. All datasets are accessed at the MiniAOD or NanoAOD data tier, with the NanoAOD datasets correponding to the `v7` campaign, also known as `02Apr2020`.

Data set name	Cross section (pb)	Order in QCD
TTJets_TuneCP5_13TeV-amcatnloFXFX-pythia8	831.76	NLO
ST_t-channel_top_4f_inclusiveDecays_TuneCP5_13TeV-powhegV2-madspin-pythia8	137.458	NLO
ST_t-channel_antitop_4f_inclusiveDecays_TuneCP5_13TeV-powhegV2-madspin-pythia8	83.0066	NLO
ST_tW_top_5f_inclusiveDecays_TuneCP5_*_13TeV-powheg-pythia8	35.85	NLO
ST_tW_antitop_5f_inclusiveDecays_TuneCP5_*_13TeV-powheg-pythia8	35.85	NLO
WW_TuneCP5_13TeV-pythia8	75.91	LO
WZ_TuneCP5_13TeV-pythia8	27.56	LO
ZZ_TuneCP5_13TeV-pythia8	12.14	LO
QCD_HT1000to1500_TuneCP5_13TeV-madgraph-pythia8	1095	LO
QCD_HT1000to1500_TuneCP5_13TeV-madgraph-pythia8	1095	LO
QCD_HT100to200_TuneCP5_13TeV-madgraph-pythia8	2.369e+07	LO
QCD_HT1500to2000_TuneCP5_13TeV-madgraph-pythia8	99.27	LO
QCD_HT2000toInf_TuneCP5_13TeV-madgraph-pythia8	20.25	LO
QCD_HT200to300_TuneCP5_13TeV-madgraph-pythia8	1.554e+06	LO
QCD_HT300to500_TuneCP5_13TeV-madgraph-pythia8	324300	LO
QCD_HT300to500_TuneCP5_13TeV-madgraph-pythia8	324300	LO
QCD_HT500to700_TuneCP5_13TeV-madgraph-pythia8	29990	LO
QCD_HT50to100_TuneCP5_13TeV-madgraphMLM-pythia8	1.85e+08	LO
QCD_HT700to1000_TuneCP5_13TeV-madgraph-pythia8	6374	LO
QCD_HT700to1000_TuneCP5_13TeV-madgraph-pythia8	6374	LO

Table 4: Simulated datasets for the modelling of sub-dominant background processes. All datasets are accessed at the MiniAOD or NanoAOD data tier, with the NanoAOD datasets correponding to the `v7` campaign, also known as `02Apr2020`.

2.3 Signal simulation samples

The theoretical signal scenarios for this analysis are described in this section. The status of the signal sample production is summarized on the analysis twiki page.

The sample names and cross sections for all signal samples are listed in Appendix G.

2.3.1 Higgs Invisible Model

The Higgs boson is the latest addition to the set of particles included in the SM. While constraints on its properties are rapidly tightening, values of the branching fraction of the Higgs boson to invisible final states of about 20% are still viable [24]. The expected SM branching fraction through decays $H \to ZZ \to 4\nu$ is smaller than one percent, leaving ample room for the possibility of decays to new invisible particles.

Simulation samples for this signal hypothesis are generated using powheg in an identical fashion to SM-like Higgs boson samples. At the matrix element level, the Higgs boson is not decayed, and invisible decays are enforced in PYTHIA8, which is also used for parton showering and modelling of the underlying event. Samples for all Higgs production modes are considered (gluon fusion, VH associated production, and vector boson fusion).

2.3.2 DMSimp Models

The text in this section is adapted from [25].

One of the simplest scenarios for DM production at the LHC is that of a single bosonic mediator that couples to the SM quarks as well as the DM particle χ. The mediator serves as a portal between the SM and the dark sector [1] and defines the way DM is produced. By considering different hypotheses for the properties of the mediator and its coupling structure to different particles, a large range of experimental signatures can be described. This type of model, where only the particles relevant to the specific interaction under study are included, and the interaction is described in an ultraviolet complete manner, is referred to as a *simplified model* [26].

While the ability to cover many collider searches with one model is attractive, care has to be taken in order not to violate constraints from well-established sectors of physics. Particularly, the introduction of new bosons can give rise to enhanced flavour-changing neutral currents, which are already strongly constrained by measurements of flavour observables such as $K^0 - \bar{K}^0$ mixing. To avoid the possibility of such violations entirely, the simplified models are designed to obey *Minimal flavour violation* (MFV) [27]. MFV simply requires that flavour and CP violation in the extended theory follow from terms containing the CKM or Yukawa matrices. MFV variation is implemented in different ways for the different scenarios described below.

In this search, scenarios with a single spin-0 or spin-1 mediator and a Dirac fermion DM candidate are considered. The implementation of Refs. [28–30] is used, and the topology is therefore referred to as DMSIMP in the following. Formulas for the relevant Lagrangian terms, as well as those for the mediator widths are obtained from Ref. [31]. Example Feynman diagrams for associated production of DM particles and jets in this model are shown in Fig. 1. Unless otherwise specified, the mediator is assumed decay with experimentally negligible decay length. The DM candidate is assumed to be stable, and a singlet under the SM gauge groups.

In the spin-1 case, MFV is implemented by setting the quark couplings to flavour-independent

---

[1] *Dark sector* refers to the full set of particles that either make up the DM component of the universe, or interact only with this component, but not the SM particles.

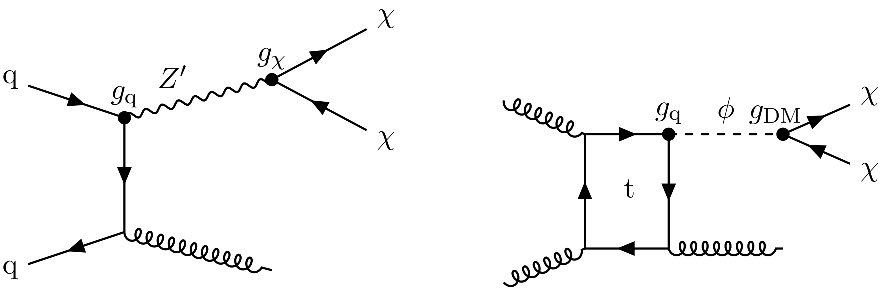

Figure 1: Example Feynman graphs for the DMSIMP model with a spin-1 mediator (Z', left) and spin-0 mediator (ϕ, right). DM particles are produced via a mediator that couples to SM quarks. Jets are produced from initial state radiation. Note that while all quark flavours could contribute to the loop on the right-hand side, only top quarks give a significant contribution.

values:

$$\mathcal{L} \;\subset\; \sum_{\mathrm{q}} Z'_\mu \bar{\mathrm{q}}\gamma^\mu (g_q^V - g_q^A\gamma_5)\mathrm{q} - Z'_\mu \bar{\chi}\gamma^\mu (g_{DM}^V - g_{DM}^A\gamma_5)\chi\,, \tag{1}$$

where Z'_μ is the DM mediator, χ is the DM candidate, and $\mathrm{q}/\bar{\mathrm{q}}$ denote the SM quarks. The free parameters are the masses m_med and m_DM of mediator and DM candidate, as well as the four coupling parameters g_q^V, g_q^A, g_{DM}^V and g_{DM}^A, which define the chiral properties of the mediator coupling to the SM quarks and DM candidate. This interaction structure is a generalized version of the SM Z boson, which couples to SM fermions with a mixture of axial-vector (A) and vector (V) couplings. In order to simplify the parameter space, only mediators with pure A couplings ($g_q^A \neq 0$, $g_{DM}^A \neq 0$, but $g_q^V = g_{DM}^V = 0$) or pure V couplings ($g_q^V \neq 0$, $g_{DM}^V \neq 0$, but $g_q^A = g_{DM}^A = 0$) are considered. Additionally the quark couplings are assumed to be identical for all quark flavours. The coupling shorthands g_q and g_{DM} are used to represent the A or V couplings in either case:

$$\mathcal{L}_V \subset g_q \sum_{\mathrm{q}} Z'_\mu \bar{\mathrm{q}}\gamma^\mu \mathrm{q} - g_{DM} Z'_\mu \bar{\chi}\gamma^\mu \chi\,, \tag{2}$$

and

$$\mathcal{L}_A \subset -g_q \sum_{\mathrm{q}} Z'_\mu \bar{\mathrm{q}}\gamma^\mu \gamma_5 \mathrm{q} + g_{DM} Z'_\mu \bar{\chi}\gamma^\mu \gamma_5 \chi\,. \tag{3}$$

This choice of couplings reduces the number of free parameters to four: m_DM, m_med, g_q and g_{DM}.

In a similar manner to the separation of the vector and axial-vector components of the couplings of the spin-1 mediator, separate scalar (S) and pseudo-scalar (P) coupling scenarios are considered for the spin-0 mediator. The MFV assumption is implemented by requiring the couplings of the mediator to the quarks be proportional to $y_\mathrm{q} = \sqrt{2}m_\mathrm{q}/v$, where $v = 246$ GeV is the vacuum expectation value of the SM Higgs boson:

$$\mathcal{L}_S \subset -\frac{g_q}{\sqrt{2}} \sum_{\mathrm{q}} \Phi y_q \bar{\mathrm{q}}\mathrm{q} - g_{DM}\Phi\bar{\chi}\chi\,, \tag{4}$$

$$\mathcal{L}_P \subset -i\frac{g_q}{\sqrt{2}} \sum_{\mathrm{q}} \Phi y_q \bar{\mathrm{q}}\gamma_5 \mathrm{q} - i g_{DM}\Phi\bar{\chi}\gamma_5\chi\,, \tag{5}$$

where Φ denotes the mediator. Like in the spin-1 case, this interaction is inspired by the familiar structure of the SM, in this case the Higgs interaction is a blueprint for the scalar mediator.

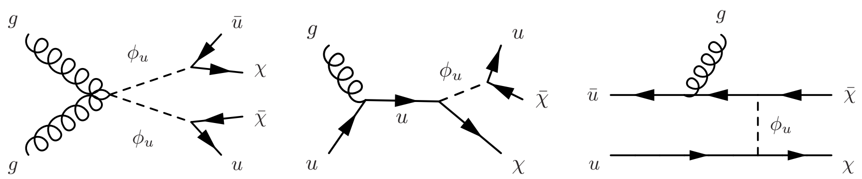

Figure 2: Example Feynman graphs for the production of DM candidates χ in association with jets in the t-channel mediator scenario. Taken from Ref. [16].

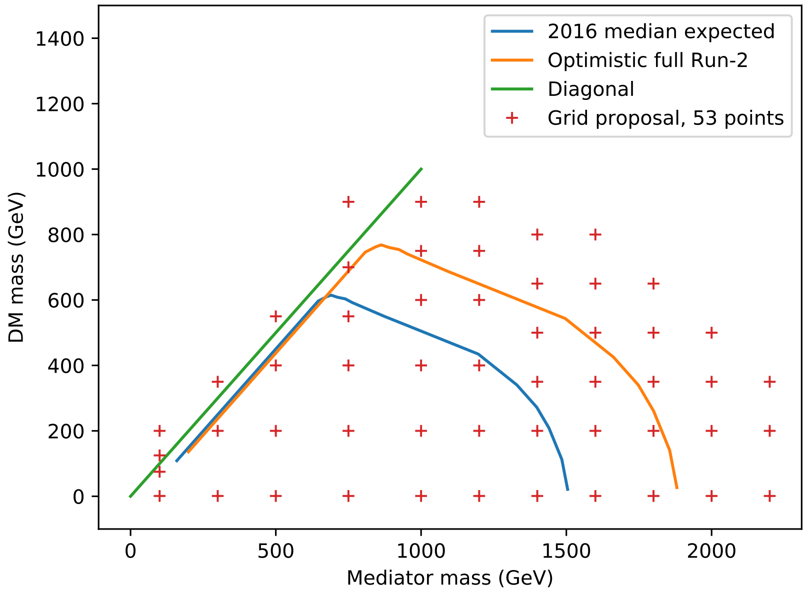

Figure 3: Parameter points considered in the t-channel dark matter signal scan.

Note that the coupling of the mediator to the DM particles does not depend on m_{DM}. This choice reflects an agnostic view of mass generation in the dark sector: no assumption is made as to how the DM candidate acquires a mass, and a full model of the dark sector physics would need to account for this question. The practical result of this choice is that the coupling of the mediator to DM is much larger than that of the SM fermions, with the exception of the top quark. A signal in this scenario would be faint, but detectable, whereas any further suppression (induced by e.g. the introduction of democratic fermion couplings) would reduce the expected signal yields below the threshold of detectability with the available data sets.

Simulation samples for the DMsimp processes are obtained using Madgraph5_aMC@NLO. For the spin-1 case, samples are produced at NLO in QCD with up to two partons at the matrix-element level in addition to the DM pair. Parton showering is performed usign PYTHIA8, and matching uses the FXFX method. For the spin-0 case, samples are simulated at effective LO in QCD, since the signal process is loop induced. The final state in this case consists of the DM pair with one additional parton at the matrix element level. In both cases, separate samples are generated for the associated production of DM particles with partonic jets, hadronically decaying W bosons, and hadronically decaying Z bosons.

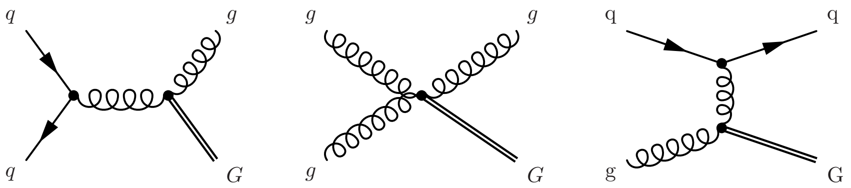

Figure 4: Example Feynman graphs for the production of ADD gravitons in association with jets. Taken from Ref. [16].

2.3.3 t-channel mediators

A more complex scenario of DM production is tested in a scenario termed “Fermion portal”. A detailed discussion of this model and its relevant for the monojet phase space can be found in Ref. [32]. Example Feynman diagrams for this type of interaction are shown in Fig. 2.

The parameters for this model are chosen to agree with those used in Ref. [16]. The technical implementation in the `DMsimp_t` UFO model is used [33], in which this set of parameters is referred to as `S3D_uR`. In this scenario, the mediator is assumed to couple to DM candidates and right-handed up quarks. The associated coupling λ is set to 1. Separate signal samples are generated for the case of mediator pair production with subsequent decays of the mediator into DM-quark pair, and pair production of DM candidates with an associated yet from either QCD radiation or the decay of a single mediator. In oth cases, samples are generated in a two-dimensional grid of DM and mediator masses, which is shown in Fig. 3. The scan is optimized to be most dense in the region around the 2016-based exclusion from Ref. [16] and the approximate expected exclusion region of the full Run-2 search.

2.3.4 ADD Model

Beyond the search for dark matter, a scenario of large extra dimensions suggested by Arkani-Hamed, Dimopulous and Dvali (ADD) is tested. In this model, the existence of additional spacetime dimensions beyond the known four can account for the as-of-yet unexplained difference in strength between gravitational and electromagnetic interactions, also known as the Hierarchy Problem. In this scenario, gravitons can be produced produced in proton-proton collisions and escape detection by escaping into the new dimensions, which are not directly accessible to experimental methods. Feynman diagrams for this process are shown in Fig. 4.

The signal hypothesis is parametrized as a function of the bulk mass M_D and the number of additional dimensions d.

2.3.5 Leptoquark Model

A leptoquark (LQ) is a Beyond the Standard Model particle which has simultaneous coupling to leptons and quarks. Models involving LQ particles include two types of LQs: Scalar LQs with spin 0, and vector LQs with spin 1. LQ models recently attracted attention because some LQ models may provide an explanation to several physics anomalies, such as the anomalies in rare B-meson decays, as observed in LHCb.

A subset of LQ models involve one LQ at a time, coupling to only one SM lepton and one quark field. These models are termed as ”Minimal Leptoquark Models” (MLQ). In the context of monojet search, MLQ models will be of interest, where LQ only couples to a neutrino and a quark. Such LQ particles produce jet + MET as a result of their decay, so their signature is identical to monojet signature.

There are three main production modes of LQ particles in collider experiments. First production mode is pair production, where a pair of LQ-antiLQ particle is produced from incoming partons, and each particle decays into a lepton and a quark. Second production mode is single production, where a single LQ is produced with another lepton, and LQ further decays to a lepton and a quark. Last production mode is Drell-Yan like prouction, where a virtual LQ is exchanged in a Drell-Yan process. Leading order Feynman digrams for all production modes can be found in Fig. 5, where scalar and vector LQ particles are collectively denoted as ϕ. Feynman diagrams are taken from Ref. [34].

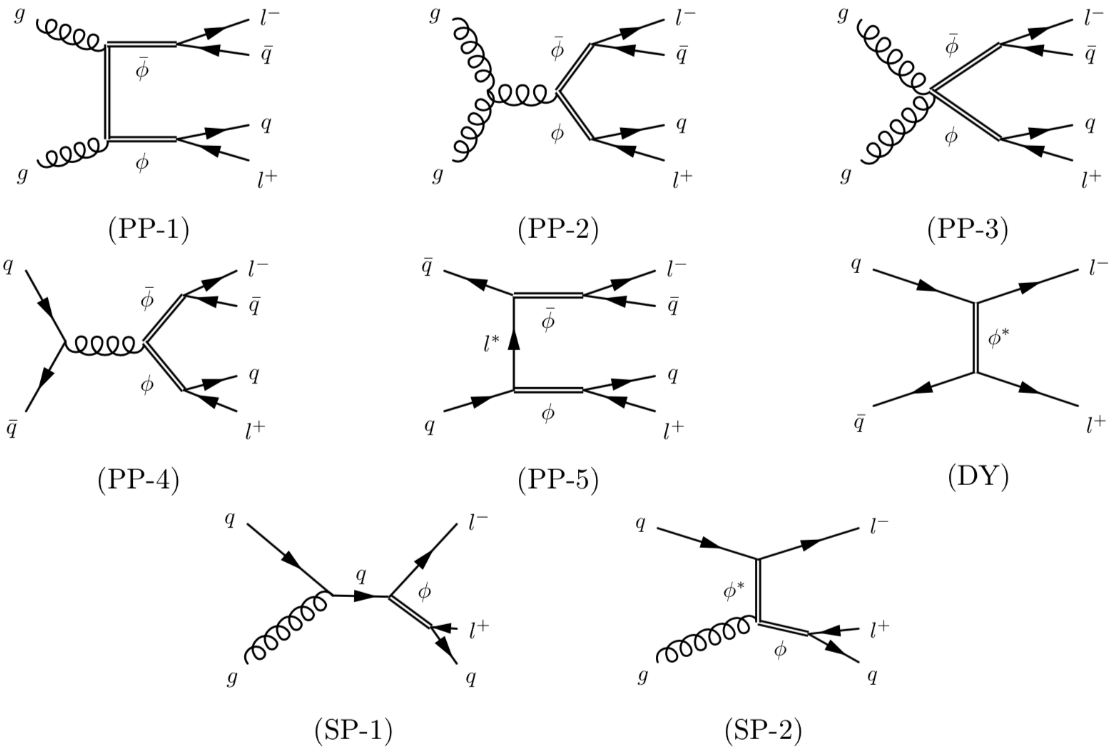

(PP-1) (PP-2) (PP-3)

(PP-4) (PP-5) (DY)

(SP-1) (SP-2)

Figure 5: Leading order Feynman Diagrams for all production modes of leptoquarks. PP indicates pair production mode, SP indicates single production mode and DY indicates Drell-Yan like production mode. Scalar and vector LQ particles are collectively denoted as ϕ. Feynman diagrams are taken from Ref. [34]

Two free parameters of LQ models are the mass of the LQ particle, m_{LQ} and coupling of leptoquark to quarks and leptons (neutrinos in our models of interest), λ. It should be noted that in these models, it is assumed that the coupling of LQ particles to neutrinos and quarks is the same value, λ.

The value of coupling λ is influential in determining the dominant production mode of LQ particles in colliders. For pair production, due to 2 QCD vertices, cross section scales as square of strong coupling, g_s^2. For single production, the cross section is instead proportional to $g_s\lambda$, and for Drell-Yan like production, it is proportional to λ^2. Therefore, in the regime where $\lambda \ll g_s$ the dominant production mode is pair production. The contribution from other two modes, single production and DY-like production, increases with increasing λ.

The signal samples simulated for this search have a minimal scalar LQ model, in which the LQ particle only couples to an up quark and an electron neutrino. In the m_{LQ}-λ grid, samples for 23 different points are generated for 2016, 2017 and 2018. For each year, 1.2 million events are generated in total. In these samples, m_{LQ} ranges from 500 GeV to 2.5 TeV, while the coupling λ ranges from 0.01 to 1.5.

3 Physics objects

3.1 Jets

In this analysis, jets are reconstructed by clustering PF candidates using the infrared and collinear safe anti-k_T algorithm [35]. Jets clustered with distance parameters of 0.4 and referred to as AK4 jets. The reconstructed vertex with the largest value of summed physics-object p_T^2 is taken to be the primary pp interaction vertex. The physics objects are those returned by a jet finding algorithm [35, 36] applied to all charged PF candidates associated with the vertex, plus the corresponding associated missing transverse momentum.

Jet momentum is determined as the vector sum of all particle momenta in the jet, and is found from simulation to be within 5 to 10% of the true momentum over the full p_T spectrum and detector acceptance. An offset correction is applied to jet energies to take into account the contribution from additional proton-proton interactions within the same or nearby bunch crossings (pileup). Jet energy corrections are derived from simulation, and are confirmed with *in situ* measurements of the energy balance in dijet, multijet, γ+jet, and leptonic Z+jet events [37]. The `Fall17_17Nov2017_V32` and `Autumn18_V19` versions of the jet energy corrections are used for the 2017 and 2018 data sets, respectively. After the jet energy scale calibration, jets are observed to still have different energy resolutions in data and simulation. To correct for this effect, jet energy resolution (JER) corrections are applied. The `Fall17_V3` and `Autumn18_V7b` versions of these corrections are used for the 2017 and 2018 data sets, respectively. The effect of this correction on the momenta of AK4 jets is propagated to the PF $p_\mathrm{T}^\mathrm{miss}$ in a similar manner as done for the T1 correction.

The AK4 jets used in this analysis is further required to have a p_T larger than 30 GeV and $|\eta| < 2.5$, except for the purpose of b tagging, where the p_T threshold is lowered (cf. sec. 3.1.1). Such jets are also required to pass tight jet identification criteria [38, 39]. Jet-lepton overlap removal is implemented by identifying and removing jets that are within a cone of size $\Delta R = \sqrt(\Delta\phi^2 + \Delta\eta^2) < 0.4$ around a lepton or photon. Only lepton and photon candidates passing one of the object selections described below are taken into account.

Lastly, to suppress the contributions due to non-collision backgrounds, the following requirements are applied on the leading AK4 jet:

- Charged hadron energy fraction > 0.1
- Neutral hadron energy fraction < 0.8

These requirements have very little effect in the analysis control regions, where contamination from artifical $p_\mathrm{T}^\mathrm{miss}$ sources is not an issue. They are designed to reject pathological tails in the hadronic signal regions, where this contamination is more. To demonstrate the behavior in the control regions, the distribution of the charged and neutral hadron fractions in the single electron control regions are shown in Fig. 6. The distributions employ the full set of selection criteria defined in section 5.1, with the exception of the requirements on the energy fractions. The energy fraction requirements reject a vanishingly small portion of good events in the single electron region, and the other control regions show a similar behavior.

3.1.1 b tagged jets

B jets with $p_\mathrm{T} > 20$ GeV and $|\eta| < 2.4$ are identified using the "DeepCSV" algorithm [40], adopting a working point (medium) corresponding to correctly identifying a b jet with a probability of 80%, and misidentifying a light-flavor jet with a probability of 10%. Events with identified b jets are rejected to reduce the contamination from top quark processes.

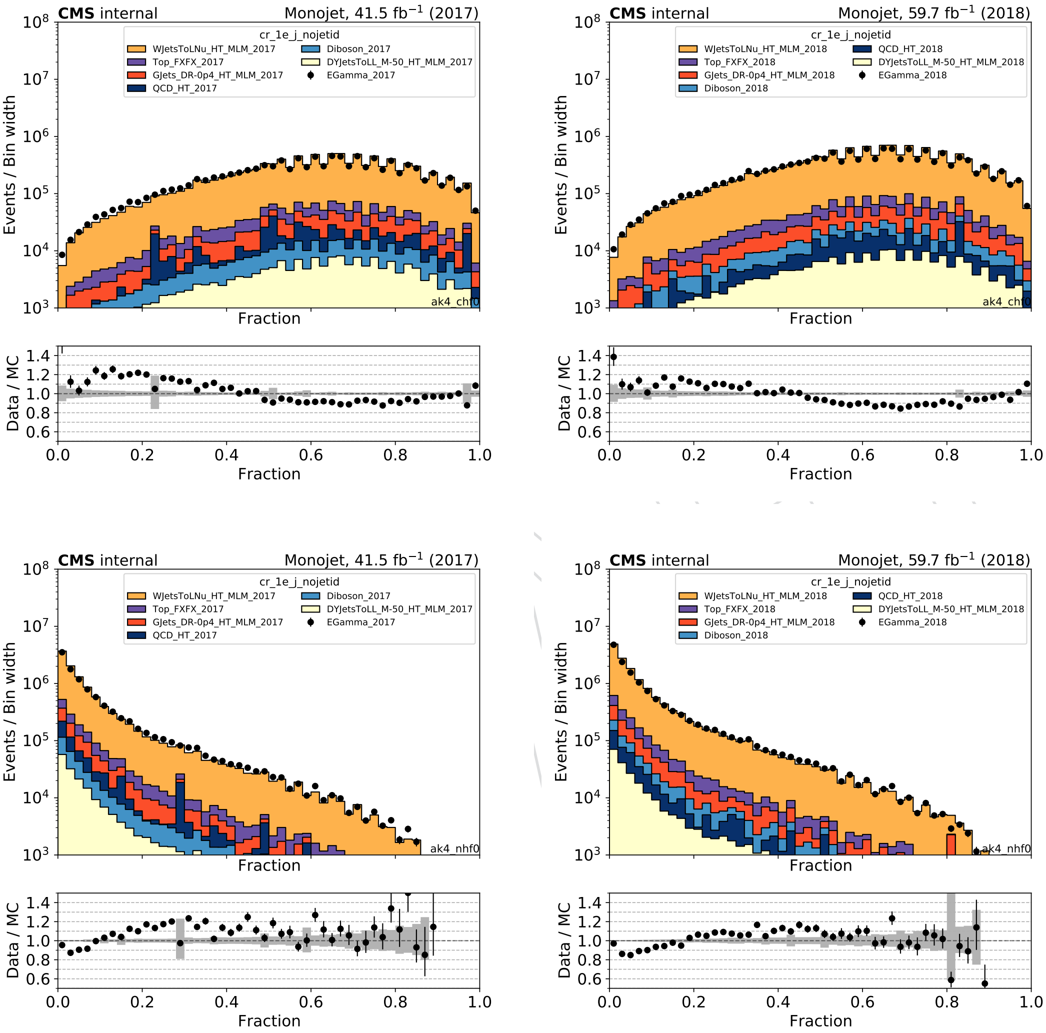

Figure 6: The charged (top) and neutral hadron energy fractions (bottom) of the leading jet in the single electron control region in the 2017 (left) and 2018 data sets (right). All selection requirements are applied with the exception of the requirements on the energy fractions themselves.

3.2 V tagged fat jets

Hadronic decays of high-p_T vector bosons are selected by tagging large-radius (“fat”) jets compatible with such decays. The tagging is performed using the “DeepAK8” algorithm. Different versions of the DeepAK8 tagger are applied on fat jets clustered using the anti-k_T algorithm [35] with a distance parameter of 0.8 (“AK8” jets). Two variants of DeepAK8 tagging are explored. In the first, dubbed “nominal”, the tagger is trained by optimizing solely with respect to tagging performance, i.e. the ability to discriminate real V jets from QCD jets. This method yields the best tagging performance. In the second variant, called “mass-decorrelated” (MD), an adversarial training is performed in which a second neural network is made to extract the jet mass from the output of the tagger network. A good performance of this second network yields to a penality on the joint cost function of the two networks. Therefore, this tagging method optimizes the ability to correctly identify the origin of a jet while systematically decorrelating the output score from the jet mass. This approach is less powerful than the nominal, but avoids shaping the jet mass distribution in background events. Since the strategy for this analysis does not rely on the jet mass shape for background estimation, the nominal tagger is a-priori more attractive. To better understand the differences in performance, as well as data/simulation agreement, both taggers are studied and a decision between tagging options is finally made based on the best expected sensitivity.

For each of the two tagging schemes, two identification working points are used to define a non-overlapping low- and high-purity regions. For the nominal tagger, an AK8 jet with tagged score above 0.458 is defined as a “loose” V tagged jet, while jets with a score above 0.961 are defined as “tight” tags. For the MD tagger, the thresholds for loose and tight V tagged jet are set at 0.245 and 0.806, respectively.

The tagger performs differently in data and simulation. This difference is compensated by applying different scale factors for jets that are correctly tagged as V jets (“tagging SF”) and those incorrectly identified as V jets (“mistagging SF”). The two are defined by their matching to generator-level information: If a jet overlaps within $\Delta R \leq 0.8$ with a generator-level Z or W boson, it is considered to be a “real” V jet. The V-jets tagging efficiency is defined as the fraction of events with V-jets that pass the tagger cut, divided by all events with V-jets. The SF fof the V-jets is thus obtained by taking the ratio of the V-jets tagging efficiencies in data and in MC. The SFs for the V-jets are summarized in Tab 5-6. They are provided centrally in CMS, refer to [41] for more information.

Table 5: The deepAK8 W tagger scale factors for the V-jets for working points recommended by JMAR for 2017 data, numbers taken from [41]

Working point	Loose	Tight	Loose MD	Tight MD
$200-300$GeV	1.05	1.00	1.00	0.90
$300-400$GeV	1.04	0.78	0.94	0.78
$400-800$GeV	1.09	0.82	0.95	0.79

Mistag scale factors are not centrally available at this time and are therefore derived here. Samples depleted of real V jets are selected by applying the full analysis selection for the mono-V photon control region, including the mass cut of $65-120$GeV, but without applying any tagging requirement. The measurement is performed in 3 control regions: photon CR, W CR, and Z CR, where the W CR corresponds to combination the single-electron CR and the single-muon CR, and the Z CR corresponds to combination of the di-electron CR and the di-muon

Table 6: The deepAK8 W tagger scale factors for the V-jets for working points recommended by JMAR for 2018 data, numbers taken from [41]

Working point	Loose	Tight	Loose MD	Tight MD
200 – 300GeV	1.04	0.87	0.96	0.73
300 – 400GeV	1.03	0.86	0.93	0.67
400 – 800GeV	1.07	0.85	0.96	0.75

CR. The mistagging rate is then measured as the ratio of the number of events passing the tagging requirement and the number of all events in the control region before the tagger selection. To account for the contamination of real V jets in data, contributions from diboson, top, or V+photon processes are estimated from simulation, matched to generator-level vector boson, and are subtracted from data before calculating the mistagging efficiency for data.

The efficiency measurement is performed separately in data and simulation and the scale factor is calculated as the ratio of rates in data and simulation. Fig 7 shows an example illustrating the ingredients in the mistagging efficiencies calculation. Result are shown in Figs. 8-11.

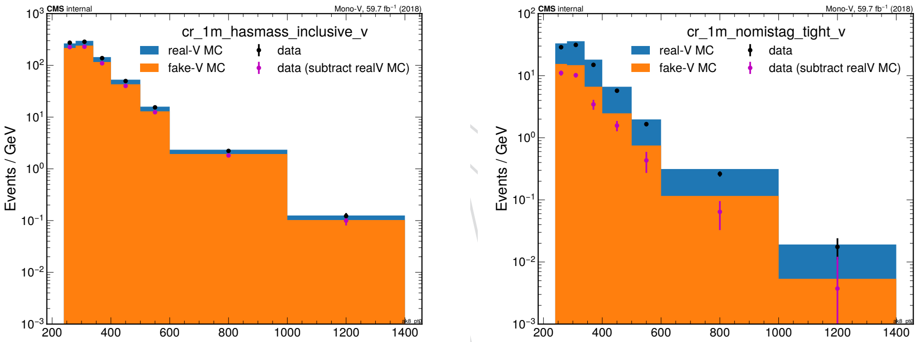

Figure 7: Ingredients used in calculation of mistagging efficiencies. Left is before applying tagger cut and right is after applying tagger cut. The data efficiency is calculated as the data (real-V subtracted) after tagger cut, divided by the same before the tagger cut. MC efficiency is calculated as the fake-V MC after tagger cut divided by before the tagger cut. Plot showing the example for tight V-tagger in the 1m Control Region with 2018 data.

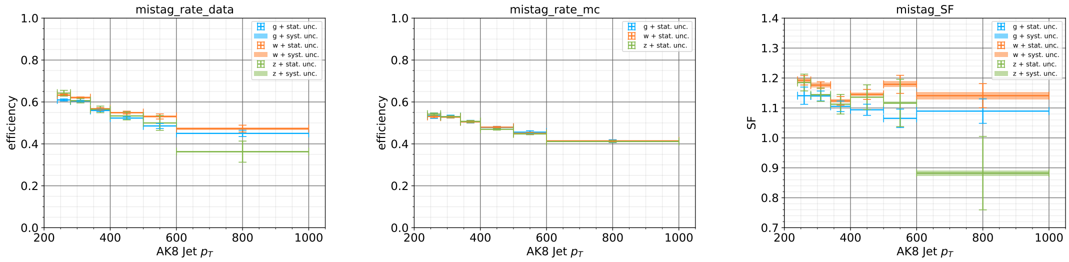

Figure 8: “DeepAK8” W nominal tagger mistagging rate measured in 2017 data(left) and MC(middle), and the data/MC scale factor(right) for the loose working point

Since the measured SFs from the 3 different CRs do not agree with each other entirely, with the difference between them being around the size of the uncertainties, we decide to apply them separately on relevant processes. For example, the SF measured in Z CR is applied

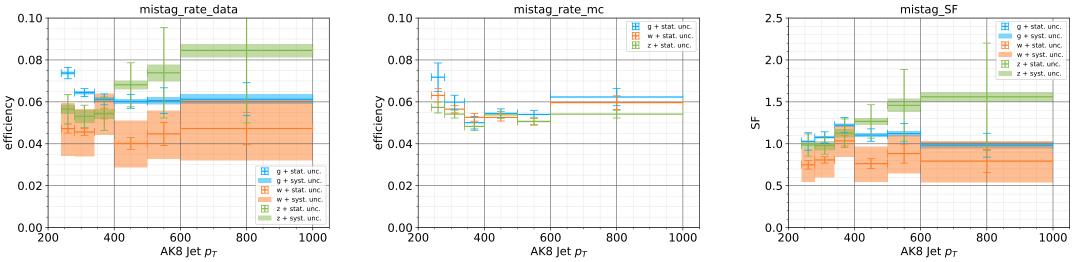

Figure 9: “DeepAK8” W nominal tagger mistagging rate measured in 2017 data(left) and MC(middle), and the data/MC scale factor(right) for the tight working point

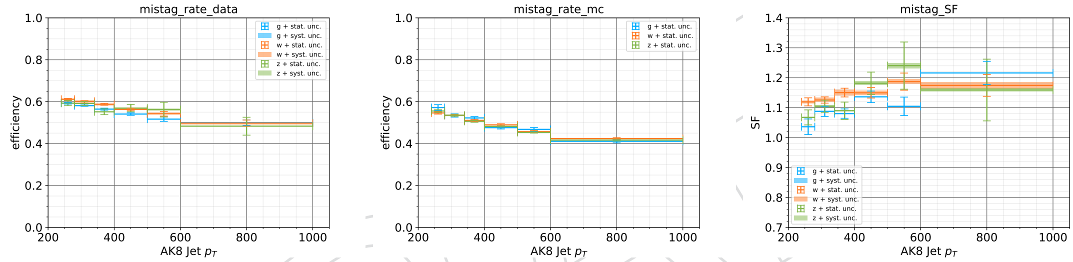

Figure 10: “DeepAK8” W nominal tagger mistagging rate measured in 2018 data(left) and MC(middle), and the data/MC scale factor(right) for the loose working point

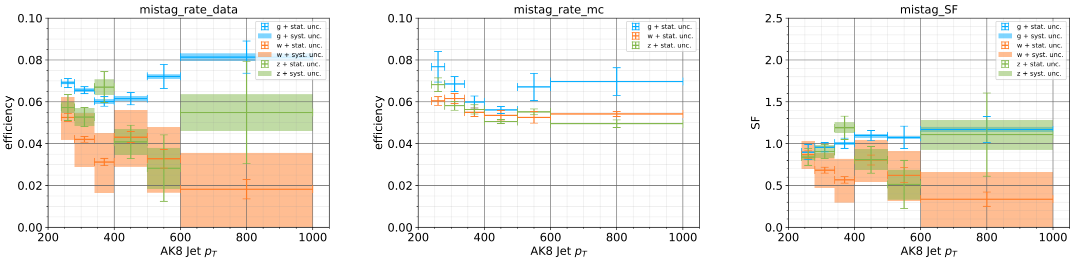

Figure 11: “DeepAK8” W nominal tagger mistagging rate measured in 2018 data(left) and MC(middle), and the data/MC scale factor(right) for the tight working point

on Z(vv)+Jets, Z(ll)+Jets, VBF produced invisible Higgs and gluon fusion produced invisible Higgs. The SF measured in W CR is applied on W(lv)+Jets, and the SF measured in photon CR is appled on photon+Jets and QCD multijet process. Additional uncertainty is assigned to QCD multijet process due to this arbitrary choice of SF application.

It is also observed that the scale factors have significant trends as functions of jet p_{T}. Given that the measurement is dominated by statistical uncertainties, to reduce the statistical fluctuations while also maintaining these trends, the binned scale factors are fitted to linear functions.

The uncertainty of this measurement has 2 parts, statistical uncertainty and systematic uncertainty. The statistical uncertainties are evaluated from the uncertainties of the fit parameters. Naturelly for each SF measurement there are 2 uncertainties corresponds to the 2 fit parameters of the linear function. Due to the strong correlation between the fit parameters, the parameters uncertainties are linearly transformed into 2 decorrelated variations, and are implemented into the analysis fit as uncertainties that varies with the hadronic recoil (which approximately equals to the leading AK8 jet p_{T}). The statistical uncertainties as functions of the leading AK8 jet p_{T} are shown in Figs 12.

The systematic uncertainties are measured by varying the overall normalization of the V(qq) MC events, when subtracting them from data, and the relevant V(qq) MC here include top-quark events, di-boson events, and vector boson + photon events. The efficiencies measured in data are very sensitive to these variations, especially for the tight WP, since the proportion of V(qq) is enlarged by the powerful deepAK8 taggers. The uncertainties on the normalization of the V(qq) MC events comes from the cross-section theory uncertainty, the uncertainty on b quark veto, and the uncertainty on the tagging scale factor of the deepAK8 tagger. By combining all three effect it is estimated that each V(qq) process can vary by about 15%. Tab 7 shows the variation on the mistagging scale factors when varying each of these V(qq) processes.

Table 7: Systematic variations of mistagging scale factors due to variations of V(qq) MC, columns are the varied MC process and rows are the flavors of mistagging SF

flavors of mistagging SF	varying top	varying di-boson	arying v+gamma
Z for loose WP	0	0.1%	0
W for loose WP	0.4%	0.3%	0
photon for loose WP	0	0	0
Z for tight WP	1%	5%	0
W for tight WP	15%	10%	0
photon for tight WP	0	0	1%

The tagging and mistagging uncertainties are implemented as partially correlated between the monojet, monoV-loose, and monoV-tight categories, in a way that if the yield in the tighter category is varied, the next looser category will be impacted in the opposite direction, by a factor of the ratio between the yields in 2 categories.

3.3 Missing transverse momentum and recoil

The vector $\vec{p}_{\mathrm{T}}^{\mathrm{miss}}$ is defined as the imbalance in the transverse momentum of all particles that interact with the detectors. Due to momentum conservation in the plane transverse to the beam axis, $\vec{p}_{\mathrm{T}}^{\mathrm{miss}}$ corresponds to the transverse momentum that is carried by undetected particles such as neutrinos. Practically, $\vec{p}_{\mathrm{T}}^{\mathrm{miss}}$ is computed as the negative of the vectorial sum of transverse

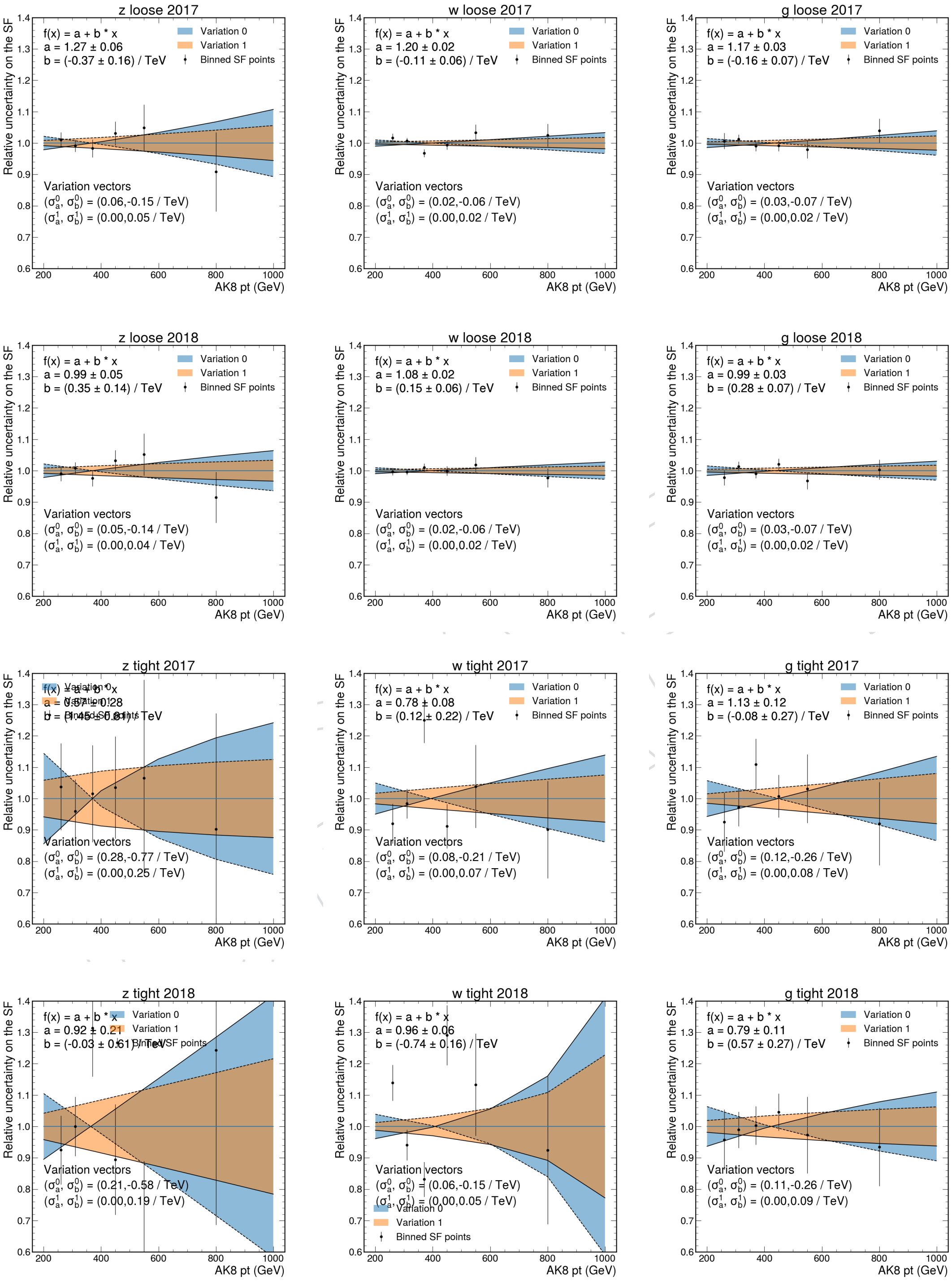

Figure 12: statistical variations of mistagging scale factors as functions of AK8 jet p_{T}

momenta of all PF candidates and is therefore also referred to as PF $\vec{p}_{\mathrm{T}}^{\mathrm{miss}}$. The magnitude of the $\vec{p}_{\mathrm{T}}^{\mathrm{miss}}$ is referred to as $p_{\mathrm{T}}^{\mathrm{miss}}$.

Minimum energy thresholds in the calorimeters, inefficiencies in the tracker, nonlinearity of the response of the calorimeter for hadronic particles can lead to an over- or underestimation of $p_{\mathrm{T}}^{\mathrm{miss}}$. The bias on the $p_{\mathrm{T}}^{\mathrm{miss}}$ measurement is reduced by propagating the effect of the jet energy corrections introduced in section 3.1 according to

$$\vec{p}_{\mathrm{T}}^{\mathrm{miss}}(\mathrm{corr}) = \vec{p}_{\mathrm{T}}^{\mathrm{miss}} - \sum_{\mathrm{jets}}(\vec{p}_{\mathrm{T,jet}}(\mathrm{corr}) - \vec{p}_{\mathrm{T,jet}}), \tag{6}$$

where the "corr" refers to the scale energy corrected measurements of the related objects.

This "type-I" correction for $\vec{p}_{\mathrm{T}}^{\mathrm{miss}}$ uses jet energy scale corrections for all corrected jets with $p_{\mathrm{T}} > 15\,\mathrm{GeV}$ that have less than 0.9 of their energy deposited in the ECAL. Furthermore, if a muon is found in a jet, its 4-momentum is subtracted from the 4-momentum of the jet when performing the correction and is added back to a corrected object. Corrections to the jet energy resolution are propagated similarly.

Since signal events in this analysis contain only jets and no other reconstructed candidates, $p_{\mathrm{T}}^{\mathrm{miss}}$ is equivalent to the total hadronic momentum in the event. For the leading backgrounds, this also corresponds to the transverse momentum of the W or Z boson. To mimic this behavior in in the control regions of this analysis, the transverse momentum of the hadronic recoil $\vec{U}$, defined as the vectorial sum of the transverse momenta of all particles except the vector boson (or its decay products), is used. The variable is computed as

$$\vec{U} = \vec{p}_{\mathrm{T}}^{\mathrm{miss}} + \sum_{i\,\in\,\text{leptons, photons}} \vec{p}_{T}^{\,i} \tag{7}$$

where the sum takes into account the leptons and photons used to define the respective control region. The uncertainty of $p_{\mathrm{T}}^{\mathrm{miss}}$ has a strong dependence on the event topology. Therefore, the uncertainty on $p_{\mathrm{T}}^{\mathrm{miss}}$ is often factorized into its components of jets, leptons and unclustered energy. Each sub-component is then varied within its scale and resolution uncertainty. In this analysis, the largest contribution on the final $p_{\mathrm{T}}^{\mathrm{miss}}$ uncertainty is due to the variations of the jet energy scale correction.

Anomalous high-$p_{\mathrm{T}}^{\mathrm{miss}}$ events can appear due to various phenomena. In the ECAL, spurious deposits may appear due to particles striking sensors in the ECAL photodetectors, or from real showers with non-collision origins such as those caused by beam halo particles. ECAL dead cells can cause real energy to be missed, again leading to a spurious imbalance. In the HCAL, spurious energy can arise due to noise in the hybrid photodiode and readout box electronics, as well as direct particle interactions with the light guides and photomultiplier tubes of the forward calorimeter. A number of filters has been developed by the POG/DPG groups to identify and supress anomalous high $p_{\mathrm{T}}^{\mathrm{miss}}$ events [42]. The recommended filters are listed in Tab. 8 and are applied in the analysis.

To further miminize the contribution of anomalous high-$p_{\mathrm{T}}^{\mathrm{miss}}$ events (specifically due to spurious charged hadrons) in this analysis, a quantity based on the relative ratio of calorimetry based $p_{\mathrm{T}}^{\mathrm{miss}}$ and PF based $p_{\mathrm{T}}^{\mathrm{miss}}$ is employed.

In the 2017 data set, it has been observed that significant noise contributions in the endcap ECAL lead to the enhanced presence of jets with misreconstructed energies. If not accounted for, these jets lead to anomalous contributions to $p_{\mathrm{T}}^{\mathrm{miss}}$. To remedy this issue, a mitigation

Table 8: The $p_{\mathrm{T}}^{\mathrm{miss}}$ filters recommended by the JME POG [42]. The recommendations apply to both 2017 and 2018. Except for the bad super cluster filter ("ee badSC"), all filters are applied both in data and simulation.

Filter	Name in NanoAOD	Applied in data (MC)
primary vertex filter	Flag_goodVertices	✓(✓)
beam halo filter	Flag_globalSuperTightHalo2016Filter	✓(✓)
HBHE noise filter	Flag_HBHENoiseFilter	✓(✓)
HBHEiso noise filter	Flag_HBHENoiseIsoFilter	✓(✓)
ECAL TP filter	Flag_EcalDeadCellTriggerPrimitiveFilter	✓(✓)
Bad PF Muon Filter	Flag_BadPFMuonFilter	✓(✓)
ee badSC noise filter	Flag_eeBadScFilter	✓(×)
ECAL bad calibration filter update	Flag_ecalBadCalibFilterV2	✓(✓)

method is applied, in which jets and unclustered PF candidates with $2.65 < |\eta| < 3.139$ and uncorrected $p_{\mathrm{T}} < 50\,\mathrm{GeV}$ are excluded from the $p_{\mathrm{T}}^{\mathrm{miss}}$ calculation ("EE noise mitigation") [43].

3.4 Leptons

3.4.1 Electrons

Electrons within the geometrical acceptance of $|\eta| < 2.5$ are reconstructed by associating tracks reconstructed in the silicon detector with clusters of energy in the ECAL [44]. Well-identified electron candidates are required to satisfy additional identification criteria based on the shower shape of the energy deposit in the ECAL and the consistency of the electron track with the primary vertex [45]. Electron candidates that are identified as coming from photon conversions in the detector material are removed. An isolation variable is calculated based on the sum of the energies of the PF candidates within a cone of $\Delta R < 0.3$ around the electron. The mean energy deposit in the isolation cone of the electron coming from pileup is estimated following the method described in Ref. [44] and subtracted from the isolation sum. In this note, 'veto' [46] electrons with a minimum p_{T} of 10 GeV are selected with an average efficiency of 95% and their presence is used as a condition to reject events, whereas 'tight' [46] electrons with a minimum p_{T} of 40 GeV and an average efficiency of 70% are used to select the events in the control regions. Full selection criteria are shown in Table 9.

3.4.2 Muons

Muons within the geometrical acceptance of $|\eta| < 2.4$ are reconstructed by combining information from the silicon tracker and the muon system [47]. The muons are required to pass set of quality criteria based on the number of spatial points measured in the tracker and in the muon system, the fit quality of the muon track and its consistency with the primary vertex of the event. Similar to electron case, the isolation requirements for muons are also based on the sum of the energies of the PF candidates, but a different cone size of a $\Delta R < 0.4$ is used. The muon isolation variable is corrected for pileup effects by subtracting half of the sum of the transverse momenta of charged particles that are inside the isolation cone and not associated with the primary vertex. In this note, "loose" [48] muons with $p_{\mathrm{T}} > 10$ GeV are selected with an average efficiency of 98% and are used as a condition to reject events, whereas "tight" [49]

Table 9: Tight and veto electron identification criteria.

Variable	Selection Tight	Selection Veto
	Barrel (Endcaps)	Barrel (Endcap)
Full 5x5 $\sigma_{i\eta i\eta}$	< 0.0104 (< 0.0353)	< 0.0126 (< 0.0457)
$\lvert\Delta\eta_{in}\rvert$	< 0.00255 (< 0.00501)	< 0.00463 (< 0.00814)
$\lvert\Delta\phi_{in}\rvert$	< 0.022 (< 0.0236)	< 0.148 (< 0.19)
H/E	$< 0.026 + 1.15/E_{SC} + 0.0324\rho/E_{SC}$ $(< 0.0188 + 2.06/E_{SC} + 0.183 * \rho/E_{SC})$	$< 0.05 + 1.16/E_{SC} + 0.0324\rho/E_{SC}$ $(< 0.05 + 2.54/E_{SC} + 0.183\rho/E_{SC})$
Relative isolation (ρ correction)	$< 0.0287 + 0.506/pT$ $(< 0.0445 + 0.963/p_{\mathrm{T}})$	$< 0.198 + 0.506/p_{\mathrm{T}}$ $(< 0.203 + 0.963/p_{\mathrm{T}})$
1/E - 1/p	< 0.159 (< 0.0197)	< 0.209 (< 0.132)
$\lvert\mathrm{d_{xy}(vtx)}\rvert$	< 0.050 (< 0.100)	< 0.050 (< 0.100)
$\lvert\mathrm{d_{z}(vtx)}\rvert$	< 0.100 (< 0.200)	< 0.100 (< 0.200)
Expected Inner Missing Hits	$<= 1$ $(<= 1)$	$<= 2$ $(<= 3)$
Pass conversion veto	Yes (Yes)	Yes (Yes)

muons with $p_{\mathrm{T}} > 20$ GeV are selected with an average efficiency of 95% and are used to select events in the control samples. A full list of tight identification criteria is given here:

- Muon reconstructed as a global muon
- Muon reconstructed as a particle flow muon
- Normalized χ^2 of the global track less than 10
- At least one muon chamber hit included in the global track fit
- Muon segments in at least two muon stations
- Transverse impact parameter w.r.t. the primary vertex less than 2 mm.
- Longitudinal impact parameter w.r.t. the primary vertex less than 5 mm.
- At least one pixel hit
- Hits on at least 5 tracker layers
- $\Delta\beta$ relative isolation less than 0.15

3.4.3 Taus

Hadronically decaying τ leptons are required to pass identification criteria using the hadron-plus-strips algorithm [50]. The algorithm identifies a jet as an hadronically decaying tau lepton candidate if a subset of the particles assigned to the jet is consistent with the decay products of a τ candidate. Candidate τ jets are required to pass the "OldDecayMode" identifiers ("Tau_idDecayMode" in NanoAOD).

In addition, τ candidates are required to be isolated from other activity in the event. The isolation requirement is computed by summing the p_{T} of the charged PF candidates and PF photon candidates within an isolation cone of $\Delta R = 0.5(0.3)$, around the tau candidate direction. The charged and photon candidates associated with the tau candidate are removed from this sum and further described in Ref. [50]. The "VLoose_IsolationMVArun2017v2DBoldDMwLT2017" isolation working point [51] is employed in this analysis for tau candidates with p_{T} larger than 18 GeV within $|\eta| < 2.3$.

3.5 Photons

Photon candidates are reconstructed from energy deposits in the ECAL using algorithms that constrain the clusters to the size and shape expected from a photon [52]. The identification of the candidates is based on shower-shape and isolation variables. For isolated photons, scalar sums of the p_{T} of PF candidates within a cone of $\Delta R < 0.3$ around the photon candidate are required to be below the bounds defined. Only the PF candidates that do not overlap with the EM shower of the candidate photon are included in the isolation sums.

Two candidate definitions are employed. "Loose" photons are used to reject events with unwanted photons. These photons are required to pass the EGamma POG 'loose' identification criteria [53], have a transverse momentum of at least 15 GeV and be within $|\eta| < 2.5$. The exact identification criteria are summarized in Table 10. A "tight" photon definition is used for the photon in the dedicated photon control region. These photons are required to be in the barrel ($|\eta| < 1.479$), and have $p_{\mathrm{T}} > 230$ GeV. The POG medium ID is employed, which is summarized in Table 11.

Variable	Selection
	Barrel (Endcap)
Full 5x5 $\sigma_{i\eta i\eta}$	< 0.0106 (< 0.0272)
H/E	< 0.04596 (< 0.0590)
charged hadron isolation	< 1.694 (< 2.089)
neutral hadron isolation	$< 24.032(19.722) + 0.01512(0.0117) \times p_T + 2.259(2.3) \times 10^{-5} \times {p_T}^2$
photon isolation	$< 2.876(4.162) + 0.004017(0.0037) \times p_T$
Conversion safe electron veto	Yes (Yes)

Table 10: Loose photon identification criteria.

3.5.1 Photon purity

Photons are reconstructed from ECAL clusters, and can discriminated from other sources of ECAL deposits due to the properties of the cluster, as well as their lack of other associated signatures such as tracks or HCAL deposits. This discrimination is not perfect, however, and in some cases, non-photon objects will incorrectly be identified as photons ("fakes"). The leading source of fake photons is QCD production of multijet events, where a jet is misidentified. This process is relevant mainly because of its large cross-section, which yields non-negligible contributions to the photon selection even if the per-jet probability of misreconstruction is small.

Variable	Selection
	Barrel
Full 5x5 $\sigma_{i\eta i\eta}$	< 0.01015
H/E	< 0.02197
charged hadron isolation	< 1.141
neutral hadron isolation	$< 1.189 + 0.01512 \times p_T + 2.259 \times 10^{-5} \times {p_T}^2$
photon isolation	$< 2.08 + 0.004017 \times p_T$
Conversion safe electron veto	Yes

Table 11: Tight photon identification criteria. The criteria are only given for the barrel region since endcap photons are not taken into account.

To estimate the fake contribution to the photon control region, a purity measurement is performed. The photon purity is defined as the fraction of reconstructed photons that is actually due to an isolated photon from the hard scattering event, as opposed to a fake. The purity is obtained from a template fit to the distribution of the $\sigma_{i\eta i\eta}$ variable in data, which $\sigma_{i\eta i\eta}$ variable represents the width of the ECAL shower in the η direction. Due to the different shower behavior of photons and hadrons, the $\sigma_{i\eta i\eta}$ distribution shows characteristically different behavior between these two classes of reconstructed photons: Real photons show a large peak with a cut-off around $\sigma_{i\eta i\eta} \approx 0.01$, while fake photons will have a smaller peak (stemming from actual photons inside jets), and an additional non-peaking bulk region at larger $\sigma_{i\eta i\eta}$ (stemming from hadrons interacting in the ECAL). The inputs to the fit are defined as follows:

- Photons in data are selected by applying the same identification criteria as for the tight selection defined above, with the exception of the $\sigma_{i\eta i\eta}$ requirement. By removing this requirement, the full $\sigma_{i\eta i\eta}$ distribution can be observed.
- A real photon template is obtained from GJETS simulation. The same identification criteria are applied as in data.
- A fake photon template is obtained from data. In this case, the identification criteria are modified by requiring that at least one of the isolation criteria is not passed. Therefore, the photons in this template do not overlap with the the 'data' template, and represent reconstructed photons inside jets.

The templates are derived in separate bins of the photon p_{T} and the measurement is performed separately for 2017 and 2018. Events are selected using the following criteria:

- At least one jet with $p_{\mathrm{T}} > 100$ and $|\eta| < 2.4$, which is not overlapping with a photon of interest.
- The event must pass the `HLT_Photon200` trigger, as well as the MET filters.
- The event must have $p_{\mathrm{T}}^{\mathrm{miss}} < 60\,\mathrm{GeV}$.

The fits are shown in Figs. 13 and 14. The resulting impurity values as a function of photon p_{T} are shown in Fig. 15. While the fits are performed in the range of $0.04 < \sigma_{i\eta i\eta} < 0.15$, the purity is evaluated only taking into account the contributions with $\sigma_{i\eta i\eta} < 0.010$, which is the requirement posed in the identification criteria used in the analysis. Overall, good fit performance is observed and the impurity is found to range between 1 and 4%, with a decreasing trend with photon p_{T}. Residual differences between the best fit and the data appear because the template shapes do not match the data shapes perfectly. To take this effect into account, the measurement is repeated with four alternative binning schemes that range from being very fine to very coarse and are shown in Fig. 16. By varying the binning choice, the effect of shape differences can be amplified or mitigated, and its impact on the final impurity values can be tested. The spread of the resulting values per bin is found to be small and a 25% uncertainty is assigned to the impurity and thus the QCD background estimate. For application in the analysis, the nominal impurity values are interpolated using an exponential function fit.

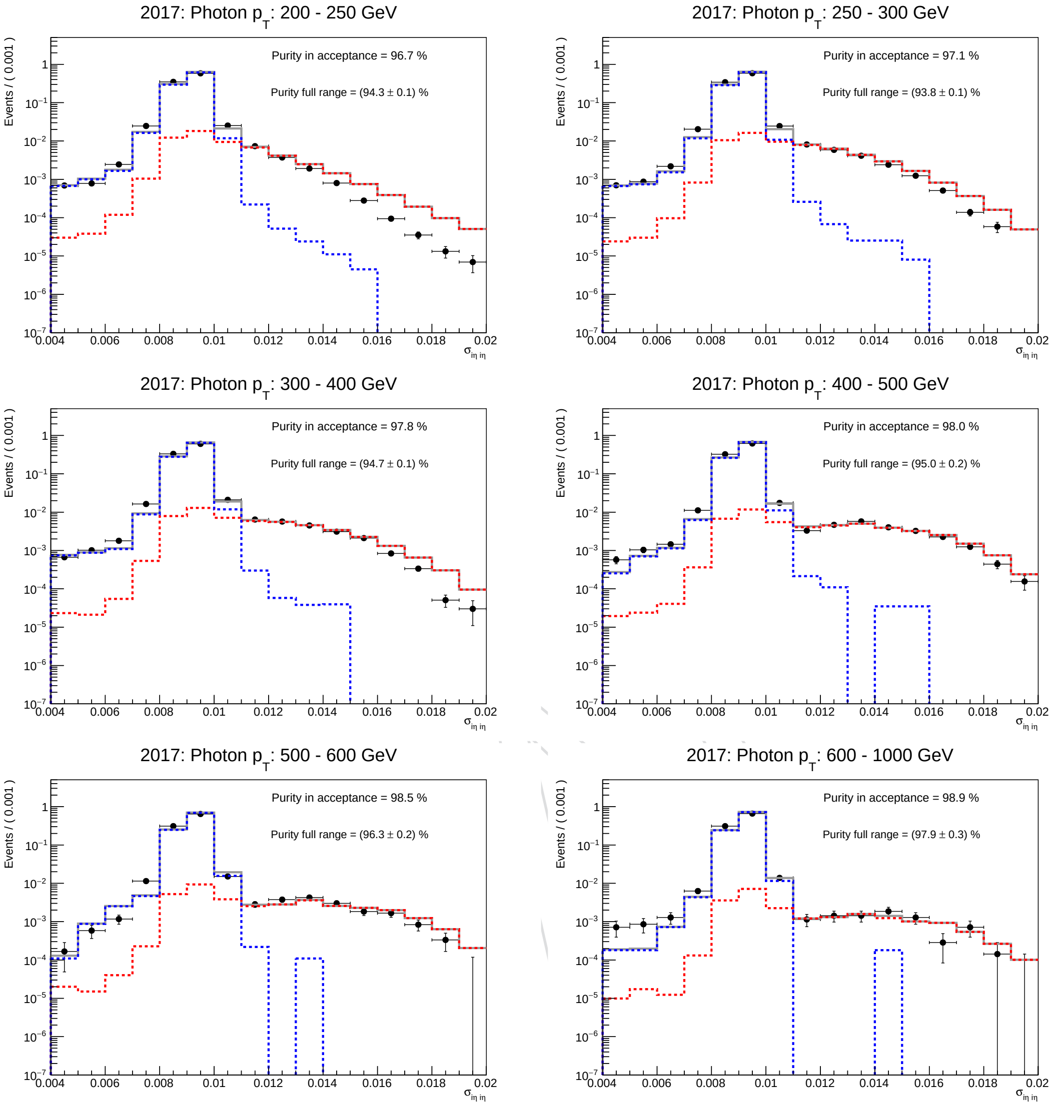

Figure 13: Template fits used to determine the photon purity in the 2017 dataset. The fits are shown in bins of photon p_T, increasing from left to right and top to bottom. The “nominal” binning scheme is used.

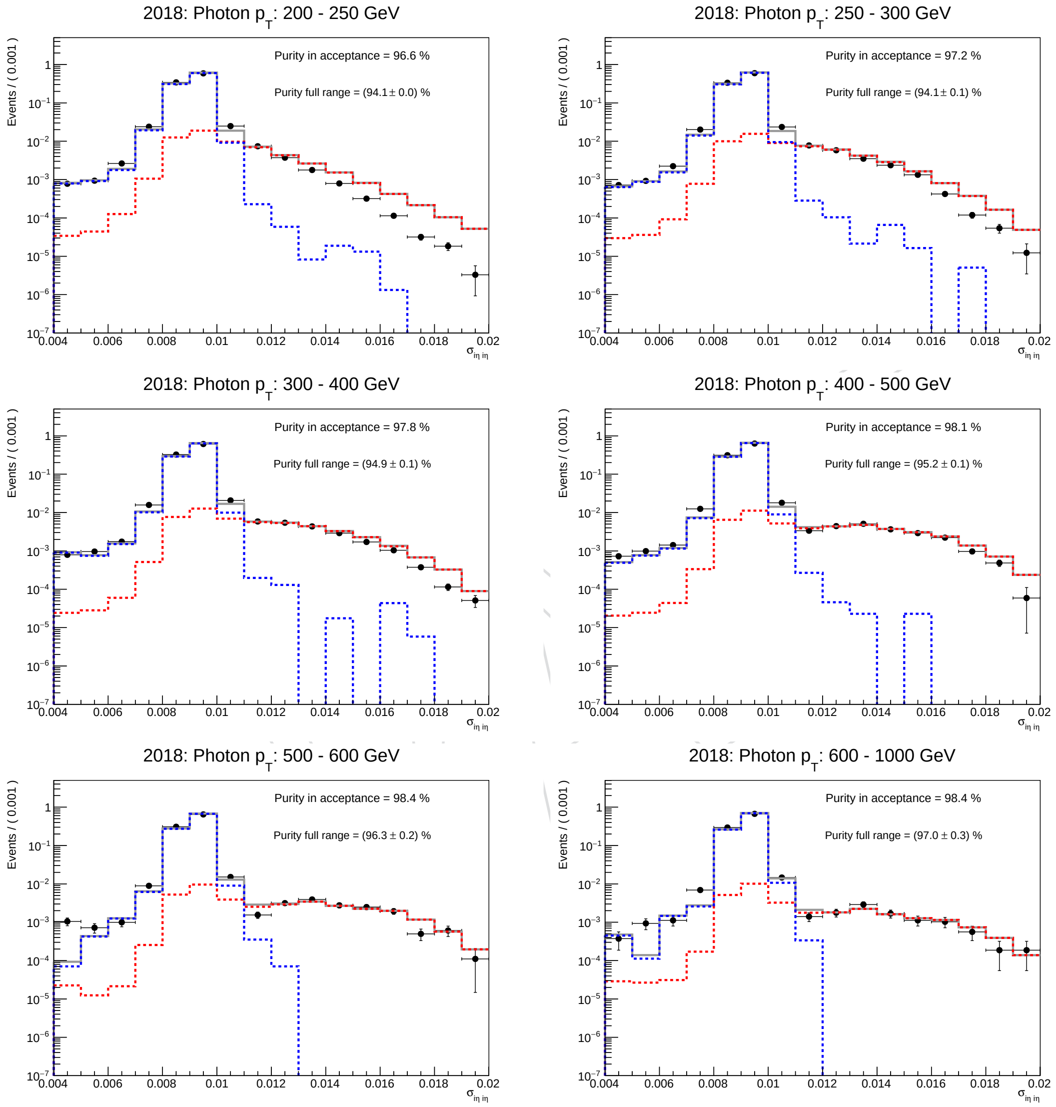

Figure 14: Template fits used to determine the photon purity in the 2018 dataset. The fits are shown in bins of photon p_T, increasing from left to right and top to bottom. The “nominal” binning scheme is used.

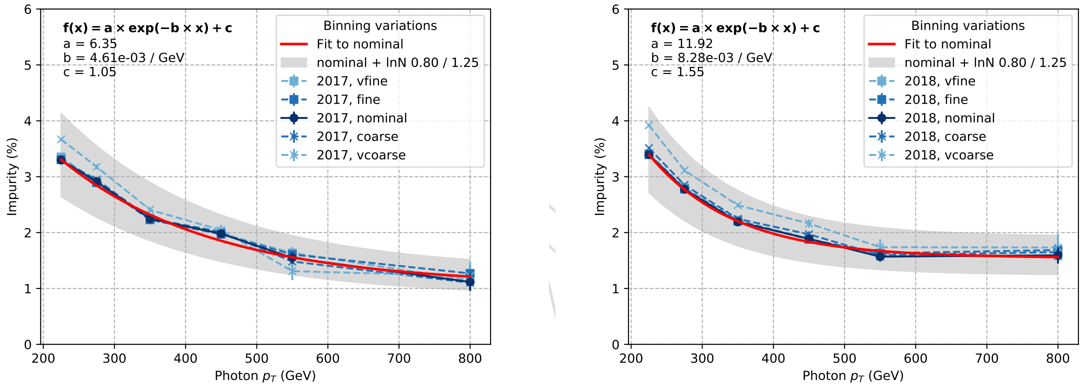

Figure 15: Photon impurity as a function of photon p_T for 2017 (left) and 2018 (right). The measured values for different binning choices are shown in the blue shaded lines and markers. The nominal result is interpolated using an exponental function fit, which is shown in the red solid line. The gray band represents a 25% uncertainty around the interpolated nominal result.

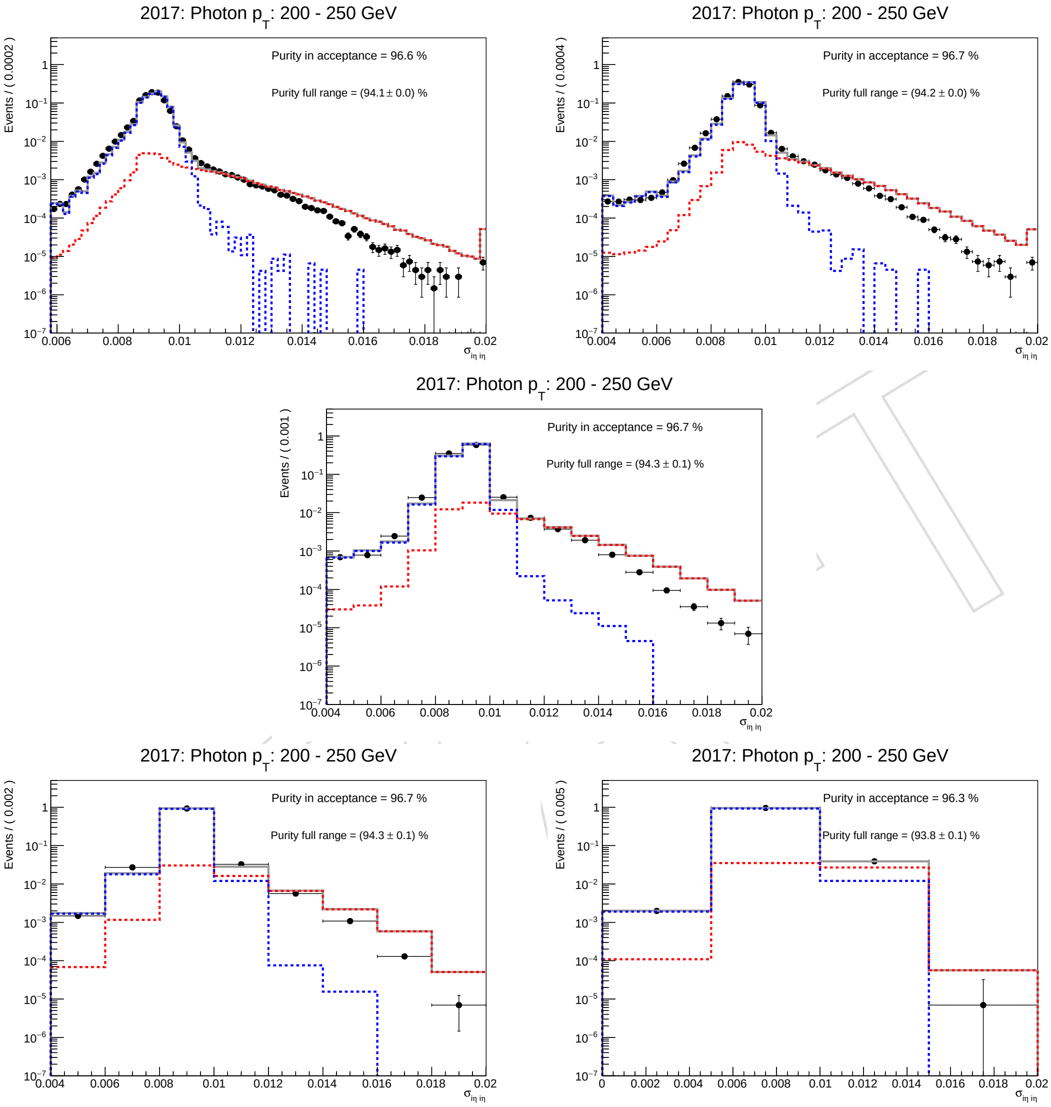

Figure 16: Comparison of binning schemes used to define a systematic uncertainty on the purity measurement. In all cases, the $200 < p_{\mathrm{T}} < 250$ GeV bin of the 2017 data set is shown. The binning choices are very fine and fine (top row), nominal (middle row) and coarse and very coarse (bottom row).

4 Reweighting of simulated events

Simulated signal and background samples are corrected for various effects through reweighting procedures outlined in this section.

4.1 Trigger efficiency reweighting

4.1.1 $p_{\mathrm{T}}^{\mathrm{miss}}$ +$H_{\mathrm{T}}^{\mathrm{miss}}$ triggers

The performance of the $p_{\mathrm{T}}^{\mathrm{miss}}$ +$H_{\mathrm{T}}^{\mathrm{miss}}$ triggers is measured using single muon events. The events are selected from the SingleMuon using the `HLT_IsoMu27` (`HLT_IsoMu24`) trigger for 2017 (2018), and the offline muon is required to be well-identified and have p_{T} larger than 40 GeV. The same selection is required as for the single-muon control region used in the final fit (cf. sec. 5.2):

1. Veto on additional leptons, photons, b jets, τ_{had} candidates.
2. $\Delta\phi(jet, \vec{p}_{\mathrm{T}}^{\mathrm{miss}}) > 0.5$ for the four leading jets with $p_{\mathrm{T}} > 30$ GeV.
3. (Calo $p_{\mathrm{T}}^{\mathrm{miss}}$- PF $p_{\mathrm{T}}^{\mathrm{miss}}$) / recoil < 0.5
4. $M_T(\ell, p_{\mathrm{T}}^{\mathrm{miss}}) < 160$ GeV.
5. Central AK4 jet with $p_{\mathrm{T}} > 100\,\mathrm{GeV}$, passing the tight jet ID.

The efficiency is calculated as a function of the hadronic recoil p_{T} and is shown in Fig. 17. The trigger is found to be more than 95% efficient for events with a recoil larger than 250 GeV, and more than 99% efficient for events with a recoil larger than 375 GeV. The MC-to-data scale factor is found to be within 1% of unity everywhere except for the lowest recoil bin at 250 GeV, where it is within 2%.

To investigate the stability of the measurement in single muon events, the same method is used to extract the efficiency from samples of double muon and single electron events. Again, an identical selection to the analysis control regions is used (cf. sec. 5.4 and 5.3), with the exception of requiring the leading muon p_{T} to be larger than 40 GeV and omitting the $p_{\mathrm{T}}^{\mathrm{miss}}$ cut in the electron region. The H_{T}-binned `WJets` and `DYJets` simulation samples are used. The resulting data-to-MC efficiency scale factors for all regions are shown in Fig. 18. For 2017, a clear trend is present: The scale factor in dimuon events is larger in absolute terms then the one from the single muon region, and the scale factor from single electron events is the smallest. The difference between all regions is within 1% relative to the single muon region. For 2018, no clear trend is observed above a recoil of 250 GeV: The scale factors from all three regions agree within the available statistical precision. Finally, the scale factors obtained form the single muon region are used to reweight the simulation. The difference to the other regions is taken into account by assigning an overall 1% uncertainty.

4.1.2 Photon trigger

The photon trigger efficiency is measured using events from the JetHT dataset collected with the `HLT_PFHT1050` trigger, which was fully unprescaled in 2017 and 2018 [2]. Events are selected in the same way as for the photon analysis control region (cf. sec. 5.6), except for the photon p_{T}, recoil, H_{T} and trigger requirements. To ensure an unbiased measurement, an offline H_{T} of

---

[2] The other, prescaled `HLT_PFHTXXX` paths yield lower statistical precision.

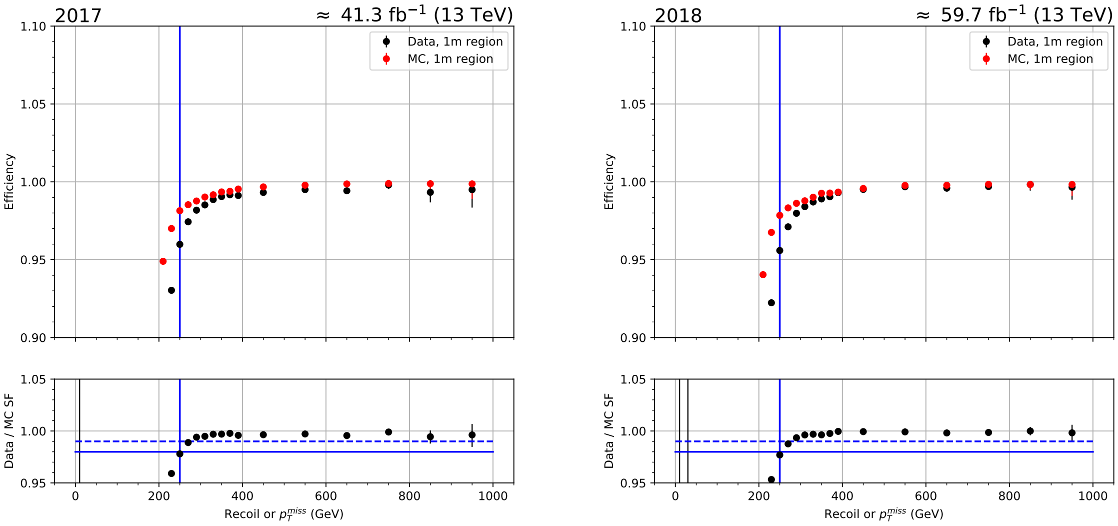

Figure 17: MET trigger turn-on curve measured in single muon events as a function of hadronic recoil p_{T} in the 2017 and 2018 `SingleMuon` datasets and H_{T}-binned `WJets` simulation samples. The vertical blue line indicates a recoil value of 250 GeV, which is the requirement used in the analysis selection. The bottom panel shows the MC-to-data scale factor, with the blue horizontal lines indicating deviations of 1% and 2% from unity, respectively.

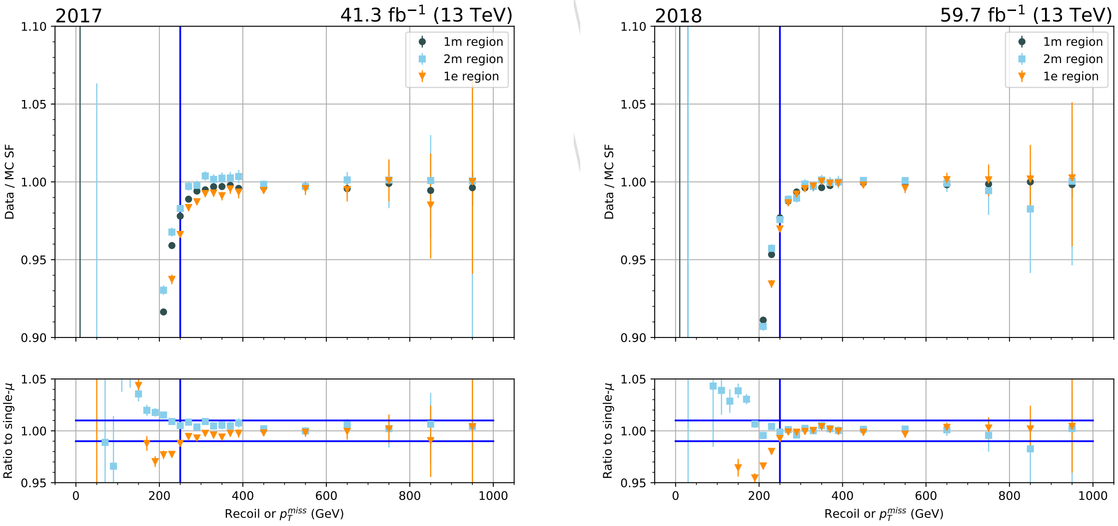

Figure 18: MC-to-data efficiency scale factors measured single muon events ('1m'), dimuon events ('2m') and single electron events ('1e'). For the single-lepton regions, the H_{T}-binned `WJets` are used, and the H_{T}-binned `DY` samples are used for the dimuon region. The bottom panel shows the ratio of the scale factors obtained from each individual region to the scale factor obtained from the single muon region. The vertical blue line indicates a recoil value of 250 GeV, which is the requirement used in the analysis selection, while the horizontal lines indicate deviations of ±1% from unity.

at least 1.5 TeV. The H_T is calculated from jets passing the POG tight ID and do not overlap with the selected photon within $\Delta R < 0.4$. The trigger efficiency ϵ is then determined as:

$$\epsilon(\texttt{HLT\_Photon200}) = \frac{\text{Offline selection \&\& } \texttt{HLT\_PFHT1050} \text{ \&\& } \texttt{HLT\_Photon200}}{\text{Offline selection \&\& } \texttt{HLT\_PFHT1050}}$$

The resulting efficiency in data and `GJets` H_T-binned simulation is shown in Fig. 19. In both data and simulation, the binned turn-on is fit using sigmoid functions, which are used to extract all further information. The trigger efficiency in data is found to be larger than 95% for photon p_T values of more than 230 GeV, which is used as the offline requirement. The MC-to-data scale factor is evaluated as the ratio of the sigmoid functions in data and simulation and is found to be within 1% of unity consistent within an uncertainty of 1% with all individual points. In the analysis implementation, the scale factor is implemented as an event-by-event weight based on the ratio of the sigmoid functions. A kinematically flat normalization uncertainty of 2% is assumed on the $\gamma +$ jets process in the photon control region to account for the trigger efficiency uncertainty (cf. Tab. 17).

4.1.3 Electron trigger

This analysis uses the logical OR of three triggers for the selection of electron events: `HLT_Ele32/35*` (threshold varies by year), `HLT_Ele115*` and `HLT_Photon200`. The higher-threshold triggers are advantageous in that they either do not contain isolation requires (`Ele115`) or do not require a well-reconstructed track (`Photon200`), both of which enhance the selection efficiency at large electron p_T.

The efficiency of the electron trigger is measured in data and simulation using a “tag and probe“ method. Tag electrons are required to pass a logical or of all triggers considered here. Both tag and probe electrons are required to pass the tight identification criteria used for the analysis selection. In data, events are separated based on whether the probe electron passes the same trigger criteria as the tag. In both of these categories, separate fits to the distribution of the invariant mass of the tag-probe system are performed to extract the number of signal-like Z events in each category, and the efficiency is defined as the ratio of the number of passing signal events and the number of all signal events. The efficiency in simulation is measured in a DY sample, and the signal event counts are defined by simply counting all events in the passing and failing categories. The MC-to-data scale factor is then defined as the ratio of the efficiency in data and that in simulation. The efficiency in data, as well as the scale factors are shown in Fig. 20.

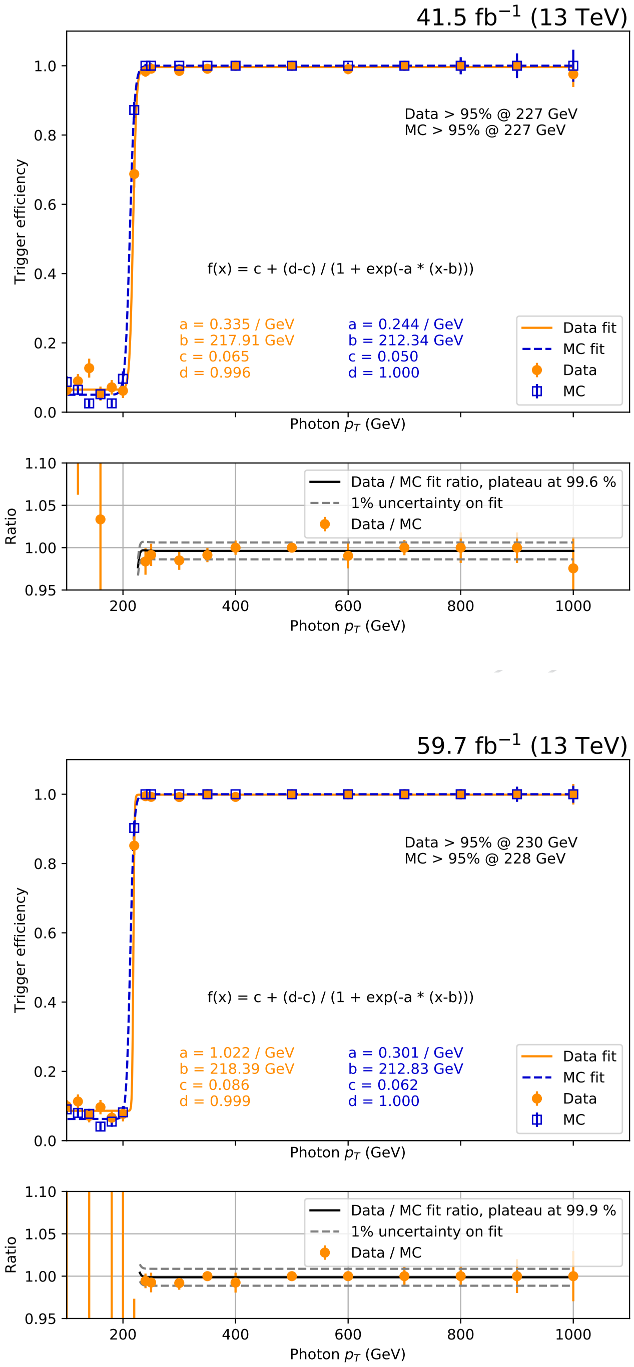

Figure 19: Efficiency of the `HLT_Photon200` trigger in data (orange) and H_T-binned `GJets` simulation (blue) for 2017 (top) and 2018 (bottom) as a function of photon p_T. The solid orange and dashed blue lines respectively represent sigmoid function fits to the turn-on in data and simulation, with the fit function and best-fit parameter values given in the respectively colored labels. The bottom panel shows the ratio of the values measured in data over those in simulation using orange markers. The solid black line corresponds to the ratio of the sigmoid fits to data and simulation, which is used as a p_T-dependent scale factor in the analysis starting at a photon p_T of 230 GeV.. The two gray dashed lines show a 1%-variation around the nominal scale factor, which covers any residual differences between the best-fit model and the individual points.

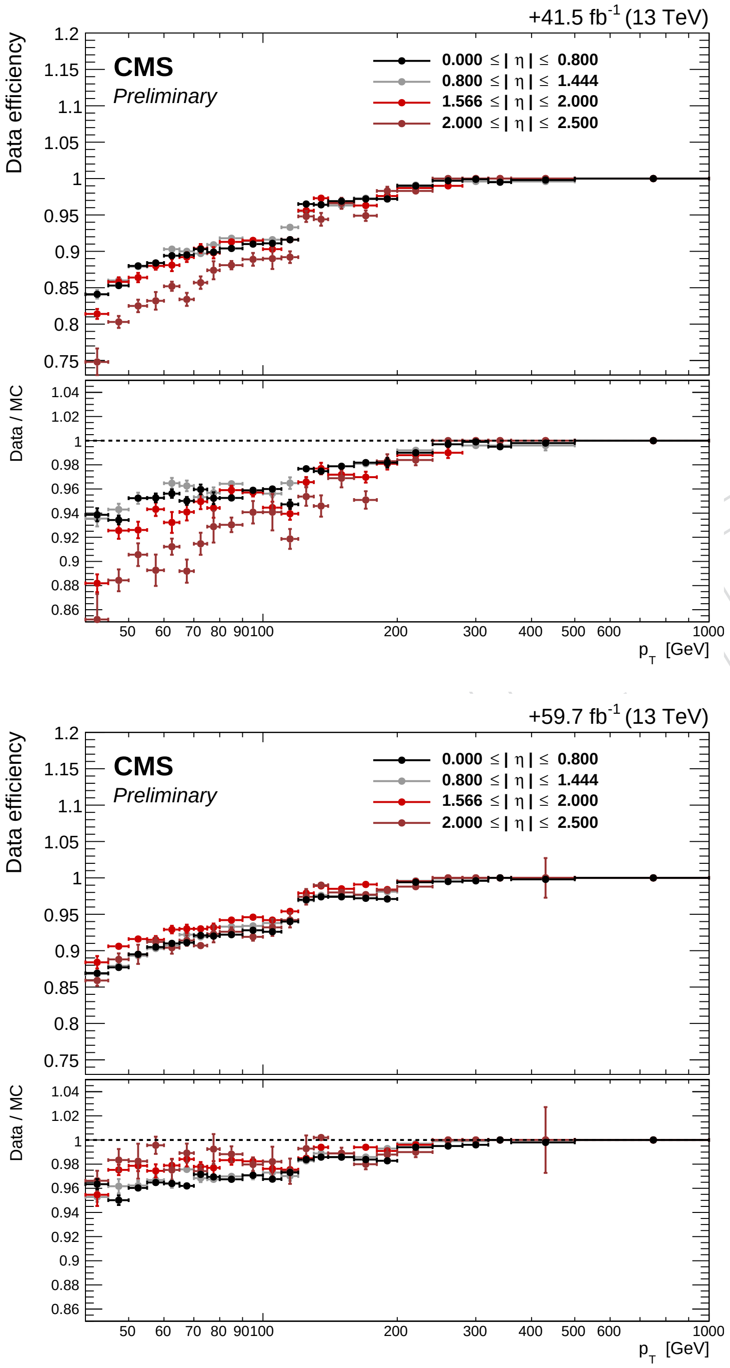

Figure 20: Efficiency of the OR of the three electron triggers for 2017 (top) and 2018 (bottom) as a function of the electron transverse momentum. The efficiency is shown for multiple regions of absolute electron pseudorapidity. In each plot, the upper panel shows the efficiency in data, while the lower panel shows the ratio of the efficiency in data and that in simulation.

4.2 Pileup reweighting

The pileup (PU) conditions in the simulated samples are not identical to the ones observed measured in data, and a reweighting is applied to remove the difference. The reweighting is performed by matching the true pileup distribution of each simulated sample with the pileup distribution in data, obtained through the pileupCalc tool assuming a minimum bias cross section of 69.2±4.6% mb, following the recommendations in in Ref. [54]. The true pileup distributions in data and simulation are shown in Fig. 21. The distribution of the number of reconstructed vertices for $W \to \mu\nu$ events before and after PU reweighting is shown in Fig. 22. In this variable, the PU reweighting method does not clearly improve the overall agreement between data and simulation. Since the number of identified primary vertices critically depends on the tracking and vertexing efficiencies, it is not an optimal measure of the number of pileup interactions in the event. As an improved variable, we consider the energy density ρ. The energy density can either be determined from the full detector or just the central region of the detector, allowing to differentiate between the modelling behavior in the forward and central regions. The full energy density is shown in Fig. 23, and the central energy density is shown in Fig. 24, again before and after PU reweighting. In these variables, which are more robust against tracking nonlinearities, modelling is improved by the reweighting procedure. In both the peak region, which contains the majority of events, as well as the shape of the high-energy tail, the agreement between data and simulation is improved. Espeically the central energy density agrees well after the reweighting, indicating that the residual disagreement in the full detector density is driven by the forward regions of the detector.

Other analysis regions show qualitatively similar behavior.

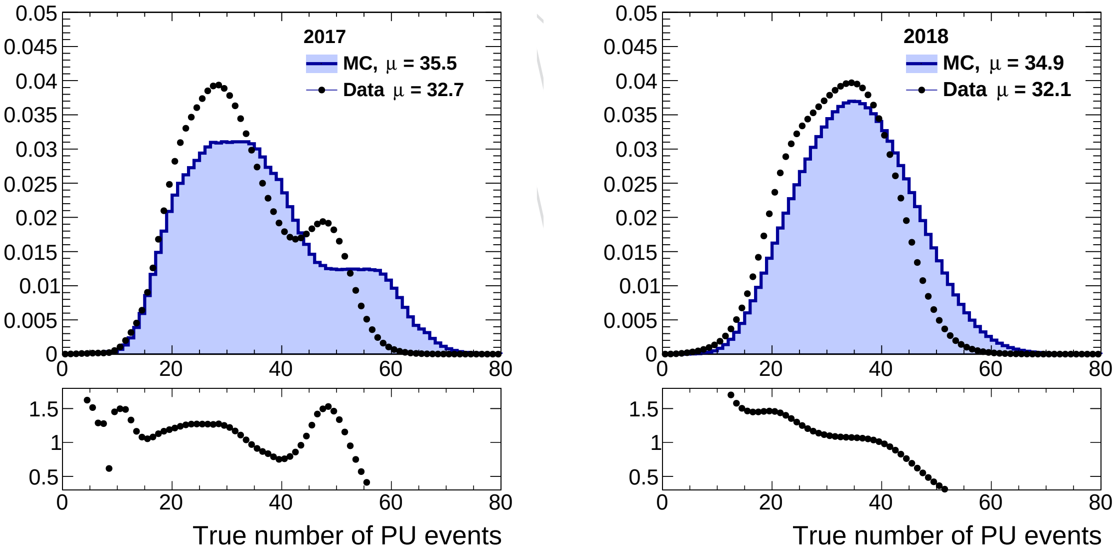

Figure 21: Distribution of the true number of PU events in data and simulation for 2017 (left) and 2018 (right). The distributions for data are extracted assuming a minimum bias cross section of 69.2 mb.

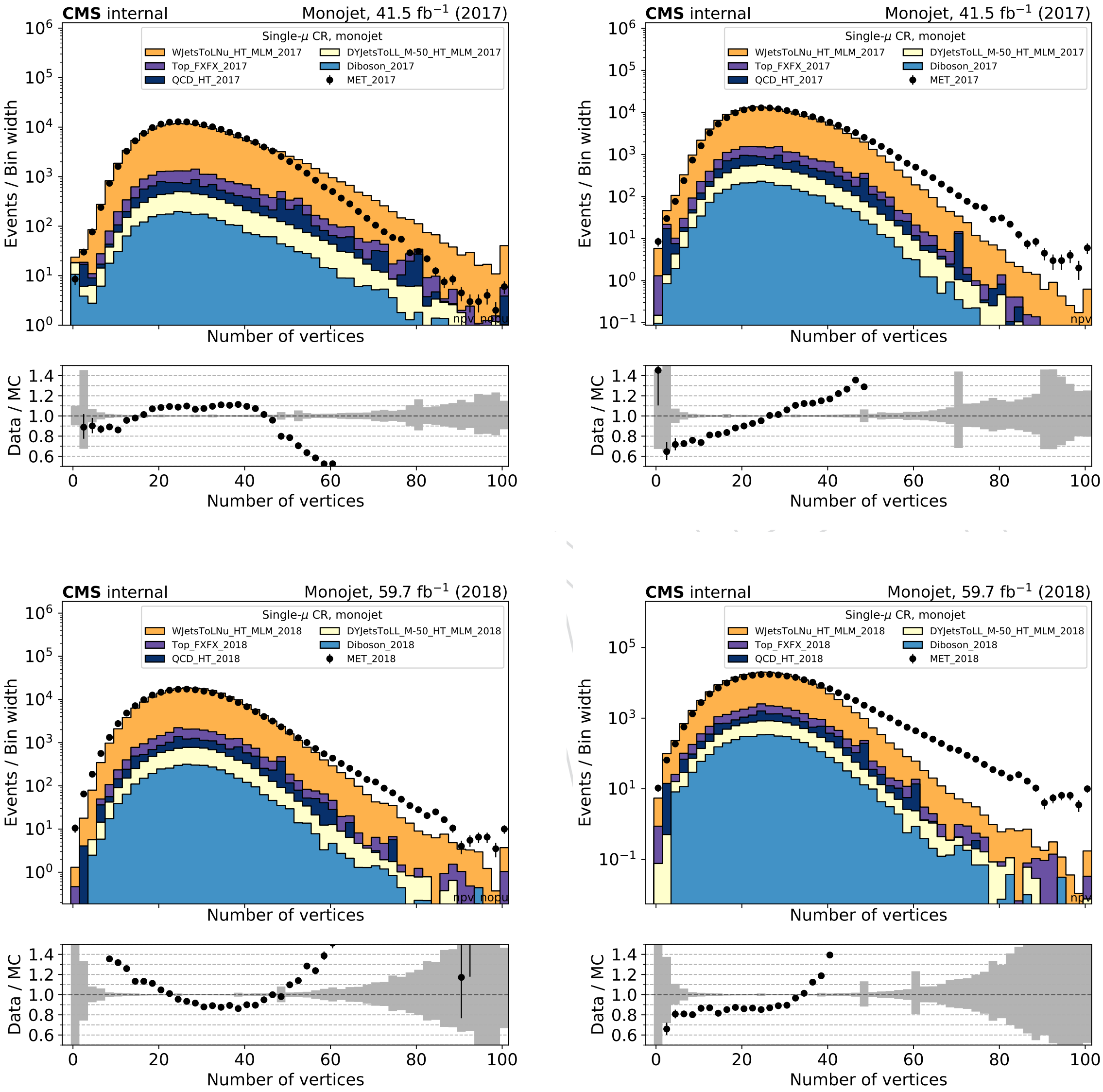

Figure 22: Distribution of the number of reconstructed vertices in $W \to \mu\nu$ events in data and simulation before pileup re-weighting (left) and after pileup reweighting (right).

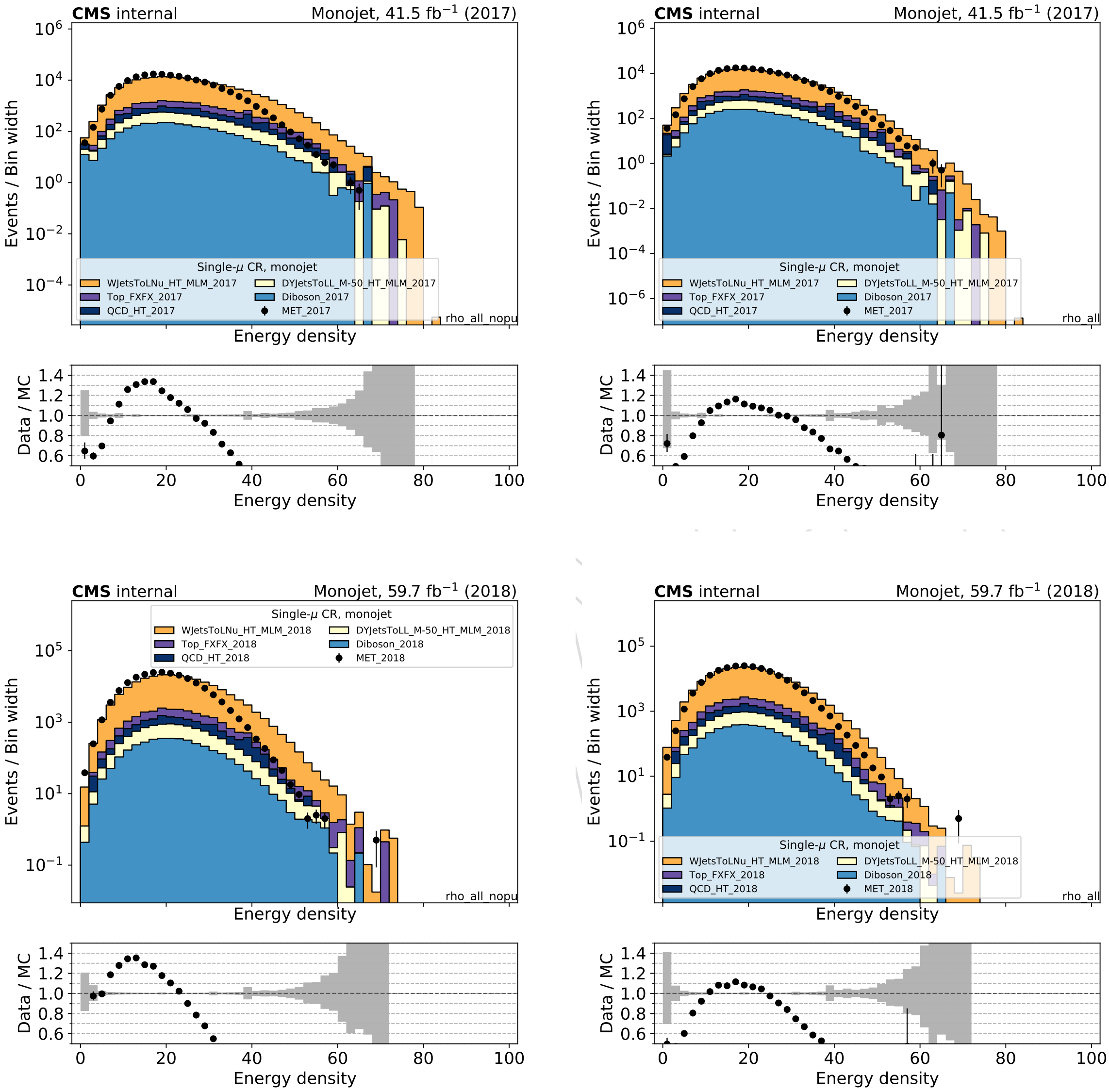

Figure 23: Distribution of the event energy density ρ calculated in the full detector volume in W $\rightarrow \mu\nu$ events in data and simulation before pileup re-weighting (left) and after pileup reweighting (right).

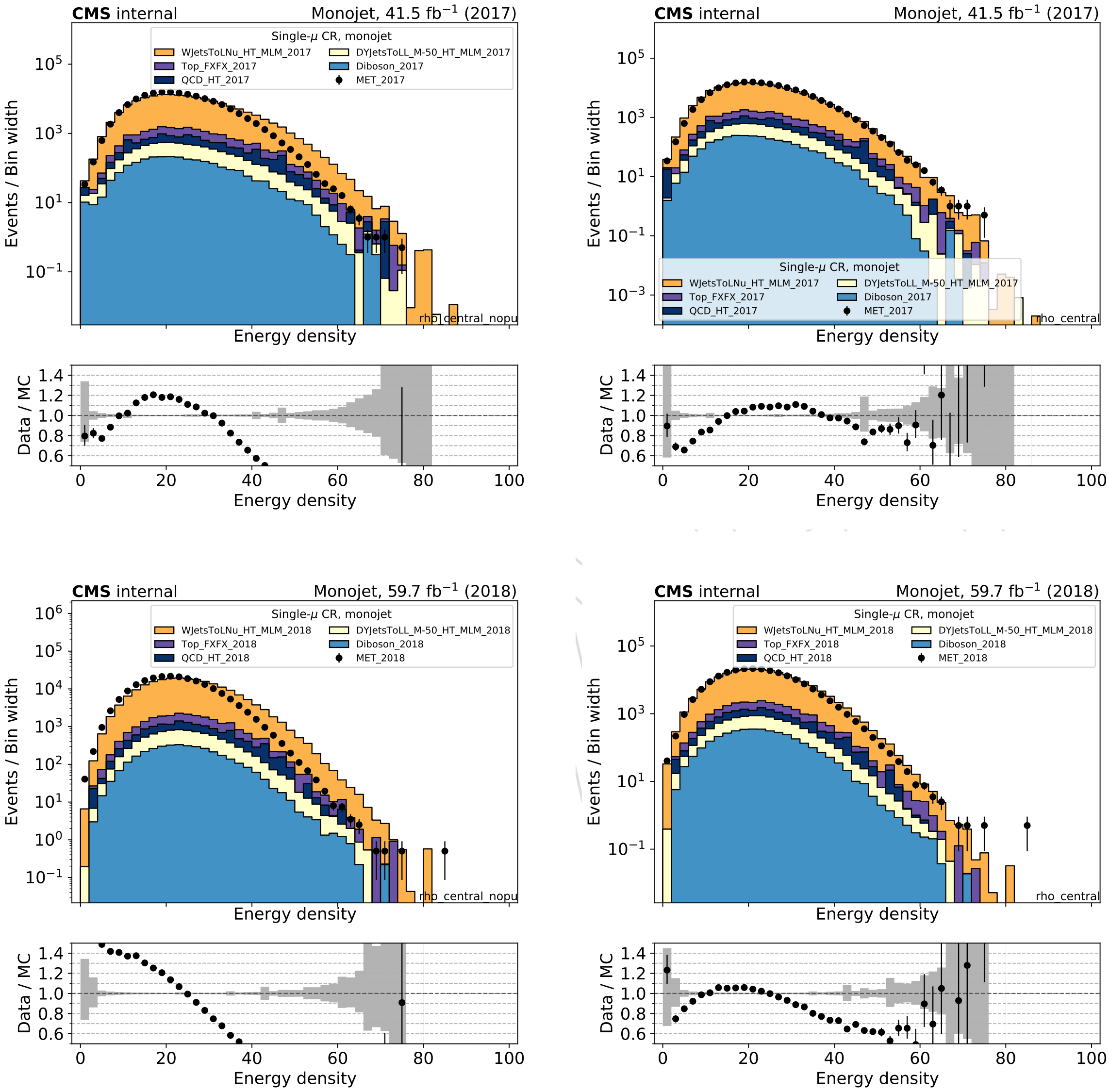

Figure 24: Distribution of the event energy density ρ calculated in the central detector region in W $\to \mu\nu$ events in data and simulation before pileup re-weighting (left) and after pileup reweighting (right).

4.3 Prefiring

In the 2017 dataset, so-called “prefiring” is present. Prefiring is caused by L1 trigger primitives in the endcap regions of the ECAL that are assigned to an incorrect earlier bunch crossing due to a timing problem. In most cases, the events to which the trigger is assigned do not pass the HLT selection and are discarded, at which point the trigger rule system prevents the event to which the trigger originally belonged from being recorded. This effect leads to an overall decrease of the trigger efficiency that is not detectable with standard offline measurements. A solution has been developed by parametrizing the probability of a jet or photon the event to cause prefiring in terms of their transverse momenta and pseudorapidity. In this analysis, the prefiring weights are applied based on the parametrization provided by the JME POG [55], and a central implementation in the nanoaod-tools framework [56]. In this implementation, a per-event prefiring weight w are calculated as:

$$w = 1 - P(\text{Prefiring}) = \prod_{i=\text{photons, jets}} (1 - \epsilon_i^{pref}(\eta, p_\mathrm{T}))$$

,

where ϵ_i^{pref} is the prefiring probability for a single photon or jet.

There are two different approaches to deriving and applying the prefiring weights. In the first approach, the full transverse momentum of jets is used for derivation and evaluation of the weights. This approach is useful because the total momentum is used in many experimental contexts and its properties are therefore well understood. In the second method, the full momentum is replaced by the electromagnetic momentum, $p_\mathrm{T}^\mathrm{EM} = p_\mathrm{T} \times f_\mathrm{charged}$, where f_charged is the charged energy fraction of the jet. This approach is attractive because the root cause of the prefiring effect is a malfunctioning of the ECAL, and it is therefore natural to assume that the charged fraction of the jet is the quantity that best parametrizes the effect. However, this approach has the disadvantage that the charged momentum is not necessarily as well calibrated as the overall momentum, and possibly not well-modeled in simulation.

To better understand the differences between the two approaches, both are tested using the separately derived input maps provided by the JME POG and their associated uncertainty variations. The differences of the different variations relative to each other is shown in Figs. 25 and 26 for the usual background and signal processes in all regions. In all regions and for all processes, the choice of the overall reweighting scheme, as well as the uncertainty variations of each of the schemes have effect of less than 2% in all bins of the recoil distribution. The differences between the approaches are most pronounced at low recoil values, where it is more likely for jets and leptons from the hard interaction to be located in the forward detector regions. As the recoil increases, these objects are more likely to be located in the central part of the detector, where no prefiring occurs.

The prescription using the full jet p_T is used as the nominal choice. The uncertainties in the transfer factors resulting from prefiring variations are discussed in detail in Section 6.4.1.

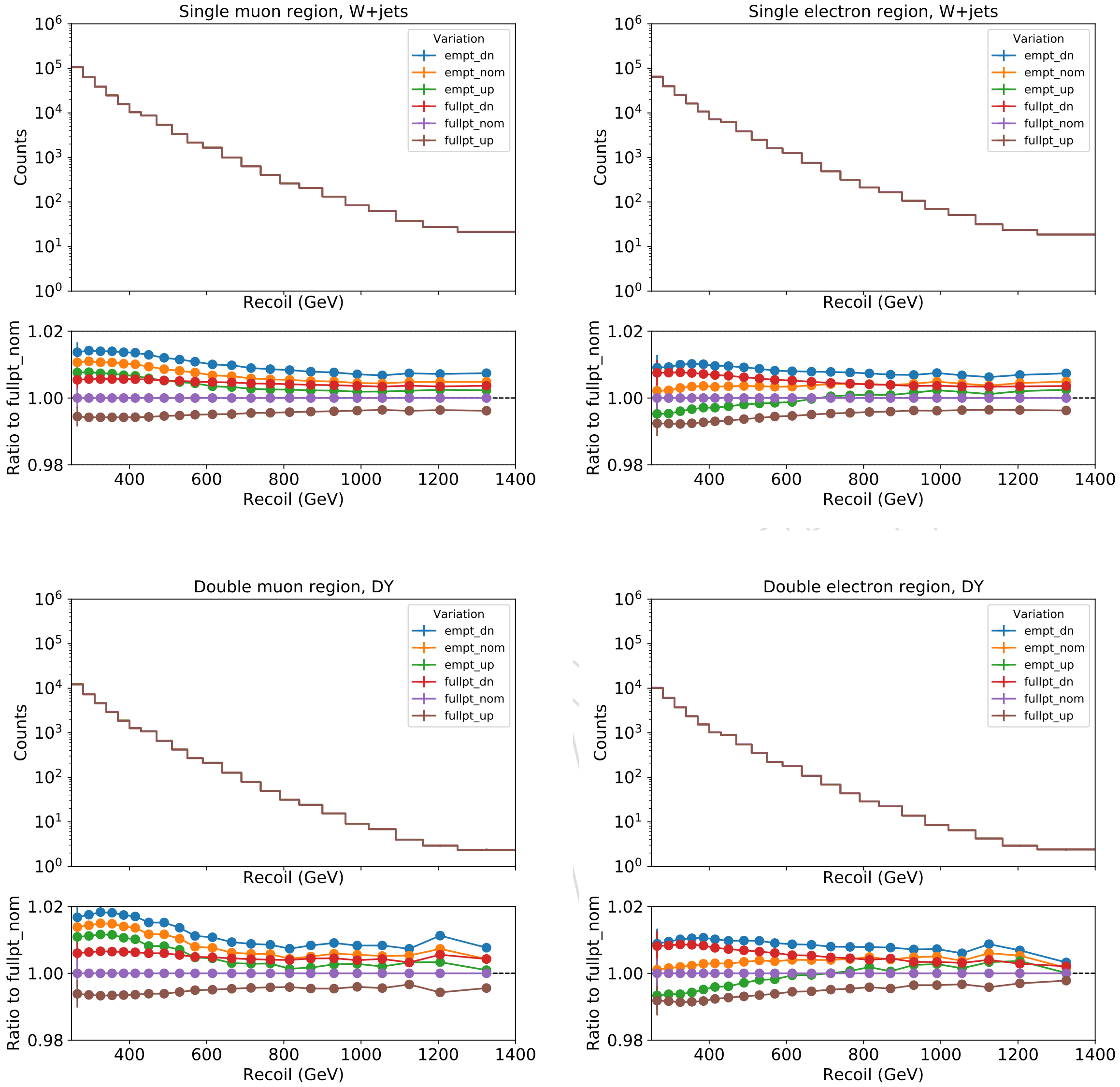

Figure 25: Comparison of the effect of the different prefiring correction approaches on the recoil distributions in the control regions. The panels represent W + jets in the single lepton regions (top) and DY in the double lepton regions (bottom), with the left and right columns corresponding to electron and muon regions, respectively. Each of the panels shows the variations of the recoil distributions in its top part. Curves labeled “empt” refer to using the electromagnetic fraction of the jet p_{T}, while entries labeled “fullpt” use the full jet p_{T}. Entries labeled “nom”, “up” and “down” are the nominal, upward and downward varations of each of the two schemes. In the bottom part of each panel, the ratio of each variation relative to the nominal correction using the full p_{T} is shown.

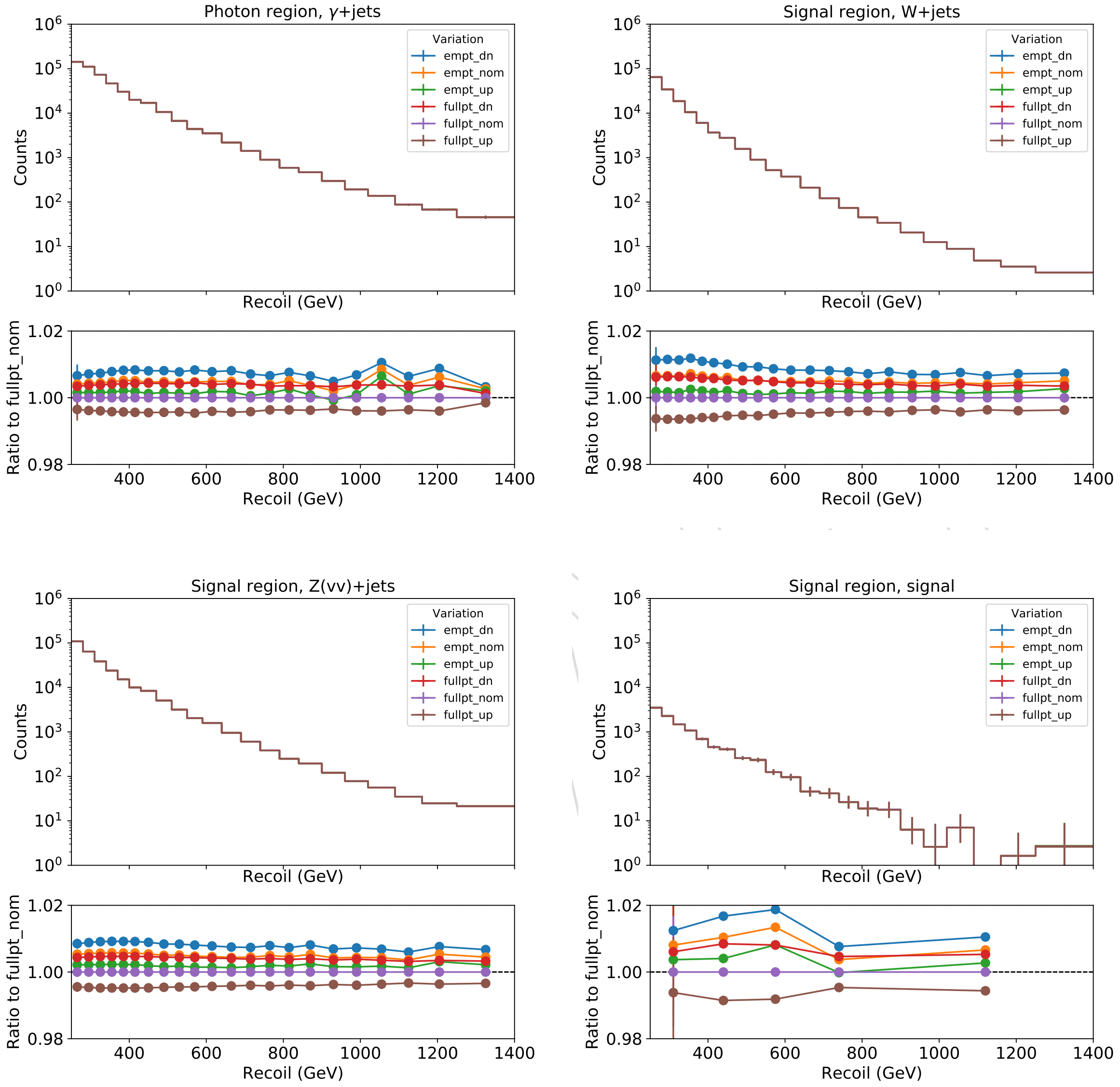

Figure 26: Same as Fig. 25 but showing the $\gamma +$ jets production in the photon CR (top left) Wjets and Z + jets in the SR (top right and bottom left, respectively), and the H(inv) signal in the signal region (bottom right). Note that due limited amount of available simulation events, the ratio for the signal panel has been rebinned.

4.4 Lepton and photon identification/reconstruction efficiency reweighting

Data-to-simulation scale factors are applied to events in the control regions to account for differences in the reconstruction, identification and isolation of leptons between data and simulationn. These data-to-MC scale factors are derived from the efficiencies that are measured for the electron and muon selections in bins of p_T and η in both data and simulation. These reconstruction scale factors and the muon identification scale factors are provided by the relevant POGs. The electron and photon identification scale factors are measured using a tag-and-probe method, and the result are reviewed and approved by the EGamma POG.

The reconstruction scale factors for electrons are shown in Fig. 27.

Dedicated measurement for the electron cut-base identification scale factors are performed such that the dataset choice and the event selections are tailored to the main analysis. The corresponding identification scale factors for veto and tight electrons are shown in Fig. 28, and include the effect of the isolation efficiency.

The identification scale factors for muons are shown in Fig. 29. Here, isolation scale factors are applied separately and are shown in Fig. 30. The corresponding corrections for muons are deemed negligible [57].

The scale factors for hadronically decaying tau leptons are shown in Fig. **??**. The scale factors are parametrized in the tau candidate pt and have been derived by the CMS TAU POG [51].

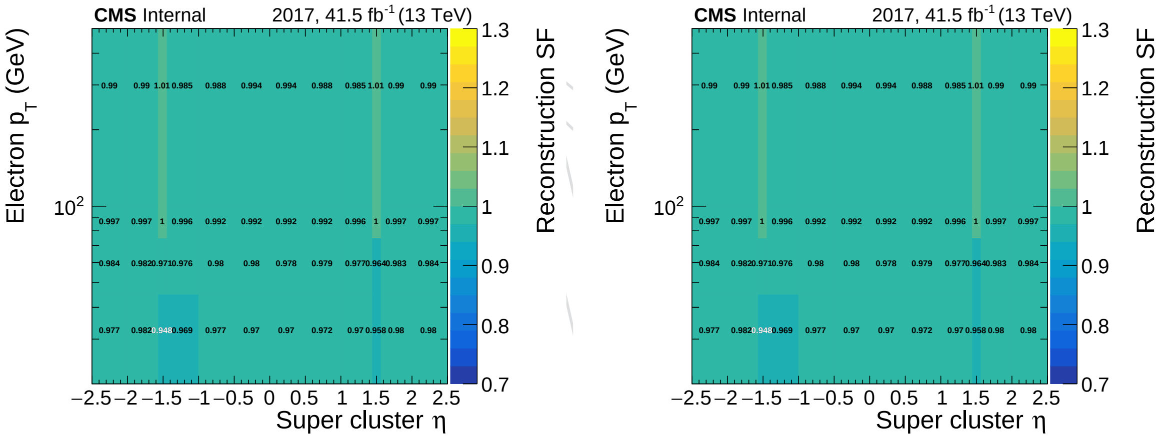

Figure 27: Scale factors for the reconstruction efficiency of electrons starting from a super cluster for 2017 (left) and 2018(right)

For photons, a dedicated measurement of the tight photon identification efficiency at high p_T is performed. The tag-and-probe method is used in $Z(ee)$ events, and the resulting efficiency scale factor at $p_T > 200\,\text{GeV}$ is determined to be between 1.01 and 1.02, depending on the data set and photon $|\eta$. The same central value of the scale factor is used for all high-p_T photons. Two uncertainty sources are considered:

1. A base uncertainty that is the combination of all uncertainties related to the fitting method used to extract the efficiency in the tagprobe measurement. This includes uncertainty variations from alternative signal and background fit functions as well as statistiscal uncertainties from data and simulation.
2. An extrapolation uncertainty that accounts for the limited knowledge of the scale factor evolution towards high p_T. It is extracted by performing the scale factor measurement in

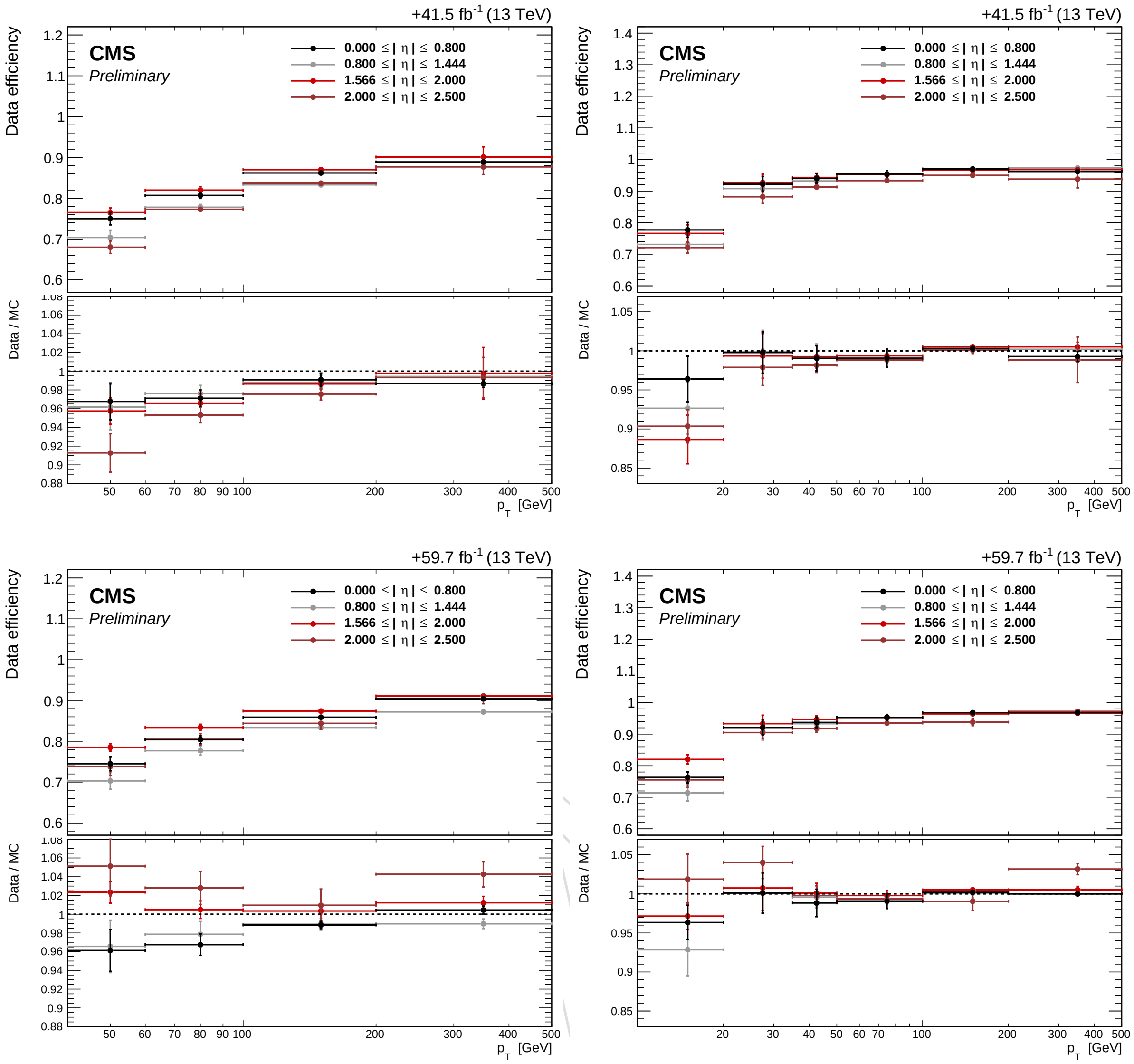

Figure 28: Scale factors for tight (left) and veto (right) electrons are shown for 2017 (top) and 2018 (bottom). The scale factors are measured in bins of electron p_T and η.

finer bins of p_T, fitting the resulting behavior with a first-order polynominal. The slope of the polynominal is found to be consistent with zero (i.e. a stable scale factor value) and the uncertainty on the slope is used to define the systematic uncertainty.

In both cases, the nominal uncertainty values are doubled in order to be conservative. The resulting central values and uncertainties are tabulated in Table 12. More details on the method and results can be found in Ref. [58].

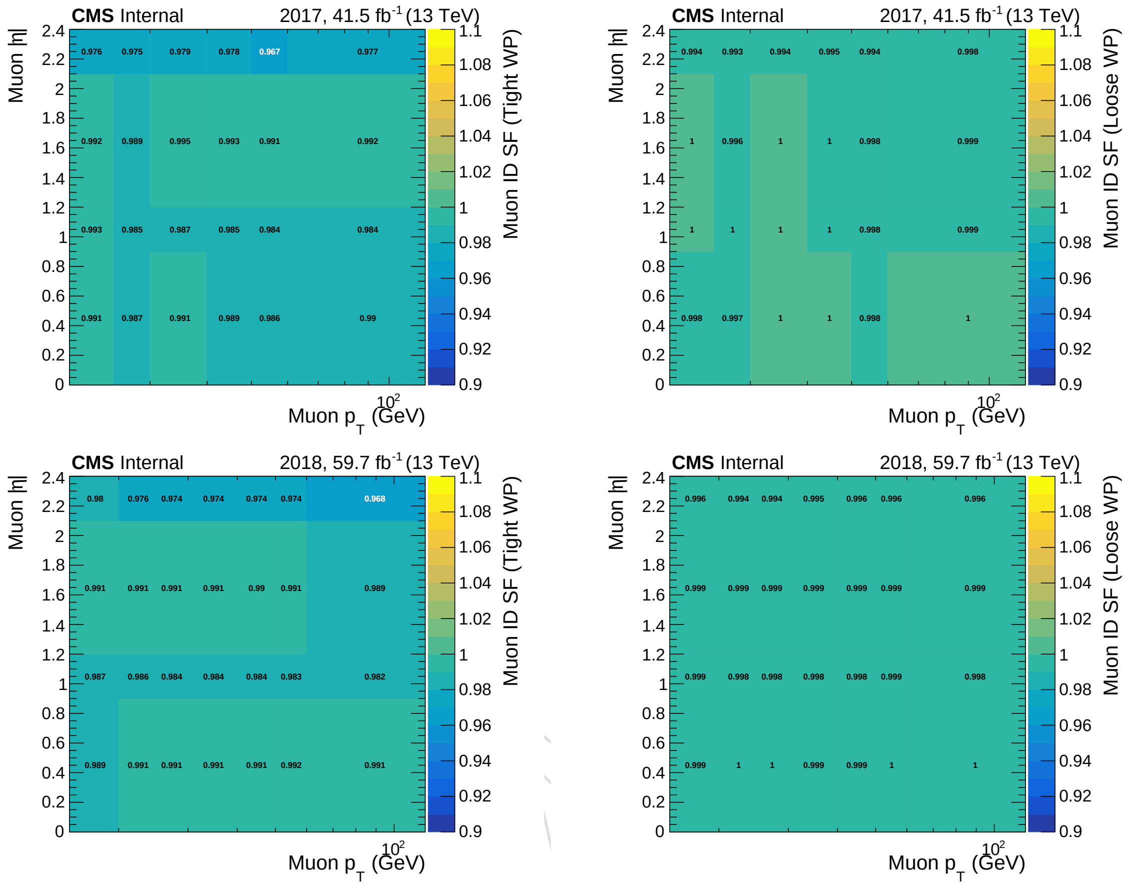

Figure 29: Scale factors for tight (left) and loose (right) muon identification are shown for 2017 (top) and 2018 (bottom). The scale factors are provided in bins of electron p_T and η.

Table 12: Central value and uncertainties of the photon medium ID scale factor at photon $p_T > 200$ GeV. The extrapolation uncertainty value given here must be multiplied by $p_T - 0.15$ TeV in order to obtain the absolute uncertainty for a given photon p_T.

Year	$\|\eta\|$	**central value**	**base uncertainty**	**extrapolation uncertainty (1/TeV)**
2017	< 0.8	1.019	0.030	0.12
	> 0.8	1.015	0.028	0.14
2018	< 0.8	1.017	0.032	0.72
	> 0.8	1.013	0.032	0.90

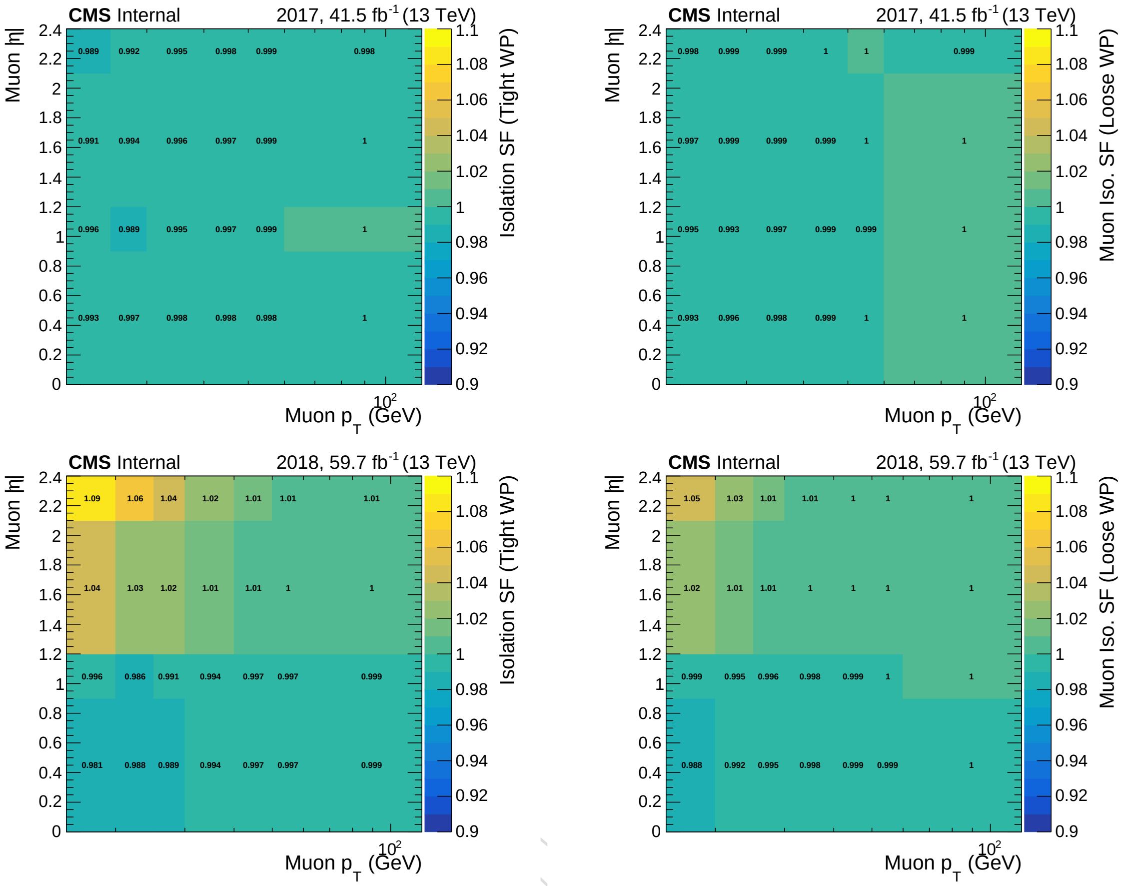

Figure 30: Scale factors for tight (left) and veto (right) muon isolation are shown for 2017 (top) and 2018 (bottom). The scale factors are provided in bins of electron p_{T} and η.

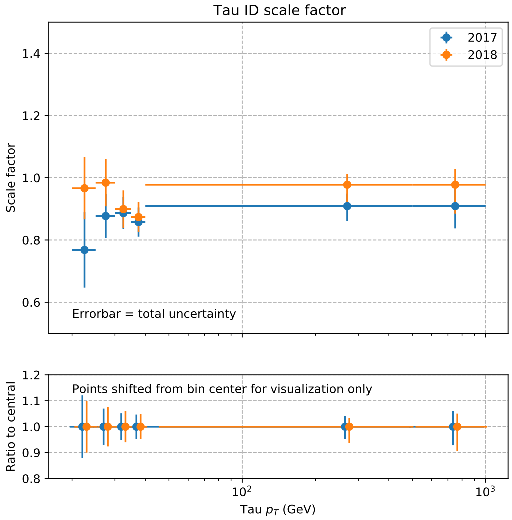

Figure 31: Scale factors for the tau lepton ID efficiency. The scale factors are provided in bins of tau p_{T}, and are shown separately for the 2017 and 2018 data sets. In the bottom panel, the ratio of each curve to its central value is shown to illustrate the relative uncertainty per bin.

4.5 Efficiency reweighting for lepton vetos

Signal-region events are required to not have any identified charged lepton (electron, muon, or tau) in order to reject contributions from $\mathrm{W}+\text{jets}$ events. Due to finite efficiencies of the reconstruction and identification of these candidates, $\mathrm{W}+\text{jets}$ events still contribute significantly, and veto efficiency differences between data and simulation need to be taken into account. For this purpose, the "veto weight" method is used. In this method, the signal object vetos of interest are removed from the signal region selection for simulated events, which causes events with identified leptons to enter the signal region. These events are then assigned a weight that is based on the identification, isolation and reconstruction efficiency scale factors for the identified objects in the event. The weight w is calculated as:

$$w = \prod_{i \in \text{ objects}} (1 - \mathrm{SF}_i)$$

,

where the sum runs over all identified veto objects in the event (electrons, muons, taus) and SF_i is the total scale factor for object i, evaluated at the approriate kinematic values of object i. It is easy to see that for the case of constant $SF \equiv 1$, all additional events are assigned a weight of zero, which is equivalent to the ordinary rejection method. For typical scale factor values that are close to and slightly smaller than one, the typical weights are close to zero, leading to small corrections of the expected yield caused by events with reconstructed leptons.

The uncertainty on this veto correction are calculated by varying the scale factors within their uncertainties and propagating the effect to the event weights, and finally to the recoil shapes in the signal region. The nominal effect of the uncertainty, as well as the variations are demonstrated in Fig. 32. In the case shown here, the uncertainties of different kinematic bins of the same scale factor are assumed to be fully correlated. For the case of the tau veto, the resulting correction is approximately 2% (0.5%) in 2017 (2018), with an uncertainty of $1 - -1.5\%$, depending on the recoil bin. For muons, all efficiency components are very close to one, leading to a very small correction and uncertainty on the veto. Finally, the electron veto leads to a correction of $2 - -5\%$ (1%) in 2017 (2018), with associated uncertainties between 0.5 and 2.5% depending on the value of the hadronic recoil. The different magnitude in correction between the data sets is driven by electrons in the endcap, for which the scale factors are significantly further from unity in 2017 than in 2018.

Finally, the nominal correction for electrons, muons and taus is applied, and the uncertainties estimated here are used in the final $\mathrm{W}+\text{jets}$ estimate. To evade some of the statistical limitation of the bin-by-byn reweighting, the binned variations shown in Fig. 32 are interpolated using a smooth curve, which is then used to model the template variation in the fit. The interpolation is shown in Fig. 97.

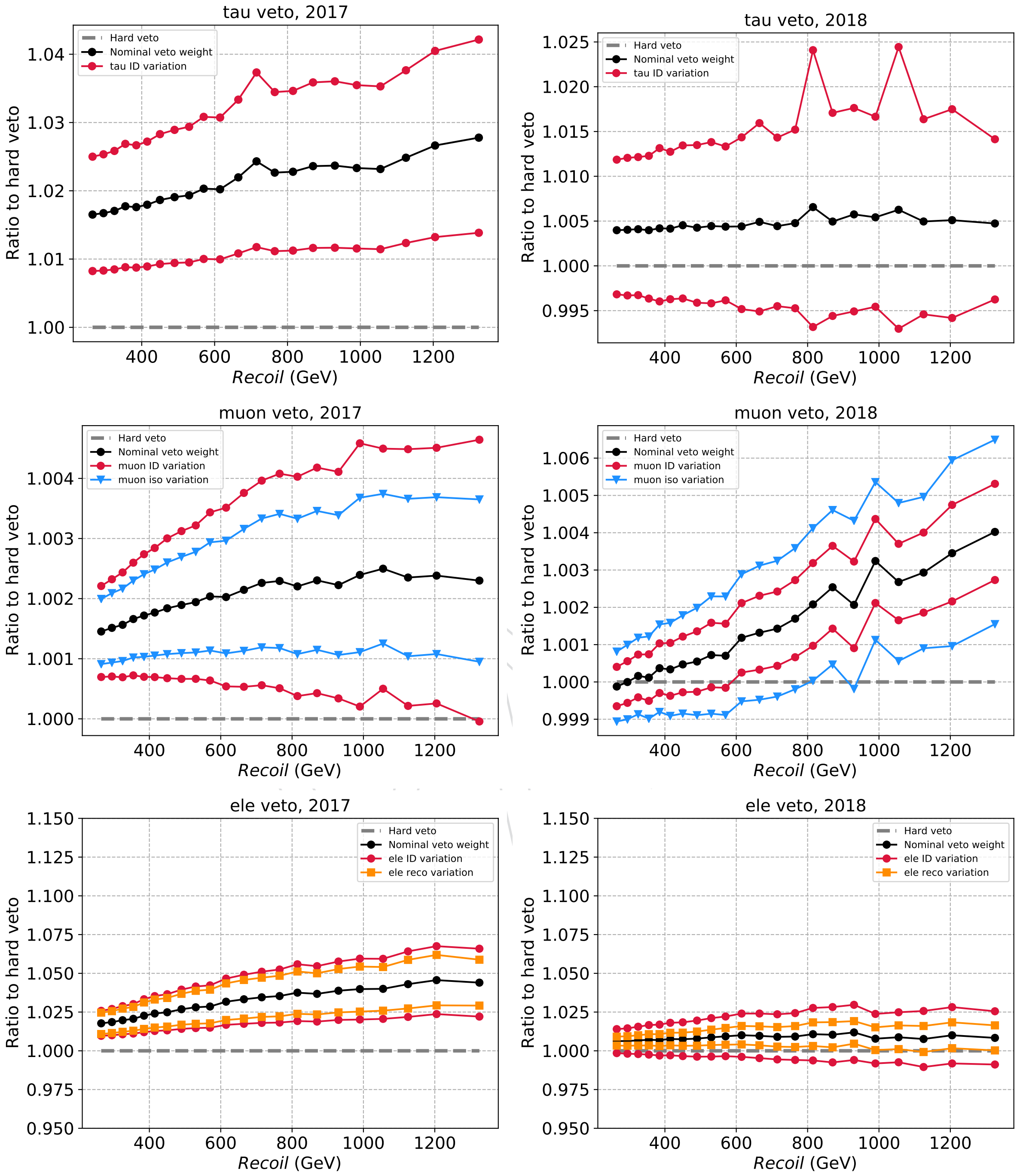

Figure 32: Effect of the veto weight correction on the recoil distribution of W + jets in the signal region. The correction is shown relative to the case of applied lepton veto without correction. The panels show the effect for the tau (top), muon (middle) and electron veto (bottom). The left and right columns correspond to the 2017 and 2018 data sets, respectively.

4.6 Efficiency reweighting for b jet vetos

For the b jet veto, the same reweighting method is applied as described for leptons in Section 4.5. The `DeepCSV_94XSF_WP_V4_B_F` and `DeepCSV_102XSF_WP_V1` scale factors provided by the the CMS BTV group are used [59, 60]. The flavor of each jet is determined using the ghost clustering method, and separate scale factors are applied for jets determined to be of light quark (u, d, s, g) or heavy quark (c, b) origin.

In order to estimate the effect of the b tagging efficiency uncertainty on the analysis, recoil templates for all processes are derived with the nominal b tagging correction, as well as the up and down variations of the correction. The behavior of the backgrounds is split into groups:

1. V + jets backgrounds: These processes have few real b jets. While a precise estimate of the V + jets processes is important, the analysis is only sensitive to the transfer factors between different V + jets processes, rather than the individual absolute corrections and uncertainties. The effect of the veto correction and its variations for these processes is demonstrated in Figs. 33 and 34 for the 2017 and 2018 data sets, respectively. Generally, it is observed that the nominal and varied corrections have an effect that is independent of the hadronic recoil. The nominal correction amounts to $\leq$ 0.5% in the 2017 data set and $\leq$ 1% in 2018, and the up/down variations are of similar size as the nominal correction. The effect on the different processes is identical to a few permille, and the resulting uncertainty on the transfer factors is therefore negligible. The only deviation from this full cancellation is observed for the W + jets process in the signal region in the 2018 data set. For this process, the nominal correction is larger than in the other processes by about one percentage point. However, the variations relative to the nominal correction are still of the same size and cancel accordingly. Therefore, it is concluded that the nominal correction should be applied to all processes, but no uncertainty is assumed on the transfer factors.

2. Top backgrounds: These processes have a large number of real b jets. The effect of the corrections on top processes is shown in Figs. 35 and 36. Here, the nominal correction can be larger than before, ranging from 6 to 15%, depending on the analysis region and data set. The correction is again found to be independent of the hadronic recoil, and a normalization uncertainty of up to 6% is assigned.

3. Others: All other processes behave quantitatively like the V + jets processes. Since these processes are not estimated using transfer factors, no cancellation takes place and the absolute uncertainty must be taken into account. A 2% normalization uncertainty is assigned to these processes.

To summarize, the nominal b tagging correction is applied to all processes. No uncertainty is assigned to the V + jets transfer factors. Top processes are assigned a 6% normalization uncertainty, and all processes that are neither V + jets nor top-related are assigned a 2% normalization uncertainty. The normalization uncertainties are decorrelated between top and non-top processes (to account for the flavor difference), as well as decorrelated between the data sets. It has been verified that these conclusions hold for the mono-V category, as well, and the same approach is adopted.

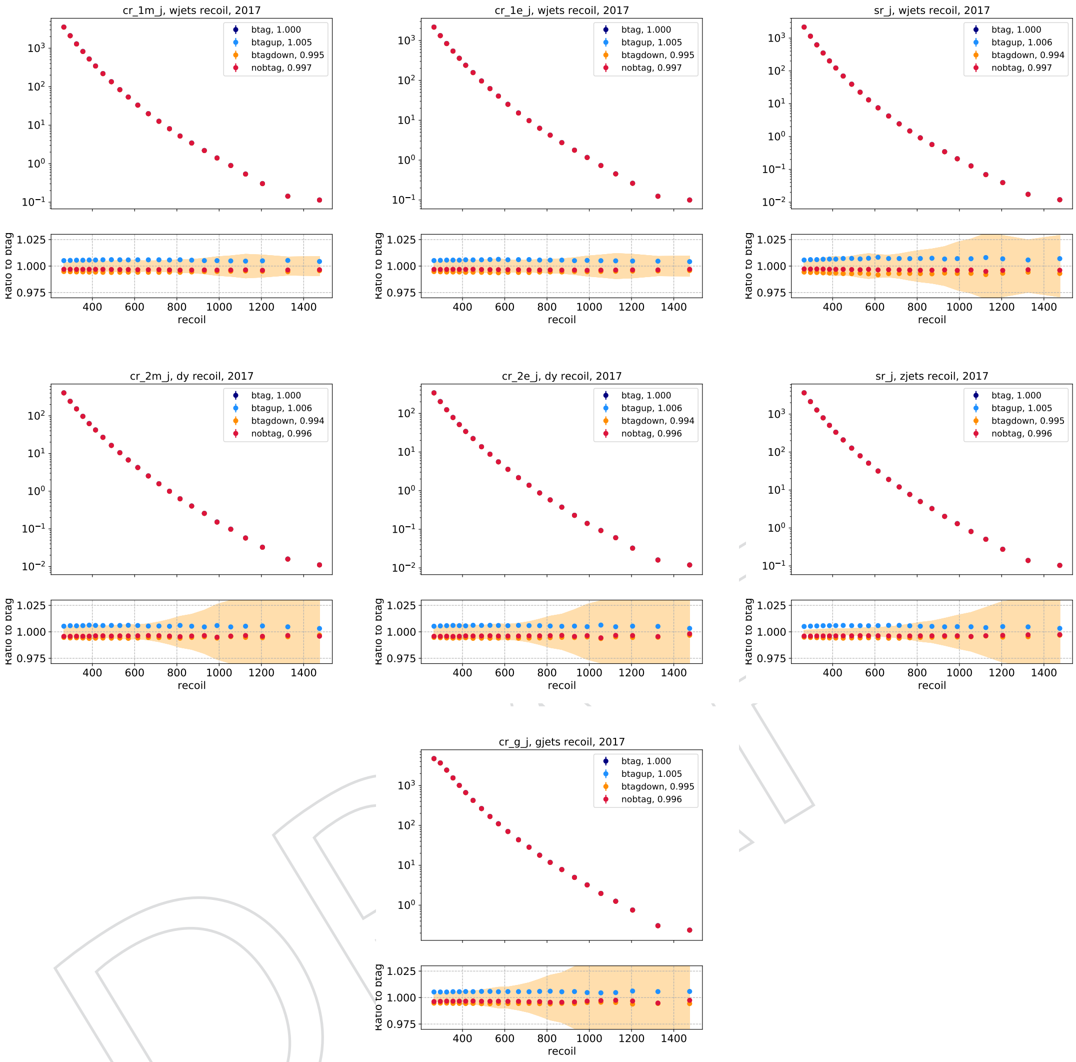

Figure 33: Effect of the b veto efficiency correction the recoil distribution of V + jets processes in the various regions in the 2017 data set. The corrections are shown for Wjets (top row) in the single muon (left), electron (middle) and signal regions (right). The second row similarly shows DY/Z + jets in the double muon (left), electron (middle) and signal regions (right). The bottom row shows the γ + jets process in the photon region. In each plot, the top panel shows the absolute recoil spectra without a b tagging correction ("nobtag"), as well as with the nominal ("btag") and varied corrections ("btagup", "btagdown"). In each of the legend entries, the ratio of the total yield of each spectrum to the total yield of the nominally corrected spectrum is given. The bottom panel then shows the ratio of each of the spectra relative to the nominal correction. For reference, the light orange band shows the limited sample size uncertainty.

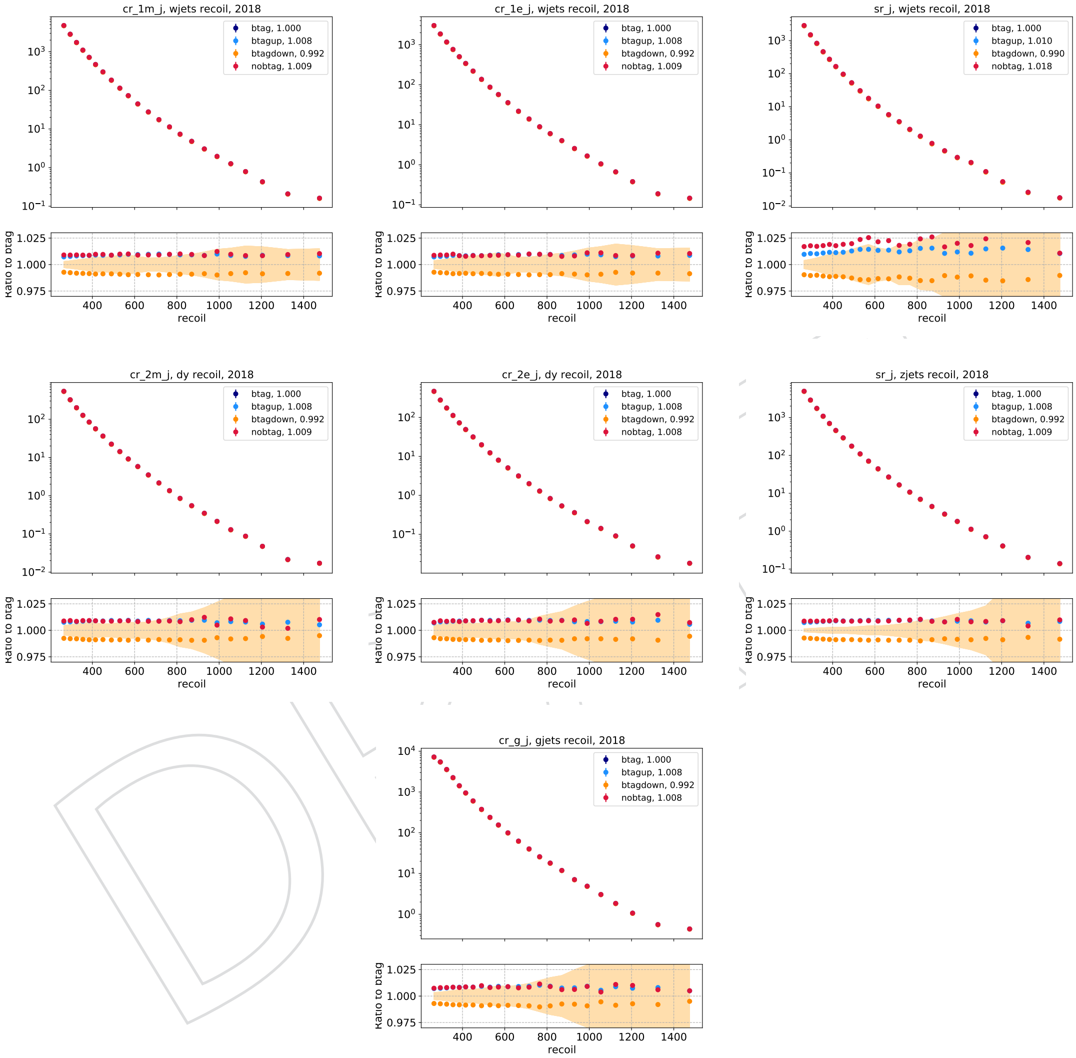

Figure 34: Same as Fig. 33, but for the 2018 data set.

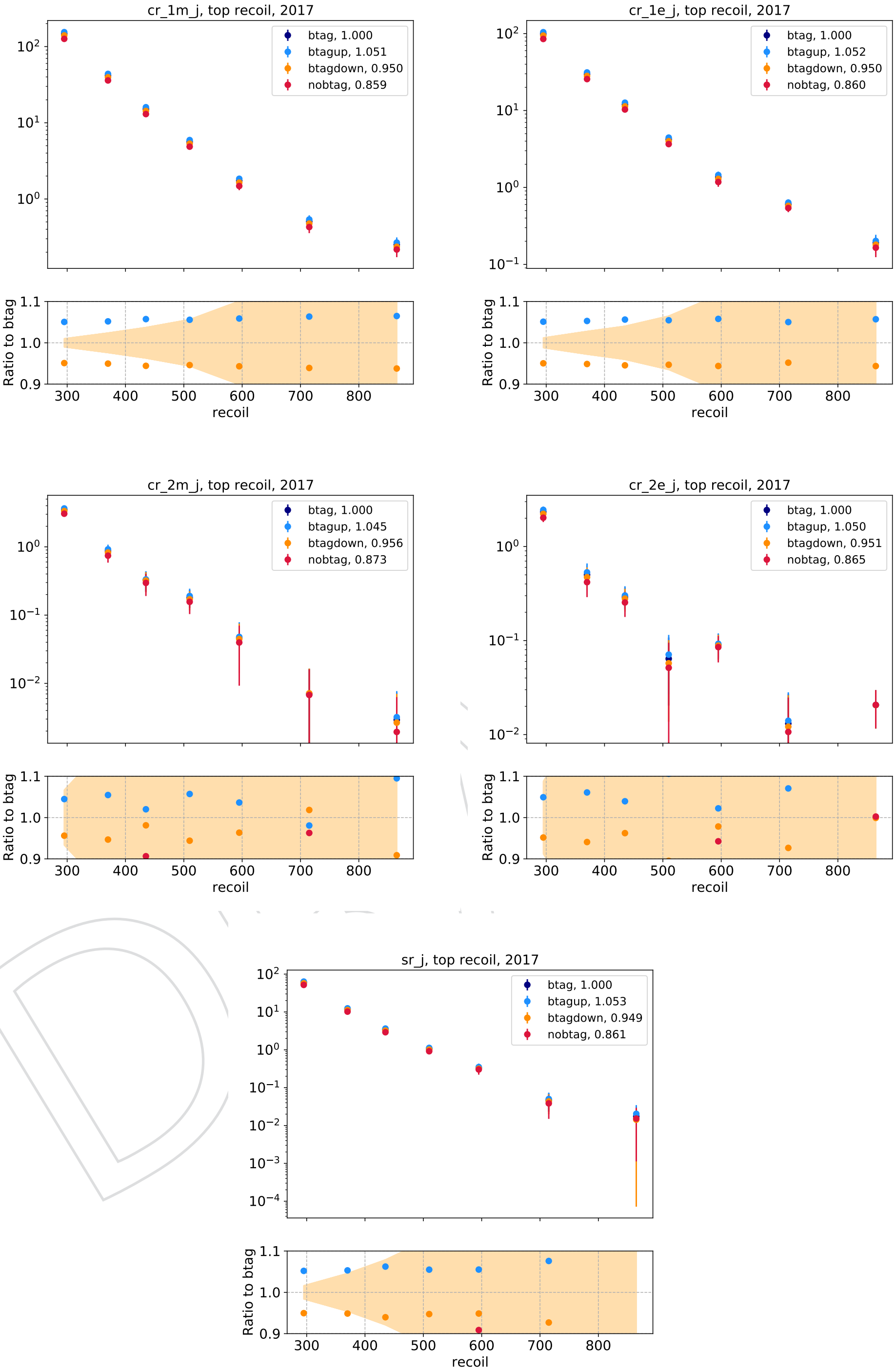

Figure 35: Same as Fig. 33, but showing the top quark-related processes instead of V + jets. The corrections are shown for the single electron and muon regions (top row), double electron and muon regions (middle row), and signal region (bottom row).

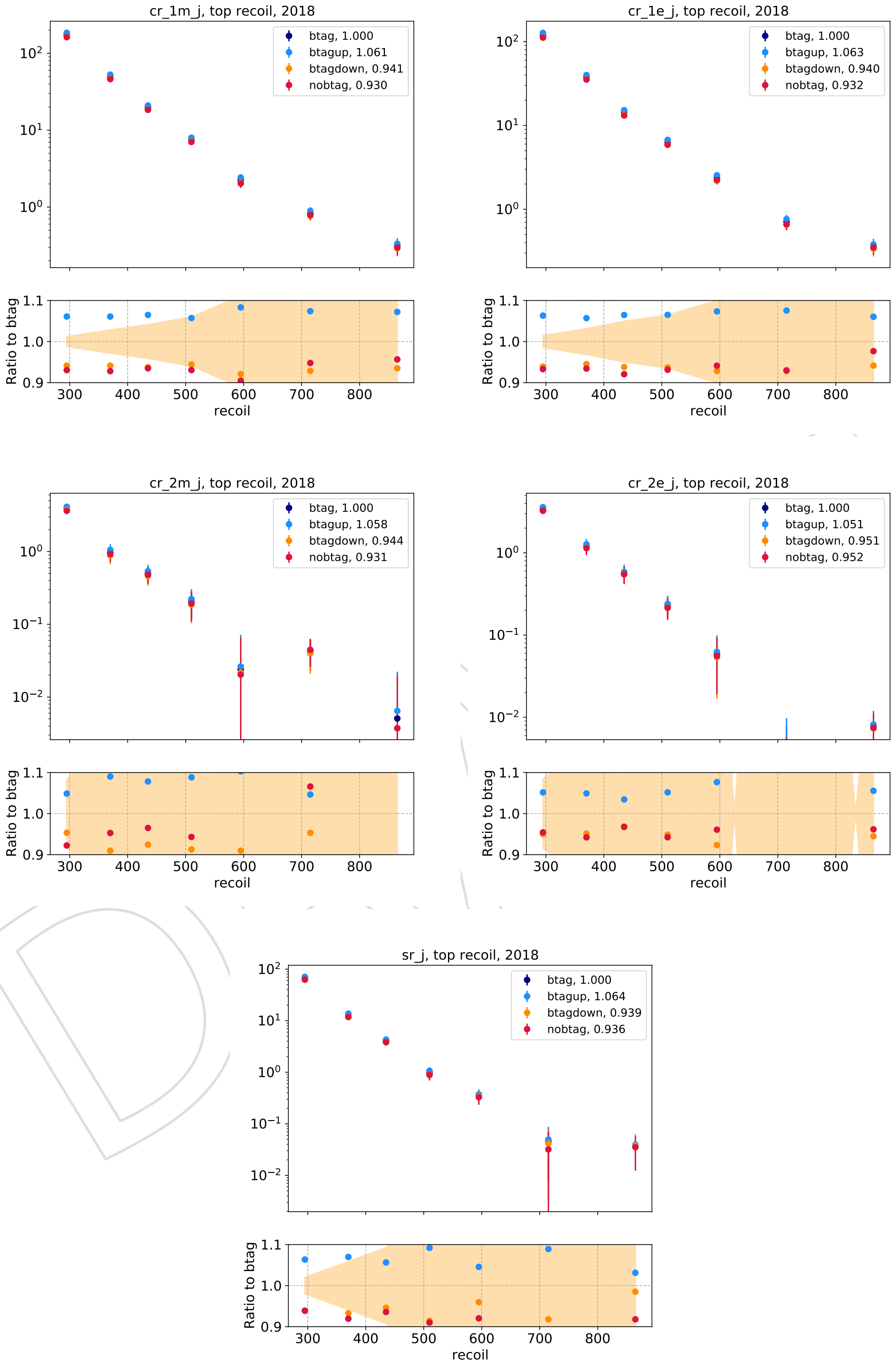

Figure 36: Same as Fig. 35, but for the 2018 data set.

4.7 Higher-order reweighting for V+jets

This analysis uses the ratios of the recoil distributions in signal and control regions to constrain the final background estimate in a partially data driven way. As signal and control regions both have large statistical power, precise predictions of these ratios are necessary. To achieve this goal, the simulation samples for the samples W, DY and photon backgrounds are reweighted using higher-order corrections.

4.7.1 Generator-level boson construction

All theory-based corrections of the W, DY and photon backgrounds are parametrized as a function of the generator-level p_{T} of the respective boson $p_{\mathrm{T},V}$. For each simulated event, this quantity is calculated as follows. For DY and W samples, the record of generator-level particles is searches for a Z or W boson with status 62, and if one is found, this particle is used to determine the boson properties. If no such boson is found, generator-level dilepton candidates are built from:

1. "dressed" final-state electrons and muons. Lepton dressing means to collect all photons radiated off the lepton within a cone of $\Delta R < 0.1$ and adding their four-momenta back to the lepton four-momentum. This procedure is meant to undo the effect of final state photon radiation, which would otherwise distort the value of the reconstructed boson four-momentum. This effect is especially relevant as electrons and muons follow different radiation patterns. Lepton dressing is performed in central NanoAOD production following the procedure used in the RIVET software.
2. τ leptons with generator status 2. As τ leptons are unstable, they are not present as final state particles (status 1) in the generator record. The τ lepton before its decay has status 2.
3. neutrinos with generator status 1.

The dilepton candidates are checked for flavour consistency with the desired boson candidate. If multiple candidates are found in an event, the one invariant mass closest to the Z or W boson mass is used. If no such dilepton candidate can be found, the dressed leptons are replaced by bare status-1 leptons and the procedure is repeated.

For photon events, the generator photon with highest p_{T} and status 1 is used.

4.7.2 EW NLO

Scale factors corresponding to NLO EW corrections are obtained from Ref. [17] and applied as a function of the generator-level boson p_{T}. The scale factors are shown in Fig. 37.

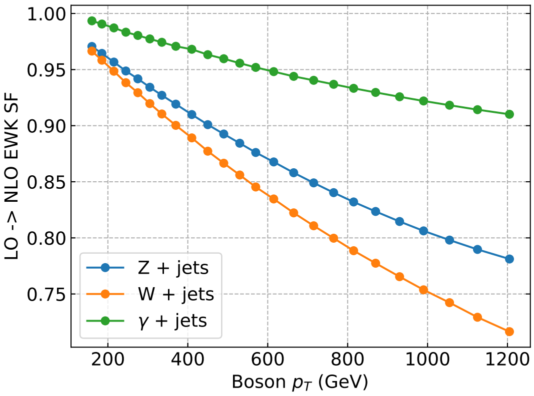

Figure 37: EW NLO scale factors for DY, W and photon production as a function of $p_{\mathrm{T},V}$.

4.8 Higher-order reweighting for VV+jets

Higher-order corrections are also defined for the diboson processes, which contribute significantly to the mono-V category. The WW, WZ and ZZ processes are modeled using samples generated at next-to-leading-logarithm order in QCD with PYTHIA8, and normalized to the inclusive cross section at NNLO in QCD. The $Z\gamma$ and $W\gamma$ processes are modeled using samples generated at NLO in QCD with Madgraph5_aMC@NLO.

QCD NLO corrections are applied to the WW, WZ and ZZ processes. The corrections are derived in a similar way as for the V+jets processes: The boson p_T spectra are compared between the default LO samples and samples generated at NLO in QCD with Madgraph5_aMC@NLO or Powheg. In each case, both samples are normalized to the same inclusive cross sections, since the normalization effect of higher-order corrections is already taken into account by normalizing to the NNLO cross section.

The corresponding EW NLO corrections are obtained from Ref. [61] for WZ, ZZ and WW, and from Refs. [62, 63] for $V\gamma$ production.

The individual and total correction factors are shown in Figs. 38 and 39. Two uncertainties are assigned:

1. A shape uncertainty $\sigma_{\rm rel} = (1 - {\rm SF}_{\rm EWK}) \times (1 - {\rm SF}_{\rm QCD})$, which models the effect of missing mixed EWK-QCD corrections. This uncertainty is equivalent to the difference between the QCD×EWK and QCD+EWK schemes. In the case of $V\gamma$ production, since no QCD NLO correction is directly applied, a flat value of ${\rm SF}_{\rm QCD} = 0.25$ is assumed.
2. A flat 10% normalization uncertainty to parametrize other effects, such as the effect of NNLO corrections to event kinematics, and the $\sqrt{s}$ dependence of the corrections.

The two uncertainties are treated as decorrelated between each other and are further decorrelated between the different diboson processes.

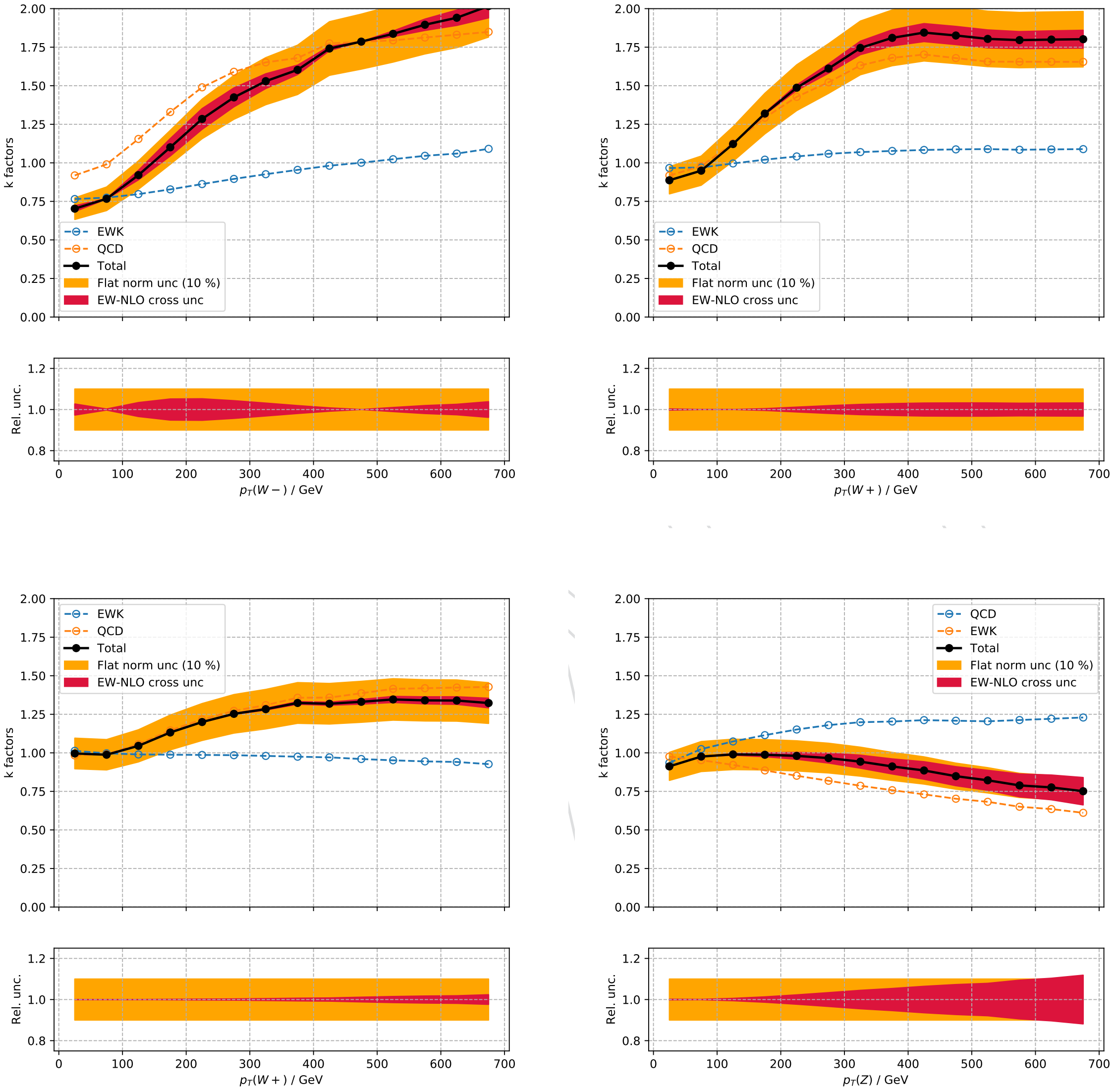

Figure 38: Higher-order correction factors for the W^-Z (top left), W^+Z (top right), WW (bottom left) and ZZ (bottom right) processes. The individual EWK and QCD corrections are shown separately in the dashed orange and blue lines. The black solid markers and line indicate the product of EWK and QCD corrections. The colored bands represent the uncertainties on the correction as described in the text.

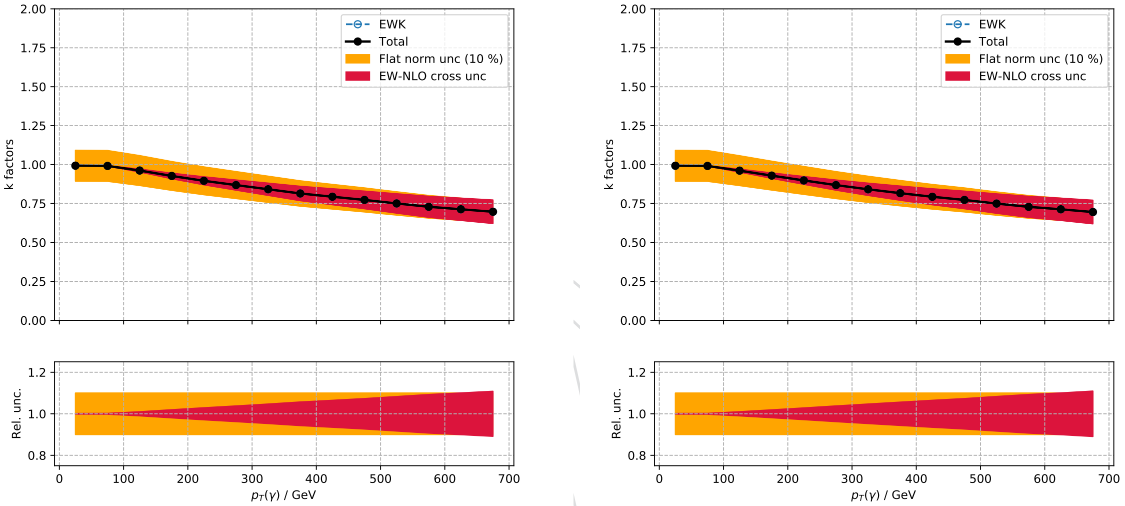

Figure 39: EWK higher-order correction factors for the Wγ (left) and Zγ (right) processes. The colored bands represent the uncertainties on the correction as described in the text. The default simulation samples are already generated at NLO in QCD, so no QCD correction is included and the EWK correction is identical to the total correction.

5 Event selection

5.1 Signal region selection

Signal region events are selected using triggers with thresholds of 120 GeV on both $p_{\mathrm{T,trig}}^{\mathrm{miss}}$ and $H_{\mathrm{T,trig}}^{\mathrm{miss}}$. The $p_{\mathrm{T,trig}}^{\mathrm{miss}}$ corresponds to the magnitude of the vector $\vec{p}_{\mathrm{T}}$ sum of all the PF candidates reconstructed at the trigger level, while the $H_{\mathrm{T,trig}}^{\mathrm{miss}}$ is computed as the magnitude of the vector $\vec{p}_{\mathrm{T}}$ sum of jets with $p_{\mathrm{T}} > 20\,\mathrm{GeV}$ and $|\eta| < 5.0$ reconstructed at the trigger level. The energy fraction attributed to neutral hadrons in these jets is required to be smaller than 0.9. This requirement suppresses anomalous events with jets originating from detector noise. To be able to use the same triggers for selecting events in the muon control samples used for background prediction, muon candidates are not included in the $p_{\mathrm{T,trig}}^{\mathrm{miss}}$ nor $H_{\mathrm{T,trig}}^{\mathrm{miss}}$ computation. The trigger efficiency is measured to be 96% for events passing the analysis selection for $p_{\mathrm{T}}^{\mathrm{miss}} > 250\,\mathrm{GeV}$ and becomes more than 99% efficient for events with $p_{\mathrm{T}}^{\mathrm{miss}} > 350\,\mathrm{GeV}$.

Candidate events are required to have a hadronic recoil of at least 250 GeV, where the hadronic recoil in the signal region corresponds to PF $p_{\mathrm{T}}^{\mathrm{miss}}$. In the monojet category, the highest p_{T} (leading) AK4 jet in the event is required to have $p_{\mathrm{T}} > 100\,\mathrm{GeV}$ and $|\eta| < 2.4$, whereas in the mono-V category, the leading AK8 jet is required to have $p_{\mathrm{T}} > 250\,\mathrm{GeV}$ and $|\eta| < 2.4$. In both categories, the leading jet is also required to have at least 10% of its energy coming from charged particles and less than 80% of its energy attributed to neutral hadrons as discussed in section 3. This selection helps to remove events originating from beam-induced backgrounds. In addition, the analysis employs various event filters to reduce events with large misreconstructed $p_{\mathrm{T}}^{\mathrm{miss}}$ [64] originating from noncollision backgrounds.

The main background processes in this search are the $\mathrm{Z}(\nu\nu)+$jetsand $\mathrm{W}(\ell\nu)+$jets processes. The $\mathrm{Z}(\nu\nu)+$jetsprocess is an irreducible background and constitutes the largest background in the search. In contrast, the background from $\mathrm{W}(\ell\nu)+$jets is suppressed by imposing a veto on events containing one or more loose muons or electrons with $p_{\mathrm{T}} > 10\,\mathrm{GeV}$, or hadronically decaying τ leptons with $p_{\mathrm{T}} > 18\,\mathrm{GeV}$. Events that contain a loose, isolated photon with $p_{\mathrm{T}} > 15\,\mathrm{GeV}$ and $|\eta| < 2.5$ are also rejected. This helps to suppress electroweak (EW) backgrounds in which a photon is radiated from the initial state. To reduce the contamination from top quark backgrounds, events are rejected if they contain a b tagged jet with $p_{\mathrm{T}} > 20\,\mathrm{GeV}$ and $|\eta| < 2.4$. These jets are identified using the DeepCSV algorithm [40, 65], adopting the "medium" working point, which corresponds to correctly identifying a jet originating from a bottom quark with a probability of 80% and misidentifying a jet originating from a charm quark (light-flavor jet) with a probability of 12 (2)%. To avoid events with anomalous MET due to reconstruction failures of the PF algorithm, events are required to have $\Delta p_{\mathrm{T}}^{\mathrm{miss}}(\mathrm{PF},\mathrm{Calo}) = (\mathrm{PF}\,p_{\mathrm{T}}^{\mathrm{miss}} - \text{calorimeter}\,p_{\mathrm{T}}^{\mathrm{miss}})/\mathrm{recoil}) < 0.5$. In a similar manner to the requirements on the leading jet enery fractions, this requirement is designed to be very efficient in the control regions, where artificial $p_{\mathrm{T}}^{\mathrm{miss}}$ is not an issue, and act as a tail rejection mechanism for the hadronic signal region. Similarly, it is required that the angle between the track $\vec{p}_{\mathrm{T}}^{\mathrm{miss}}$ and PF $\vec{p}_{\mathrm{T}}^{\mathrm{miss}}$ vectors is smaller than 2 rad in the transverse plane. Lastly, QCD multijet background with $E_{\mathrm{T}}^{\mathrm{miss}}$ arising from mismeasurements of the jet momenta is suppressed by requiring the minimum azimuthal angle between the $\vec{p}_{\mathrm{T}}^{\mathrm{miss}}$ direction and each of the first four leading jets with p_{T} greater than 30 GeV and $|\eta| < 2.4$ to be larger than 0.5 radians.

To select an event in the mono-V category, a leading AK8 jet is identified as a jet arising from hadronic decays of Lorentz-boosted W or Z bosons. Such jets typically have an invariant mass, computed from the momenta of jet's constituents, between 65 and 120 GeV [66]. The mass of the leading AK8 jet is computed after applying the soft drop algorithm to remove soft and wideangle radiation [67]. This technique yields improved jet mass resolution owing to reduced effects coming from the underlying event and pileup.

For events with an AK8 jet passing the mass requirement, separate analysis regions are defined based on whether the jet passes the different tagger working points described in sec. 3.2. A low-purity region is defined by requiring that the jet pass the loose, but not the tight working point of the nominal tagger, and a corresponding high-purity region is populated with jets passing the tight tagger requirement. These selection requirements are summarized in Tab. 14.

Fig. 40, **??**, 43, **??**, shows the distribution of the $E_{\mathrm{T}}^{\mathrm{miss}}$, the number of jets, as well as the p_{T} and η distribution of the leading jet (AK4 for monojet, AK8 for mono-V) for events in the monojet and mono-V signal categories respectively for 2017 and 2018 datasets. For the monojet category, the leading jet energy fractions are additionally shown in Figs. 41 and 44.

5.1.1 HEM effect

During a large part of data-taking in 2018, a submodule of the HCAL was not functioning. As a result, no HCAL deposits have been recorded in the region of $-3.0 < |\eta| < -1.3$ and $-1.57 < \phi < -0.87$ for the affected portion of the data set. The missing HCAL deposits have two immediate consequences for this analysis:

1. Affected jets will often be reconstructed as an isolated offline electron. The electron identification criteria rely on HCAL deposits to differentiate between cases where ECAL clusters are deposited by true isolated electrons and cases where the clusters result from hadronic jets. These “fake” electrons will often pass the analysis object selection and can contaminate the selection.
2. Affected jets are not calibrated correctly. Without HCAL deposits, the jet energy as reconstructed using the the standard PFCHS reconstruction with the nominal calibration constants is not reliable. This mis-measurement of the true jet energy will lead to anomalous $p_{\mathrm{T}}^{\mathrm{miss}}$ in affected events.

The impact of the HEM effect is studied in detail in Appendix . To mitigate the effect of the HEM failure on this analysis, two selection criteria are added for the analysis of the 2018 data set:

1. Events where an electron is found to be in the HEM $\eta - \phi$ range are not taken into account in the single-electron region (see below).
2. Events with $-1.62 < \phi(\vec{p}_{\mathrm{T}}^{\mathrm{miss}}) < -0.62$ are rejected from the signal region if they have $p_{\mathrm{T}}^{\mathrm{miss}} < 470\,\mathrm{GeV}$.

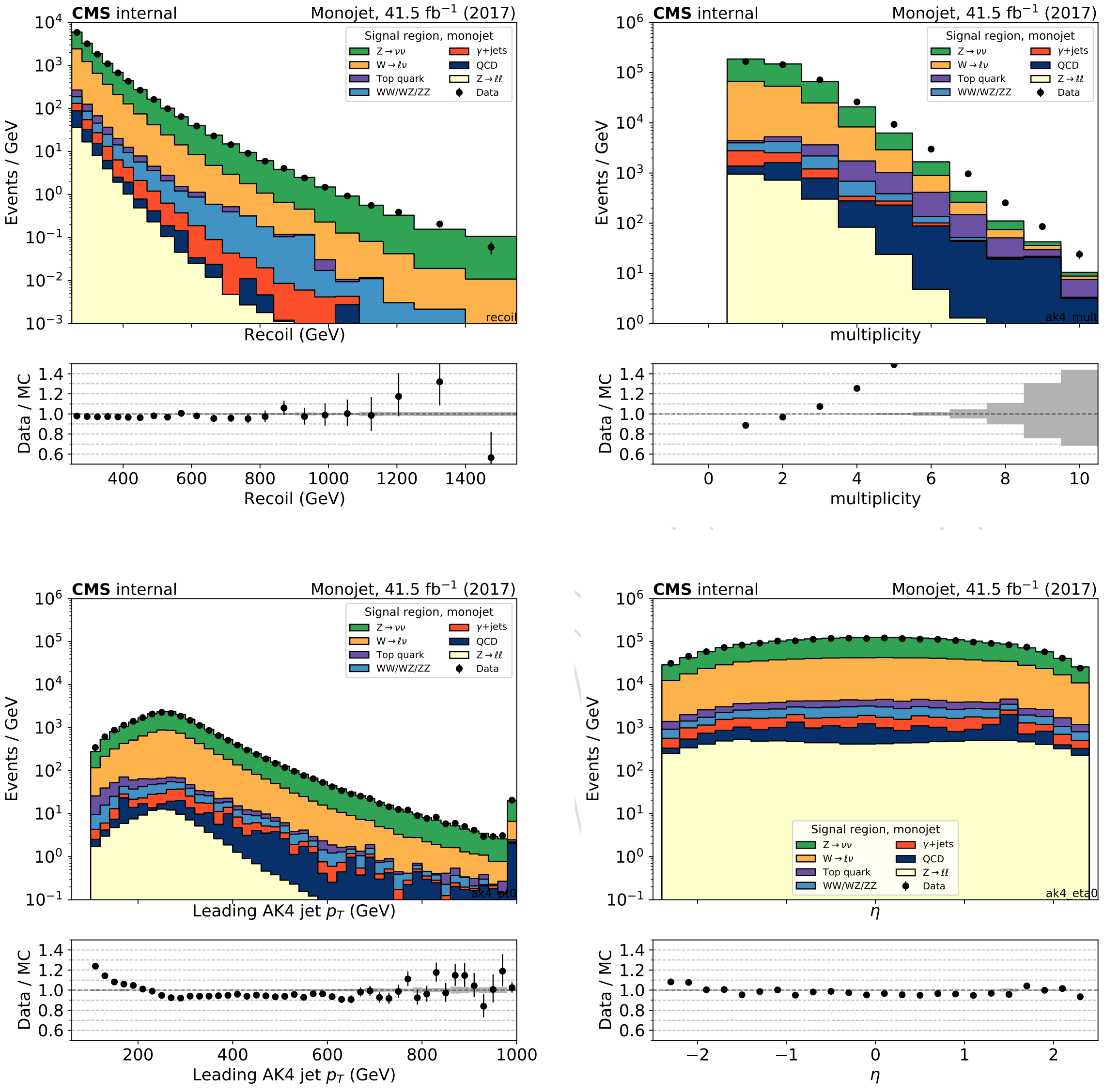

Figure 40: Comparison between 2017 data and monte carlo simulation in the signal sample for the recoil distribution, the AK4 jet multiplicity distribution, p_{T} and η distribution of the leading AK4 jet with the monojet selection. The bottom panel shows the ratio between data and prediction, with the gray band representing the statistical uncertainty due to limited size of the simulated samples.

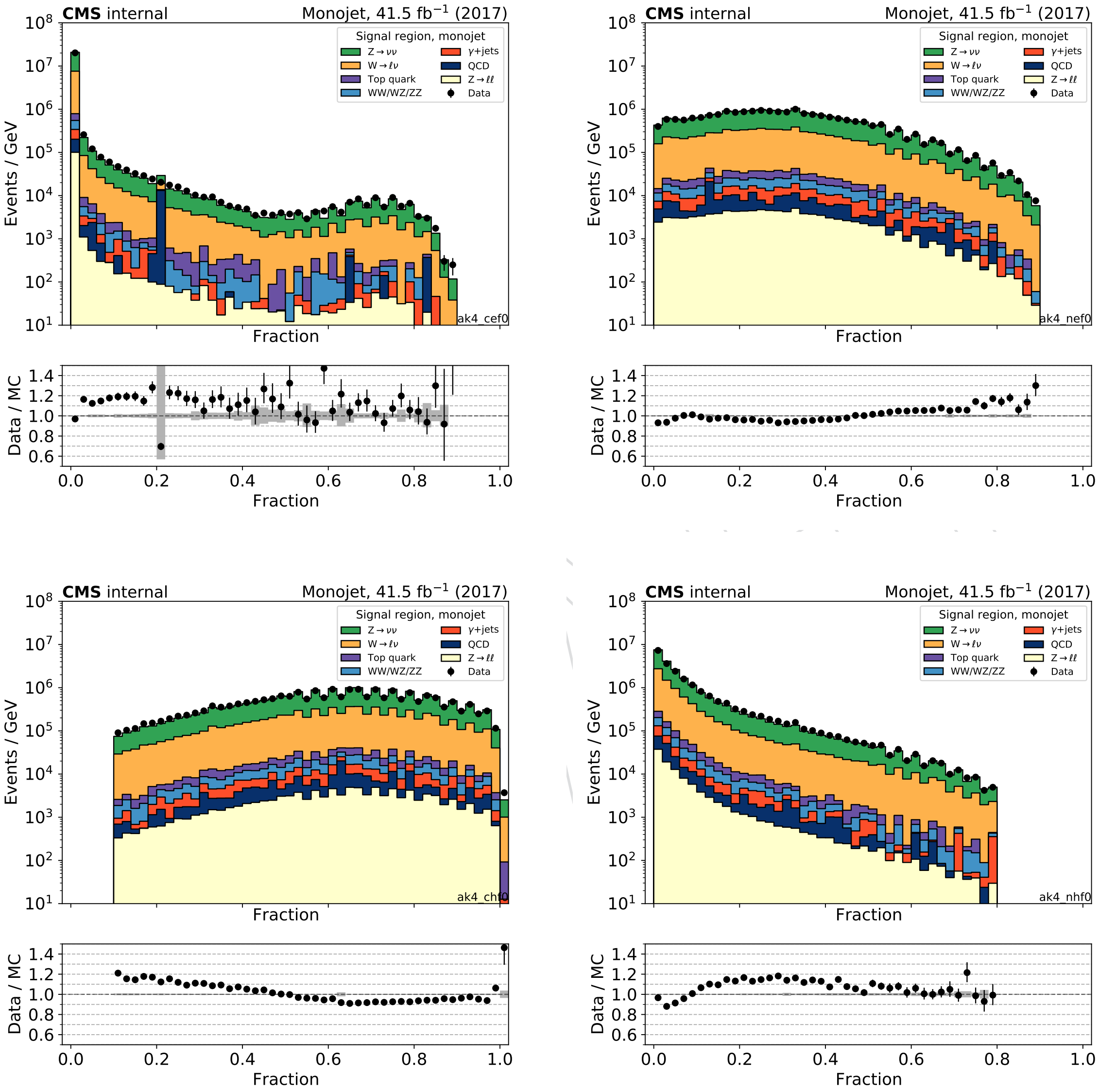

Figure 41: Comparison between 2017 data and monte carlo simulation in the signal sample for the distriutions of the jet energy fractions: Electron and photon energy fraction (top left and right, respectively), as well as charged and neutral hadron fractions (bottom left and right).

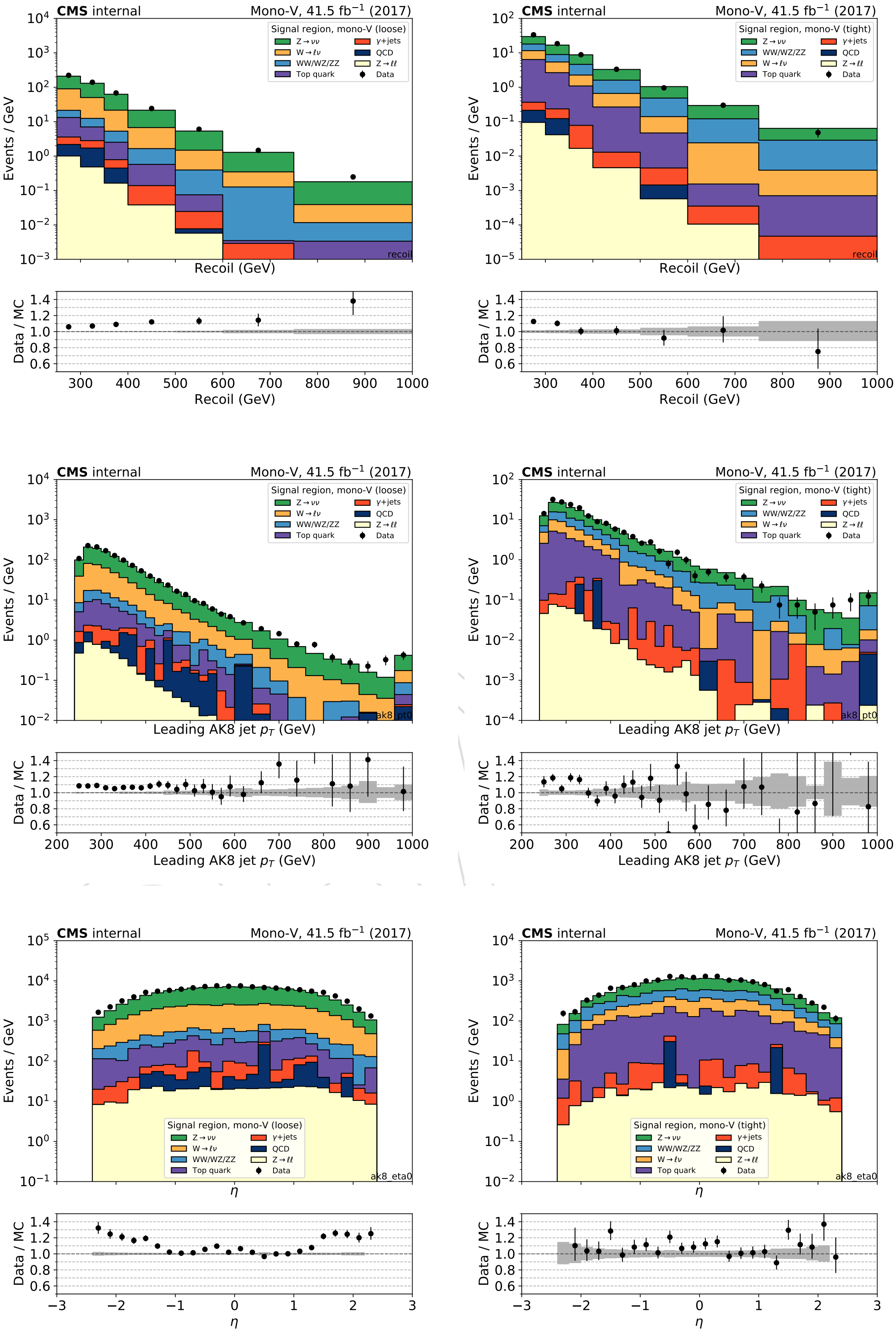

Figure 42: Comparison between 2017 data and monte carlo simulation in the signal sample for the recoil distribution, and the AK8 jet p_T and η distribution in the low-purity (left) and high-purity (right) regions. The bottom panel shows the ratio between data and prediction, with the gray band representing the statistical uncertainty due to limited size of the simulated samples.

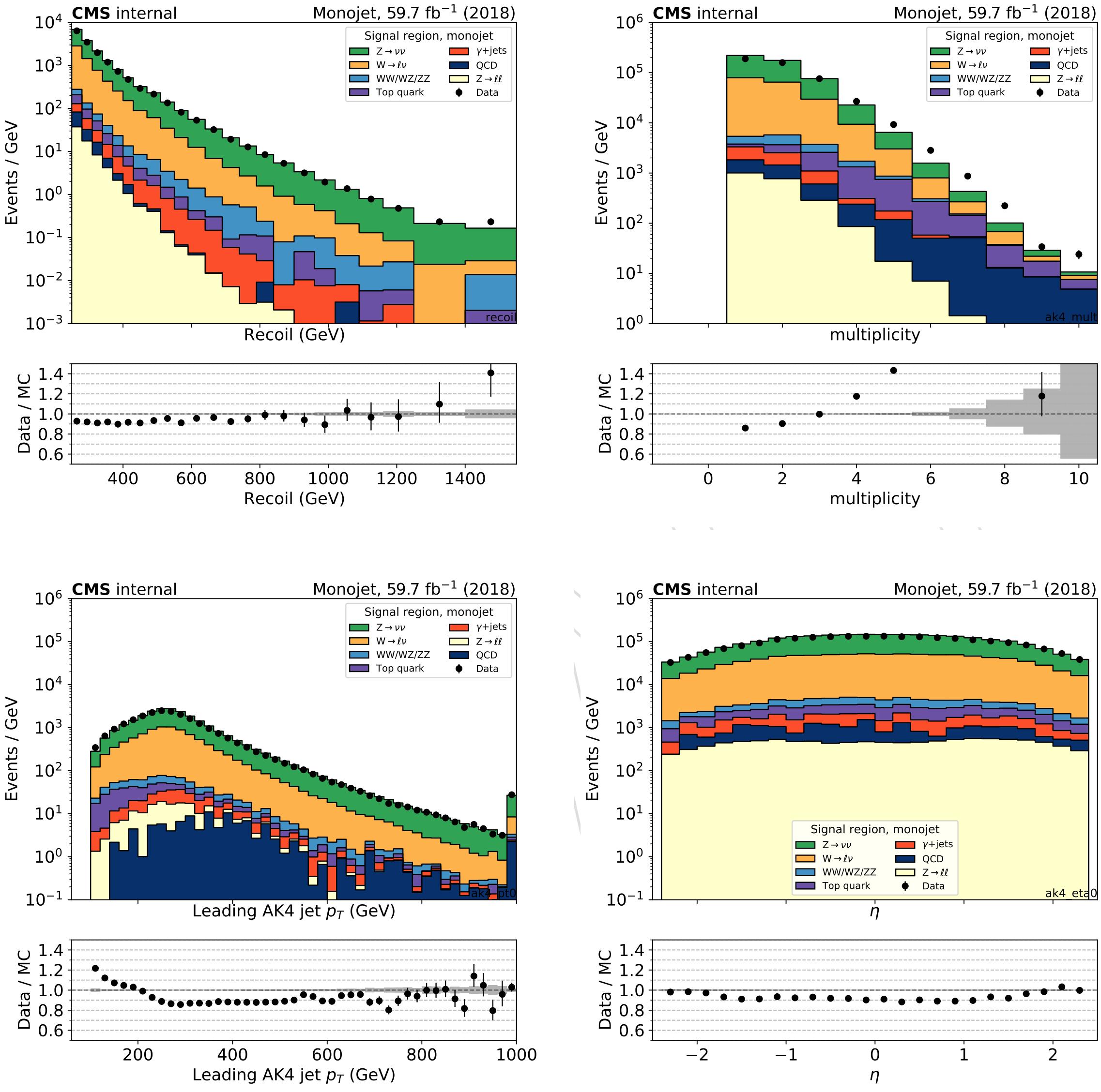

Figure 43: Comparison between 2018 data and monte carlo simulation in the signal sample for the recoil distribution, the AK4 jet multiplicity distribution, p_{T} and η distribution of the leading AK4 jet with the monojet selection. The bottom panel shows the ratio between data and prediction, with the gray band representing the statistical uncertainty due to limited size of the simulated samples.

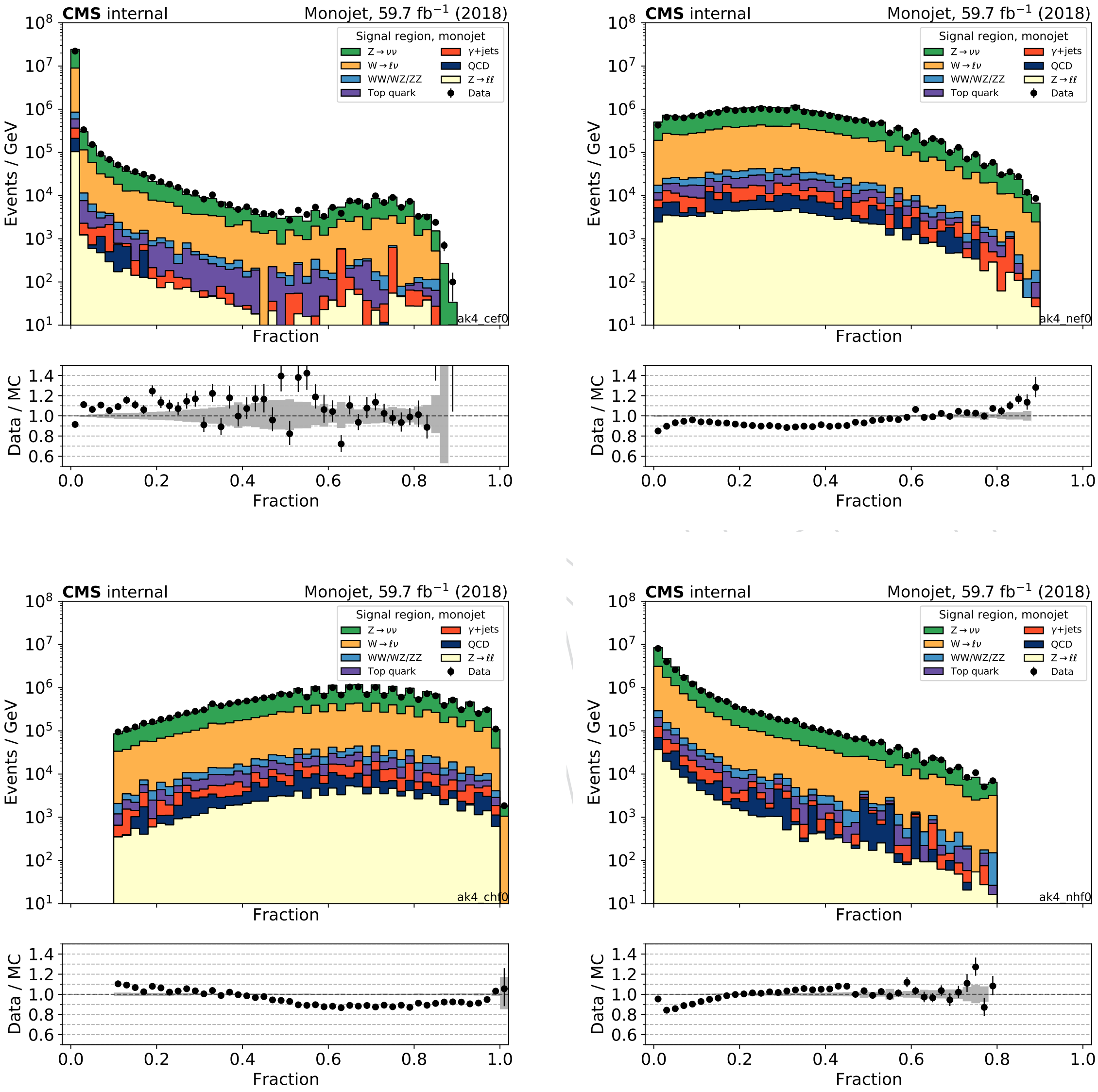

Figure 44: Comparison between 2018 data and monte carlo simulation in the signal sample for the distriutions of the jet energy fractions: Electron and photon energy fraction (top left and right, respectively), as well as charged and neutral hadron fractions (bottom left and right).

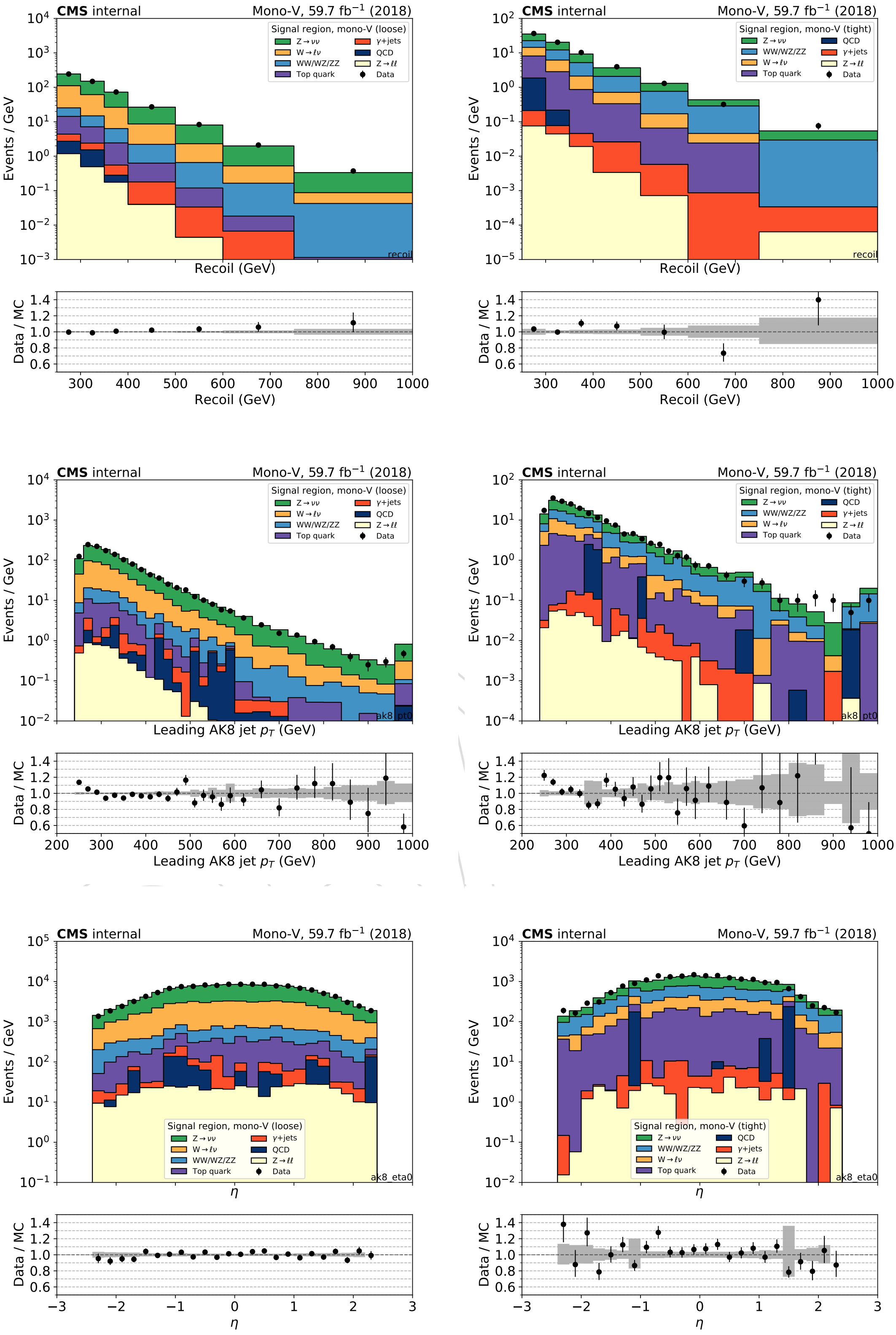

Figure 45: Comparison between 2018 data and monte carlo simulation in the signal sample for the recoil distribution, and the AK8 jet p_T and η distribution in the low-purity (left) and high-purity (right) regions. The bottom panel shows the ratio between data and prediction, with the gray band representing the statistical uncertainty due to limited size of the simulated samples.

Table 13: Summary of the common selection requirements for mono-V and monojet categories. Note that for the control region selections, the requirements on $\vec{p}_{\mathrm{T}}^{\mathrm{miss}}$ are replaced by the hadronic recoil, which is calculated as the vector sum of $\vec{p}_{\mathrm{T}}^{\mathrm{miss}}$ and the respective lepton or photon momenta used to define the control region selection. The $\Delta p_{\mathrm{T}}^{\mathrm{miss}}(\mathrm{PF, Calo})$ requirement is always evaluated based on $p_{\mathrm{T}}^{\mathrm{miss}}$, and not the hadronic recoil.

Variable	Selection	Target background
Muon (electron) veto	$p_{\mathrm{T}} > 10\,\mathrm{GeV}$, $\lvert\eta\rvert < 2.4(2.5)$	$\mathrm{Z}(\ell\ell)+\mathrm{jets}$, $\mathrm{W}(\ell\nu)+\mathrm{jets}$
τ lepton veto	$p_{\mathrm{T}} > 18\,\mathrm{GeV}$, $\lvert\eta\rvert < 2.3$	$\mathrm{Z}(\ell\ell)+\mathrm{jets}$, $\mathrm{W}(\ell\nu)+\mathrm{jets}$
Photon veto	$p_{\mathrm{T}} > 15\,\mathrm{GeV}$, $\lvert\eta\rvert < 2.5$	$\gamma+\mathrm{jets}$
Bottom jet veto	DeepCSV medium $< 0.4941/0.4184$ (2017 / 2018) for all jets with $p_{\mathrm{T}} > 20\,\mathrm{GeV}$, $\lvert\eta\rvert < 2.4$	Top quark
recoil	$>250\,\mathrm{GeV}$	QCD, top quark, $\mathrm{Z}(\ell\ell)+\mathrm{jets}$
$\Delta p_{\mathrm{T}}^{\mathrm{miss}}(\mathrm{PF, Calo})$	<0.5	QCD
$\Delta\phi(\mathrm{PF, Tk})$	<2	QCD
$\Delta\phi(\vec{p}_{\mathrm{T}}^{\mathrm{jet}}, \vec{p}_{\mathrm{T}}^{\mathrm{miss}})$	>0.5 radians	QCD
Leading AK4 jet p_{T} and η	$>100\,\mathrm{GeV}$ and $\lvert\eta\rvert < 2.4$	All

Table 14: Summary of the selection requirements for the mono-V category. Events that fail the mono-V selection are assigned to the monojet category.

Leading AK8 jet	Low-purity region	High-purity region
p_{T} and η	$>250\,\mathrm{GeV}$ and $\lvert\eta\rvert < 2.4$	
Mass (m_{jet})	$65 < m_{\mathrm{jet}} < 120\,\mathrm{GeV}$	
DeepAK8 Tag	loose but not tight	tight

5.2 Single muon control region selection

Single-muon control sample events are selected using full signal region criteria of monojet and mono-V categories with the exception of the muon veto. The $p_{\mathrm{T}}^{\mathrm{miss}}$ requirement is replacement an identical requirement on the hadronic recoil, which is defined as the sum of $\vec{p}_{\mathrm{T}}^{\mathrm{miss}}$ and the muon $\vec{p}_{\mathrm{T}}$, and thus corresponds to the distribution of the W p_{T}. In the single-muon control sample, exactly one tightly identified, isolated muon with $p_{\mathrm{T}} > 20$ GeV is required. No additional loose muons or electrons with $p_{\mathrm{T}} > 10$ GeV are allowed. In addition, the transverse mass of the muon-$\vec{p}_{\mathrm{T}}^{\mathrm{miss}}$ system is required to be smaller than than 160 GeV. The transverse mass (M_{T}) is computed as $M_{\mathrm{T}} = \sqrt{2E_{\mathrm{T}}^{\mathrm{miss}} p_{\mathrm{T}}^{\mu}(1-\cos\Delta\phi)}$, where p_{T}^{μ} is the p_{T} of the muon, and $\Delta\phi$ is the angle between $\vec{p}_{\mathrm{T}}^{\mu}$ and $\vec{p}_{\mathrm{T}}^{\mathrm{miss}}$.

Figs. 46 and 49 show the distributions of the recoil, the number of jets, and the p_{T} and η distribution of the leading AK4 jet for events in the single-muon control sample for the monojet category in 2017 and 2018 datasets, respectively. Figs. 47 and 50 show the distributions of the leading muon p_{T} and η, as well as the muon-$p_{\mathrm{T}}^{\mathrm{miss}}$ transverse mass, again for 2017 and 2018, respectively.

Figs. 48 and 51 show the distributions of the recoil, as well as the leading AK8 jet p_{T} and η in the low-purity and high-purity mono-V regions in the 2017 and 2018 datasets, respectively.

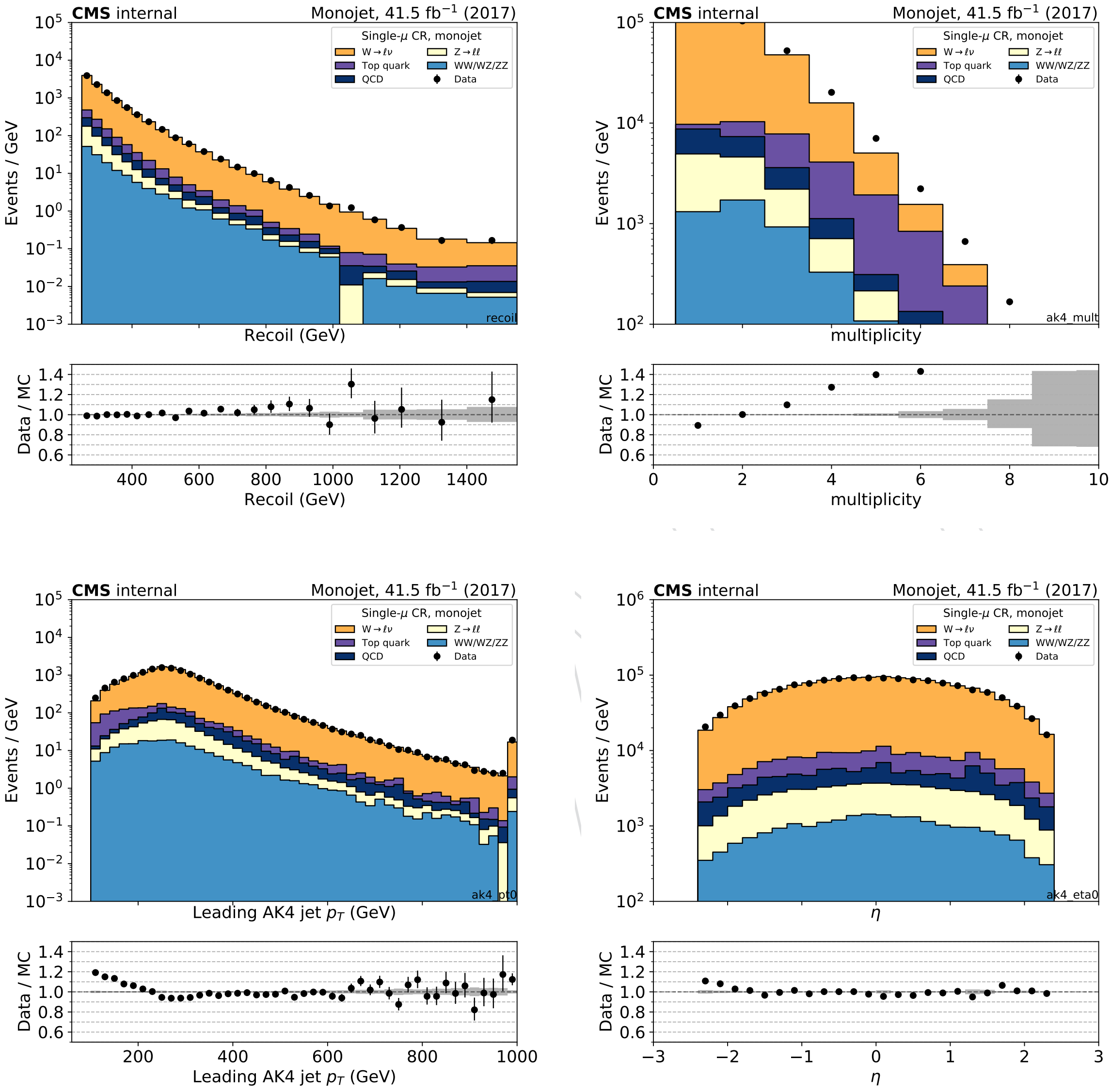

Figure 46: Comparison between 2017 data and monte carlo simulation in the single muon control sample for the recoil distribution, the AK4 jet multiplicity distribution, p_T and η distribution of the leading AK4 jet with the monojet selection. The bottom panel shows the ratio between data and prediction, with the gray band representing the statistical uncertainty due to limited size of the simulated samples.

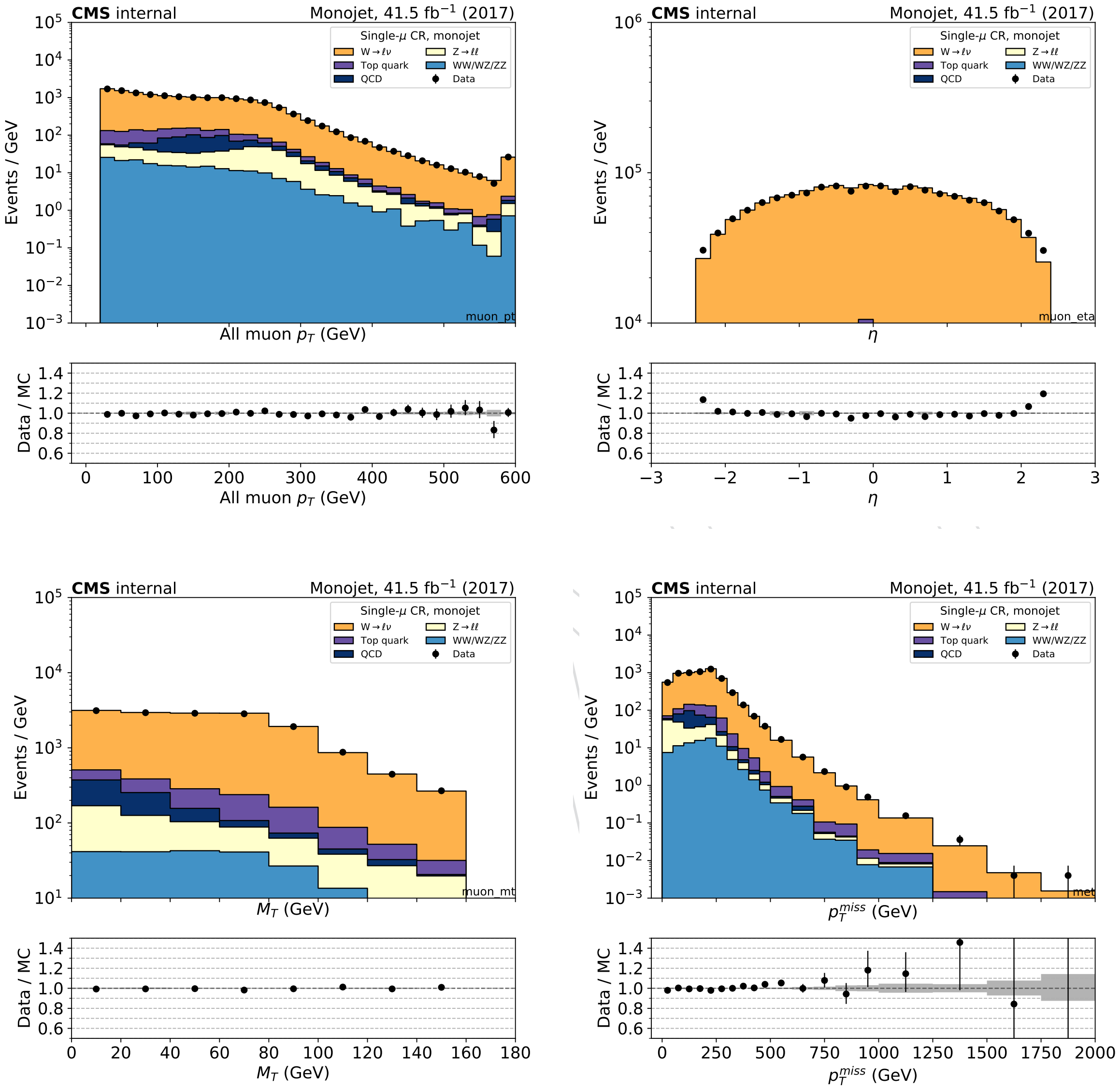

Figure 47: Comparison between 2017 data and monte carlo simulation in the single muon control sample for the p_{T} and η of the muon (top row) and the transverse mass and $p_{\mathrm{T}}^{\mathrm{miss}}$ (bottom row) in the monojet category. The bottom panel shows the ratio between data and prediction, with the gray band representing the statistical uncertainty due to limited size of the simulated samples.

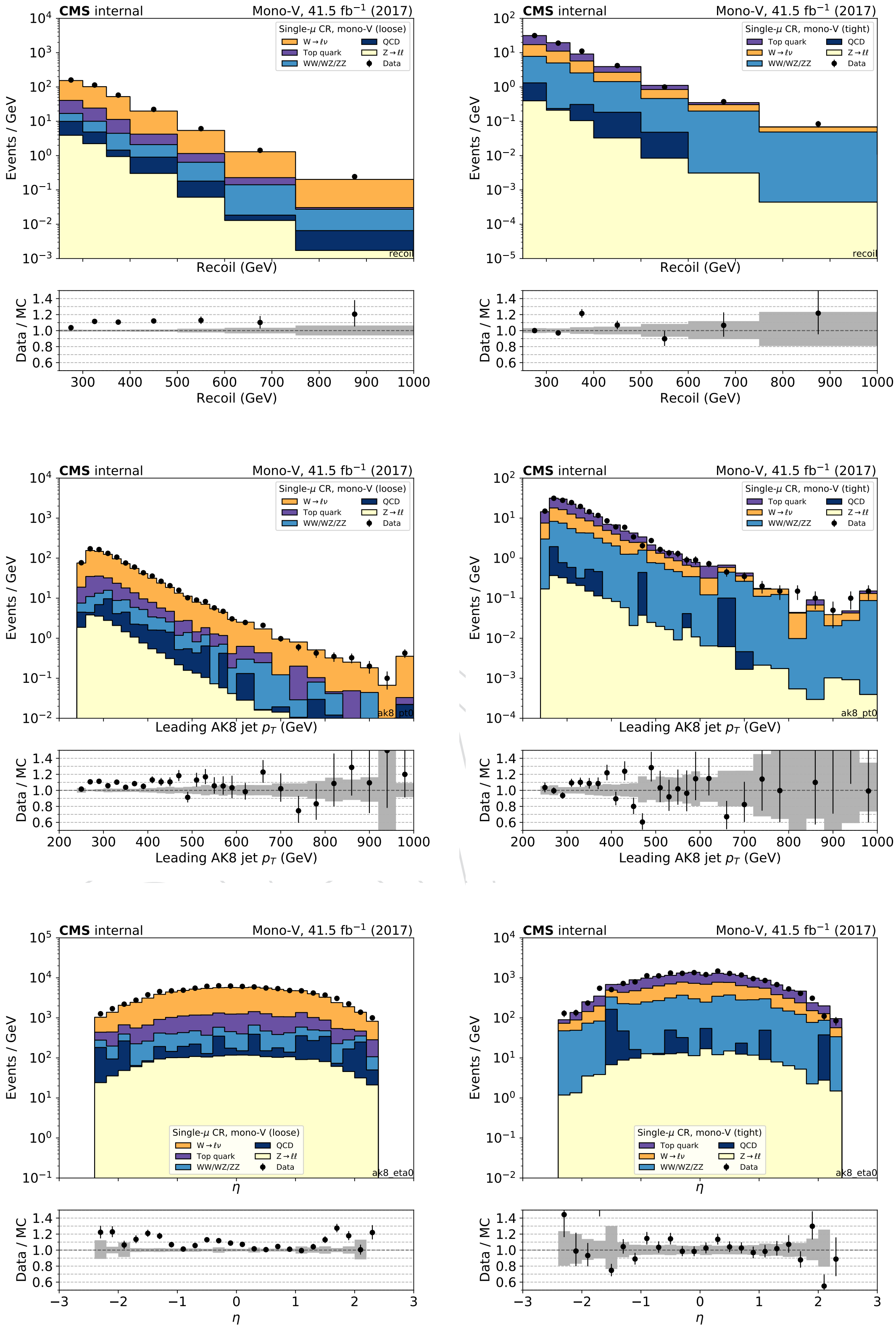

Figure 48: Comparison between 2017 data and monte carlo simulation in the single muon control sample for the recoil distribution, and the AK8 jet p_{T} and η distribution in the low-purity (left) and high-purity (right) regions. The bottom panel shows the ratio between data and prediction, with the gray band representing the statistical uncertainty due to limited size of the simulated samples.

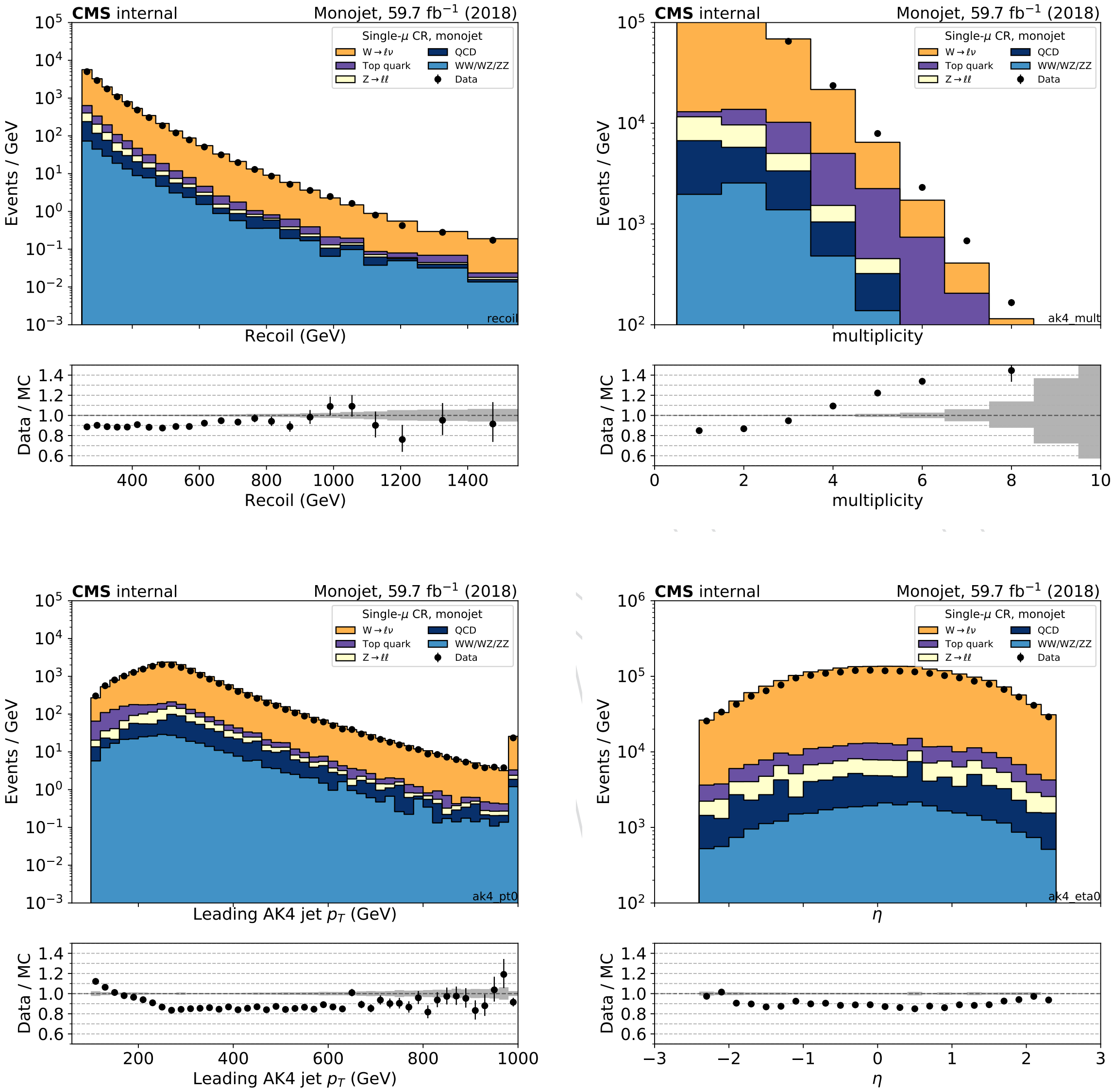

Figure 49: Comparison between 2018 data and monte carlo simulation in the single muon control sample for the recoil distribution, the AK4 jet multiplicity distribution, p_T and η distribution of the leading AK4 jet with the monojet selection. The bottom panel shows the ratio between data and prediction, with the gray band representing the statistical uncertainty due to limited size of the simulated samples.

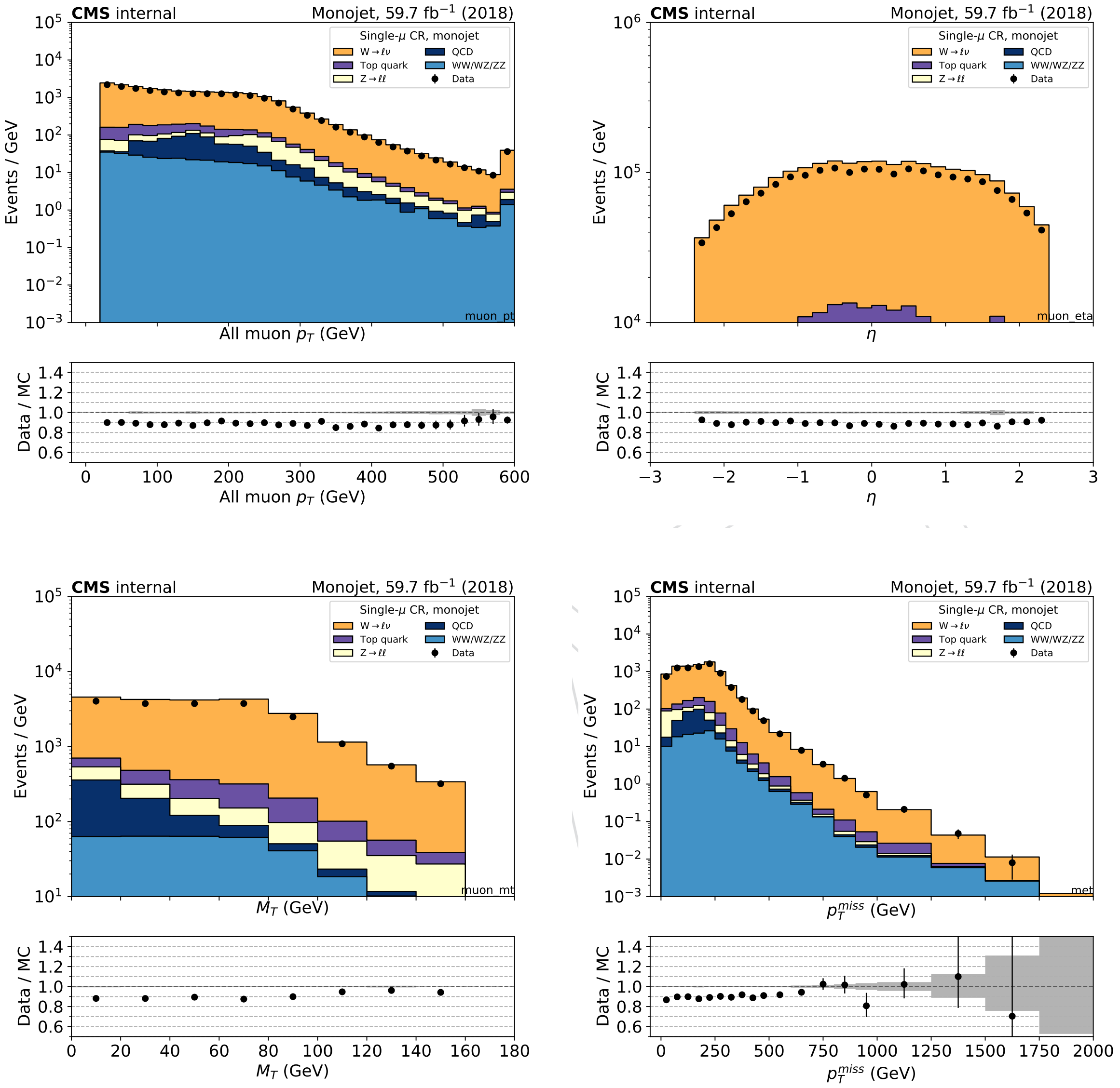

Figure 50: Comparison between 2018 data and monte carlo simulation in the single muon control sample for the p_{T} and η of the muon (top row) and the transverse mass and $p_{\mathrm{T}}^{\mathrm{miss}}$ (bottom row) in the monojet category. Note: The M_{T} distribution is made after N-1 selection while all others are after final selection. The bottom panel shows the ratio between data and prediction, with the gray band representing the statistical uncertainty due to limited size of the simulated samples.

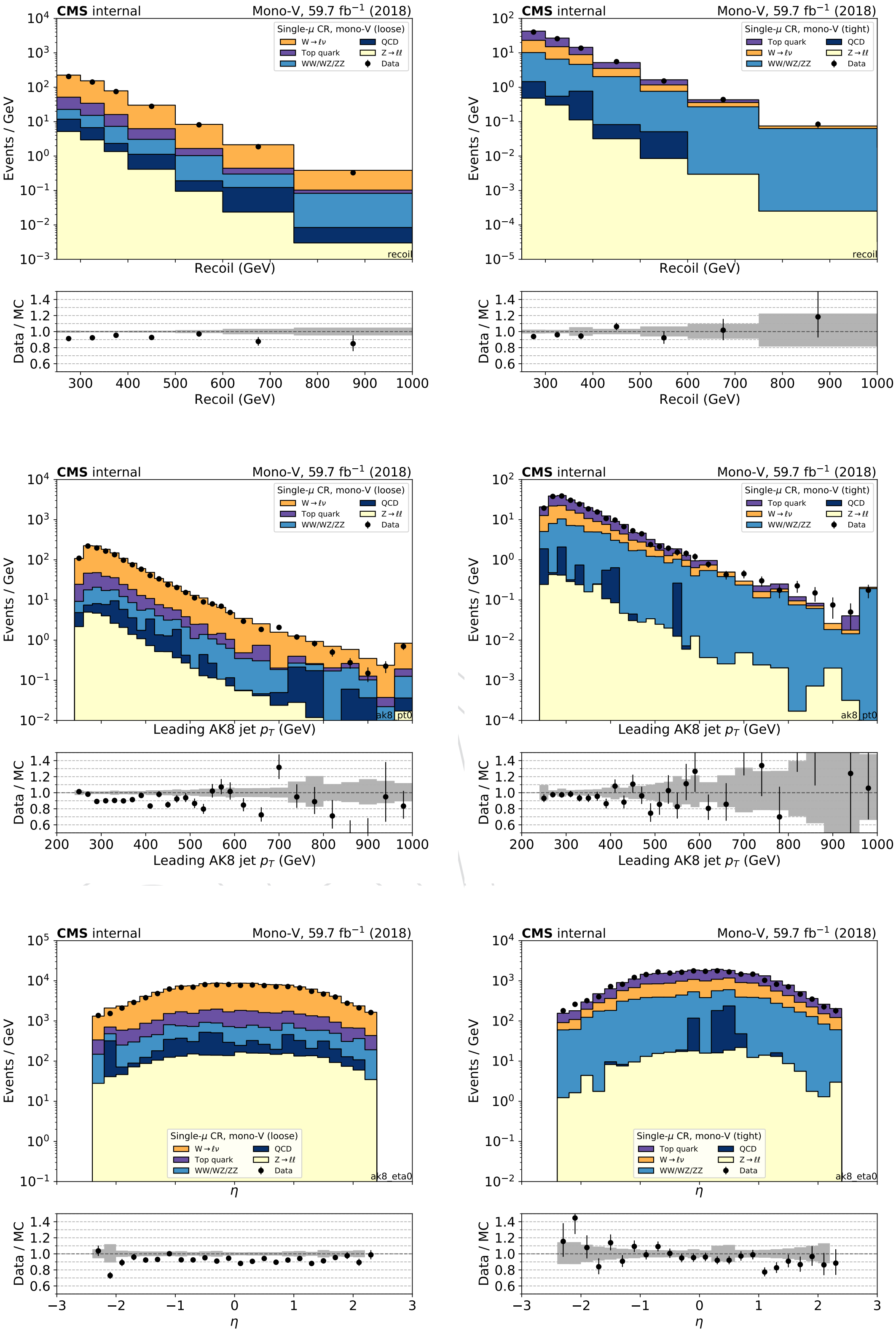

Figure 51: Comparison between 2018 data and monte carlo simulation in the single muon control sample for the recoil distribution, and the AK8 jet p_{T} and η distribution in the low-purity (left) and high-purity (right) regions. The bottom panel shows the ratio between data and prediction, with the gray band representing the statistical uncertainty due to limited size of the simulated samples.

5.3 Single electron control region selection

Events for the single-electron control sample are collected with the single-electron and photon triggers described in Sec. 2. The $p_{\mathrm{T}}^{\mathrm{miss}}$ requirement is replacement an identical requirement on the hadronic recoil, which is defined as the sum of $\vec{p}_{\mathrm{T}}^{\mathrm{miss}}$ and the electron $\vec{p}_{\mathrm{T}}$, and thus corresponds to the distribution of the W p_{T}. The events in the single-electron control sample are required to contain exactly one tightly identified and isolated electron with $p_{\mathrm{T}} > 40$ GeV. In addition, the contamination from QCD multijet events in this control sample is suppressed by requiring $E_{\mathrm{T}}^{\mathrm{miss}} > 50$ GeV and $M_{\mathrm{T}} < 160\,\mathrm{GeV}$.

Figs. 52 and 55 show the distributions of the recoil, the number of jets, and the p_{T} and η distribution of the leading AK4 jet for events in the single-electron control sample for the monojet category in 2017 and 2018 datasets, respectively. Figs. 53 and 56 show the distributions of the leading electron p_{T} and η, as well as the electron-$p_{\mathrm{T}}^{\mathrm{miss}}$ transverse mass, again for 2017 and 2018, respectively.

Figs. 54 and 57 show the distributions of the recoil, as well as the leading AK8 jet p_{T} and η in the low-purity and high-purity mono-V regions in the 2017 and 2018 datasets, respectively.

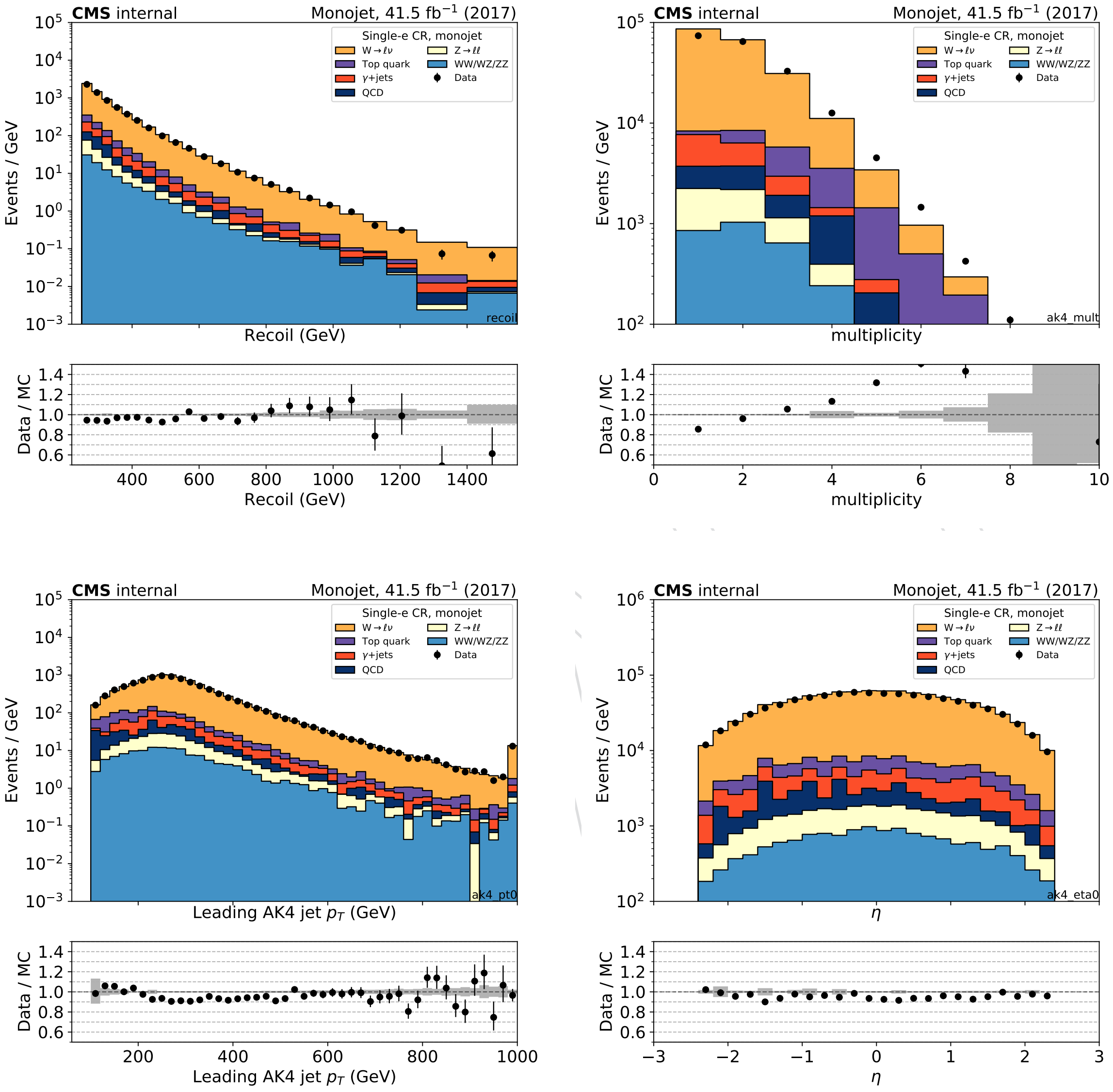

Figure 52: Comparison between 2017 data and monte carlo simulation in the single electron control sample for the recoil distribution, the AK4 jet multiplicity distribution, p_{T} and η distribution of the leading AK4 jet with the monojet selection. The bottom panel shows the ratio between data and prediction, with the gray band representing the statistical uncertainty due to limited size of the simulated samples.

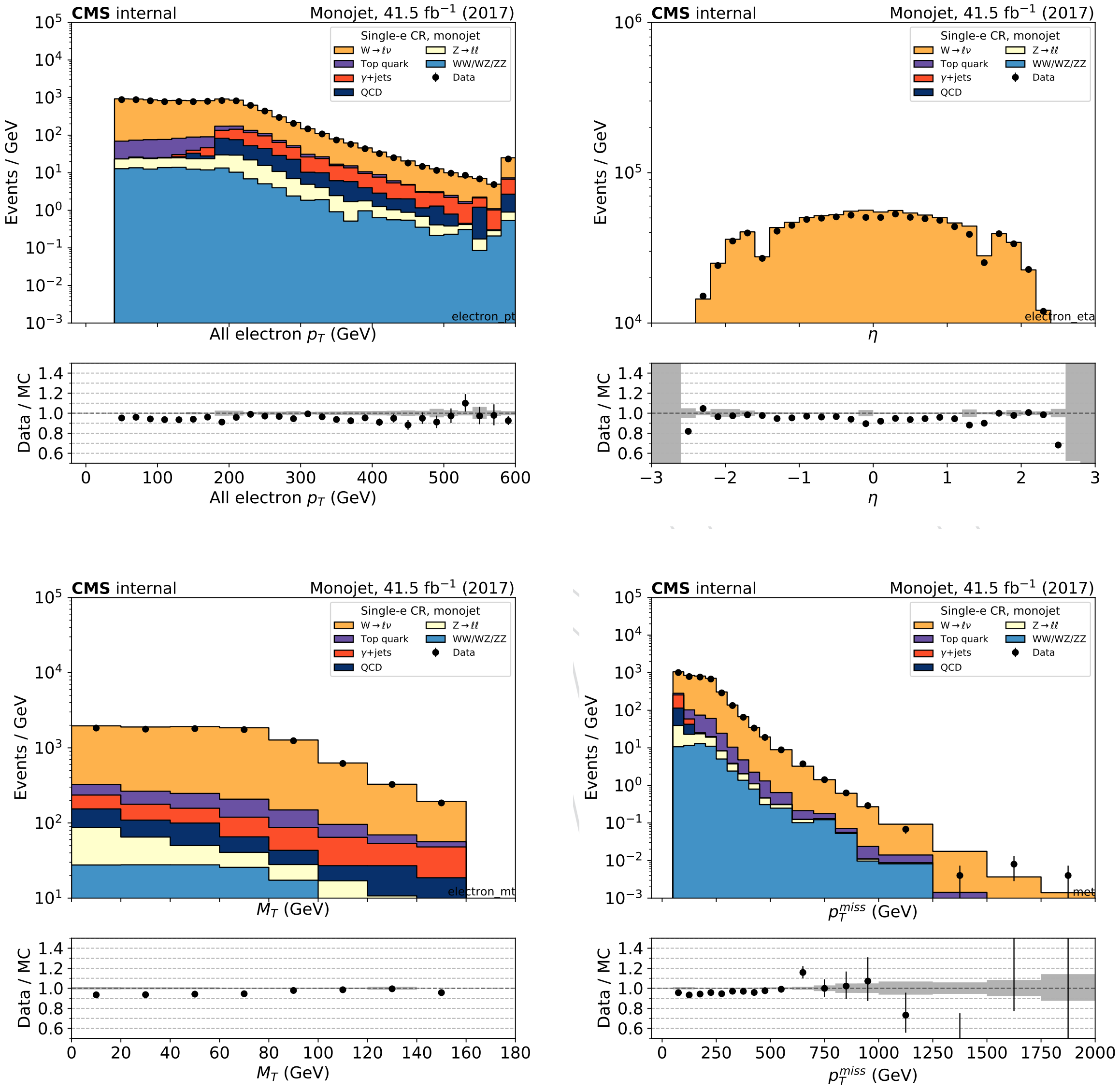

Figure 53: Comparison between 2017 data and monte carlo simulation in the single electron control sample for the p_{T} and η of the electron (top row) and the transverse mass and $p_{\mathrm{T}}^{\mathrm{miss}}$ (bottom row) in the monojet category. The bottom panel shows the ratio between data and prediction, with the gray band representing the statistical uncertainty due to limited size of the simulated samples.

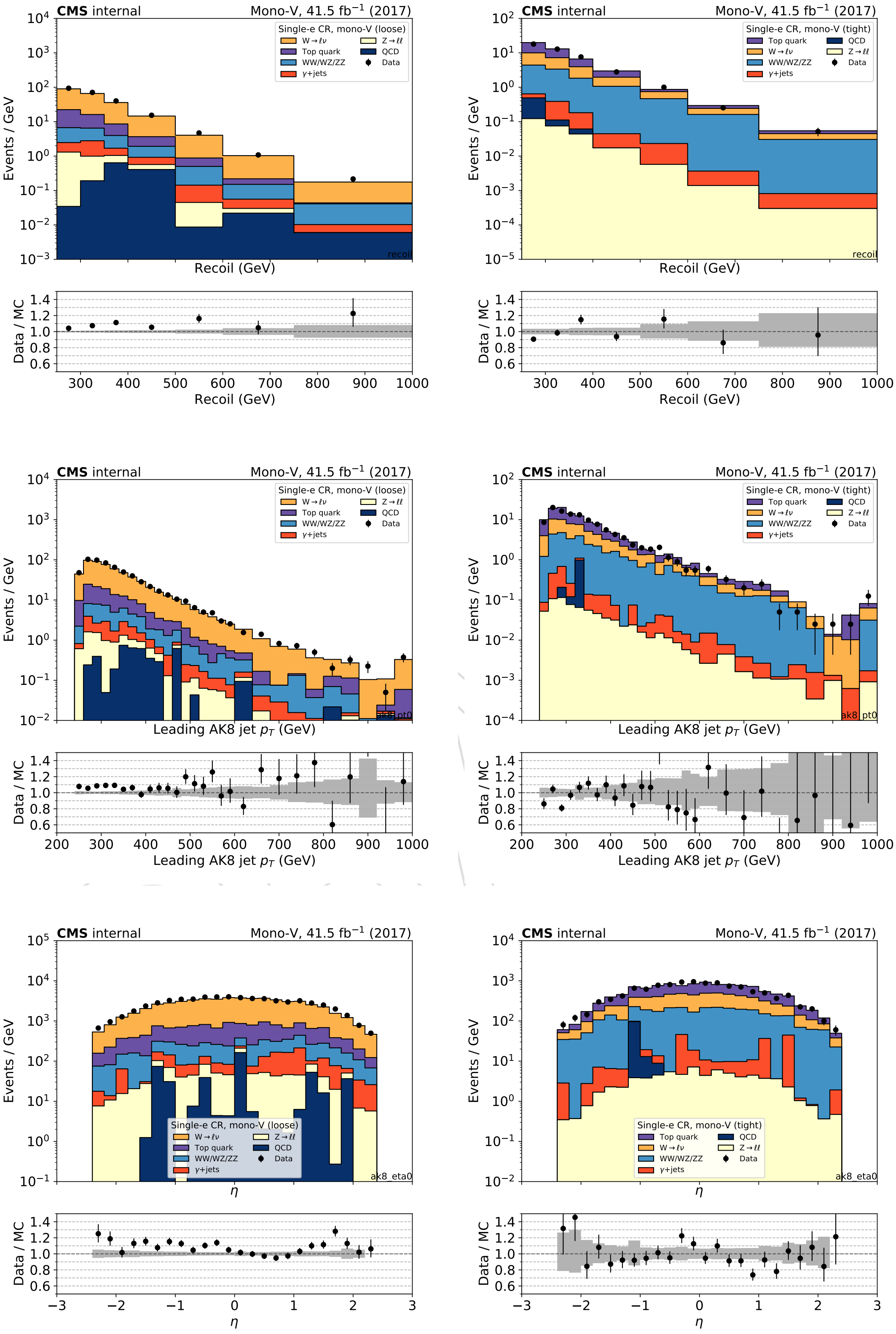

Figure 54: Comparison between 2017 data and monte carlo simulation in the single electron control sample for the recoil distribution, and the AK8 jet p_{T} and η distribution in the low-purity (left) and high-purity (right) regions. The bottom panel shows the ratio between data and prediction, with the gray band representing the statistical uncertainty due to limited size of the simulated samples.

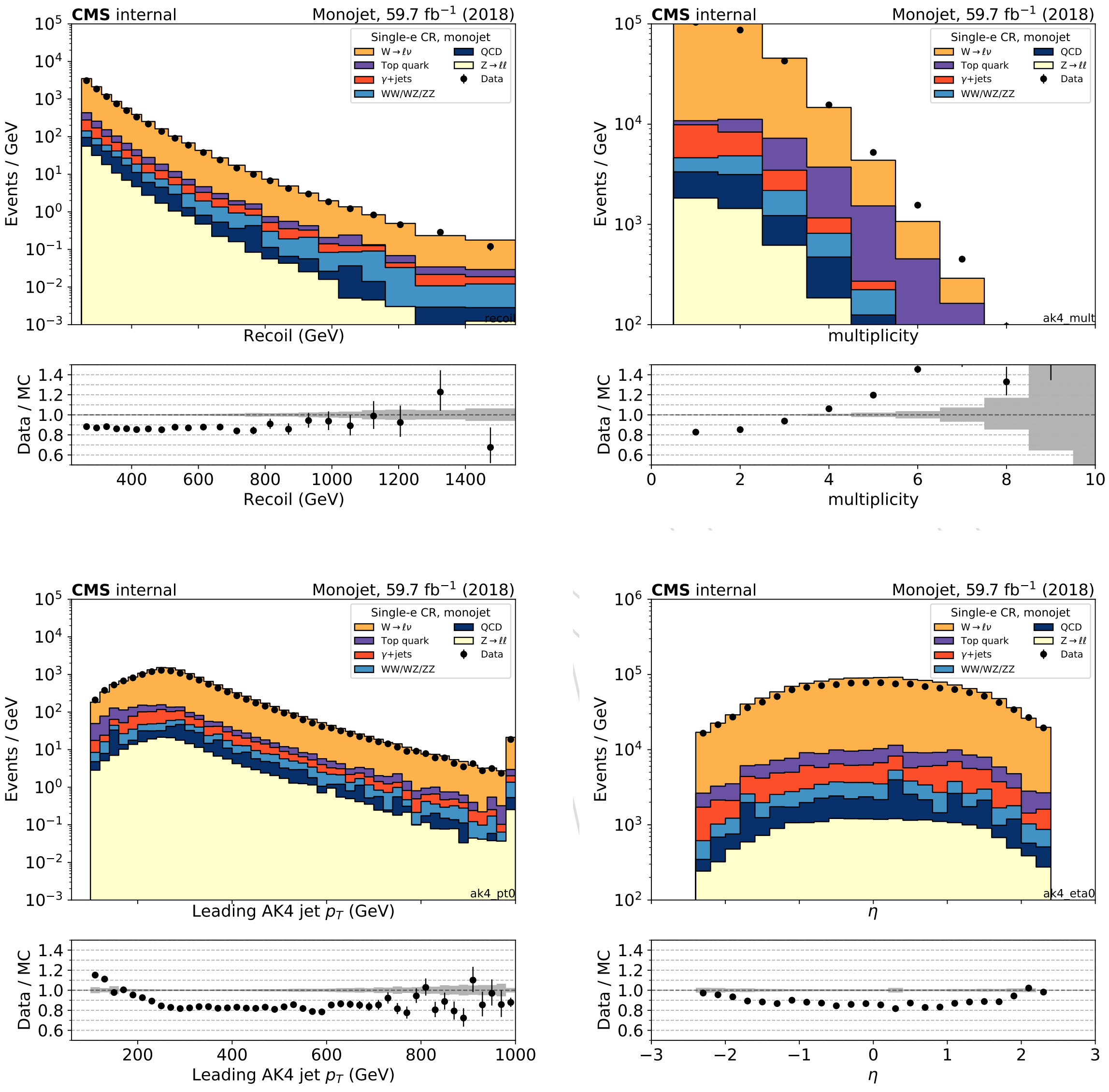

Figure 55: Comparison between 2018 data and monte carlo simulation in the single electron control sample for the recoil distribution, the AK4 jet multiplicity distribution, p_{T} and η distribution of the leading AK4 jet with the monojet selection. The bottom panel shows the ratio between data and prediction, with the gray band representing the statistical uncertainty due to limited size of the simulated samples.

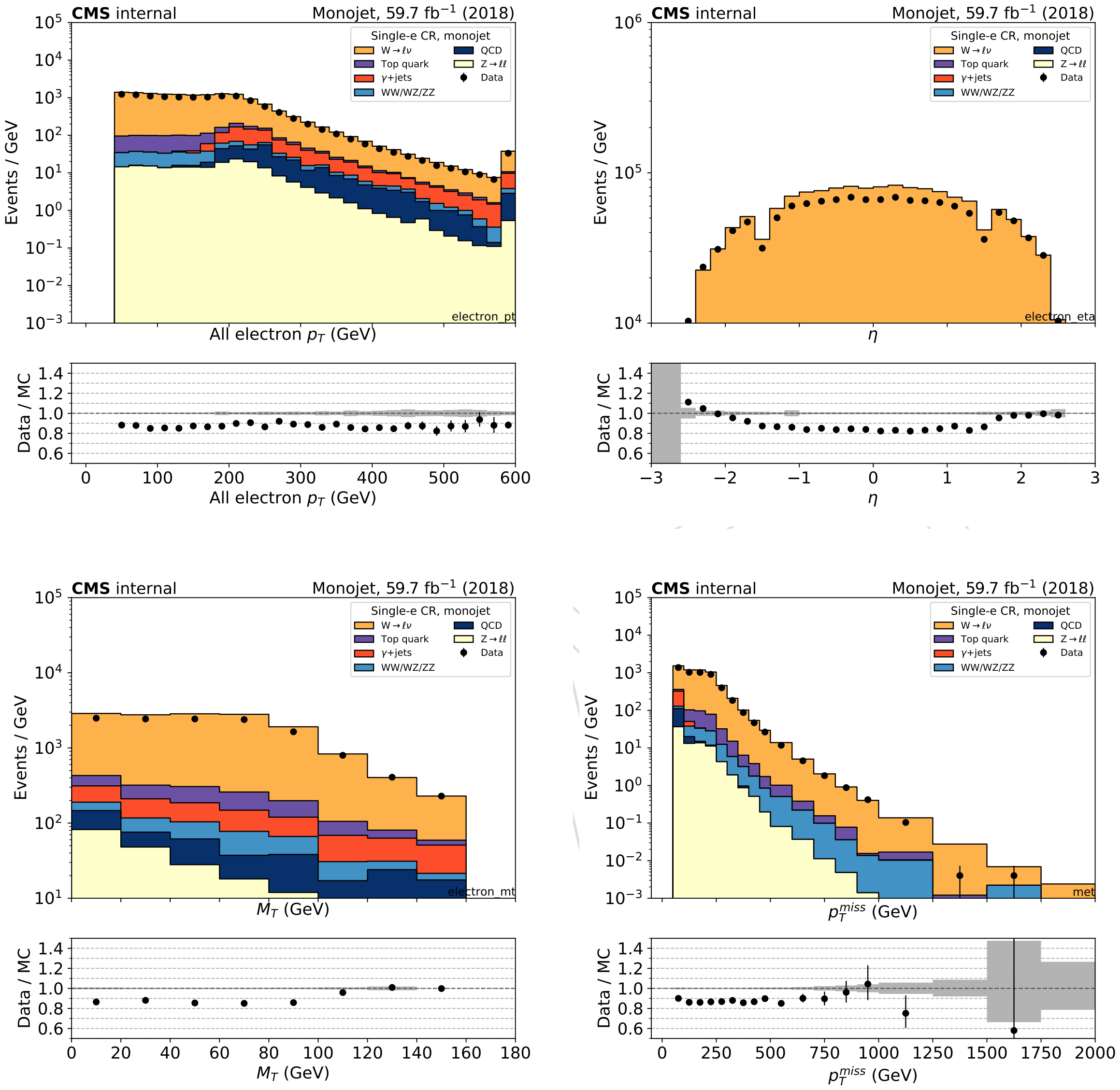

Figure 56: Comparison between 2017 data and monte carlo simulation in the single electron control sample for the p_T and η of the electron (top row) and the transverse mass and p_T^{miss} (bottom row) in the monojet category. Note: The M_T distribution is made after N-1 selection while all others are after final selection. The bottom panel shows the ratio between data and prediction, with the gray band representing the statistical uncertainty due to limited size of the simulated samples.

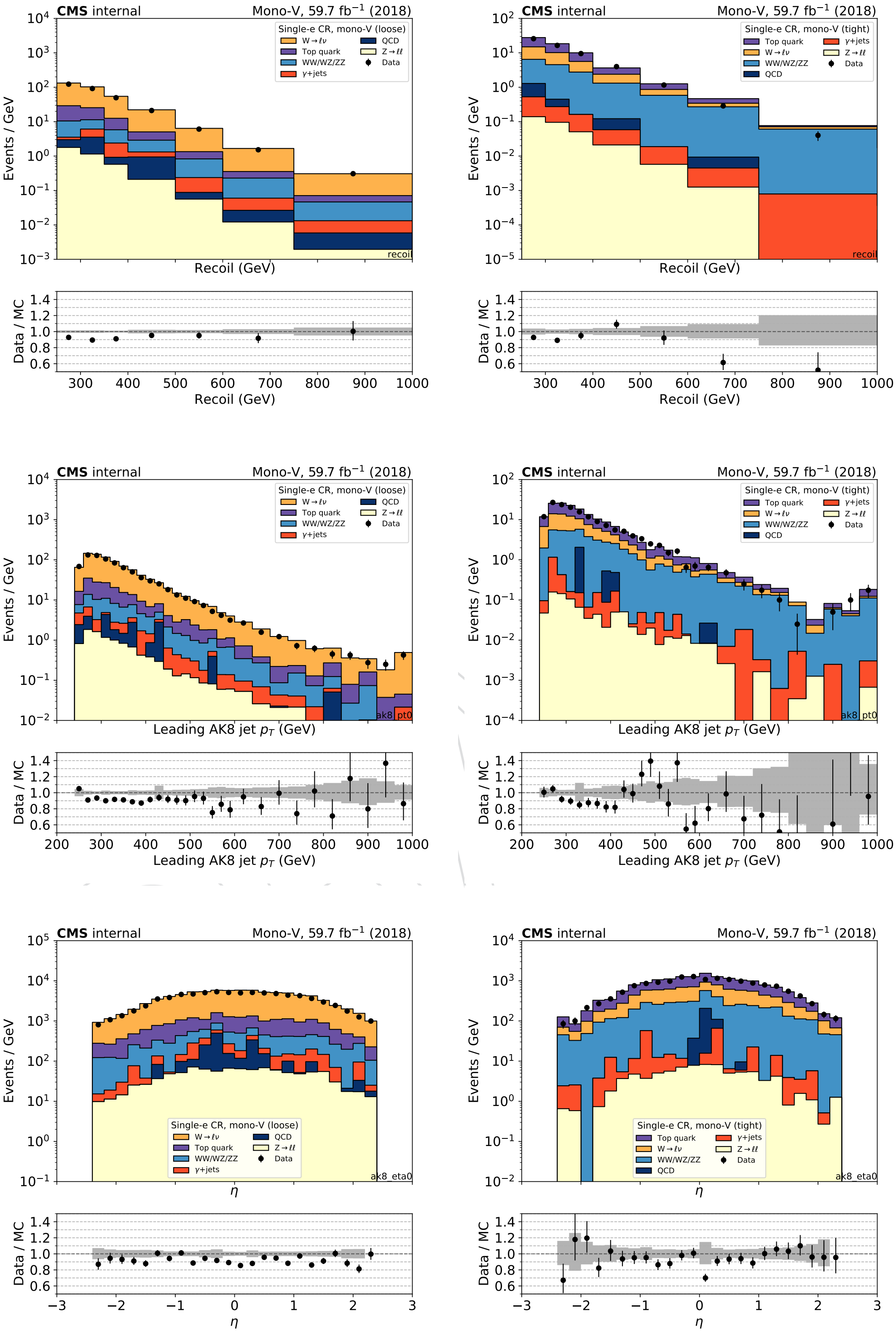

Figure 57: Comparison between 2018 data and monte carlo simulation in the single electron control sample for the recoil distribution, and the AK8 jet p_T and η distribution in the low-purity (left) and high-purity (right) regions. The bottom panel shows the ratio between data and prediction, with the gray band representing the statistical uncertainty due to limited size of the simulated samples.

5.4 Double muon control region selection

Double-muon control sample events are selected using full signal region criteria of monojet and mono-V categories with the exception of the muon veto. In the double-muon control sample, events are selected requiring leading (subleading) muon p_{T} greater than 20 (10) GeV and an invariant mass in the range 60 to 120 GeV, compatible with a Z boson decay. At least one of the two muons is required to pass the tight candidate definition. Events are rejected if there is an additional loose muon or electron with $p_{\mathrm{T}} > 10\,\mathrm{GeV}$. The SR $p_{\mathrm{T}}^{\mathrm{miss}}$ requirement is replacement an identical requirement on the hadronic recoil, which is defined as the sum of $\vec{p}_{\mathrm{T}}^{\mathrm{miss}}$ and the muon $\vec{p}_{\mathrm{T}}$, and thus corresponds to the distribution of the Z p_{T} smeared with the $p_{\mathrm{T}}^{\mathrm{miss}}$ resolution.

Figs. 58 and 61 shows the distributions of the recoil, the number of jets, and the p_{T} and η distribution of the leading AK4 jet for events in the double-muon control sample for the monojet category in 2017 and 2018 datasets, respectively. Figs. 59 and 62 show the distributions of the leading muon p_{T} and η, as well as the dimuon mass and p_{T}, again for 2017 and 2018, respectively.

Figs. 60 and 63 show the distributions of the recoil, as well as the leading AK8 jet p_{T} and η in the low-purity and high-purity mono-V regions in the 2017 and 2018 datasets, respectively.

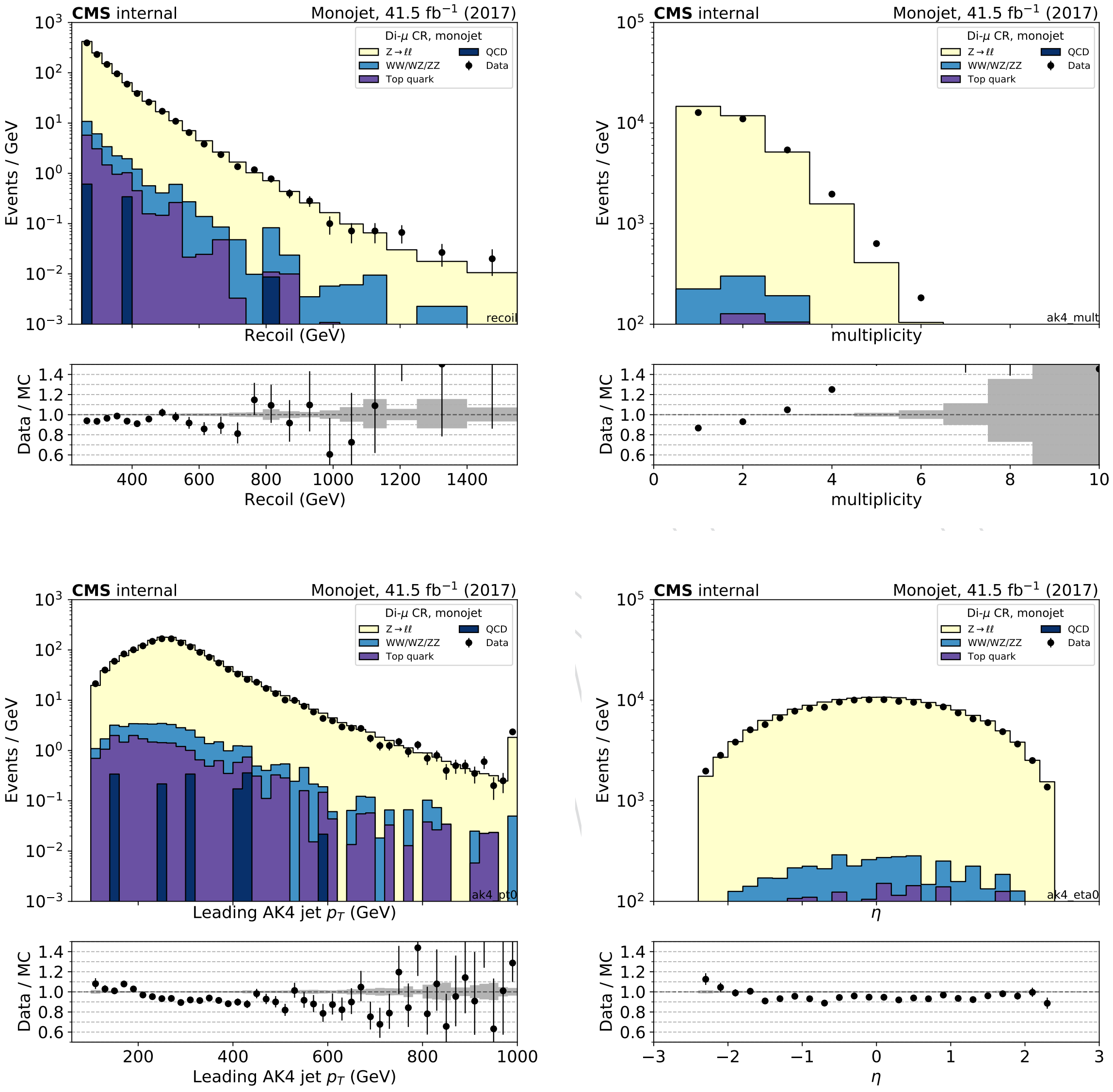

Figure 58: Comparison between 2017 data and monte carlo simulation in the double muon control sample for the recoil distribution, the AK4 jet multiplicity distribution, p_T and η distribution of the leading AK4 jet with the monojet selection. The bottom panel shows the ratio between data and prediction, with the gray band representing the statistical uncertainty due to limited size of the simulated samples.

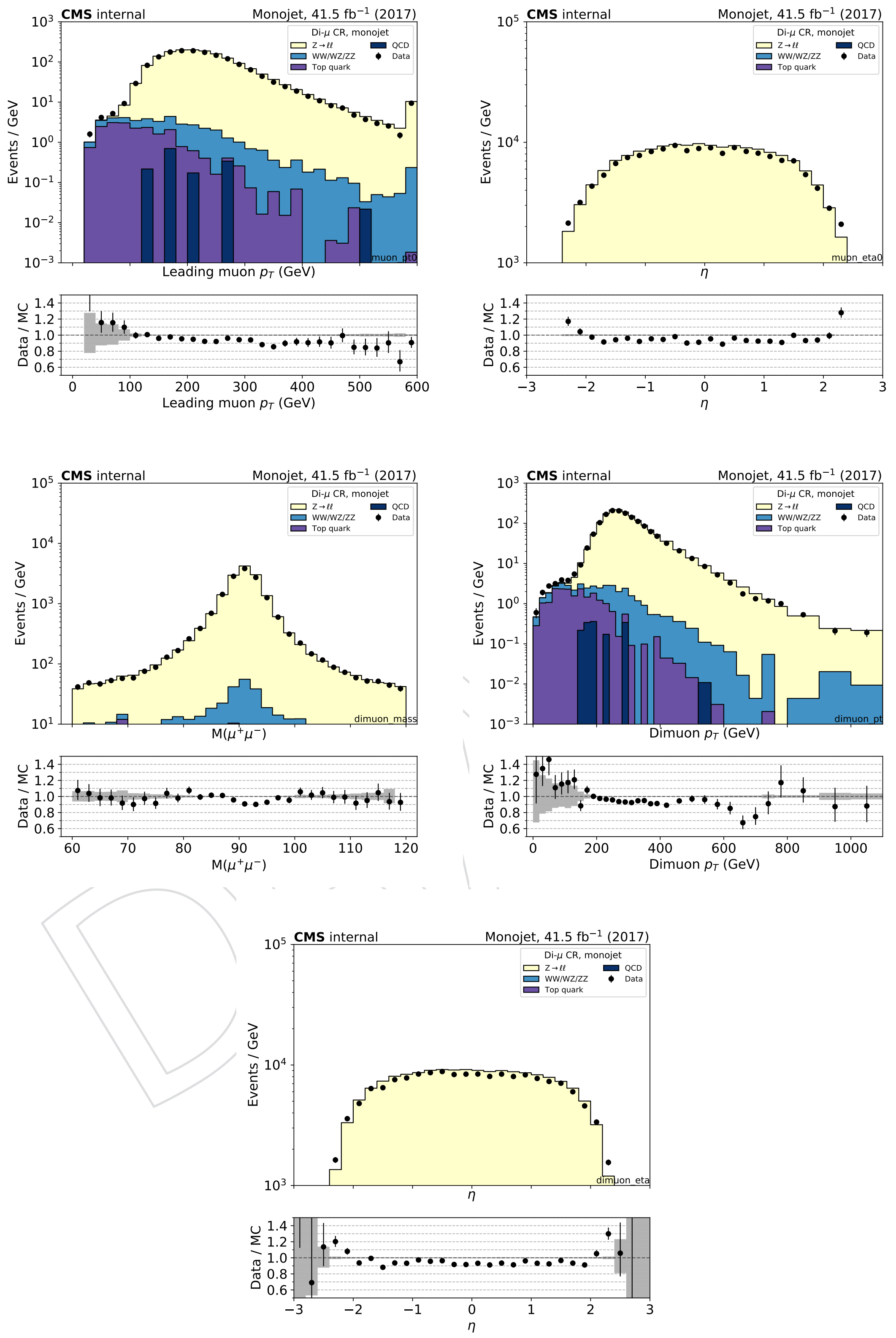

Figure 59: Comparison between 2017 data and monte carlo simulation in the double muon control sample for the p_{T} and η of the leading muon and the transverse mass, p_{T}, and η of the dimuon candidate with the monojet selection. The bottom panel shows the ratio between data and prediction, with the gray band representing the statistical uncertainty due to limited size of the simulated samples.

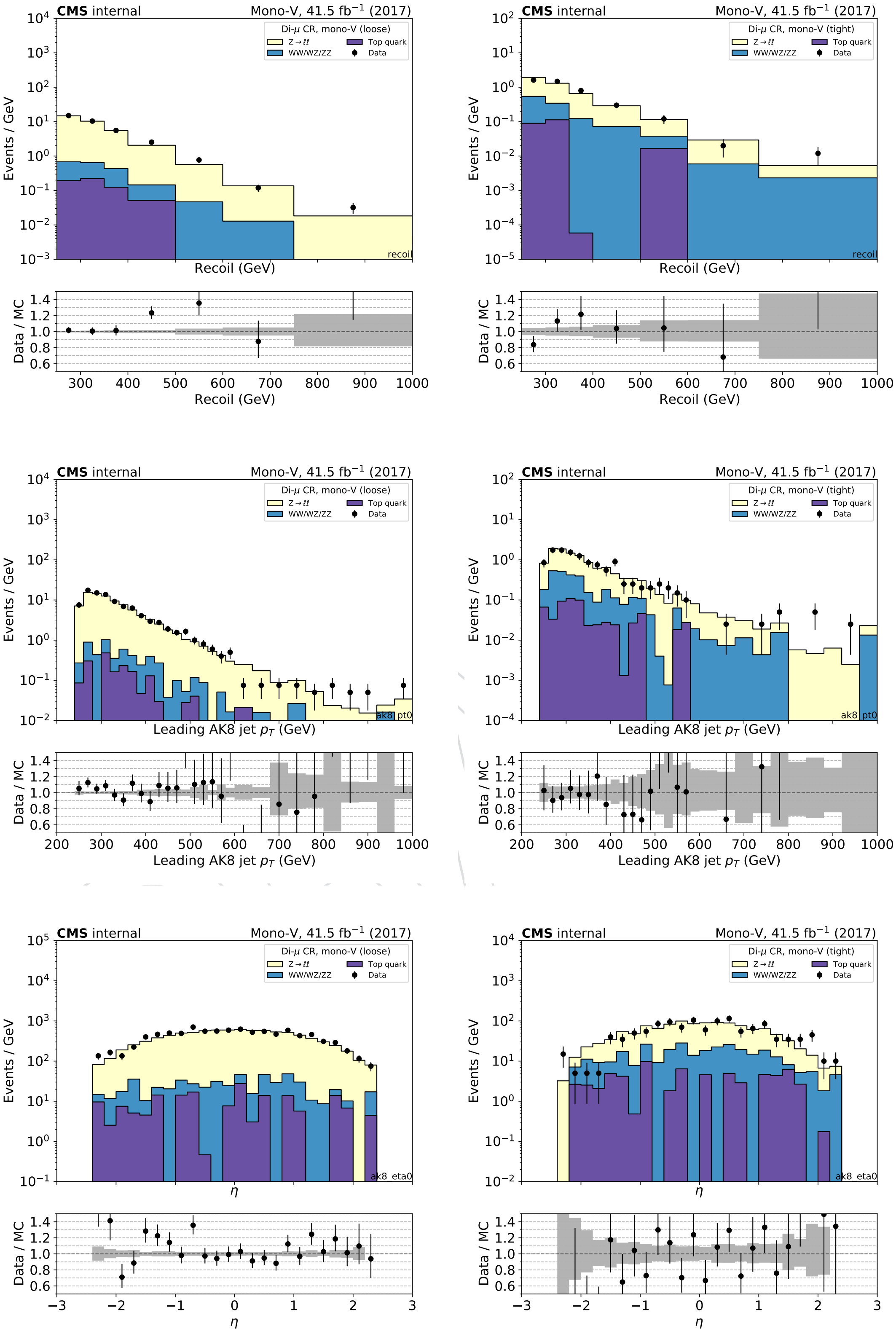

Figure 60: Comparison between 2017 data and monte carlo simulation in the double muon control sample for the recoil distribution, and the AK8 jet p_T and η distribution in the low-purity (left) and high-purity (right) regions. The bottom panel shows the ratio between data and prediction, with the gray band representing the statistical uncertainty due to limited size of the simulated samples.

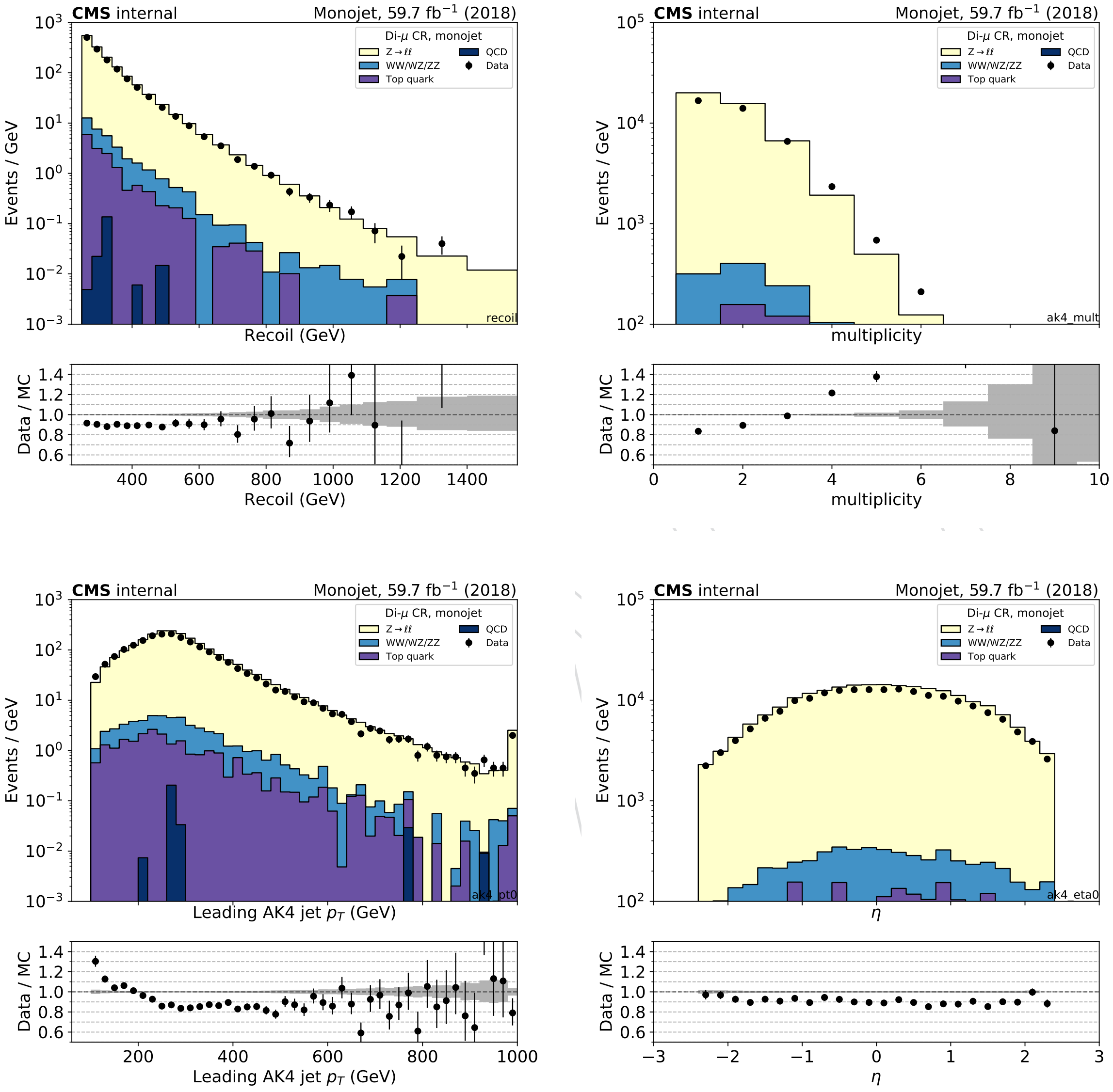

Figure 61: Comparison between 2018 data and monte carlo simulation in the double muon control sample for the recoil distribution, the AK4 jet multiplicity distribution, p_T and η distribution of the leading AK4 jet with the monojet selection. The bottom panel shows the ratio between data and prediction, with the gray band representing the statistical uncertainty due to limited size of the simulated samples.

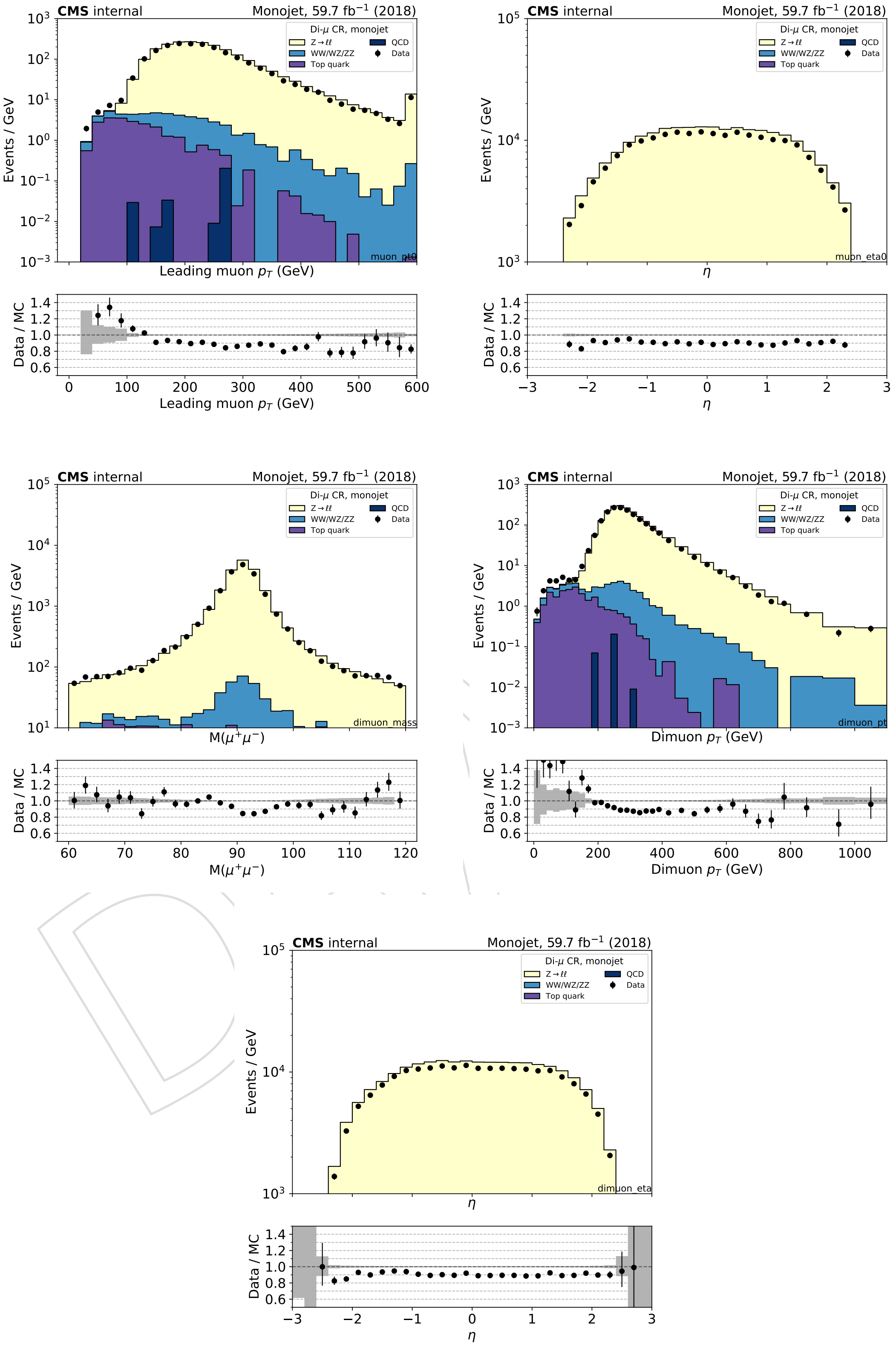

Figure 62: Comparison between 2018 data and monte carlo simulation in the double muon control sample for the p_T and η of the leading muon and the transverse mass, p_T, and η of the dimuon candidate with the monojet selection. The bottom panel shows the ratio between data and prediction, with the gray band representing the statistical uncertainty due to limited size of the simulated samples.

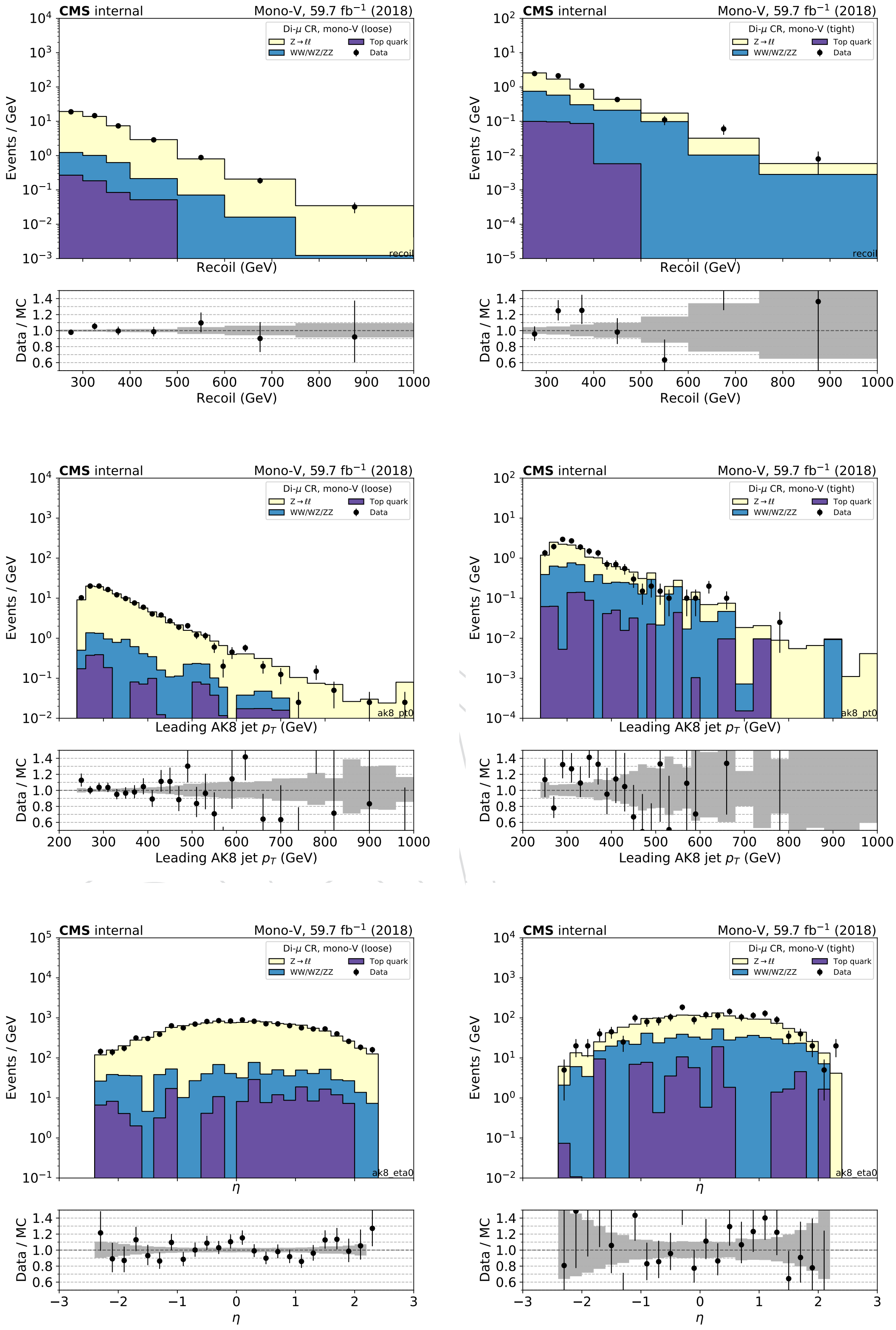

Figure 63: Comparison between 2018 data and monte carlo simulation in the double muon control sample for the recoil distribution, and the AK8 jet p_T and η distribution in the low-purity (left) and high-purity (right) regions. The bottom panel shows the ratio between data and prediction, with the gray band representing the statistical uncertainty due to limited size of the simulated samples.

5.5 Double electron control region selection

Events for the double-electron control sample are collected with the single-electron and photon triggers described in Sec. 2. In the offline analysis, events in the dielectron control sample are required to contain exactly two oppositely charged electrons with leading (trailing) electron p_{T} greater than 40 (10) GeV, with at least one of the two passing the tight candidate definition. The SR $p_{\mathrm{T}}^{\mathrm{miss}}$ requirement is replacement an identical requirement on the hadronic recoil, which is defined as the sum of $\vec{p}_{\mathrm{T}}^{\mathrm{miss}}$ and the muon $\vec{p}_{\mathrm{T}}$, and thus corresponds to the distribution of the Z p_{T} smeared with the $p_{\mathrm{T}}^{\mathrm{miss}}$ resolution. Similar to the dimuon control sample case, the invariant mass of the dielectron system is required to be between 60 and 120 GeV to be consistent with a Z boson decay.

Figs. 64 and 67 shows the distributions of the recoil, the number of jets, and the p_{T} and η distribution of the leading AK4 jet for events in the double-electron control sample for the monojet category in 2017 and 2018 datasets, respectively. Figs. 65 and 68 show the distributions of the leading electron p_{T} and η, as well as the dielectron mass and p_{T}, again for 2017 and 2018, respectively.

Figs. 66 and 69 show the distributions of the recoil, as well as the leading AK8 jet p_{T} and η in the low-purity and high-purity mono-V regions in the 2017 and 2018 datasets, respectively.

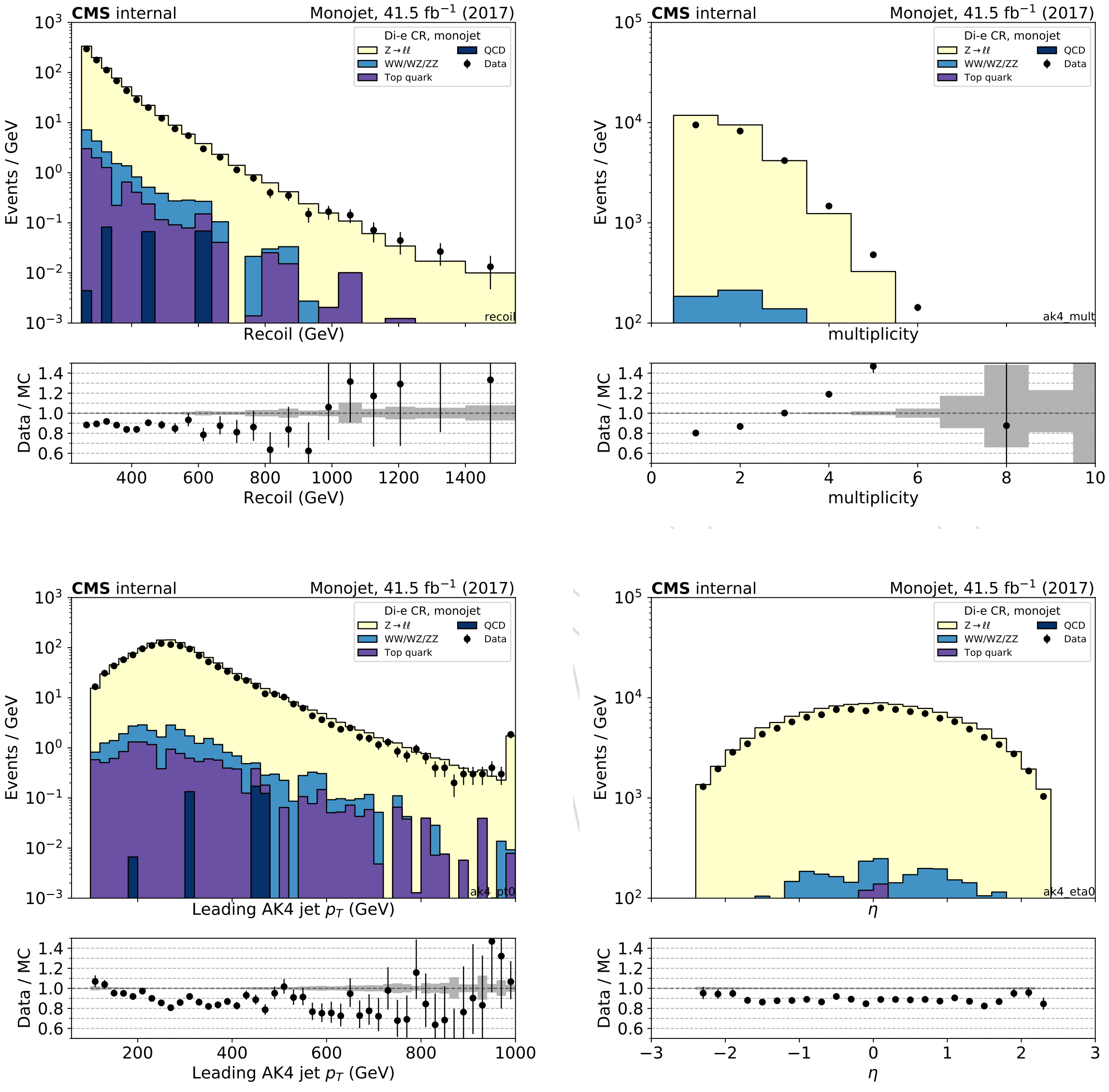

Figure 64: Comparison between 2017 data and monte carlo simulation in the double electron control sample for the recoil distribution, the AK4 jet multiplicity distribution, p_T and η distribution of the leading AK4 jet with the monojet selection. The bottom panel shows the ratio between data and prediction, with the gray band representing the statistical uncertainty due to limited size of the simulated samples.

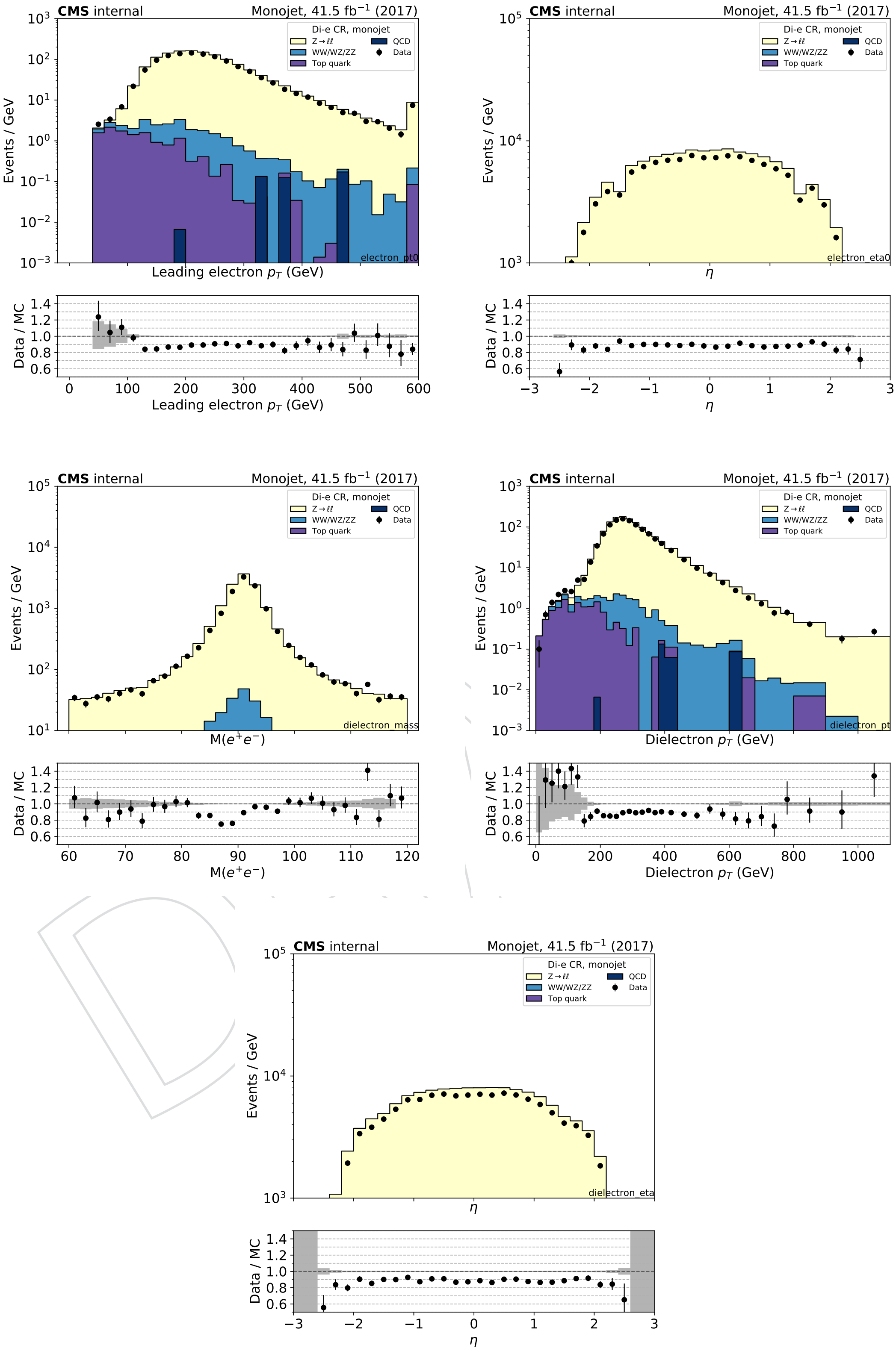

Figure 65: Comparison between 2017 data and monte carlo simulation in the double electron control sample for the p_T and η of the leading electron and the transverse mass, p_T, and η of the dielectron candidate with the monojet selection. The bottom panel shows the ratio between data and prediction, with the gray band representing the statistical uncertainty due to limited size of the simulated samples.

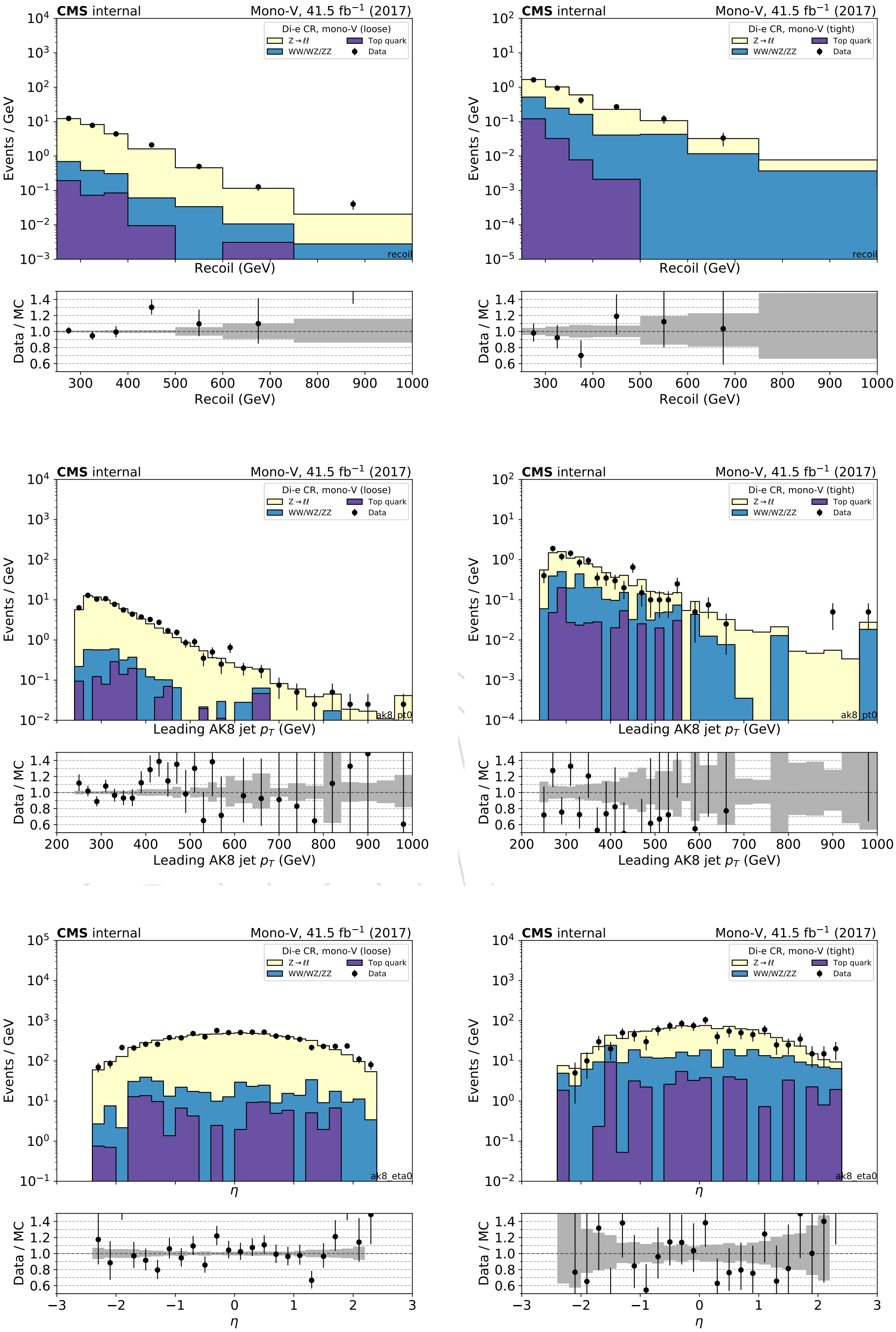

Figure 66: Comparison between 2017 data and monte carlo simulation in the double electron control sample for the recoil distribution, and the AK8 jet p_T and η distribution in the low-purity (left) and high-purity (right) regions. The bottom panel shows the ratio between data and prediction, with the gray band representing the statistical uncertainty due to limited size of the simulated samples.

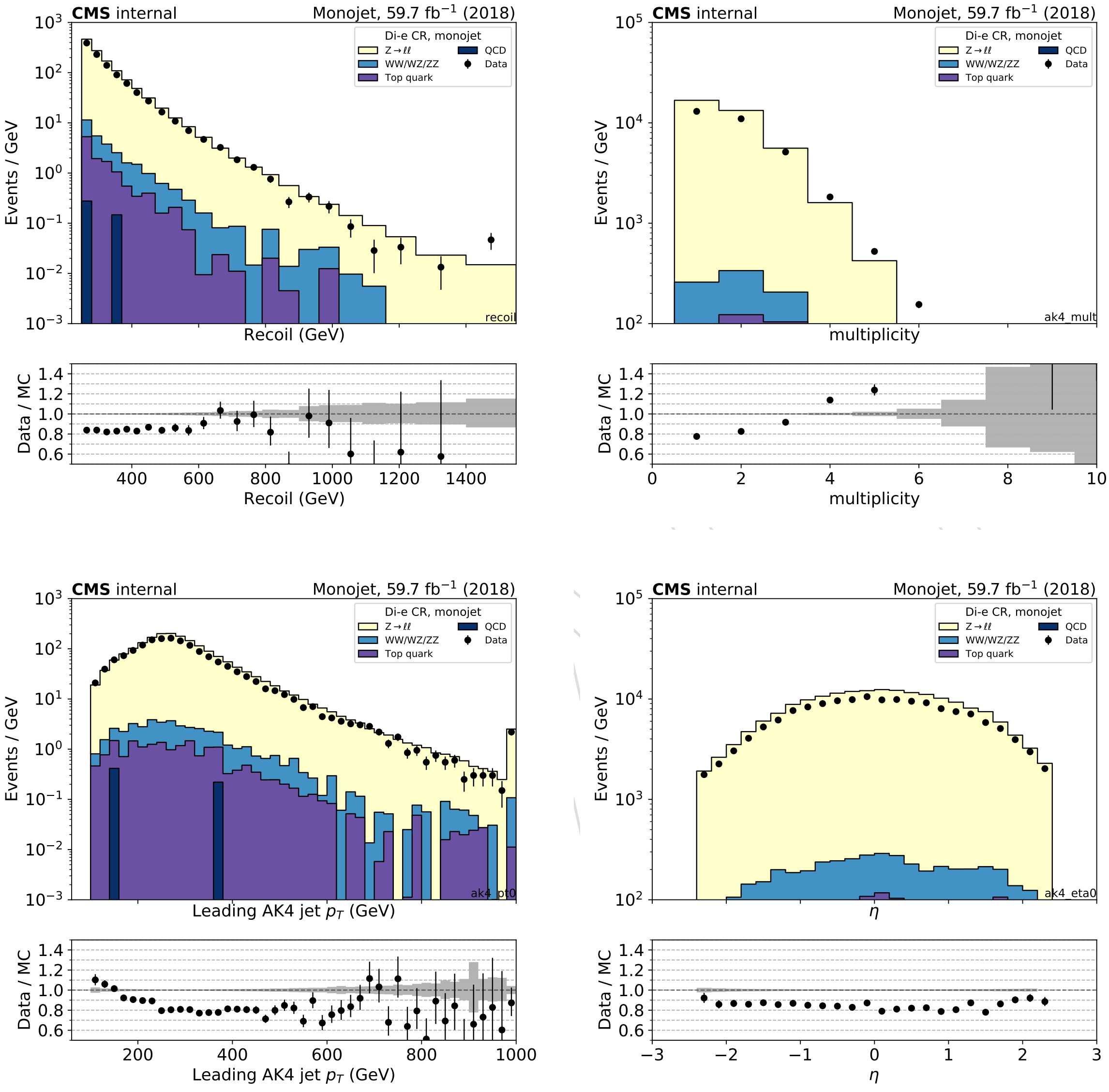

Figure 67: Comparison between 2018 data and monte carlo simulation in the double electron control sample for the recoil distribution, the AK4 jet multiplicity distribution, p_T and η distribution of the leading AK4 jet with the monojet selection. The bottom panel shows the ratio between data and prediction, with the gray band representing the statistical uncertainty due to limited size of the simulated samples.

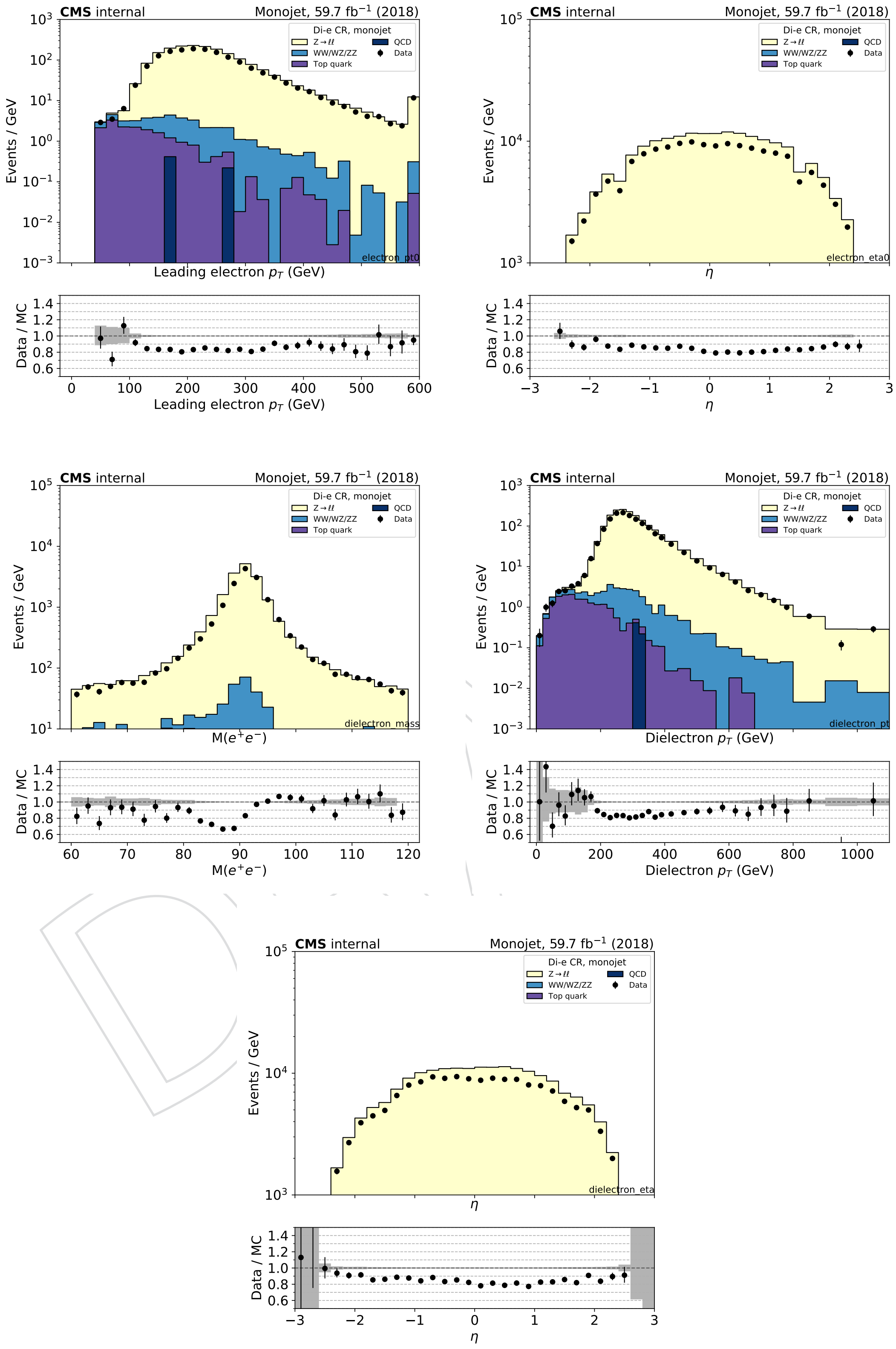

Figure 68: Comparison between 2018 data and monte carlo simulation in the double electron control sample for the p_{T} and η of the leading electron and the transverse mass, p_{T}, and η of the dielectron candidate with the monojet selection. The bottom panel shows the ratio between data and prediction, with the gray band representing the statistical uncertainty due to limited size of the simulated samples.

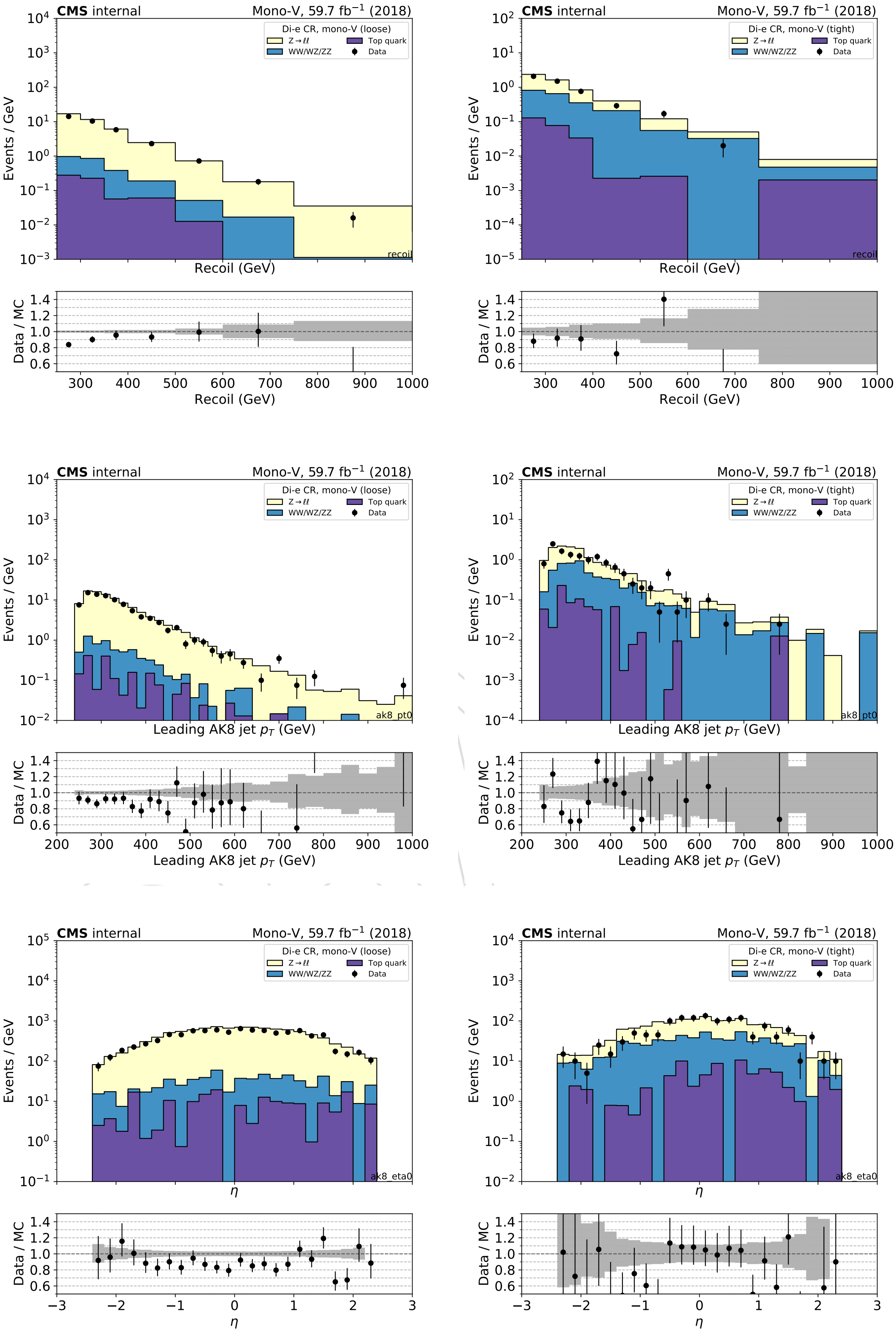

Figure 69: Comparison between 2018 data and monte carlo simulation in the double electron control sample for the recoil distribution, and the AK8 jet p_T and η distribution in the low-purity (left) and high-purity (right) regions. The bottom panel shows the ratio between data and prediction, with the gray band representing the statistical uncertainty due to limited size of the simulated samples.

5.6 Photon control region

The $\gamma+$jets control sample is selected using events with one high-p_{T} photon collected using single-photon triggers with a p_{T} threshold of 200 GeV. The photon is required to have $p_{\mathrm{T}} >$ 230 GeV and to pass tight identification and isolation criteria, to ensure a high trigger efficiency of 95% and an efficiency difference between data and simulation of less than one percent.

Figs. 70 and 70 show the distributions of the recoil, the number of jets, p_{T} and eta distribution of the leading AK4 jet for events in the photon control sample for the monojet category in the 2017 and 2018 datasets, respectively. Similarly, Figs. 71 and 74 show the distributions of the photon p_{T} and η.

Figs. 72 and 75 show the distributions of the recoil, as well as the leading AK8 jet p_{T} and η in the low-purity and high-purity mono-V regions in the 2017 and 2018 datasets, respectively.

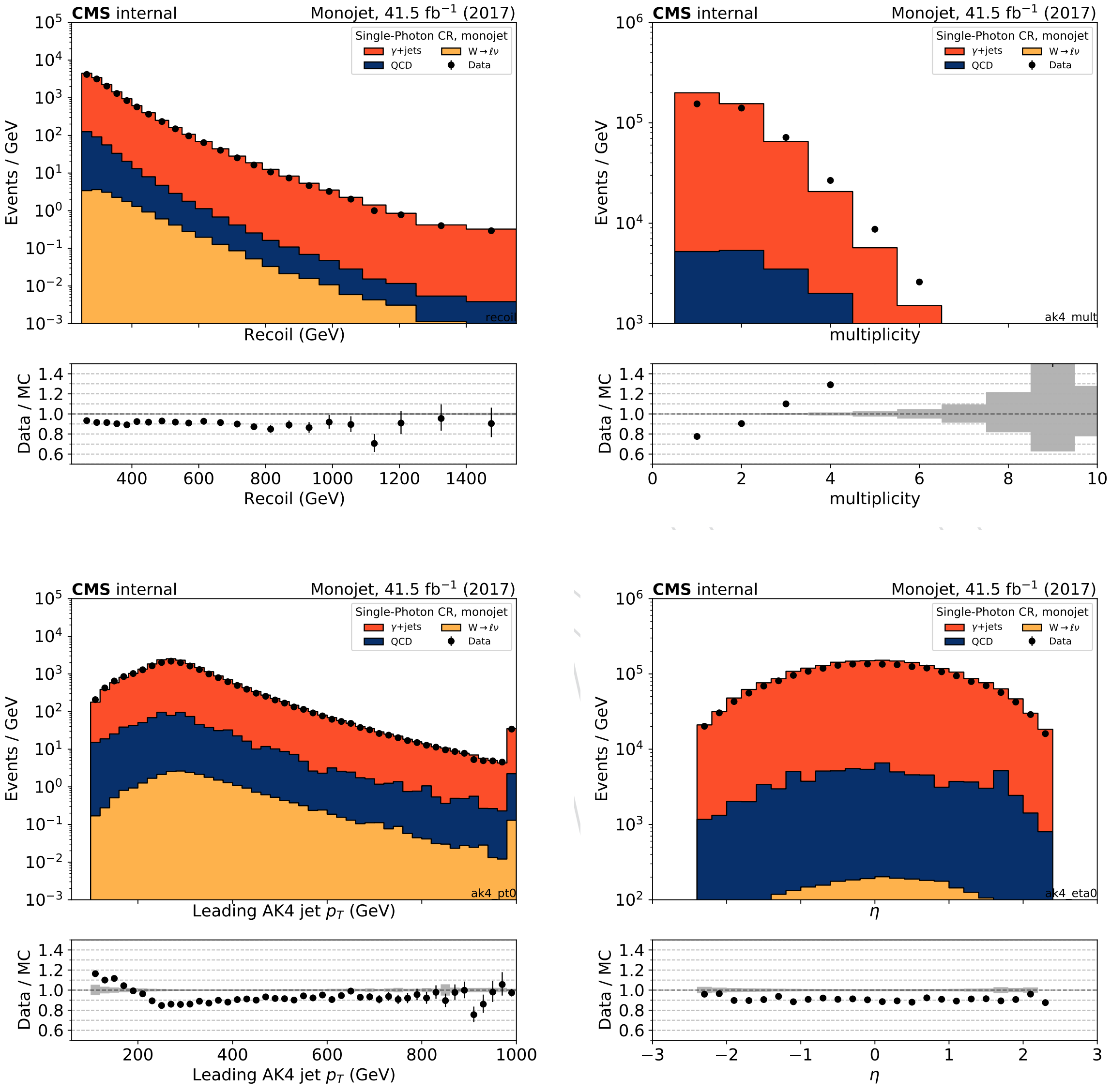

Figure 70: Comparison between 2017 data and monte carlo simulation in the photon control sample for the recoil distribution, the AK4 jet multiplicity distribution, p_{T} and η distribution of the leading AK4 jet with the monojet selection. The bottom panel shows the ratio between data and prediction, with the gray band representing the statistical uncertainty due to limited size of the simulated samples.

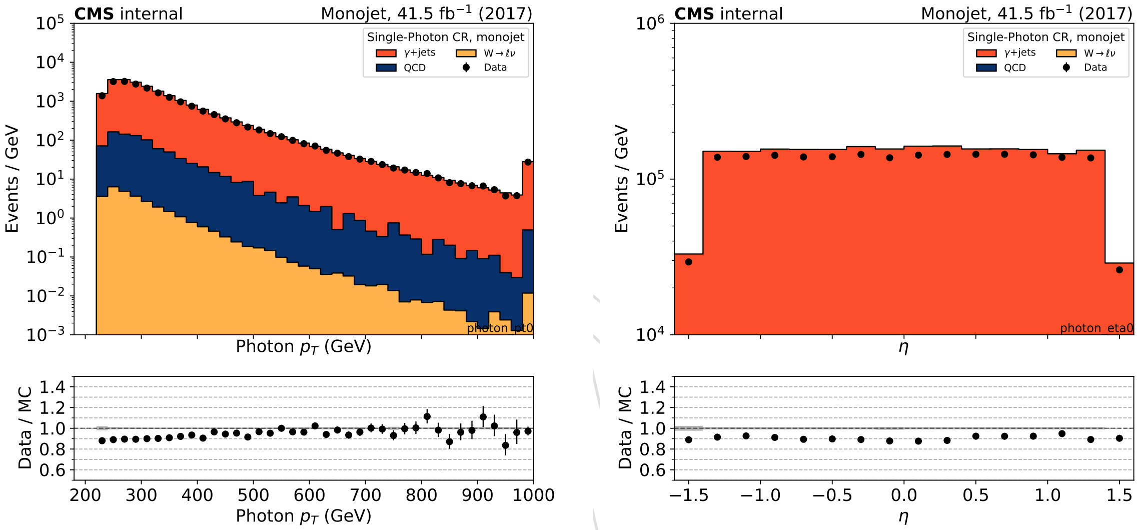

Figure 71: Comparison between 2017 data and monte carlo simulation in the photon control sample for the p_{T} and η of the leading photon with the monojet selection. The bottom panel shows the ratio between data and prediction, with the gray band representing the statistical uncertainty due to limited size of the simulated samples.

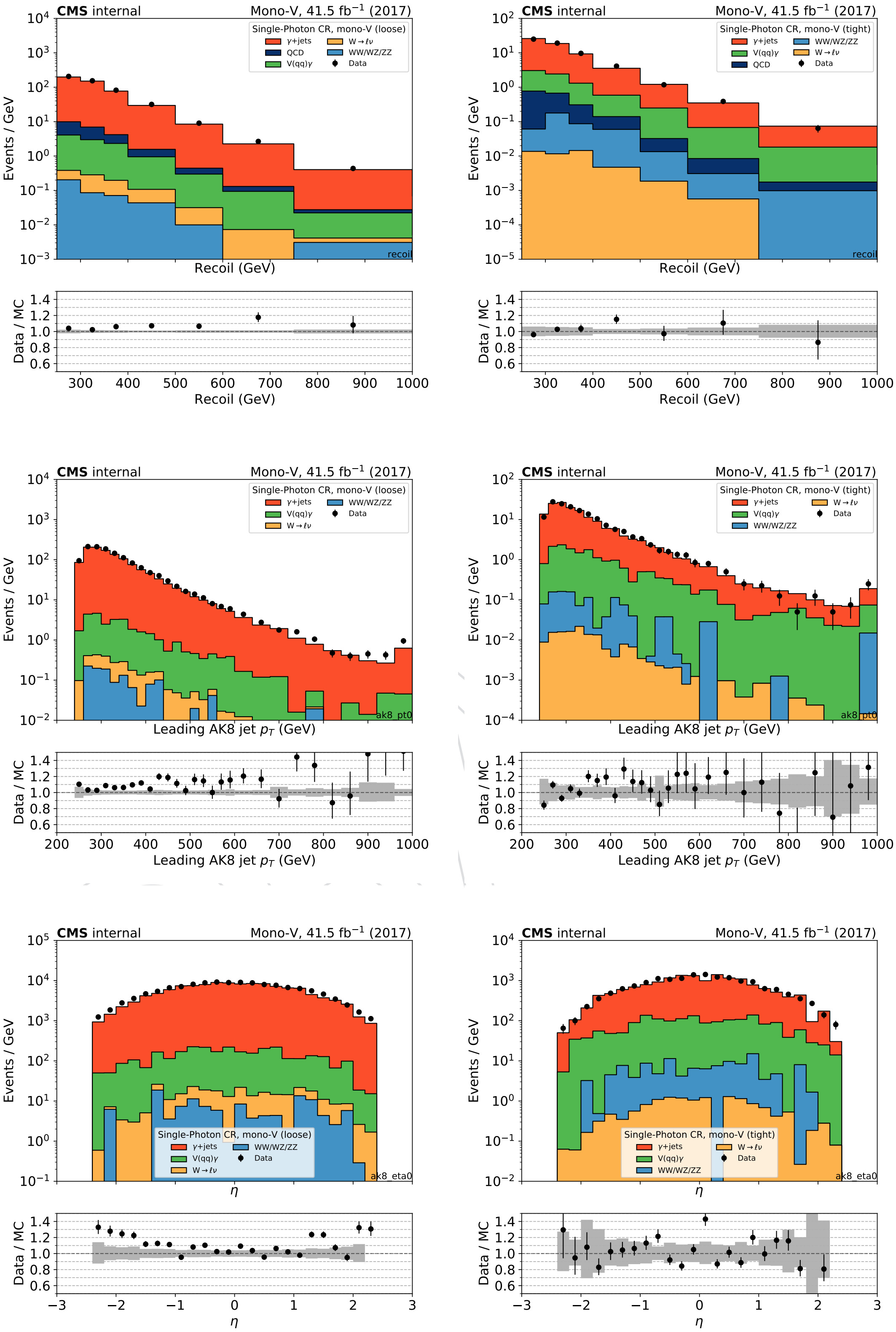

Figure 72: Comparison between 2017 data and monte carlo simulation in the photon control sample for the recoil distribution, and the AK8 jet p_T and η distribution in the low-purity (left) and high-purity (right) regions. The bottom panel shows the ratio between data and prediction, with the gray band representing the statistical uncertainty due to limited size of the simulated samples.

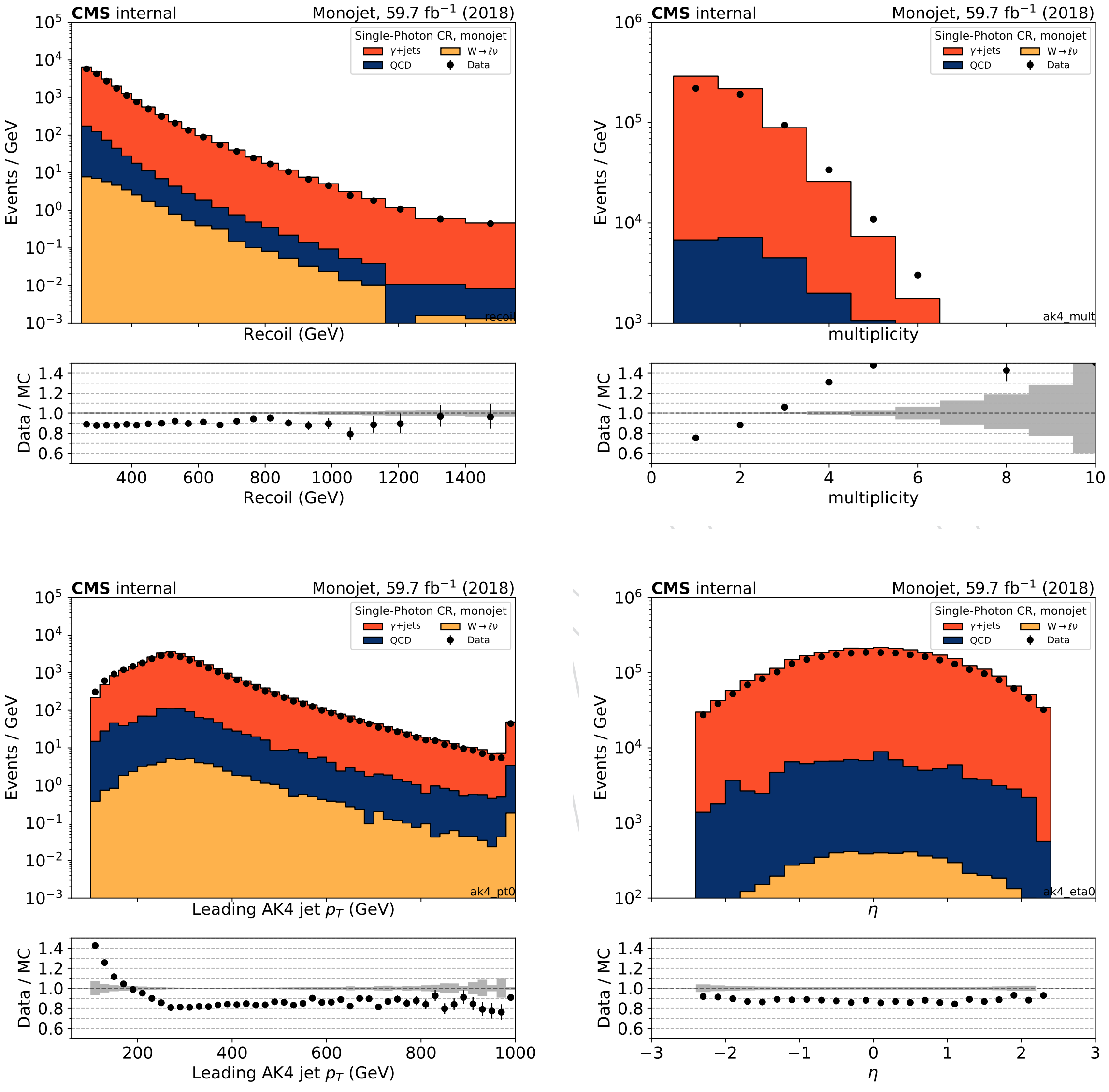

Figure 73: Comparison between 2018 data and monte carlo simulation in the photon control sample for the recoil distribution, the AK4 jet multiplicity distribution, p_{T} and η distribution of the leading AK4 jet with the monojet selection. The bottom panel shows the ratio between data and prediction, with the gray band representing the statistical uncertainty due to limited size of the simulated samples.

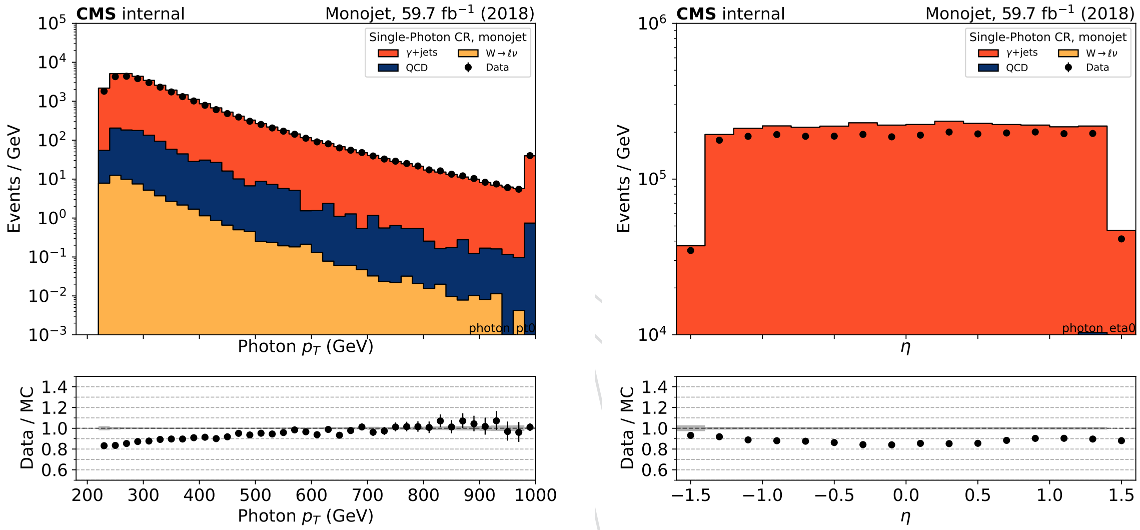

Figure 74: Comparison between 2018 data and monte carlo simulation in the photon control sample for the p_{T} and η of the leading photon with the monojet selection. The bottom panel shows the ratio between data and prediction, with the gray band representing the statistical uncertainty due to limited size of the simulated samples.

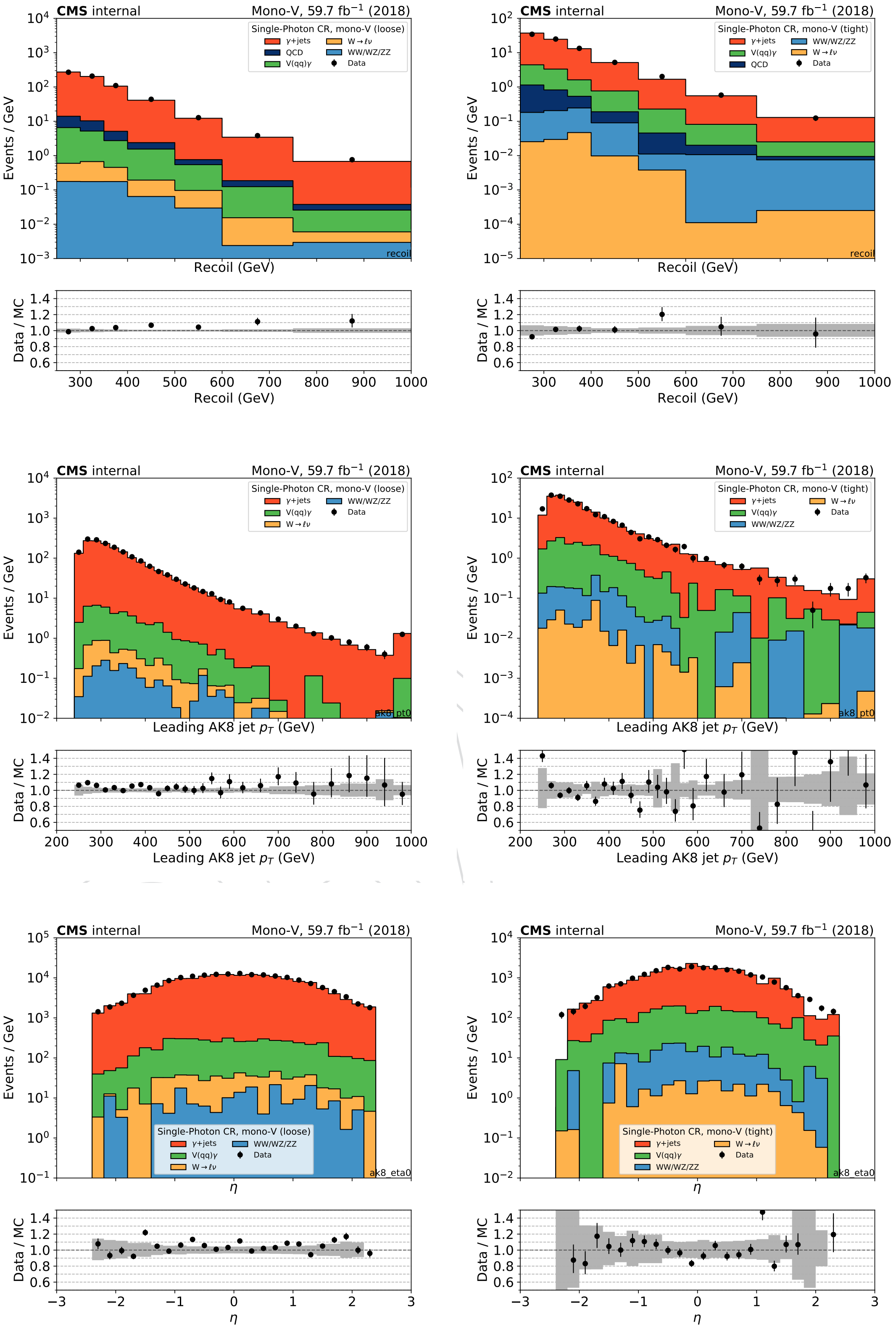

Figure 75: Comparison between 2018 data and monte carlo simulation in the single muon control sample for the recoil distribution, and the AK8 jet p_{T} and η distribution in the low-purity (left) and high-purity (right) regions. The bottom panel shows the ratio between data and prediction, with the gray band representing the statistical uncertainty due to limited size of the simulated samples.

6 Signal extraction strategy

The largest background contributions, from $\mathrm{Z}(\nu\nu) + \text{jets}$and $\mathrm{W}(\ell\nu) + \text{jets}$ processes, are estimated using data from five mutually exclusive control samples selected from dimuon, dielectron, single-muon, single-electron, and $\gamma + \text{jets}$ final states as explained below. The hadronic recoil p_{T} is used as a proxy for the signal-region $p_{\mathrm{T}}^{\mathrm{miss}}$ in these control samples, and is defined by excluding identified leptons or photons from the $p_{\mathrm{T}}^{\mathrm{miss}}$ calculation.

The remaining backgrounds that contribute to the total event yield in the signal region yield relatively smaller contributions. These smaller backgrounds include QCD multijet production, which is predicted from data in a side-band using a $\Delta\phi$ extrapolation method and will be dicussed in 6.2. Top quark and diboson processes are estimated directly from simulation.

6.1 Choice of mono-V tagging working point

Three schemes are considered for the categorization of mono-V events:

- One category defined using τ_{21}: This category serves as a benchmark and corresponds to the strategy used in the 2016 analysis.
- Two categories defined using the mass-decorrelated DeepAK8 tagger. The two categories are separated by purity, with the high-purity region containing events passing the tight tagging working point, while the low-purity category contains events passing the loose, but failing the tight working point. The regions are non-overlapping and are combined.
- Two categories defined using the nominal DeepAK8 tagger. The same low-/high-purity scheme is used.

For each of the schemes, the resulting expected H(inv) branching fraction limit is shown in Tab. 15. The expected exclusion is determined from a combined Asimov fit to the control and signal regions. Both nominal and mass-decorrelated DeepAK8 taggers outperform the τ_{21}-based selection by approximately 10% (mass-decorrelated) and 30% (nominal tagger). In both cases, the combination of low- and high-purity regions does not yield a significant improvement over the tight category alone, indicating that the tight category contributes most of the signal sensitivity. Based on the outcome of this comparison, the mono-V category is defined as a single category based on the tight nominal tagger for the rest of the analysis.

The DeepAK8 approach presents a significant improvement over the techniques used in previous results.

Table 15: Sensitivity comparison of different mono-V categorization schemes.

Tagger type	Working point	Expected H(inv) limit		
		2017	2018	combined
τ_{21}	< 0.6	65%	59%	46%
Mass-decorrelated	loose	94%	92%	69%
	tight	60%	64%	45%
	combined	55%	57%	41%
Nominal	loose	93%	83%	65%
	tight	50%	48%	36%
	combined	46%	44%	33%

6.2 Multijet background estimation

QCD multijet production mostly yields events without large $p_{\mathrm{T}}^{\mathrm{miss}}$ and thus rarely enters the signal region. However, jet energy mismeasurements, as well as neutrinos from meson decays give rise to $p_{\mathrm{T}}^{\mathrm{miss}}$. Although only a small fraction of multijet events will have high $p_{\mathrm{T}}^{\mathrm{miss}}$, the large overall rate of these events ensures that a non-negligible component exists at high $p_{\mathrm{T}}^{\mathrm{miss}}$. The event selection for the signal region is constructed to suppress contributions from multijet events to less than one percent of the total background yield. Since mismeasurement effects are not always well-modeled in simulation, a data-driven method is used.

The data-driven estimate makes use of a QCD control region, which is defined by inverting the $\Delta\phi$ cut. I.e. in the QCD control region, $\min \Delta\phi(\mathrm{jet}, \mathrm{E}_{\mathrm{T}}^{\mathrm{miss}}) <= 0.5$ is required. The $\min \Delta\phi(\mathrm{jet}, \mathrm{E}_{\mathrm{T}}^{\mathrm{miss}})$ variable is highly effective at discriminating multijet events from other processes since jet momentum mismeasurements resulting in large $E_{\mathrm{T}}^{\mathrm{miss}}$ will necessarily yield an angular alignment of the mismeasured jet and the $\vec{p}_{\mathrm{T}}^{\mathrm{miss}}$ vector.

The QCD yield in the control region is estimated by substracting all non-QCD background MC from data, and is scaled to the QCD estimate in signal region by a transfer factor.

The transfer factor is defined by the taking ratio of the QCD MC in the signal region and the QCD MC in the control region. To avoid satatistics fluctuations, an analytical function $f(x) = a\exp(-bx) + c$ is used to fit the transfer factor that is binned in $p_{\mathrm{T}}^{\mathrm{miss}}$. The fit plots are shown in Fig. 76 for monojet, and in Figs. 77 and 78 for the loose and tight mono-V regions, respectively. The function fits well to the low $p_{\mathrm{T}}^{\mathrm{miss}}$ region where the QCD background are mostly relevant.

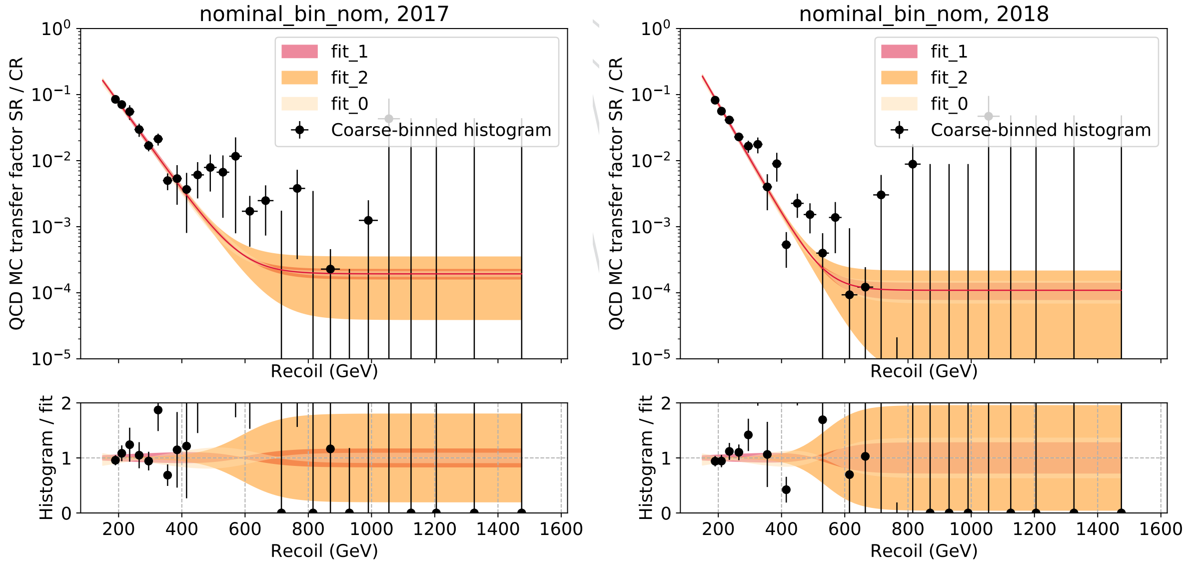

Figure 76: Fitting function $f(x) = a\exp(-bx) + c$ to the binned transfer factor in the monojet QCD control region. Left is 2017 and right is 2018. The function fits well to the low $p_{\mathrm{T}}^{\mathrm{miss}}$ region where the QCD background are mostly relevant. The black points show the binned transfer factor obtained from MC. The red solid represents the best fit result, and the shaded bands represent the 1 s.d. variations of the fit parameters along the directions of the three eigenvectors of the covariance matrix of the parameters.

To account for the shape mismatch at high $p_{\mathrm{T}}^{\mathrm{miss}}$ region, 3 alternative binnings are used: the first alternative binning makes the $p_{\mathrm{T}}^{\mathrm{miss}}$ start from 250 GeV; the second has coarser binning at high $p_{\mathrm{T}}^{\mathrm{miss}}$; and the third binning is coarser everywhere. The fits using the alternative binnings

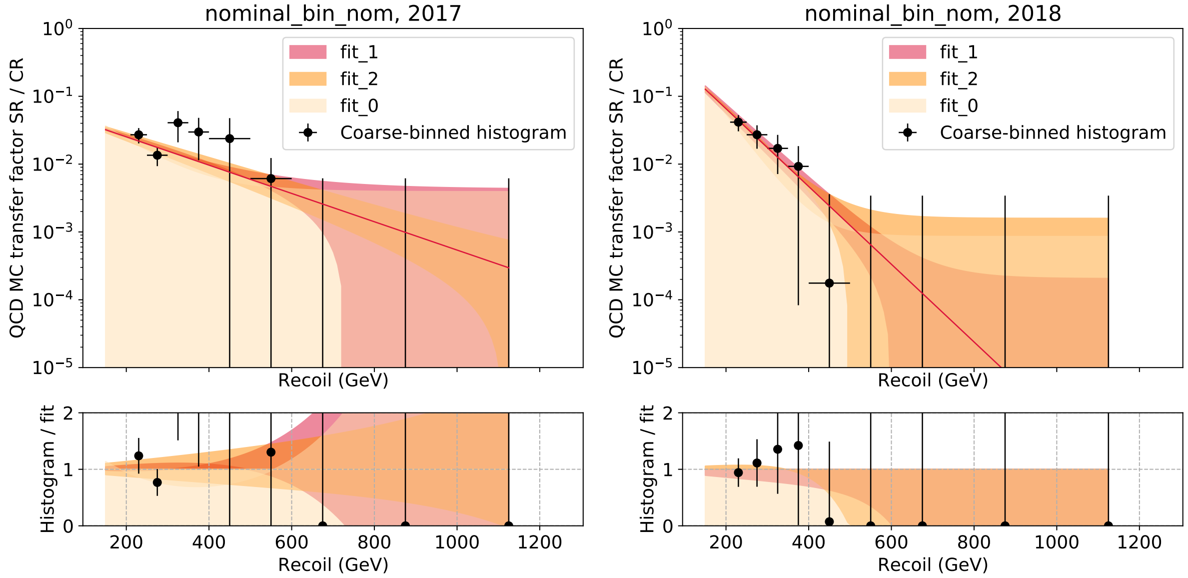

Figure 77: Fitting function $f(x) = a\exp(-bx) + c$ to the binned transfer factor in the mono-V QCD control region. Left is 2017 and right is 2018. The function fits well to the low $p_{\mathrm{T}}^{\mathrm{miss}}$ region where the QCD background are mostly relevant.

are shown in Fig. 79, and the resultant transfer factors derived from each alternative binning are compared in Fig. 80. The third binning ”alt3” gives the largest deviation from the nominal binning, and this deviation is used as the binning uncertainty.

To address the potential mis-modeling of non-QCD background in the QCD control region, we performed a closure test which derives the transfer factor from a lower $\Delta\phi$ region ($\min\Delta\phi(\mathrm{jet}, \mathrm{E}_{\mathrm{T}}^{\mathrm{miss}}) \leq x$) and tests it in rest of the control region ($x < \min\Delta\phi(\mathrm{jet}, \mathrm{E}_{\mathrm{T}}^{\mathrm{miss}}) \leq 0.5$). The divide point x is chosen to be 0.2, 0.3, and 0.4. Fig. 81-82 show the comparisons between the fitted transfer factor from the inference (low $\min\Delta\phi$) region and the binned transfer factors from the target (high $\min\Delta\phi$) region. According to the discrepancy (about $10-20\%$) observed in the first $p_{\mathrm{T}}^{\mathrm{miss}}$ bins, where the QCD purity is high and thus the closure test is reliable, a closure uncertainty 25% is assigned.

Fig. 83 and Fig. 84 are the final QCD multijet predictions in the signal region, for monojet region and mono-V region respectively. The fit uncertainty, binning uncertainty, and closure uncertainty are plotted separately, and the QCD MC in the signal region is also plotted for reference. Due to the limited statistics in the mono-V region, the transfer factor is binned more coarsly and no alternative binnings are used.

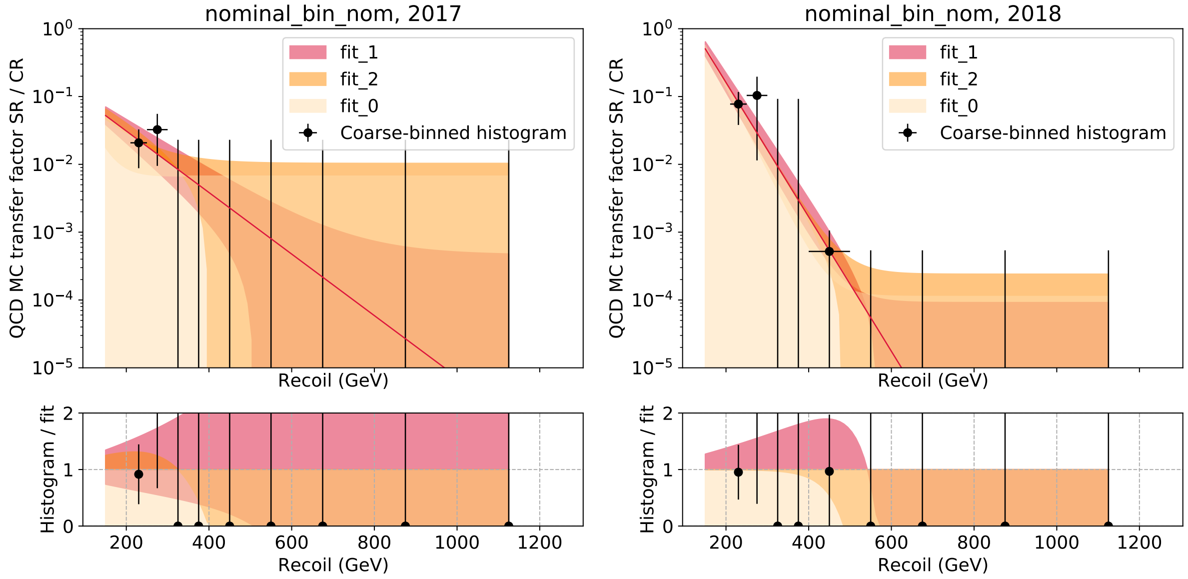

Figure 78: Fitting function $f(x) = a \exp(-bx) + c$ to the binned transfer factor in the mono-V QCD control region. Left is 2017 and right is 2018. The function fits well to the low $p_{\mathrm{T}}^{\mathrm{miss}}$ region where the QCD background are mostly relevant.

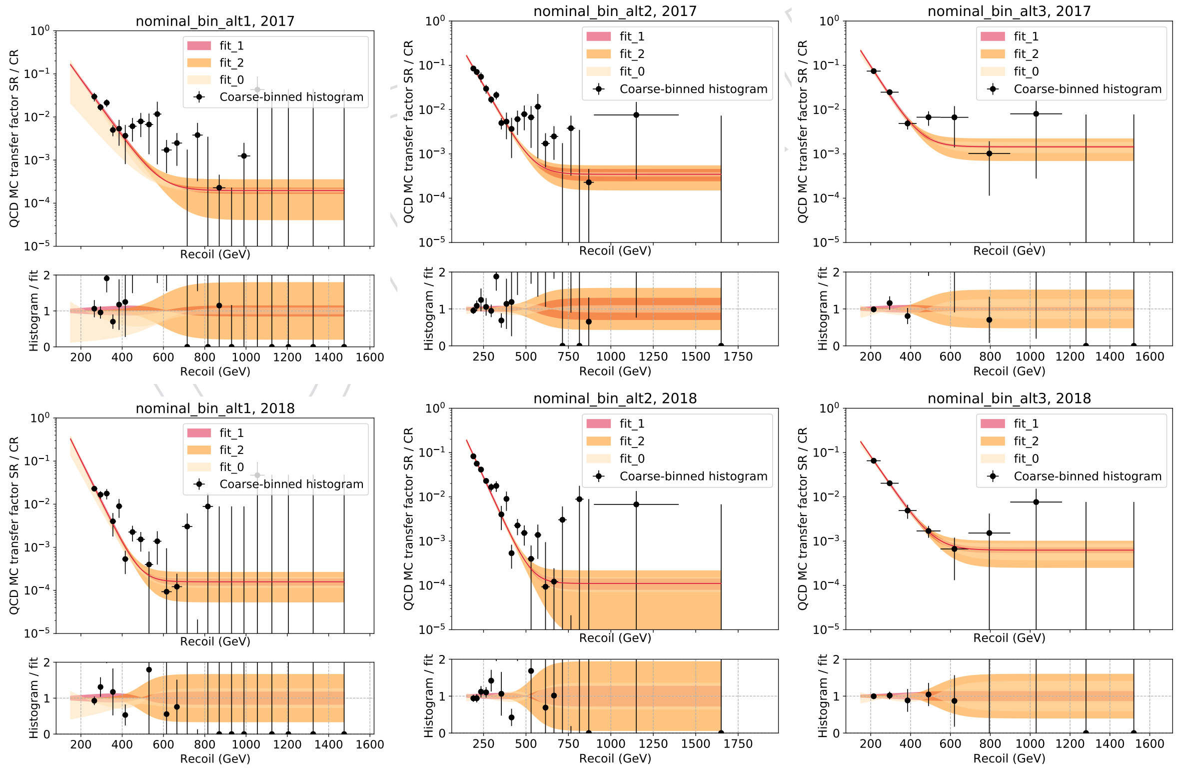

Figure 79: Alternative binnings used when fitting to the binned transfer factor in the monojet QCD control region. 2017 plots on the upper row and 2018 plots on the lower row.

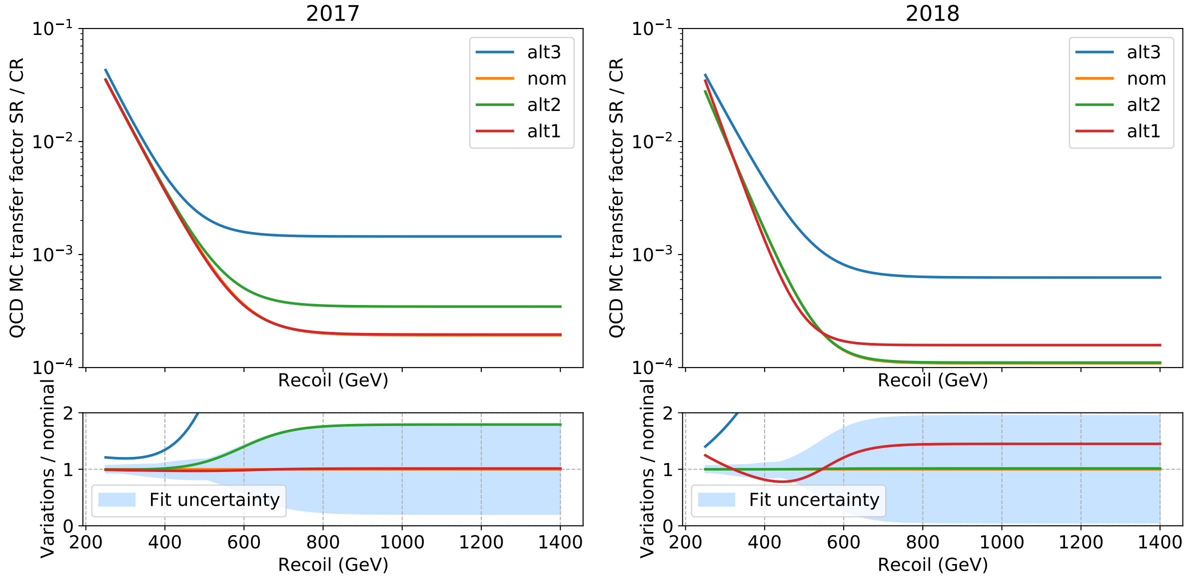

Figure 80: Compare the fitted transfer factors using alternative binnings to the one using the nominal binning, in monojet region. Left is 2017 and right is 2018. The binning ”alt3” gives largest deviation from the nominal binning, and is used to assign the binning uncertainty.

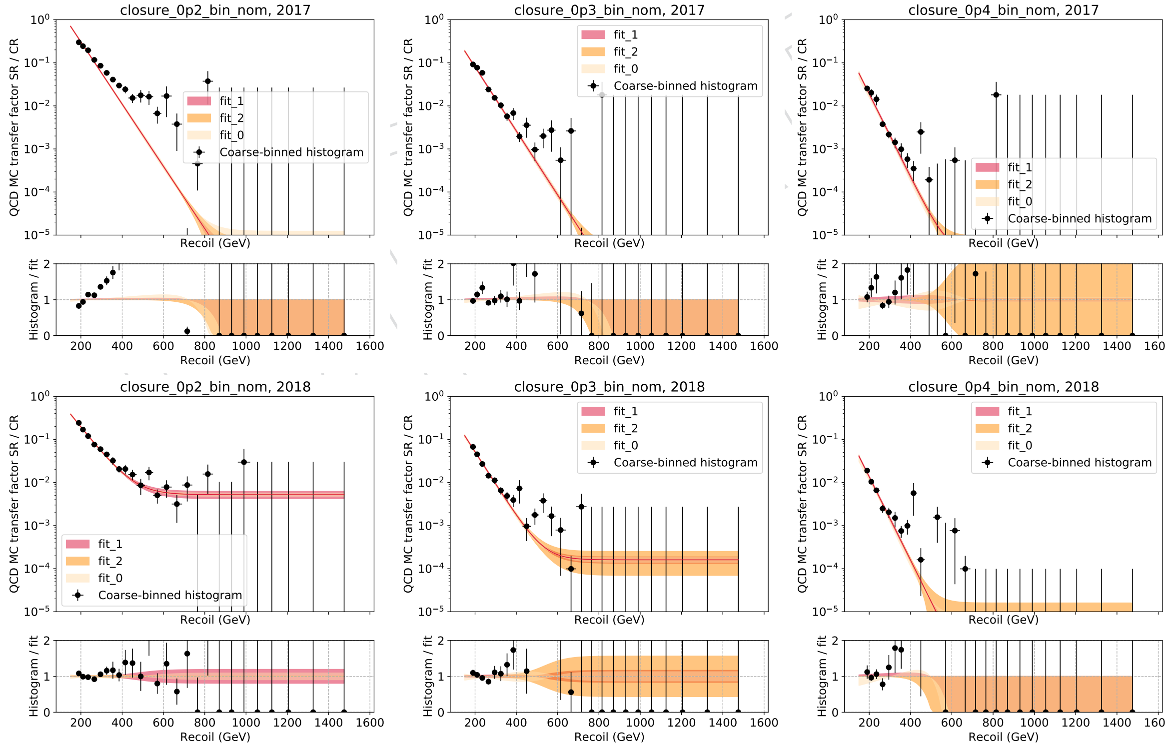

Figure 81: Closure test for QCD estimate in monojet region. Fit transfer factor in a $\min \Delta\phi(\text{jet}, \text{E}_{\text{T}}^{\text{miss}}) \leq x$ sub region and test in the $x < \min \Delta\phi(\text{jet}, \text{E}_{\text{T}}^{\text{miss}}) \leq 0.5$ sub region, the divide point x is set to 0.2, 0.3, and 0.4 for the three columns respectively. 2017 plots on the upper row and 2018 plots on the lower row.

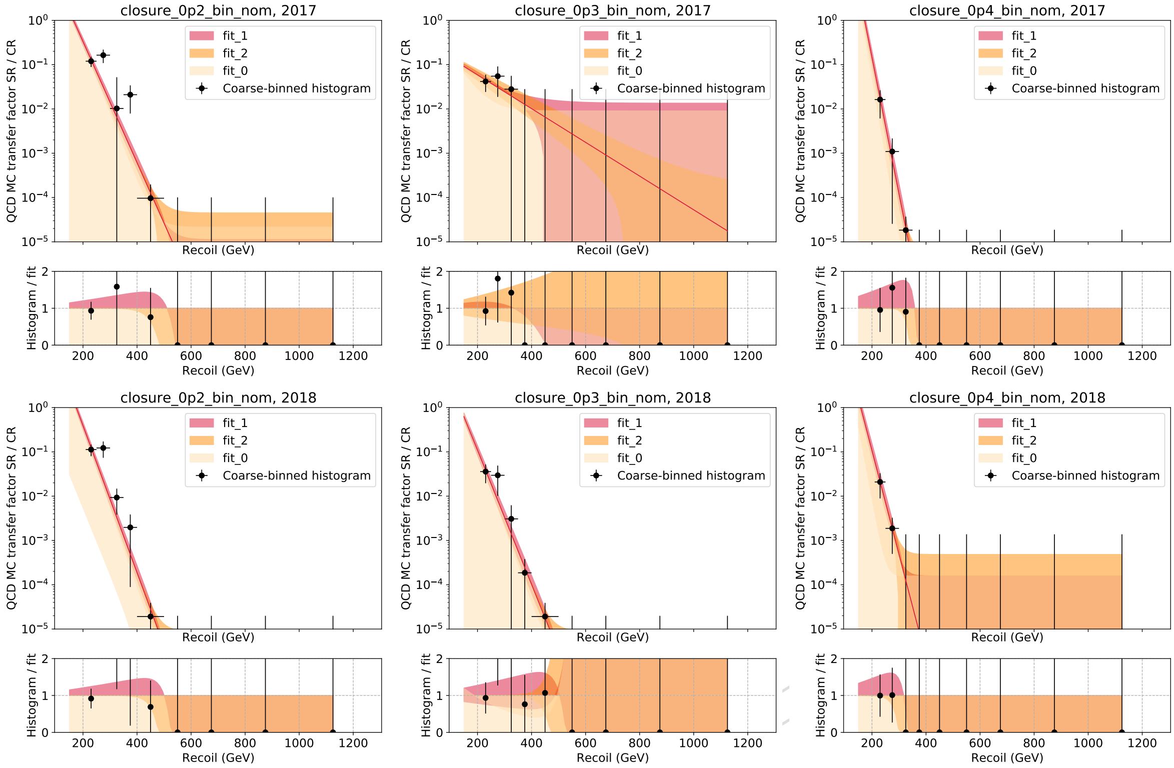

Figure 82: Closure test for QCD estimate in mono-V region. Fit transfer factor in a $\min \Delta\phi(\mathrm{jet}, \mathrm{E}_{\mathrm{T}}^{\mathrm{miss}}) <= x$ sub region and test in the $x < \min \Delta\phi(\mathrm{jet}, \mathrm{E}_{\mathrm{T}}^{\mathrm{miss}}) <= 0.5$ sub region, the divide point x is set to 0.2, 0.3, and 0.4 for the three columns respectively. 2017 plots on the upper row and 2018 plots on the lower row.

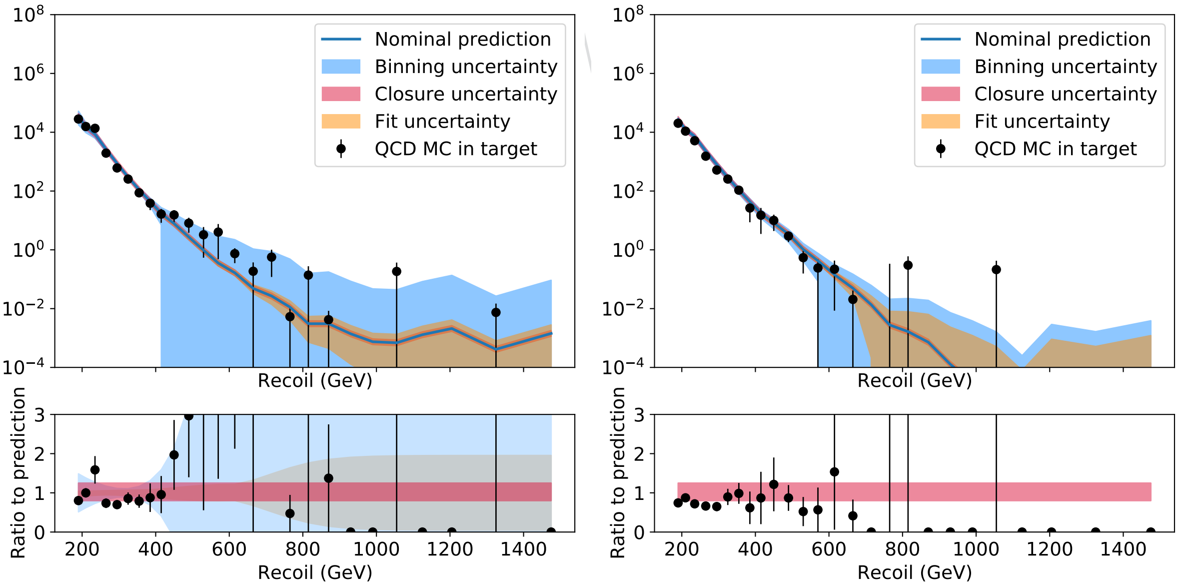

Figure 83: Final QCD background estimate in monojet signal region. Left is 2017 and right is 2018. The different uncertainties are shown in different color bands. The simulated QCD background yields are also plotted for reference.

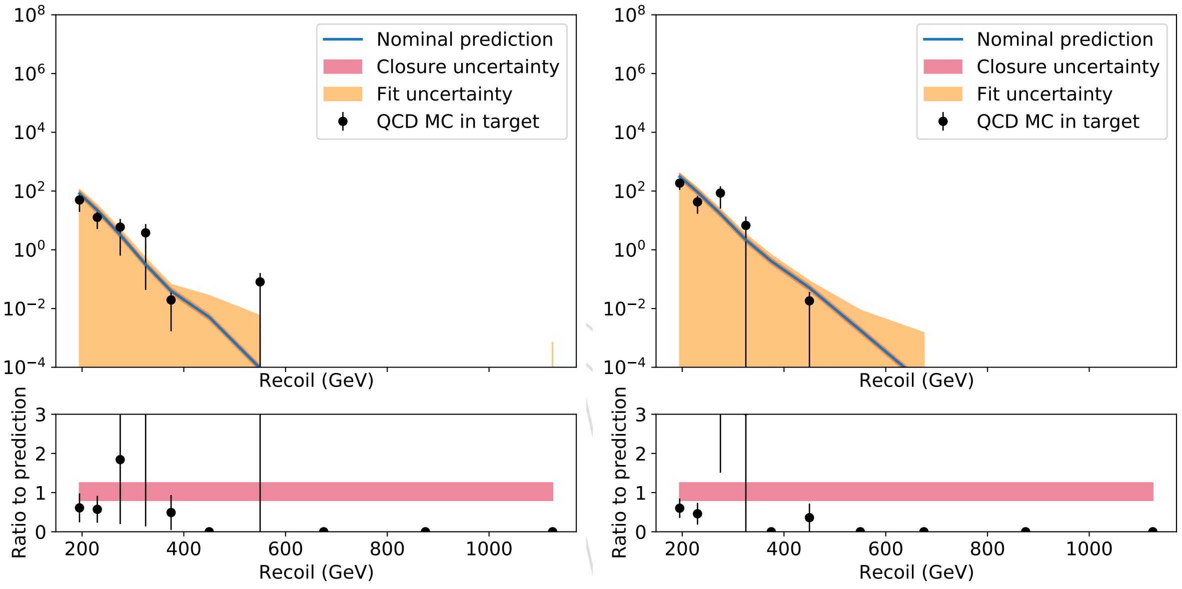

Figure 84: Final QCD background estimate in mono-V signal region. Left is 2017 and right is 2018. The different uncertainties are shown in different color bands. The simulated QCD background yields are also plotted for reference.

6.3 EW background estimation and fitting procedure

The V + jets background processes are estimated using a fit to the data. In the following sections, we first provide a simplified explanation of the fit procedure in order to build practical intuition for the fit behaviors. In the section after that, we provide all the necessary details to fully define the procedure in more precise terms.

6.3.1 Practical explanation without details

The main features of the fit employed here are in short:

- The yield of the $Z \rightarrow \nu\nu$ process in each bin of the signal region is represented by an **unconstrained nuisance parameter**. In practice, that means that the fit can move these parameters at will, without paying a likelihood cost to do so. The unconstrained nuisances only affect the likelihood indirectly by either improving or worsening the agreement between the model and the data. If you were to fit the signal region without any control regions, this freedom means that any possible data shape could be fit.
- To reign in the $Z \rightarrow \nu\nu$ parameters, we use control regions. In each of the control regions, the leading background (e.g. $Z \rightarrow \ell\ell$) is directly coupled to the yield of per bin. If goes up, $Z \rightarrow \ell\ell$ goes up, and so does every other V + jets process. The ratio between any given V + jets process and $Z \rightarrow \nu\nu$ is determined from simulation, and is not affected by the unconstrained nuisance parameters.
- The only way to change the **ratios** of two different V + jets contributions is through **constrained nuisance parameters**, which represent uncertainties (theory and experiment). In constrast to the unconstrained parameters, the likelihood function incurs a large cost for moving the constrained nuisance parameters from their nominal value.
- The signal strength parameter control the signal yield in the signal region. It is unconstrained.

The most important consequences of the above are:

- We do not use any pre-made prediction of the shape of the recoil distribution. We only predict the ratios between processes/regions.
- Anything that cancels out in these ratios can be absorbed by the unconstrained nuisance parameters. This is true for both normalization and shape effects without any constraint.
- Anything that does not cancel out will cause the constrained nuisances to move. The constrained nuisances allow us to correct the transfer factors within some small range.
- Given that the signal strength is not constrained, it can be "cheaper" for the fit to increase the signal strength rather than move more constrained nuisance parameters in order to achieve the same goal.

Some additional terminology:

- Nuisance correlation: Later on, we will define the nuisance correlations in different contexts. Corelation means that a single nuisance parameter is used to parametrize the effect of the uncertainty on the model in this context. For example, we might say "Correlated in p_{T}/ recoil" to say that there is only one nuisance parameter controlling the movement of all recoil bins. The parametrization of each bin as a function of this nuisance parameter can still be completely independent in both magnitude and direction of the uncertainty effect (e.g. for a given nuisance parameter value of X, bin 1 might go up by 5%, bin 2 might go down by 3%, according to the shapes discussed in the uncertainties section). Correlation is a statement about the number of nuisance parameters used.

- Prefit: The prefit background estimate is the estimate from MC simulation, with all the corrections applied plus the data-driven estimates for QCD in the signal and photon control regions. As the name suggests, there is no fitting done, yet. The unconstrained nuisance parameters are simply set to the $\mathrm{Z} \rightarrow \nu\nu$ yield in MC in each bin, and all nuisance parameters are zero. The transfer factors are identical to the ratio of the yields from simulation.
- Postfit: Both the constrained and unconstrained nuisance parameters have been optimized in order to maximize the likelihood function. If we are speaking about the background-only fit, that's all. If we are speaking about the signal+background fit, then the signal strength parameter has also been optimized at the same time as all other parameters.

6.3.2 Detailed description

A binned likelihood fit to the data as presented in Ref. [14] is performed simultaneously in the five different control samples and in the signal region, for events selected in both the monojet and mono-V categories, to estimate the $\mathrm{Z}(\nu\nu) + \mathrm{jets}$and $\mathrm{W}(\ell\nu) + \mathrm{jets}$ rate in each $p_{\mathrm{T}}^{\mathrm{miss}}$ bin. The full likelihood can be seen below:

$$\begin{aligned} \mathcal{L}_{\mathrm{c}}(\boldsymbol{\mu}^{\mathrm{Z}\rightarrow\nu\nu}, \boldsymbol{\mu}, \boldsymbol{\theta}) = & \prod_i \mathrm{Poisson}\left(d_i^{\gamma} | B_i^{\gamma}(\boldsymbol{\theta}) + \frac{\mu_i^{\mathrm{Z}\rightarrow\nu\nu}}{R_i^{\gamma}(\boldsymbol{\theta})} \right) \\ & \times \prod_i \mathrm{Poisson}\left(d_i^{Z} | B_i^{Z}(\boldsymbol{\theta}) + \frac{\mu_i^{\mathrm{Z}\rightarrow\nu\nu}}{R_i^{Z}(\boldsymbol{\theta})} \right) \\ & \times \prod_i \mathrm{Poisson}\left(d_i^{W} | B_i^{W}(\boldsymbol{\theta}) + \frac{f_i(\boldsymbol{\theta})\mu_i^{\mathrm{Z}\rightarrow\nu\nu}}{R_i^{W}(\boldsymbol{\theta})} \right) \\ & \times \prod_i \mathrm{Poisson}\left(d_i | B_i(\boldsymbol{\theta}) + (1 + f_i(\boldsymbol{\theta}))\mu_i^{\mathrm{Z}\rightarrow\nu\nu} + \mu S_i(\boldsymbol{\theta}) \right) \end{aligned} \quad (8)$$

In the above likelihood, $d_i^{\gamma/Z/W}$ are the observed number of events in each bin of the photon, dimuon/dielectron and single-muon/single-electron control regions, and $B_i^{\gamma/Z/W}$ is the background in the respective control regions. The systematic uncertainties ($\boldsymbol{\theta}$) enter the likelihood as additive perturbations to the transfer factors $R_i^{\gamma/Z/W}$, and are modeled as Gaussians. The parameter $\boldsymbol{\mu}^{\mathrm{Z}\rightarrow\nu\nu}$ represents the yield of the $\mathrm{Z} \rightarrow \nu\nu$ background in the signal region, and is left freely floating in the fit. The function $f_i(\boldsymbol{\theta})$ is the transfer factor between the $\mathrm{Z} \rightarrow \nu\nu$ and W+jets backgrounds in the signal region and represents a constraint between these backgrounds. The likelihood also includes the signal region with B_i representing all the backgrounds, S representing the nominal signal prediction, and μ being the signal strength parameter also left floating in the fit.

In this likelihood, the expected numbers of $\mathrm{Z}(\nu\nu) + \mathrm{jets}$events in each bin of $p_{\mathrm{T}}^{\mathrm{miss}}$ are the free parameters of the fit. Transfer factors, derived from simulation, are used to link the yields of the $\mathrm{Z}(\ell\ell) + \mathrm{jets}$, $\mathrm{W}(\ell\nu) + \mathrm{jets}$ and $\gamma + \mathrm{jets}$ processes in the control regions with the $\mathrm{Z}(\nu\nu) + \mathrm{jets}$and

$\mathrm{W}(\ell\nu) + \text{jets}$ background estimates in the signal region. These transfer factors are defined as the ratio of expected yields of the target process in the signal region and the process being measured in the control sample.

To estimate the $\mathrm{W}(\ell\nu) + \text{jets}$ background in the signal region, the transfer factors between the $\mathrm{W}(\mu\nu) + \text{jets}$ and $\mathrm{W}(e\nu) + \text{jets}$ event yields in the single-lepton control samples and the estimates of the $\mathrm{W}(\ell\nu) + \text{jets}$ background in the signal region are constructed. These transfer factors take into account the impact of lepton acceptances and efficiencies, lepton veto efficiencies, and the difference in the trigger efficiencies in the case of the single-electron control sample.

The $\mathrm{Z} \to \nu\nu$ background prediction in the signal region is connected to the yields of $\mathrm{Z} \to \mu^+\mu^-$ and $\mathrm{Z} \to e^+e^-$ events in the dilepton control samples. The associated transfer factors account for the differences in the branching ratio of Z bosons to charged leptons relative to neutrinos and the impact of lepton acceptance and selection efficiencies. In the case of dielectron events, the transfer factor also takes into account the difference in the trigger efficiencies. The resulting constraint on the $\mathrm{Z}(\nu\nu) + \text{jets}$process from the dilepton control samples is limited by the statistical uncertainty in the dilepton control samples because of the large difference in branching fractions between Z boson decays to neutrinos and Z boson decays to muons and electrons.

The $\gamma + \text{jets}$ control sample is also used to predict the $\mathrm{Z}(\nu\nu) + \text{jets}$process in the signal region through a transfer factor, which accounts for the difference in the cross sections of the $\gamma + \text{jets}$ and $\mathrm{Z}(\nu\nu) + \text{jets}$processes, the effect of acceptance and efficiency of identifying photons along with the difference in the efficiencies of the photon and $p_{\mathrm{T}}^{\mathrm{miss}}$ triggers. The addition of the $\gamma + \text{jets}$ control sample mitigates the impact of the limited statistical power of the dilepton constraint, because of the larger production cross section of $\gamma + \text{jets}$ process compared to that of $\mathrm{Z}(\nu\nu) + \text{jets}$process.

Finally, a transfer factor is also defined to connect the $\mathrm{Z}(\nu\nu) + \text{jets}$and $\mathrm{W}(\ell\nu) + \text{jets}$ background yields in the signal region, to further benefit from the larger statistical power that the $\mathrm{W}(\ell\nu) + \text{jets}$ background provides, making it possible to experimentally constrain $\mathrm{Z}(\nu\nu) + \text{jets}$production at high $p_{\mathrm{T}}^{\mathrm{miss}}$.

These transfer factors rely on an accurate prediction of the ratio of $\mathrm{Z} + \text{jets}$, $\mathrm{W} + \text{jets}$, and $\gamma + \text{jets}$ cross sections. Therefore, LO simulations for these processes are corrected using boson p_{T}-dependent NLO QCD K-factors derived using MADGRAPH5_aMC@NLO. They are also corrected using p_{T}-dependent higher-order EW corrections extracted from theoretical calculations [68–73]. The higher-order corrections are found to improve the data-to-simulation agreement for both the absolute prediction of the individual $\mathrm{Z} + \text{jets}$, $\mathrm{W} + \text{jets}$, and $\gamma + \text{jets}$ processes, and their respective ratios. The transfer factors for all regions are shown in Figs. 85-87 for the monojet category and in Figs. **??**-90 and 91-93 for the low- and high-purity mono-V categories, respectively. Note that the transfer factors between signal and control region processes in the 2018 data set exhibit a step-like feature at recoil values of 470 GeV. This is a result of the HEM mitigation selection described in sec. 5.1.1, which rejects events below this recoil value, but not above.

The remaining backgrounds that contribute to the total event yield in the signal region are much smaller than those from $\mathrm{Z}(\nu\nu) + \text{jets}$and $\mathrm{W}(\ell\nu) + \text{jets}$ processes. These smaller backgrounds include QCD multijet events which are measured from data using a $\Delta\phi$ extrapolation method [14, 74], and top quark and diboson processes, which are obtained directly from simulation.

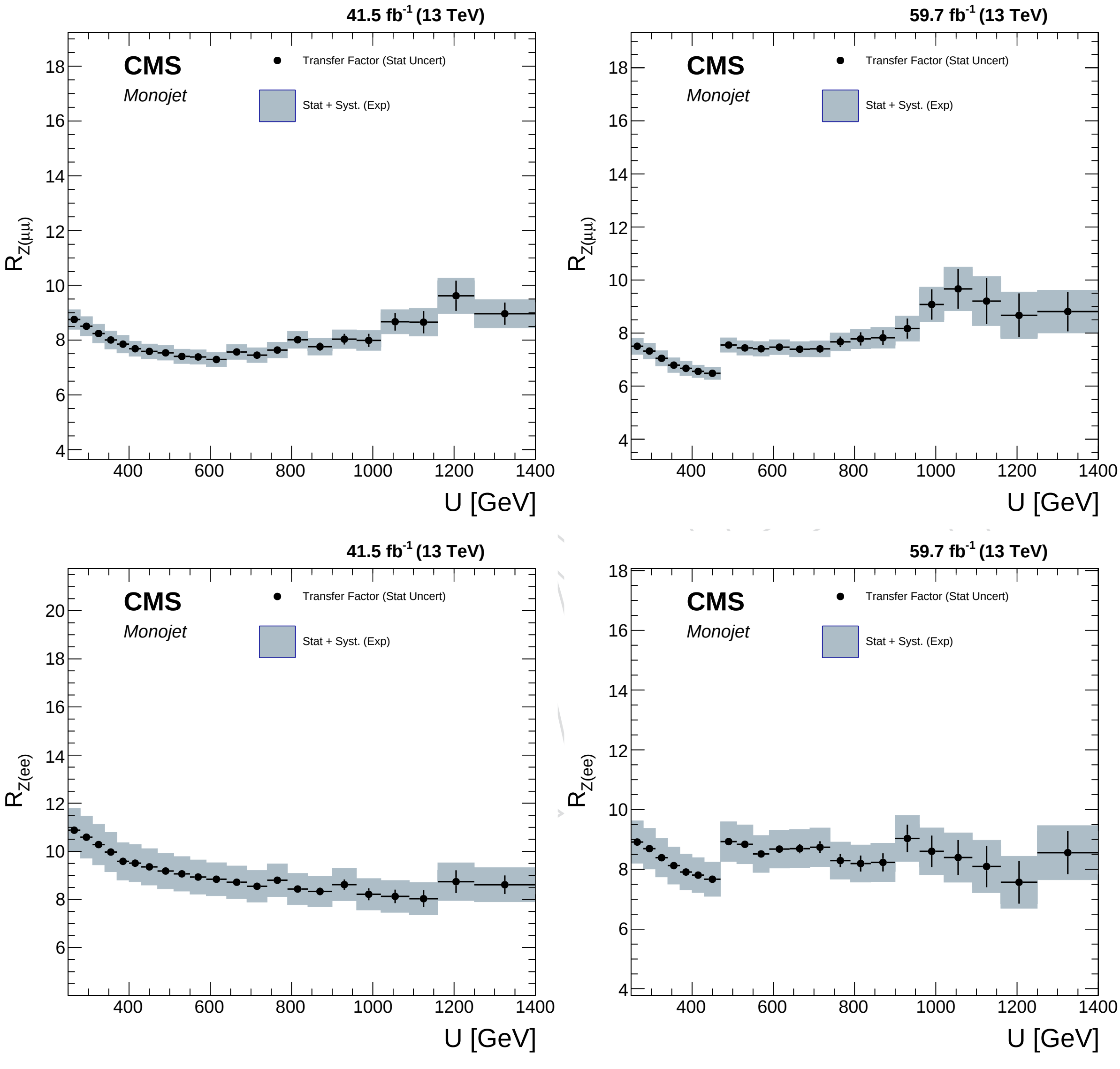

Figure 85: Transfer factors for the $Z \rightarrow \nu\nu$ background as a function of the recoil using the dimuon and dielectron control regions in the monojet category for the 2017 (left) and 2018 datasets (right). The gray band shows the total systematic uncertainty on the ratios.

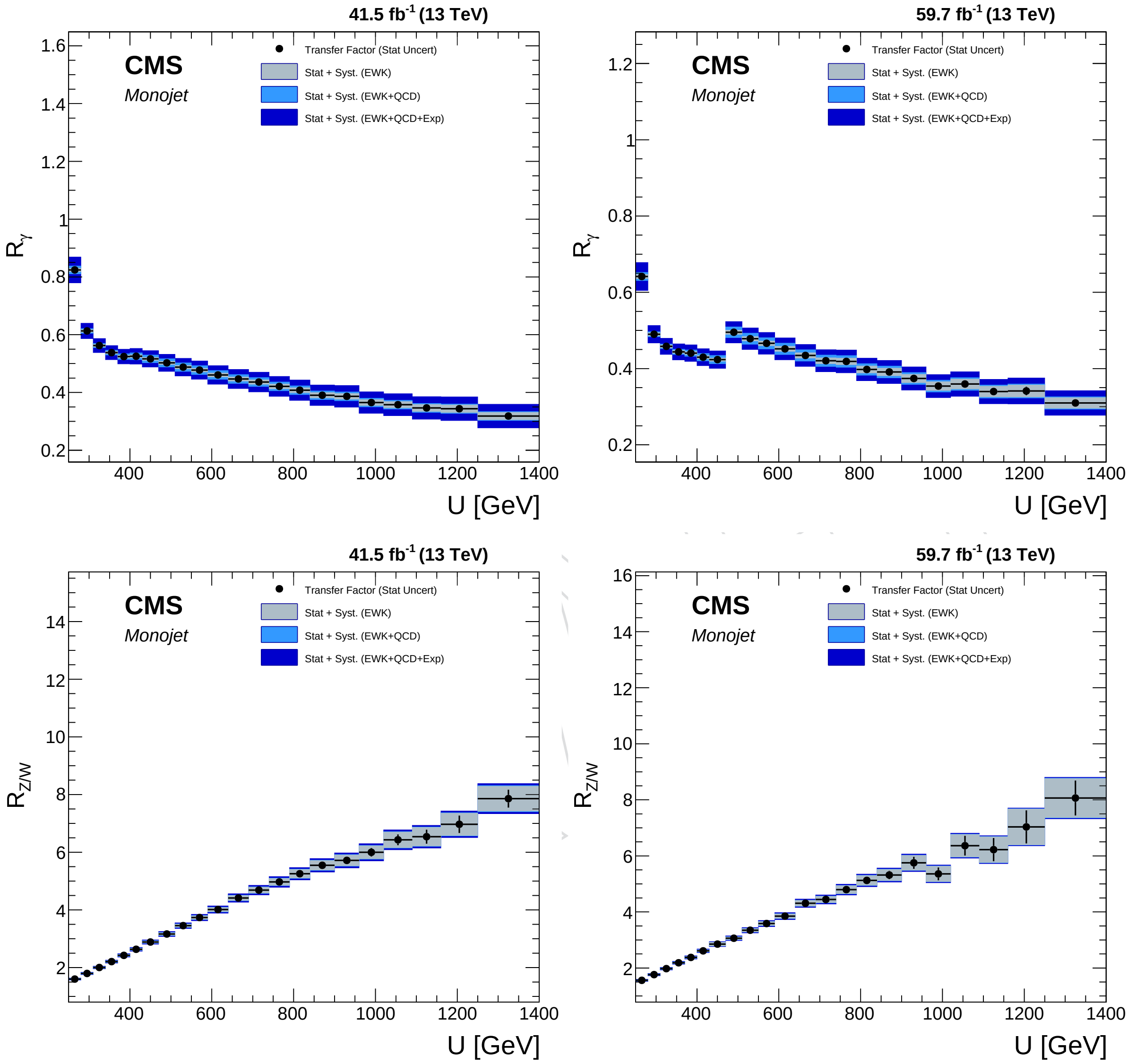

Figure 86: Transfer factors for the to estimate the $Z \rightarrow \nu\nu$ background from the photon control region and W+jets in the signal region as a function of the recoil in the monojet category for the 2017 (left) and 2018 datasets (right). The gray band shows the total systematic uncertainty on the ratios.

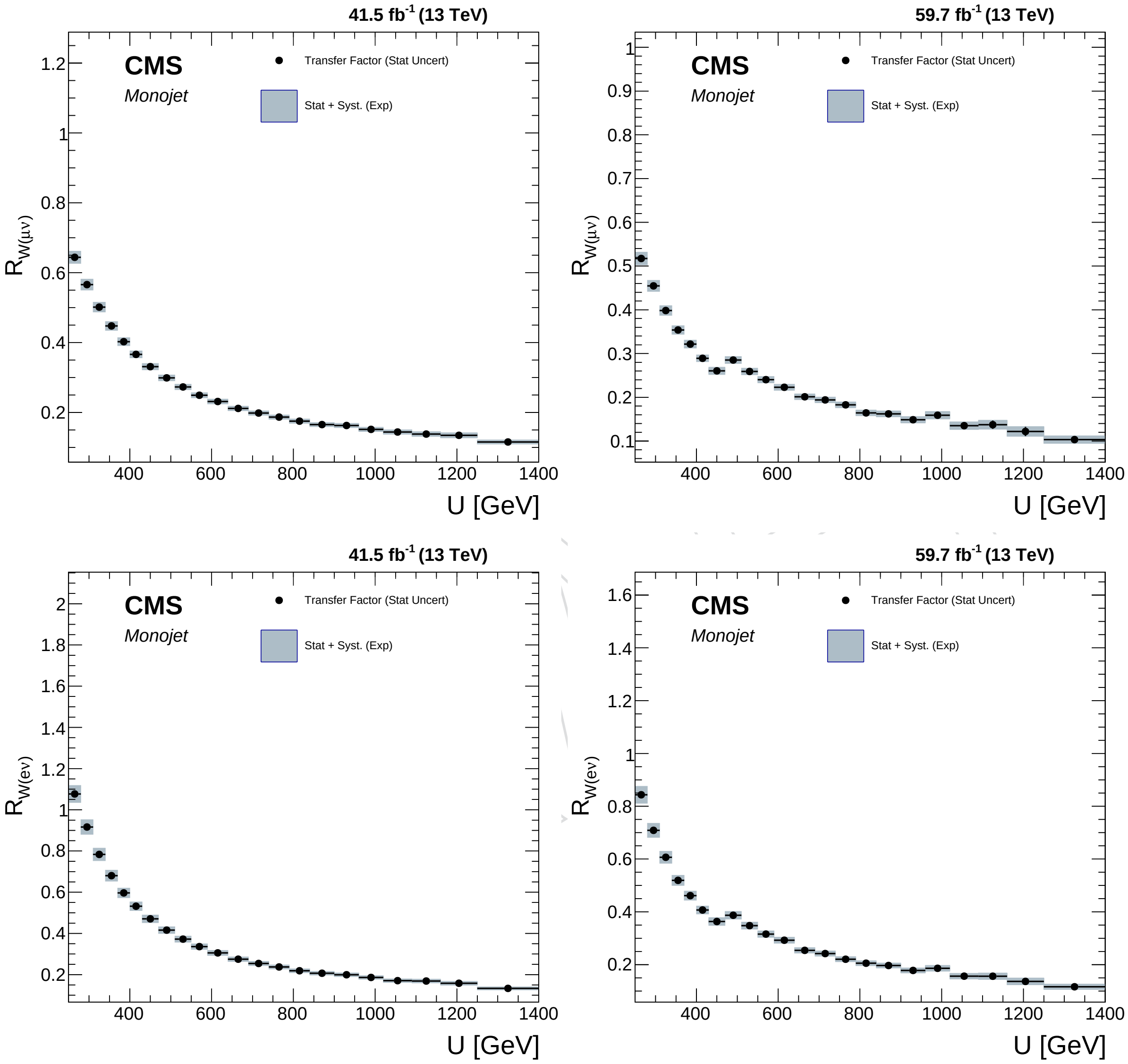

Figure 87: Transfer factors for the $W(\ell\nu) +$ jets background as a function of the recoil using the single muon and single electron control regions in the monojet category for the 2017 (left) and 2018 datasets (right). The gray band shows the theoretical uncertainties on the ratios.

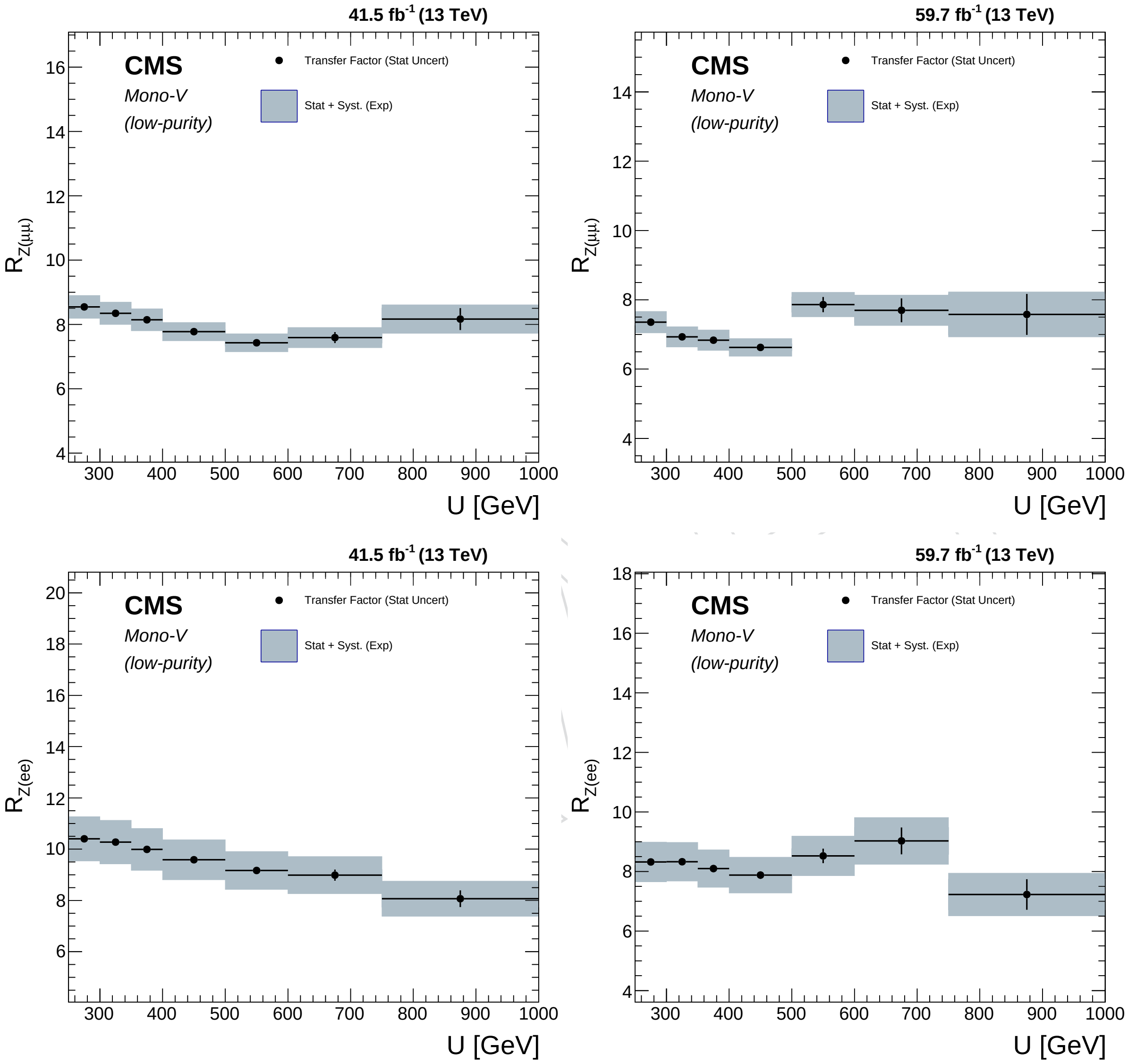

Figure 88: Transfer factors for the $Z \rightarrow \nu\nu$ background as a function of the recoil using the dimuon and dielectron control regions in the low-purity mono-V category for the 2017 (left) and 2018 datasets (right). The gray band shows the total systematic uncertainty on the ratios.

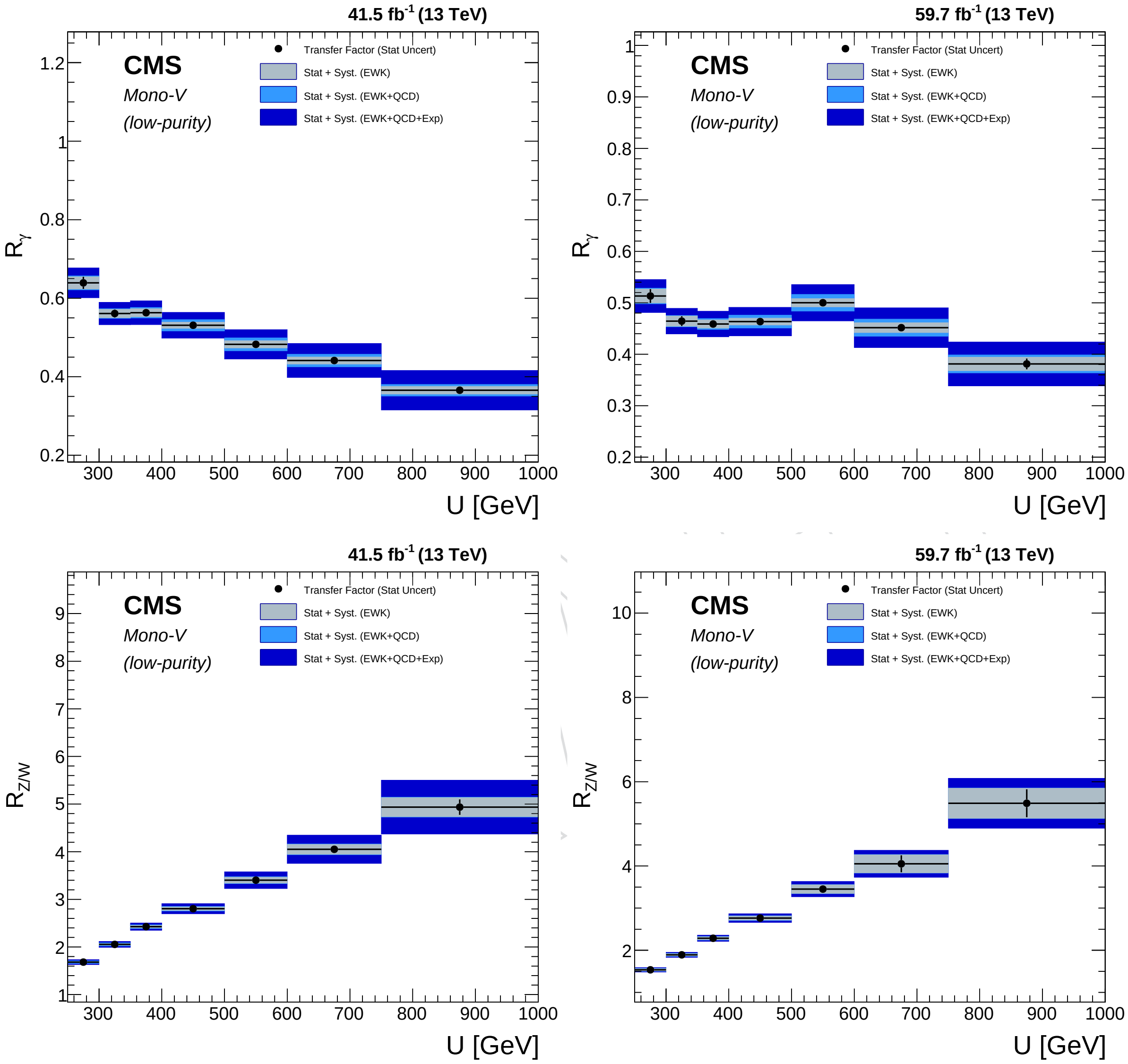

Figure 89: Transfer factors for the to estimate the $Z \rightarrow \nu\nu$ background from the photon control region and W+jets in the signal region as a function of the recoil in the low-purity mono-V category for the 2017 (left) and 2018 datasets (right). The gray band shows the total systematic uncertainty on the ratios.

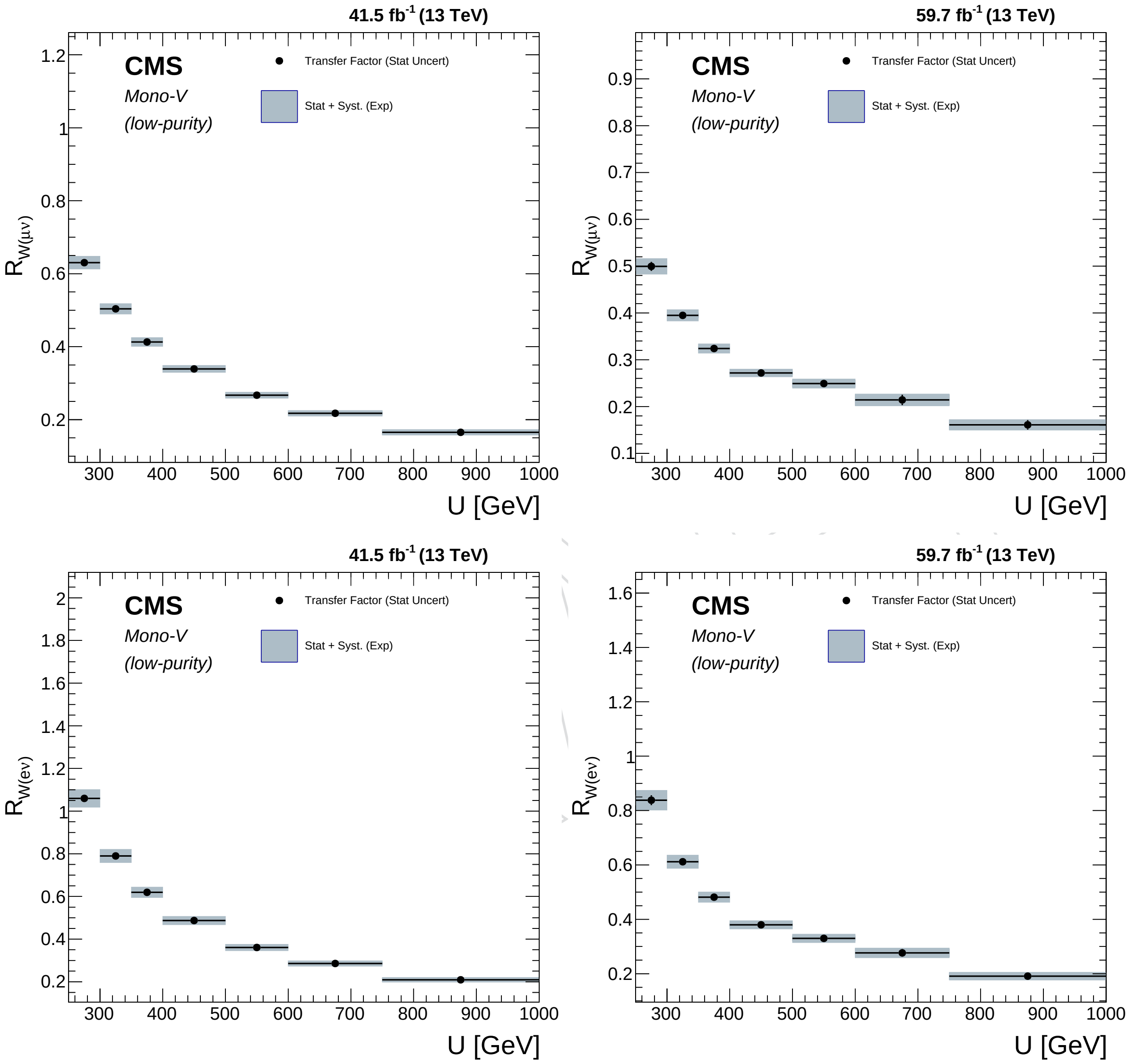

Figure 90: Transfer factors for the $W(\ell\nu) +$ jets background as a function of the recoil using the single muon and single electron control regions in the low-purity mono-V category for the 2017 (left) and 2018 datasets (right). The gray band shows the theoretical uncertainties on the ratios.

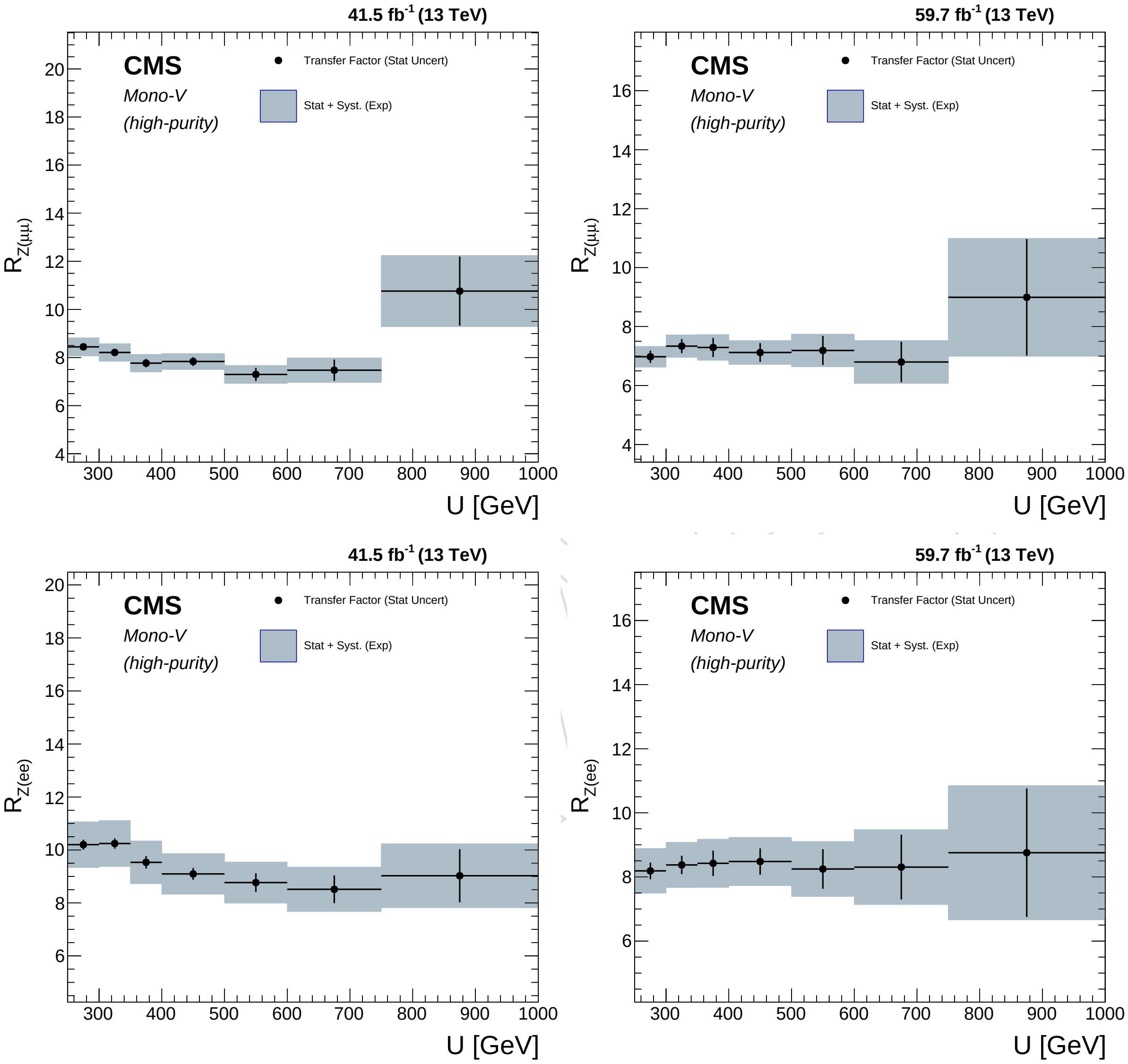

Figure 91: Transfer factors for the $Z \rightarrow \nu\nu$ background as a function of the recoil using the dimuon and dielectron control regions in the high-purity mono-V category for the 2017 (left) and 2018 datasets (right). The gray band shows the total systematic uncertainty on the ratios.

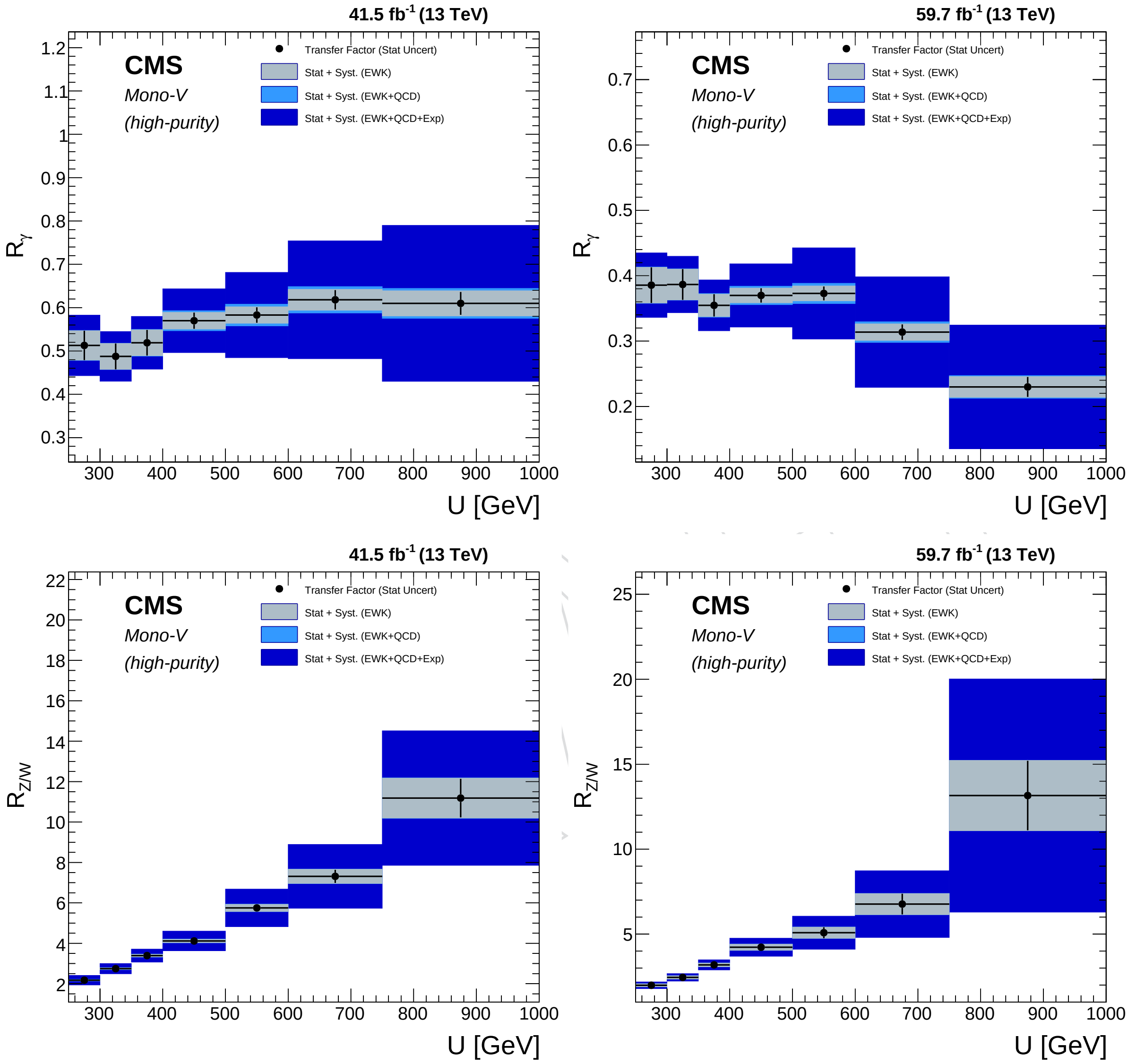

Figure 92: Transfer factors for the to estimate the $Z \rightarrow \nu\nu$ background from the photon control region and W+jets in the signal region as a function of the recoil in the high-purity mono-V category for the 2017 (left) and 2018 datasets (right). The gray band shows the total systematic uncertainty on the ratios.

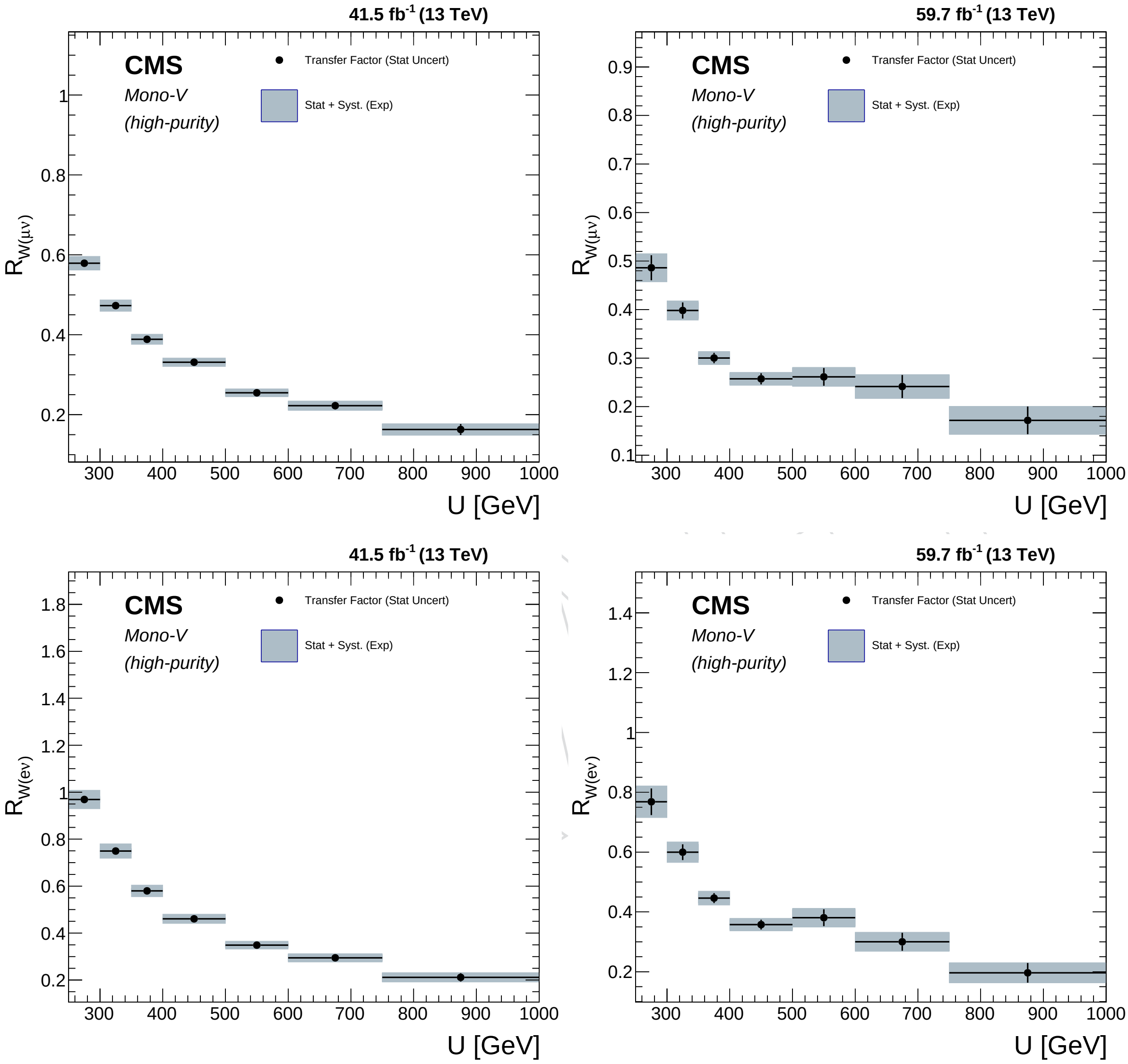

Figure 93: Transfer factors for the $W(\ell\nu) +$ jets background as a function of the recoil using the single muon and single electron control regions in the high-purity mono-V category for the 2017 (left) and 2018 datasets (right). The gray band shows the theoretical uncertainties on the ratios.

6.4 Systematic Uncertainties

Systematic uncertainty discussion is divided into sections separating out the uncertainties in the transfer factors from the ones in the MC based backgrounds.

The theory uncertainty prescription remains unchanged relative to the 2016 analysis. Based on the prescription of Ref. [17], per-event weights are used to derive the uncertainties on the 2017 and 2018 data sets.

Reminder: There is a practical explanation of the fit model, as well as a definition of related terminology in section 6.3.1.

6.4.1 Uncertainties in the transfer factors

Systematic uncertainties in the transfer factors are modeled as constrained nuisance parameters and include both experimental and theoretical uncertainties in the $\gamma + \text{jets}$ to $\text{Z} + \text{jets}$ and $\text{W} + \text{jets}$ to $\text{Z} + \text{jets}$ differential cross section ratios.

Theoretical uncertainties in V-jets and $\gamma + \text{jets}$ processes include effects from QCD and EW higher-order corrections along with PDF modeling uncertainty. To estimate the theoretical uncertainty in the V-jets and $\gamma + \text{jets}$ ratios due to QCD and EW higher-order effects as well as their correlations across the processes and p_{T} bins, the recommendations of Ref. [17] are employed, as detailed in the following explanation.

Three separate sources of uncertainty associated with QCD higher order corrections are used. One of the uncertainties considered comes from the variations around the central renormalization and factorization scale choice. It is evaluated by taking the differences in the NLO cross section as a function of boson p_{T} after changing the renormalization and factorization scales by a factor of two and a factor of one-half with respect to the default value. These constant scale variations mainly affect the overall normalization of the boson p_{T} distributions and therefore underestimate the shape uncertainties that play an important role in the extrapolation of low-p_{T} measurements to high-p_{T}. A second, conservative shape uncertainty derived from altered boson p_{T} spectra is used to supplement the scale uncertainties and account for the p_{T} dependence of the uncertainties. The modeling of the correlations between the processes assumes a close similarity of QCD effects between all V-jets and $\gamma + \text{jets}$ processes. However, the QCD effects in $\gamma + \text{jets}$ production could differ compared to the case of $\text{Z} + \text{jets}$ and $\text{W} + \text{jets}$ productions. In order to account for this variation, a third uncertainty is computed based on the difference of the known QCD K-factors of the $\text{W} + \text{jets}$ and $\gamma + \text{jets}$ processes with respect to $\text{Z} + \text{jets}$ production. All QCD uncertainties are correlated across the $\text{Z} + \text{jets}$, $\text{W} + \text{jets}$, $\gamma + \text{jets}$ processes, and also correlated across the bins of the hadronic recoil p_{T}.

For the V-jets and $\gamma + \text{jets}$ processes, nNLO EW corrections are applied, which correspond to full NLO EW corrections [68–70, 73] supplemented by two-loop Sudakov EW logarithms [71, 75–77]. We also considered three separate sources of uncertainty arising from the following: pure EW higher-order corrections failing to cover the effects of unknown Sudakov logarithms in the perturbative expansion beyond NNLO, missing NNLO effects that are not included in the nNLO EW calculations, and the difference between the next-to-leading logarithmic (NLL) Sudakov approximation at two-loop and simple exponentiation of the full NLO EW correction. The variations due to the effect of unknown Sudakov logs are correlated across the $\text{Z} + \text{jets}$, $\text{W} + \text{jets}$, and $\gamma + \text{jets}$ processes and are also correlated across the bins of hadronic recoil p_{T}. On the other hand, the other two sources of EW uncertainties are treated as uncorrelated across the V-jet and $\gamma + \text{jets}$ processes, and an independent nuisance parameter is used for each process.

Uncertainties related to the PDF choice for sample generation are estimated using the replicas of the PDF4LHC15 NNLO PDF set. For each transfer factor, the numerator and denominator are varied in a correlated manner, and the transfer factor is recalculated based on the varied inputs, in order to define the variation of the transfer factor. The resulting uncertainties are shown in Fig. 94. The uncertainty cancels almost perfectly between the analysis regions, and the small residual uncertainty is taken into account in the fit. For simplicity, the PDF variations for the different transfer factors are kept decorrelated (Otherwise, it would be necessary to include the more than 100 PDF variations as separate nuisances, which would be wildly impractical as well as unnecessary.).

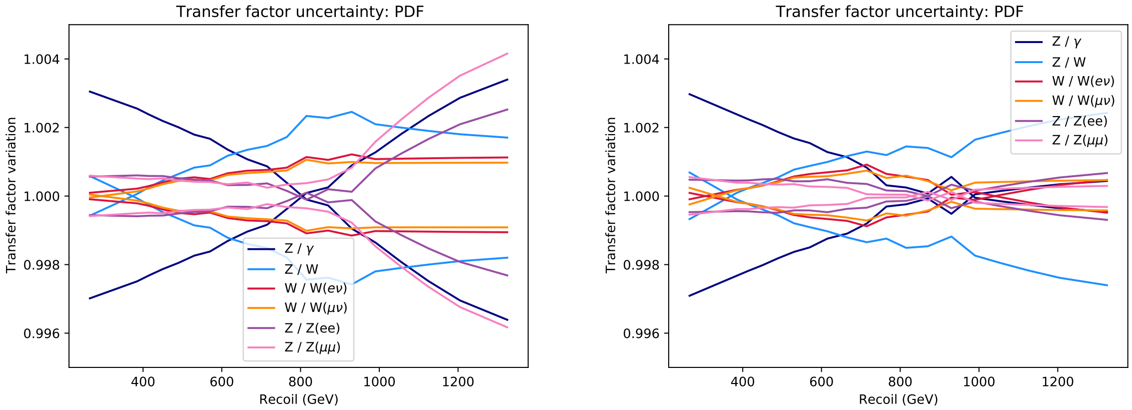

Figure 94: PDF uncertainties on the transfer factors between different analysis regions in the 2017 (left) and 2018 data sets (right).

A recommendation that includes a factorized approach to partially include mixed QCD-EW corrections is outlined in Ref. [17]. An additional uncertainty is introduced to account for the difference between the corrections done in the multiplicative and the additive approaches, to account for the non-factorized mixed EW-QCD effects.

The summary of the aforementioned theoretical uncertainties including their magnitude and correlation is outlined in Table 16. The uncertainty templates used in the fits are shown in Fig. 95.

Experimental uncertainties including the reconstruction efficiency and the selection efficiencies of leptons, photons ($4-13\%$, cf Fig. 96) are also incorporated. Uncertainties in in the efficiency of the electron (2%), photon (2%), and $p_{\mathrm{T}}^{\mathrm{miss}}$ (up to 2%) triggers, are included and are fully correlated across all the bins of hadronic recoil p_{T} and $p_{\mathrm{T}}^{\mathrm{miss}}$. The uncertainty in the efficiency of the b jet veto is estimated to be 6% (2)% for the contribution of the top quark (diboson) background.

In addition, the lepton veto uncertainties are also included in the transfer factors and are estimated as described in Section 4.5. The effects of the uncertainties in the vetos on the respective lepton flavors are shown in Fig. 97. The overall magnitude of the lepton-veto uncertainty is found to increase from 1.5 to 3% with increasing recoil, with dominant contributions from the electron and tau lepton veto, and negligible contributions from muons.

In the 2017 data set, the prefiring issue has necessitated the use of a correction based on event weights. As detailed in Section 4.3, differenct reweighting schemes lead to different results, which are taken into account as a systematic uncertainty in the transfer factors between the main background processes. The uncertainty is derived by calculating the relevant transfer

Table 16: Theoretical uncertainties considered in the V-jets and $\gamma+$ jets processes, and their ratios. The correlation between each process and between the p_{T} bins are described.

Uncertainty source	Process (magnitude)	Correlation
Fact. & renorm. scales (QCD)	$\mathrm{Z}\to\nu\nu/\mathrm{W}\to\ell\nu$ (0.1 – 0.5%) $\mathrm{Z}\to\nu\nu/\gamma+$jets (0.2 – 0.5%)	Correlated between processes and in p_{T}
p_{T} shape dependence (QCD)	$\mathrm{Z}\to\nu\nu/\mathrm{W}\to\ell\nu$ (0.4 – 0.1%) $\mathrm{Z}\to\nu\nu/\gamma+$jets (0.1 – 0.2%)	Correlated between processes and in p_{T}
Process dependence (QCD)	$\mathrm{Z}\to\nu\nu/\mathrm{W}\to\ell\nu$ (0.4 – 1.5%) $\mathrm{Z}\to\nu\nu/\gamma+$jets (1.5 – 3.0%)	Correlated between processes and in p_{T}
Effects of unknown Sudakov logs (EW)	$\mathrm{Z}\to\nu\nu/\mathrm{W}\to\ell\nu$ (0 – 0.5%) $\mathrm{Z}\to\nu\nu/\gamma+$jets (0.1 – 1.5%)	Correlated between processes and in p_{T}
Missing NNLO effects (EW)	$\mathrm{Z}\to\nu\nu$ (0.2 – 3.0%) $\mathrm{W}\to\ell\nu$ (0.4 – 4.5%) $\gamma+$jets (0.1 – 1.0%)	Uncorrelated between processes correlated in p_{T}
Effects of NLL Sudakov approx. (EW)	$\mathrm{Z}\to\nu\nu$ (0.2 – 4.0%) $\mathrm{W}\to\ell\nu$ (0 – 1.0%) $\gamma+$jets (0.1 – 3.0%)	Uncorrelated between processes correlated in p_{T}
Unfactorized mixed QCD-EW corrections	$\mathrm{Z}\to\nu\nu/\mathrm{W}\to\ell\nu$ (0.15 – 0.3%) $\mathrm{Z}\to\nu\nu/\gamma+$jets (<0.1%)	Correlated between processes and in p_{T}
PDF	$\mathrm{Z}\to\nu\nu/\mathrm{W}\to\ell\nu$ (0 – 0.3%) $\mathrm{Z}\to\nu\nu/\gamma+$jets (0 – 0.6%)	Correlated between processes and in p_{T}

factors for each of the weight variations, and the largest difference to the nominal prescription is used as an uncertainty. The resulting uncertainties are shown in Fig. 98 as a function of the recoil. It is observed that the overall uncertainty is dominated by a single variation, the upward variation of the reweighting scheme based on the electromagnetic jet energy, which is found to be anticorrelated for electron and muon regions. Therefore, a single nuisance parameter is used for the prefiring uncertainty in all recoil bins and analysis channels, and it is implemented to affect transfer factors with electrons and muons in opposite directions.

The uncertainty in the efficiency of the V tagging requirements is estimated to be 9% in the mono-V category. The uncertainty in the modeling of $p_{\mathrm{T}}^{\mathrm{miss}}$ in simulation [78] is estimated to be 4% and is dominated by the uncertainty in the jet energy scale. For the calculation of jet energy scale (JES) uncertainties, an 11-source splitting is used, in accordance with the correlation scheme defined by JME, which can be found in Ref. [79]. For each of the subsources, the up and down variations are derived by varying the jet p_T and MET, and calculating the change in the final event yield, as a function of $p_{\mathrm{T}}^{\mathrm{miss}}$. For the case of TFs, flat uncertainties are being used since there is no strong shape dependence of the variations as a function of $p_{\mathrm{T}}^{\mathrm{miss}}$. Therefore, each up and down variation is represented by a single value. In the figures below, plots show JES and JER uncertainties for different transfer factors for 2017 and 2018. In Fig. 99, uncertainties on $\mathrm{Z}\to\nu\nu/\mathrm{W}\to\ell\nu$ and $\gamma+\text{jets}/\mathrm{Z}\to\nu\nu$ transfer factors are shown. Uncertainties on $\mathrm{Z}\to\nu\nu/\mathrm{Z}\to e^+e^-$ and $\mathrm{Z}\to\nu\nu/\mathrm{Z}\to\mu^+\mu^-$ transfer factors are shown in Fig. 100, and uncertinties on $\mathrm{W}\to\ell\nu/\mathrm{W}\to e\nu$ and $\mathrm{W}\to\ell\nu/\mathrm{W}\to\mu\nu$ are shown in Fig. 101.

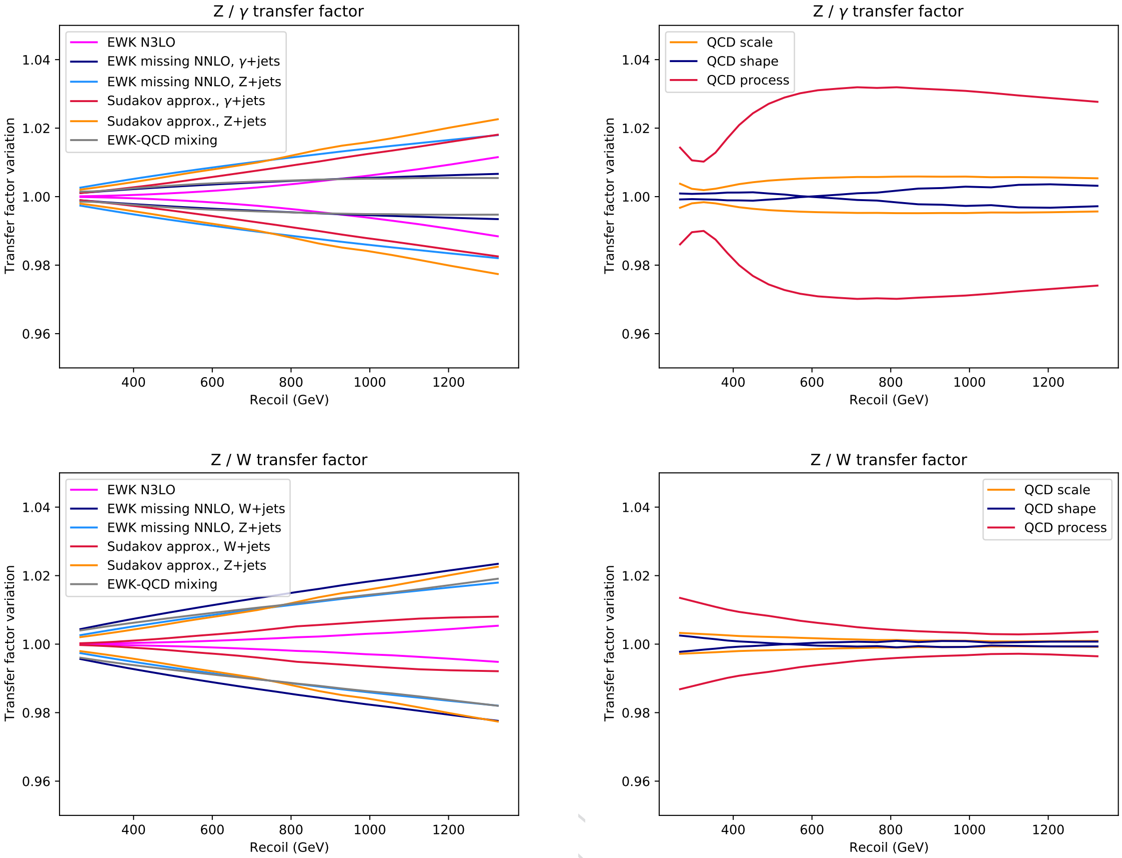

Figure 95: Transfer factor variations used to model the theoretical uncertainties. The variations are shown separately for the $Z\gamma$ ratio (top row) and the Z ratio (bottom). The left (right) panels show the variations related to QCD and EWK variations, respectively.

From Figs. 99, 100 and 101, it can be seen that the JES and JER uncertainties on transfer factors mostly cancel, up to $1-2\%$. Total JES uncertainties are found to be slightly larger in 2018, with the Relative Sample 2018 uncertainty source generally being the largest uncertainty source, within the 11 sub-sources.

An additional scale uncertainty is associated with the photon pt determination. This uncertainty is particularly relevant due as a result of the small numerical difference between the selection thresholds for hadronic recoil (250 GeV) and the leading photon in the photon CR (230 GeV). In this regime, small changes of the photon p_{T} determination have an amplified effect to the acceptance at low recoil. Note that by consturction, such a scale change will not affect value of the hadronic recoil for a given event, as the change in photon momentum – if propagated consistently – will cancel with a corresponding opposite change in the $p_{\mathrm{T}}^{\mathrm{miss}}$. The scale uncertainty is estimated by varying the photon p_{T} scale up and down by each 2% and observing the change in the recoil spectrum of γ+jets events in the CR, which is shown in Fig. 102. The resulting shape variation is applied an an uncertainty on the transfers of between the photon and other regions.

The full list of uncertainties on the transfer factors are summarized in Table 17. It should be noted that uncertainties that are common both in the denominator and the numerator of these transfer factors, such as jet energy scale, jet energy resolution, luminosity cancel either partially

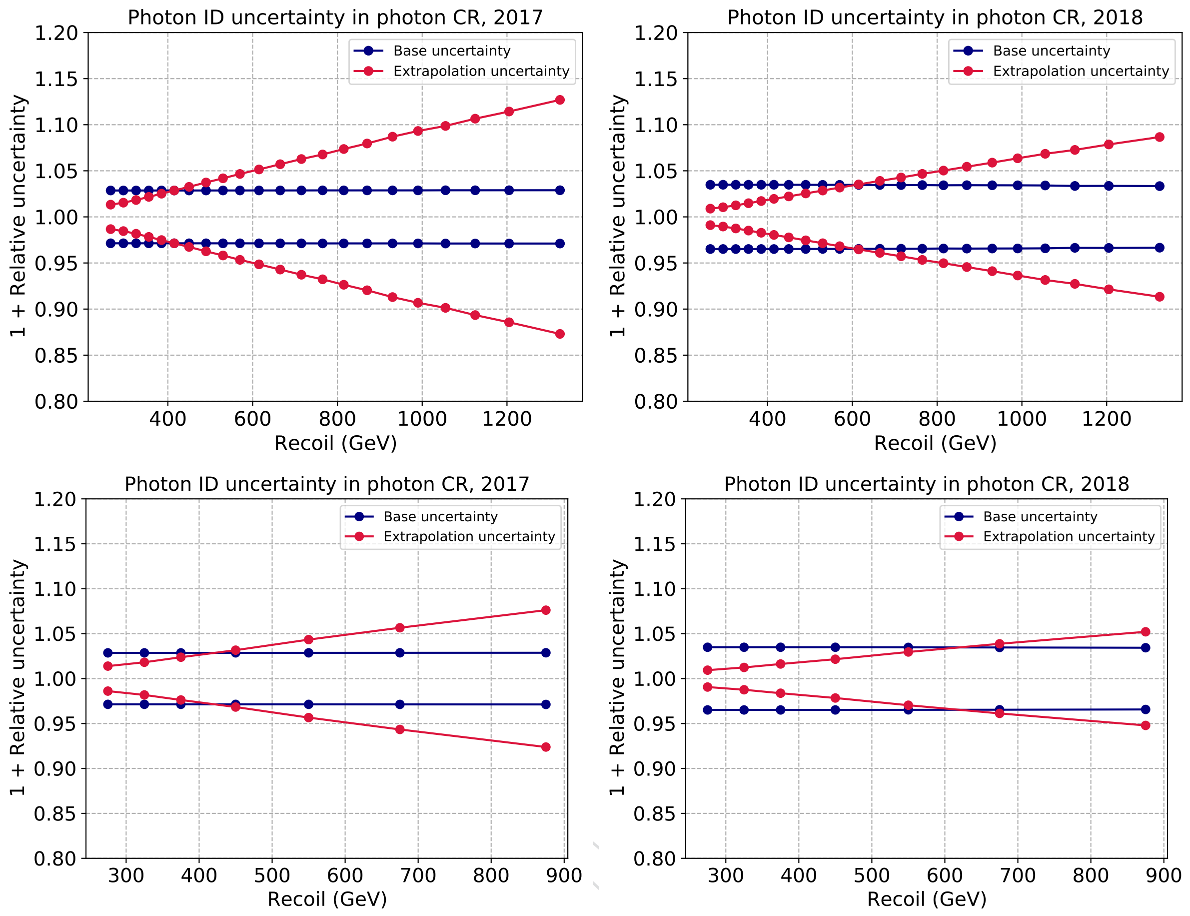

Figure 96: Photon identification related uncertainties on the Z/γ transfer factor for 2017 (left) and 2018 (right). The top row shows the monojet category, the botton row shows the mono-V category.

or fully.

6.4.2 Uncertainties assigned to the MC based processes

Uncertainties assigned to the simulation based processes include the uncertainty in the efficiency of the b-jet veto and is estimated to be 6(2)% for the top quark (other) background. A systematic uncertainty of 10% is included for the top quark background normalization due to the modeling of the top quark p_{T} distribution in simulation, and a second uncertainty of 10% is assigned to the top quark overall cross section [80].

For the diboson backgrounds, both a shape and a normalization uncertainty are included to account for theoretical corrections to the process model (cf. sec. 4.8). The uncertainties are decorrelated between the separate diboson processes.

The uncertainty of the jet energy and $p_{\mathrm{T}}^{\mathrm{miss}}$ calibration is estimated and split into components in the same way as for the transfer factors (cf. Sec. 6.4.1). The resulting uncertainties are shown in Fig. 103. The variations are found to be consistent between processes and regions, and the total combined uncertainty ranges up to 4% (6%) for 2017 (2018), depending on $p_{\mathrm{T}}^{\mathrm{miss}}$.

All the above mentioned uncertainites are summarized 18.

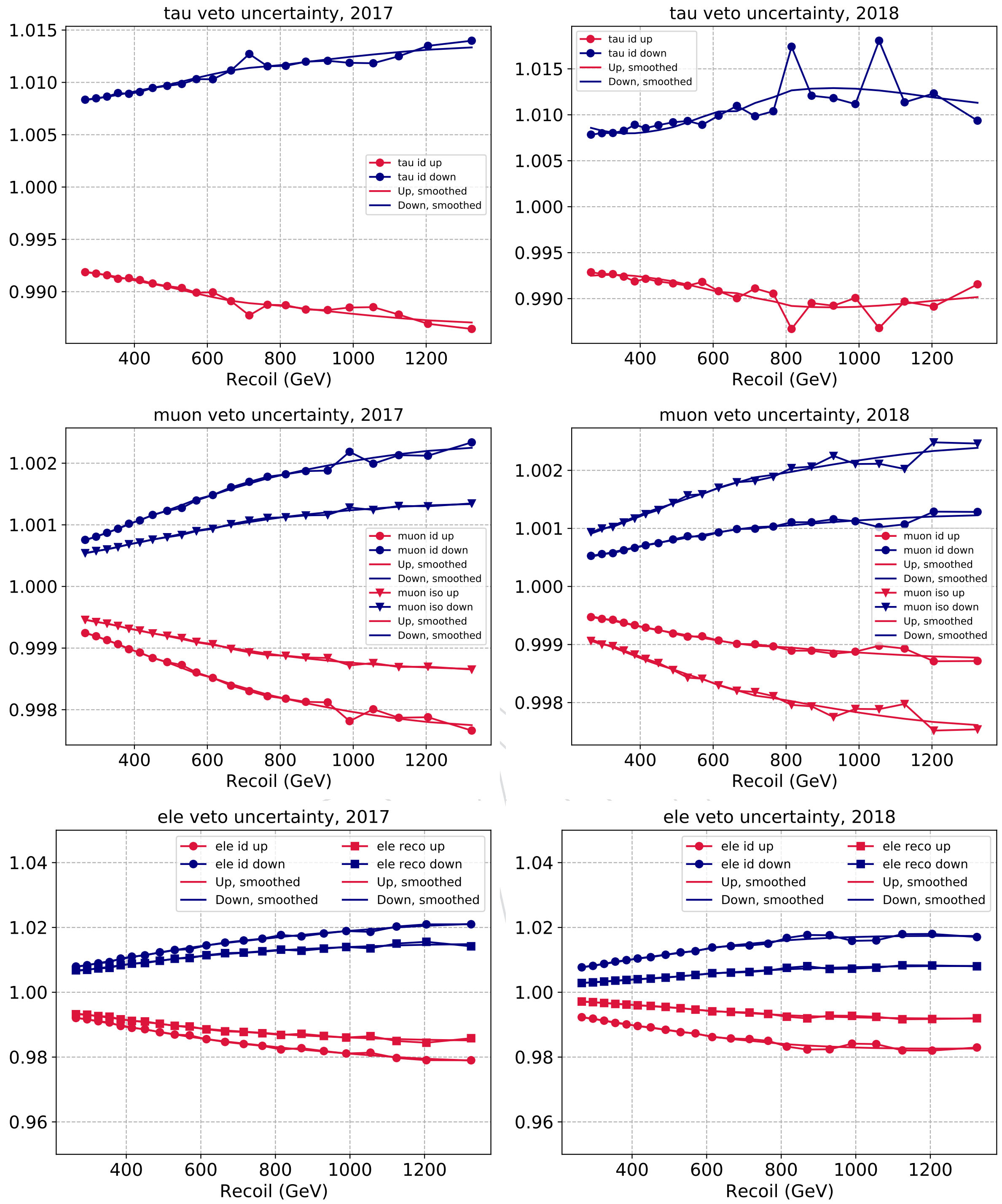

Figure 97: Veto uncertainties in the yields of the W + jets process in the signal region for the tau (top), muon (middle) and electron vetos (bottom). The smoothed template variations are used as inputs to the transfer factor uncertainties.

1414
6.4.3 Uncertainties assigned to the signals

1415 In addition to the uncertainties described in Section 6.4.2, additional theory uncertainties are
1416 applied to the signal processes.

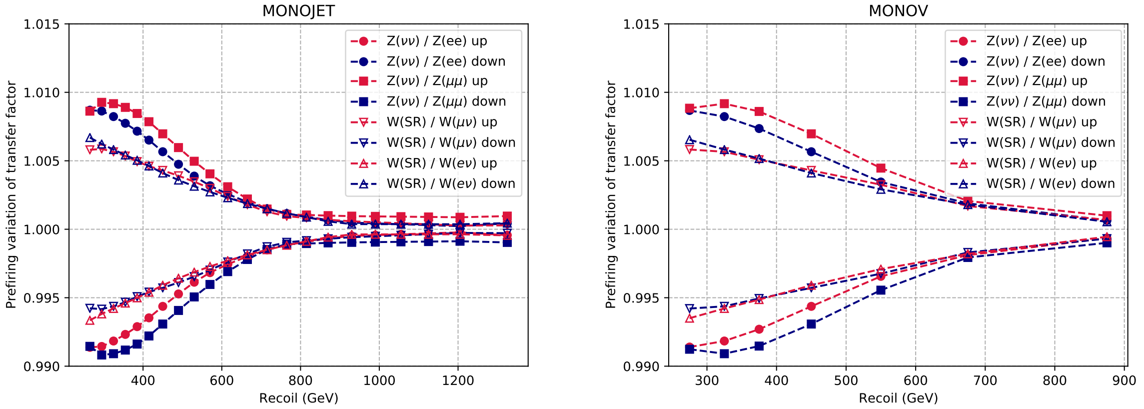

Figure 98: Transfer factor uncertainties based on the prefiring variations for the monojet (left) and mono-V categories (right). The variations for the Z-to-W, as well as the photon-to-Z ratio are not shown because they are found to be negligible.

Table 17: Experimental uncertainties affecting transfer factors used in the analysis to estimate the W $\rightarrow \ell\nu$ and Z $\rightarrow \nu\nu$ backgrounds in the signal region. The last column indicates whether the respective uncertainty value has been vetted for the 2017/2018 data set

Source	Process	Uncertainty	Up-to-date?
Electron trigger	$W_{\mathrm{SR}}/W_{e\nu}$, Z_{SR}/Z_{ee}	1%	✓
$E_{\mathrm{T}}^{\mathrm{miss}}$ trigger	$W_{\mathrm{SR}}/W_{e(\mu)\nu}$	1-2% (shape)	✓
	$Z_{\mathrm{SR}}/Z_{\mu\mu}$	2-3% (shape)	✓
Photon trigger	$Z_{\mathrm{SR}}/\gamma_{\mathrm{CR}}$	2%	✓
Photon p_{T} scale	$Z_{\mathrm{SR}}/\gamma_{\mathrm{CR}}$	$<4\%$ (shape)	✓
Muon-reco efficiency per muon	$W_{\mathrm{SR}}/W_{\mu\nu}$, $Z_{\mathrm{SR}}/Z_{\mu\mu}$	1%	✓
Muon-ID efficiency per muon	$W_{\mathrm{SR}}/W_{\mu\nu}$, $Z_{\mathrm{SR}}/Z_{\mu\mu}$	1%	✓
Muon-iso. efficiency per muon	$W_{\mathrm{SR}}/W_{\mu\nu}$, $Z_{\mathrm{SR}}/Z_{\mu\mu}$	1%	✓
Electron-reco efficiency per ele.	$W_{\mathrm{SR}}/W_{e\nu}$, Z_{SR}/Z_{ee}	1%	✓
Electron-ID efficiency per ele.	$W_{\mathrm{SR}}/W_{e\nu}$, Z_{SR}/Z_{ee}	3%	✓
Photon-ID efficiency	$Z_{\mathrm{SR}}/\gamma_{\mathrm{CR}}$	$4-13\%$ (shape)	✓
Muon veto	$W_{\mathrm{SR}}/W_{e(\mu)\nu}$ $Z_{\mathrm{SR}}/W_{\mathrm{SR}}$	$<1\%$ (shape)	✓
Electron veto	$W_{\mathrm{SR}}/W_{e(\mu)\nu}$ $Z_{\mathrm{SR}}/W_{\mathrm{SR}}$	2% (shape)	✓
Tau veto	$W_{\mathrm{SR}}/W_{e(\mu)\nu}$,$Z_{\mathrm{SR}}/W_{\mathrm{SR}}$	1–2% (shape)	✓
Prefiring	$Z_{\mathrm{SR}}/Z_{\mathrm{CR}}$,$W_{\mathrm{SR}}/W_{\mathrm{CR}}$	$<1\%$ (shape)	✓

Theoretical uncertainties are based on the 7-point QCD scale variations , as well as the PDF variations. For the scale variations, the envelope of the 7-point scale variations are employed (μ_R, μ_F up/down by factor of two with the exception of the two extreme points). PDF uncertainties are derived based on the 30 replicas of the PDF4LHC15 PDF set. In both cases, only the acceptance part of the uncertainties is considered, i.e. the effect on the inclusive signal normalization is neglected.

For the invisible Higgs signal model, the acceptance uncertainties are derived from the centrally produced signal samples via an event-by-event reweighting. To smoothen out the tem-

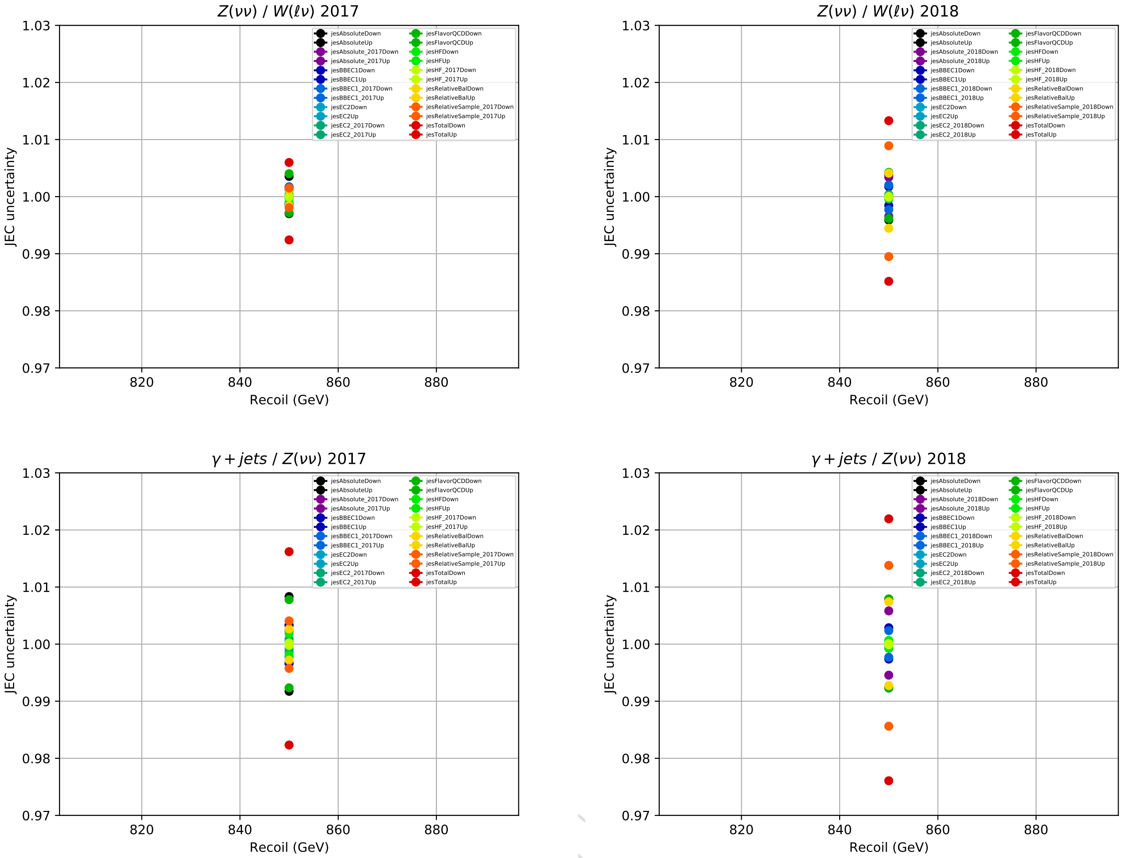

Figure 99: Jet energy scale (JES) and resolution (JER) uncertainties with the 11-source splitting used for JES uncertainties. Plots on the top show the uncertainites for $Z \to \nu\nu / W \to \ell\nu$, and the plots on the bottom show the uncertainties for $\gamma + \text{jets}/Z \to \nu\nu$, for 2017 and 2018.

plate variations, polynominal fits are performed to the up/down variations, and the values from the fits are used for up/down templates in combine. The template variations are shown in Fig. 104. Since the samples are normalized to the cross section values from the yellow report, the corresponding normalization uncertainties for PDF and scale variations are taken from the yellow report and added as independent nuisance parameters.

For the other signal models, the relative per-bin template variations from the invisible Higgs interpretation are copied, sicne the relevant weights are not available in all samples. For DM+Z and DM+W production, the ucnertainties are taken from WH and ZH, respectively. For the DM+jet signatures, as well as for the ADD and LQ interpretations, the ggH-based uncertainties are used.

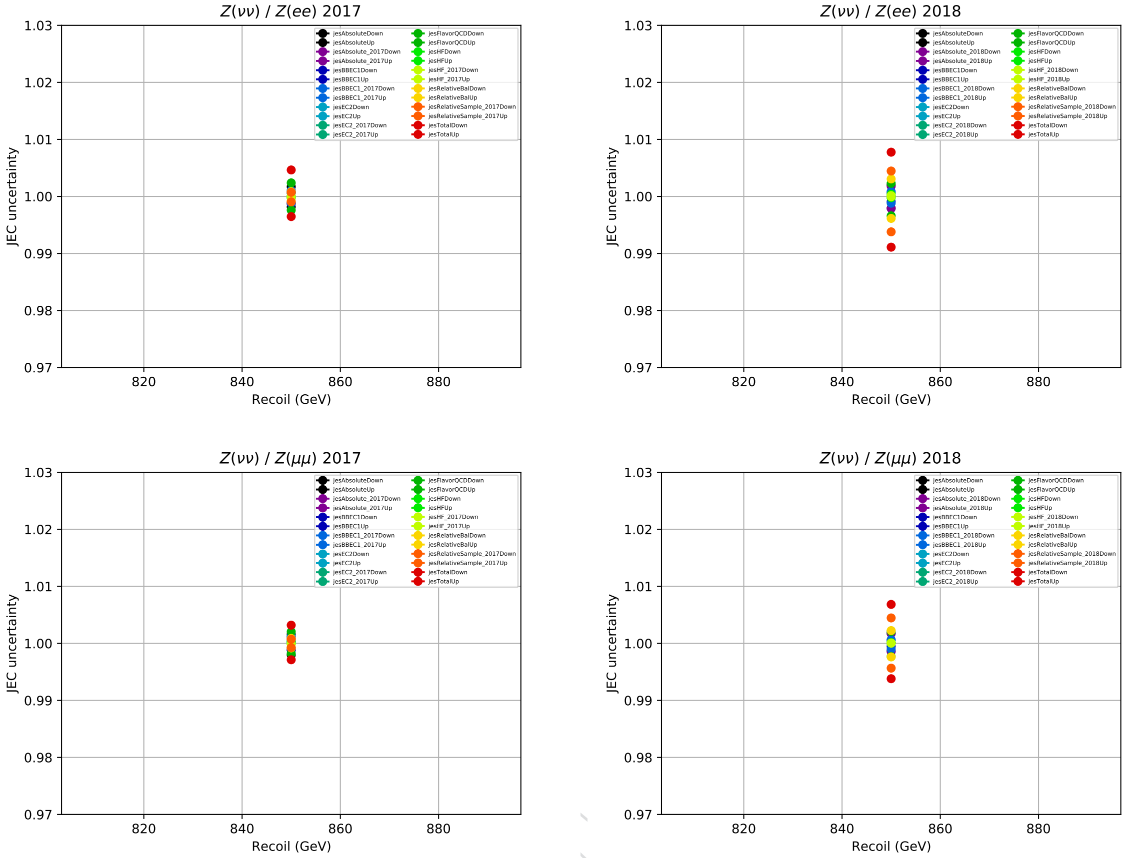

Figure 100: Jet energy scale (JES) and resolution (JER) uncertainties with the 11-source splitting used for JES uncertainties. Plots on the top show the uncertainites for $Z \to \nu\nu / Z \to e^+e^-$, and the plots on the bottom show the uncertainties for $Z \to \nu\nu / Z \to \mu^+\mu^-$, for 2017 and 2018.

6.5 Control sample validation

An important cross-check of the application of p_{T}-dependent NLO QCD and EW corrections is represented by the agreement between data and simulation in the ratio of $\mathrm{Z} + \text{jets}$ events to both $\gamma + \text{jets}$ events and $\mathrm{W} + \text{jets}$ events in the control samples, as a function of hadronic recoil p_{T}.

The ratios between $\mathrm{Z}(\ell\ell) + \text{jets}$ and $\gamma + \text{jets}$, $\mathrm{Z}(\ell\ell) + \text{jets}$ and $\mathrm{W}(\ell\nu) + \text{jets}$, and the one between $\mathrm{W}(\ell\nu) + \text{jets}$ and $\gamma + \text{jets}$ processes are shown in Fig. 105 for the monojet category and and Figs. 107 and 107 for the low- and high-purity mono-V categories, respectively. While we do not explicitly use a $\mathrm{W}(\ell\nu) + \text{jets}/\gamma + \text{jets}$ constraint in the analysis, the two cross sections are connected through the $\mathrm{Z} + \text{jets}/\gamma + \text{jets}$ and $\mathrm{Z} + \text{jets}/\mathrm{W} + \text{jets}$ constraints. Therefore, it is instructive to examine the data-MC comparison of the $\mathrm{W}(\ell\nu) + \text{jets}/\gamma + \text{jets}$ ratio.

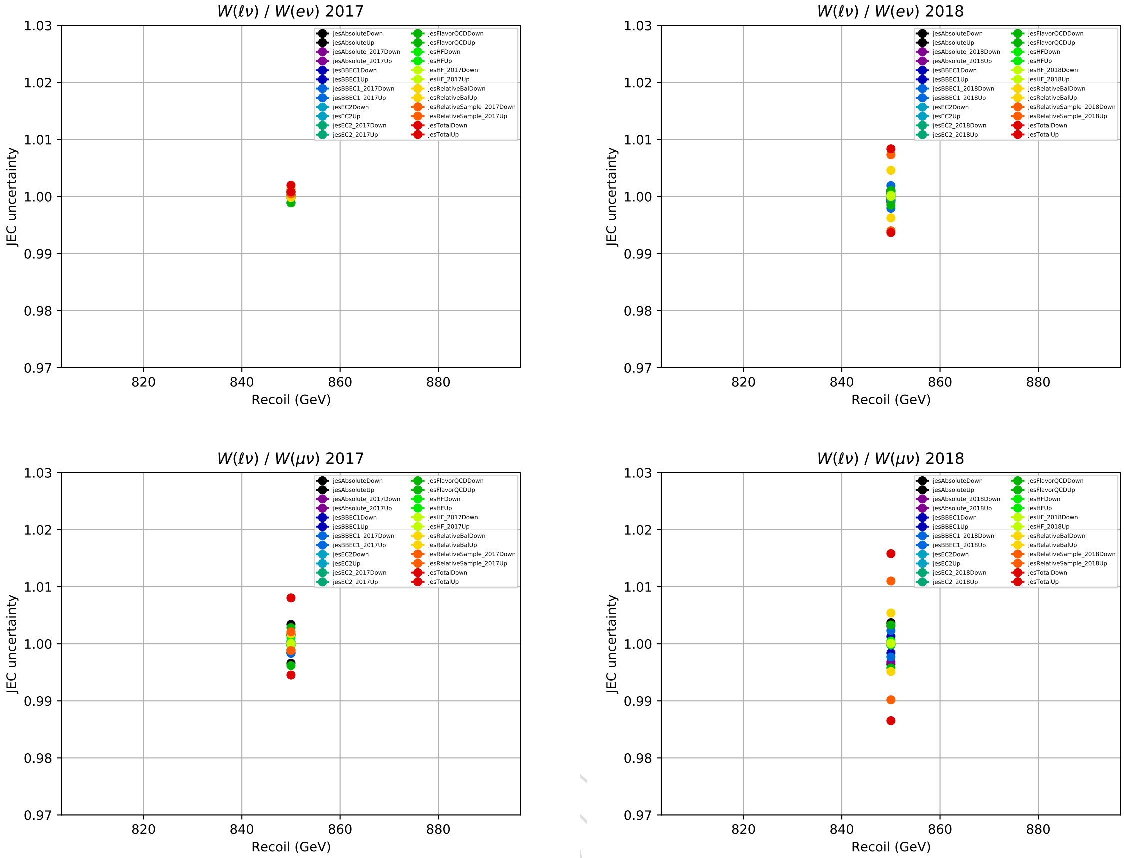

Figure 101: Jet energy scale (JES) and resolution (JER) uncertainties with the 11-source splitting used for JES uncertainties. Plots on the top show the uncertainites for $W \to \ell\nu / W \to e\nu$, and the plots on the bottom show the uncertainties for $W \to \ell\nu / W \to \mu\nu$, for 2017 and 2018.

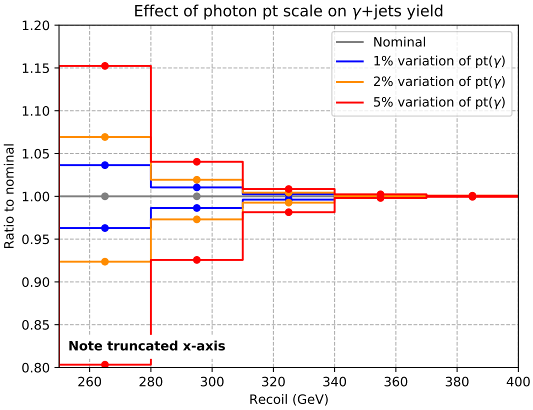

Figure 102: The effect of a photon p_T scale on the background prediction in the photon CR. Note that the x axis is truncated from its full range in order to better show the low-recoil bins.

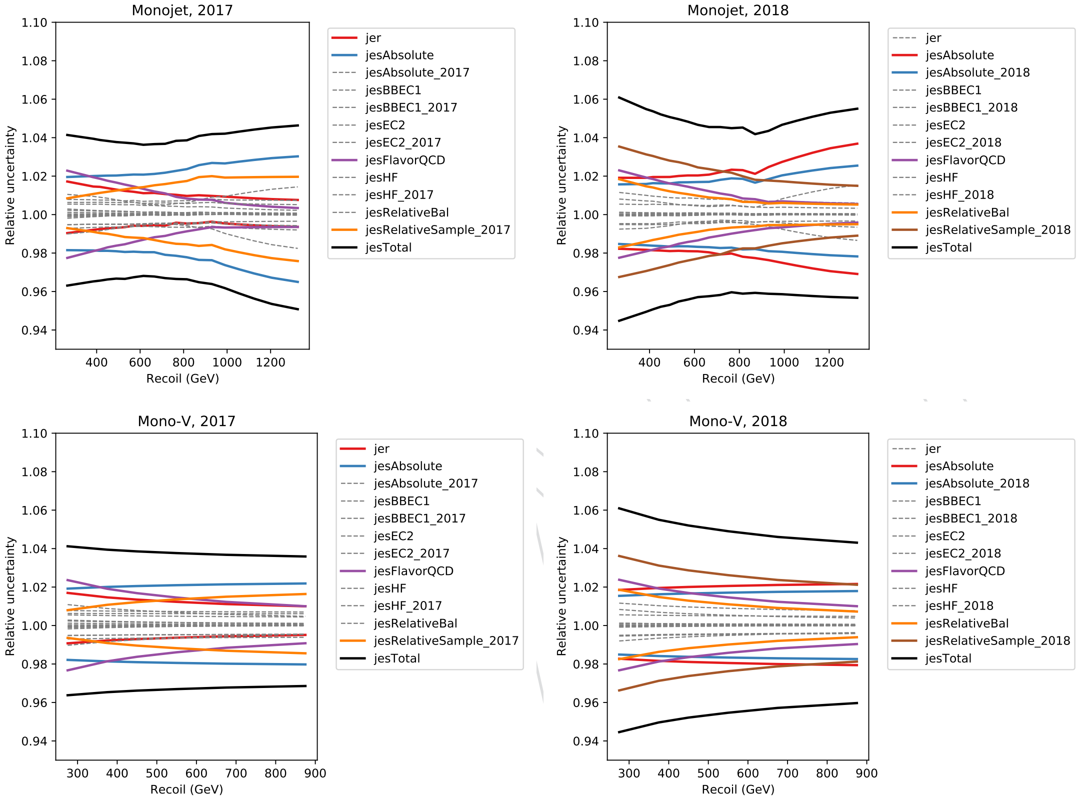

Figure 103: Uncertainties related to jet calibration for the monojet (top) and mono-V categories (bottom), for the 2017 (left) and 2018 (right) data sets. In each panel, all sources shown are taken into account in the final fit. For demonstrational calrity, all components with an average per-bin effect of less than 1% are shown in the same grey color. Components with a larger average effect are shown in separate colors and thicker lines.

Table 18: Uncertainties assigned to the simulation based processes. If two values are given, the first refers to 2017, the second to 2018.

Source	Process	Uncertainty	Up-to-date?
Luminosity	All	2.5 %/ 2.3%	✓
Electron trigger	All in 1e CR	1%	✓
$E_{\mathrm{T}}^{\mathrm{miss}}$ trigger	All in SR and 1μ CR	2%	✓
Jet/$E_{\mathrm{T}}^{\mathrm{miss}}$ energy calibration	All	5% (shape)	✓
Muon-reco efficiency per muon	All in muon CRs	1%	✓
Muon-ID efficiency per muon	All in muon CRs	1%	✓
Muon-iso efficiency per muon	All in muon CRs	1%	✓
Electron-reco efficiency per ele.	All in electron CRs	1%	✓
Electron-ID efficiency per ele.	All in electron CRs	3%	✓
b-jet veto	Top in SR and all CRs	6%	✓
	All remaining in SR and all CRs	2%	✓
Top p_{T} reweight	Top	10%	✓
Top norm	Top	10%	✓
Diboson mixed EWK-QCD corr.	Diboson	up to 10% (shape)	✓
Diboson normalization	Diboson	10%	✓
$\mathrm{Z}(\ell\ell) +$ jets norm	$\mathrm{Z}(\ell\ell) +$ jets (SR)	20%	✓
`QCD`	`QCD` in SR	from 20% up to $>$ 100% (shape)	✓
Fake muons	`QCD` in $W_{\mu\nu}$	50%	✓
Jet-to-electron fakes	`QCD` in $W_{e\nu}$	75%	✓
Photon-to-electron fakes	$\gamma +$ jets in $W_{e\nu}$	20%	✓

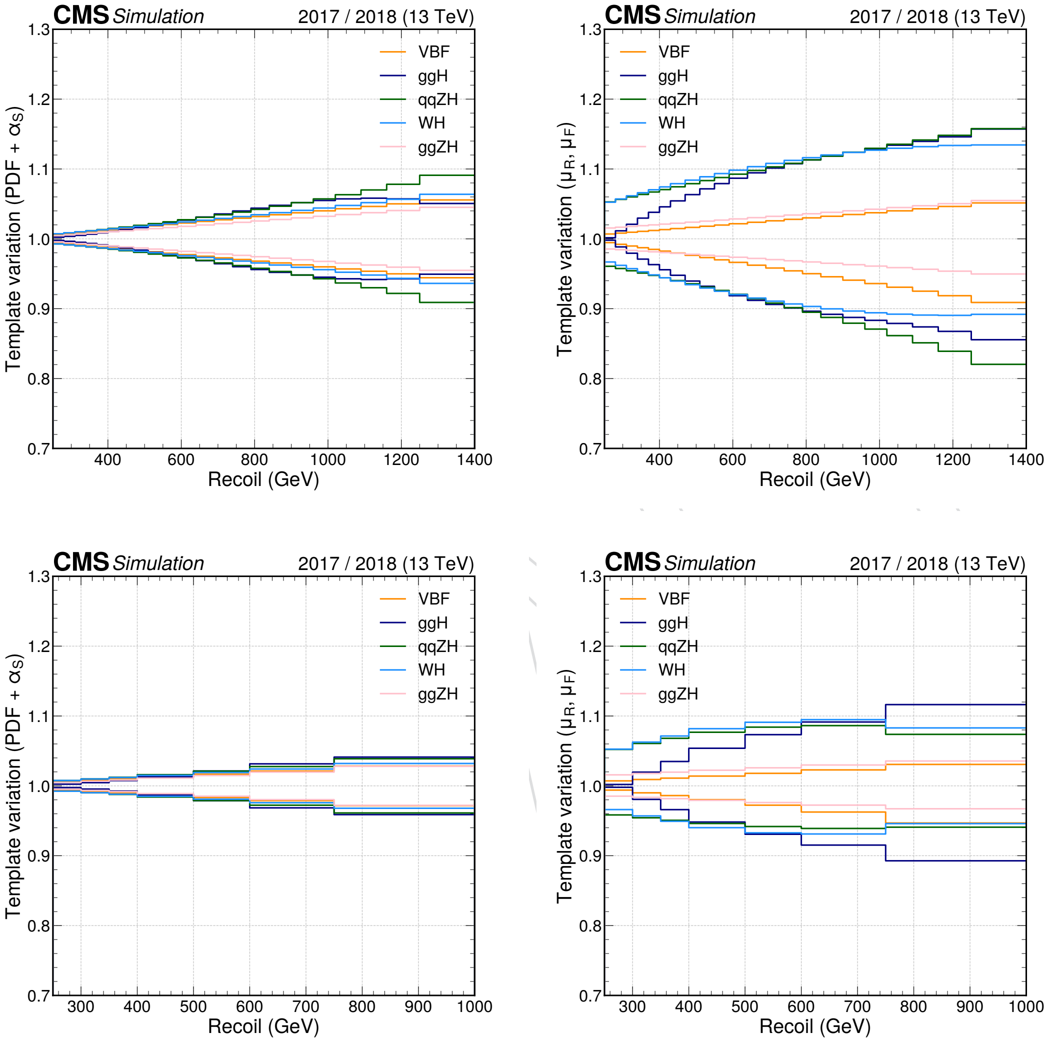

Figure 104: Signal theory uncertainties for the monojet (top) and mono-V analyses (bottom). The left (right) column shows the template variations related to the acceptance parts of the PDF (QCD scale) uncertainties. The template variations are derived from the H(inv) signal samples with various production modes. For other interpretations, the template variations for the most closely related H(inv) production mode are copied.

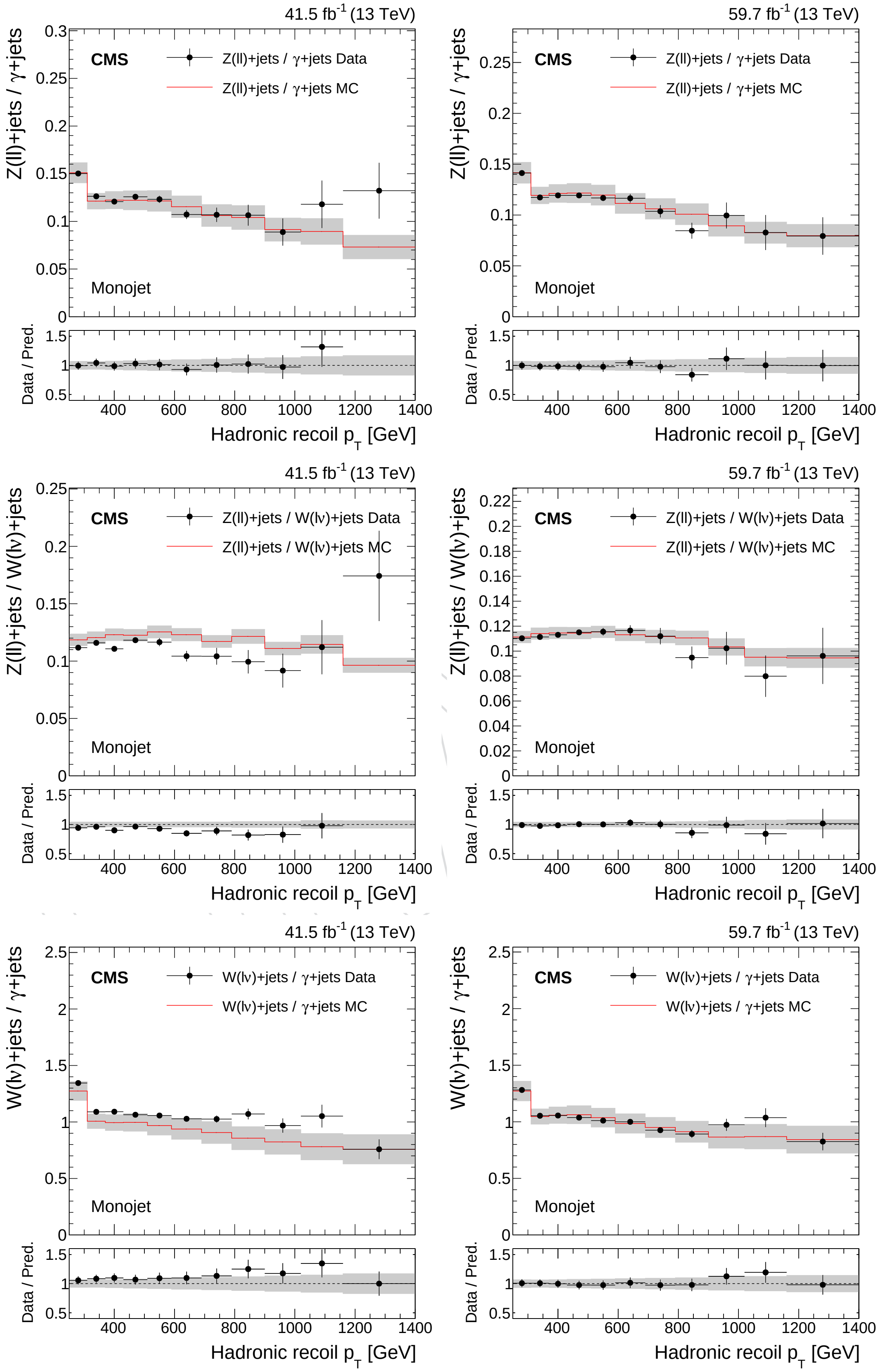

Figure 105: Comparison between data and MC simulation for the $Z(\ell\ell)/\gamma+$jets (top row), $Z(\ell\ell)/W(\ell\nu)$ (middle row), and $W(\ell\nu)/\gamma+$jets ratios (bottom row) as a function of the hadronic recoil in the monojet category. The left and right columns correspond to the 2017 and 2018 datasets, respectively. In each case, the left column shows the muon regions, while the right column shows the electron regions. In each of the lower panels, ratios of data with the pre-fit background prediction are shown. The shaded bands represent the statistical uncertainty in the simulation.

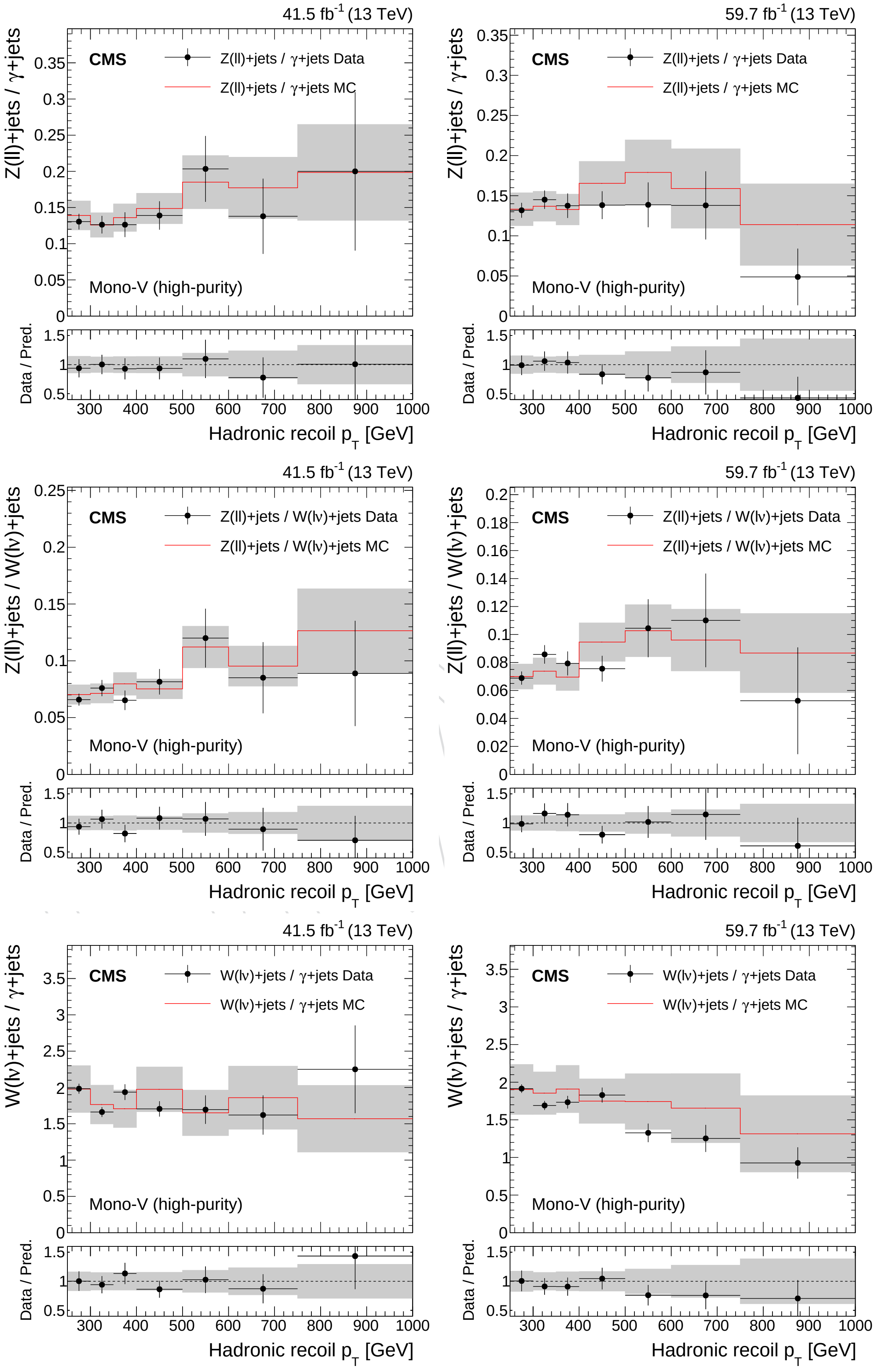

Figure 106: Same as Fig. 105, but for the high-purity mono-V category.

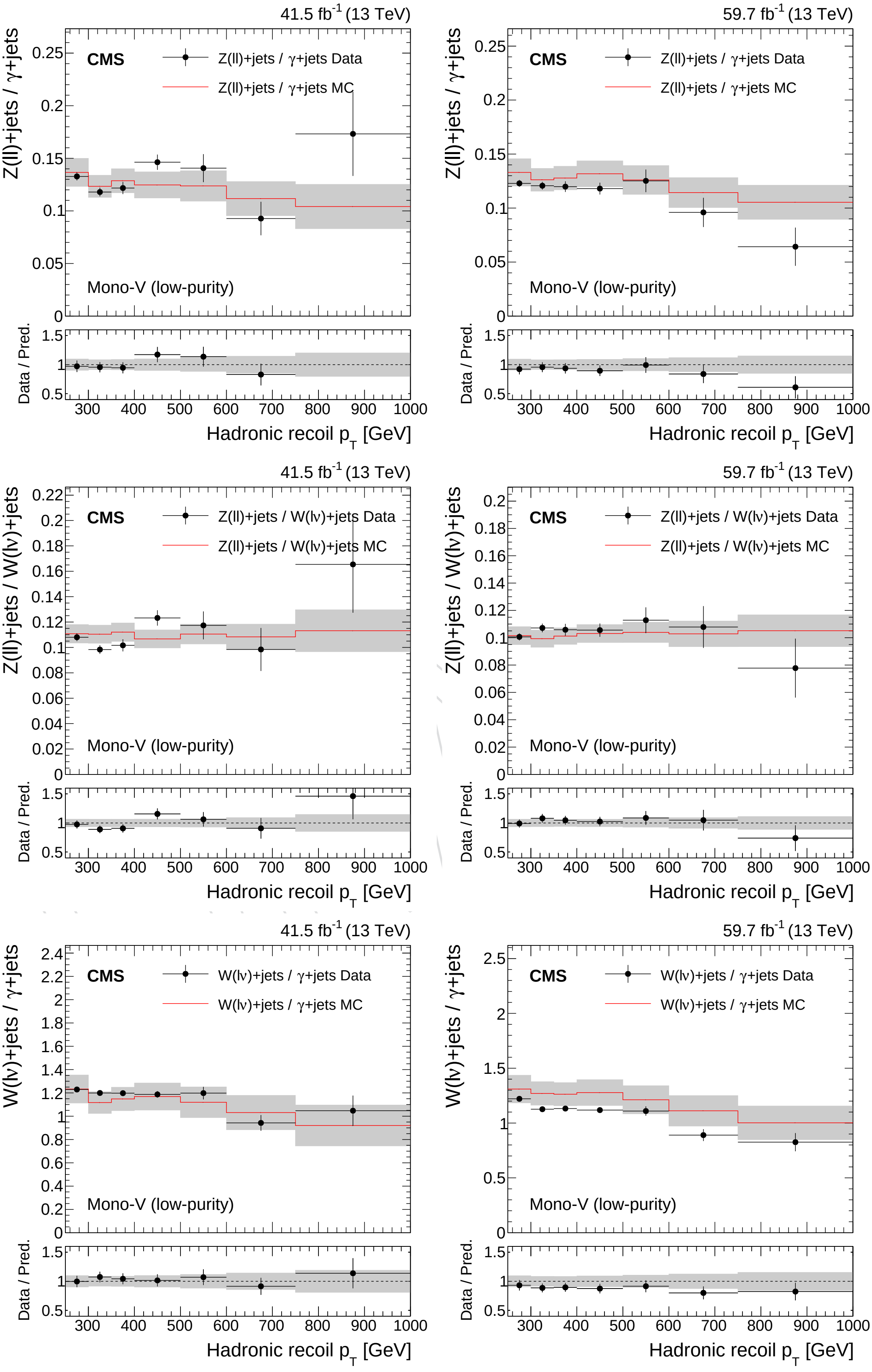

Figure 107: Same as Fig. 105, but for the low-purity mono-V category.

7 Results

In this section, fit results and final sensitivies are discussed. All fits are performed by combining the 2017 and 2018 data sets, as well as combining the monojet and mono-V categories, which are orthogonal in event selection, but share some common systematic uncertainties, such as uncertainties related to theoretical predictions.

7.1 Control region + signal region fit

A fit is performed using the full comination of control and signal regions, as well as categories. The 2017 and 2018 datasets are combined and fit using a common likelihood function, in which most experimental uncertainties are decorrelated between the years, but theoretical uncertainties are correlated. Due to common correlated sources, the uncertainties related to the jet energy calibration as well as the uncertainty related to the luminosity determination are partially correlated between years. We follow the partial correlation scheme defined by the relevant POGs. In all following plots, note that nuisance parameters that have a year in their name (e.g. "CMS_eff2017_e") are decorrelated between the years, while parameters that do not have a year in their name (e.g. "ewk") are correlated between the years.

7.1.1 Post-fit agreement in the control regions

Figures 108–110 (111–113 and 114–116) show the results of the combined fit in all control samples and the signal region in the monojet (loose and tight mono-V, respectively) category. Data in the are compared to the pre-fit predictions from simulation and the post-fit estimates obtained after performing the fit.

The postfit version of the background prediction is in very good agreement with the spectra observed in data. In the bulk of the distributions, where systematic and statistical uncertainties are small, only very few significant pulls (data $-$ prediction/uncertainty $\approx$ 2) are observed, with most bins agreeing to significantly better precision. In the mono-V categories, the overall behavior of the control regions is much more dominated by statistical uncertainties than in the monojet case.

The prefit and postfit yields for all processes in all regions, categories and years are shown in Tables 19, 20 and 21. The nuisance parameter pulls, as well as a quantitative goodness-of-fit evaluation are provided in Appendix F.

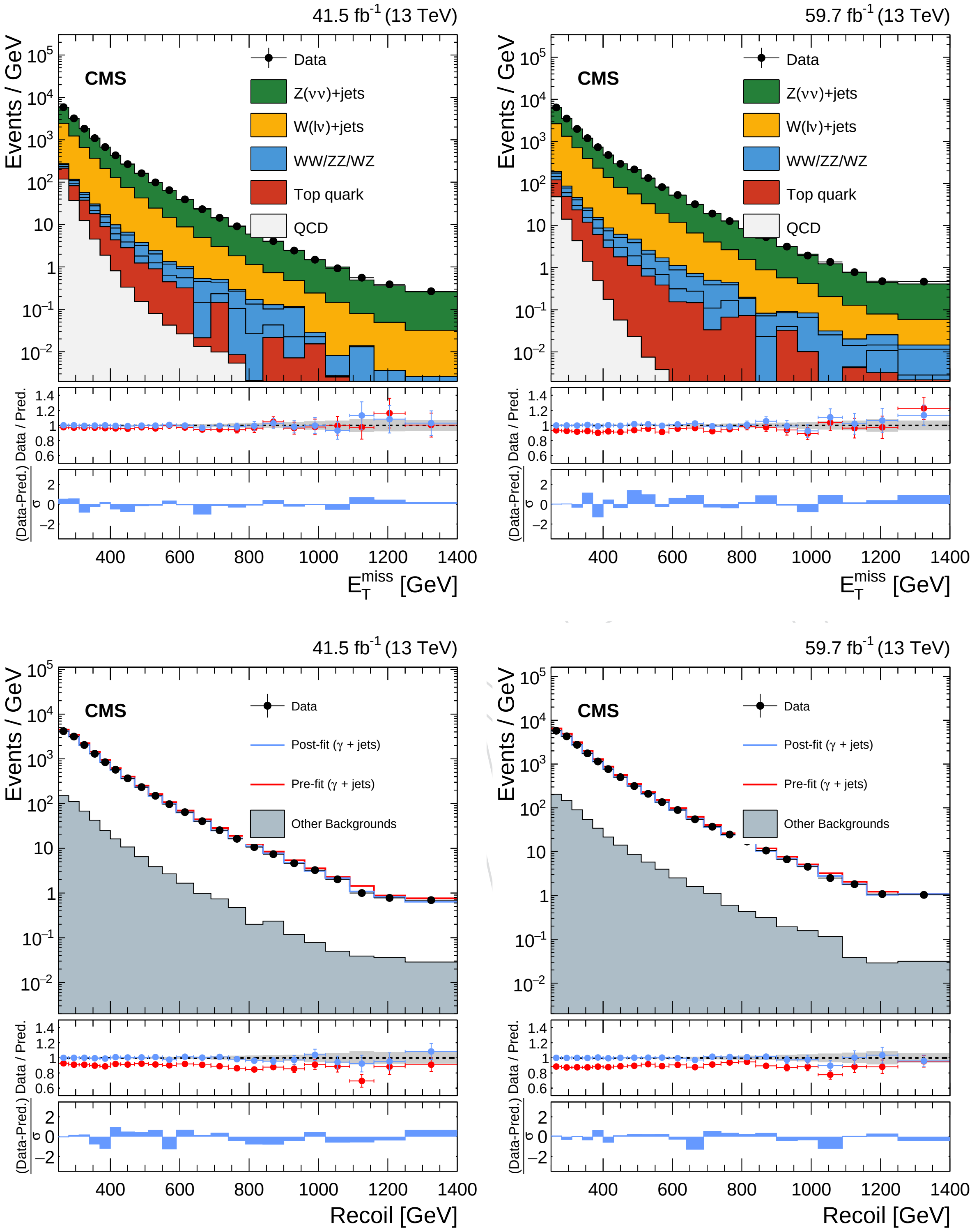

Figure 108: Comparison between data and MC simulation in the signal region (top) and $\gamma+$jets control sample (bottom) before and after the simultaneous fit. The fit includes all control samples and the partially unblinded signal region in all categories and both years. The resulting distributions are shown separately for 2017 (left) and 2018 (right). The hadronic recoil p_{T} in $\gamma+$jets events is used as a proxy for $p_{\mathrm{T}}^{\mathrm{miss}}$ in the signal region. The last bin includes overflow. In the lower panels, ratios of data with the pre-fit background prediction (red open points) and post-fit background prediction (blue full points) are shown. The gray band in the lower panel indicates the post-fit uncertainty after combining all the systematic uncertainties. Finally, the distribution of the pulls, defined as the difference between data and the post-fit background prediction relative to the quadrature sum of the post-fit uncertainty in the prediction and statistical uncertainty in data, is shown in the lowest panel.

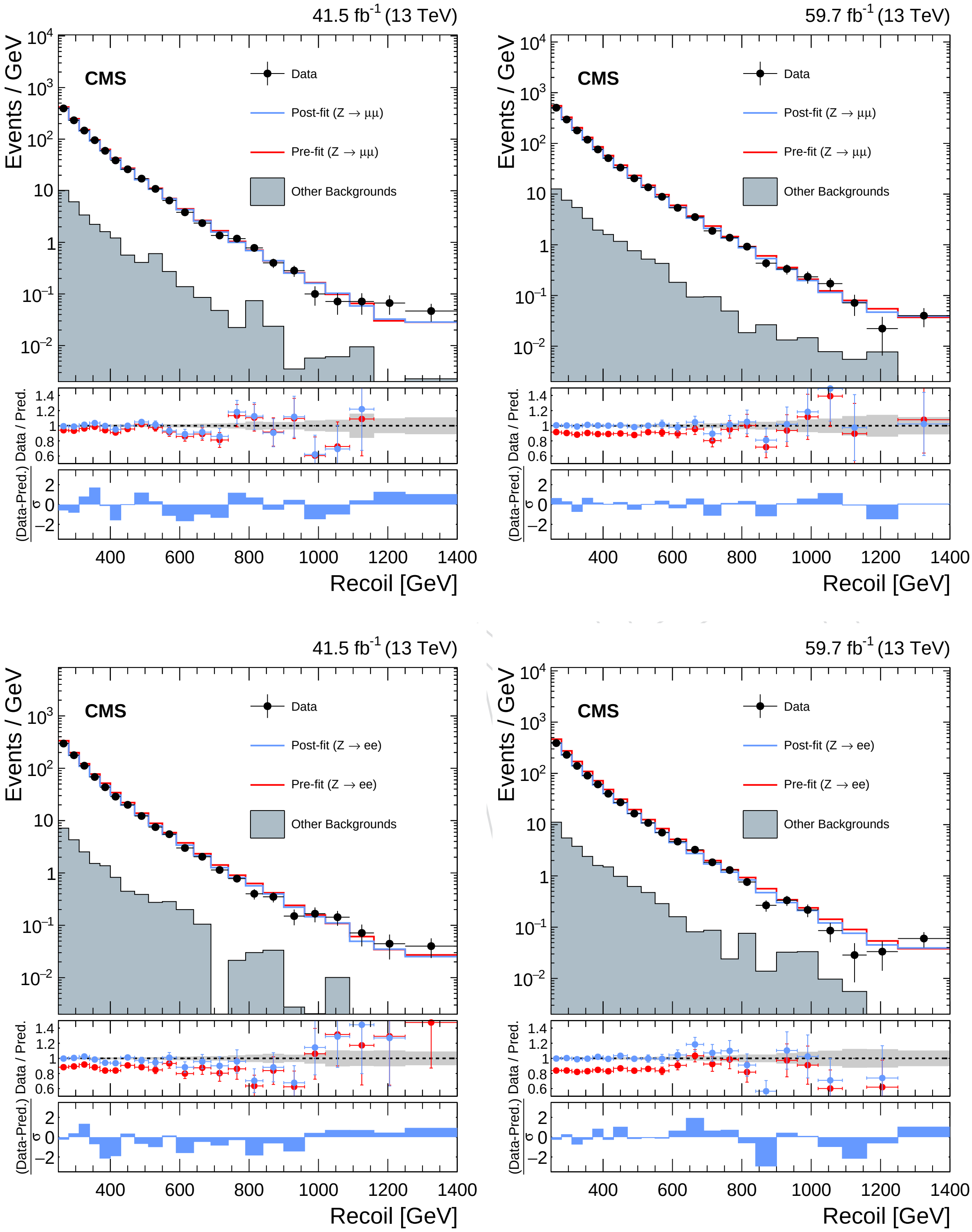

Figure 109: Same as Fig. 108 but for the dilepton CRs. The other backgrounds include top quark, diboson, and W + jets processes.

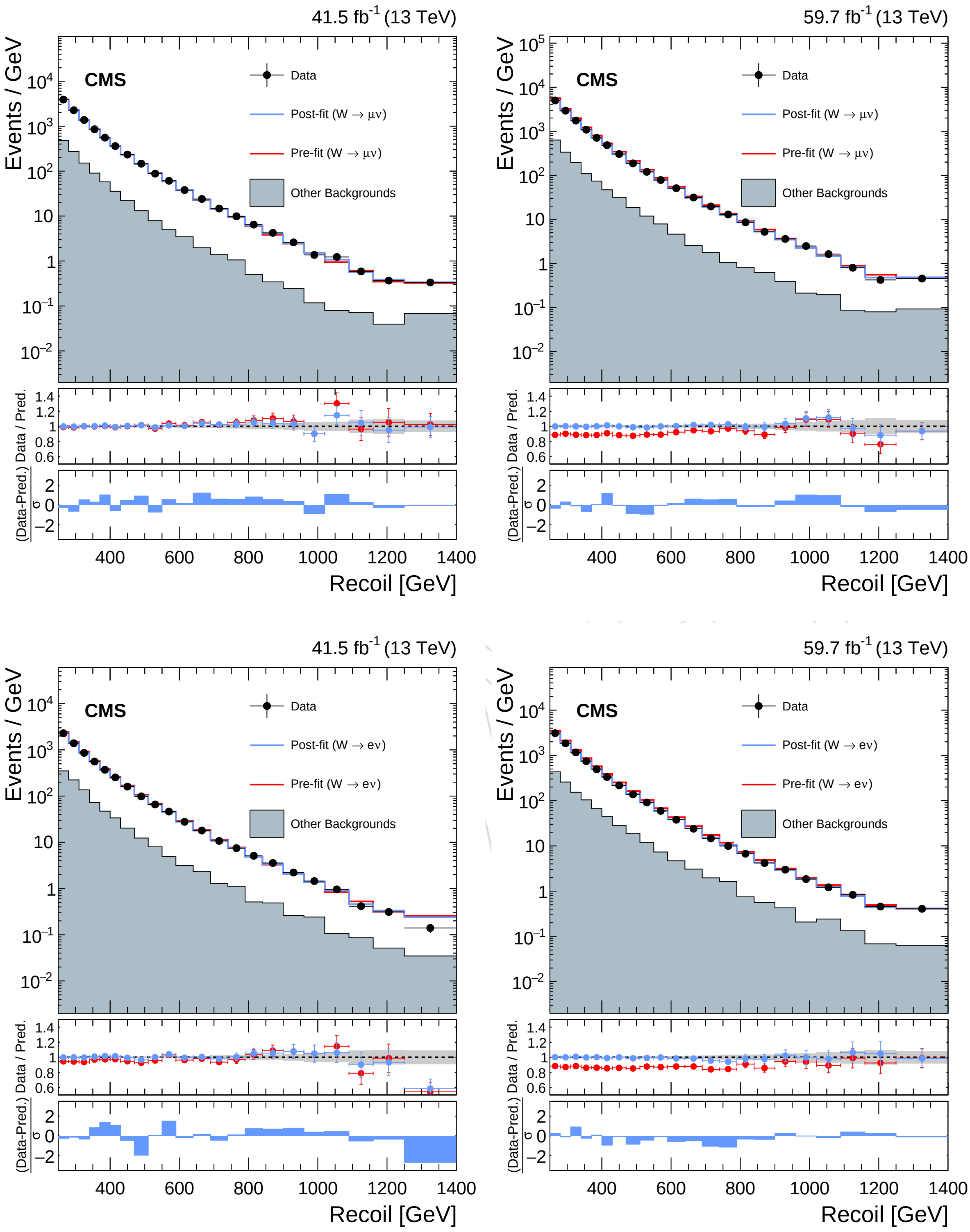

Figure 110: Same as Fig. 108 but for the single-lepton CRs. The other backgrounds include top quark, diboson, and QCD multijet processes. The description of the lower panels is the same as in Fig. 108.

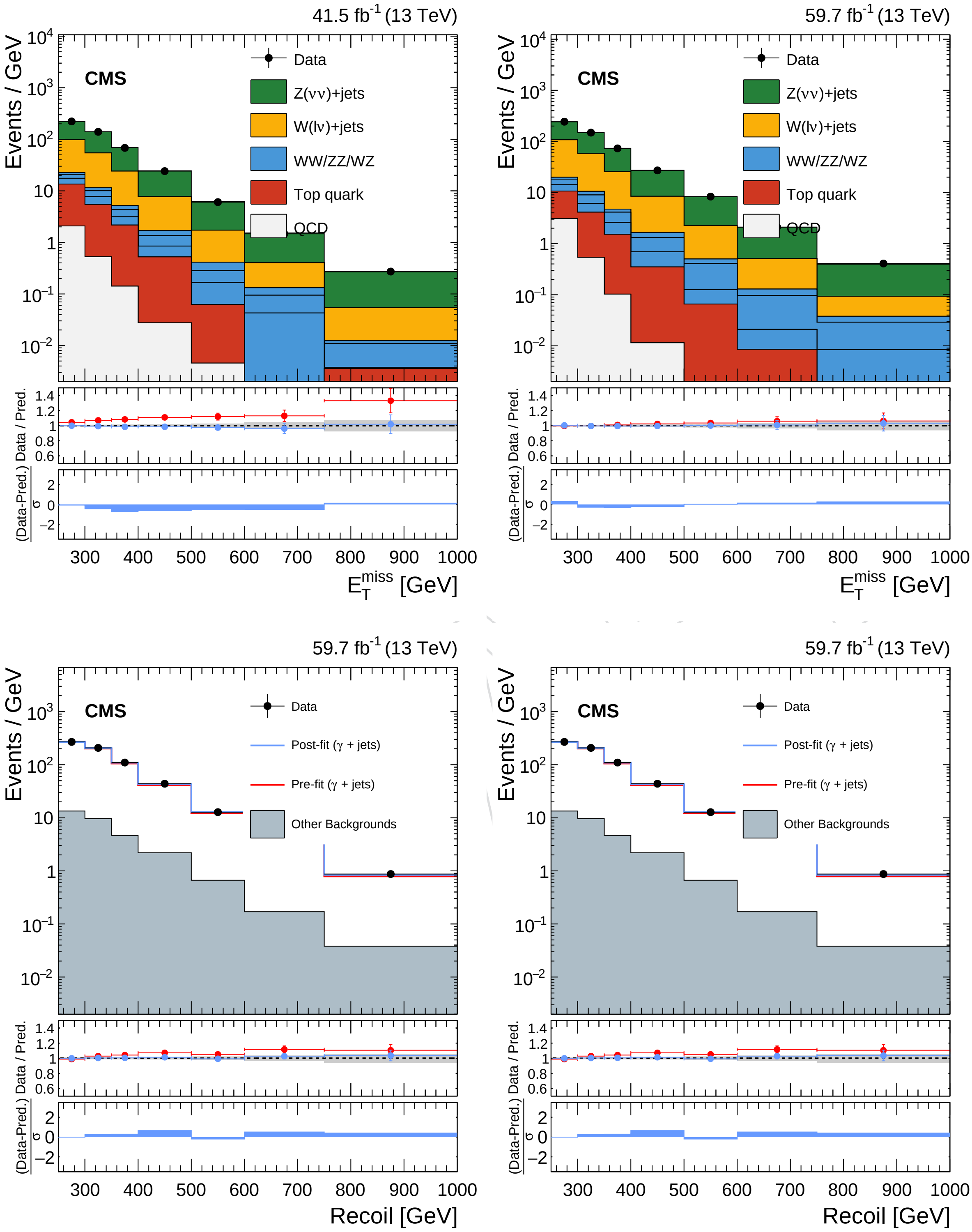

Figure 111: Same as Fig. 108, but for the low-purity mono-V category.

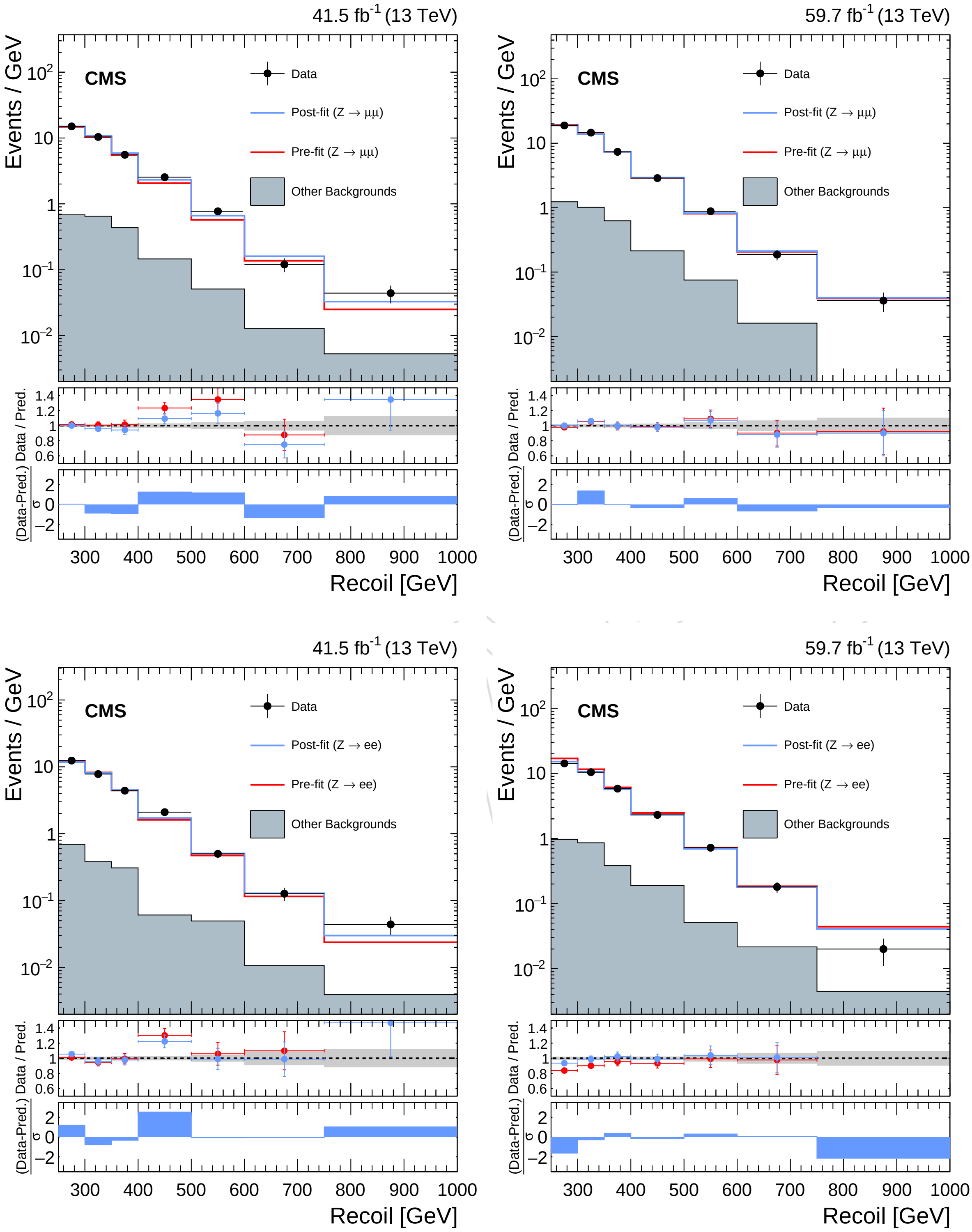

Figure 112: Same as Fig. 109, but for the low-purity mono-V category.

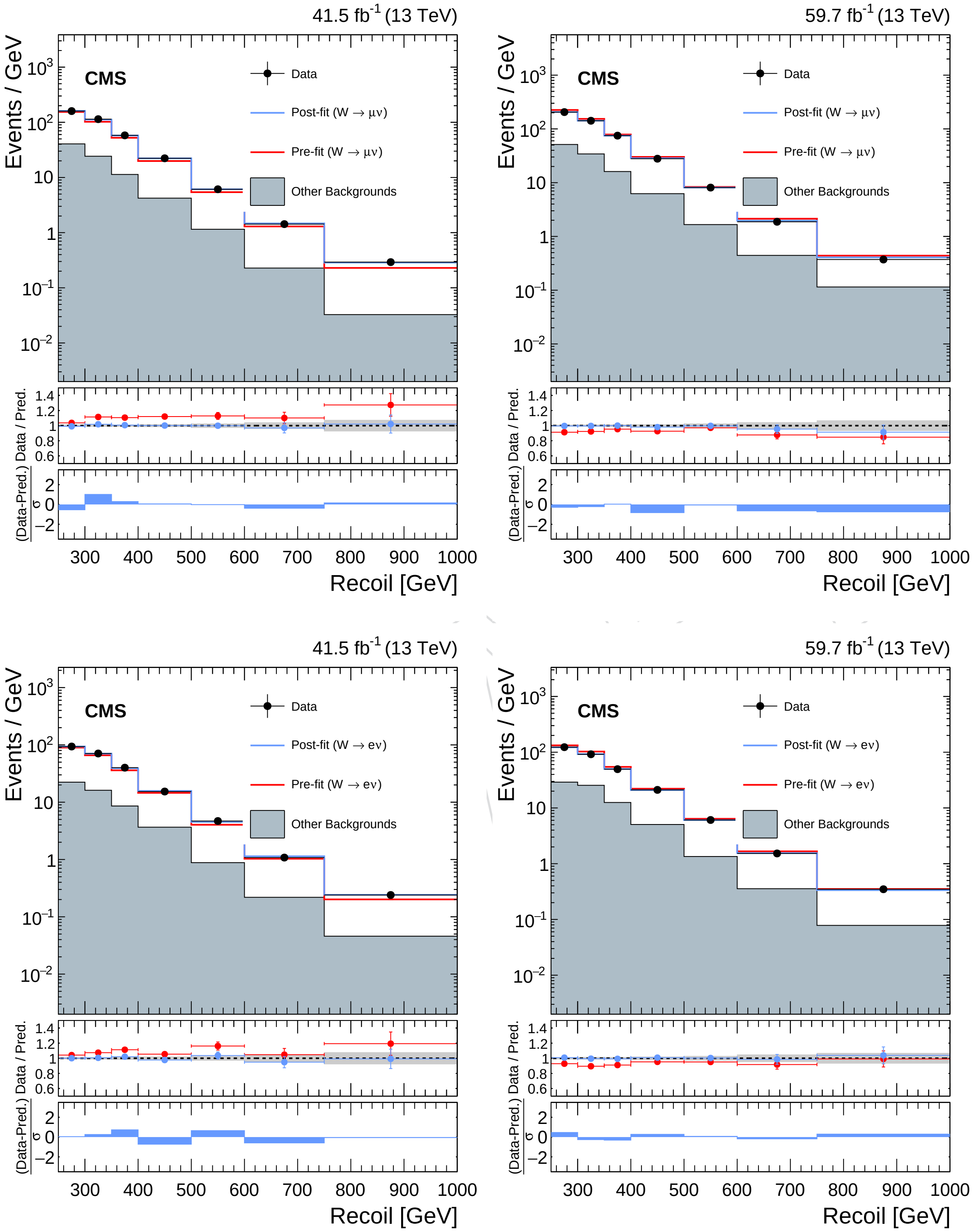

Figure 113: Same as Fig. 110, but for the low-purity mono-V category.

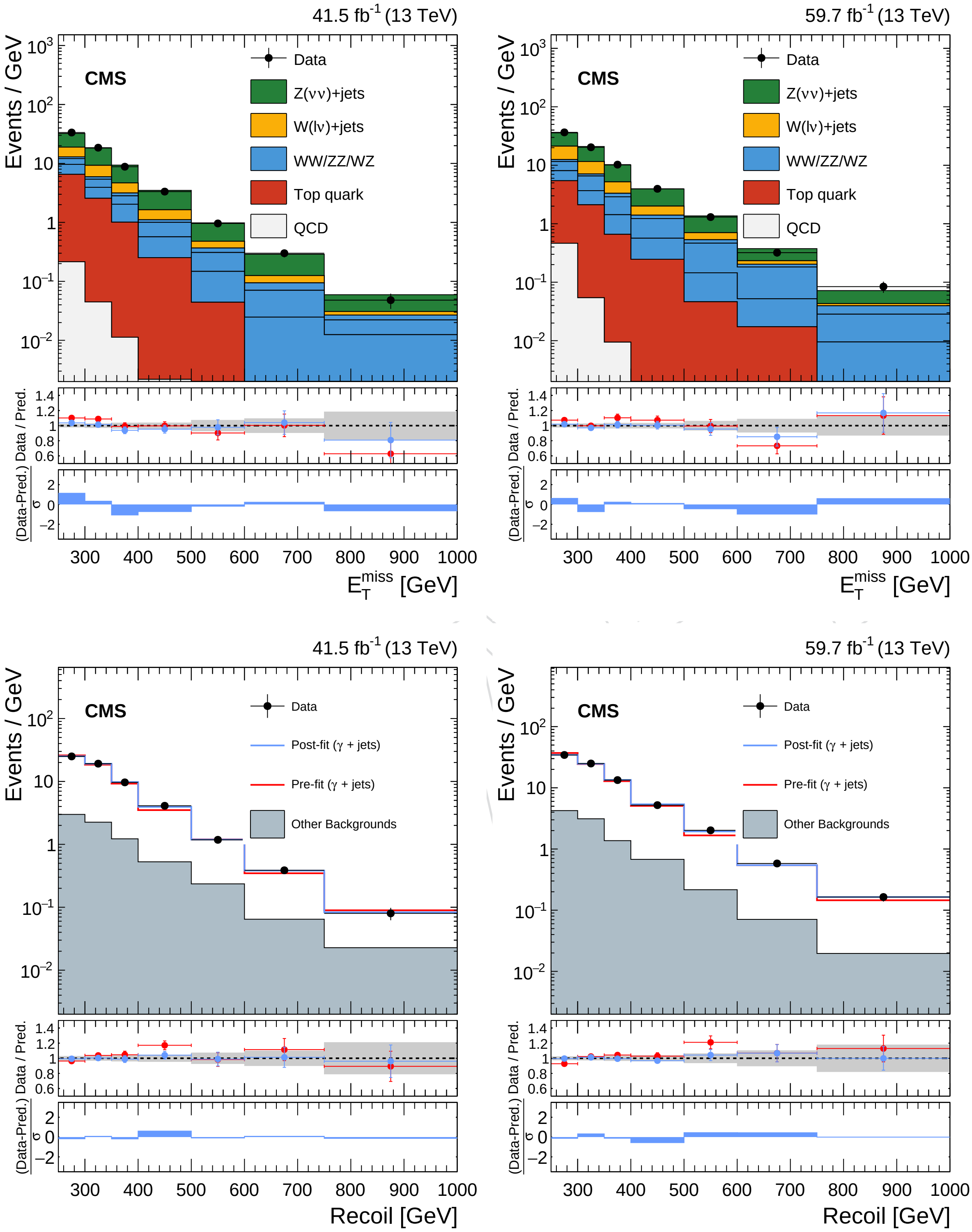

Figure 114: Same as Fig. 108, but for the high-purity mono-V category.

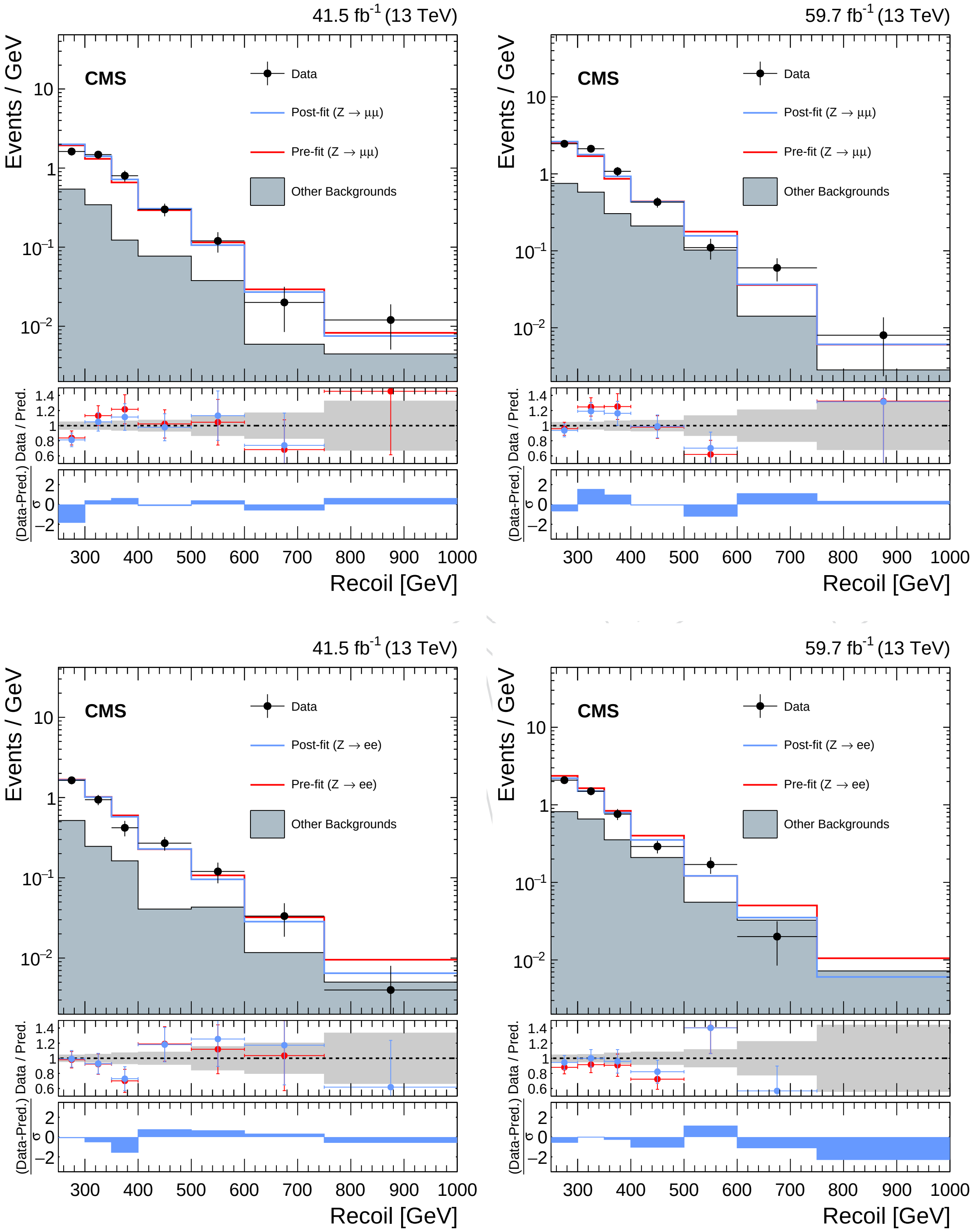

Figure 115: Same as Fig. 109, but for the high-purity mono-V category.

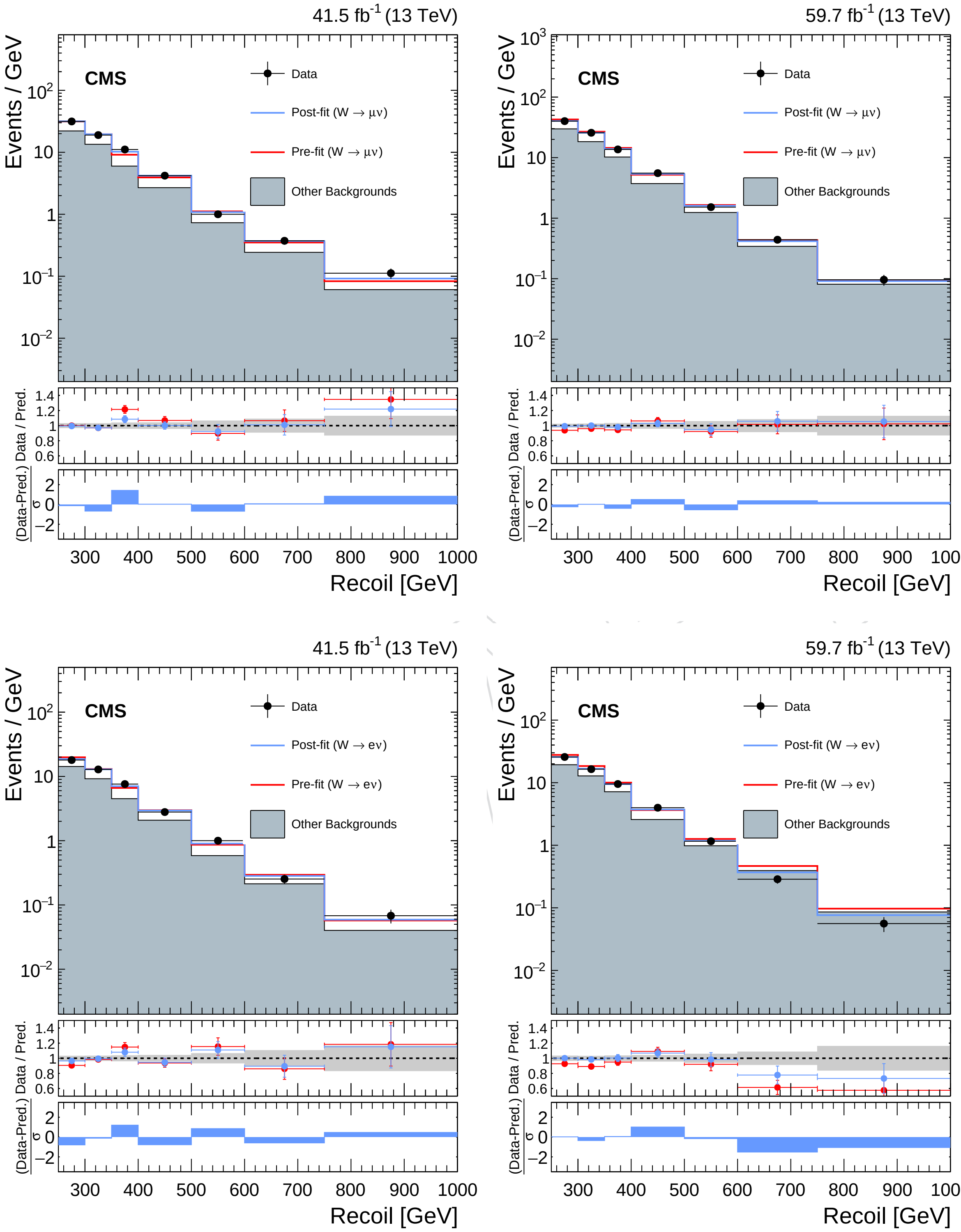

Figure 116: Same as Fig. 110, but for the high-purity mono-V category.

Table 19: Event yield per process before the fit. The yields are rounded to 3 significant digits.

year	channel	region	$W\gamma$	WW	DY	$W + \text{jets}$	ZZ	$Z \to \nu\nu$	WZ	$Z\gamma$	$\gamma + \text{jets}$	QCD	Top	Total BG	Data
2017	monojet	γ CR	2290	-	-	-	-	-	-	842	430000	10500	-	444000	405000
		1μ CR	-	3540	8300	273000	34.5	-	846	-	-	8550	13700	308000	306000
		1e CR	-	2280	3240	172000	14.2	-	555	-	7960	4780	9450	201000	191000
		2μ CR	-	118	32900	-	136	-	203	-	-	-	382	33700	32000
		2e CR	-	75.9	26500	-	108	-	173	-	-	-	252	27100	24000
		SR	-	1460	-	146000	1030	275000	2010	-	-	2720	5390	434000	-
	monovloose	γ CR	354	-	-	-	-	-	-	204	24300	666	-	25500	26800
		1μ CR	-	788	394	13800	6.30	-	157	-	-	533	2520	18200	19800
		1e CR	-	560	145	8810	3.30	-	104	-	236	89.7	1730	11700	12500
		2μ CR	-	4.29	1710	-	30.1	-	44.8	-	-	-	32.1	1820	1910
		2e CR	-	4.23	1400	-	24.2	-	36.0	-	-	-	18.9	1480	1520
		SR	-	372	-	7090	220	14200	412	-	-	147	880	23300	-
	monovtight	γ CR	222	-	-	-	-	-	-	110	2810	82.4	-	3230	3300
		1μ CR	-	803	40.2	1110	2.48	-	83.1	-	-	76.6	1470	3590	3690
		1e CR	-	535	14.7	711	0.816	-	62.3	-	32.3	21.1	1040	2420	2360
		2μ CR	-	1.70	178	-	14.9	-	35.6	-	-	-	11.8	242	243
		2e CR	-	2.48	147	-	9.42	-	37.6	-	-	-	8.26	205	195
		SR	-	337	-	531	102	1450	348	-	-	12.1	536	3320	-
2018	monojet	γ CR	3060	-	-	-	-	-	-	1170	611000	14000	-	629000	554000
		1μ CR	-	4720	11100	397000	47.1	-	1790	-	-	10800	16900	442000	394000
		1e CR	-	3200	4140	258000	21.7	-	1180	-	10400	4210	11900	293000	256000
		2μ CR	-	142	43800	-	183	-	334	-	-	-	458	44900	40600
		2e CR	-	115	36900	-	158	-	274	-	-	-	352	37800	31700
		SR	-	1600	-	171000	1150	316000	2710	-	-	1990	5080	500000	-
	monovloose	γ CR	508	-	-	-	-	-	-	336	33300	868	-	35000	35800
		1μ CR	-	1180	530	21200	8.74	-	364	-	-	665	3240	27200	25100
		1e CR	-	777	205	13600	3.88	-	254	-	286	278	2260	17700	16300
		2μ CR	-	7.68	2270	-	44.2	-	92.0	-	-	-	31.0	2450	2460
		2e CR	-	4.62	1950	-	34.2	-	65.8	-	-	-	34.2	2090	1860
		SR	-	442	-	8590	262	16100	685	-	-	181	900	27200	-
	monovtight	γ CR	297	-	-	-	-	-	-	136	3970	109	-	4510	4490
		1μ CR	-	1070	49.5	1490	4.87	-	179	-	-	103	2090	4990	4780
		1e CR	-	712	17.3	986	0.624	-	116	-	39.6	54.0	1470	3390	3160
		2μ CR	-	1.54	209	-	19.3	-	80.8	-	-	-	14.7	326	348
		2e CR	-	1.53	180	-	18.7	-	91.6	-	-	-	13.0	305	266
		SR	-	338	-	603	131	1490	646	-	-	24.0	537	3770	-

Table 20: Event yield per process after the SR+CR fit, with the signal strength fixed to zero. The yields are rounded to 3 significant digits.

			Wγ	WW	DY	W + jets	ZZ	$Z \rightarrow \nu\nu$	WZ	Zγ	γ + jets	QCD	Top	Total BG	Data
year	channel	region													
2017	monojet	γ CR	2320	-	-	-	-	-	-	853	393000	9500	-	406000	405000
		1μ CR	-	3630	8630	258000	36.6	-	835	-	-	19200	14900	306000	306000
		1e CR	-	2250	3300	163000	14.4	-	526	-	8670	3180	9810	191000	191000
		2μ CR	-	122	31200	-	146	-	202	-	-	-	417	32000	32000
		2e CR	-	73.1	23500	-	108	-	160	-	-	-	257	24100	24000
		SR	-	1510	-	141000	1100	264000	2000	-	-	5600	5890	422000	-
	monovloose	γ CR	390	-	-	-	-	-	-	223	25400	717	-	26700	26800
		1μ CR	-	845	431	14900	7.21	-	157	-	-	646	2750	19700	19800
		1e CR	-	587	149	9430	3.71	-	101	-	254	81.5	1850	12500	12500
		2μ CR	-	4.65	1810	-	34.3	-	45.1	-	-	-	34.9	1920	1910
		2e CR	-	4.31	1380	-	27.2	-	34.7	-	-	-	19.9	1470	1520
		SR	-	388	-	7690	246	15200	397	-	-	142	938	25000	-
	monovtight	γ CR	222	-	-	-	-	-	-	110	2870	83.1	-	3290	3300
		1μ CR	-	790	43.9	1180	2.58	-	75.9	-	-	109	1470	3670	3690
		1e CR	-	504	14.7	751	0.865	-	54.6	-	34.3	18.9	994	2370	2360
		2μ CR	-	1.52	186	-	15.6	-	31.8	-	-	-	11.7	246	243
		2e CR	-	2.41	144	-	9.27	-	31.7	-	-	-	7.76	195	195
		SR	-	359	-	562	115	1540	338	-	-	12.6	610	3530	-
2018	monojet	γ CR	2930	-	-	-	-	-	-	1120	538000	11900	-	554000	554000
		1μ CR	-	4450	9120	359000	45.8	-	1620	-	-	5270	14800	394000	394000
		1e CR	-	2940	3900	226000	20.7	-	1040	-	9080	2810	10200	256000	256000
		2μ CR	-	133	39500	-	178	-	300	-	-	-	397	40500	40600
		2e CR	-	101	30900	-	144	-	232	-	-	-	286	31600	31700
		SR	-	1540	-	159000	1140	293000	2510	-	-	2070	4520	464000	-
	monovloose	γ CR	436	-	-	-	-	-	-	288	34000	1020	-	35700	35800
		1μ CR	-	944	462	20900	7.54	-	272	-	-	336	2330	25300	25100
		1e CR	-	610	188	13200	3.25	-	186	-	259	280	1590	16300	16300
		2μ CR	-	6.17	2290	-	38.5	-	69.1	-	-	-	22.4	2430	2460
		2e CR	-	3.48	1810	-	27.2	-	45.2	-	-	-	22.7	1910	1860
		SR	-	364	-	8720	231	16600	524	-	-	188	664	27300	-
	monovtight	γ CR	269	-	-	-	-	-	-	123	3990	109	-	4490	4490
		1μ CR	-	914	51.3	2010	4.47	-	142	-	-	77.9	1590	4790	4780
		1e CR	-	587	17.5	1290	0.559	-	88.8	-	36.0	54.4	1090	3170	3160
		2μ CR	-	1.41	239	-	18.4	-	63.6	-	-	-	11.5	334	348
		2e CR	-	1.18	189	-	15.5	-	65.7	-	-	-	9.00	280	266
		SR	-	295	-	825	123	1740	517	-	-	25.9	425	3950	-

Table 21: Event yield per process after the SR+CR fit, with floating signal strength. The yields are rounded to 3 significant digits.

			$W\gamma$	WW	DY	$W + \text{jets}$	ZZ	$Z \to \nu\nu$	WZ	$Z\gamma$	$\gamma + \text{jets}$	QCD	Top	Total BG	Data
year	channel	region													
2017	monojet	γ CR	2320	-	-	-	-	-	-	853	393000	9500	-	406000	405000
		1μ CR	-	3620	8630	258000	36.6	-	835	-	-	19200	14900	306000	306000
		1e CR	-	2250	3300	163000	14.4	-	526	-	8670	3200	9800	191000	191000
		2μ CR	-	122	31200	-	146	-	202	-	-	-	417	32000	32000
		2e CR	-	73.1	23500	-	108	-	160	-	-	-	257	24100	24000
		SR	-	1510	-	141000	1100	264000	2000	-	-	5600	5890	422000	-
	monovloose	γ CR	389	-	-	-	-	-	-	223	25400	717	-	26700	26800
		1μ CR	-	845	431	14900	7.20	-	157	-	-	646	2750	19700	19800
		1e CR	-	586	149	9430	3.71	-	101	-	254	81.4	1850	12500	12500
		2μ CR	-	4.65	1810	-	34.3	-	45.0	-	-	-	34.9	1920	1910
		2e CR	-	4.31	1380	-	27.2	-	34.6	-	-	-	19.9	1470	1520
		SR	-	388	-	7690	246	15200	397	-	-	142	938	25000	-
	monovtight	γ CR	222	-	-	-	-	-	-	110	2870	83.1	-	3290	3300
		1μ CR	-	789	43.9	1180	2.58	-	75.8	-	-	109	1470	3670	3690
		1e CR	-	503	14.7	751	0.865	-	54.6	-	34.3	18.9	994	2370	2360
		2μ CR	-	1.52	186	-	15.5	-	31.8	-	-	-	11.7	246	243
		2e CR	-	2.41	144	-	9.26	-	31.6	-	-	-	7.76	195	195
		SR	-	359	-	563	115	1540	337	-	-	12.6	610	3530	-
2018	monojet	γ CR	2920	-	-	-	-	-	-	1120	538000	11900	-	554000	554000
		1μ CR	-	4440	9130	359000	45.7	-	1620	-	-	5240	14800	394000	394000
		1e CR	-	2940	3900	226000	20.7	-	1040	-	9070	2790	10200	256000	256000
		2μ CR	-	133	39500	-	178	-	300	-	-	-	397	40500	40600
		2e CR	-	101	30900	-	143	-	232	-	-	-	286	31600	31700
		SR	-	1540	-	159000	1140	293000	2510	-	-	2050	4520	464000	-
	monovloose	γ CR	435	-	-	-	-	-	-	287	34000	1030	-	35700	35800
		1μ CR	-	943	461	20900	7.54	-	271	-	-	336	2330	25300	25100
		1e CR	-	609	187	13200	3.25	-	185	-	259	279	1590	16300	16300
		2μ CR	-	6.16	2290	-	38.5	-	69.0	-	-	-	22.4	2430	2460
		2e CR	-	3.47	1810	-	27.2	-	45.2	-	-	-	22.7	1910	1860
		SR	-	364	-	8720	231	16600	523	-	-	188	664	27300	-
	monovtight	γ CR	269	-	-	-	-	-	-	123	3990	109	-	4490	4490
		1μ CR	-	913	51.2	2010	4.46	-	142	-	-	77.8	1590	4790	4780
		1e CR	-	586	17.5	1290	0.558	-	88.6	-	35.9	54.4	1090	3170	3160
		2μ CR	-	1.40	239	-	18.3	-	63.5	-	-	-	11.5	334	348
		2e CR	-	1.17	189	-	15.5	-	65.6	-	-	-	8.99	280	266
		SR	-	295	-	826	123	1740	517	-	-	25.9	425	3950	-

7.2 Unblinding strategy

As this analysis uses a signal region with jets, $p_{\mathrm{T}}^{\mathrm{miss}}$ and no other well-identified objects, special care must be taken to avoid contamination from pathological sources of $p_{\mathrm{T}}^{\mathrm{miss}}$. This is partially accomplished by integrating safety measures into the analysis selection (e.g. tighter jet ID criteria and the $\Delta p_{\mathrm{T}}^{\mathrm{miss}}(\mathrm{PF},\mathrm{Calo})$ criterion). The study of the control regions also allows to derive some confidence in the performance of the reconstruction algorithms, but is not entirely sufficient simply because the control regions have at least one well-identified high-p_{T} lepton or photon, which provides a great reconstruction advantage over the more fragile hadronic final state. To ensure that there really are no unexpected sources of pathological $p_{\mathrm{T}}^{\mathrm{miss}}$, a partial unblinding strategy is proposed, which allows to study the behavior of $p_{\mathrm{T}}^{\mathrm{miss}}$ in the hadronic signal region specifically. In this strategy, a fraction of the full dataset, e.g. every fifth event, is unblinded. The published analysis of the 2016 dataset was performed using approximately $36\mathrm{fb}^{-1}$ of data, and no signal was found. Therefore, unblinding a fifth of the 2017 and 2018 datasets (≈ 8 and $12\ \mathrm{fb}^{-1}$, respectively) will not reveal any signals.

In the partially unblinded dataset, a well-known set of tools is available to test for pathologic $p_{\mathrm{T}}^{\mathrm{miss}}$ contributions:

1. The $\phi(p_{\mathrm{T}}^{\mathrm{miss}})$ distribution allows to check for spikes from non-collision backgrounds.
2. The jet energy fraction distributions allow to test for the presence of low-quality jets, which are often accompanied by fake $p_{\mathrm{T}}^{\mathrm{miss}}$.
3. The two-dimensional jet $\eta - \phi$ distribution can reveal the presence of hot towers and other noise-related jet sources that are well located in the detector.
4. Comparisons between PF $p_{\mathrm{T}}^{\mathrm{miss}}$ and other reconstruction types, e.g. track-based or PUPPI $p_{\mathrm{T}}^{\mathrm{miss}}$, can test the performance of the reconstruction algorithms and be a tool to identify events in which reconstruction failures appear.
5. The number of reconstructed primary vertices is useful to identify contributions from events with extremely large PU.

Each of the quantities listed here will be studied both in the full signal region, as well as in subsets of signal region events. For example, it is useful to specifically select the high-$p_{\mathrm{T}}^{\mathrm{miss}}$ tails of the region in order to gain confidence these events are not enriched in pathological features such as low-quality jets, very high PU, etc.

In addition to these general tests of $p_{\mathrm{T}}^{\mathrm{miss}}$ reconstruction quality, the 2018 dataset requires additional attention due to the presence of the HEM effect. To achieve maximal independence from the HEM effect, a strict vetoing method has been used in the development of this analysis, where all events with a jet in the affected region are rejected (cf. sec. 5.1.1). While this method is successful at mitigating the negative consequences of the HEM effect, it is also likely not optimally efficient. Therefore, the partially unblinded dataset will be used to optimize this criterion to achieve the highest possible signal efficiency while still mitigating the HEM effect. The method can be tuned by changing the p_{T} requirement applied to jets in order to trigger a veto from its a-priori value of 30 GeV. Specifically, the $p_{\mathrm{T}}^{\mathrm{miss}}$ distribution will be studied for a range of values of the p_{T} requirement. Any impact of the HEM effect on the $p_{\mathrm{T}}^{\mathrm{miss}}$ distribution, such as high-$p_{\mathrm{T}}^{\mathrm{miss}}$ outlier events, will then become increasingly apparant as the veto is loosened. This effect will be clearly separable from physical processes, the yield of which should increase mostly uniformly across the $p_{\mathrm{T}}^{\mathrm{miss}}$ spectrum.

7.3 Combination with 2016

The results of this analysis are combined with the previous CMS analysis of the 2016 data set [16]. The different data sets are treated as independent analysis regions in the same way as done for the 2017 and 2018 data sets, as well as the monojet and mono-V region. If physically motivated, nuisance parameters are correlated between the regions.

The same correlation scheme is adopted as in the combination of the 2017 and 2018 data sets:

- Most experimental uncertainties are decorrelated between different years. The luminosity uncertainty is partially correlated between years.
- Theoretical uncertainties are correlated between different years. Most notably, this includes the theoretical uncertainties on the $\mathrm{V}+\mathrm{jets}$ transfer factors. Care is taken to ensure that the correlated nuisances are defined in the same directions between the years, and the definition of the 2017/18 nuisances is adapted where necessary. In addition to the transfer factor uncertainties, the flat normalization uncertainties for the small backgrounds and signals are also correlated between years.

7.3.1 H(invisible) branching fraction

The analysis sensitivity is estimated using the scenario of invisible decays of the Higgs boson. The resulting signal strength limits are shown in Fig. 117 and summarized in Tab. **??**. The combined 2016+2017+2018 expected limit on the invisible branching fraction of the Higgs boson is found to be $\mathrm{BR}(\mathrm{H} \to \mathrm{inv}) < 24.5\%$ (25.1% expected).

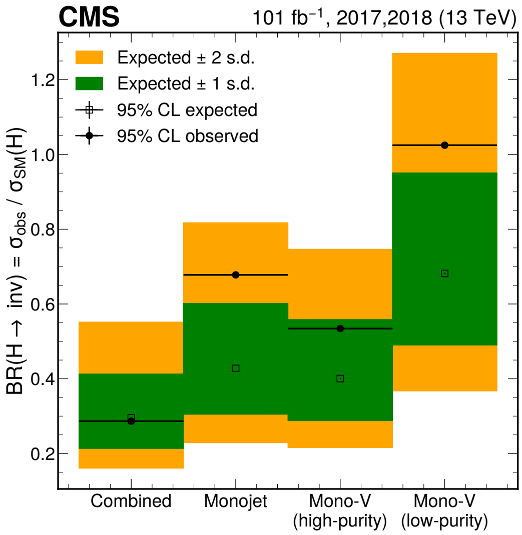

Figure 117: Sensitivity comparison of different categories.

7.3.2 Simplified DM model with a spin-1 mediator

In a model with spin-1 mediator, exclusion limits are calculated in the two-dimensional parameter space of the dark matter and mediator masses, m_{DM} and m_{med}. The coupling between the mediator and SM quarks is set to a constant value of $g_q = 0.25$, and the mediator-DM coupling is set to $g_\chi = 1.0$, and both vector and axial vector type coupling are considered in separate interpretations. The resulting exclusion limits at 95% CL on the signal strength μ are shown

Table 22: Expected signal strength exclusion limits. The values are derived based on a combined fit of the signal region and the five control regions.

Category	Year	Expected signal strength limit	Observed signal strength limit
Monojet	2016	64.7%	73.8%
	2017	59.0%	43.0%
	2018	55.1%	107.9%
Mono-V(low-purity)	2016	–	–
	2017	96.5%	86.2%
	2018	90.6%	200.1%
Mono-V (high-purity)	2016	–	–
	2017	55.5%	60.2%
	2018	56.5%	79.6%
Mono-V	2016	54.5%	53.5%
	2017	53.3%	49.3%
	2018	49.4%	71.6%
Combined	combined	25.3%	27.8%

in Fig. 118 for both coupling types. Values of the mediator mass m_{med} of up to 2.35 TeV are expected to be excluded for small values of $m_{\mathrm{DM}} \approx 1\,\mathrm{GeV}$. The excluded value of m_{med} reduces with increasing values of m_{DM}, as the branching fraction for decays of the mediator into dark matter candidates is reduced. The results are compared to those from direct detection experiments in Fig. 119.

In addition to constraints in the m_{DM}-m_{med} plane, we also formulate exclusion limits in the planes of m_{med} and g_q, as well as m_{med} and g_χ, which are shown in Fig. 120. The coupling exclusion is derived analytically from the signal strength exclusion at the default coupling values by rescaling the signal cross section according to the production cross section and decay branching fractions of the mediator according to the formulas from Ref. [81]. The DM candidate mass m_{DM} is fixed to $m_{\mathrm{med}}/3$. For low mediator masses, values of g_q down to 0.02, as well as g_χ down to 0.06 can be excluded, providing significant additional insight into the probed parameter space relative to the mass exclusion for fixed couplings.

7.3.3 Simplified DM model with a spin-0 mediator

The expected upper limits on the signal strength for cases with spin-0 mediators are shown in Fig. 121. In this scenario, only the monojet signature is taken into account, i.e. the production of a mediator with a QCD ISR jet. The mediator couplings are assumed to be $g_q = 1.0$ and $g_\chi = 1.0$, and the DM candidate mass is fixed to a value of $m_{\mathrm{DM}} = 1\,\mathrm{GeV}$. For scalar mediators, signal strengths of larger than 1.4 can be excluded at mediator mass values of $m_{\mathrm{med}} \approx 300\,\mathrm{GeV}$. A pseudoscalar mediator with mass below $m_{\mathrm{med}} = 450\,\mathrm{GeV}$ are excluded. In both cases, the signal strength limits show distinctive features around the threshold of $m_{\mathrm{med}} = 2m_{\mathrm{top}}$. As the

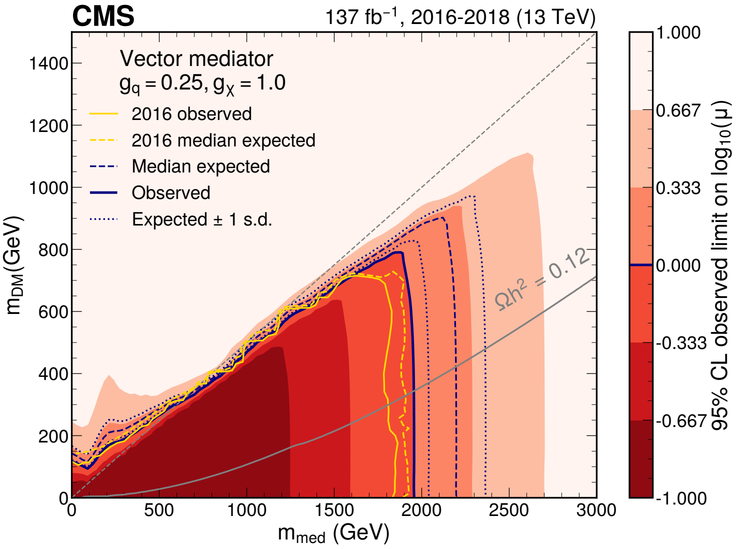

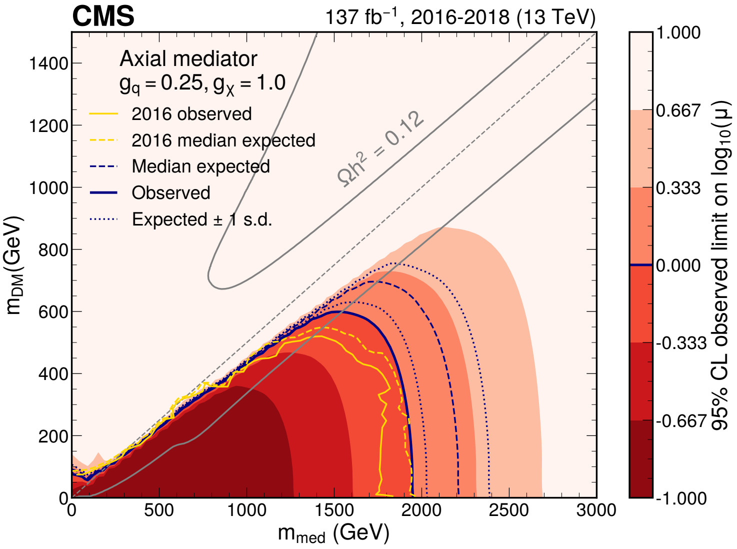

Figure 118: Expected exclusion limits at 95% CL on the signal strength $\mu = \sigma/\sigma_{\text{theo}}$ in the m_{med}-m_{DM} plane for a scenario with a vector (axial) mediator in the top (bottom panel), with coupling values of $g_q = 0.25$, $g_\chi = 1.0$. The blue solid line indicates the exclusion boundary $\mu = 1$. Parameter combinations with larger values of μ (indicated by a darker shade in the color scale) are excluded. The expected exclusion reaches up to $m_{\text{med}} = 2.35\,\text{TeV}$ for low values of $m_{\text{DM}} = 1\,\text{GeV}$. The grey dashed line indicates the diagonal $m_{\text{med}} = 2m_{\text{DM}}$, above which only off-shell mediator production contributes to the jet+$p_{\text{T}}^{\text{miss}}$ final state. The gray solid lines represent parameter combinations for which the simplified model correctly reproduces the DM relic density, assuming DM production through thermal freeze-out [81, 82].

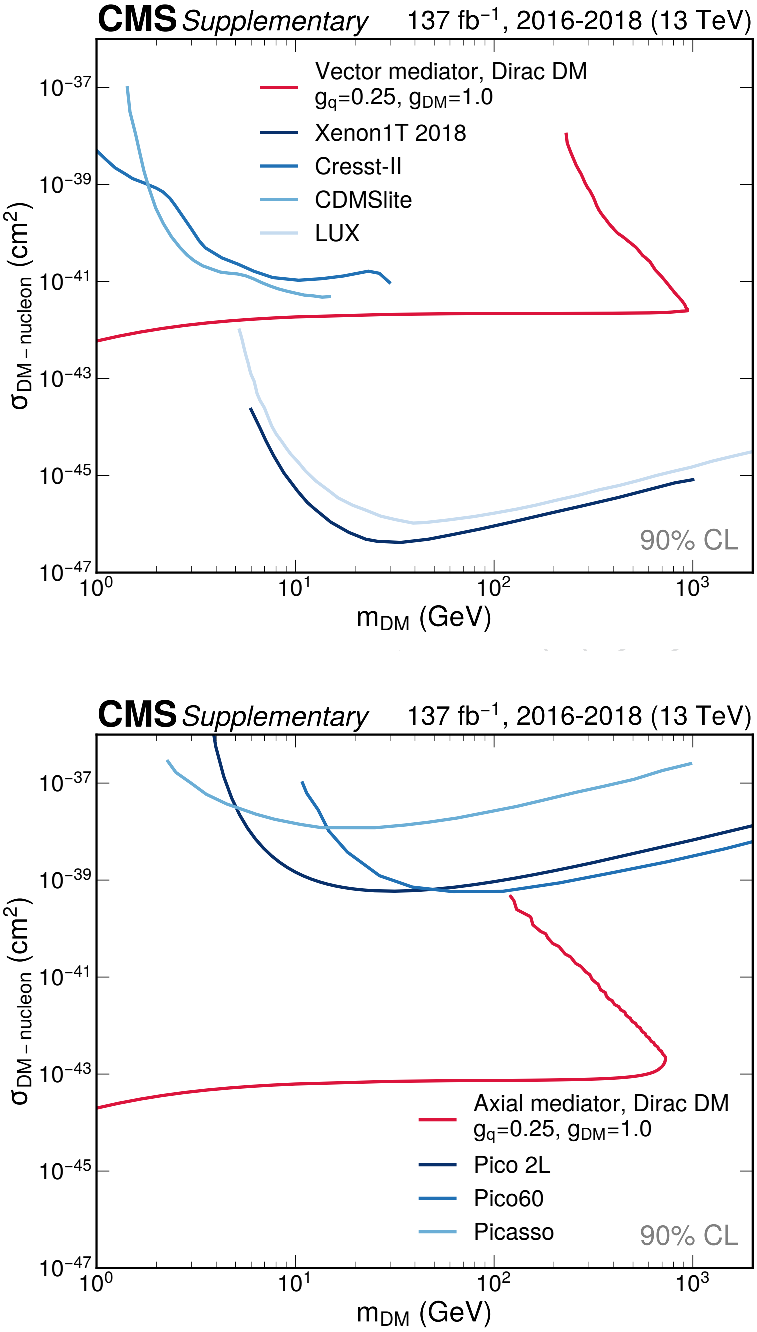

Figure 119: Expected exclusion limits at 90% CL on the DM-nucleon cross section as a function of $m_{\rm DM}$.

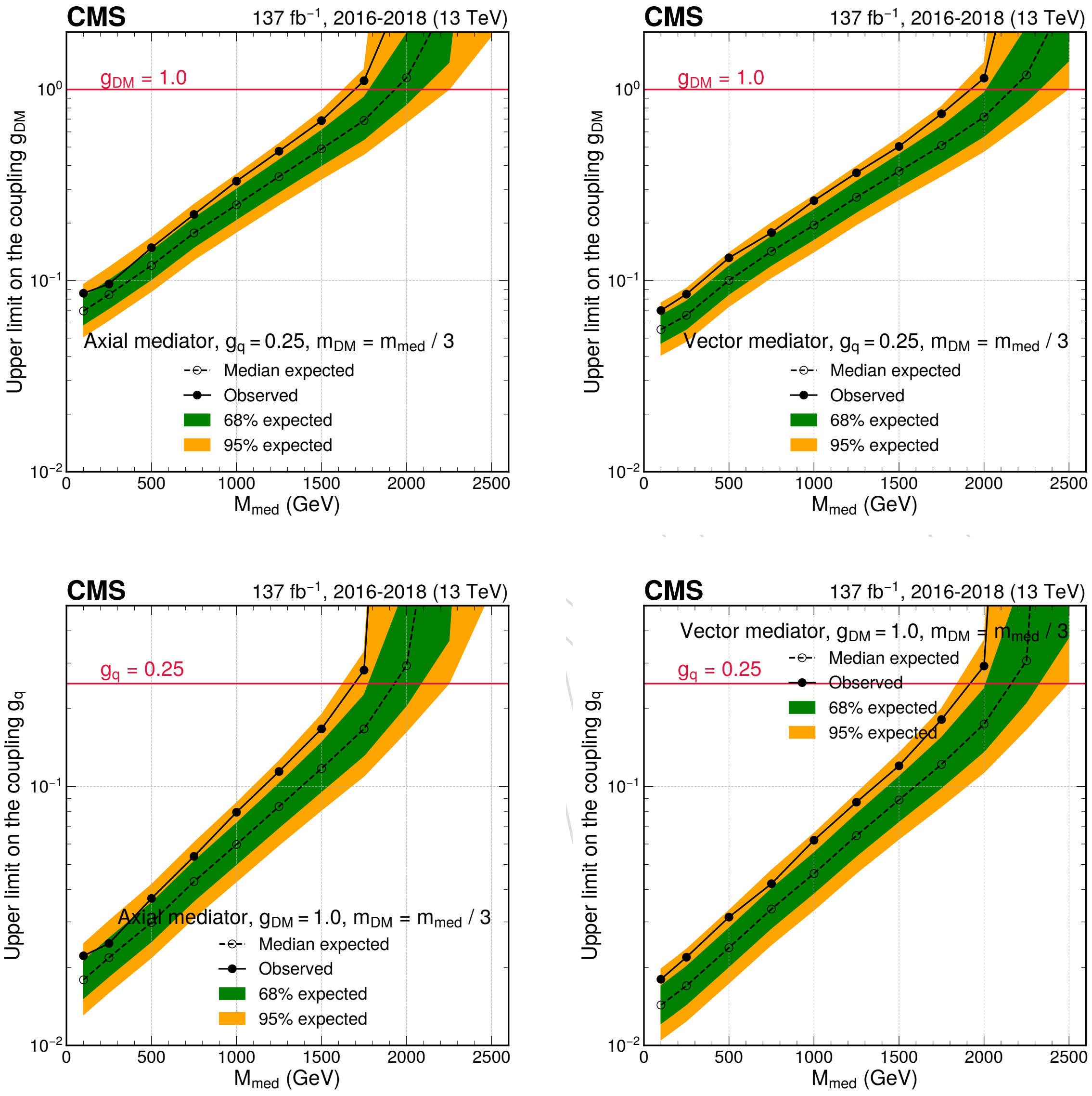

Figure 120: Exclusion limits at 95% CL on the signal strength couplings g_χ (top) and g_q (bottom row) for axial (left) and vector mediators (right column). In each panel, the result is shown as a function of the mediator mass m_{med}, and the mass of the DM candidate is fixed to $m_{\text{DM}} = m_{\text{med}}/3$. In all cases, only one coupling is varied, and the respective other coupling is fixed at its default value ($g_q = 0.25$, $g_\chi = 1.0$).

mediator is produced via a top quark loop, the signal cross section is enhanced as the mediator mass approaches the threshold from below. Above the threshold, the decay of the mediator into a pair of top quarks becomes possible, leading to a significant suppression of the branching fraction to DM candidates, and therefore the effective signal cross section. This result is based on the signal templates from Ref. [16].

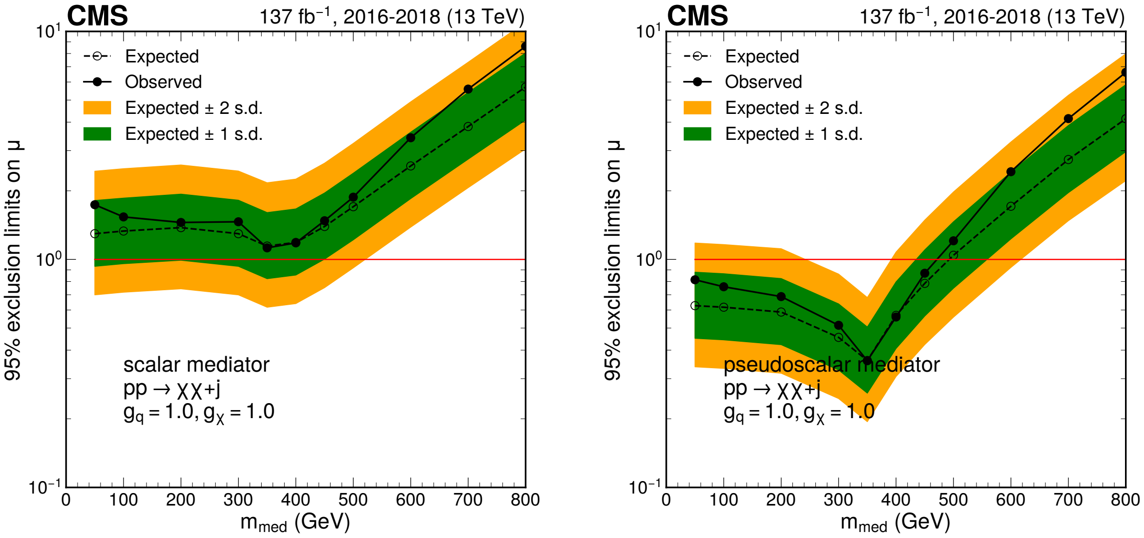

Figure 121: Expected exclusion limits at 95% CL on the signal strength $\mu = \sigma/\sigma_{\text{theo}}$ as a function of m_{med} for scenarios with a scalar (left) and pseudoscalar (right) mediators and coupling values of $g_q = 1.0$, $g_\chi = 1.0$, as well as a constant value of $m_{\text{DM}} = 1\,\text{GeV}$. The red solid line indicates the exclusion boundary $\mu = 1$. Parameter combinations with larger values of μ are excluded. In the case of a pseudoscalar mediator, mediator masses of up to 450 GeV can be excluded.

7.3.4 Simplified DM model with a t-channel mediator

7.3.5 ADD

The exclusion limits on the bulk mass M_D in the ADD scenario as a function of the number of extra dimensions d is shown in Fig. 123.

7.4 Leptoquark interpretation

Finally, exclusion limits are placed on the production cross section of leptoquarks coupling to up quarks and neutrinos with a coupling value λ. The branching fraction for the decay of the leptoquark into an electron neutrino and up quark is assumed to be 100%. Coupling limits are derived by interpolating the signal strength limit as a function of the coupling λ for each value of the leptoquark mass, and finding the coupling value which corresponds to $\mu = 1$, which is demonstrated in Fig. 124. The final limits are shown in Fig. 125. Generally, production of both single and paired leptoquarks contributes to the signal, with the coupling λ mainly influencing the single production mode. The pair production mode dominates at lower masses of $m_{\text{med}} < 1\,\text{TeV}$, leading to a weaker dependence of the coupling limit on the leptoquark mass than in the high-mass regime $m_{\text{med}} > 1\,\text{TeV}$, where the relative contribution from single leptoquarks is increased. The minimal excluded coupling ranges from less than 0.01 at $m_{\text{LQ}} = 500\,\text{GeV}$ to $\lambda = 1$ at $m_{\text{LQ}} = 1.75\,\text{TeV}$ and $\lambda = 1.4$ at $m_{\text{LQ}} = 2\,\text{TeV}$.

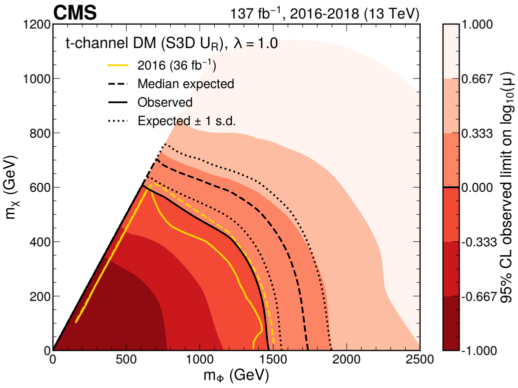

Figure 122: Expected exclusion limits at 95% CL on the signal strength $\mu = \sigma/\sigma_{\text{theo}}$ in the - m_{DM} plane for a scenario with a t-channel mediator. The coupling of the mediator to an up quark and DM candidate is assumed to be $\lambda = 1.0$. The black solid line indicates the exclusion boundary $\mu = 1$. Parameter combinations with larger values of μ are excluded. The sensitivity is truncated above the diagonal line =. Note: These plots are based on the combined full Run-2 fit, but do not include the 2016 signal contribution. While the samples for this are available, we are sitll in the process of validating our implementation of the 2016 seslection.

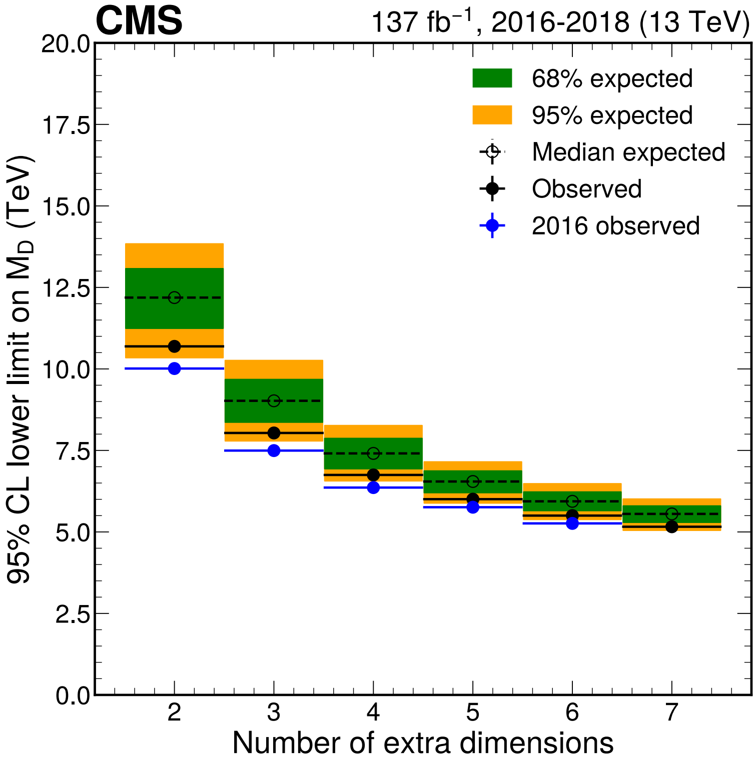

Figure 123: Expected exclusion limits at 95% CL on M_D in the ADD scenario for different values of the number of extra dimensions d.For $d = 2$, M_D values of up to 12.1 TeV are expected to be excluded. As the number of extra dimensions increases, the probed M_D value is reduced down to 6.0 TeV for a large number of $d = 6$. The result from Ref. [16] is represented with blue points for comparison.

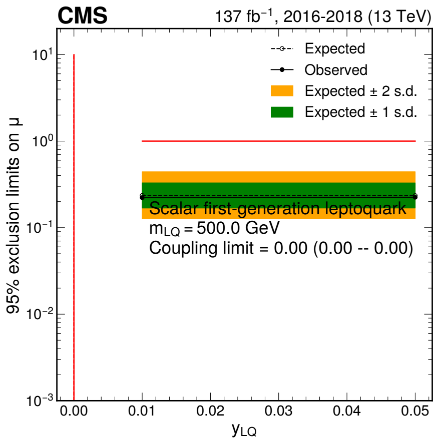
CMS
137 fb^{-1}, 2016-2018 (13 TeV)
Expected
Observed
Expected ± 2 s.d.
Expected ± 1 s.d.
Scalar first-generation leptoquark
m_{LQ} = 500.0 GeV
Coupling limit = 0.00 (0.00 -- 0.00)
95% exclusion limits on μ
y_{LQ}
10^{1}
10^{0}
10^{-1}
10^{-2}
10^{-3}
0.00
0.01
0.02
0.03
0.04
0.05

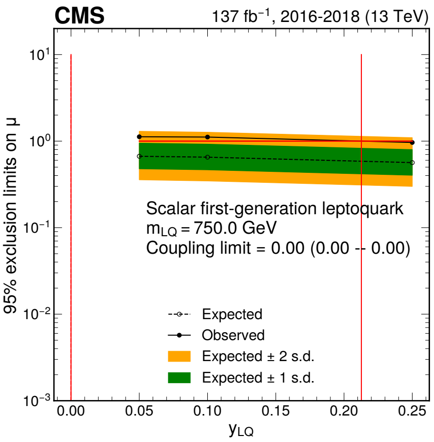
CMS
137 fb^{-1}, 2016-2018 (13 TeV)
Scalar first-generation leptoquark
m_{LQ} = 750.0 GeV
Coupling limit = 0.00 (0.00 -- 0.00)
Expected
Observed
Expected ± 2 s.d.
Expected ± 1 s.d.
95% exclusion limits on μ
y_{LQ}
10^{1}
10^{0}
10^{-1}
10^{-2}
10^{-3}
0.00
0.05
0.10
0.15
0.20
0.25

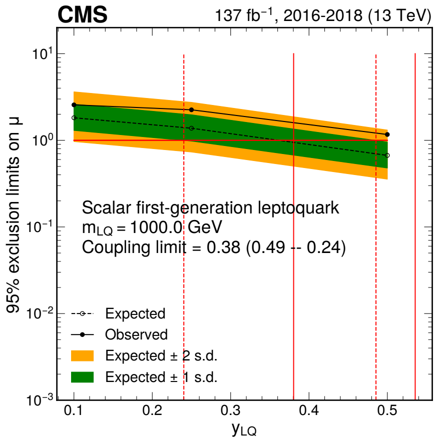
CMS
137 fb^{-1}, 2016-2018 (13 TeV)
Scalar first-generation leptoquark
m_{LQ} = 1000.0 GeV
Coupling limit = 0.38 (0.49 -- 0.24)
Expected
Observed
Expected ± 2 s.d.
Expected ± 1 s.d.
95% exclusion limits on μ
y_{LQ}
10^{1}
10^{0}
10^{-1}
10^{-2}
10^{-3}
0.1
0.2
0.3
0.4
0.5

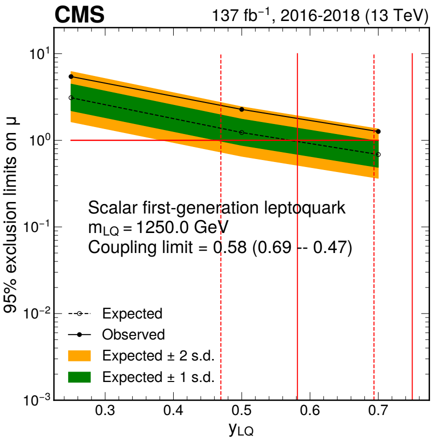
CMS
137 fb^{-1}, 2016-2018 (13 TeV)
Scalar first-generation leptoquark
m_{LQ} = 1250.0 GeV
Coupling limit = 0.58 (0.69 -- 0.47)
Expected
Observed
Expected ± 2 s.d.
Expected ± 1 s.d.
95% exclusion limits on μ
y_{LQ}
10^{1}
10^{0}
10^{-1}
10^{-2}
10^{-3}
0.3
0.4
0.5
0.6
0.7

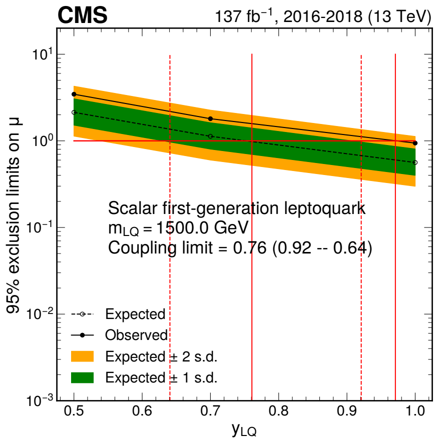
CMS
137 fb^{-1}, 2016-2018 (13 TeV)
Scalar first-generation leptoquark
m_{LQ} = 1500.0 GeV
Coupling limit = 0.76 (0.92 -- 0.64)
Expected
Observed
Expected ± 2 s.d.
Expected ± 1 s.d.
95% exclusion limits on μ
y_{LQ}
10^{1}
10^{0}
10^{-1}
10^{-2}
10^{-3}
0.5
0.6
0.7
0.8
0.9
1.0

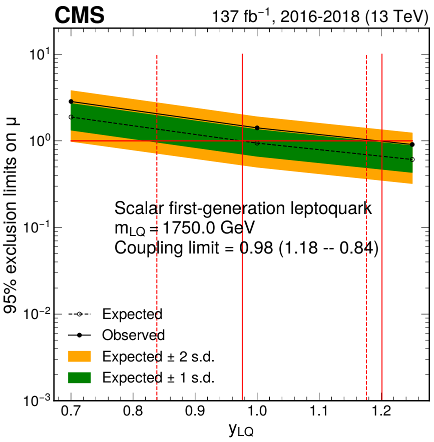
CMS
137 fb^{-1}, 2016-2018 (13 TeV)
Scalar first-generation leptoquark
m_{LQ} = 1750.0 GeV
Coupling limit = 0.98 (1.18 -- 0.84)
Expected
Observed
Expected ± 2 s.d.
Expected ± 1 s.d.
95% exclusion limits on μ
y_{LQ}
10^{1}
10^{0}
10^{-1}
10^{-2}
10^{-3}
0.7
0.8
0.9
1.0
1.1
1.2

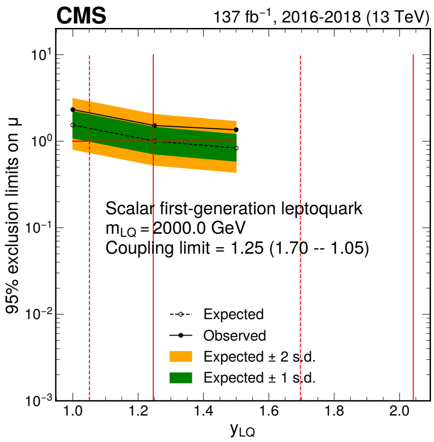
CMS
137 fb^{-1}, 2016-2018 (13 TeV)
Scalar first-generation leptoquark
m_{LQ} = 2000.0 GeV
Coupling limit = 1.25 (1.70 -- 1.05)
Expected
Observed
Expected ± 2 s.d.
Expected ± 1 s.d.
95% exclusion limits on μ
y_{LQ}
10^{1}
10^{0}
10^{-1}
10^{-2}
10^{-3}
1.0
1.2
1.4
1.6
1.8
2.0

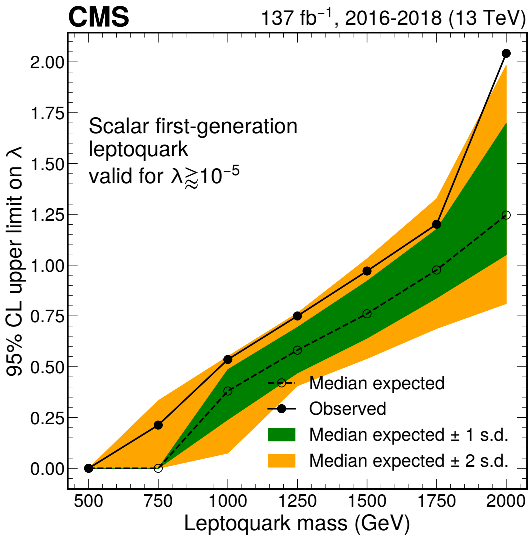

Figure 125: Expected exclusion limits at 95% CL on the leptoquark coupling λ as a function of the mass of the leptoquark. The branching fraction for the decay of the leptoquark into an electron neutrino and up quark is assumed to be 100%. The dashed line indicates the median expected exclusion contour. Parameter combinations with larger values of λ are excluded. For a leptoquark mass values, the signal scenario can be excluded for couplings as small as $\lambda = 0.01$. The value of the excluded coupling then increases with increasing leptoquark mass, reaching $\lambda = 1$ at a mass of 1.75 TeV. Note: These plots are based on the combined full Run-2 fit, but do not include the 2016 signal contribution. While the samples for this are available, we are sitll in the process of validating our implementation of the 2016 seslection.

A Synchronization efforts

A.1 CR data/MC Sync

Fig. 126 to Fig. 134 shows the comparison of the final data and MC templates obtained from **both frameworks** in the monojet category for 2017 and 2018. In the figures below, BU refers to Boston University whose results are based on nanoAOD data tier while UW refers to University of Wisconsin-Madison whose results are based on miniAOD data tier. Comparisons are shown for data and leading backgrounds for 2017 and 2018.

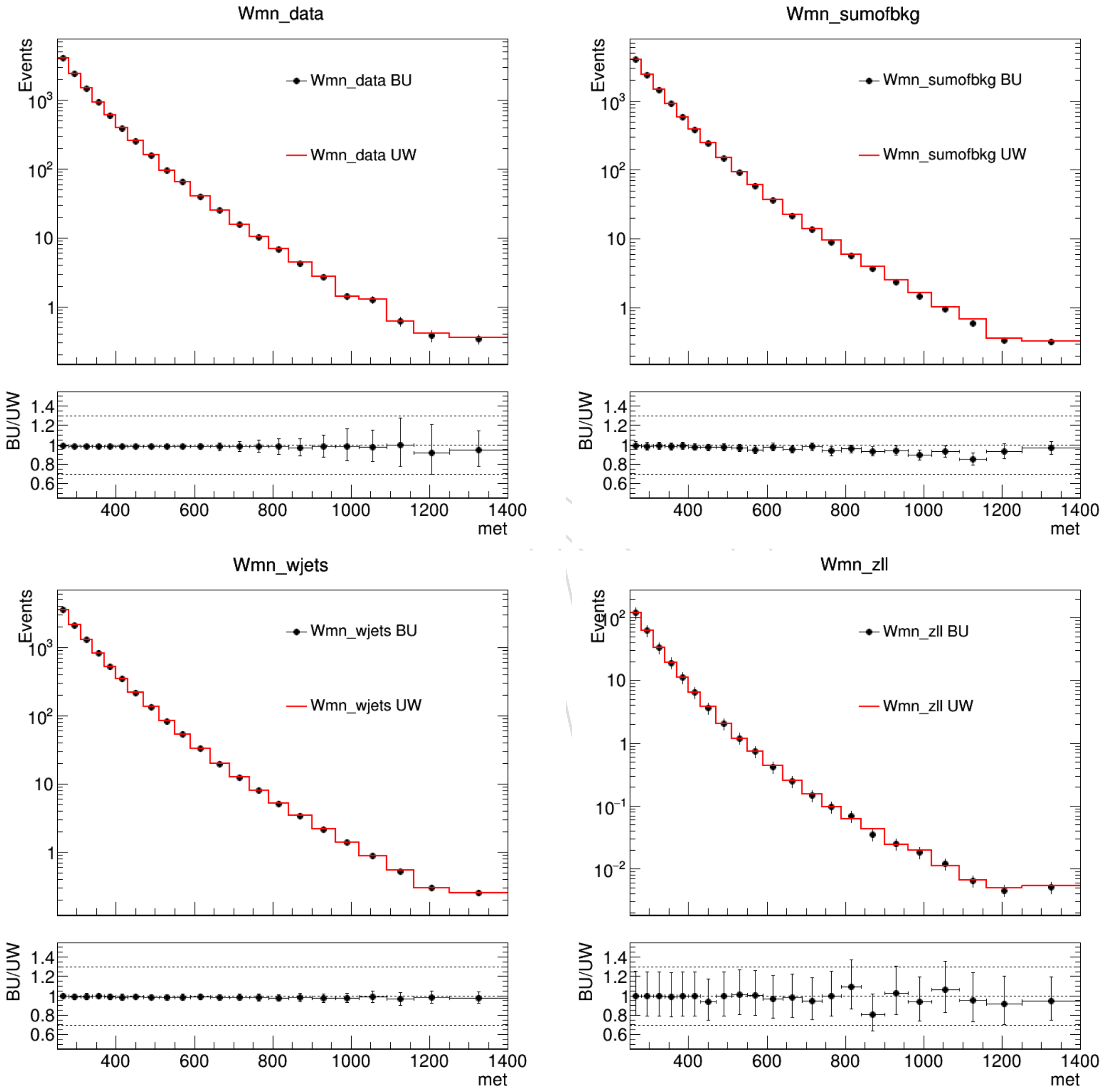

Figure 126: Comparison of BU (black bullets) and UW (red histogram) templates in W($\mu\nu$) control sample in 2017 for data (top-left), sum of all backgrounds (top-right), W($\ell\nu$)+jets background (bottom-left) and Z($\ell\ell$)+jets background (bottom-right).

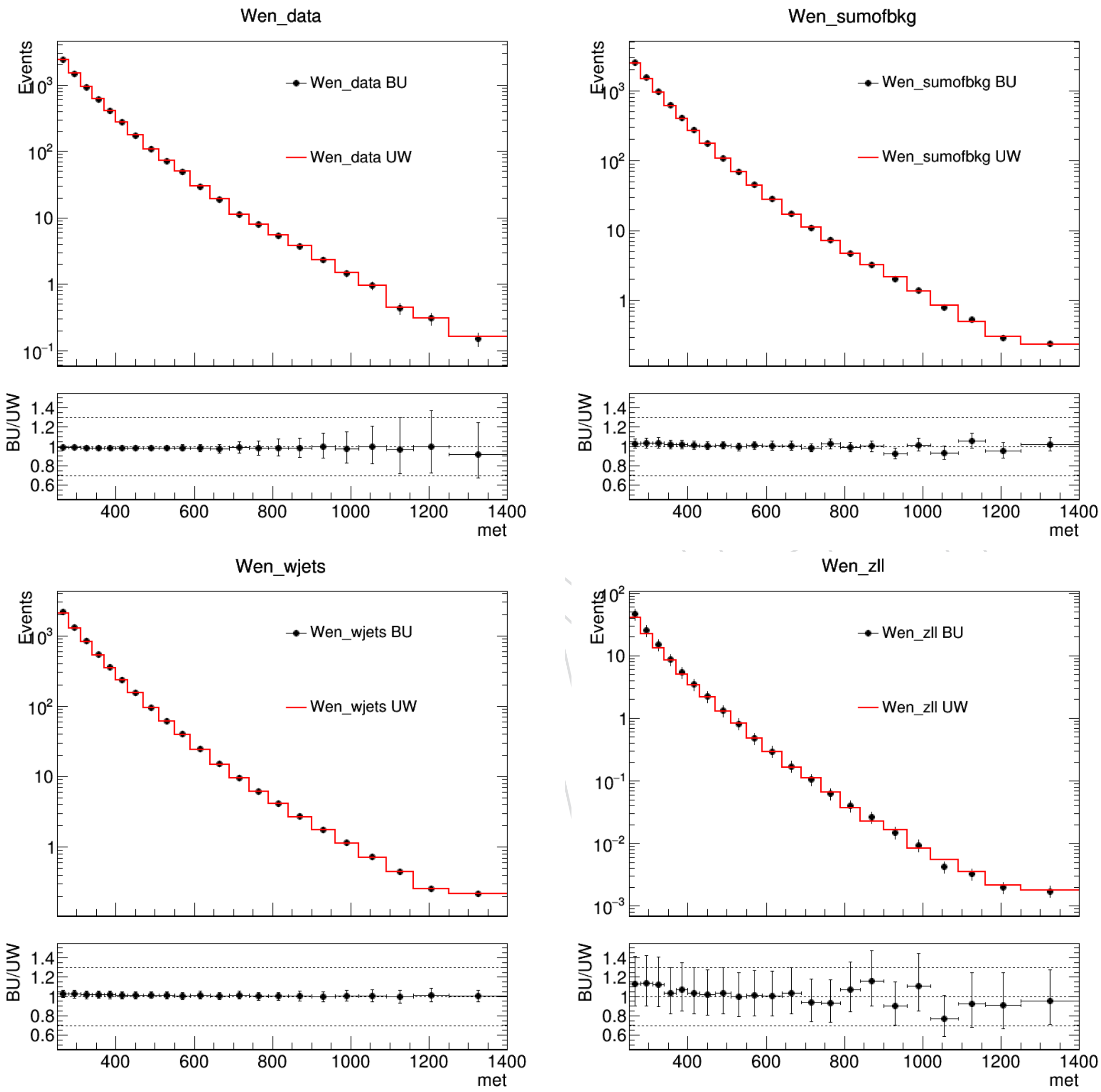

Figure 127: Comparison of BU (black bullets) and UW (red histogram) templates in W($e\nu$) control sample in 2017 for data (top-left), sum of all backgrounds (top-right), W($\ell\nu$)+jets background (bottom-left) and Z($\ell\ell$)+jets background (bottom-right).

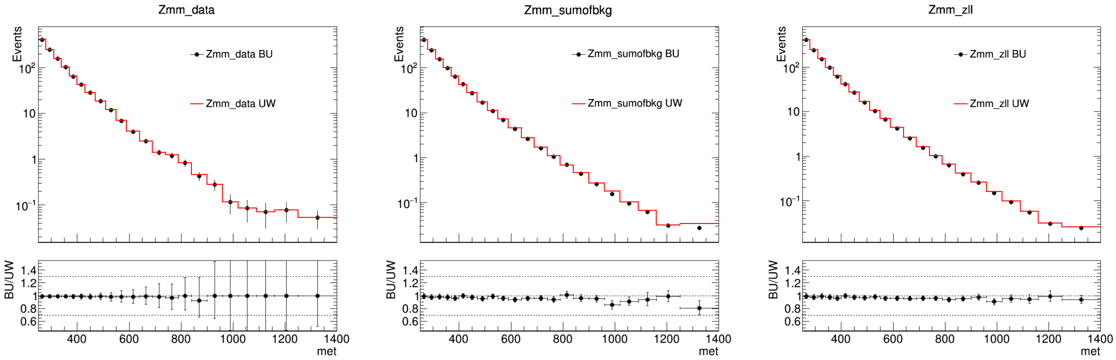

Figure 128: Comparison of BU (black bullets) and UW (red histogram) templates in Z($\mu\mu$) control sample in 2017 for data (left), sum of all backgrounds (middle) and Z($\ell\ell$)+jets background (right).

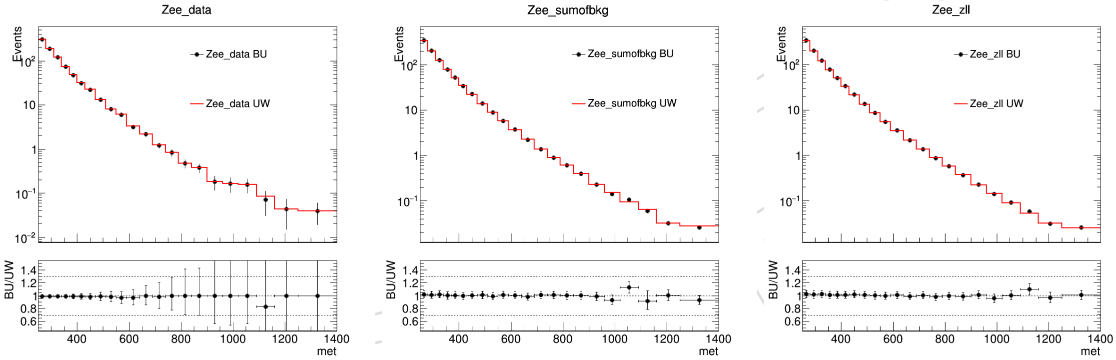

Figure 129: Comparison of BU (black bullets) and UW (red histogram) templates in Z(ee) control sample in 2017 for data (left), sum of all backgrounds (middle) and Z($\ell\ell$)+jets background (right).

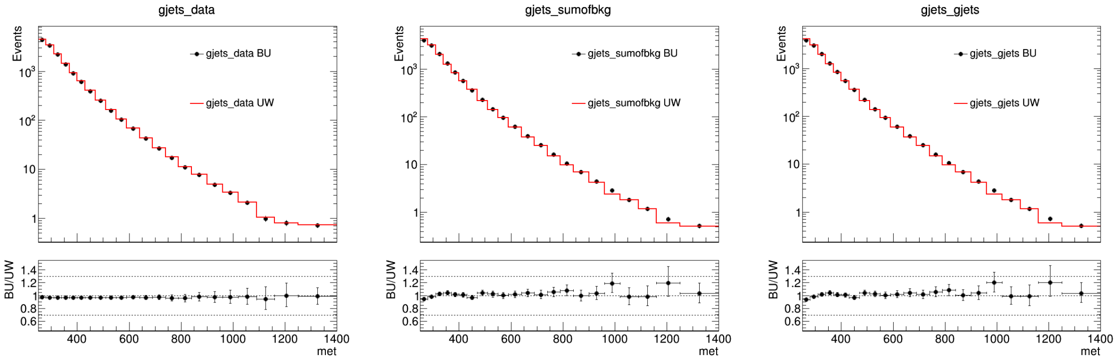

Figure 130: Comparison of BU (black bullets) and UW (red histogram) templates in γ+jet control sample in 2017 for data (left), sum of all backgrounds (middle) and γ+jets background (right).

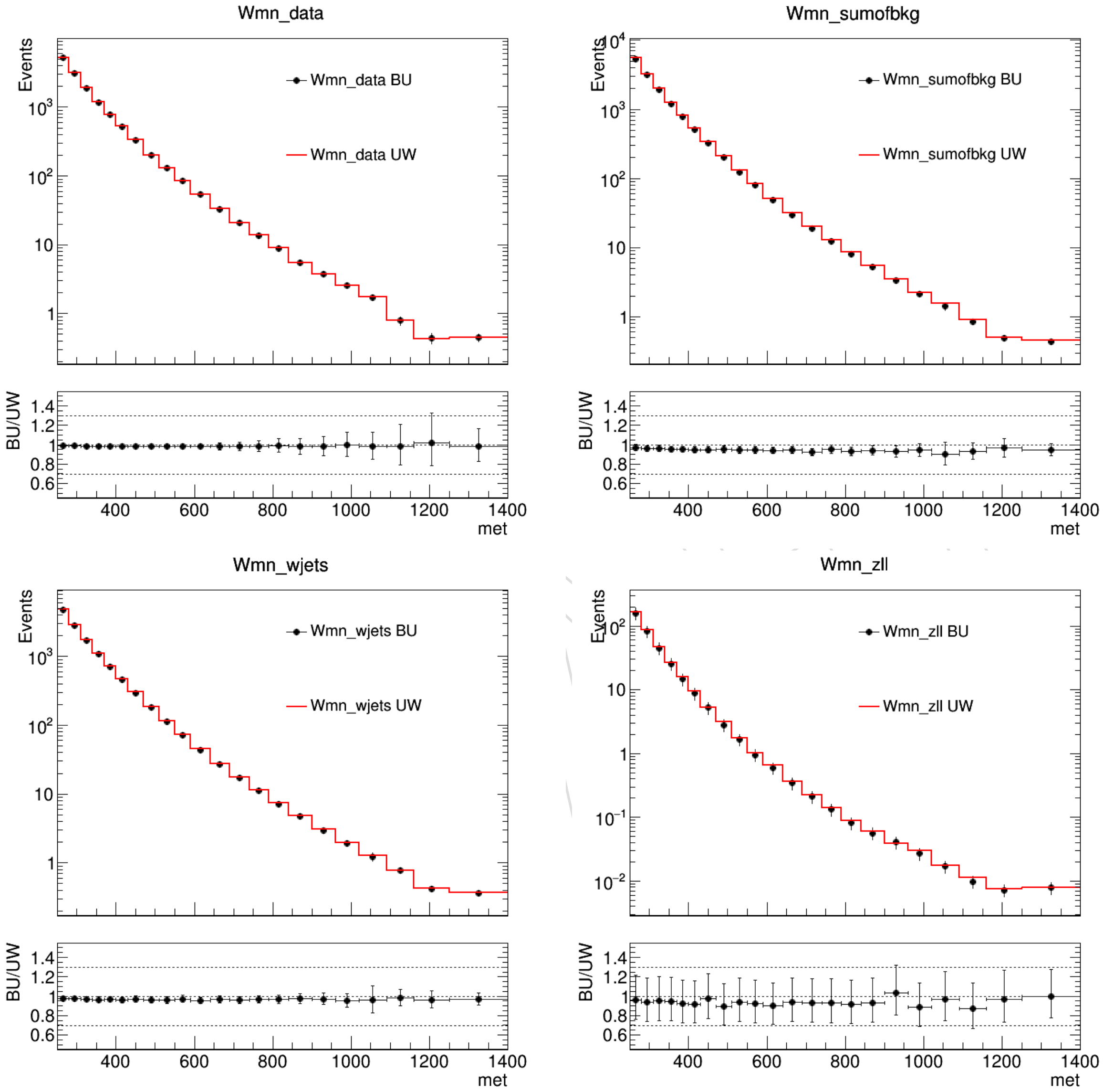

Figure 131: Comparison of BU (black bullets) and UW (red histogram) templates in W($\mu\nu$) control sample in 2018 for data (top-left), sum of all backgrounds (top-right), W($\ell\nu$)+jets background (bottom-left) and Z($\ell\ell$)+jets background (bottom-right).

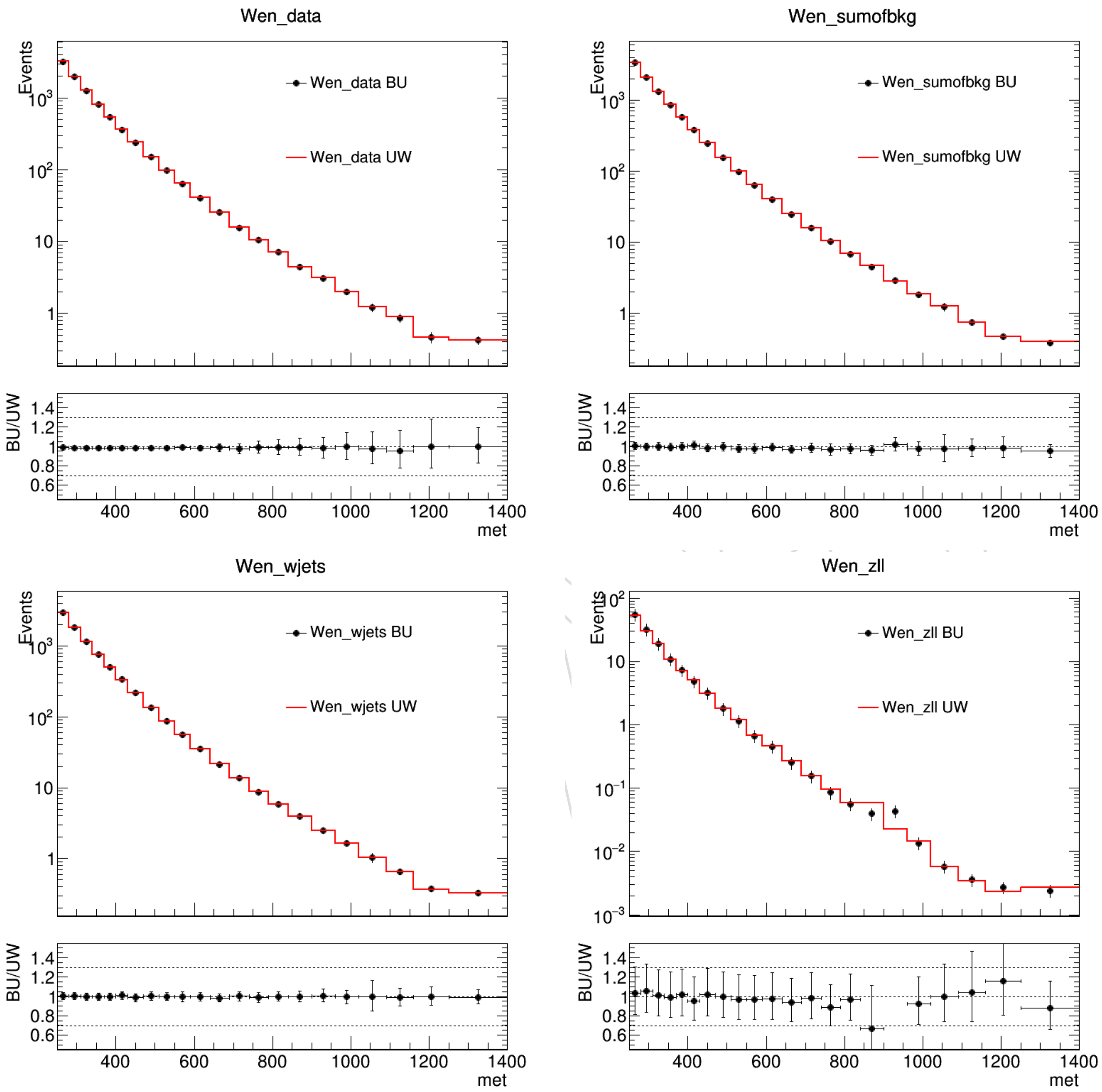

Figure 132: Comparison of BU (black bullets) and UW (red histogram) templates in $W(e\nu)$ control sample in 2018 for data (top-left), sum of all backgrounds (top-right), $W(\ell\nu)$+jets background (bottom-left) and $Z(\ell\ell)$+jets background (bottom-right).

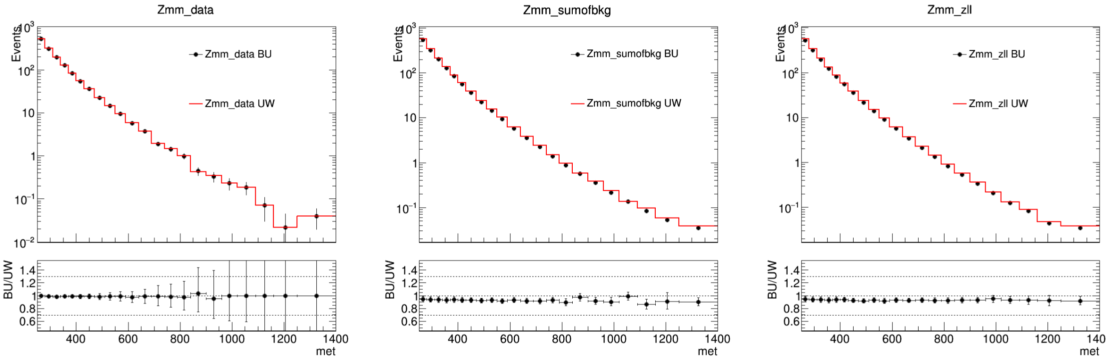

Figure 133: Comparison of BU (black bullets) and UW (red histogram) templates in Z($\mu\mu$) control sample in 2018 for data (left), sum of all backgrounds (middle) and Z($\ell\ell$)+jets background (right).

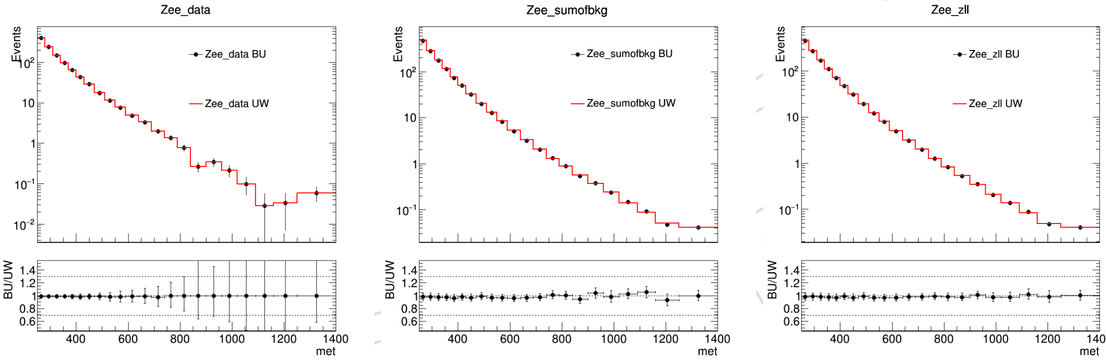

Figure 134: Comparison of BU (black bullets) and UW (red histogram) templates in Z(ee) control sample in 2018 for data (left), sum of all backgrounds (middle) and Z($\ell\ell$)+jets background (right).

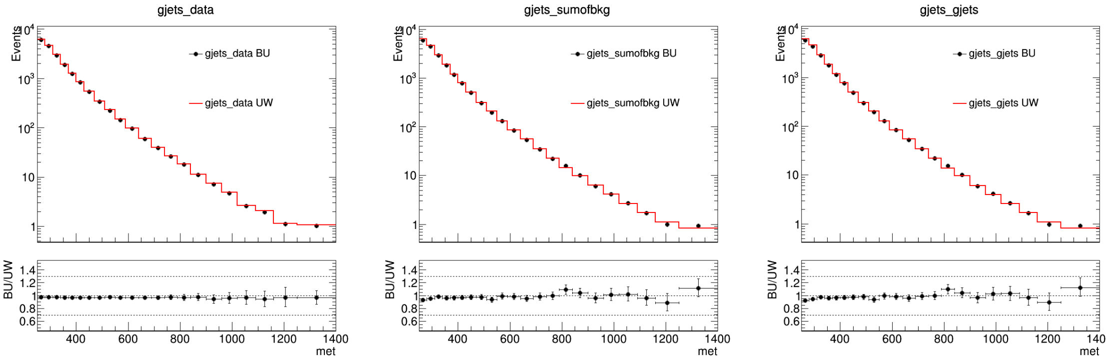

Figure 135: Comparison of BU (black bullets) and UW (red histogram) templates in γ+jet control sample in 2018 for data (left), sum of all backgrounds (middle) and γ+jets background (right).

A.2 CR-only fit comparison

Fig. 136 to Fig. 140 shows the comparison of post fit (CR-only) distributions for all control regions (single/double electron and muon and photon) for UW and BUin both 2017 and 2018. The distributions shows very good agreement across the years and for all control regions. The treatment of systematic uncertainties for all sources is described in Section **??**

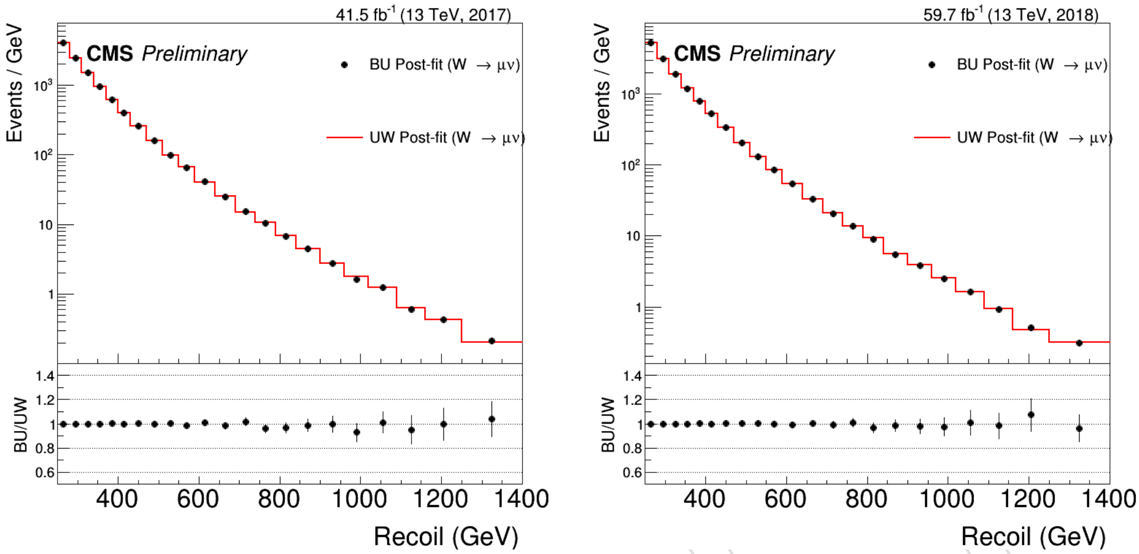

Figure 136: Comparison of BU (black bullets) and UW (red histogram) post-fit (CR only) distributions including all backgrounds in 2017 (left) and 2018 (right) for W($\mu\nu$) control sample.

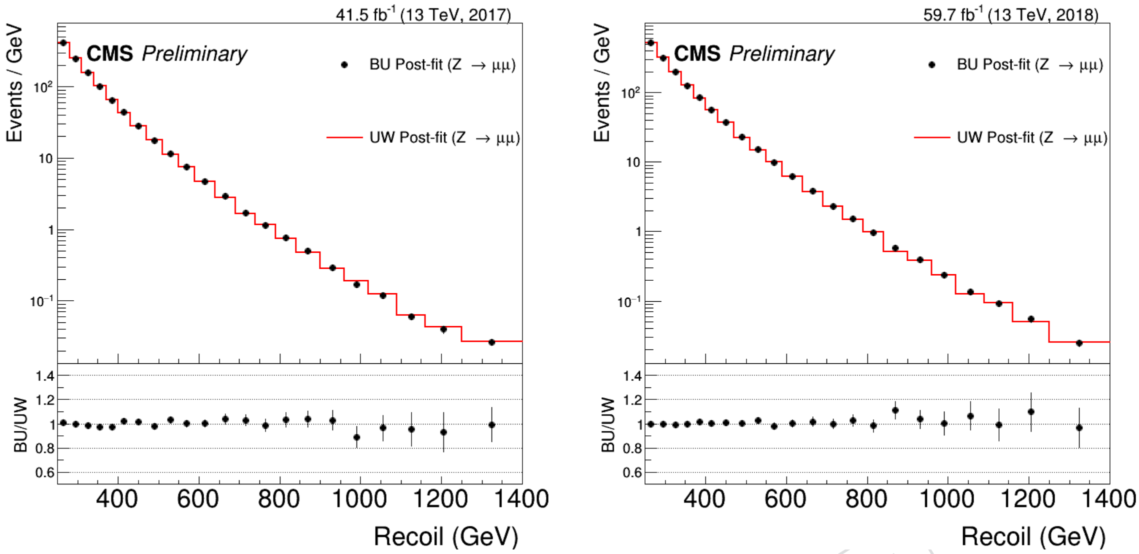

Figure 137: Comparison of BU (black bullets) and UW (red histogram) post-fit (CR only) distributions including all backgrounds in 2017 (left) and 2018 (right) for Z($\mu\mu$) control sample.

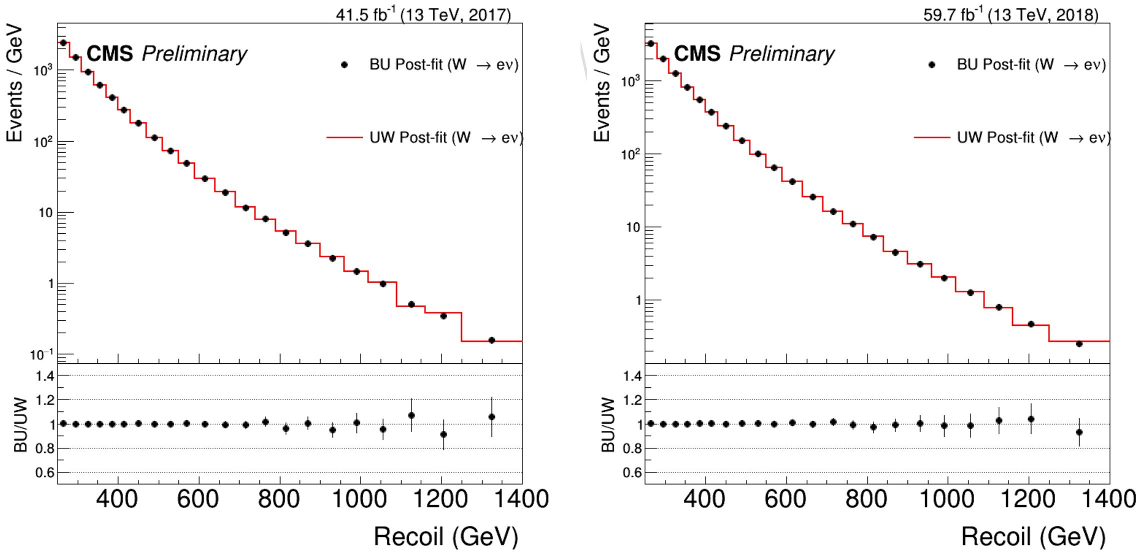

Figure 138: Comparison of BU (black bullets) and UW (red histogram) post-fit (CR only) distributions including all backgrounds in 2017 (left) and 2018 (right) for W($e\nu$) control sample.

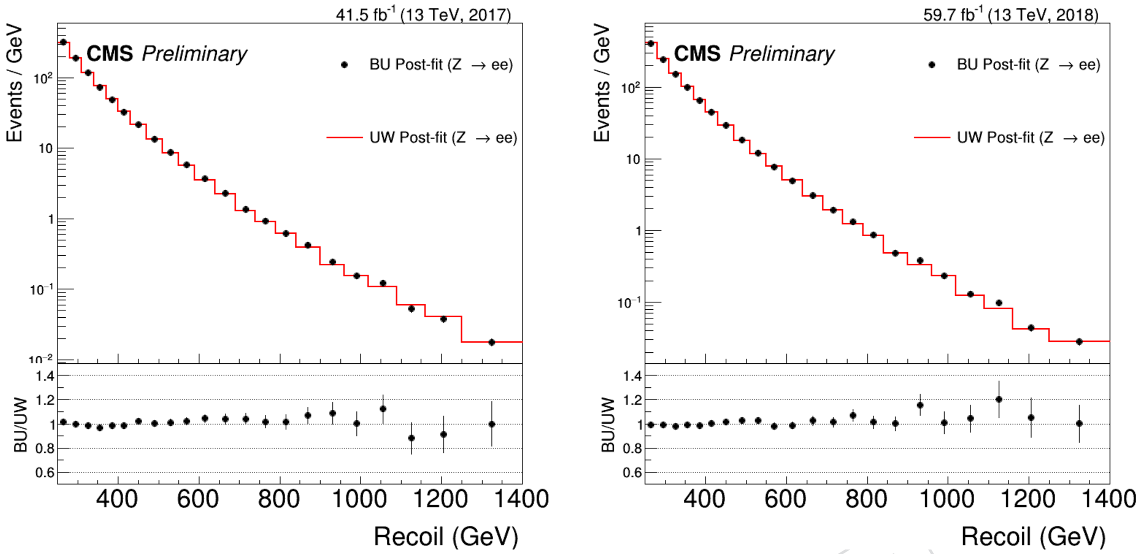

Figure 139: Comparison of BU (black bullets) and UW (red histogram) post-fit (CR only) distributions including all backgrounds in 2017 (left) and 2018 (right) for Z(*ee*) control sample.

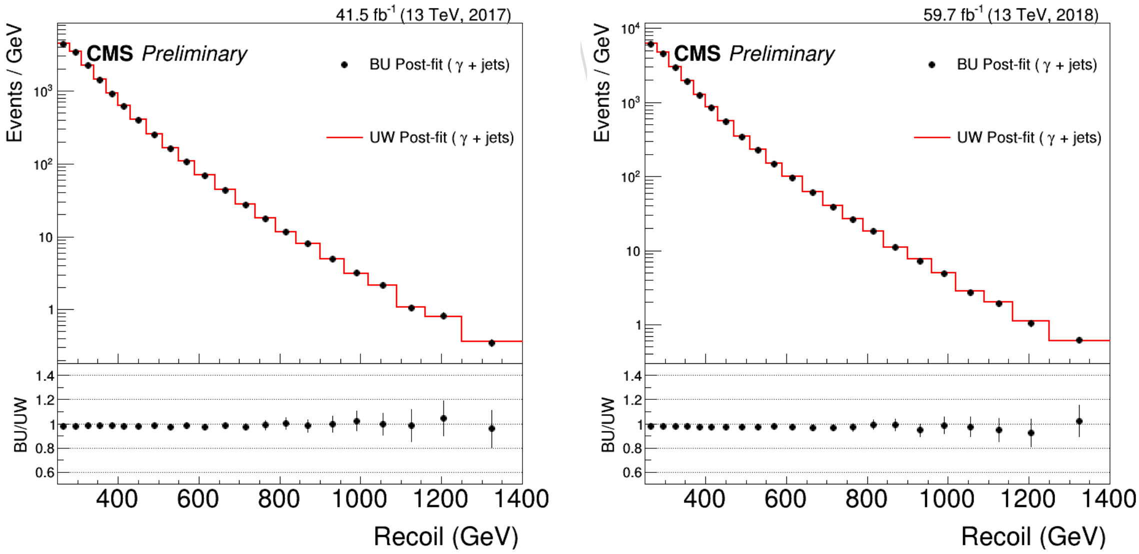

Figure 140: Comparison of BU (black bullets) and UW (red histogram) post-fit (CR only) distributions including all backgrounds in 2017 (left) and 2018 (right) for photon control sample.

A.3 MC Synchronization Updates

To ensure the reliability of the fit templates, the synchronization is conducted between the three different frameworks on some representative datasets, as listed in 23. Among the frameworks, MIT and BU groups use the nanoAOD data tier, while UW group uses the miniAOD. The value of the kinematics, the number of events that passes the final selection, and the weight from each correction are studied and compared individually. In each region, the number of events from the main background differs no more than 1% (2% for gjets), which shows that the selection efficiency is consistent between the three frameworks. The value of recoil and the weight from each correction of a same event is computed. The value from BU framework is used as the denominator, and the value of MIT and UW framework are used as the nominators. There are several components in the weights: the pileup reweighting, the SFs of the physics object reconstruction, the theoretical reweighting, the SF of the trigger, and the prefiring SF if it is 2017 MC.

Table 23: The list of testing MC samples for synchronisation.

Year	2017
DY	DYJetsToLL_M-50_HT-800to1200_TuneCP5_13TeV-madgraphMLM-pythia8
WJets	WJetsToLNu_HT-800To120_TuneCP5_13TeV-madgraphMLM-pythia8
GJets	GJets_HT-600ToInf_TuneCP5_13TeV-madgraphMLM-pythia8
$Z\nu\nu$	ZJetsToNuNu_HT-800To1200_13TeV-madgraph
Year	2018
DY	DYJetsToLL_M-50_HT-800to1200_TuneCP5_PSweights_13TeV-madgraphMLM-pythia8
WJets	WJetsToLNu_HT-800To1200_TuneCP5_13TeV-madgraphMLM-pythia8
GJets	GJets_HT-600ToInf_TuneCP5_13TeV-madgraphMLM-pythia8
$Z\nu\nu$	ZJetsToNuNu_HT-800To1200_13TeV-madgraph

The ratio of the recoil values of the same events is shown in figure 141, 142 for the major contribution in each region. In this synchronization, the jet energy smearing is considered and propagated to $p_{\mathrm{T}}^{\mathrm{miss}}$. The randomness in jet energy smearing contributes to the $\sim$ 1% deviation in the value of recoil between different frameworks, except in the 2017 DY sample. It is because that the miniAOD and nanoAOD testing DY samples have the different PU settings, with nanoAOD using PU version `new_pmx` and miniAOD using the normal version. The small trend in 2017 $Z \to \nu\nu$ testing sample is temporarily due to a small fraction ($\sim$ 5%) of genBoson reconstruction failure in miniAOD sample, which is not affecting any of the results in this note.

Each component of the weights is compared individually, the example of 2018 double muon region is shown in the figure 143. The SFs from pileup reweighting are not always the same, since the pile up set-ups are different between the groups. The mean value from pileup reweighting ratio is close to 1, and the standard deviation is around 3%, and this difference will not affect the recoil distribution. The rest components are well agreed between the three framework.

The recoil distribution is then compared in each region to demonstrate the consistency between different frameworks, as shown in figure 145. The shape and normalisation of the recoil distribution are in a good agreement within the statistical fluctuation.

In the previous synchronisation (section A.1), there were $\sim$ 5% normalization difference in the 2018 double muon CR. To ensure the consistency in this region, a closer look is conducted on all the of 2018 DY samples in the double muon CR region. The recoil distribution is then compared with all the weights considered, as shown in figure 146. Among all the seven bins of

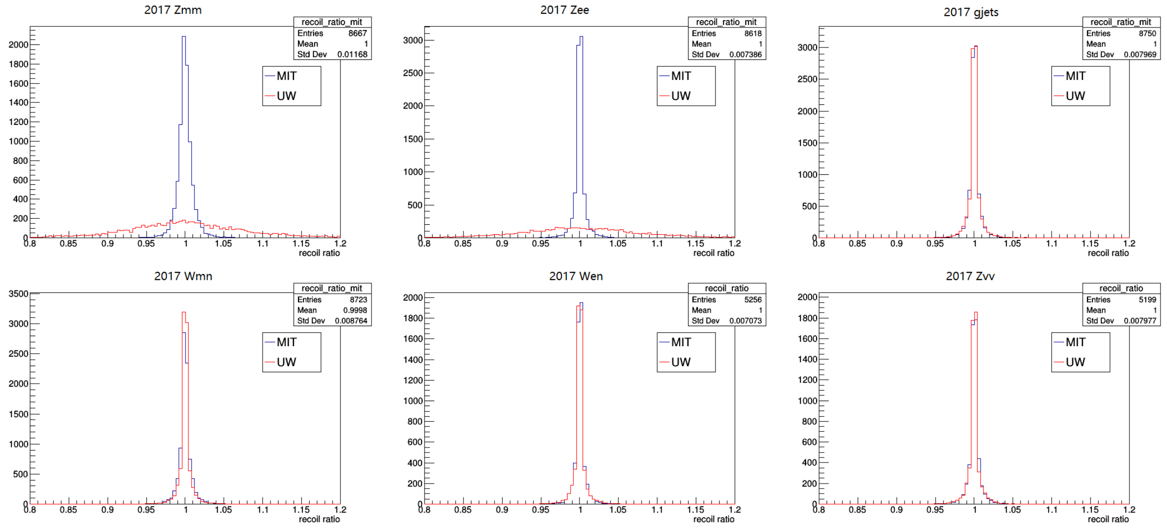

Figure 141: The recoil value of 2017 testing MC samples are compared between different frameworks in each region, including DY testing sample in double muon (top left) and double electron (top middle) control region, γ+jets testing sample in single photon region (top right), W+jets testing sample in single muon (bottom left) and single electron (bottom middle) region, and $Z \to \nu\nu$ testing sample in signal region (bottom right).

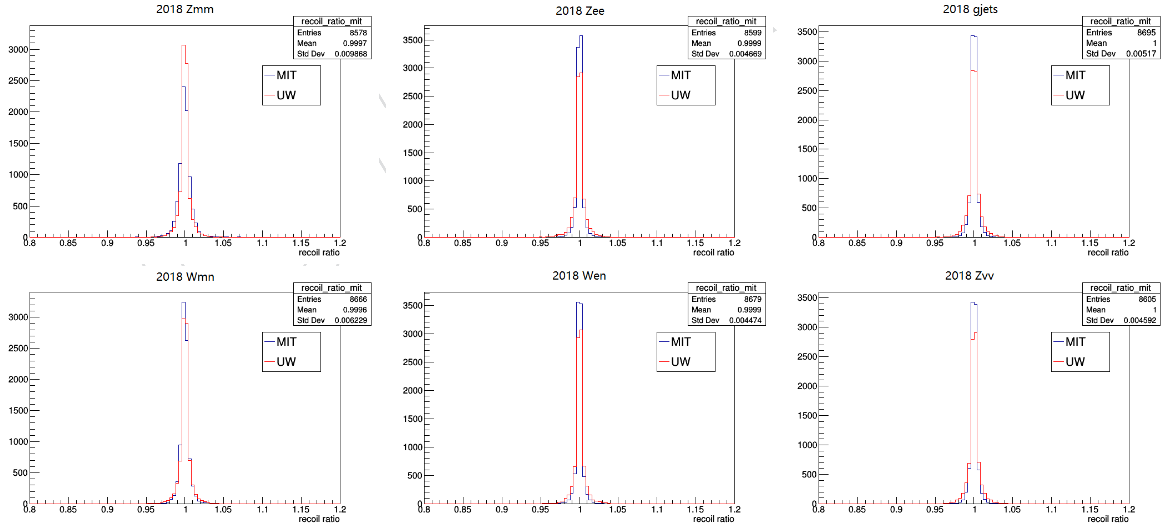

Figure 142: The recoil value of 2018 testing MC samples are compared between different frameworks in each region, including DY testing sample in double muon (top left) and double electron (top middle) control region, γ+jets testing sample in single photon region (top right), W+jets testing sample in single muon (bottom left) and single electron (bottom middle) region, and $Z \to \nu\nu$ testing sample in signal region (bottom right).

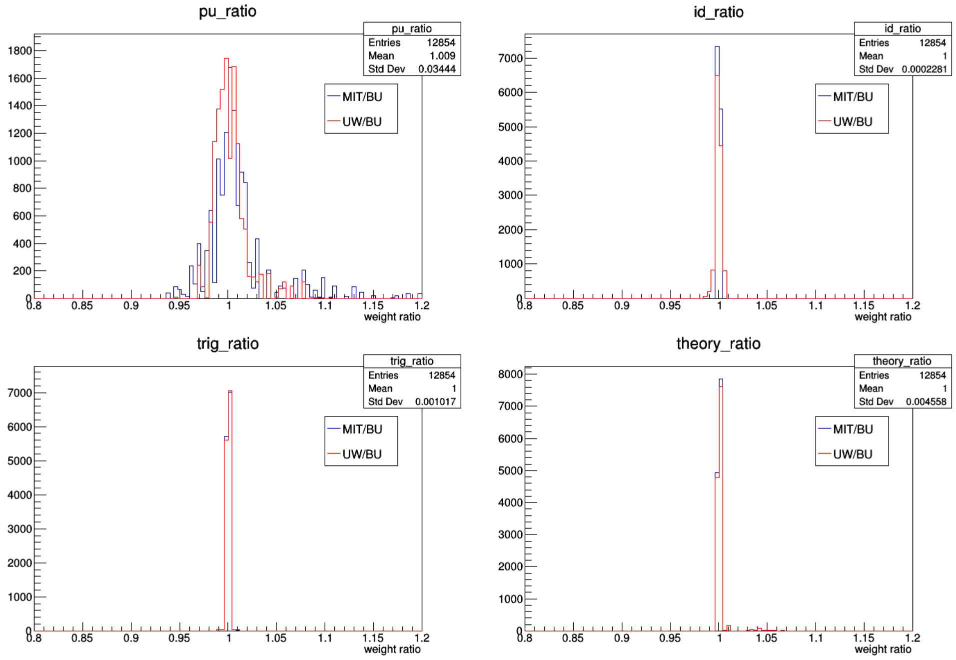

Figure 143: The recoil value of 2017 testing MC samples are compared between different frameworks in each region, including DY testing sample in double muon (top left) and double electron (top middle) control region, γ+jets testing sample in single photon region (top right), W+jets testing sample in single muon (bottom left) and single electron (bottom middle) region, and $Z \to \nu\nu$ testing sample in signal region (bottom right).

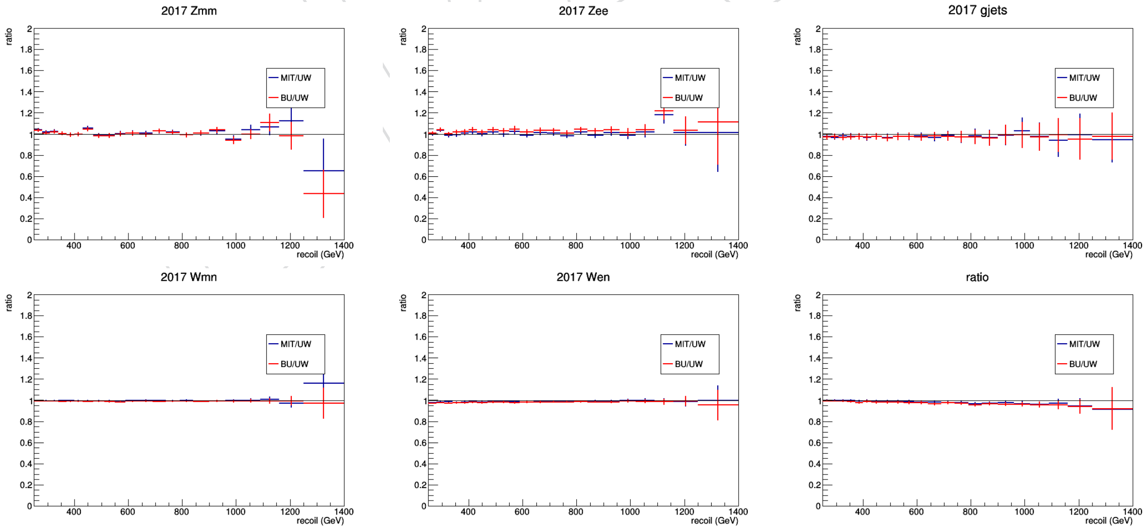

Figure 144: The recoil value of 2017 testing MC samples are compared between different frameworks in each region, including DY testing sample in double muon (top left) and double electron (top middle) control region, γ+jets testing sample in single photon region (top right), W+jets testing sample in single muon (bottom left) and single electron (bottom middle) region, and $Z \to \nu\nu$ testing sample in signal region (bottom right).

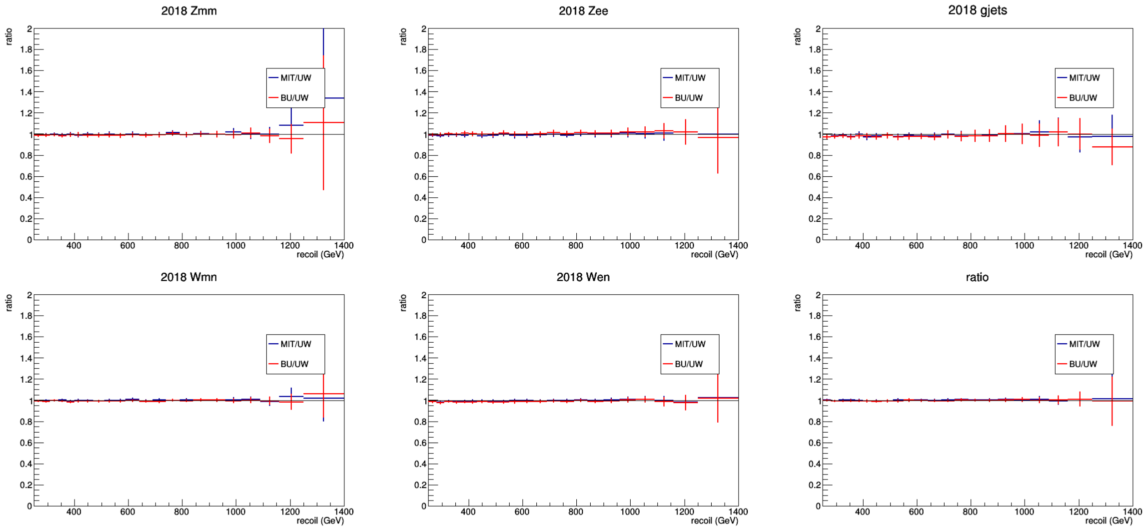

Figure 145: The recoil distributions of 2018 testing MC samples are compared between different frameworks in each region, including DY testing sample in double muon (top left) and double electron (top middle) control region, γ+jets testing sample in single photon region (top right), W+jets testing sample in single muon (bottom left) and single electron (bottom middle) region, and Z $\rightarrow \nu\nu$ testing sample in signal region (bottom right).

DY sample, the `bin400to600` sample has a slightly trend in the shapes between miniAOD and nanoAOD sample and the rest samples have a good agreement both in shapes and normalisation. The small trend in `bin400to600` is due to different sample used in miniAOD and nanoAOD. The miniAOD uses version `ext4` and nanoAOD uses `ext2`. Those two samples are also compared in the same framework, which is also shown in figure 147. The comparison shows the same trend as the comparsion between the three frameworks, which indicates that the shape difference is caused by the difference of the samples.

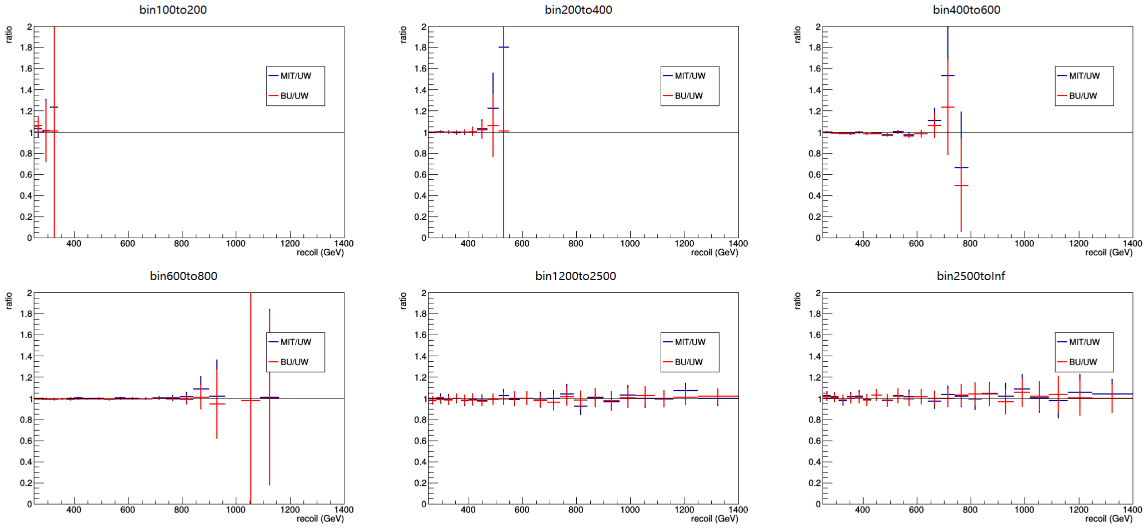

Figure 146: The recoil distribution is compared between three frameworks in 2018 double muon control region. The comparison is conducted on the rest of the bins other than DY testing sample: bin100to200 (top left), bin200to400 (top middle), bin400to600 (top right), bin600to800 (bottom left), bin1200to2500 (bottom middle), and bin2500toInf (bottom right).

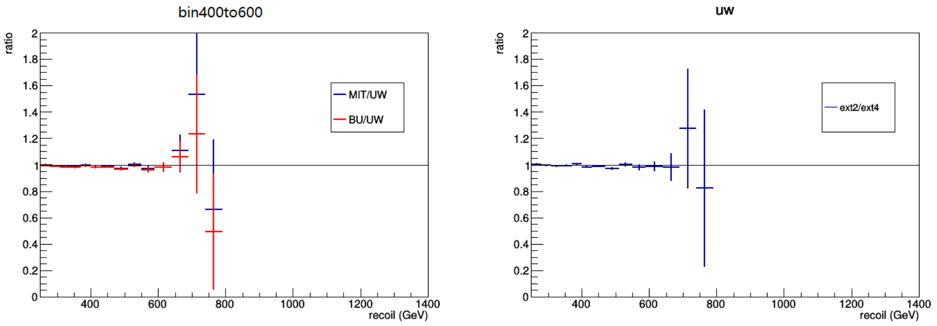

Figure 147: The comparison of recoil distribution of DY bin400to600 between three frameworks (left), and the comparison on ext2 and ext4 version using the MIT framework (right).

B DMsimp spin-1 coupling limits

In addition to the well-established interpretation of the analysis in terms of limits on the mediator and DM masses, an interpretation in terms of coupling limits is made. To this end, it is necessary to study the effect the choice of coupling values g_q and g_{DM} has on the signal. Two approaches are documented in this section:

1. A simulation-based strategy, in which signal samples with different coupling values are simulated with Madgraph, and the features of the samples are studied, cross-sections are extracted, etc. This method is robust, but takes a lot of work.
2. An analytical rescaling strategy, in which the dependence of the signal strength limits on the couplings is modeled analytically. This method is very practical, but its robustness must be established.

We are currently in the process of understanding the comparison between the two methods and using them to cross-validate.

B.1 Simulation-based strategy

In order to check the sensitivity with respect to different values of couplings, the signal samples are generated in several g_q values. From the 2016 generated signal samples, the yields are compared at different mass points in terms of different values of g_q, while the mass of the dark matter is fixed to be 1/3 of the mediator mass and g_{dm} is fixed at 1. The kinematic between different samples are similar regardless of the coupling values for each mass point, as shown in figure 148 for some of the examples. Therefore, the coupling value only affects the normalization, which ratio is shown in figure 149. The yields are not continuously increasing with larger g_q value for some of the mass points.

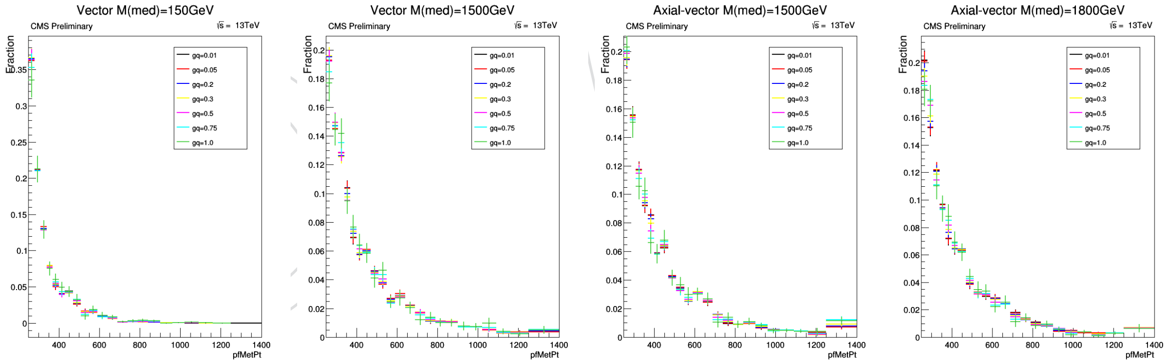

Figure 148: The generator level recoil distribution from 2016 signal samples with different g_q values. The corresponding generator level signal region selection is applied and the normalization is scaled to 1. The dark matter mass is 1/3 of the mediator mass and $g_{dm} = 1$. The plots includes signals with 150 GeV vector mediator (left), 1500 GeV vector mediator (middle left), 1500 GeV axial-vector mediator (middle right), and 1800 GeV axial-vector mediator (right).

This feature is cross checked with the signal samples generated using the setting of 2017 and 2018 sample. The signal samples are generated at LO. Their kinematics are also similar between different coupling values, as shown in figure 150, after the generator level signal region selections are applied. The selection efficiencies are similar, therefore adding selection does not affect the ratio between the yields with different coupling values. The NLO and LO cross

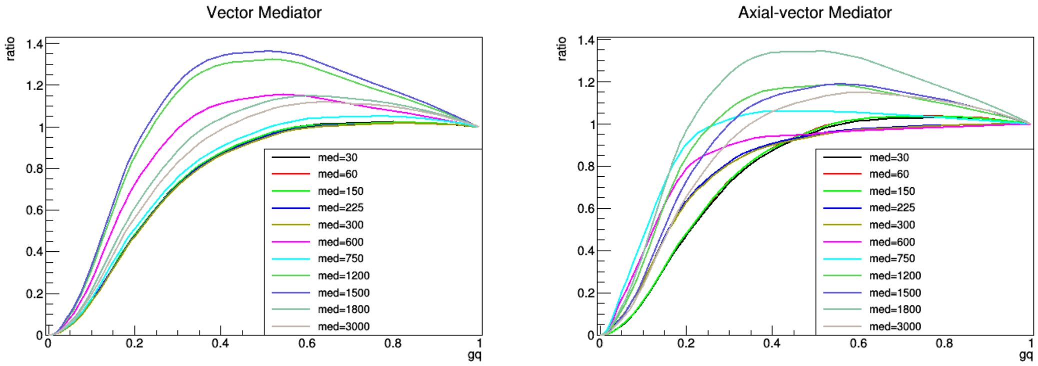

Figure 149: The ratio of signal yields of different g_q values relative to the yields of $g_q = 1$ in both vector model (left) and axial-vector model (right) from 2016 samples. The corresponding generator level signal region selection is applied. The dark matter mass is 1/3 of the mediator mass and $g_{dm} = 1$

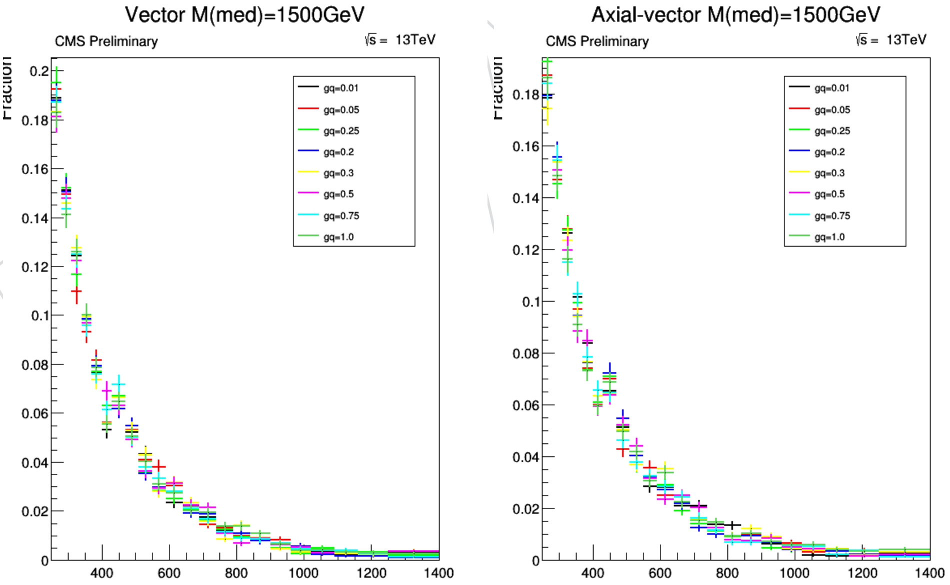

Figure 150: The generator level recoil distribution from 2017 LO signal samples with different g_q values. The corresponding generator level signal region selection is applied and the normalization is scaled to 1. The dark matter mass is 1/3 of the mediator mass and $g_{dm} = 1$. The plots includes signals with 1500 GeV vector mediator (left), and 1500 GeV axial-vector mediator (right).

section are calculated by madgraph and the NLO/LO scaling is roughly a constant regardless of the coupling values. Thus the yield ratio derived from LO samples is reliable.

The ratios with respect to different g_q values are compared between 2017 LO samples and 2016 samples, as shown in figure 151. There are some mass points that have a 20% difference. The trending remains similar as the signal yield decreases when $g_q > 0.5$ for some mass points.

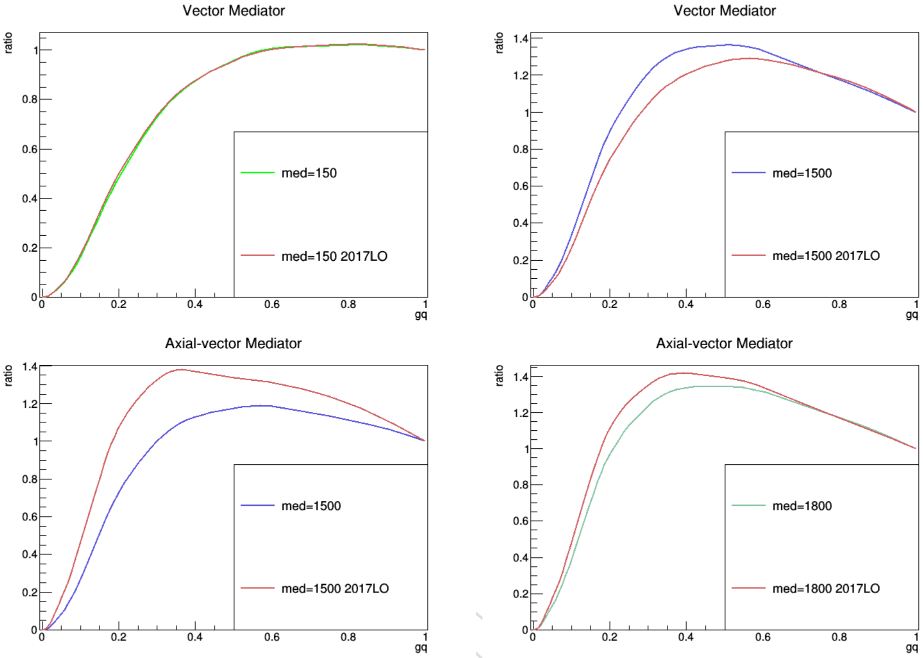

Figure 151: The ratio of signal yields of different g_q values comparison between 2017 samples and 2016 samples. The corresponding generator level signal region selection is applied. The dark matter mass is 1/3 of the mediator mass and $g_{dm} = 1$.

Since 2016 samples are hard to reproduce and no problems were found in the 2017/2018 signal samples, We decieded to use the ratio of signal yields based 2017/2018 samples. The ratio of signal yields of different g_q values relative to the yields of $g_q = 0.25$ in both vector model and axial-vector model from 2017/2018 samples are shown in figure 152.

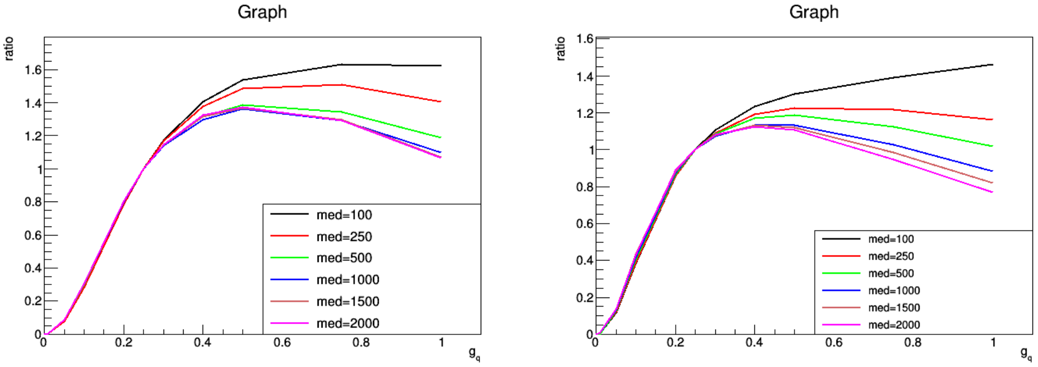

Figure 152: The ratio of signal yields of different g_q values relative to the yields of $g_q = 0.025$ in both vector model (left) and axial-vector model (right) from 2017/2018 samples. The corresponding generator level signal region selection is applied. The dark matter mass is 1/3 of the mediator mass and $g_{dm} = 1$

B.2 Analytical strategy

B.2.1 Description of method

This section is copied from Ref. [25].

The result of a search for a given signal of new physics is usually quantified by quoting the observed value of the signal strength μ, which corresponds to the ratio of the observed and predicted signal cross sections. In the case where no significant signal is observed, the results are framed as an exclusion limit on the μ parameter. In both cases, it is interesting to translate the observed signal strength into the space of the coupling parameters g_q and g_χ. In order to derive limits on the couplings g_q and g_χ, it is helpful to consider the analytical dependence of the signal cross section on the couplings. Since the mediator is always produced from a quark-antiquark-mediator vertex, its production cross section is necessarily proportional to g_q^2. An additional coupling dependence is incurred in the mediator decay, where the branching fraction to invisible particles is given by the ratio of the partial width Γ_χ, which depends on g_χ, and the total width Γ_{tot}, which depends on g_χ as well as g_q:

$$\sigma \times \mathrm{BR} \;\propto\; g_q^2 \times \frac{\Gamma_\chi(g_\chi)}{\Gamma_{tot}(g_\chi, g_q)} \,. \tag{9}$$

In a typical case, one would generate a signal sample for fixed values of g_q^{gen} and g_χ^{gen} and process the sample through the experimental analysis to determine the exclusion limit on the signal strength μ. The signal strength limit can then be translated into a coupling limit by expressing μ using the proportionality relation above:

$$\mu = \frac{(\sigma \times \mathrm{BR})_{obs}}{(\sigma \times \mathrm{BR})_{gen}} = \frac{\left(g_q^2 \frac{\Gamma_\chi(g_\chi)}{\Gamma_q(g_q)+\Gamma_\chi(g_\chi)}\right)_{obs}}{\left(g_q^2 \frac{\Gamma_\chi(g_\chi)}{\Gamma_q(g_q)+\Gamma_\chi(g_\chi)}\right)_{gen}} \,. \tag{10}$$

The labels *gen* and *obs* are short for *generated* and *observed*, respectively. Keeping one of the couplings g_χ and g_q fixed, the analytical expressions for $\Gamma_{\chi/q}$ from [81] can be inserted and the equation can be solved algebraically for the excluded value of the other coupling. To make the expression more readable, variables are understood to represent the generated values unless specified otherwise, and the "gen" label is dropped:

$$g_q^{obs} = \sqrt{\frac{\mu \times \Gamma_\chi}{C g_\chi^2 - \gamma_q \times \mu}}, \quad g_\chi^{obs} = \sqrt{\frac{\mu \times \Gamma_q}{C g_q^2 - \gamma_\chi \times \mu}} \,, \tag{11}$$

with

$$C = \frac{\Gamma_\chi + \Gamma_q}{\left(g_q g_\chi\right)^2}, \quad \gamma_i = \frac{\Gamma_i}{g_i^2} \,.$$

Since the coupling is defined as a real number, this solution of course requires that the term under the root is positive. This requirement effectively creates a maximum signal strength value μ_{max} for which a coupling value can still be derived:

$$\mu_{max} = \begin{cases} 1 + \left(\frac{\Gamma_\chi}{\Gamma_q}\right)_{generated}, & \text{when deriving a } g_q \text{ value} \\ \\ 1 + \left(\frac{\Gamma_q}{\Gamma_\chi}\right)_{generated}, & \text{when deriving a } g_\chi \text{ value} \end{cases} \quad . \tag{12}$$

In the parameter space with $m_{\text{med}} \gg m_{\text{DM}}$, where this analysis is most sensitive, the default choices of $g_q = 0.25$ and $g_\chi = 1.0$ imply $\Gamma_\chi \approx \Gamma_q$ and therefore $\mu_{max} \approx 2$. The reason for this boundary is that the expression for $\sigma \times \text{BR}$ eventually saturates since the coupling dependence in the numerators and denominators of eq. 11 cancels in the limit of $g_q \to \infty$ or $g_\chi \to \infty$. This implies that no arbitrarily large signal strength values can be accommodated by varying only one coupling parameter, and it would be necessary to vary both parameters at the same time.

The exact behavior of the translation from the signal strength to the coupling values is shown in Fig. 153. For a signal strength of $\mu = 1$, the resulting coupling values are identical to the input coupling values. For $\mu \to \mu_{max}$, the translation function diverges and no coupling value can be deduced. Note that this divergence has a dependence on the mediator mass due to the top mass threshold: The ratio of the Γ_χ and Γ_q terms is different below and above the threshold, which has opposite effects on the resulting g_χ and g_q values (cf. eq. 12). In the limit of $\mu \to 0$, the behavior simplifies again and the observed coupling values scale as $\sqrt{\mu}$.

B.2.2 Results for this analysis

The result of the analytical rescaling method for this analysis is shown in Fig. 154.

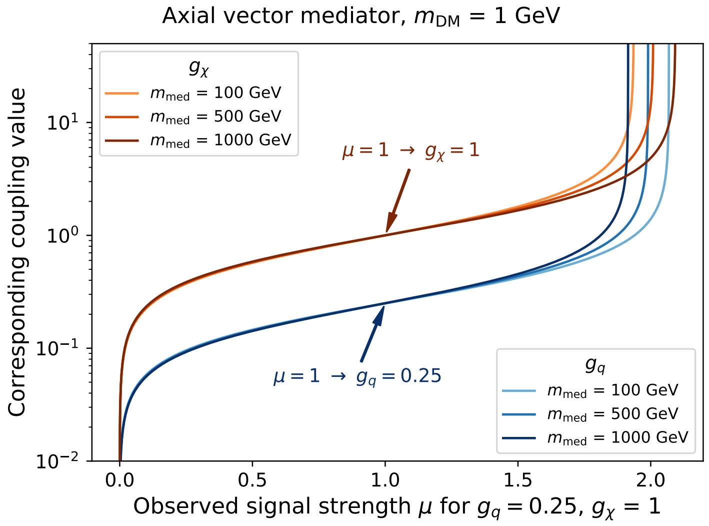

Figure 153: Relation between the observed signal strength and the corresponding coupling values for the default set of couplings discussed in the text. Curves are shown separately for g_χ (red lines) and g_q (blue lines), assuming that each coupling is varied independently, while the other one is kept constant at its starting value. The different color shadings indicate different choices for the mediator mass m_{med}. The couplings of the mediator to the fermions are assumed to be of axial vector type, and the DM mass is set to $m_{\mathrm{DM}} = 1$ GeV. The two points indicated by the colored arrows represent the cases where the observed signal cross section coincides with the generated one, in which case the translation procedure simply reproduces the generated values of the couplings. For a vector mediator, the behavior is identical to the axial vector case in the limit of $m_{\mathrm{med}} < m_{top}$ and $m_{\mathrm{med}} \gg m_{top}$, but different for $m_{\mathrm{med}} \approx m_{top}$, where the sharper turn-on behavior of the width function would lead to a more swift transition between the regimes (i.e. the line with $m_{\mathrm{med}} = 500$ GeV would be much closer to that with $m_{\mathrm{med}} = 1$ TeV).

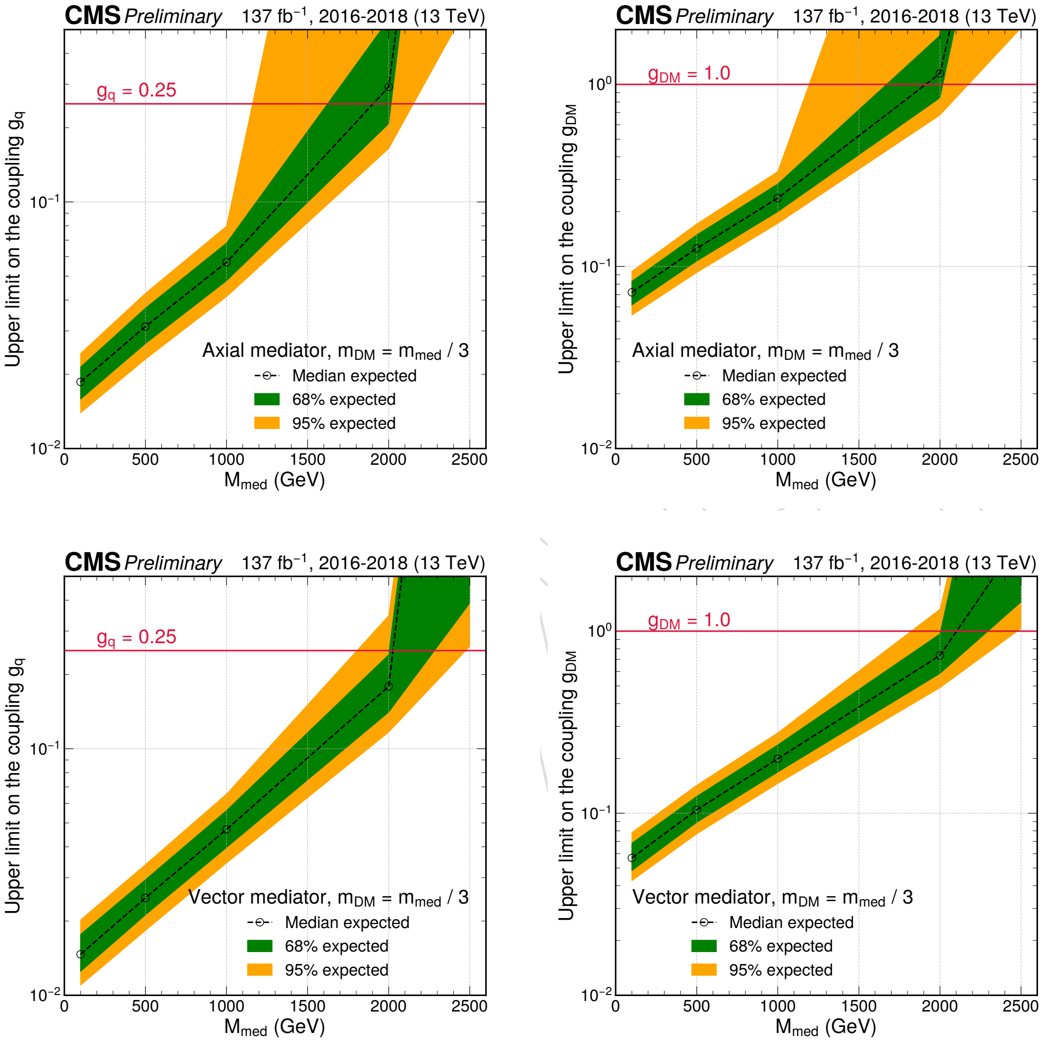

Figure 154: Coupling limits obtained with the analytica rescaling method for axial (top) and vector mediators (bottom). The limits are formulated on either g_q (left) or g_χ (right), while the other coupling is kept constant at its default value.

C Update GJets MC from LO sample to NLO sample

Currently the γ+jet samples used in the analysis, as shown in Table 33, are generated at LO (Leading Oder) precision. A k-factor as a function of generator-level photon p_T is applied to correct the LO sample towards NLO precision. The k-factor is derived by comparing 2016 LO GJets sample with 2016 NLO GJets sample. However, the k factor scheme does not fully reproduce the behavior of the NLO sample.

To get more accurate GJets simulation, 2017+2018 NLO GJets sample has been put into production. As of now, the 2018 NLO GJets samples are ready, while the 2017 NLO GJets samples are still under production. As an early check, we replaced the 2018 LO GJets sample with the 2018 NLO GJets sample, and compared the result with before in terms of data-MC agreement and nuisance parameter pulls. We observed that after the switching, both pre-fit and post-fit agreement has improved (as shown in Fig 155), and the photon-related nuisance parameters for 2018 are pulled much less compared to before (as shown in Fig 156).

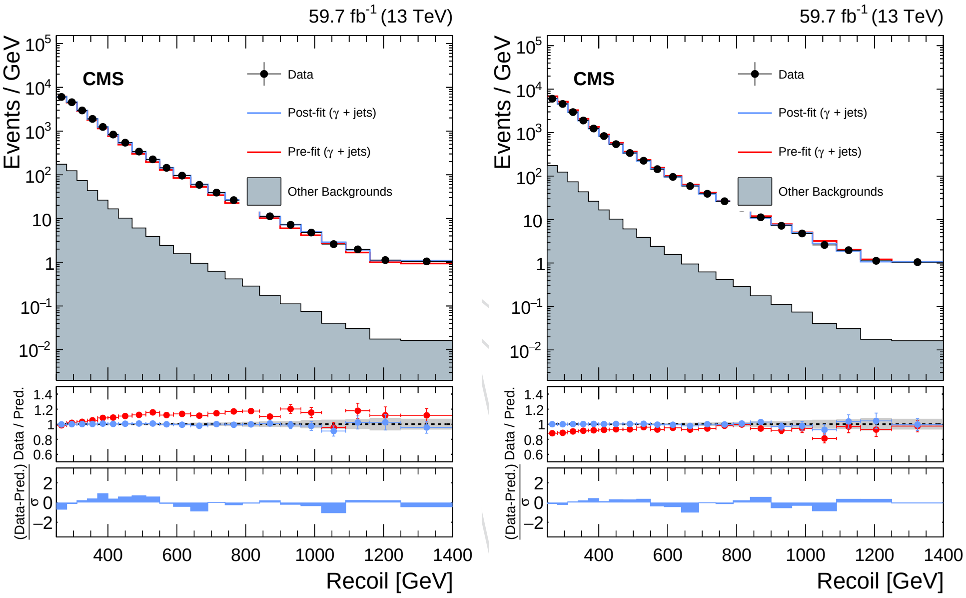

Figure 155: The comparison of data/MC agreement between using 2018 LO GJets sample(left) and 2018 NLO GJets sample(right), the plot on the right show better agreement in both pre-fit and post-fit.

The corresponding samples for 2017 are currently in production, with three out of four p_T bins close to completion. We expect the last p_T bin to be completed within a week.

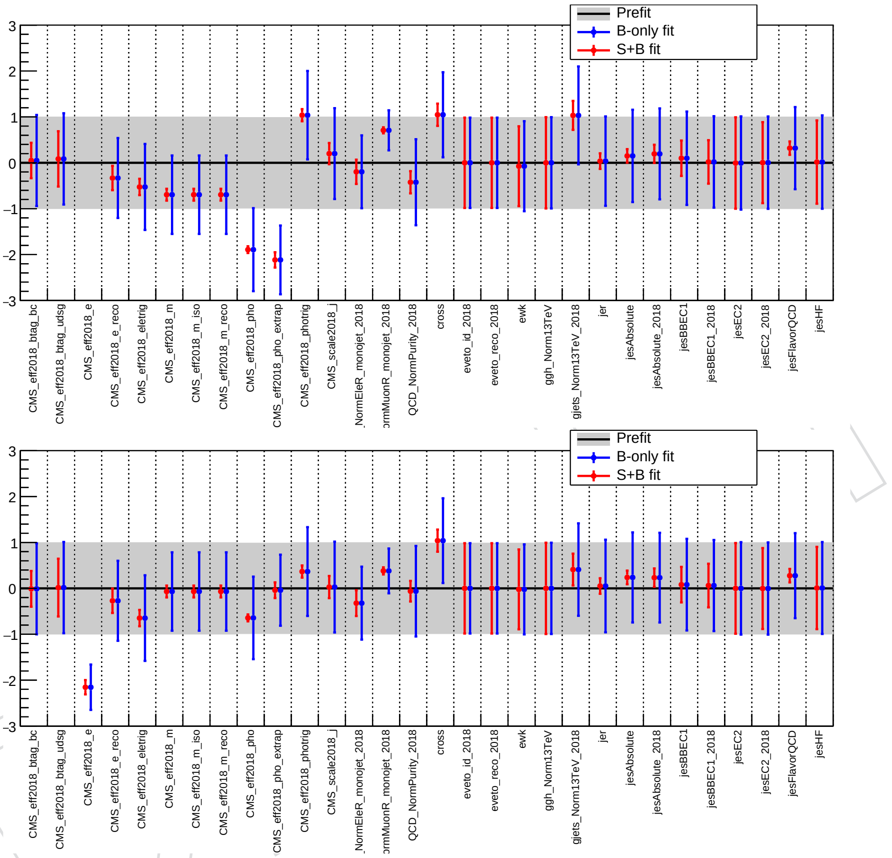

Figure 156: The comparison of select nuisance parameter pulls between using 2018 LO GJets sample (top) and 2018 NLO GJets sample(bottom), the plot on the right show smaller pulls on the photon-related parameters including: CMS_eff2018_pho, CMS_eff2018_pho_extrap, CMS_eff2018_photrig, and gjets_Norm13TeV_2018, which are related to photon identification, photon trigger, and gjets normalization respectively.

D Understand Double Ele CR Data/MC agreement

In the di-electron control regions, a normalization difference between data and MC is observed in both 2017 and 2018 as can be seen in Figs. 64 and 67, respectively, of Section 5.5, which does not happen in the double muon control region. Different set of checks are performed to investigate the cause of this normalization difference and are reported in sub-sections below.

D.1 Effect of Individual Triggers

As a first check, to verify that it is not caused by one of the triggers (Ele35_WPTight_Gsf or Ele115_CaloIdVT_GsfTrkIdT) used to collect data in double electron control region, we use individual triggers with the entire double ele CR selection. The recoil distribution from each of the category using only Ele35_WPTight_Gsf and only Ele115_CaloIdVT_GsfTrkIdT trigger as compared with the default version (OR of two triggers) can be seen in Fig. 157. No particular difference is seen from any of the triggers and similar order of difference is observed from both the triggers. The combined SFs computed for the analysis are used for all the three categories and are not expected to make a difference. The results indicate that the effect is not related to the triggers used in the double-ele control region.

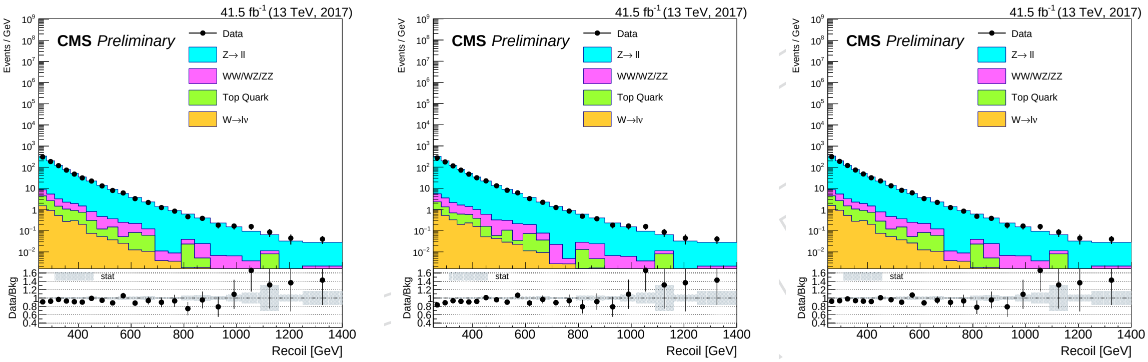

Figure 157: The comparison of the recoil distribution using events triggered by only `Ele35_WPTight_Gsf` (left), only `Ele115_CaloIdVT_GsfTrkIdT` and OR of both ele triggers.

D.2 High boost Z boson check

bosoncheck

As events in the analysis are required to satisfy recoil > 250 GeV, which may result in high boost Z $\rightarrow$ ee. The electrons may have small separation which leads to the overlapped isolation cones of two electron. This may change the isolation efficiency difference between data and simulation. The SFs of the isolation related selection may not apply, such as the single electron trigger `Ele35_WPTight_Gsf`.

The ΔR between the two electrons is presented in figure 158 using the di-electron CR selection. The majority of the events have the two electrons with separation $\Delta R > 0.5$. The discrepancy between data and MC behaves similarly in low ΔR and high ΔR region, which represents Z $\rightarrow$ ee with high and low boost, respectively. In the di-electron CR, three triggers are used for selection: `Ele35_WPTight_Gsf` for 2017 or `Ele35_WPTight_Gsf` for 2018, `Ele115_CaloIdVT_GsfTrkIdT`, and `Photon200`. The ΔR distribution is then plotted by requiring three triggers separately, as shown in Fig. 159. The combined trigger SF is applied to all of them, which leads to some normalization difference. Among the three triggers, low p_{T} single electron trigger contains the isolation. The shape of the Data/MC remains similar between different triggers. This further indicates that the discrepancy is not related to the boost of the $Z \rightarrow ee$.

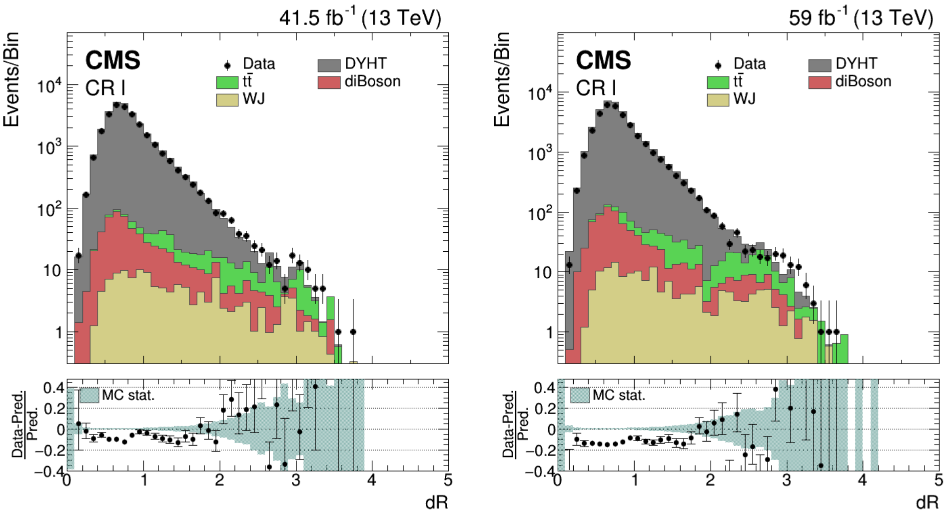

Figure 158: The comparison of the ΔR of two electrons between data and MC prediction in 2017 (left) and 2018 (right).

D.3 Check effect of the selections

The data and simulation are compared with a set of looser selection. The selection is the subset of di-electron CR selection, which requires the events to pass di-electron selection, no photon, muon or tau that pass the loose ID, recoil > 250 GeV, and a leading jet with $p_{\mathrm{T}} > 100$ GeV and $|\eta| < 2.4$. As shown in figure **??**, the discrepancy remains similar, which indicates that the difference is not caused by the removed selections. The efficiency of the leading jet is also studied in this case, where no obvious efficiency difference is spotted between data and MC, as shown in figure 161.

D.4 Effect of different electron IDs

To look further into the effect of selection bias, different combination of electron identification isolation working points as suggested by the EGamma POG were looked. In the analysis, tight WP and lepton-veto WP by the POG are used to selection leading and trailing electrons, respectively, and in-house derived scale factors are applied. For this check, a combination of tight-tight, tight-medium, tight-loose and medium-medium working points were used to identify isolate leading-trailing electrons. As in-house SFs are not available for all these permutations, POG recommended scale factors were applied and a comparison of recoil distribution for all these categories are show in Fig. 162. The left side distribution shows the absolute comparison for each category while the right side distributions show the normalized comparison.

No major difference in the normalization discrepancy is observed in any of the category. We also investigated other distributions - Z_{ee} invariant mass, Zp_{T}, p_{T}, η, ϕ of the leading and trailing electron and other variables that are used in the selection and no obvious trends could be observed in any of the variable.

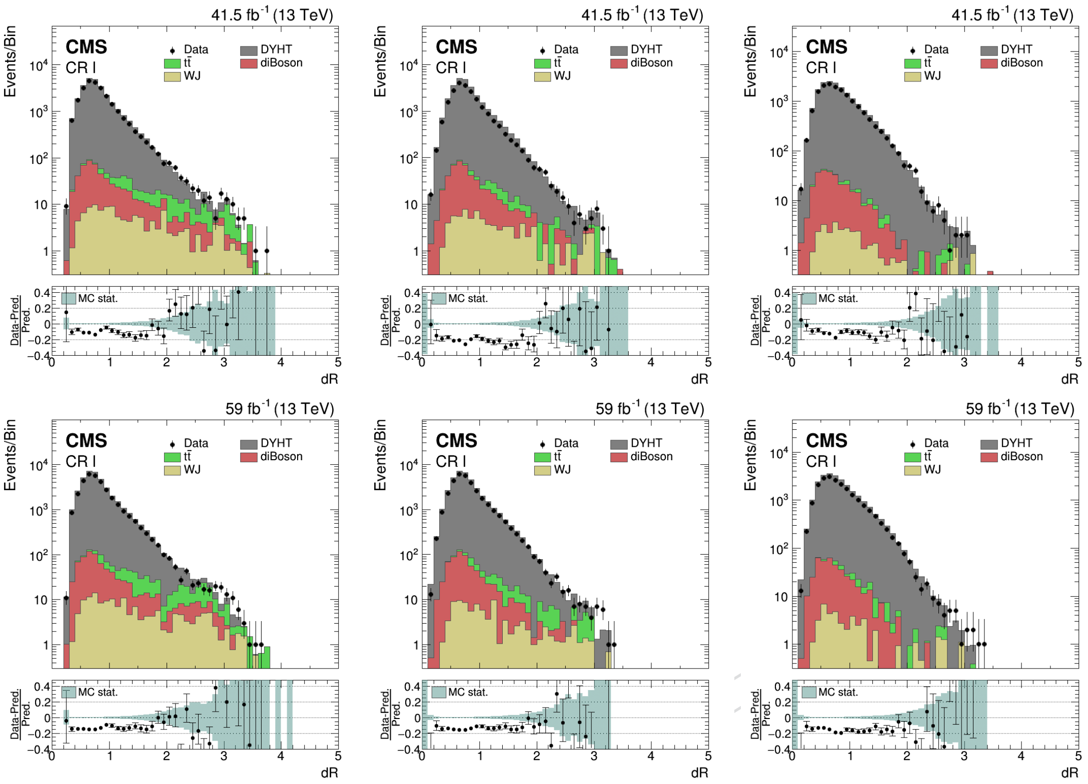

Figure 159: The comparison of the ΔR of two electrons between data and MC prediction. The top plots are the comparison with 2017 data passing trigger `Ele35_WPTight_Gsf` (left), `Ele115_CaloIdVT_GsfTrkIdT` (middle), and `Photon200`. The bottom plots are the comparison with 2018 data passing trigger `Ele32_WPTight_Gsf` (left), `Ele115_CaloIdVT_GsfTrkIdT` (middle), and `Photon200`.

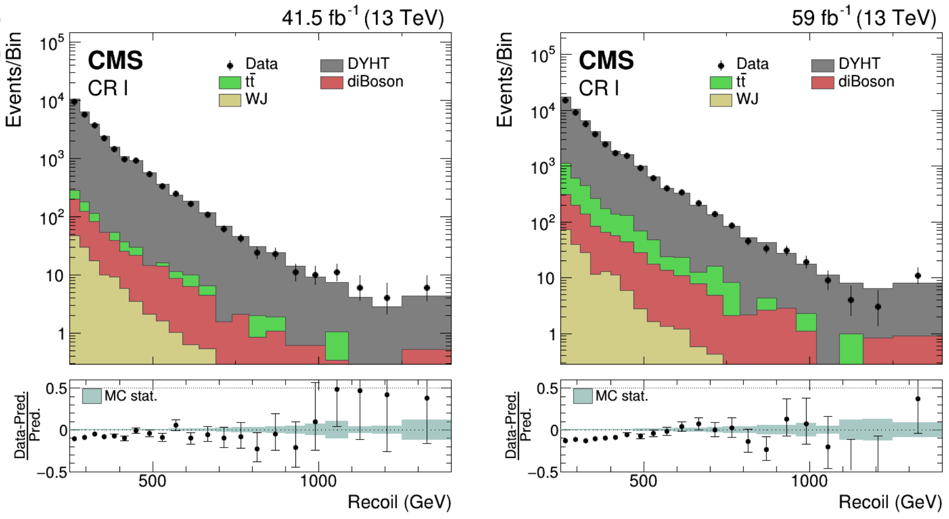

Figure 160: The comparison between data and MC prediction in 2017 (left) and 2018 (right) using the looser selection: di-electron selection with no muon, photon or tau passing loose ID, recoil > 250 GeV, and a leading jet with $p_{\mathrm{T}} > 100$ GeV and $|\eta| < 2.4$.

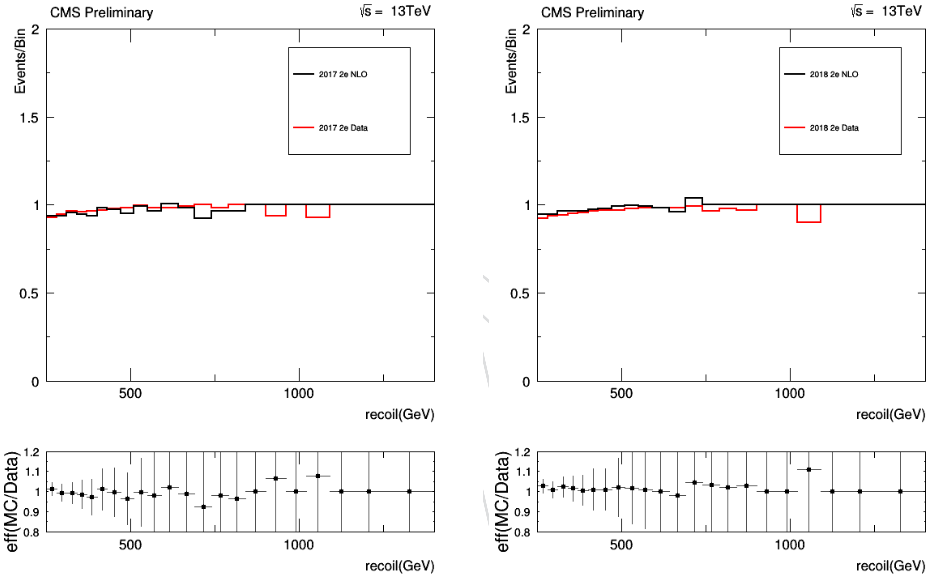

Figure 161: The efficiency comparison of leading jet selection in di-electron CR between data and MC prediction in 2017 (left) and 2018 (right).

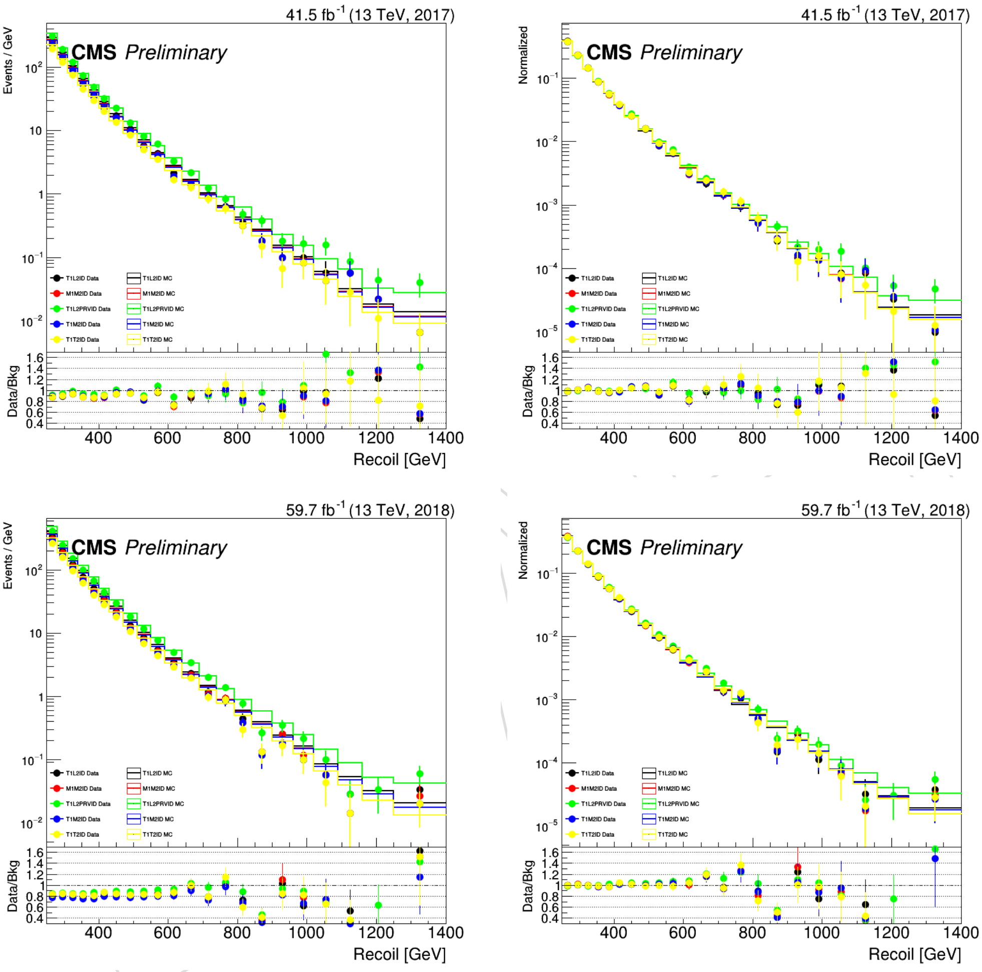

Figure 162: Comparison of Recoil distribution for different electron IDs for 2017 (top) and 2018 (bottom). The left side distribution shows the absolute comparison while right side are the normalized distributions

D.5 Split by Eras

To check the era dependence on the normalization differences, recoil distribution were made for both 2017 and 2018 separated in each data taking era for respective years. The average pileup distribution for the entire year was used for each era instead of respective pileup weights. Fig. 163 shows the recoil distributions separated in era's for 2017, B, C and D are seen to compare better than E and F data taking era but when the same separation in era is looked upon for recoil distribution in year 2018, Fig. 164 no such dependence is observed.

For what appears in 2017 could be incidently and no era-dependence is observed for the differences in normalization and hence can't be attributed to a particular problem related to data taking issue.

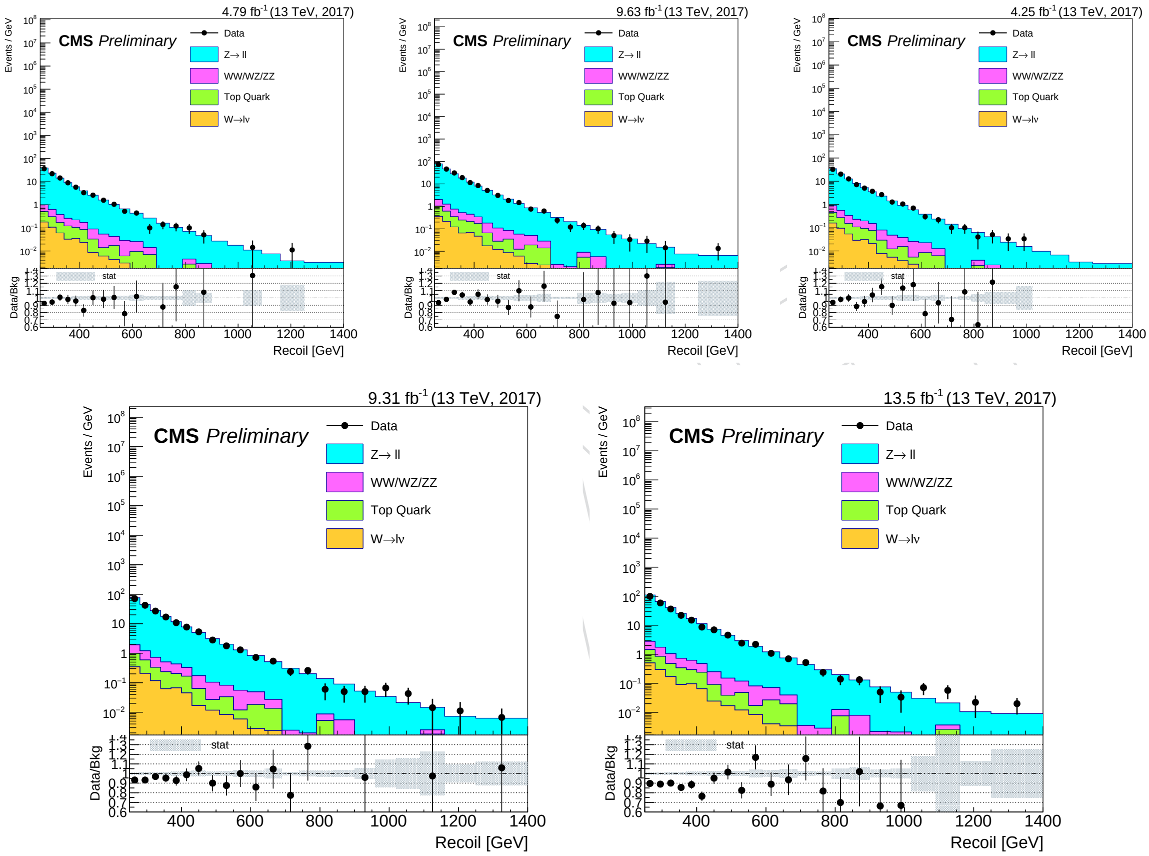

Figure 163: Comparing recoil distribution separated in each data taking era B (top-left), C (top-middle), D (top-right), E (bottom-left), and F (bottom-right) for year 2017

In conclusion, after looking at different kinematic variables for the leading and trailing lepton, other variables used in the selection and studying the trigger effect, no particular cause is found for the differences observed in the double electron control region.

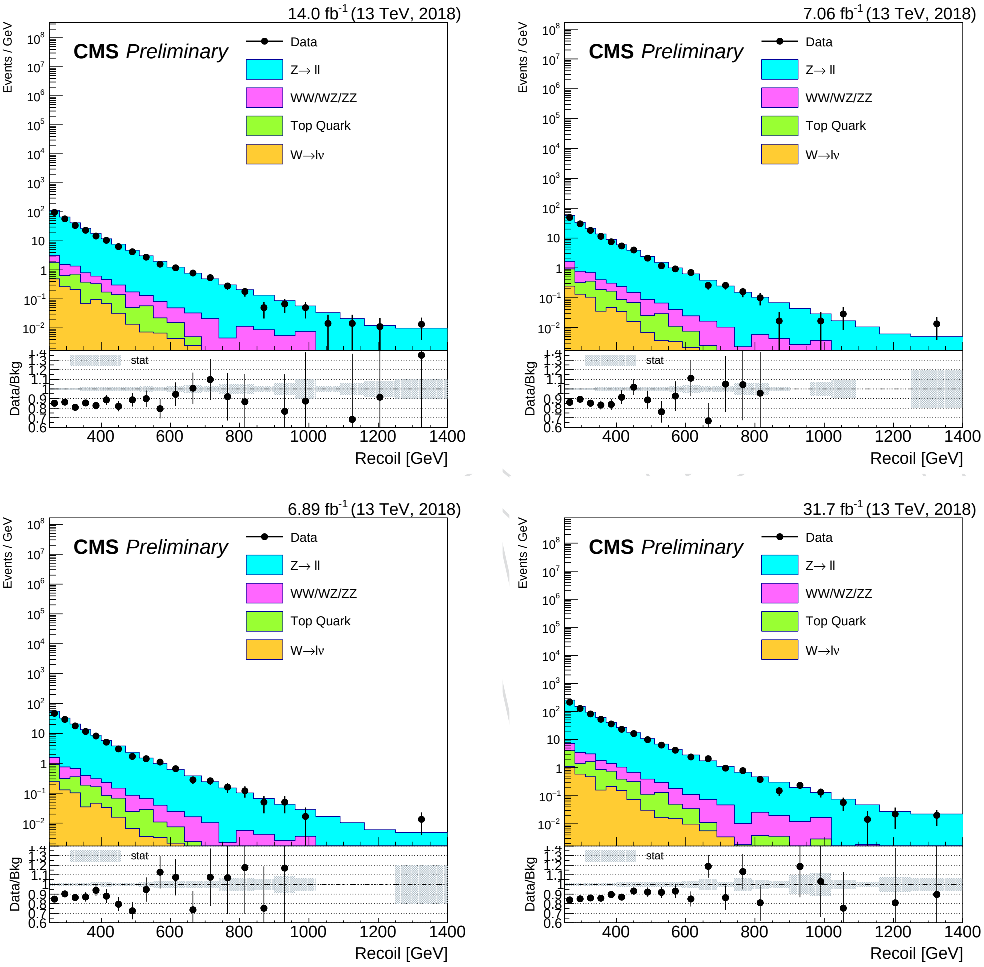

Figure 164: Comparing recoil distribution separated in each data taking era A (top-left), B (top-right), C (bottom-left), and D (bottom-right) for year 2018

E Results of partial unblinding

As outlined in Section 7.2, a partial unblinding is performed in order to check for experimental issues affecting the jet/$p_{\mathrm{T}}^{\mathrm{miss}}$ reconstruction. One fifth of each of the 2017 and 2018 data sets is considered for this study (events in data are selected if their event number is divisible by five with a remainder of zero).

In all plots shown below, the baseline event selection including the jet-based HEM veto is applied unless otherwise specific in the text.

E.1 Comparison of recoil spectra between frameworks

The unblinding study has been performed independently three analysis frameworks. It has been ensured that the agreement between the groups is within 1% or within a few events in all bins of the recoil distributions in the signal region. It has further been checked that the 20 selected events with the highest $p_{\mathrm{T}}^{\mathrm{miss}}$ values are identical between the groups.

E.2 Analysis of high-$p_{\mathrm{T}}^{\mathrm{miss}}$ events

The twenty selected events with highest $p_{\mathrm{T}}^{\mathrm{miss}}$ in both data sets are tabulated in Tables 24 and 25. In the 2017 data set, 3 events are observed with $p_{\mathrm{T}}^{\mathrm{miss}} > 1.4\,\mathrm{TeV}$, while the 2018 data set shows nine such events. The high-tail of the $p_{\mathrm{T}}^{\mathrm{miss}}$ distribution is especially sensitive to experimental sources of pathological $p_{\mathrm{T}}^{\mathrm{miss}}$ because of the low numbers of expected events from SM processes. In this region, even very rare reconstruction failures can have a significant effect on the analysis, if they produce sufficiently high $p_{\mathrm{T}}^{\mathrm{miss}}$. To understand whether contamination from such events is present, the twenty highest-$p_{\mathrm{T}}^{\mathrm{miss}}$ in both data sets are inspected manually. The vast majority of inspected events has a monojet-like topology: A single, high-p_{T} jet recoiling back-to-back against large $p_{\mathrm{T}}^{\mathrm{miss}}$. Most events do not have significant jet activity beyond the leading jet. Event displays for the two highest-$p_{\mathrm{T}}^{\mathrm{miss}}$ events in each year are shown in Fig. 166 and Fig. 167. For each event, the following quantities are checked:

1. Jet quality criteria: the composition in terms of different PF candidate types, and constituent multiplicities allow to differentiate jets from experimental failures from good jets.
2. Signs of beam halo contamination: Events with energy deposits induced by muons travelling along the beamline ("beam halo") typically show hits in the CSC system as muons enter the detector. They further show energy deposits not pointing toward the beam spot, and induce jets with low track multiplicities that can be elongated in η.
3. Presence of large multiplicities of unepxected objects such as muons, eletrons, photons, or generally unusually high calorimeter occupancy.

At the highest $p_{\mathrm{T}}^{\mathrm{miss}}$ values, it is observed that the leading jet sometimes carries enough energy to partially reach the muon system, rather than be fully absorbed by the calorimeters ("punch-through"). In such events, the jet p_{T} is likely slightly undermeasured as the particles exiting the calorimeters are not taken into account properly. This effect is a basic limitation of the calorimeters installed in CMS, which have finite thickness. While striking, this effect is not a source of "fake $p_{\mathrm{T}}^{\mathrm{miss}}$", since the events are still dominated by the single jet+$p_{\mathrm{T}}^{\mathrm{miss}}$ system. The undermeasurement of the jet energy results in a reduction of $p_{\mathrm{T}}^{\mathrm{miss}}$ in this case, since $p_{\mathrm{T}}^{\mathrm{miss}} \approx p_{\mathrm{T}}(j)$ by construction. No evidence is found of any reconstruction pathologicy issue in the inspected events.

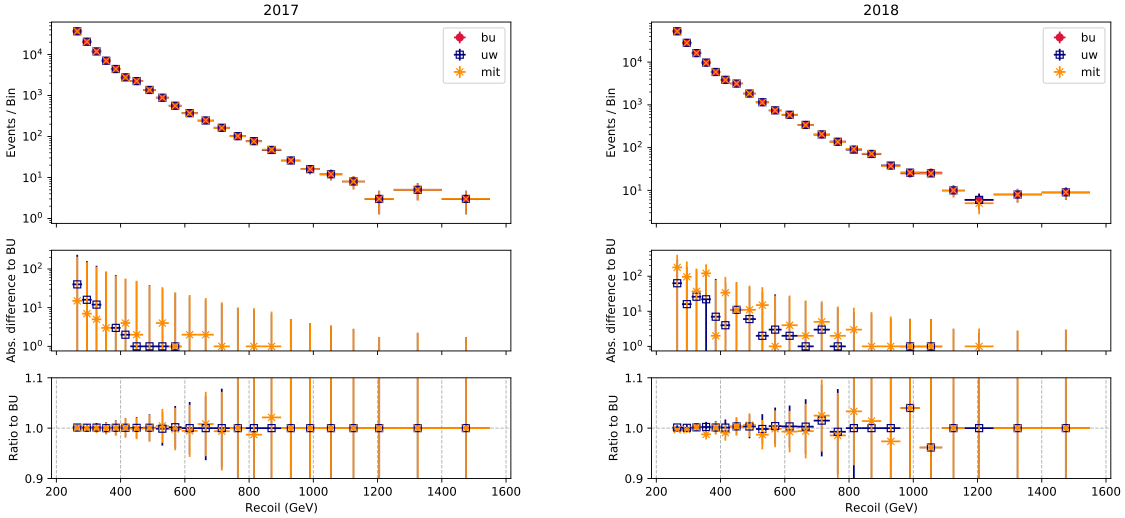

Figure 165: Comparison of the recoil spectra in data in the monojet signal region in the partially unblinded 2017 (left) and 2018 data sets (right). The different colors indicate different analysis frameworks. In the middle panel, the absolute difference of the individual curves relative to one of them is shown. Similarly, the bottom panel shows the ratio of the spectra relative to a common reference.

Table 24: List of the twenty events with highest $p_{\mathrm{T}}^{\mathrm{miss}}$ in the partially unblinded 2017 monojet signal region. Three events are observed with $p_{\mathrm{T}}^{\mathrm{miss}} > 1.4\,\mathrm{TeV}$.

Run number	**Lumi section**	**Event number**	$p_{\mathrm{T}}^{\mathrm{miss}}$ **(GeV)**	$\phi(p_{\mathrm{T}}^{\mathrm{miss}})$
300122	441	609074740	1077	-0.1
300558	157	217386075	1096	2.9
304508	1280	1486280085	1109	1.9
302525	27	37310995	1116	2.9
297485	152	262927160	1118	2.3
306041	169	324709425	1126	-0.1
304797	366	662096405	1134	3.1
300157	1045	1026592315	1142	-1.2
305237	596	1108766975	1151	1.2
297675	285	489484455	1179	-2.6
306091	591	760770745	1190	1.7
303838	1412	1797754590	1235	1.3
304333	957	1559667420	1275	-1.5
301472	485	467333845	1281	2.8
305366	856	1233795870	1293	-2.4
303948	86	61149125	1339	-2.7
300806	174	235256970	1359	-0.4
302322	406	333103125	1430	1.3
305202	216	276641240	1482	-0.6
306459	10	16127940	1499	-2.6

Table 25: List of the twenty events with highest $p_{\mathrm{T}}^{\mathrm{miss}}$ in the partially unblinded 2018 monojet signal region. Nine events are observed with $p_{\mathrm{T}}^{\mathrm{miss}} > 1.4\,\mathrm{TeV}$.

Run number	**Lumi section**	**Event number**	$p_{\mathrm{T}}^{\mathrm{miss}}$ **(GeV)**	$\phi(p_{\mathrm{T}}^{\mathrm{miss}})$
323525	316	538386495	1195	-2.9
317182	409	528535265	1211	-0.4
321712	190	364451050	1216	-1.4
321457	719	1156385440	1254	0.2
319524	1111	1659388200	1267	0.8
321283	174	238605465	1273	1.9
319853	4	5950615	1308	-0.9
317488	567	820655290	1319	0.3
321305	118	173886005	1322	-0.3
322332	330	554760245	1330	2.7
316722	246	336389195	1341	-1
324841	217	414322085	1442	0.5
320040	238	377889955	1458	-0.9
316059	145	163781840	1478	0.5
316457	879	1016946020	1494	-2.1
317319	87	78055115	1511	-3.1
322617	193	321858390	1613	-0.1
323524	82	152241545	1779	0.4
321457	1008	1610942665	1906	2.6
317626	1870	2818081770	1944	-1.2

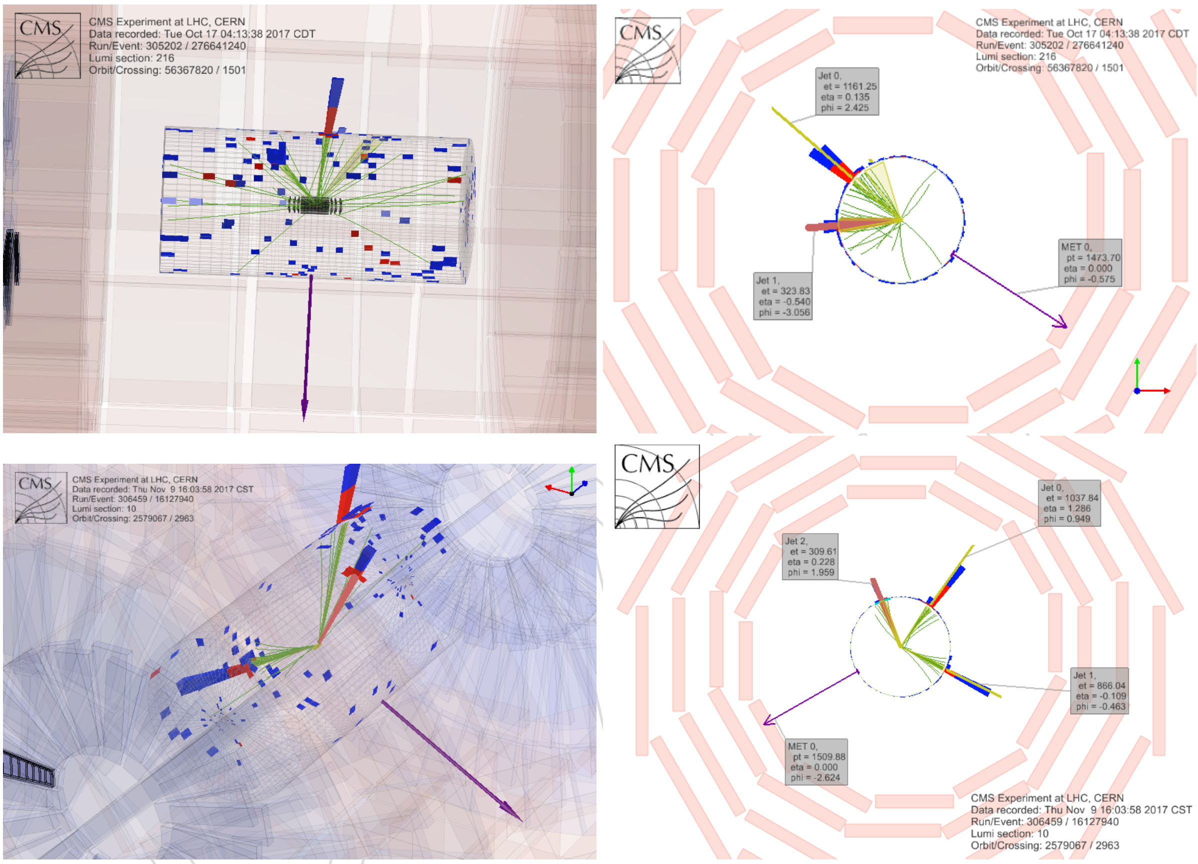

Figure 166: Event displays for the two highest-$p_{\mathrm{T}}^{\mathrm{miss}}$ events in the 2017 data set. The top (bottom) row shows run number:luminosity section:event number =305202:216:276641240 (306459:10:16127940). The left column shows the 3D view of the detector, while the right column shows the $r - \phi$ plane.

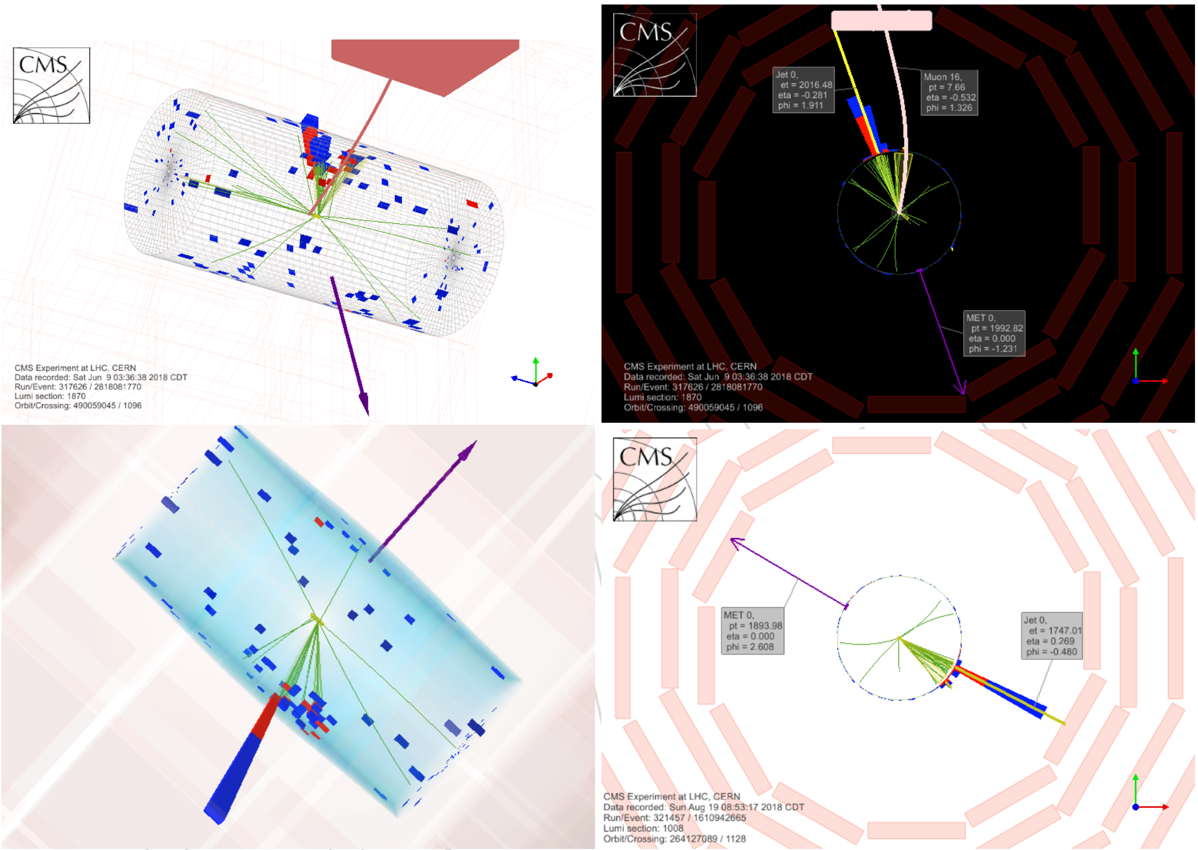

Figure 167: Event displays for the two highest-$p_{\mathrm{T}}^{\mathrm{miss}}$ events in the 2018 data set. The top (bottom) row shows run number:luminosity section:event number = 317626:1870:1610942665 (321457:1008:1610942665) The left column shows the 3D view of the detector, while the right column shows the $r - \phi$ plane.

E.3 Comparison of recoil spectra between years

As a first sanity check, the recoil spectra observed in the two data sets are compared. Fig. 168 shows the ratio between the 2018 and 2017 spectra for data and simulation. For most of the recoil range, the relationship between the 2017 and 2018 data sets in data is consistent with the expectation from simulation. A statistically significant deviation appears at low values of recoil ($\approx 250\,\mathrm{GeV}$), where the 2018 data set shows an excess with respect to the expectation. Qualitatively similar, but statistically less significant is an excess at very high values of recoil (overflow bin $p_{\mathrm{T}}^{\mathrm{miss}} > 1400\,\mathrm{GeV}$), where 2018 shows a slight excess.

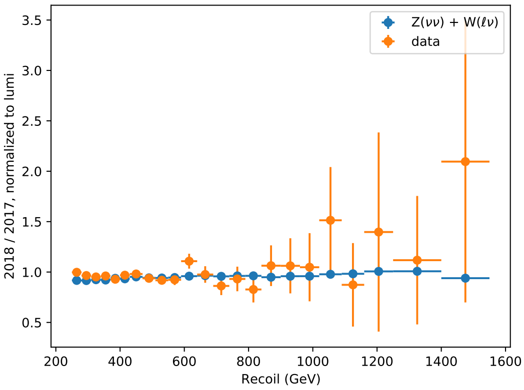

Figure 168: Ratio of the recoil spectra between in the 2018 data set over those in the 2017 data set. The ratio is shown separately for observed events in data and for the expected background contributions from W + jets and Z + jets events.

E.4 Kinematic distributions

The behavior of the data in the signal region is studied by analyzing various kinematic distributions. Fig. 169 shows the recoil p_{T} and ϕ distributions in both data sets, and compares the data with the expectation from simulation. In the 2017 data set, no unexpected features are present. The recoil spectrum, as well as the ϕ distribution show good quantitative and qualitative agreement with the simulation. In the 2018 data set, the excesses at the low and high ends of the recoil range previously observed in the comparison between years are evident. The ϕ distribution further shows a clear excess of events in data in the HEM region, which indicates that the jet-based veto used here is insufficient to fully reject contamination from events with fake $p_{\mathrm{T}}^{\mathrm{miss}}$ arising from the HEM failure.

The properties of the leading jets are further studied. Fig. 170 shows the p_{T}, η and ϕ distributions of the leading jet in each event. The leading jet p_{T} is not well modeled in simulation for events with jet p_{T} below the recoil selection threshold of 250 GeV. This behavior is also observed in the control regions (cf. Figs. 58 and 61) and related to the leading-jet-to-recoil resolution, rather than the $p_{\mathrm{T}}^{\mathrm{miss}}$ reconstruction under study here. Beyond the p_{T} distribution, good agreement is observed for the leading jet quantities in 2017. In the 2018 data set, excesses of events are observed in the negative η hemisphere, and at in the ϕ region opposite to the HEM region. These events are most likely multijet events, in which one jet from a back-to-back dijet system enters the HEM region and is lost to reconstruction, giving rise to large $p_{\mathrm{T}}^{\mathrm{miss}}$. The second jet of the system, which is typically shifted by π in ϕ relative to the first jet, is then reconstructed as the good leading jet in the signal region selection.

The baseline analysis selection incorporates a number of quantities designed to avoid contamination from low-quality jets. For the leading jets, requirements on the neutral and charged hadron energy fractions are imposed. The distributions of these quantities after the baseline selection are shown in Fig. 170. Furthermore, events are required to have consistent values of PF $p_{\mathrm{T}}^{\mathrm{miss}}$ and calorimeter-based $p_{\mathrm{T}}^{\mathrm{miss}}$. The relative different between the two is shown in Fig. 173. These quantities are directly affected by the fine-grained reconstruction mechanisms, as well as the resolution of quantities like the calorimeter $p_{\mathrm{T}}^{\mathrm{miss}}$, which is not specifically calibrated. Therefore, only qualitative agreement between data and simulation is expected. In this regard, data and simulation agree well. No qualitatively unexpected features are observed in the data.

Finally, the jet $\eta - \phi$ occupancy in data is checked for signs of hot or cold spots, which would indicate faulty detector components. The distributions are shown in Fig. 174 and no unexpected features are observed. Note that in the 2018 data set, a deficit of jets in the HEM region is observed, which is mostly a result of the jet-based veto selection we have applied here: Events tha thave jets in this region of the detector are rejected by the selection, leading to a suppression relative to neighoring regions.

E.5 Isolating the HEM contribution in 2018

As detailed above, multiple discrepancies between data and simulation are observed in the 2018 signal region. In order to identify whether or not each of these features is related to the HEM effect, a comparison is made of two samples constructed to be enriched with, or respectively depleted of HEM contamination. In both samples, the signal selection is applied, with exception of the jet-based HEM veto, which is not applied. In addition, events in the HEM-enriched sample are then selected by requiring $-1.57 < \phi(\vec{p}_{\mathrm{T}}^{\mathrm{miss}}) < -0.87$, while the depleted sample is required to have $1.57 > \phi(\vec{p}_{\mathrm{T}}^{\mathrm{miss}}) > 0.87$.

The properties of the leading jets in events in both regions are shown in Fig. 175. In the ϕ distributions of the leading jet, the effect of the $\phi(\vec{p}_{\mathrm{T}}^{\mathrm{miss}})$ is mirrored: For the vast majority of events, the leading jet-$p_{\mathrm{T}}^{\mathrm{miss}}$ system is back-to-back in ϕ, leading to a clear accumulation of leading jets in the ϕ region opposite to the selected $\phi(\vec{p}_{\mathrm{T}}^{\mathrm{miss}})$ region. As is evident from the depleted region, this correlation between leading jet ϕ and $\phi(\vec{p}_{\mathrm{T}}^{\mathrm{miss}})$ is generally well modeled in simulation. In the HEM-enriched region, the jet ϕ distribution shows a general excess of events that is not present in the well-modeled depleted region. Similarly, the jet η distriution in the enriched region shows an enhanced version of previously observed excess in the negative pseudorapidity hemisphere, while the agreement between data and simulation is much better in this distrubtion in the depleted region. From these observations, we can conclude that $\phi(\vec{p}_{\mathrm{T}}^{\mathrm{miss}})$ is a reliable predictor of HEM-related mismodeling. Finally, the recoil distributions in the two regions are shown in Fig. 176. In the depleted region, the data is generally well modelled by the simulation, and the previously observed excess of events at low recoil is not present. In the enriched region however, this excess is present and significantly enhanced relative to the $\phi(\vec{p}_{\mathrm{T}}^{\mathrm{miss}})$ inclusive selection. From this observation, we concude that the excess at low recoil is a direct result of the HEM effect: QCD multijet events generate fake $p_{\mathrm{T}}^{\mathrm{miss}}$, and thus enter the signal region.

E.6 Strategy for addressing the HEM effect

In the previous sections, it has been demonstrated that QCD contamination via the HEM effect must be taken into account. Here, two strategies are explored: in one strategy, events with $\phi(\vec{p}_{\mathrm{T}}^{\mathrm{miss}})$ in the HEM region are rejected, while in the other, the contamination from HEM-related events is estimated and included in the statistical analysis.

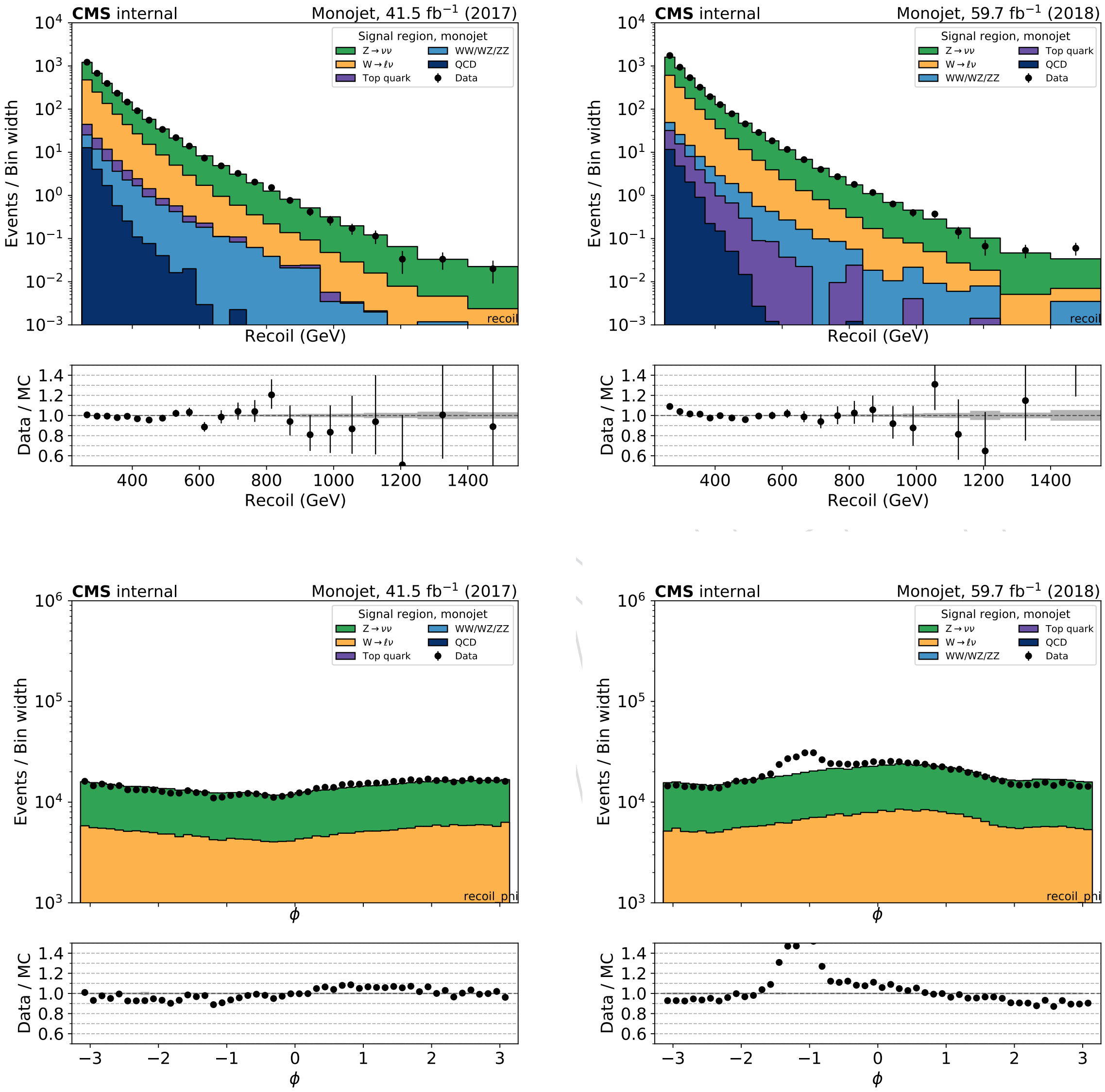

Figure 169: Comparison of data and simulation in the partially unblinded signal regions in 2017 (left) and 2018 (right). The top row shows the recoil p_{T} distribution, while the lower row shows the recoil ϕ distribution.

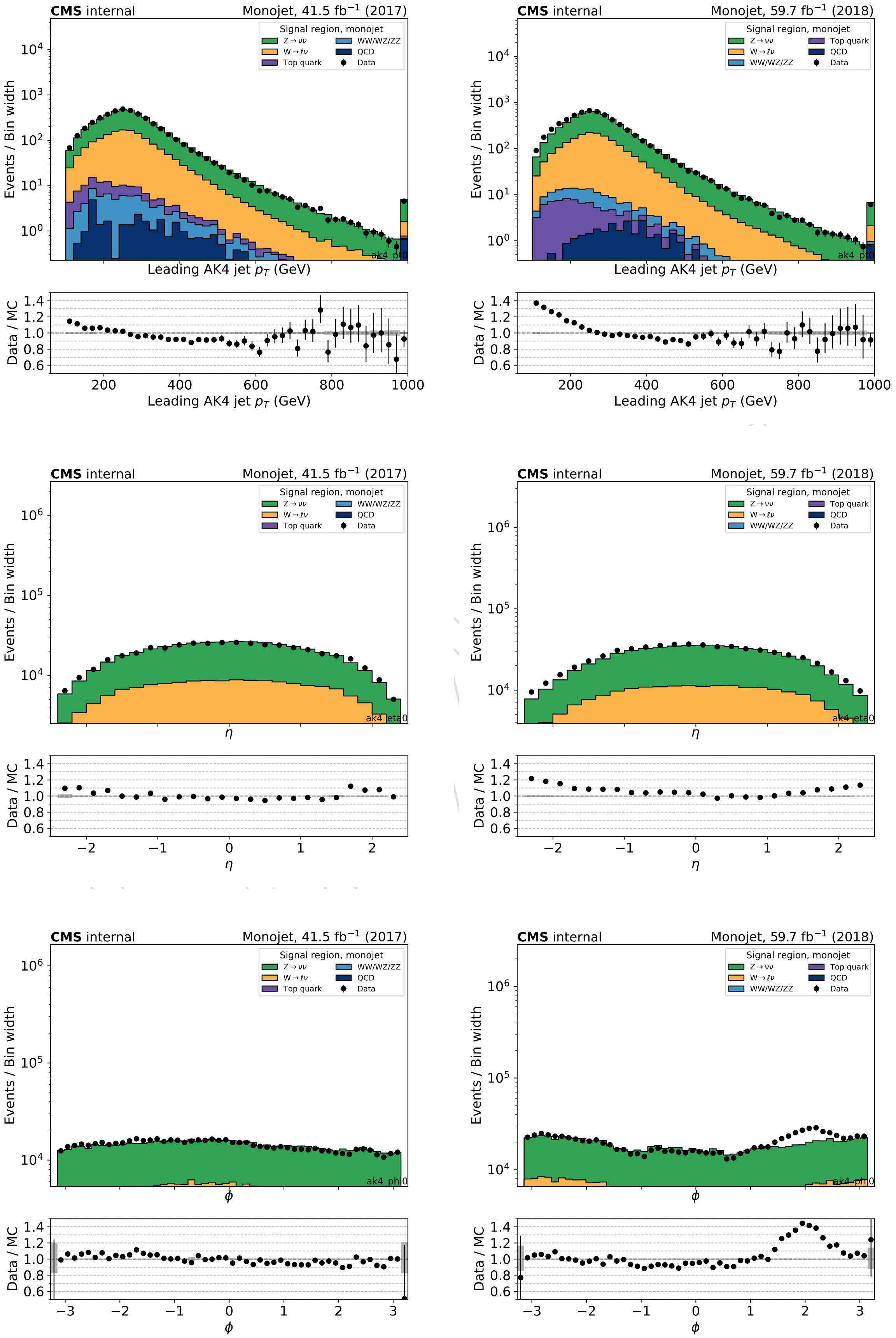

Figure 170: Comparison of data and simulation in the partially unblinded signal regions in 2017 (left) and 2018 (right). The rows show the leading jet p_{T} (top), η (middle) and ϕ distributions (bottom).

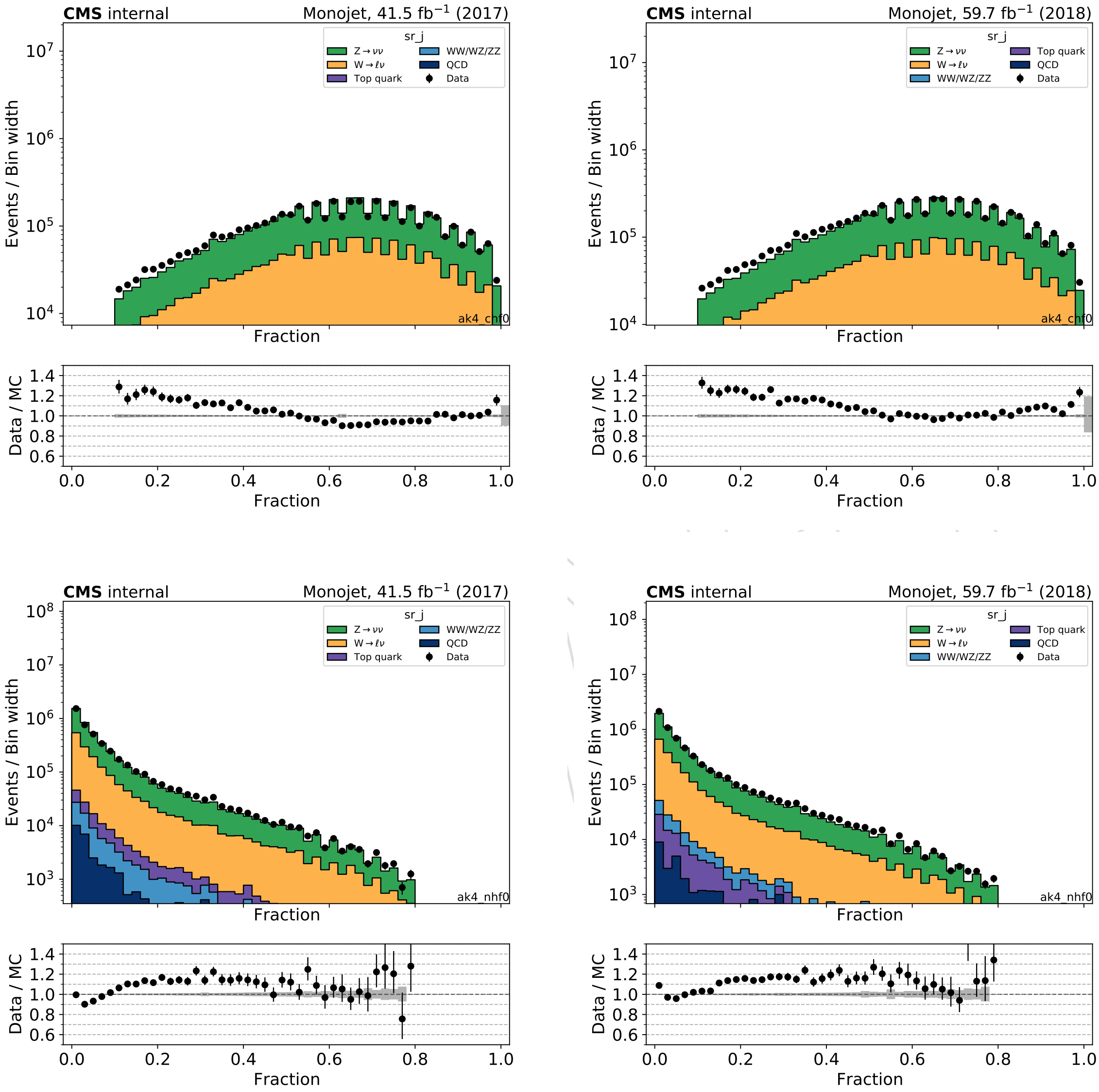

Figure 171: Comparison of data and simulation in the partially unblinded signal regions in 2017 (left) and 2018 (right). The rows show the leading jet charged hadron energy fraction (top) and neutral hadron energy fraction (bottom).

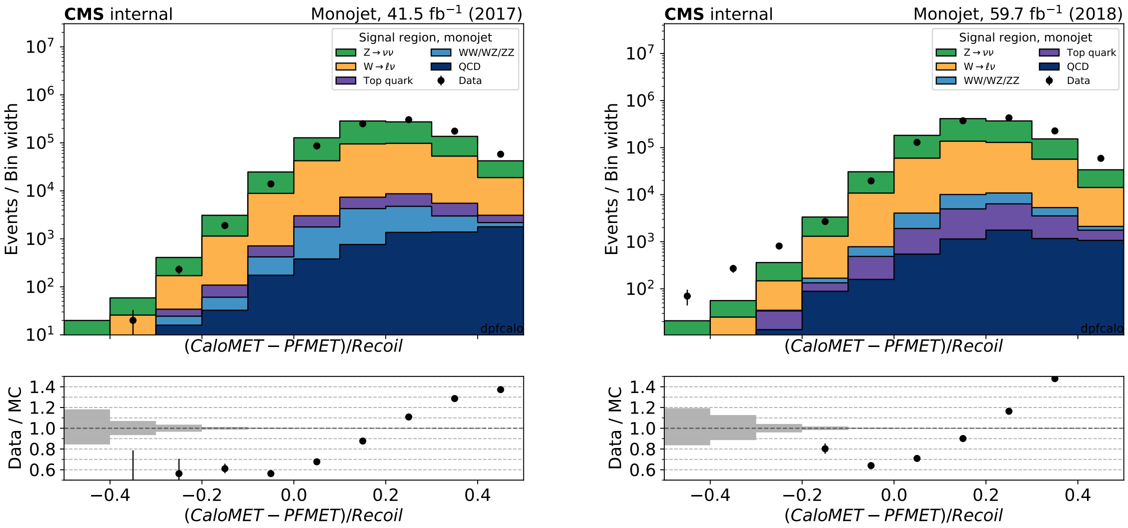

Figure 172: Comparison of data and simulation in the partially unblinded signal regions in 2017 (left) and 2018 (right). The distribution of the relative different of PF and calorimeter-based $p_{\mathrm{T}}^{\mathrm{miss}}$ is shown.

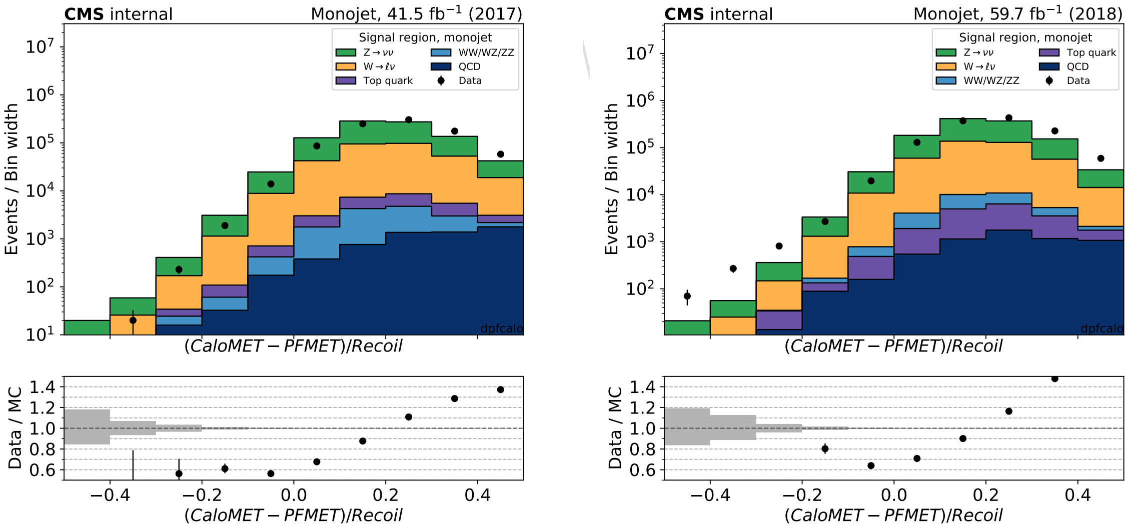

Figure 173: Comparison of data and simulation in the partially unblinded signal regions in 2017 (left) and 2018 (right). The distribution of the relative different of PF and calorimeter-based $p_{\mathrm{T}}^{\mathrm{miss}}$ is shown.

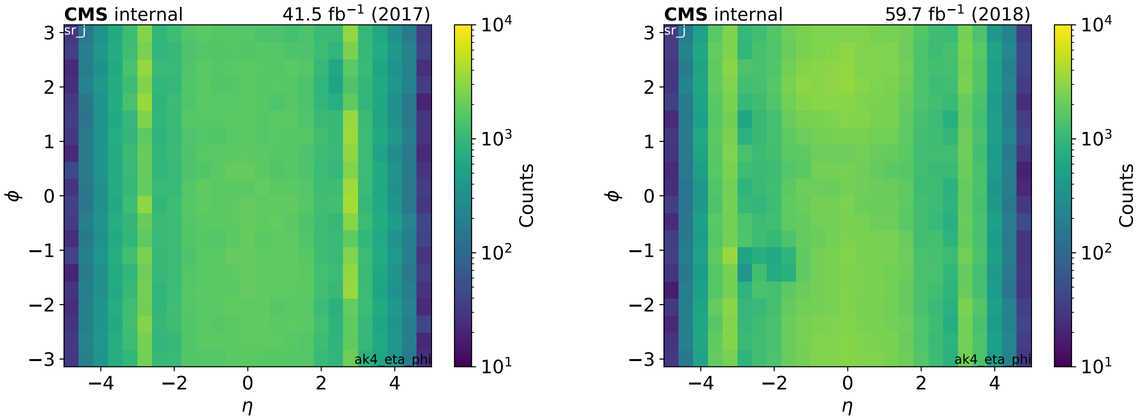

Figure 174: Two-dimensional η-ϕ occupancy of jets with $p_T > 20\,\text{GeV}$ observed in data in 2017 (left) and 2018 (right). Note that there is a deficit of events in the 2018 distribution related to the jet-based HEM veto.

After considering multiple strategies, Strategy C has been selected and is applied in the analysis.

E.6.1 Strategy A: removing the HEM contribution via an event veto

As demonstrated above, $\phi(\vec{p}_T^{\,\text{miss}})$ is a reliable predictor of contamination from HEM-related events. To remove such events, a veto method based on $\phi(\vec{p}_T^{\,\text{miss}})$ is introduced. This veto method makes obsolete the previously employed jet-based veto. Since the analysis design relies on the transfer factors between signal and control regions, the jet-based veto was previously also applied to the control regions, even though there is no direct fake p_T^{miss} contamination. The analysis selection is changed as follows:

- The jet-based event veto is removed for both the signal and control regions.
- In the single-electron region, events are rejected if their leading electron is found to be in the HEM region. This is necessary because the HEM failure results in misreconstruction of hadronic jets as electrons which can pass the analysis selection in this region. This contamination was previously implicitly removed through the jet-based veto (since every electron is also reconstructed as a jet).
- Events in the signal region are rejected if $-1.8 < \phi(\vec{p}_T^{\,\text{miss}}) < -0.6$. This rejection window is slightly enlarged relative to the direct HEM region definition in order to take into account edge effects and to fully remove the contamination.

The resulting distributions of the relevant kinematic variables of the leading and recoil are shown in Figs. 177. Good agreement between the simulation and data is observed. The $\phi(\vec{p}_T^{\,\text{miss}})$-based veto is successful in removing the pathologies previously observed in these quantities. Note that the excess of high-recoil events in 2018 is still present, as the events in this region do not favor the HEM ϕ region (as can already be determined from Tab. 25).

To estimate the effect of the new veto on the sensitivity of the analysis, two comparisons are made:

1. **Low-p_T^{miss} signal (H(inv))**: The full statistical analysis is performed, once using the baseline selection including the jet-based HEM veto, and adapting the selection as decribed above. It is found that the effect on the expected exclusion limit on the invisible branch-

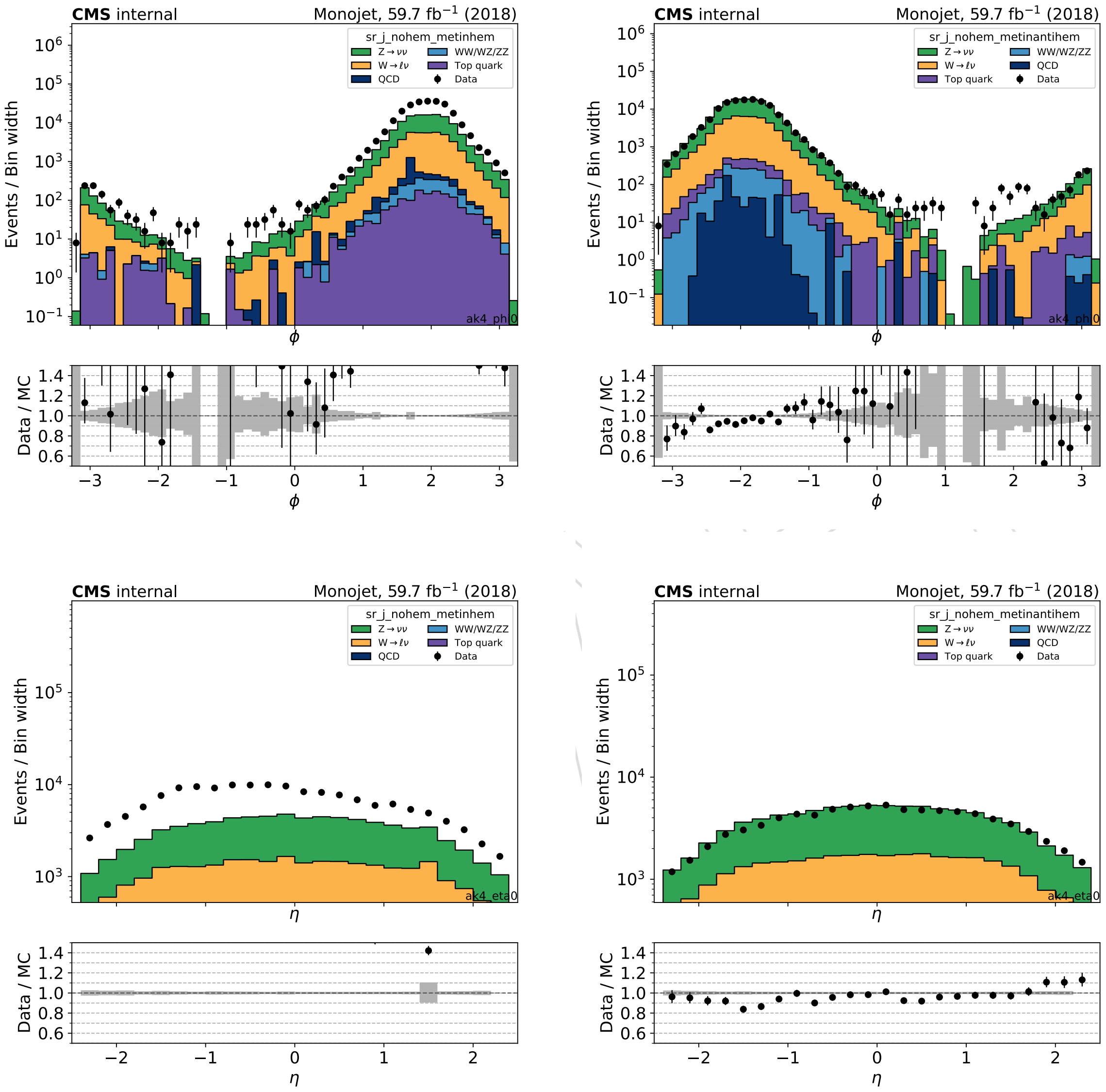

Figure 175: Distributions of the leading jet ϕ (top) and η (bottom) in the HEM enriched (left) and depleted regions (right).

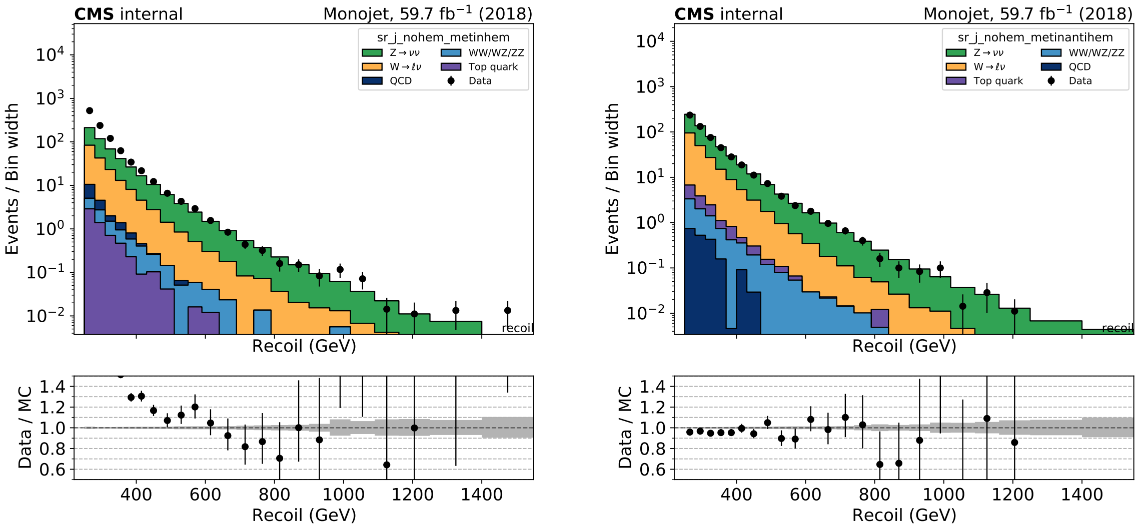

Figure 176: Distribution of the recoil in the HEM enriched (left) and depleted regions (right).

ing fraction of the Higgs boson is stable between the two cases and changes relatively by less than 1%. This is a result of the low-recoil nature of the signal: Its distribution overlaps significantly with that of the backgrounds, and the sensitivity is therefore dominated by systematic uncertainties. The difference between the selection methods contemplated here manifests itself as an effective loss of integrated luminosity in the signal region, to which the systematically limited signals are not sensitive.

2. **High-p_T^{miss} signal (DMsimp)** To estimate the effect of on high-p_T^{miss} signals, which are not yet included in this analysis note, the data cards from the 2016 analysis are used, which include signal templates for high-mass mediators. The templates of all processes in the data cards are scaled to the 2018 luminosity and the resulting signal strength limit is used as a reference value. To model the effect of the $\phi(\vec{p}_T^{miss})$-based veto, the same procedure is performed, except that the templates are scaled only to 80% of the luminosity of the 2018 data set (modelling a veto of $1.2\,2\pi \approx 20\%$ of the overall phase space). Relative to the case of the full 2018 luminosity, this results in a loss of signal strength sensitivity of 9% for a case of $m_{\text{med}} = 1.5\,\text{TeV}$ and 13% for $m_{\text{med}} = 3\,\text{TeV}$. These sensitivity losses can be seen as a worst case scenario: The estimate does not take into account that there is almost no loss of data in the control regions, and is formulated relative to the case where no sensitivity whatsoever is lost as a result of HEM.

E.6.2 Strategy B: integrating the HEM contribution into the fit

In the signal region, we mainly require a boosted jet and large p_T^{miss}. The HEM effect gives no HCAL reading in the region $-3.0 < |\eta| < -1.3$, $-1.57 < \phi < -0.87$, which leads to fake p_T^{miss} when jets fall into this region. In the signal region, the main contribution caused by HEM issue is therefore from QCD process, when high energy jets fall in the HEM region. As shown in figure 178, the HEM issue happens in 2018 era C and D data, resulting in the excess around [-1.57,-0.87] in the $\phi(p_T^{miss})$ distribution. The JetHT data in era C and D are used to estimate the QCD contribution caused by the HEM issue.

To emulate the jets in HEM region, an anti-HEM region is defined as: $-3.0 < |\eta| < -1.3$, $1.57 > \phi > -0.87$. This region is symmetric to HEM region geometrically, therefore having the

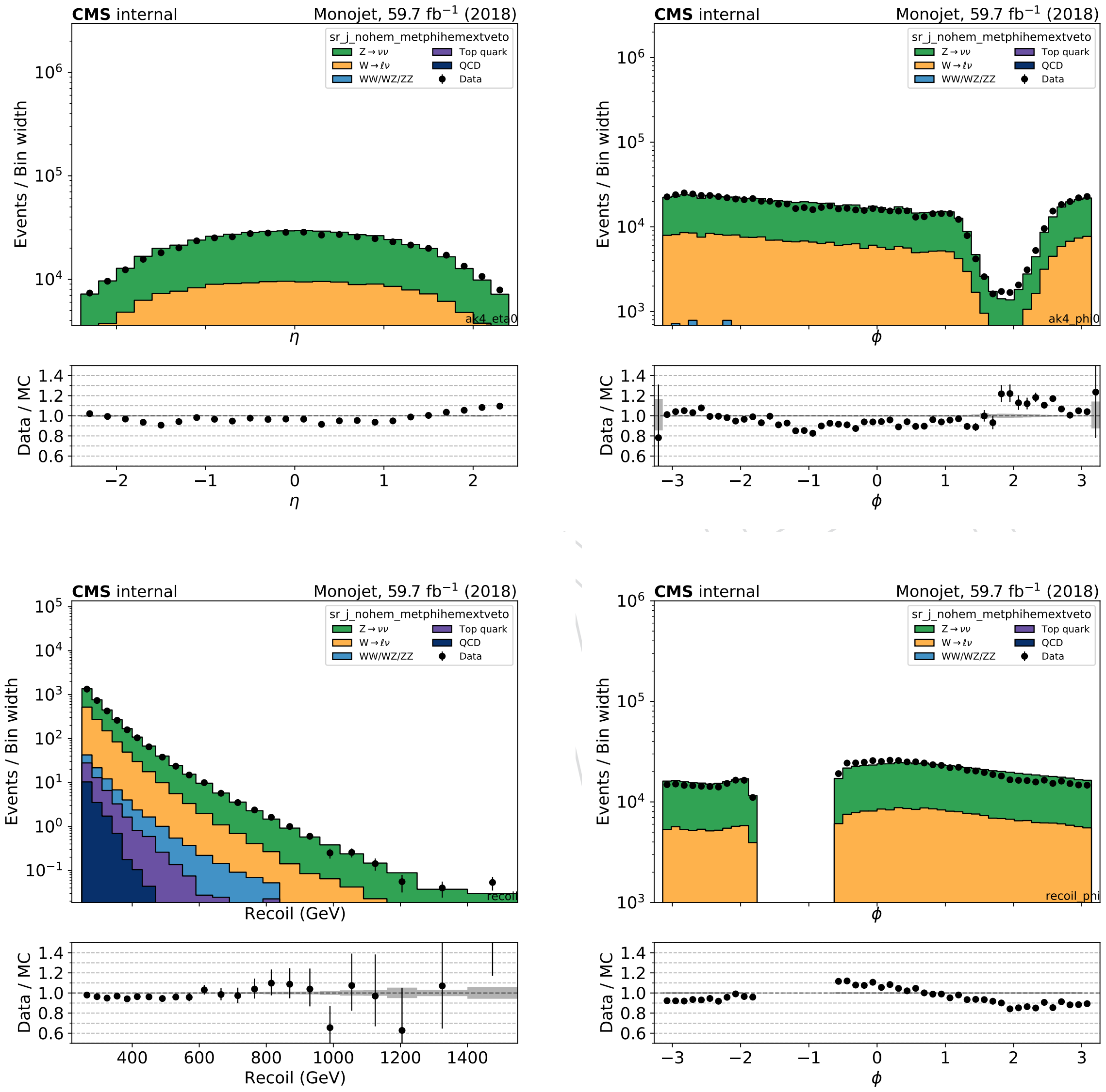

Figure 177: Distribution of the η and ϕ of the leading jet (top) and the recoil and recoil ϕ (bottom) after removing events with $-1.8 < \phi(\vec{p}_{\mathrm{T}}^{\mathrm{miss}}) < -0.6$.

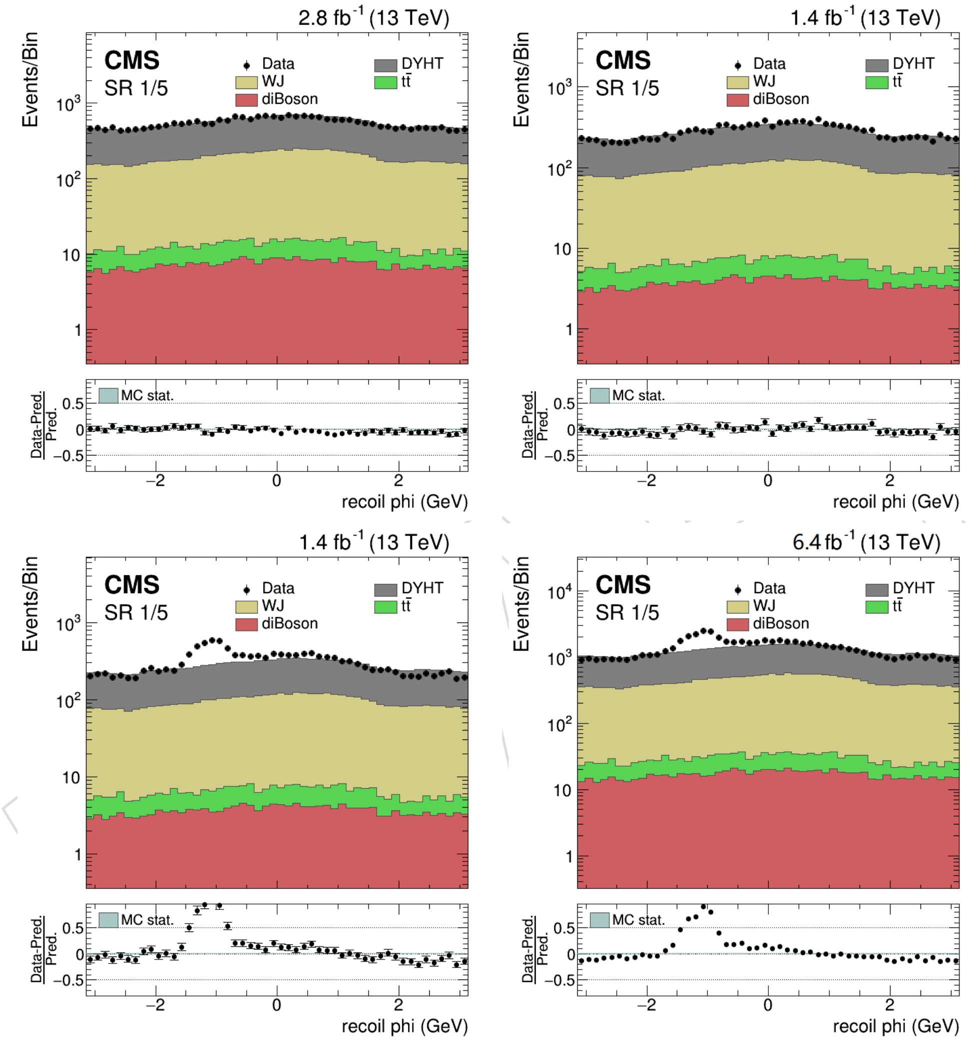

Figure 178: The recoil ϕ distribution of 1/5 unblinded 2018 data in era A (top left), B (top right), C(bottom left), and D(bottom right).

similar jets contribution from QCD process. The fake $p_{\mathrm{T}}^{\mathrm{miss}}$ in HEM region is estimated by jets in anti-HEM region assuming that their hadronic energy is missing and mistreated as $p_{\mathrm{T}}^{\mathrm{miss}}$.

Most of the reconstructed jets in HEM region have neutral hadron fraction with value of 0, while the charged hadronic fraction is mostly non-zero. It indicates that charged hadron bends in the magnetic field and may fall outside the HEM region in HCAL, therefore leaving some energy and reconstructed as AK4 Jets. For all the jets in the anti-HEM region, all of the neutral hadron fraction (NHF) and a fraction of the charged hadronic fraction (CHF) are considered missing. The magnitude of the vector sum of the jet p_{T} in the anti-HEM region is labelled as "*hempt*", as the charged and neutral hadronic part are labelled as "*hemchf*" and "*hemnhf*" respectively. The pileup also contributes to the fake $p_{\mathrm{T}}^{\mathrm{miss}}$ in HEM region. The contribution is about 8 GeV, which is estimated by average $\rho_{neutral} \times A_{HEM}$, where $\rho_{neutral}$ is the neutral hadronic density from the pileup, and A_{HEM} is the area of the HEM region. Therefore the fake $p_{\mathrm{T}}^{\mathrm{miss}}$ from the HEM region is: ${p_{\mathrm{T}}^{\mathrm{miss}}}_{HEM} = hemnhf + frac \times hemchf + 8\ GeV$, $\phi({p_{\mathrm{T}}^{\mathrm{miss}}}_{HEM}) = -\phi(hempt)$ (reverse the phi since we are using anti-HEM for the derivation). The final fake $p_{\mathrm{T}}^{\mathrm{miss}}$ is the vector sum of the ${p_{\mathrm{T}}^{\mathrm{miss}}}_{HEM}$ and the particle-flow $p_{\mathrm{T}}^{\mathrm{miss}}$: $\overrightarrow{p_{\mathrm{T}}^{\mathrm{miss}}}_{fake} = \overrightarrow{p_{\mathrm{T}}^{\mathrm{miss}}}_{HEM} + \overrightarrow{p_{\mathrm{T}}^{\mathrm{miss}}}_{PF}$.

The data driven JetHT events are selected from era C and D 2018 data using triggers with different thresholds on H_{T}. The low H_{T} trigger has larger prescale value, several H_{T} triggers are used in order to increase the statistics at high H_{T} phase space. The prescales are calculated from trigger's luminosity. As shown in figure 179, the prescales are validated by comparing the *hempt* distribution using different triggers scaled by the their values of prescales. The triggers, prescales and their corresponding *hempt* range is listed in table 26.

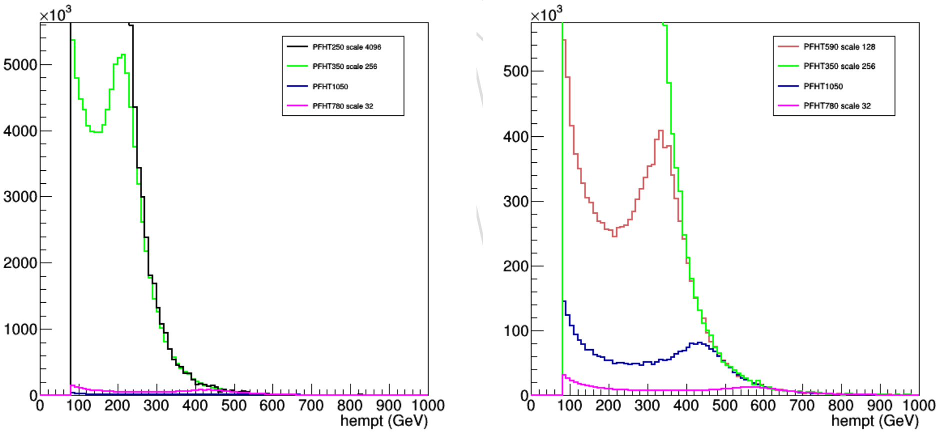

Figure 179: The distribution of *hempt* using different triggers scaled by their prescale values.

Table 26: The list of jet triggers, and their overall prescales as well as their corresponding *hempt* ranges.

Trigger	prescale	hempt
PFHT250	4096	$<$ 230 GeV
PFHT350	256	[230,400] GeV
PFHT590	128	[400,500] GeV
PFHT780	32	[500,620] GeV
PFHT1050	1	$>$ 620 GeV

The non-$p_{\mathrm{T}}^{\mathrm{miss}}$ related selections are the same as the signal region. The selected events are required to have no loose muons or electrons with $p_{\mathrm{T}} > 10$ GeV, or hadronically decay τ leptons with $p_{\mathrm{T}} > 18$ GeV. Events are also rejected if they contain a loose, isolated photon with $p_{\mathrm{T}} > 15$ GeV and $|\eta| < 2.5$ or a medium DeepCSV b-tagged jets. The $pfmet$ is required to be less than 100 GeV to suppress the overlapped events in the signal region. The final fake $p_{\mathrm{T}}^{\mathrm{miss}}{}_{fake}$ is required to be larger than 250 GeV. For the hemveto selection, the non-missing energy of the jet should be less than 30 GeV: $hempt - hemnhf - frac \times hemchf < 30$ GeV.

The prescale of trigger "PFHT250" is large, and it gives a quite limited statistics after requiring $hempt - hemnhf - frac \times hemchf < 30$ GeV in the signal region. To increase the statistics for this trigger, the similar selection is conducted by treating the remaining energy of the jet as half as a few parameters change as follow:

- the remaining energy: $(hempt - hemnhf - frac \times hemchf) \rightarrow (hempt - hemnhf - frac \times hemchf)/2$
- the $p_{\mathrm{T}}^{\mathrm{miss}}{}_{HEM}$ is $hempt$ subtracted by the remaining energy: $(hemnhf + frac \times hemchf) \rightarrow [(hemnhf + frac \times hemchf)/2 + hempt/2]$.

For events that have $hempt < 230GeV$ and pass the PFHT250 trigger, they are selected with $(hempt - hemnhf - frac \times hemchf)/2 < 30$ GeV and $p_{\mathrm{T}}^{\mathrm{miss}}{}_{HEM}$ is calculated using $(hemnhf + frac \times hemchf)/2 + hempt/2 + 8GeV$ accordingly to maintain the consistency in $p_{\mathrm{T}}^{\mathrm{miss}}{}_{HEM}$ shape. Then they are scaled down to match the actual yield for this trigger.

In the CR where the selection is the same, except requiring recoil (pfmet) between [200,250] GeV. The method is tested in order to find a fraction value that could account for the discrepancy in the HEM region. In figure 180, the data and MC could reach good agreement when fraction value equals to 0.8. Then the method is tested in signal region, where the fraction=0.83 gives the good agreement to account for the discrepancy in the HEM region, see figure 181. The fraction value technically differs with different p_{T} value of the charged hadron. A conservative systemic uncertainty is signed to this HEM contribution to cover this effect. The input template of HEM contribution is selected as fraction=0.83 ± 0.03 with some low statistic bins smoothed, as their contributions in SR are shown in figure 182.

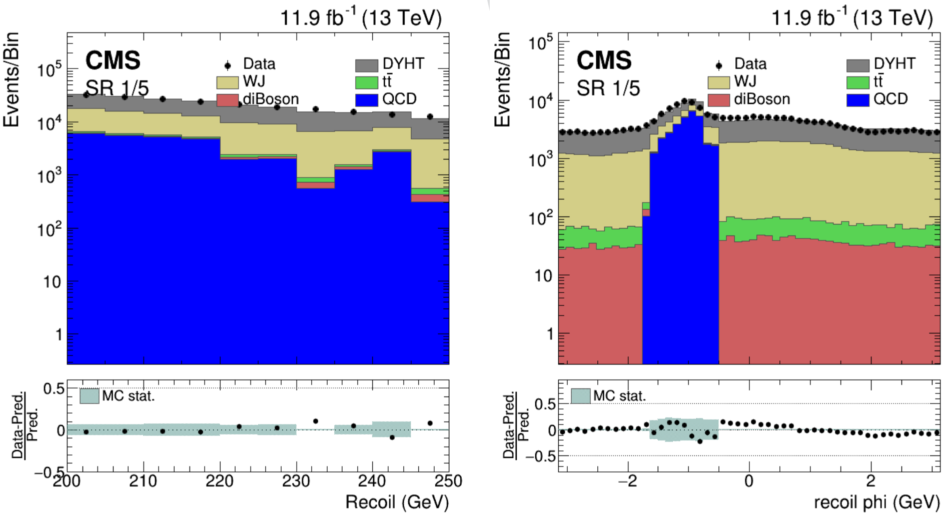

Figure 180: The recoil and recoil ϕ distribution of 1/5 unblinded in the control region of $200 < recoil < 250$GeV with the 'fraction' value of 0.80.

The sensitivity is tested with 1/5 of the unblinded 2018 data, and then scaled to full year luminosity to see how it affects our result. There are three scenarios put into comparison: the normal

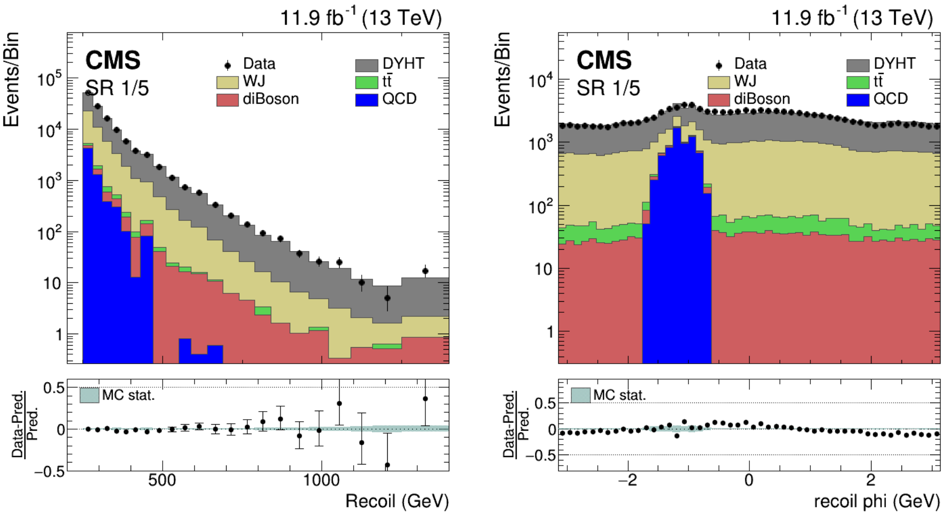

Figure 181: The recoil and recoil ϕ distribution of 1/5 unblinded in the signal region with the 'fraction' value of 0.83.

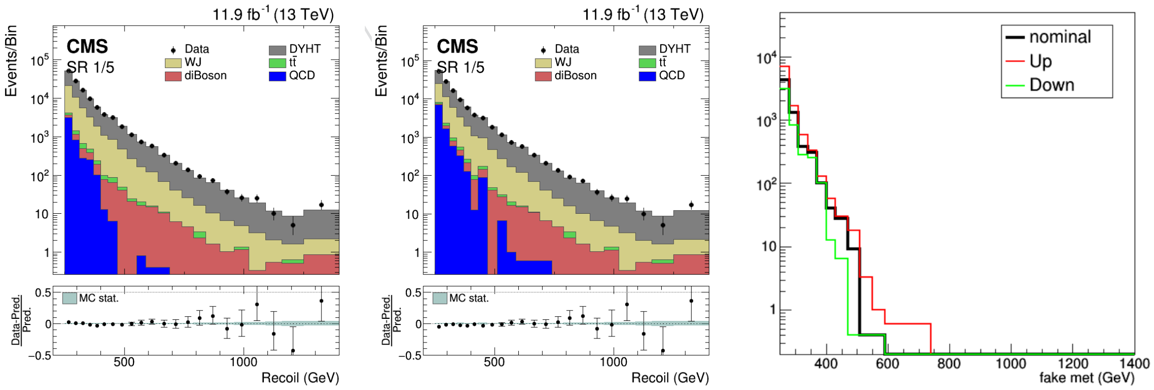

Figure 182: The recoil distribution of 1/5 unblinded in signal region, with the value of fraction 0.80(left), 0.86(middle). The corresponding input template of recoil distribution from HEM QCD contribution with low statistic bins smoothed, including nominal, up, and down distribution (right).

signal region selection including jet-based hemveto selection, labelled as “original”; the same selection but including the contribution from HEM QCD contribution, labelled as “hemqcd”; same selection as “orignal” but with additional selection $\phi(p_{\mathrm{T}}^{\mathrm{miss}}) \notin [-1.57, -0.87]$ in the signal region, labelled as “$\phi(p_{\mathrm{T}}^{\mathrm{miss}})$ veto”. Just for testing purpose, “$\phi(p_{\mathrm{T}}^{\mathrm{miss}})$ veto” method still includes hemveto selection, which is different from the previous sections. The postfit and the pulls of the main nuisance parameters are presented in figure 183, the hemqcd input template is reasonable as it receives additional constrains on the ‘fraction’ nuisance parameter. The limits are summarized in table 27. For the low $p_{\mathrm{T}}^{\mathrm{miss}}$ signal sample (H(inv)), the “hemqcd” method gives no obvious improvements in comparison to “$\phi(p_{\mathrm{T}}^{\mathrm{miss}})$ veto” method. For the high MET signal sample (DMsimp), the “hemqcd” method has more than 5% improvements in the sensitivity in comparison to “$\phi(p_{\mathrm{T}}^{\mathrm{miss}})$ veto” method.

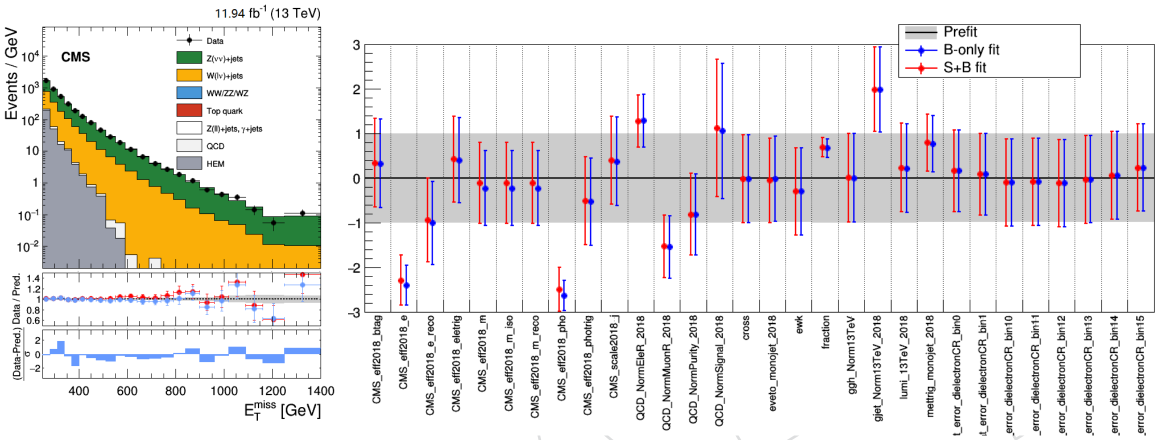

Figure 183: The comparison between 1/5 unblinded 2018 data and MC prediction before and after the fit using ‘hemqcd’ method (left) and the pulls of the main nuisance parameters (right).

Table 27: The postfit limits of three scenarios: “original”, “hemqcd”, “$\phi(p_{\mathrm{T}}^{\mathrm{miss}})$ veto”, and “dynamic” with 1/5 of the unblinded 2018 data and scaled to full year’s luminosity. For comparison, the limits are scaled relative to the “orginal” medium limit.

Data	1/5 unblinded				Scaled to full year			
signal	Higgs invisible							
Limits	original	hemqcd	$\phi(p_{\mathrm{T}}^{\mathrm{miss}})$ veto	dynamic	original	hemqcd	$\phi(p_{\mathrm{T}}^{\mathrm{miss}})$ veto	dynamic
-2	61.7%	61.2%	61.8%	61.6%	61.7%	61.3%	62.0%	61.7%
-1	76.7%	76.5%	77.1%	76.7%	76.7%	76.4%	77.0%	77.0%
0	100%	100.4%	100.8%	100.4%	100%	100%	100.5%	100%
+1	133%	134%	133%	133%	132%	133%	133%	133%
+2	173%	173%	172%	172%	171%	172%	172%	171%
signal	Dark Matter Sample							
Limits	original	hemqcd	$\phi(p_{\mathrm{T}}^{\mathrm{miss}})$ veto	dynamic	original	hemqcd	$\phi(p_{\mathrm{T}}^{\mathrm{miss}})$ veto	dynamic
-2	55.4%	55.8%	57.9%	55.8%	54.4%	55.6%	56.9%	55.0%
-1	72.9%	73.3%	76.1%	72.9%	72.3%	73.3%	75.2%	72.8%
0	100%	100.7%	104.4	100.7%	100%	100.9%	103.9%	100.6%
+1	139%	140%	145%	140%	139%	140%	145%	140%
+2	186%	188%	195%	187%	186%	188%	193%	188%

E.6.3 Strategy C: Dynamic veto based on information learned from strategy B

The “hemqcd” method has shown that the contribution of $p_{\mathrm{T}}^{\mathrm{miss}}{}_{fake}$ is mostly in low $p_{\mathrm{T}}^{\mathrm{miss}}$ region. Based on the $p_{\mathrm{T}}^{\mathrm{miss}}$ and $\phi(p_{\mathrm{T}}^{\mathrm{miss}})$ distribution in figure 181, the HEM QCD contribution is negligible when $p_{\mathrm{T}}^{\mathrm{miss}} > 470$ GeV or $\phi(p_{\mathrm{T}}^{\mathrm{miss}}) \notin [-1.62, -0.62]$. A dynamic selection is applied as the forth scenario: the events in the signal region are required to satisfy $\phi(p_{\mathrm{T}}^{\mathrm{miss}}) \notin [-1.62, -0.62]$ when $p_{\mathrm{T}}^{\mathrm{miss}} < 470$ GeV in addition to the original selections. The dynamic selection could ensure the contribution from HEM QCD is negligible ($\ll 1\%$) in any of the recoil bin. This could avoid both extra uncertainty in the low $p_{\mathrm{T}}^{\mathrm{miss}}$ region and loosing events at high $p_{\mathrm{T}}^{\mathrm{miss}}$ region. The figure 184 shows the $p_{\mathrm{T}}^{\mathrm{miss}}$ and $\phi(p_{\mathrm{T}}^{\mathrm{miss}})$ distribution in the signal region based on 1/5 of the unblinded data. This method is labelled as “dynamic”, and its limits are listed in table 27. The “dynamic” method has the similar performance as the “hemqcd” method, and it is sufficient to sustain the sensitivity after loosing events due to the HEM issue.

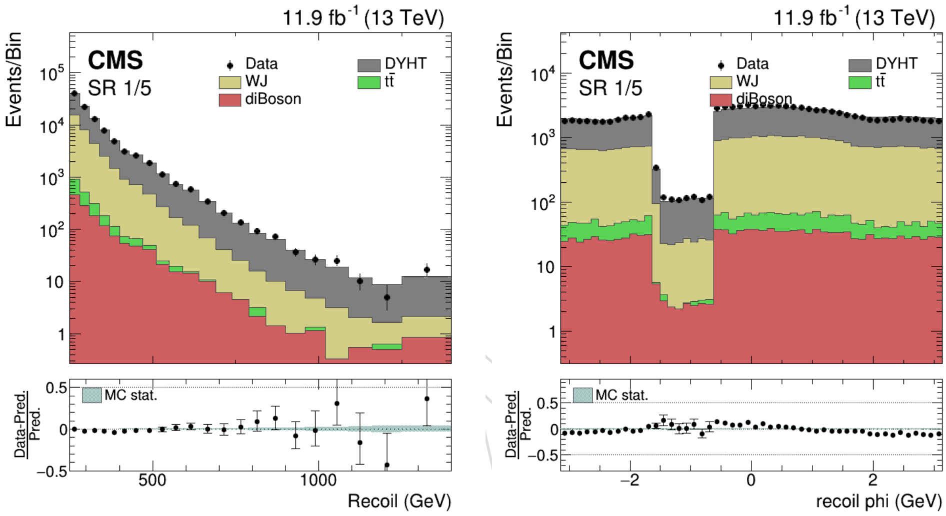

Figure 184: The comparison of the $p_{\mathrm{T}}^{\mathrm{miss}}$(left) and $\phi(p_{\mathrm{T}}^{\mathrm{miss}})$(right) distribution between 1/5 unblinded 2018 data and MC prediction using the ‘dynamic’ method.

F Fit details

F.1 CR-only fit

This section relates to the combination of the monojet and mono-V categories in the 2017 and 2018 datasets. Results shown here represent a fit in which the signal regions are not taken into account (CR-only fit).

F.1.1 Goodness-of-fit

The goodness of fit (GoF) is evaluated via a p value calculation. The underlying test statistic is a likelihood ratio, in which the likelihood is normalized to the saturated likelihood [83]. The expected distribution of the test statistic is found by generating toy experiments based on the Asimov likelihood model that serves as input to the fit. For each iteration, a toy dataset is generated by randomizing nuisance parameters as well as per-bin yields, and the test statistic is calculated based on the generated dataset. The p-value is then defined as the fraction of toy experiments giving equal or larger values of the test statistic than the one observed when fitting the actual data.

The result of the procedure is shown in Fig. 185 for the CR-only fit of the 2017+2018 monojet+mono-V combination.

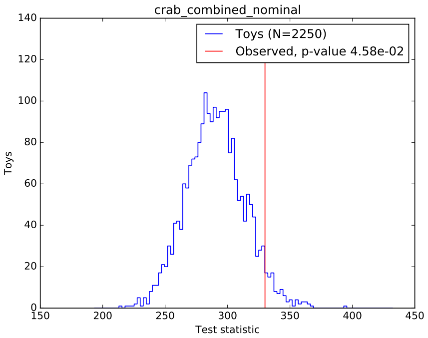

Figure 185: Evaluation of the p value based on the distribution of the likelihood ratio test statistic. The blue histogram shows the distribution of the saturated likelihood-ratio test statistic in toy experiments, and the red solid line indicates the value observed in data. The p value is defined as the fraction of toy experiments with test statistics equal to or larger then the one observed in data. The results shown here correspond to the combined CR-only fit of monojet and mono-V categories in 2017 and 2018.

F.1.2 Postfit plots

The comparisons of the prefit and postfit predictions are shown in Figs. 186 to 194.

F.1.3 Nuisance Pulls

The nuisance pulls for this fit are shown in Figs. 195–206.

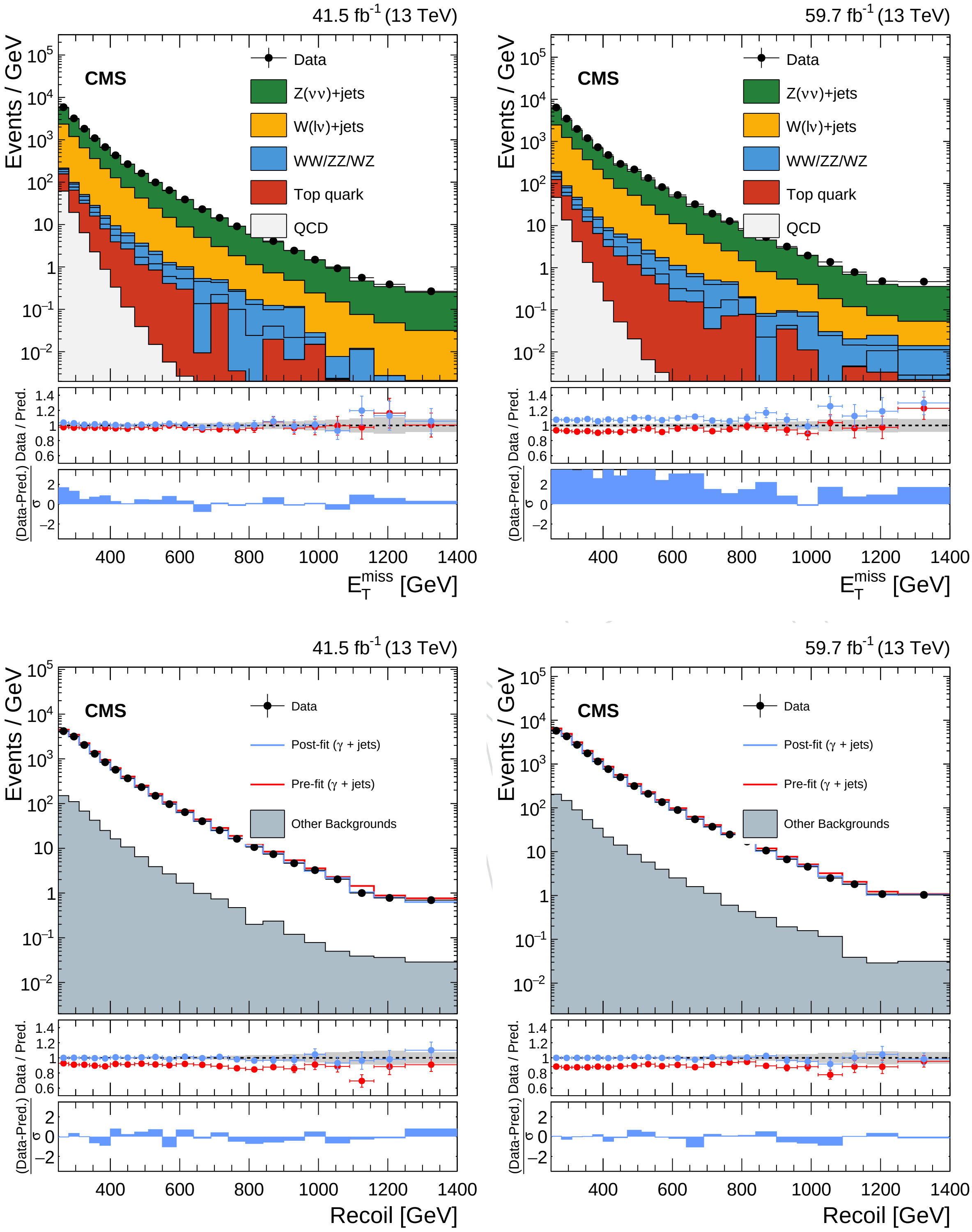

Figure 186: Comparison between data and MC simulation in the signal region (top) and $\gamma+$jets control sample (bottom) before and after the simultaneous fit. The fit includes all control samples in all categories and both years. The signal region is not included in the fit. The resulting distributions are shown separately for 2017 (left) and 2018 (right). The hadronic recoil p_{T} in $\gamma+$jets events is used as a proxy for $p_{\mathrm{T}}^{\mathrm{miss}}$ in the signal region. The last bin includes overflow. In the lower panels, ratios of data with the pre-fit background prediction (red open points) and post-fit background prediction (blue full points) are shown. The gray band in the lower panel indicates the post-fit uncertainty after combining all the systematic uncertainties. Finally, the distribution of the pulls, defined as the difference between data and the post-fit background prediction relative to the quadrature sum of the post-fit uncertainty in the prediction and statistical uncertainty in data, is shown in the lowest panel.

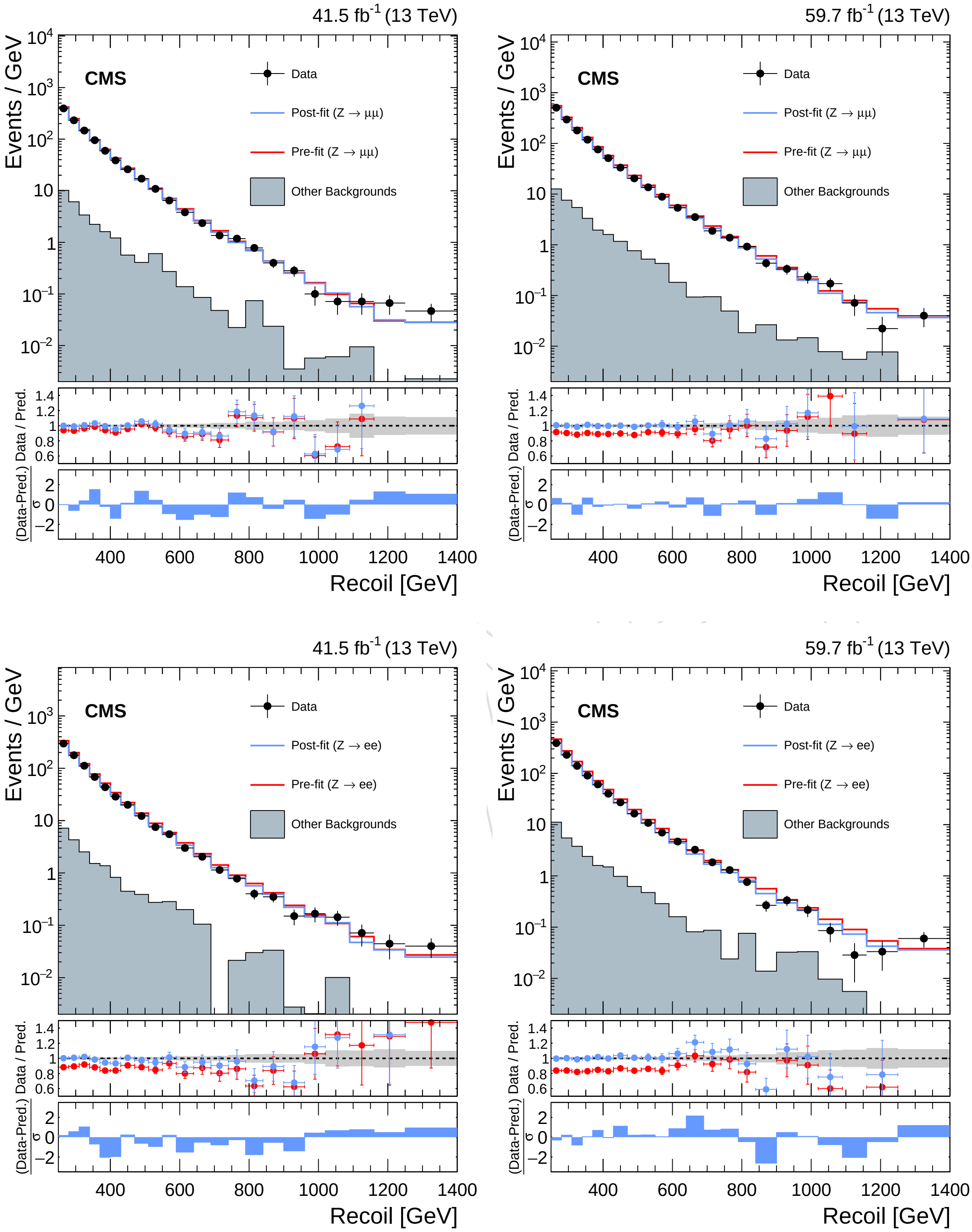

Figure 187: Same as Fig. 186 but for the dilepton CRs. The other backgrounds include top quark, diboson, and W + jets processes.

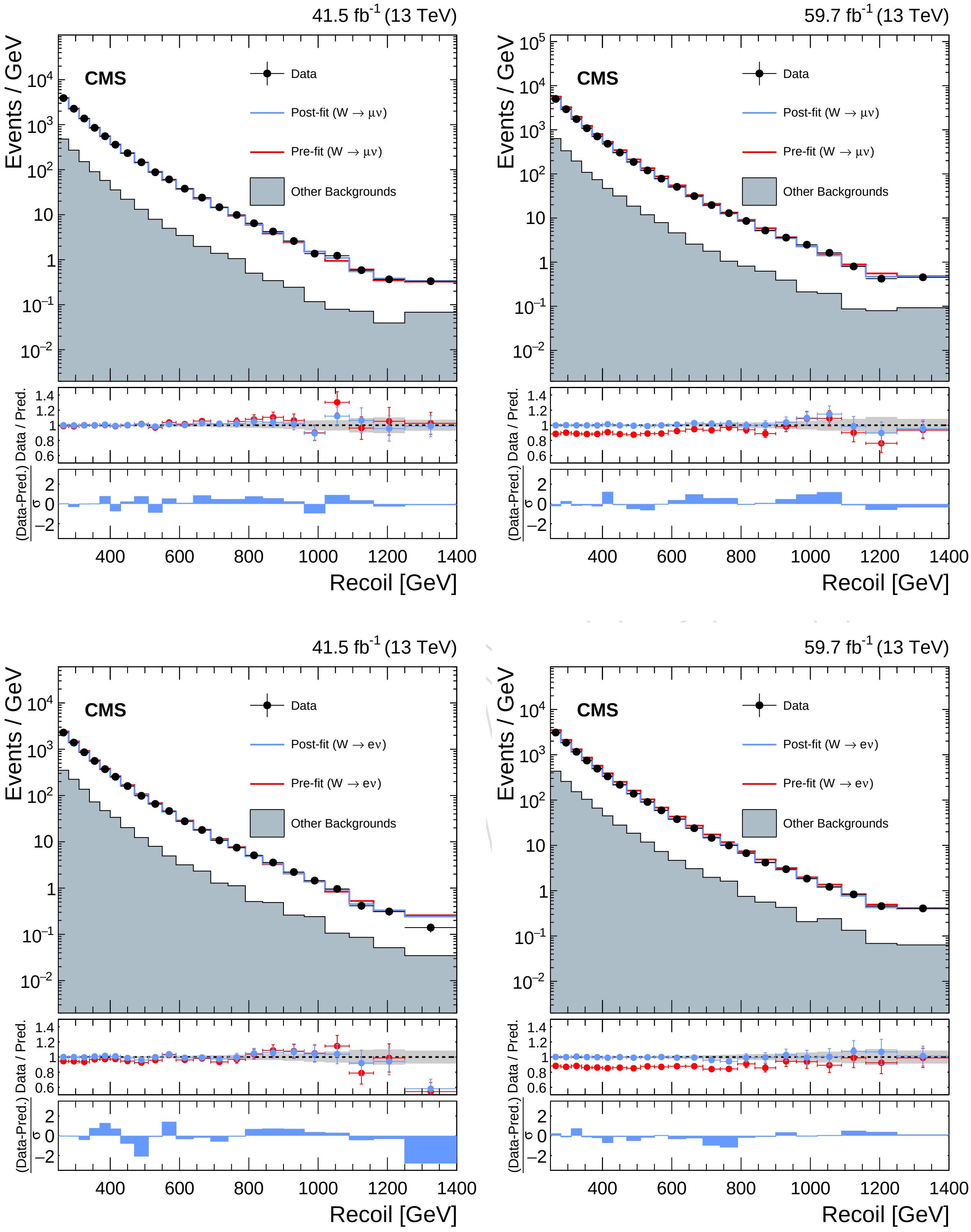

Figure 188: Same as Fig. 186 but for the single-lepton CRs. The other backgrounds include top quark, diboson, and QCD multijet processes. The description of the lower panels is the same as in Fig. 186.

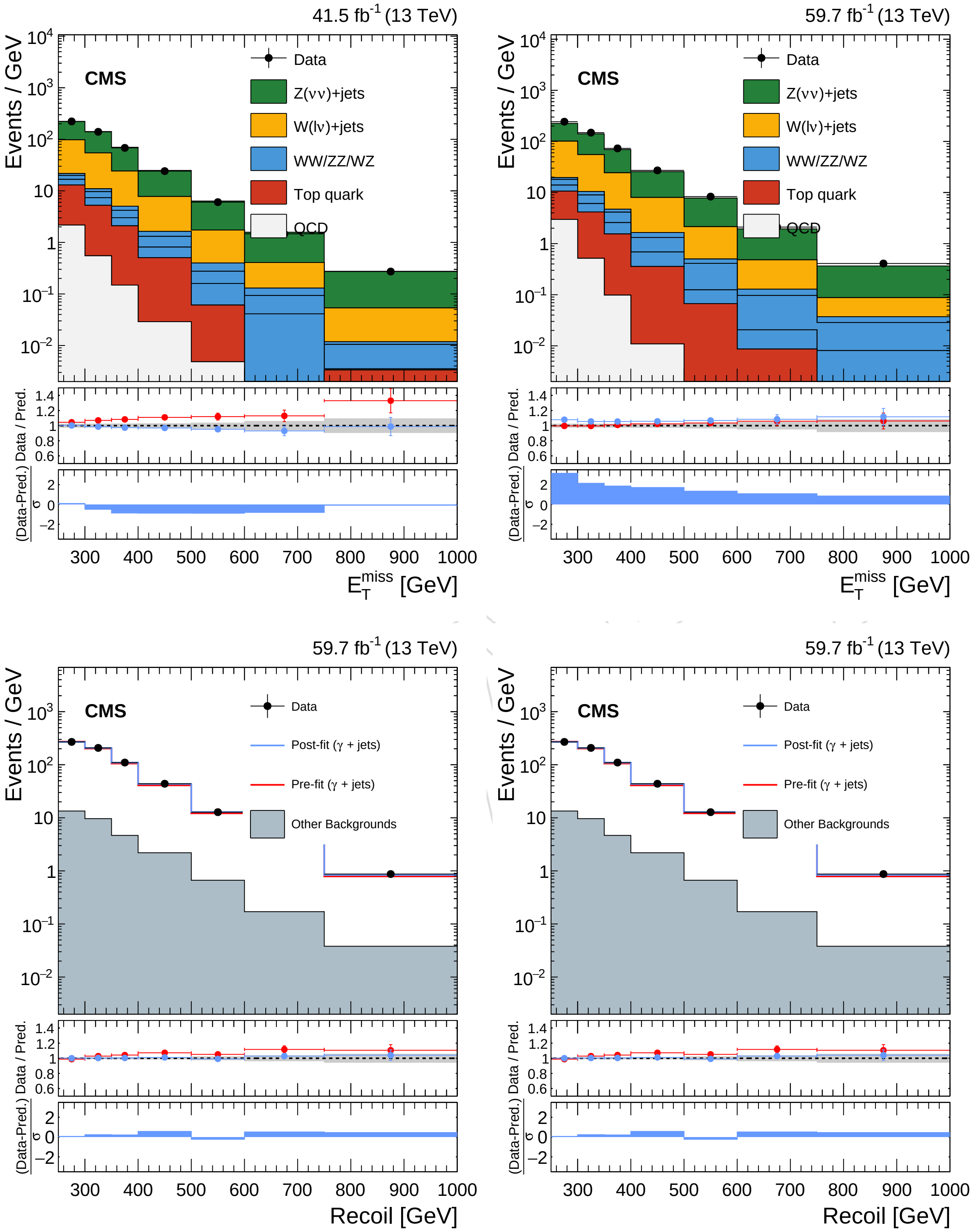

Figure 189: Same as Fig. 186, but for the low-purity mono-V category.

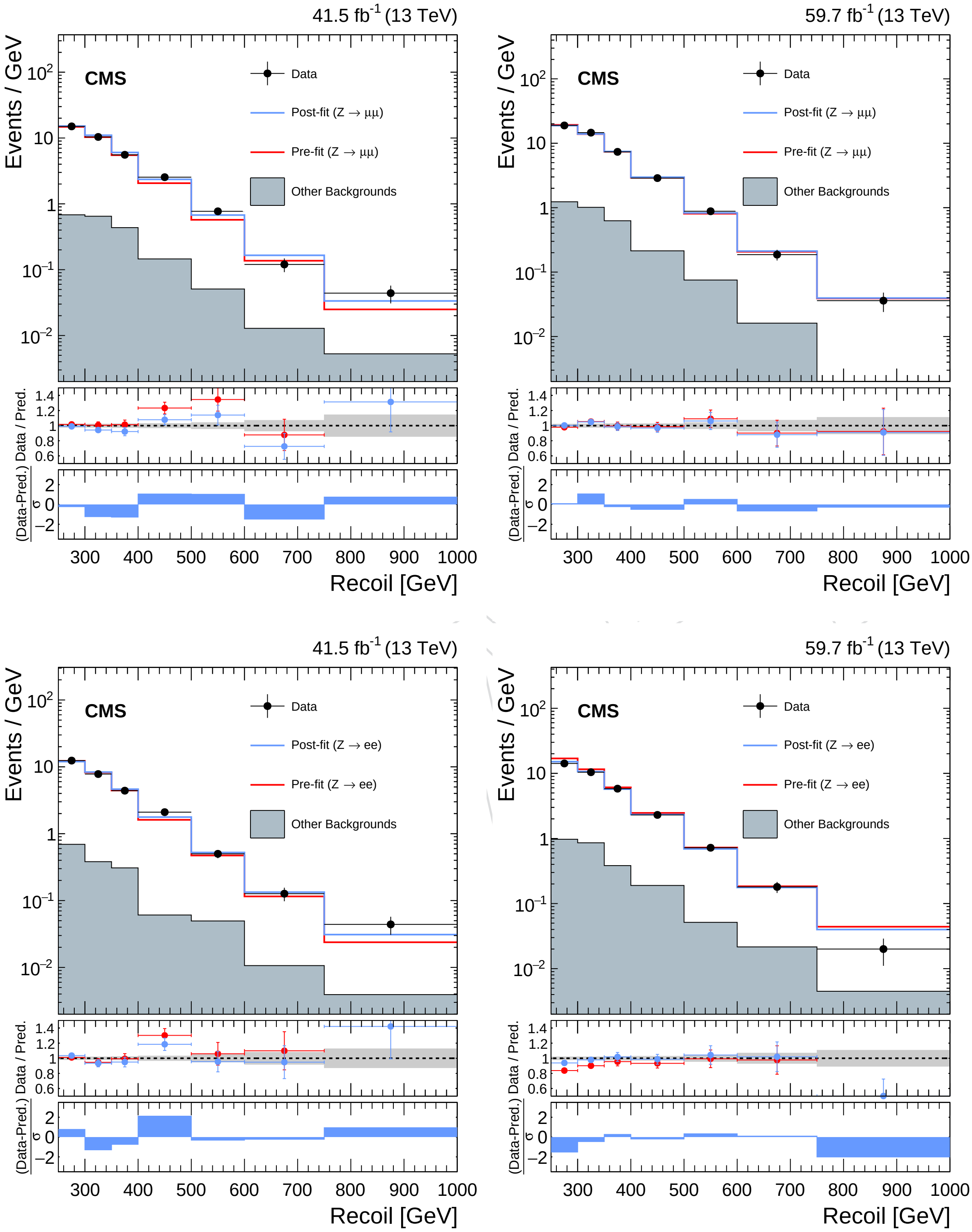

Figure 190: Same as Fig. 187, but for the low-purity mono-V category.

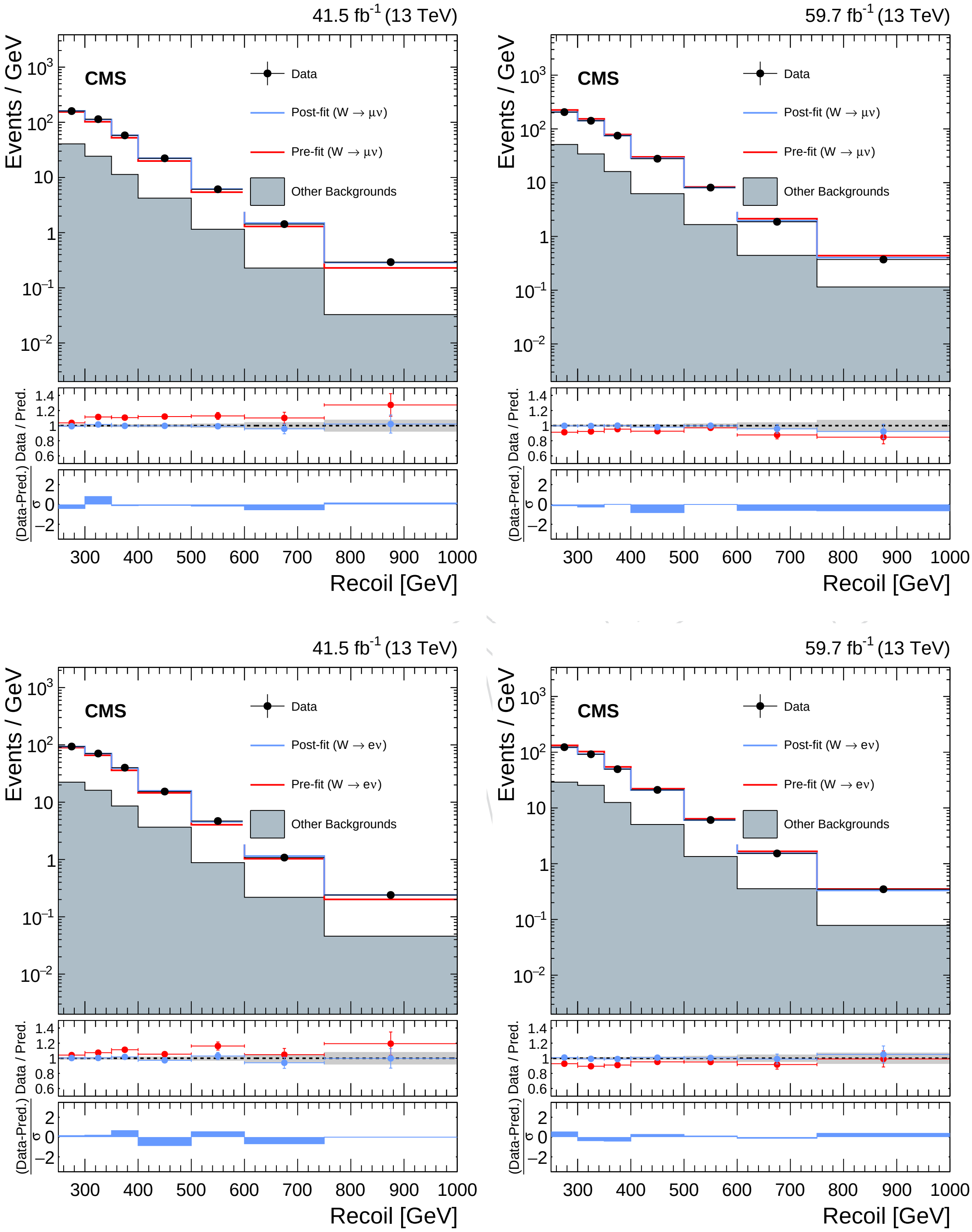

Figure 191: Same as Fig. 188, but for the low-purity mono-V category.

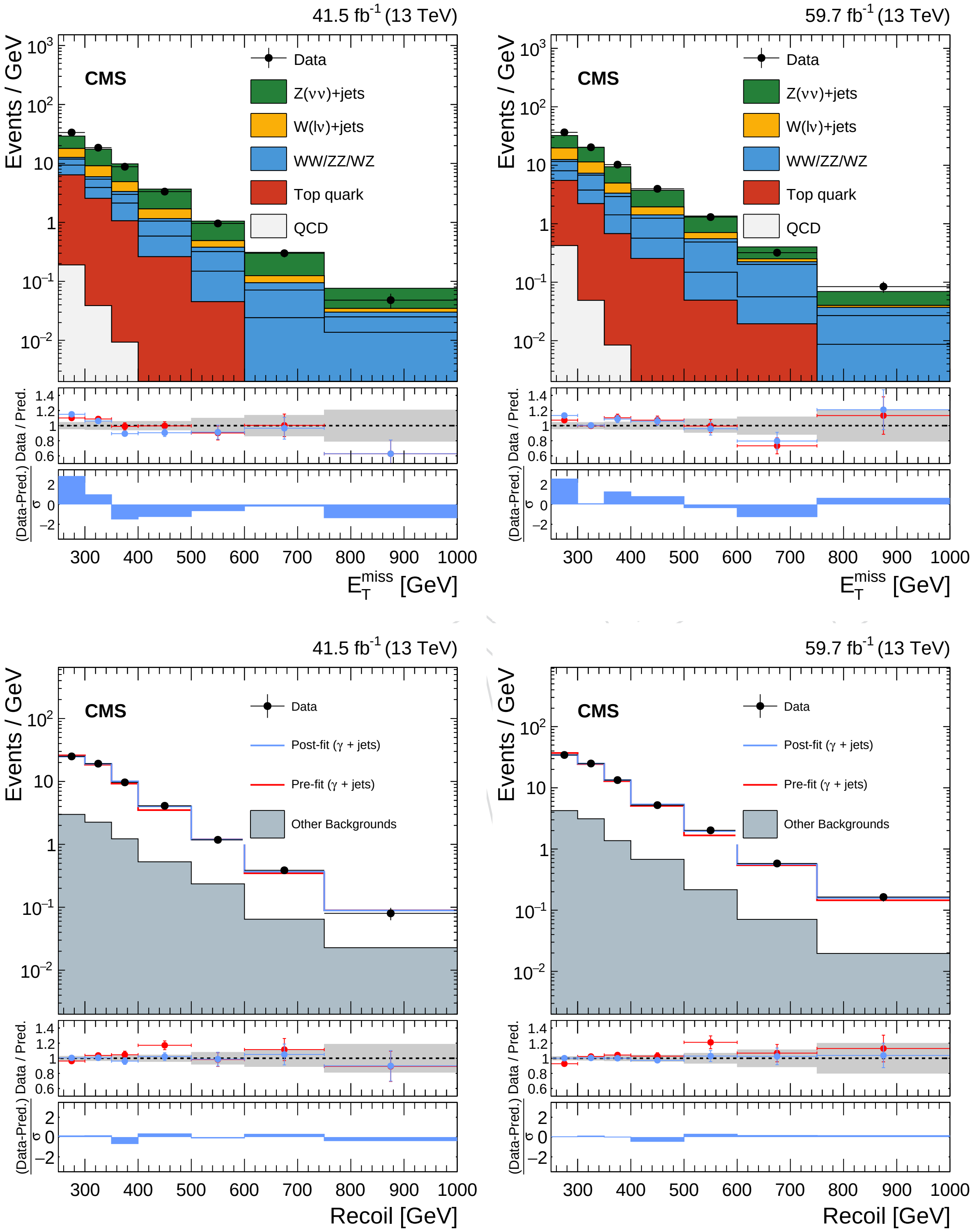

Figure 192: Same as Fig. 186, but for the high-purity mono-V category.

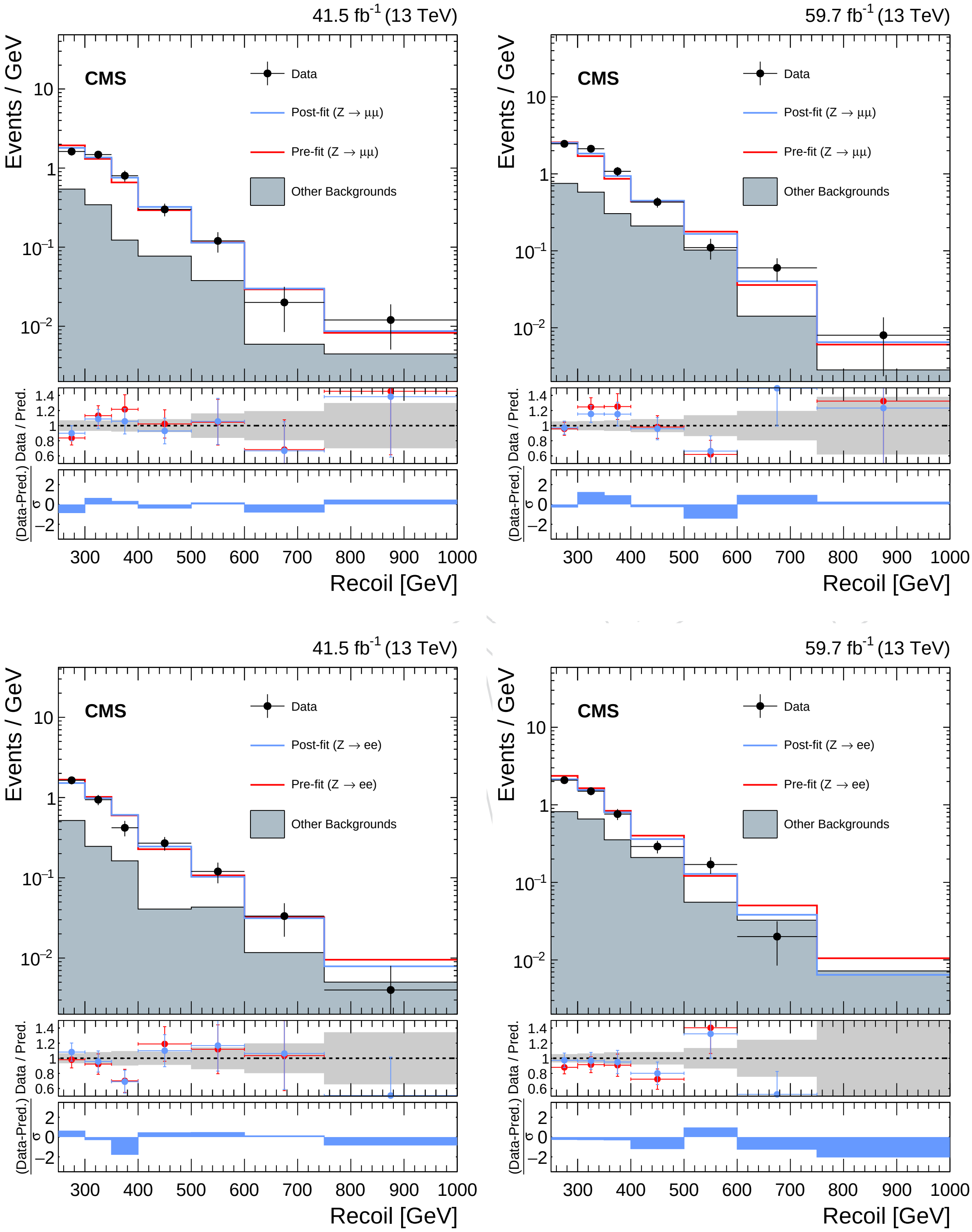

Figure 193: Same as Fig. 187, but for the high-purity mono-V category.

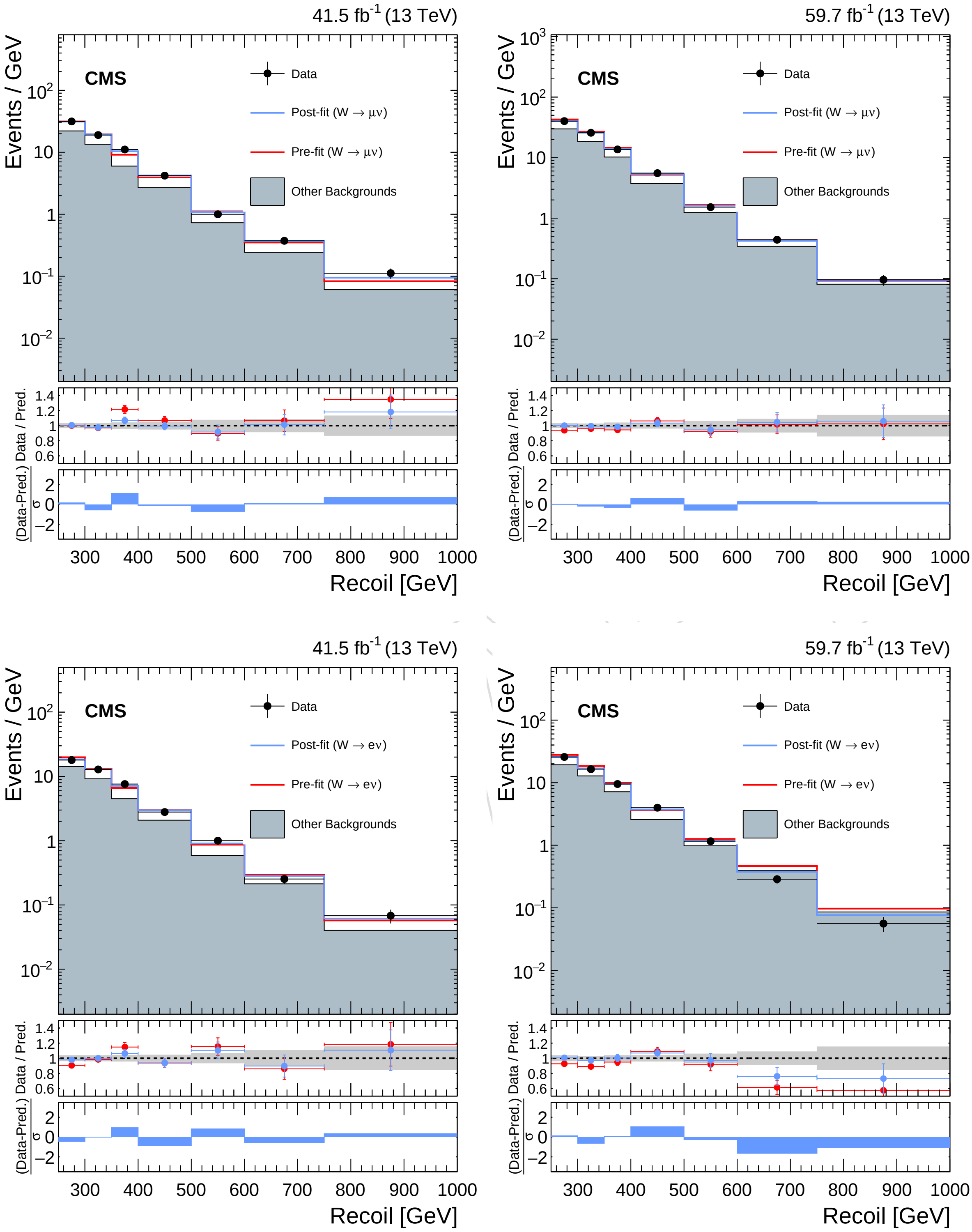

Figure 194: Same as Fig. 188, but for the high-purity mono-V category.

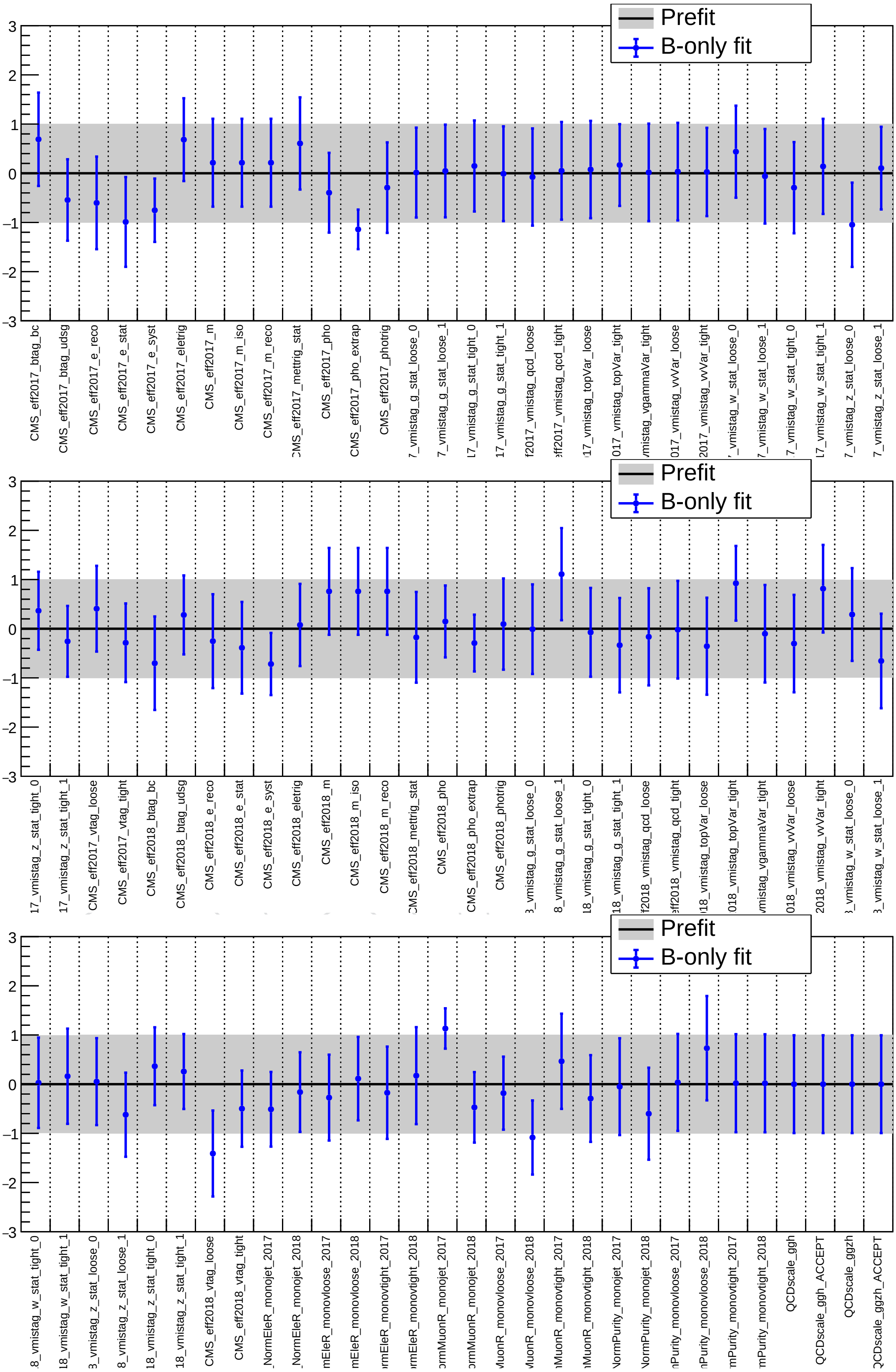

Figure 195: Nuisance parameters for the combined CR-only fit in all categories (monojet, loose mono-V, tight mono-V) and both years (2017, 2018). By definition, the prefit values of the nuisance parameters are at zero, with an uncertainty of ±1. The blue (red) points indicate the postfit value of the individual parameters under the background only (background plus signal) hypothesis. Note that red and blue coincide because only the control regions are taken into account, and there is no signal. Because of the large number of parameters, the image is split into separate panels.

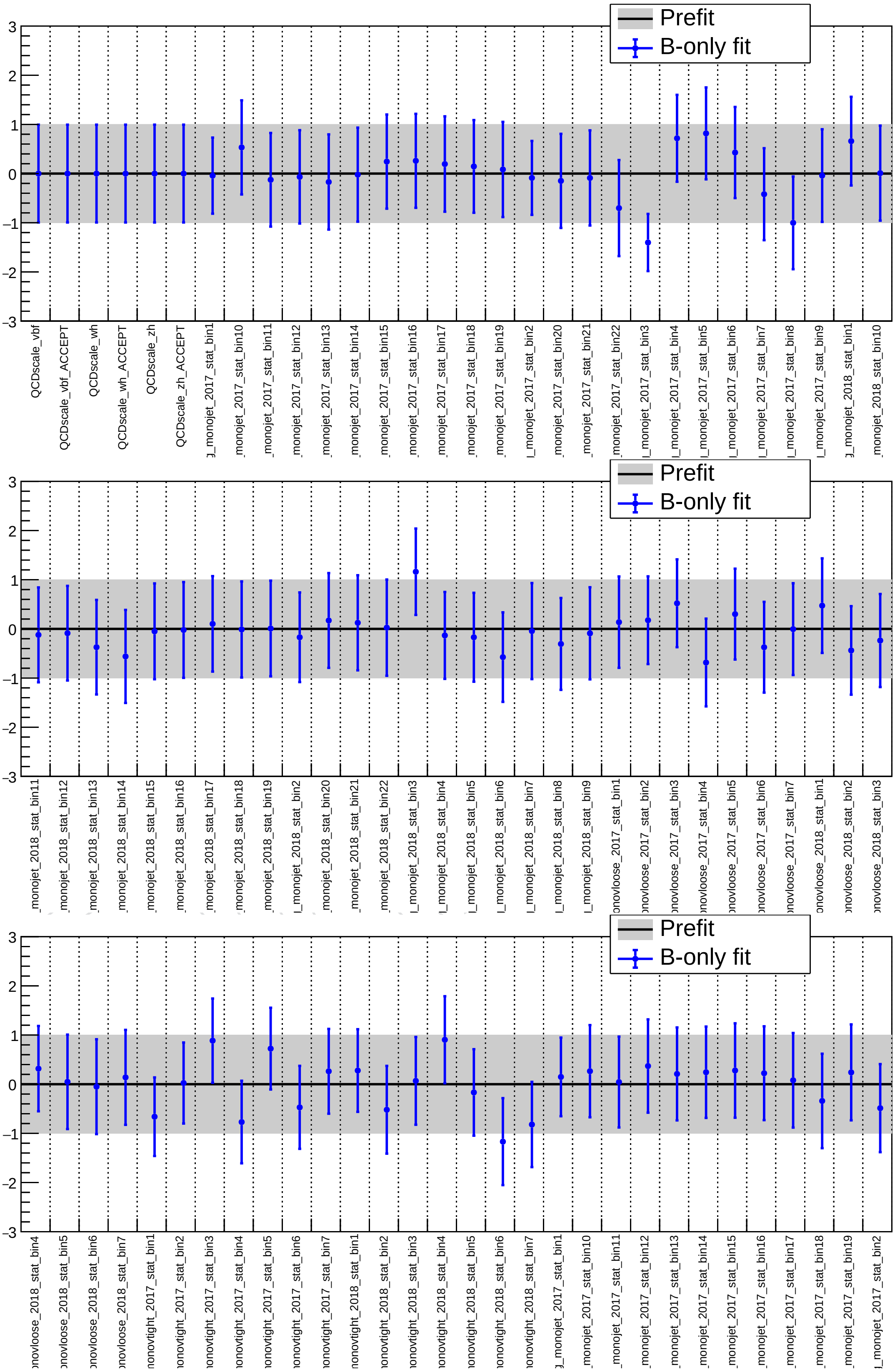

Figure 196: Continuation of Fig. 195

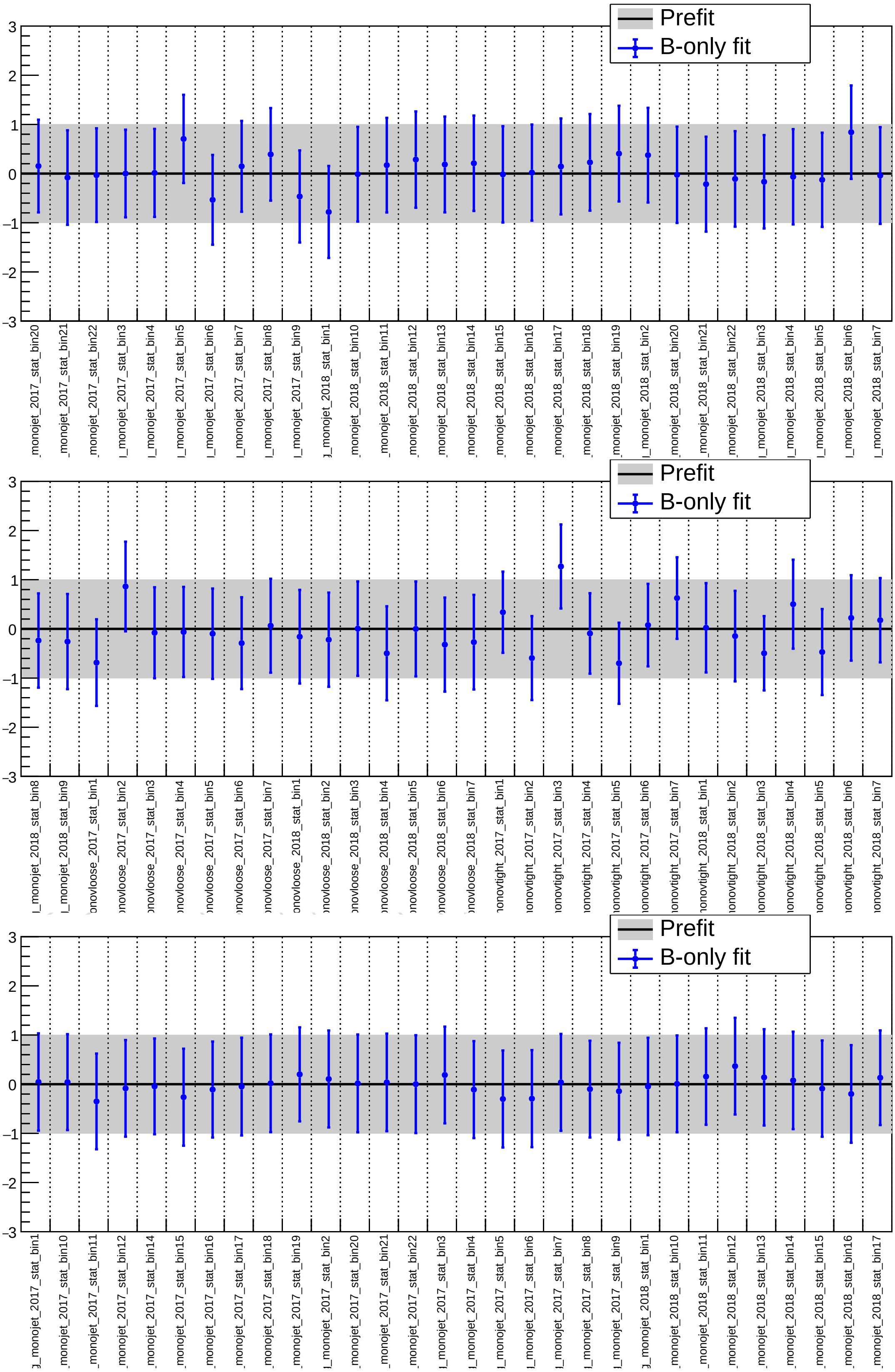

Figure 197: Continuation of Fig. 196

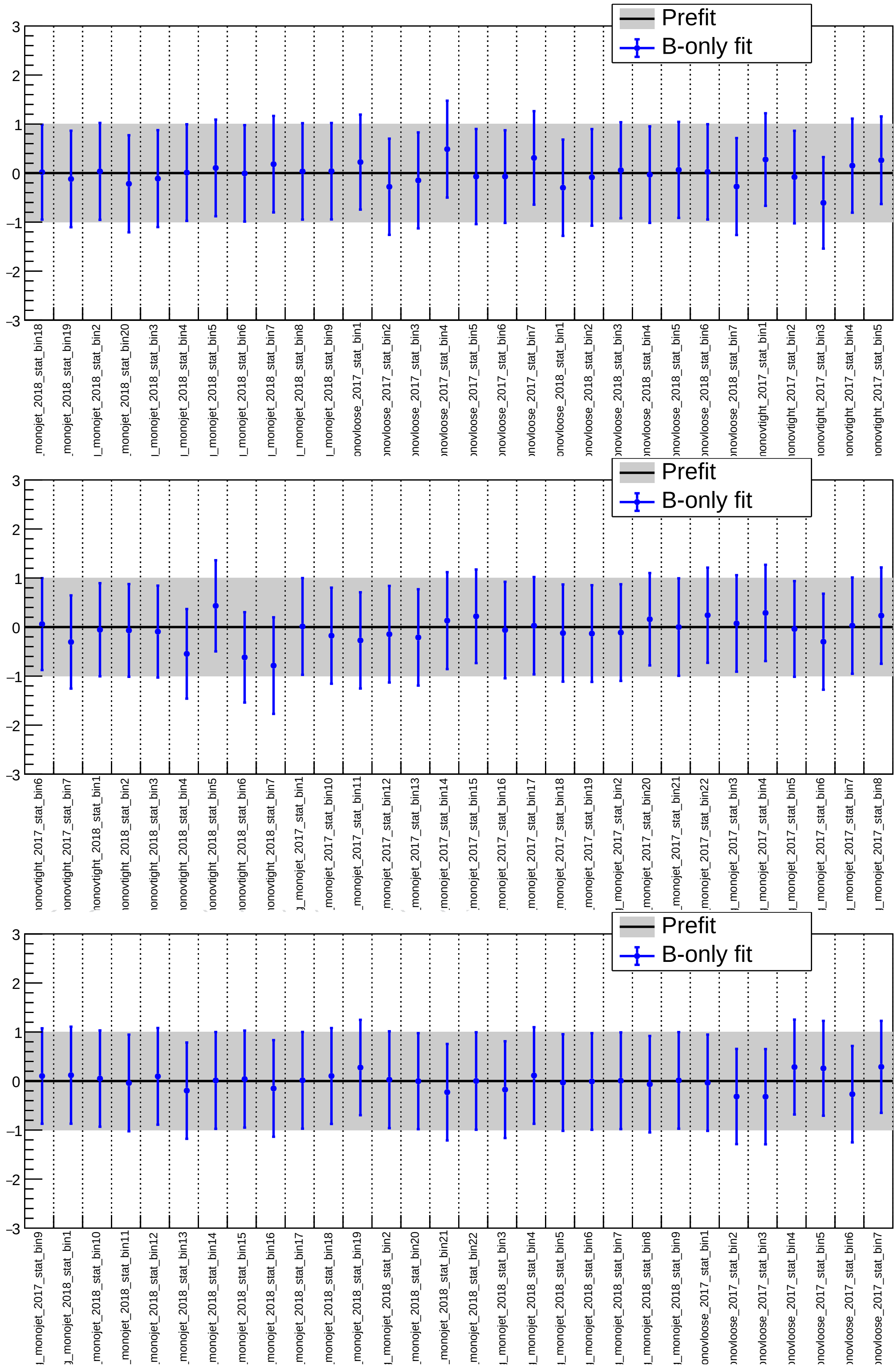

Figure 198: Continuation of Fig. 197

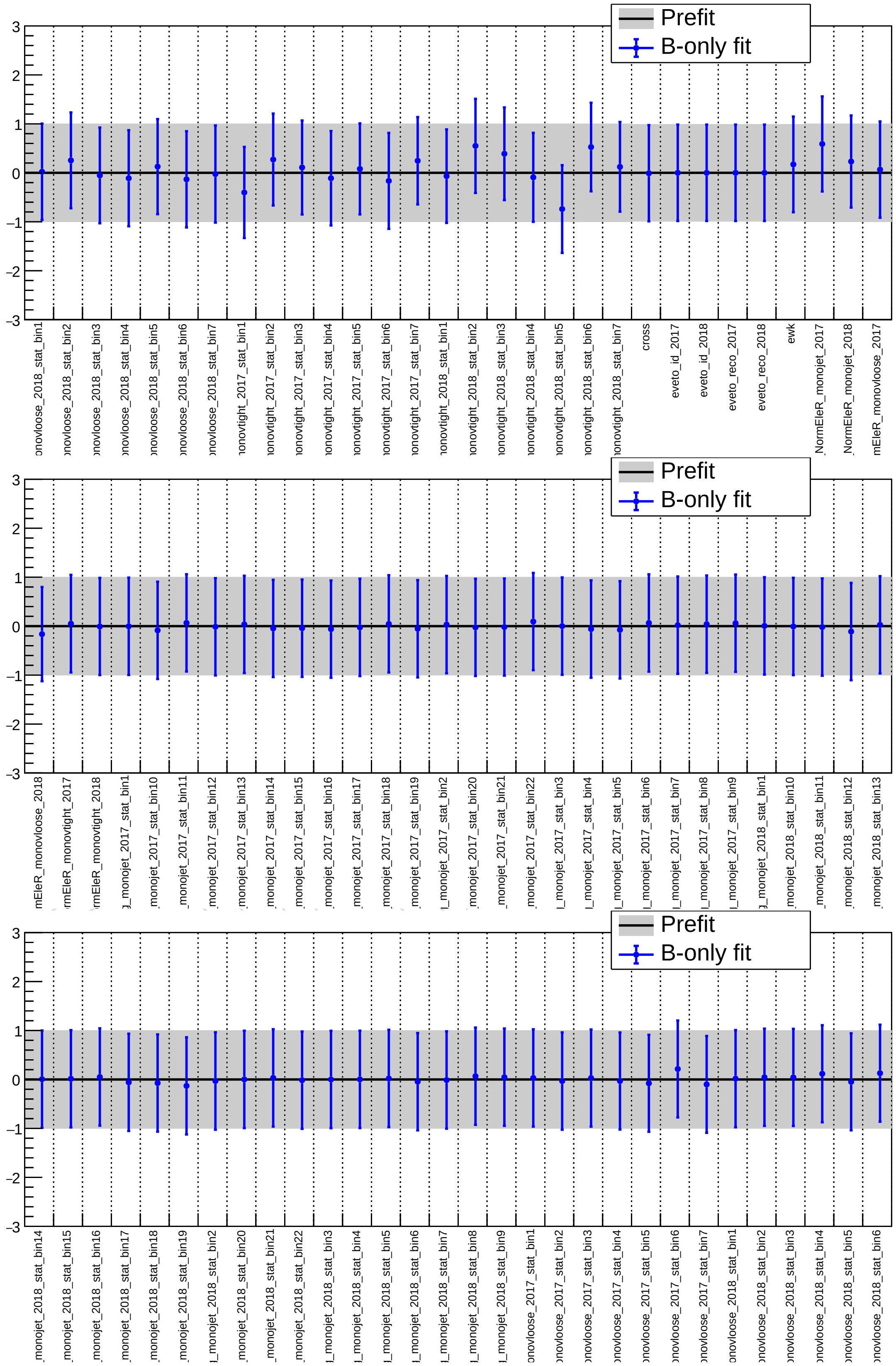

Figure 199: Continuation of Fig. 198

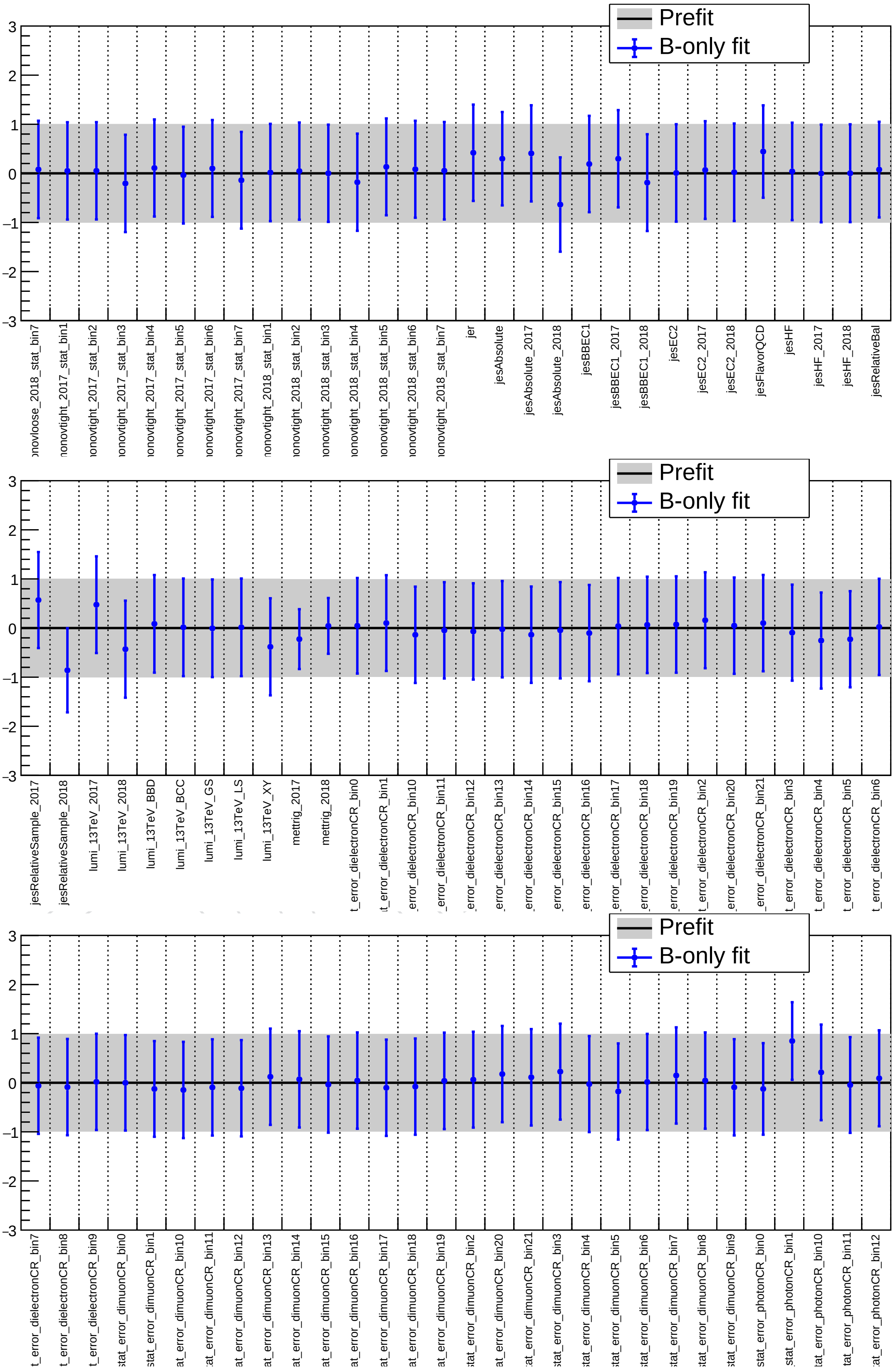

Figure 200: Continuation of Fig. 199

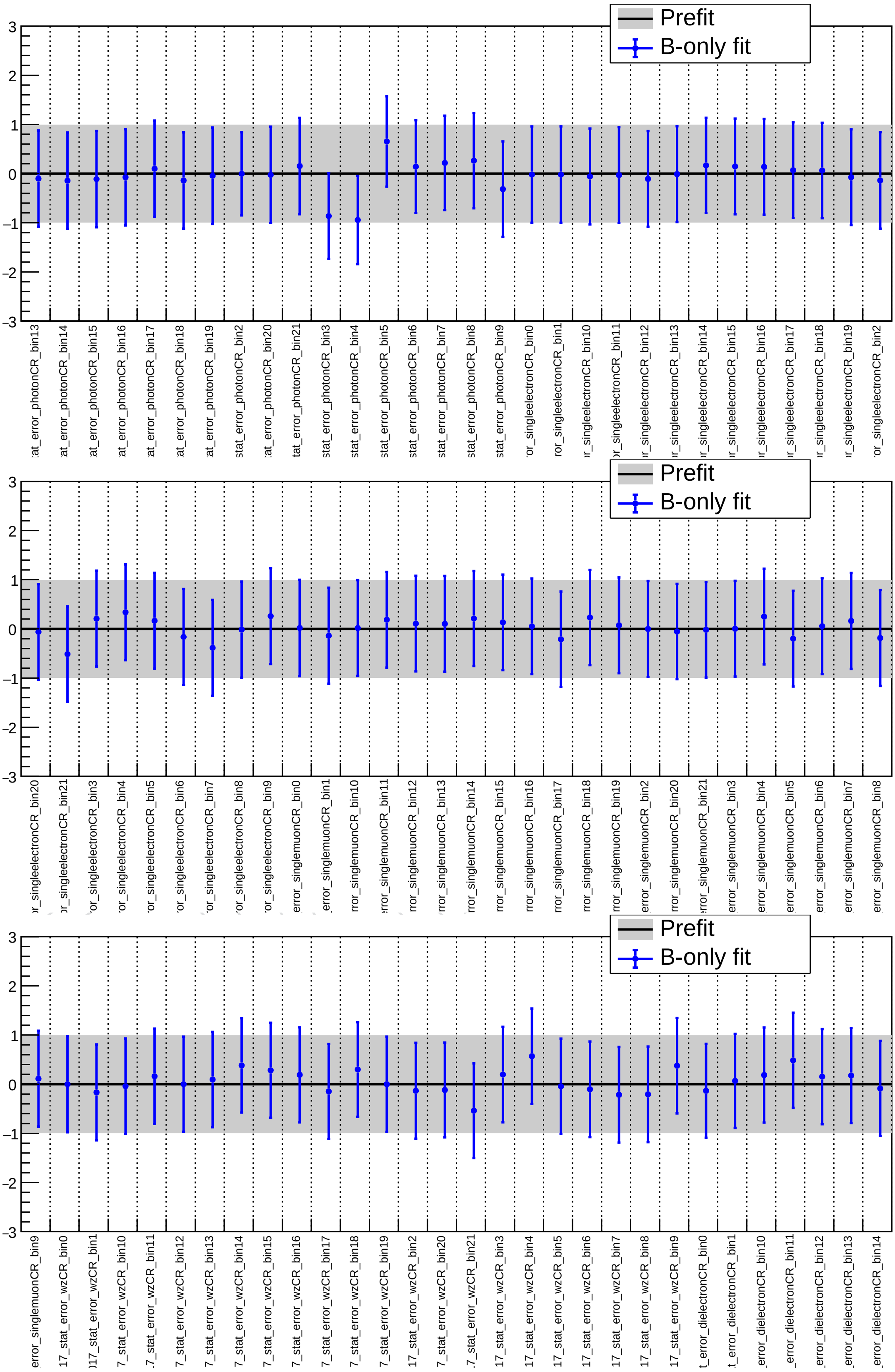

Figure 201: Continuation of Fig. 200

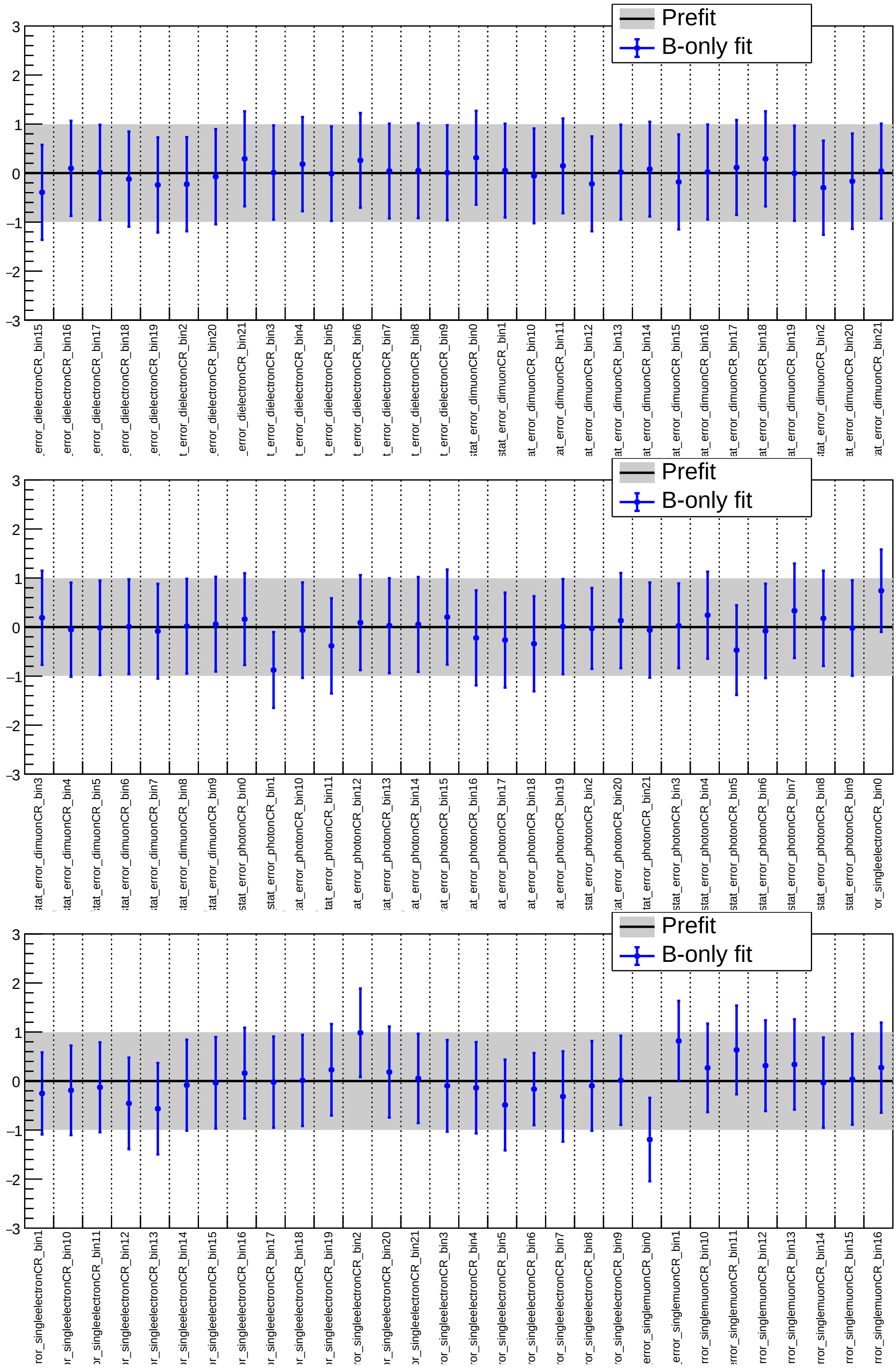

Figure 202: Continuation of Fig. 201

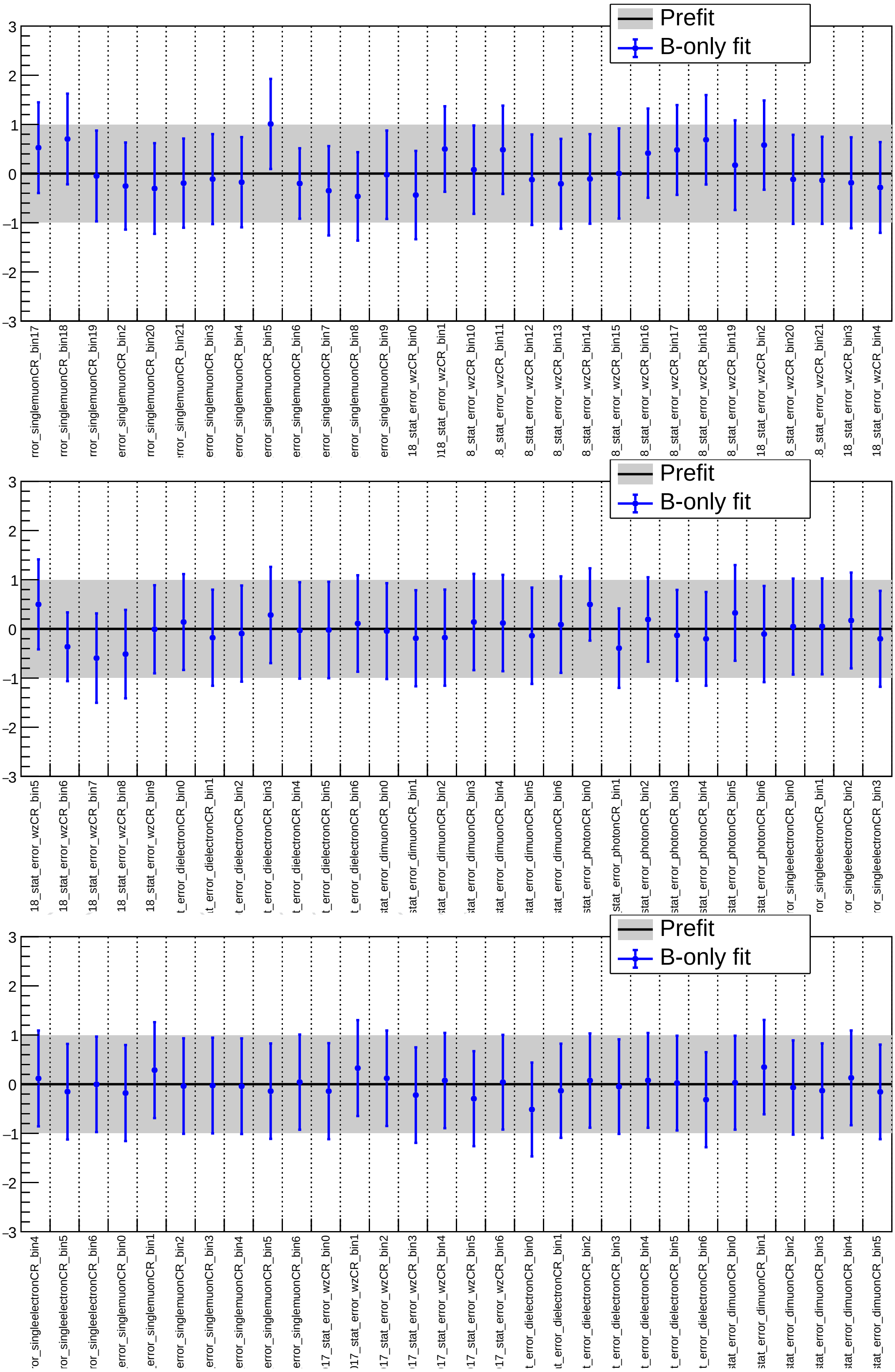

Figure 203: Continuation of Fig. 202

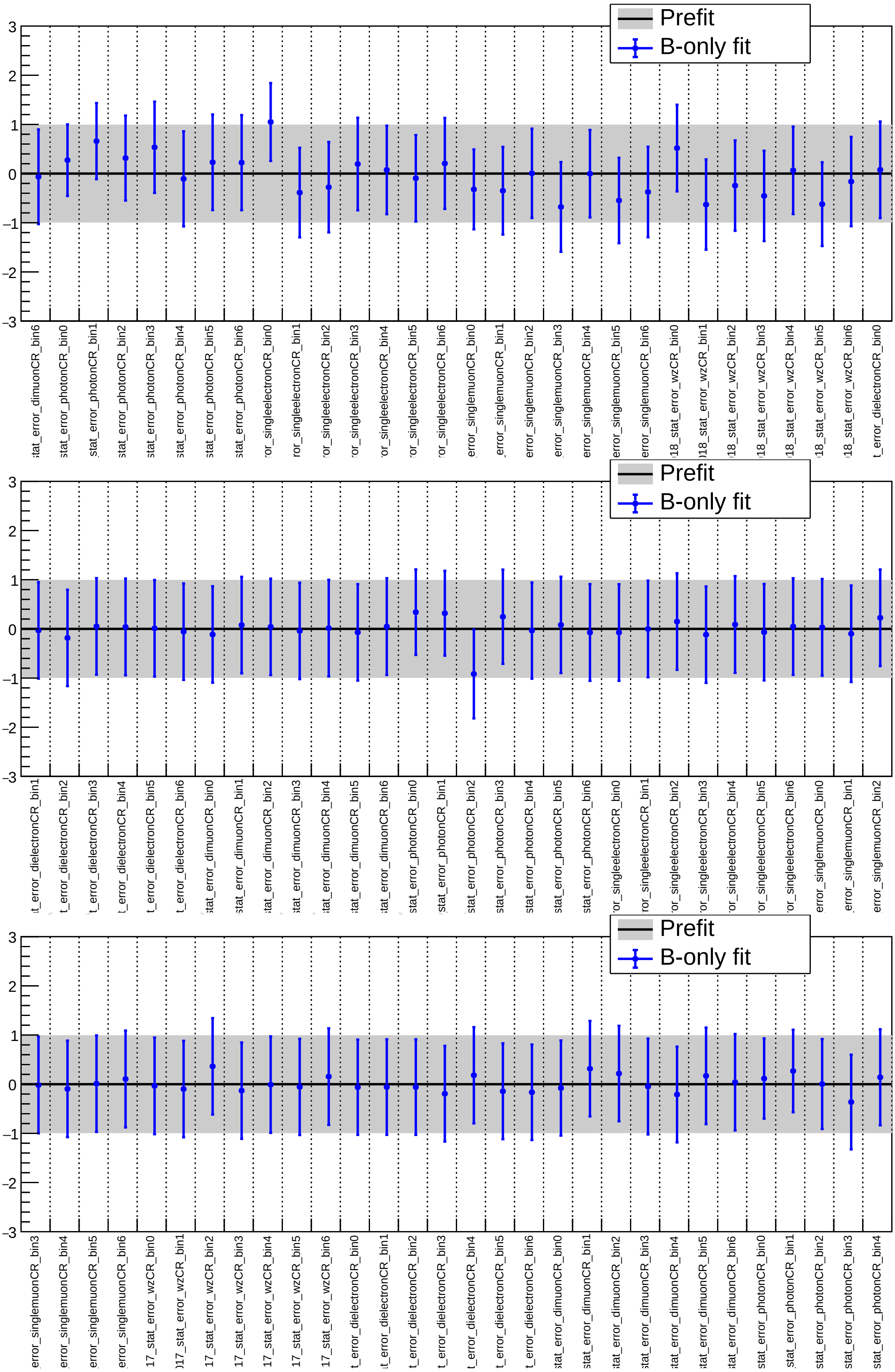

Figure 204: Continuation of Fig. 203

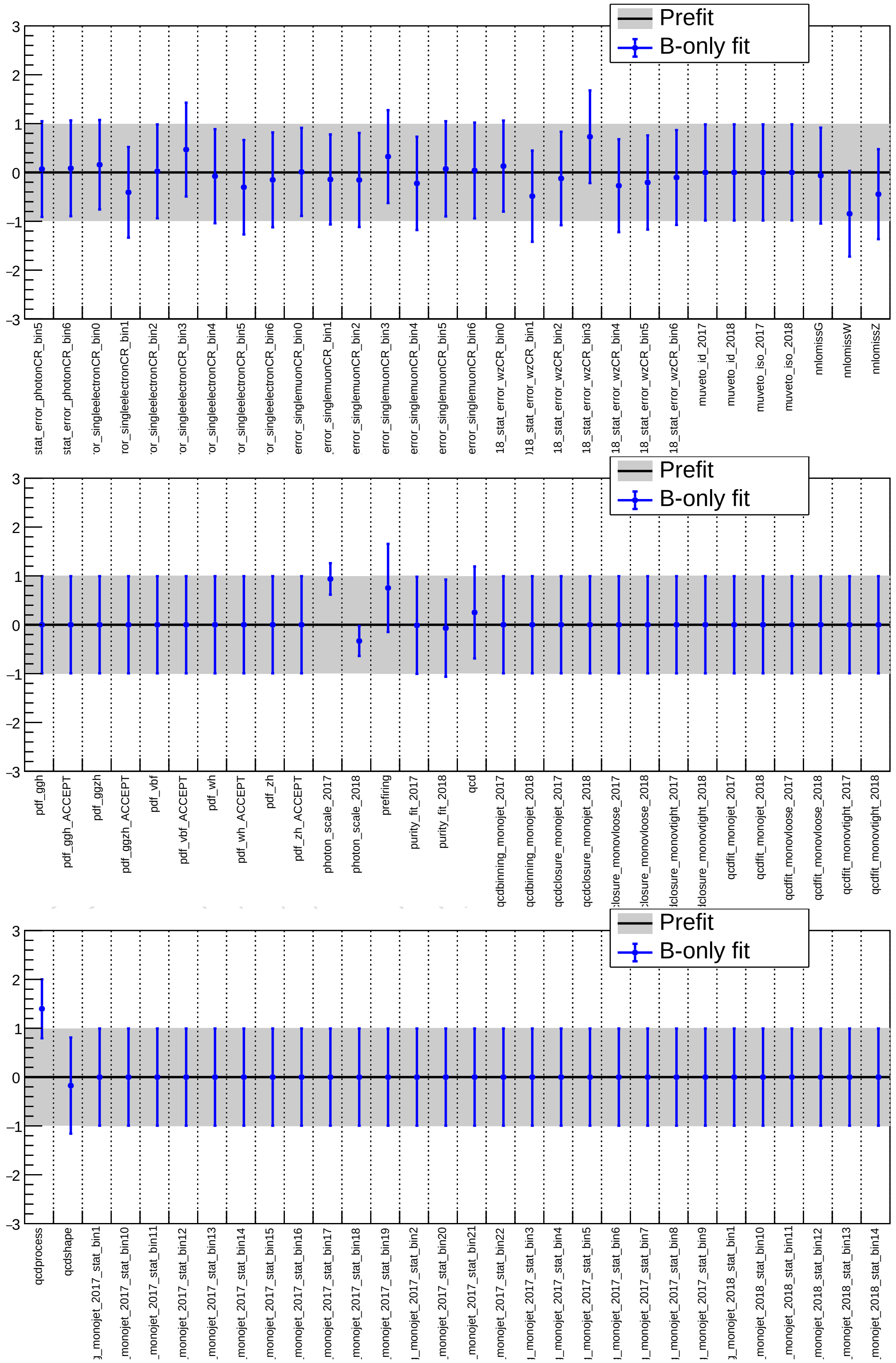

Figure 205: Continuation of Fig. 204

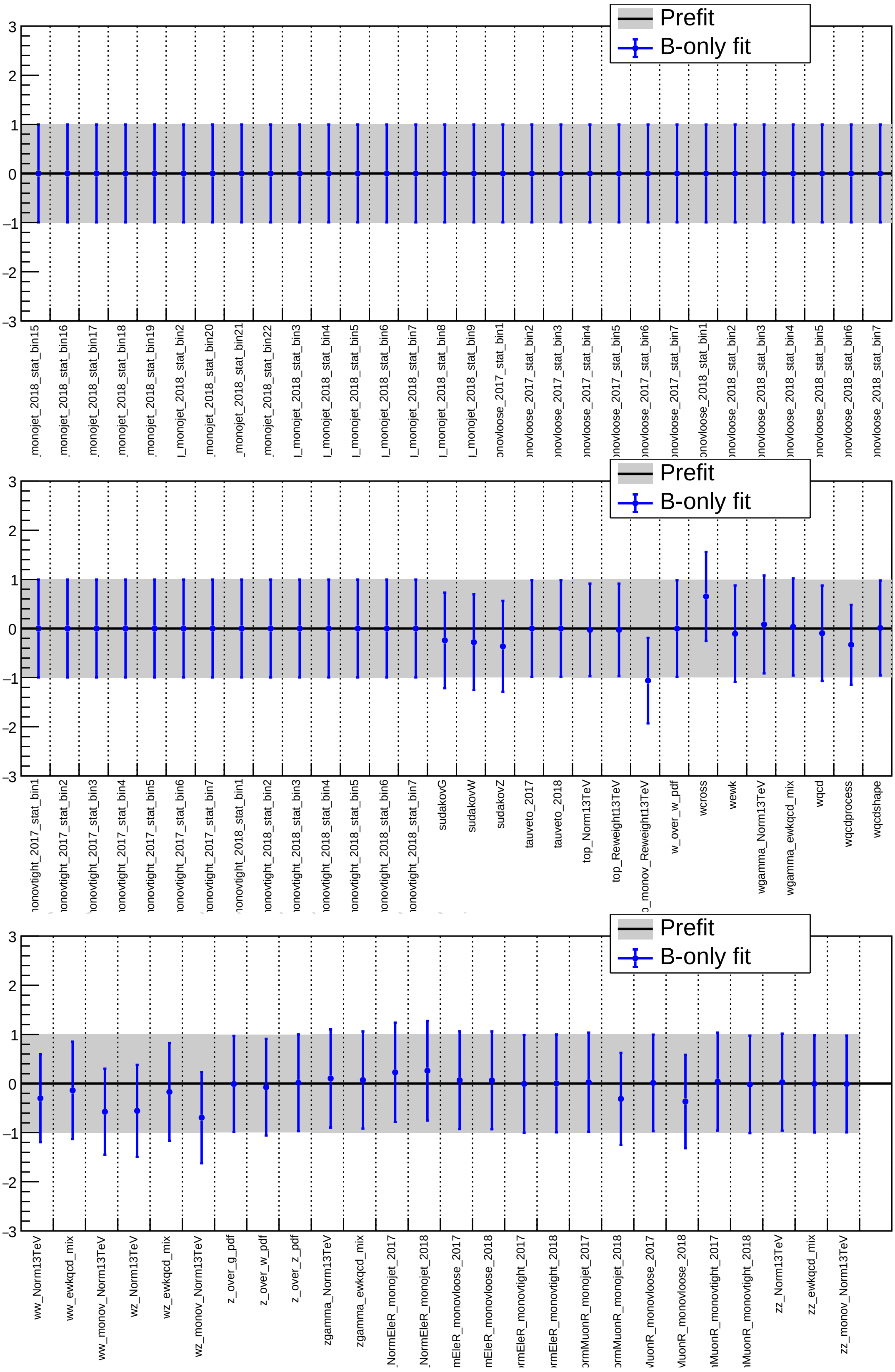

Figure 206: Continuation of Fig. 205

F.2 SR+CR fit

This section relates to the combination of the monojet and mono-V categories in the 2017 and 2018 datasets. Results shown here represent a fit in which the signal are taken into account (SR+CR fit).

F.2.1 Likelihood scan

Likelihood scans for the H(inv) signal strength are shown in Fig. 207, and 208.

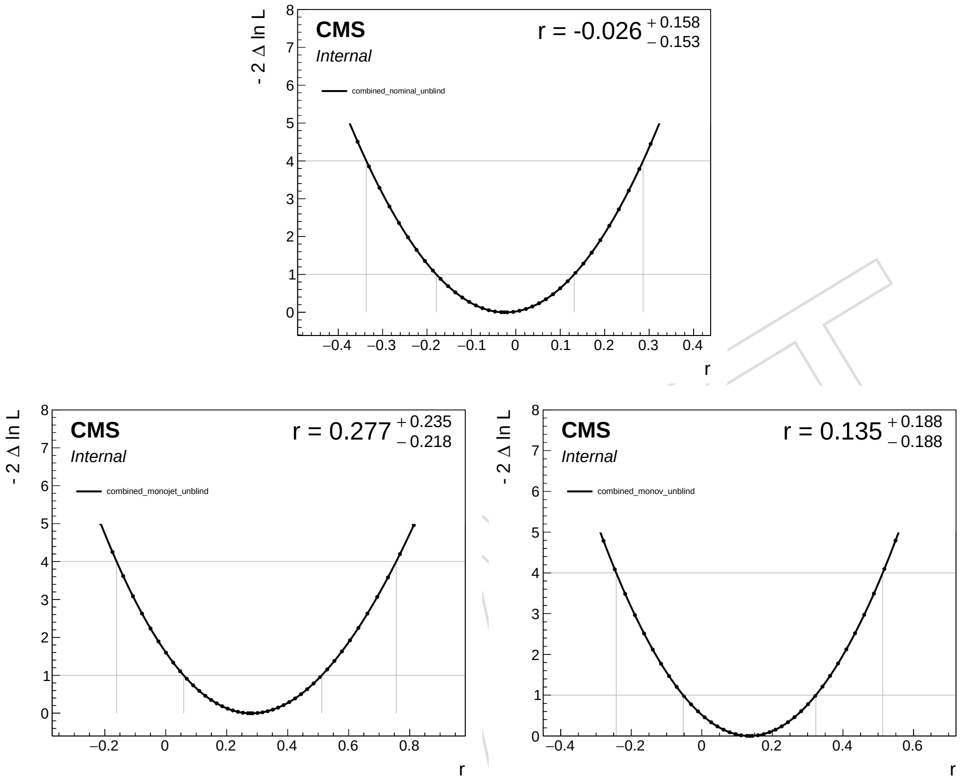

Figure 207: Likelihood scan as a function of the signal strength r. For each value of r, the nuisance parameters are profiled separately. The y axis shows the difference of two times the negative logarithm of the likelihood value to the value at the minimum. The label text inside the plot indicates the best-fit signal strength, which corresponds to the minimum of the shown curve. Note that negative signal strengths are tested here only as a matter of technical validation, but are not used in the physics result, in which $r > 0$ is enforced. In the top panel, the scan is shown for the combined fit of all categories in 2017 and 2018. In the bottom panels, the scans are shown for separate fits of just the monojet category (left), and just the mono-V categories (right).

F.2.2 Postfit plots

The comparisons of the prefit and postfit predictions are shown in the main body of the note.

F.2.3 Goodness-of-fit

The GoF result is shown in Fig. 209. Note that the signal+background fit is used here.

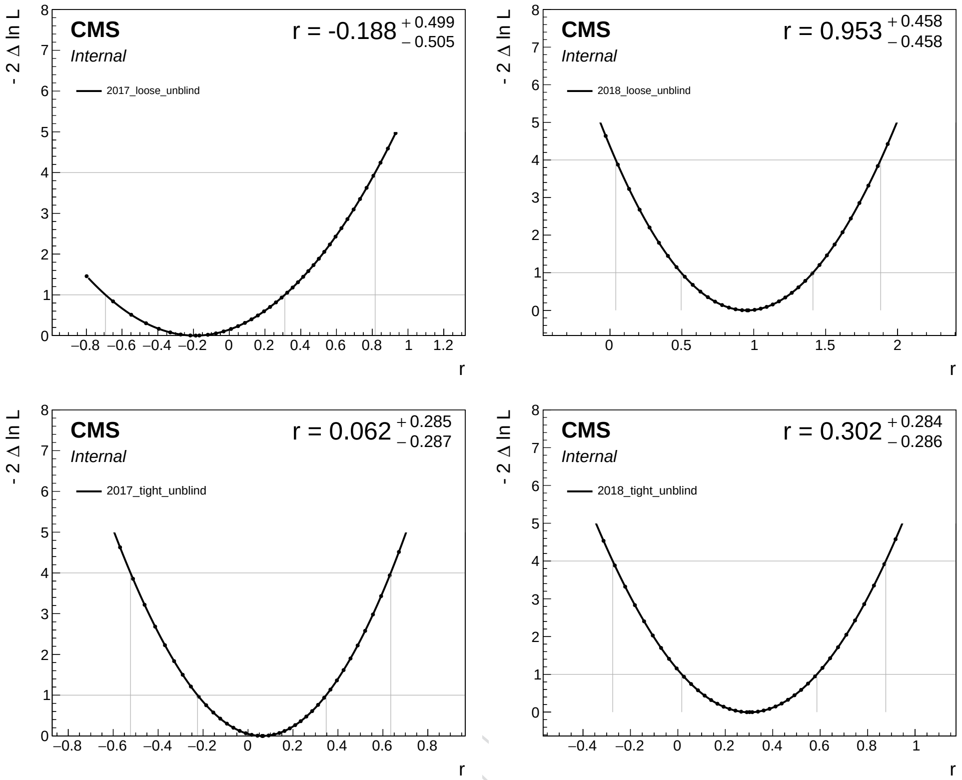

Figure 208: Likelihood scan for the low-purity (left) and high-purity mono-V categories fit by themselves. The left column shows the 2017 data set, while the right column shows 2018.

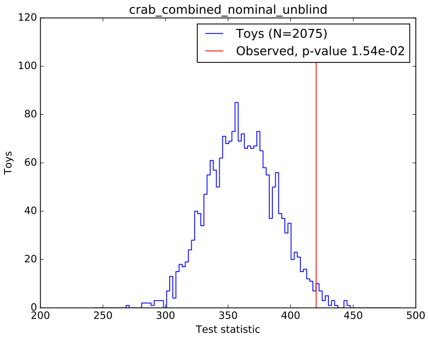

Figure 209: Same as Fig. 185, but now including the partialy unblinded signal regions with floating signal strength.

F.2.4 Nuisance pulls

The nuisance pulls for this fit are shown in Figs. 210–221.

F.3 Nuisance parameter impacts

The impacts of the 120 most relevant nuisance parameters are shown in Figs. 222 and 223 for the Asimov dataset, assuming no signal, as well as for the fit of the observed data in Fig. 224 and 225. The impacts are defined as the relative change in the best fit signal strength between the case where the nuisance paramter is left to float and the case where it is fixed to its nominal best-fit value.

Since the nuisance impacts are derived for the invisible Higgs signal hypothesis, the mono-V channel contributes significantly to the overall sensitivity. Consequently, the leading nuisance parameter for the overall fit is the WZ normalization uncertainty ("wz_Norm13TeV"), which dominantly affects the mono-V channel where diboson and top events make up a significant fraction ($\approx 25 - -50\%$) of the total background. In the monojet category, such events are significantly more rare (up to 5%) and the nuisance consequently has no appreciable effect.

Beyond the diboson normalization, the most significant nuisances represent the experimental uncertainties associated to lepton and photon selection, as well as the theory uncertainty related to process-dependent QCD corrections. These uncertainties are important because they allow the process contributions in the signal and control regions to move relative to each other, which sligthly decouples the shapes in the different regions. This decoupling then translates into increased room to fit a signal component. Additionally, the lepton uncertainties affect the dilepton control regions more strongly than they affect the single lepton regions, and consequently allow the relative contributions of $Z +$ jets and Wjets processes to change, yielding differences in the shape of the overall background in the signal region, which again translate into differences in the best-fit signal strength. Because of the large statistical power of the analysis regions, it is possible to constrain some of nuisances by factors of up to around two.

Theoretical uncertainties on the transfer factors are overall sub-leading relative to the experimental nuisances. Due to the precise nature of the theory prescriptions used to derive them, they do not represent the main constraints on the analysis sensitivy, even though they are considered to be correlated between the data-taking years.

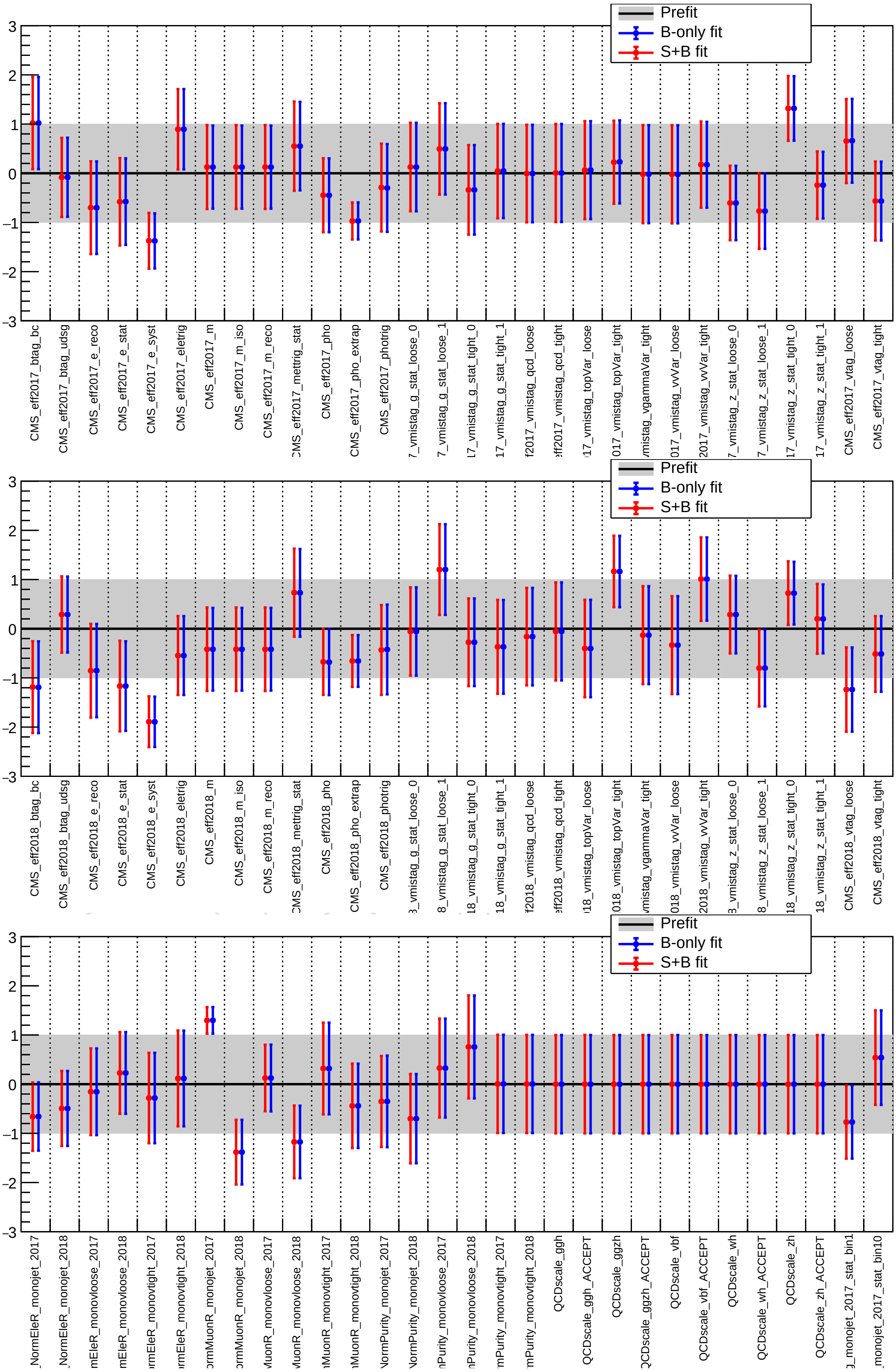

Figure 210: Nuisance parameters for the combined SR+CR fit in all categories (monojet, loose mono-V, tight mono-V) and both years (2017, 2018). By definition, the prefit values of the nuisance parameters are at zero, with an uncertainty of ±1. The blue (red) points indicate the postfit value of the individual parameters under the background only (background plus signal) hypothesis.

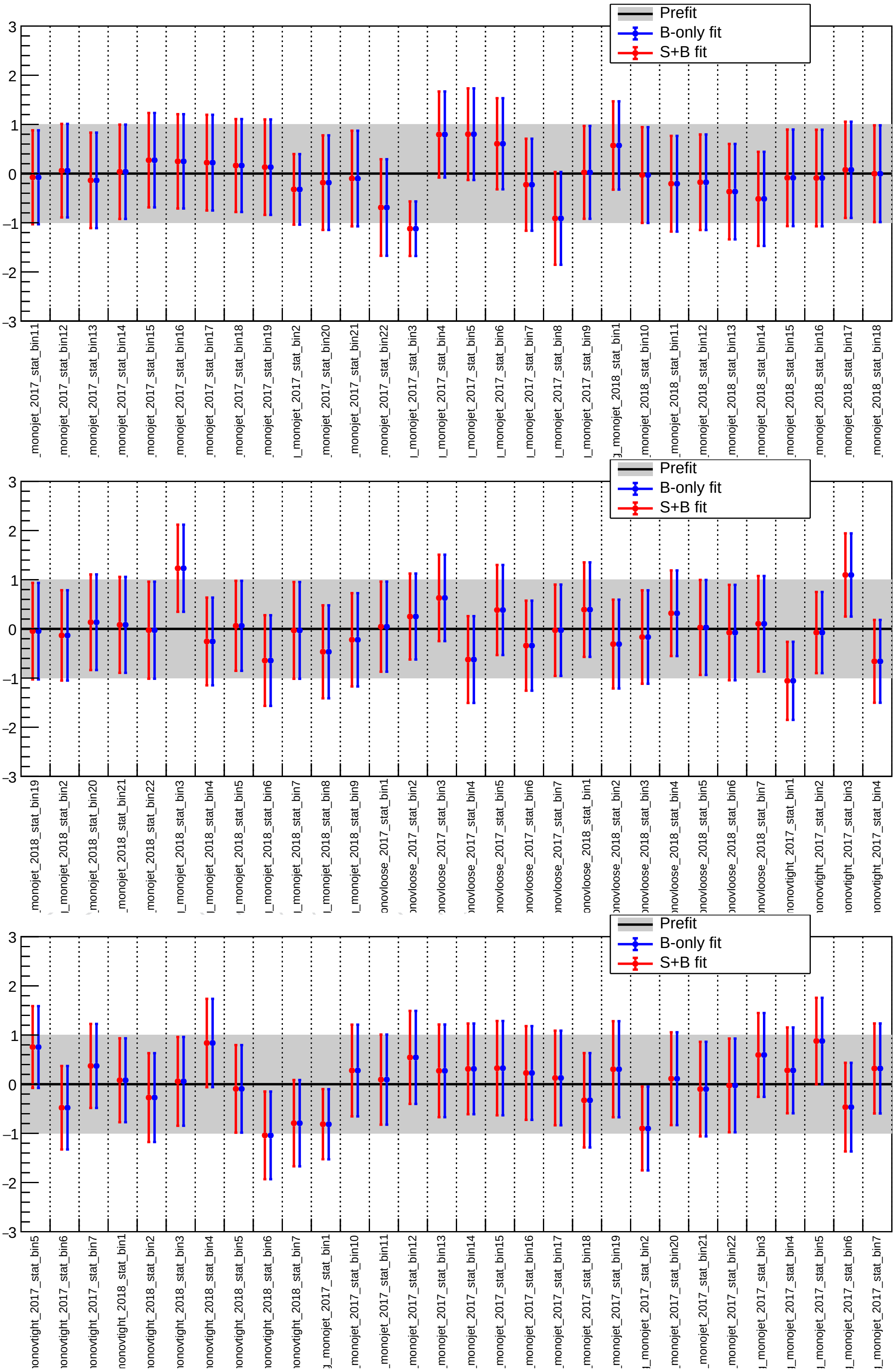

Figure 211: Continuation of Fig. 210

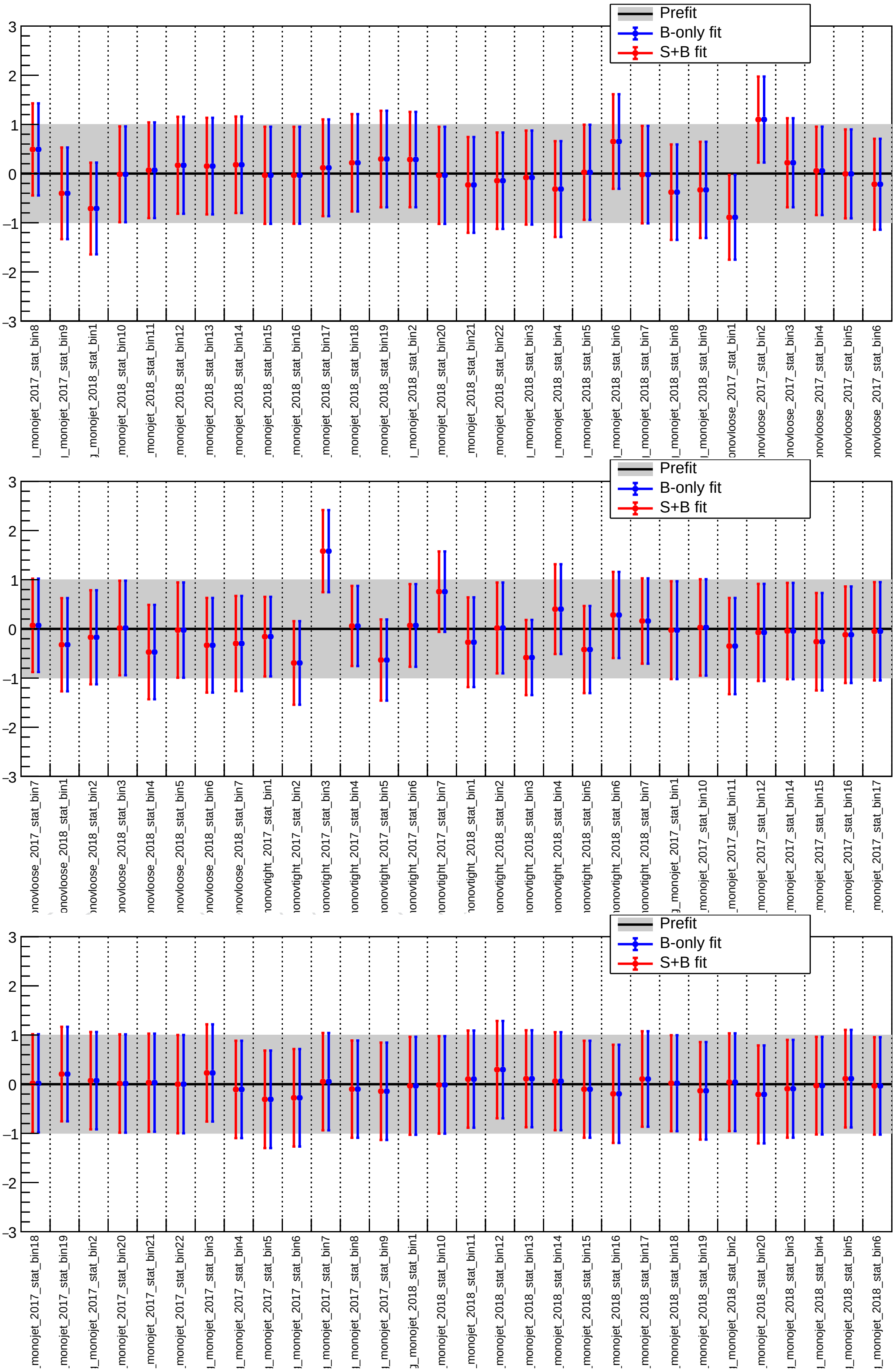

Figure 212: Continuation of Fig. 211

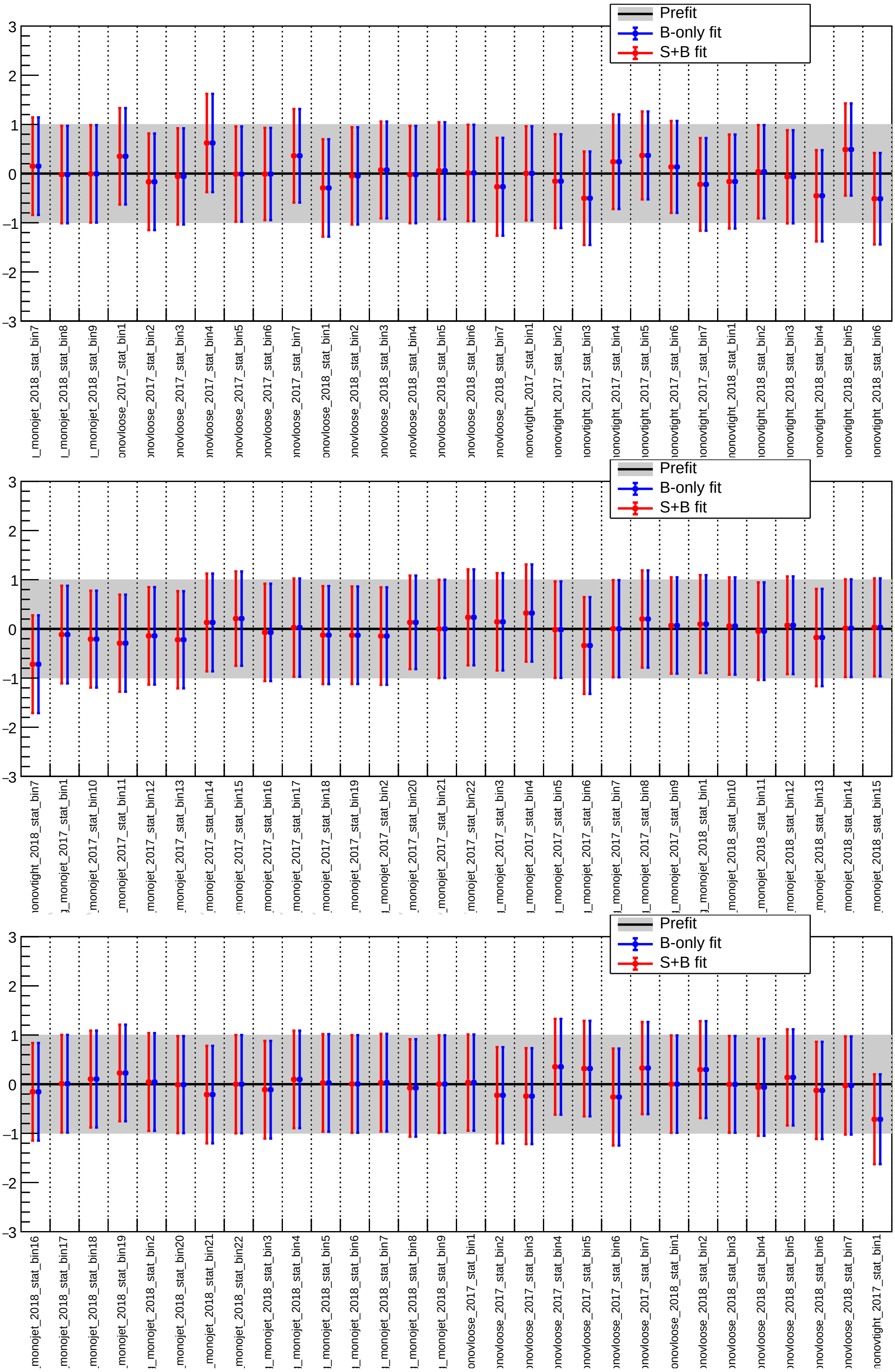

Figure 213: Continuation of Fig. 212

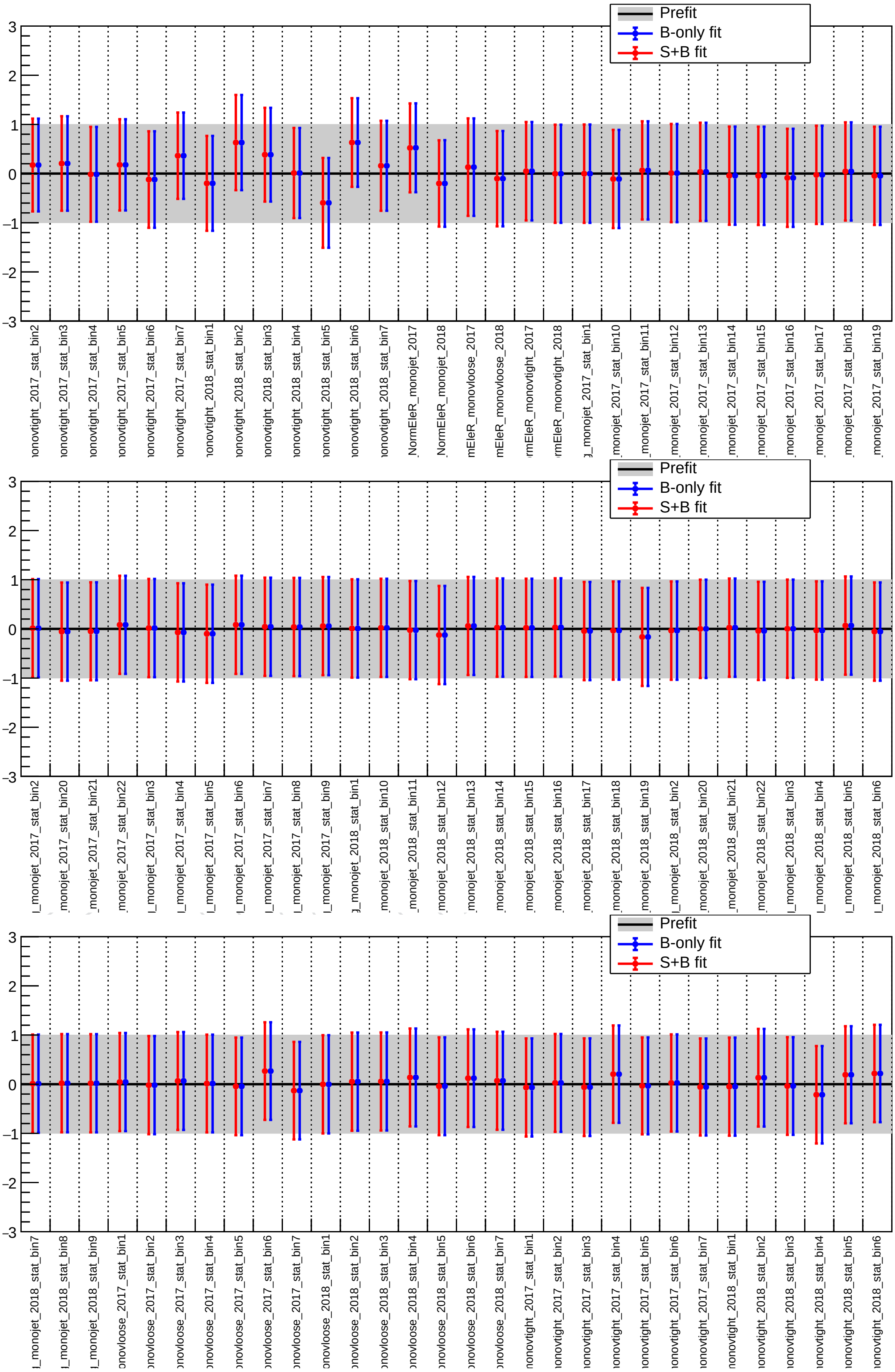

Figure 214: Continuation of Fig. 213

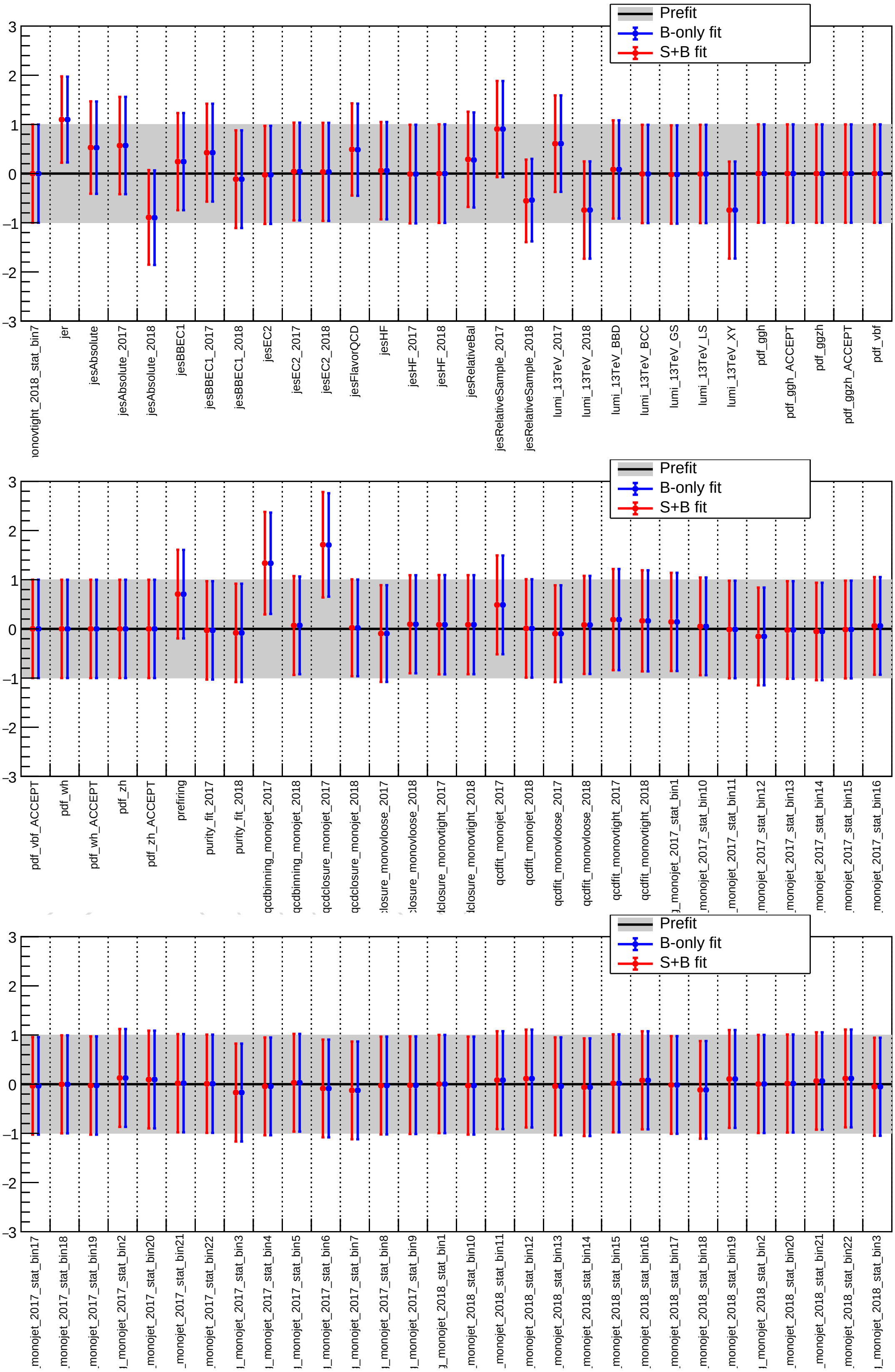

Figure 215: Continuation of Fig. 214

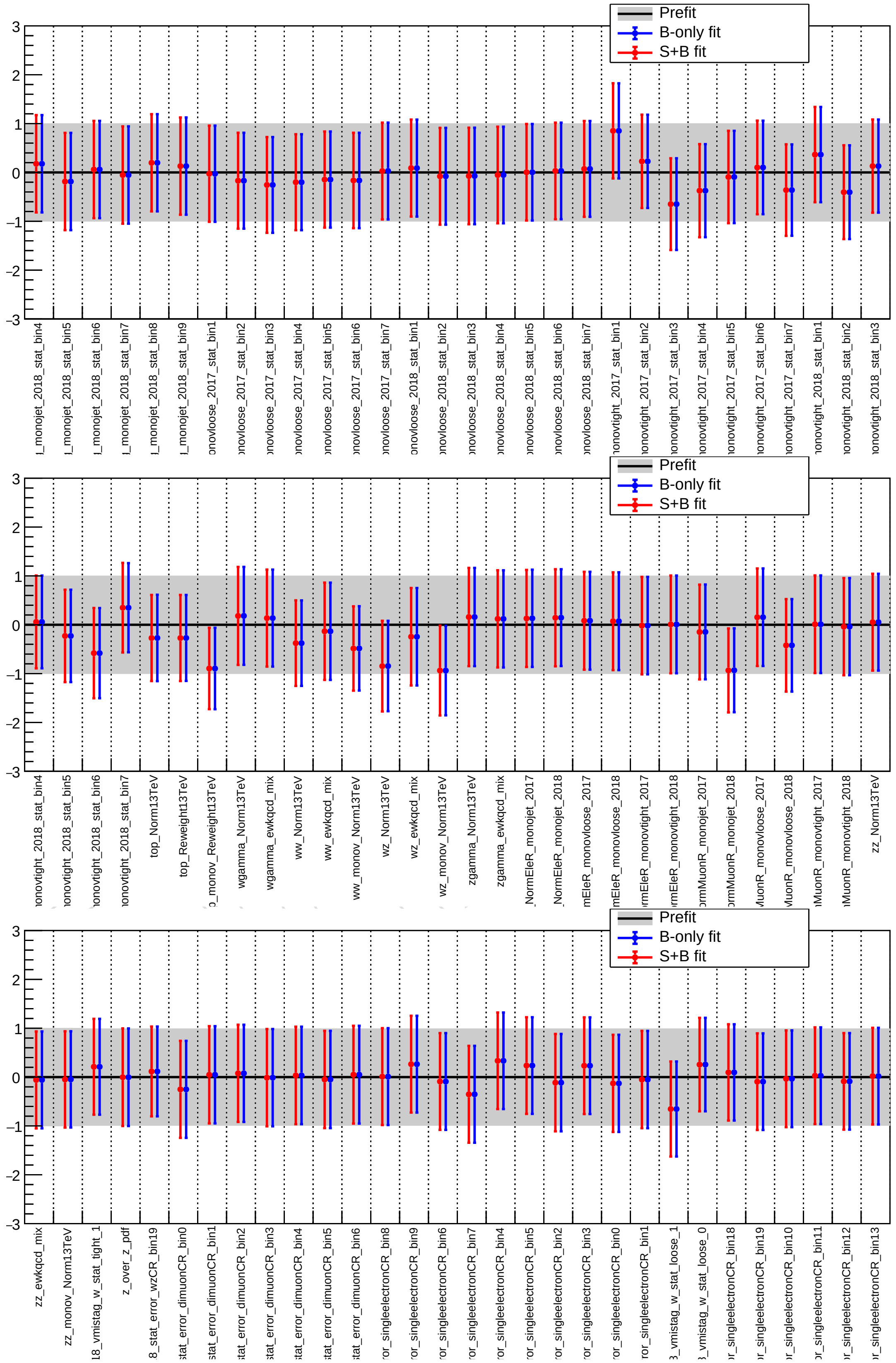

Figure 216: Continuation of Fig. 215

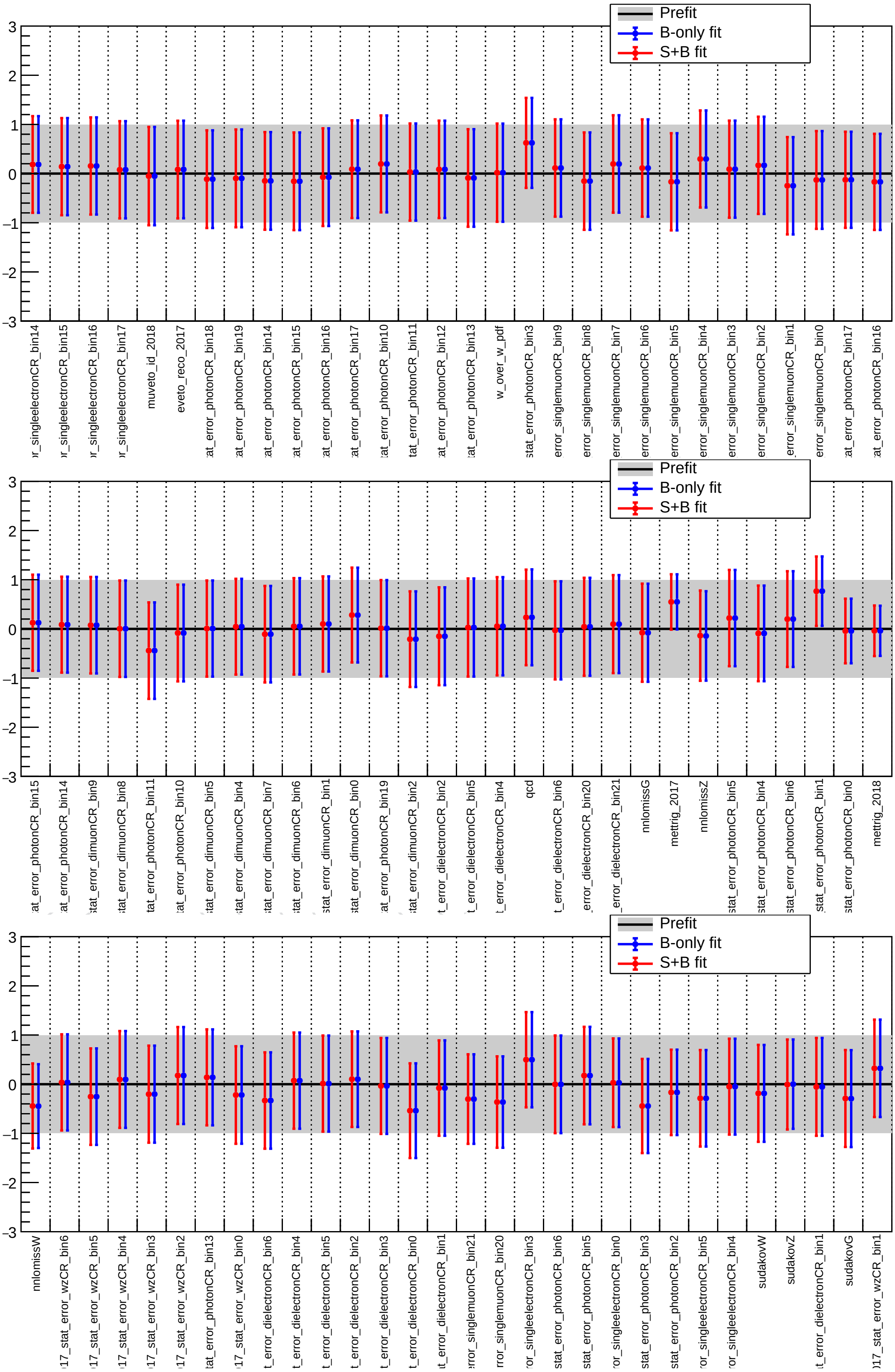

Figure 217: Continuation of Fig. 216

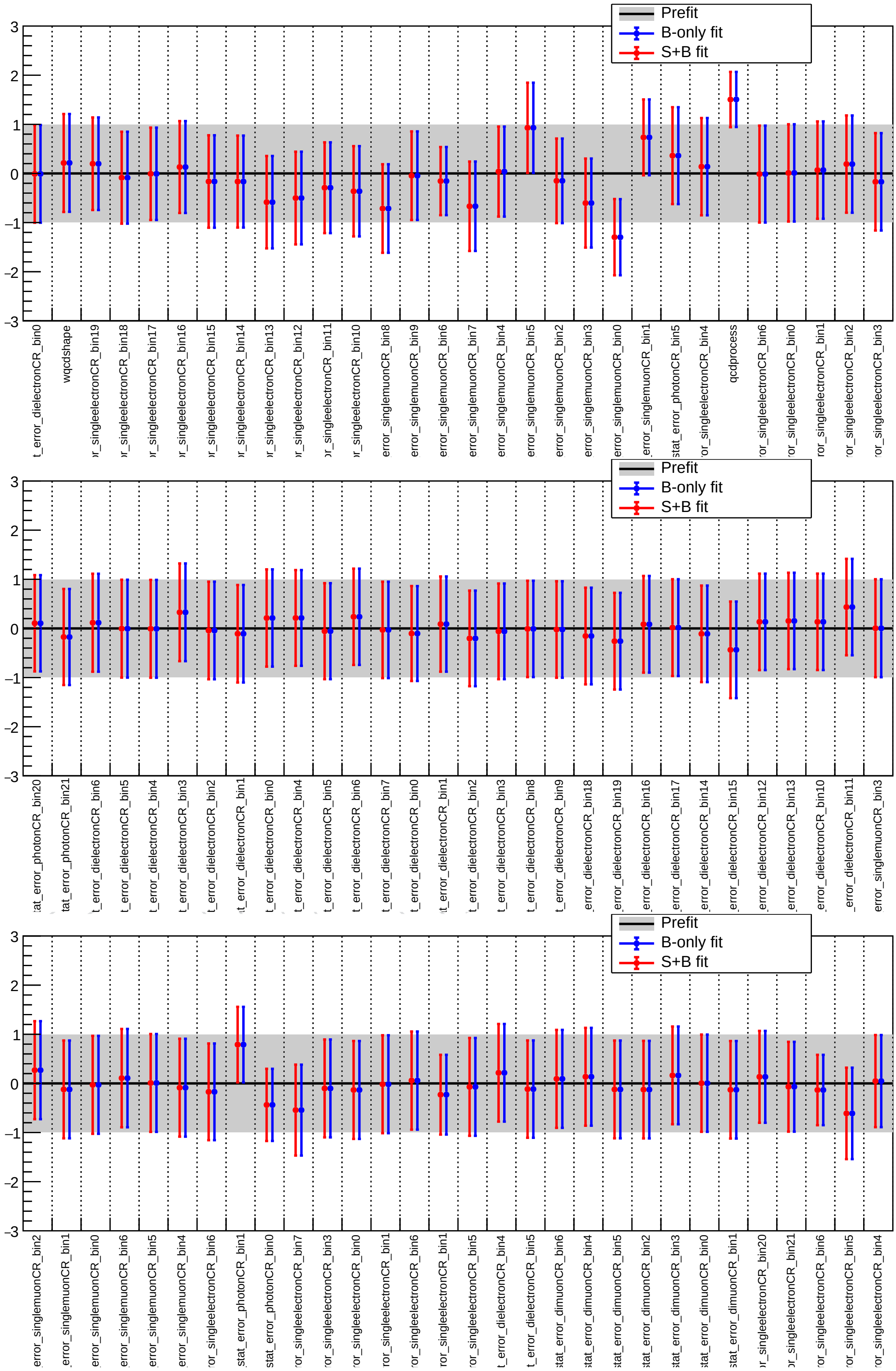

Figure 218: Continuation of Fig. 217

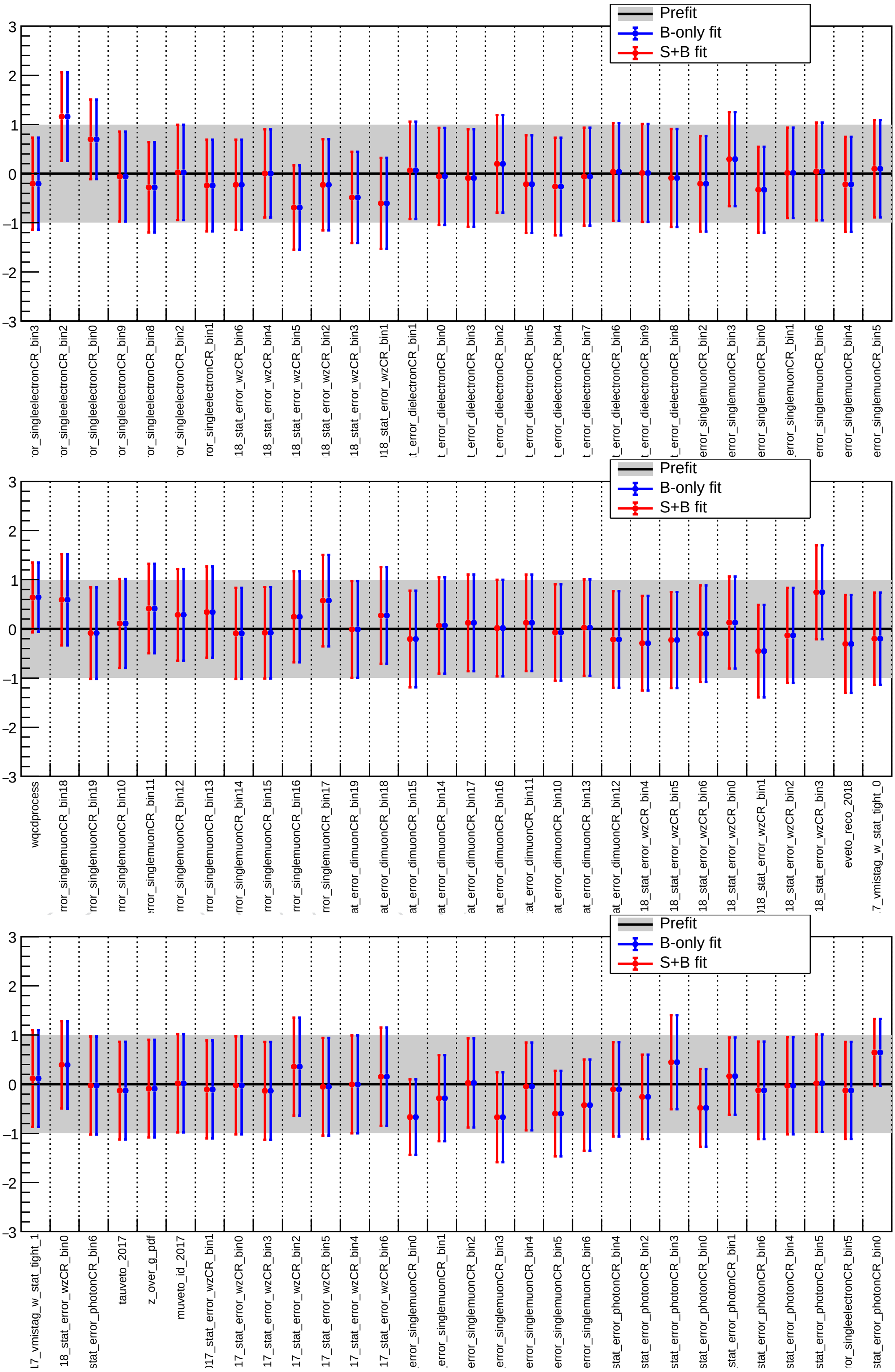

Figure 219: Continuation of Fig. 218

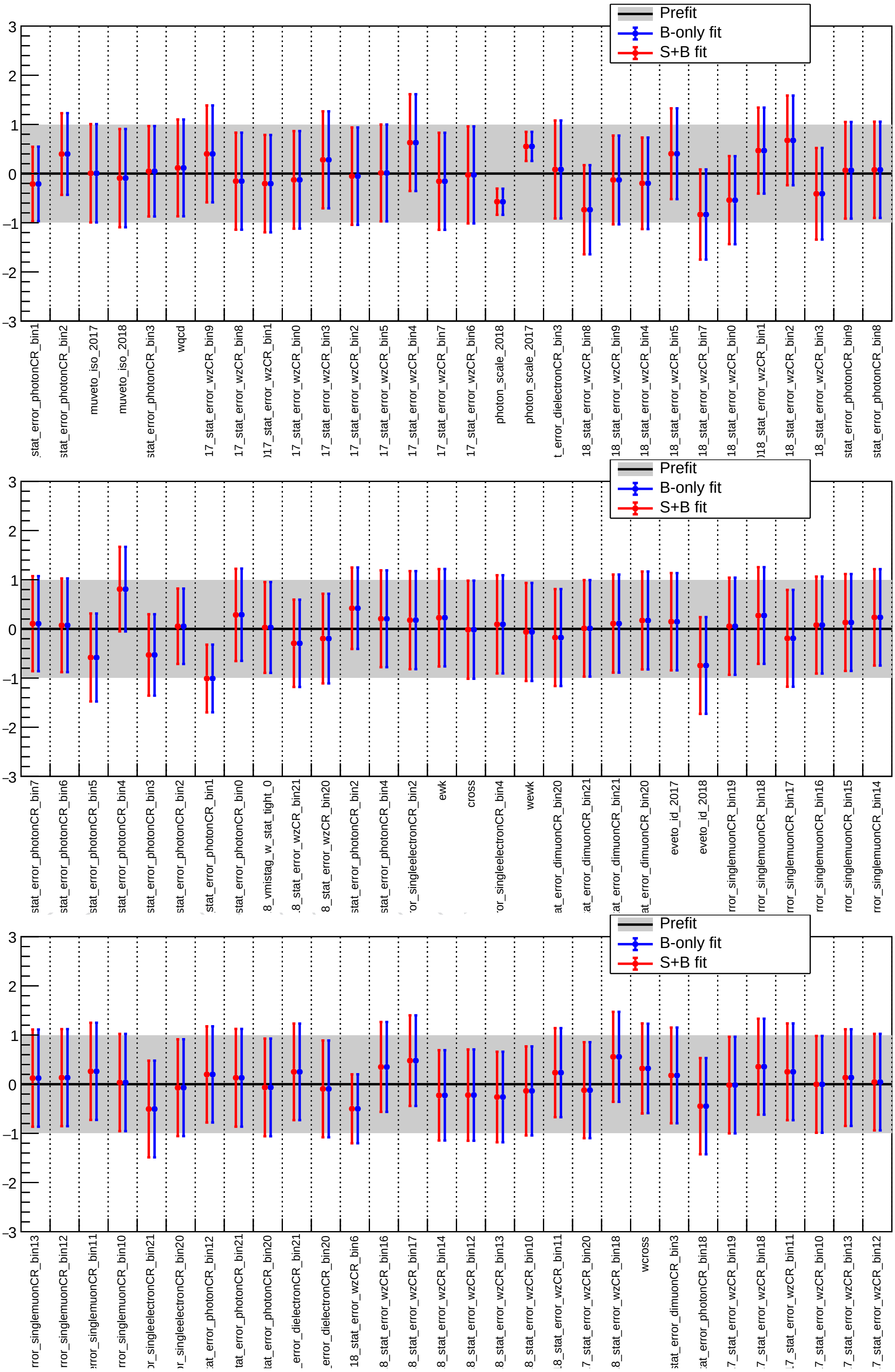

Figure 220: Continuation of Fig. 219

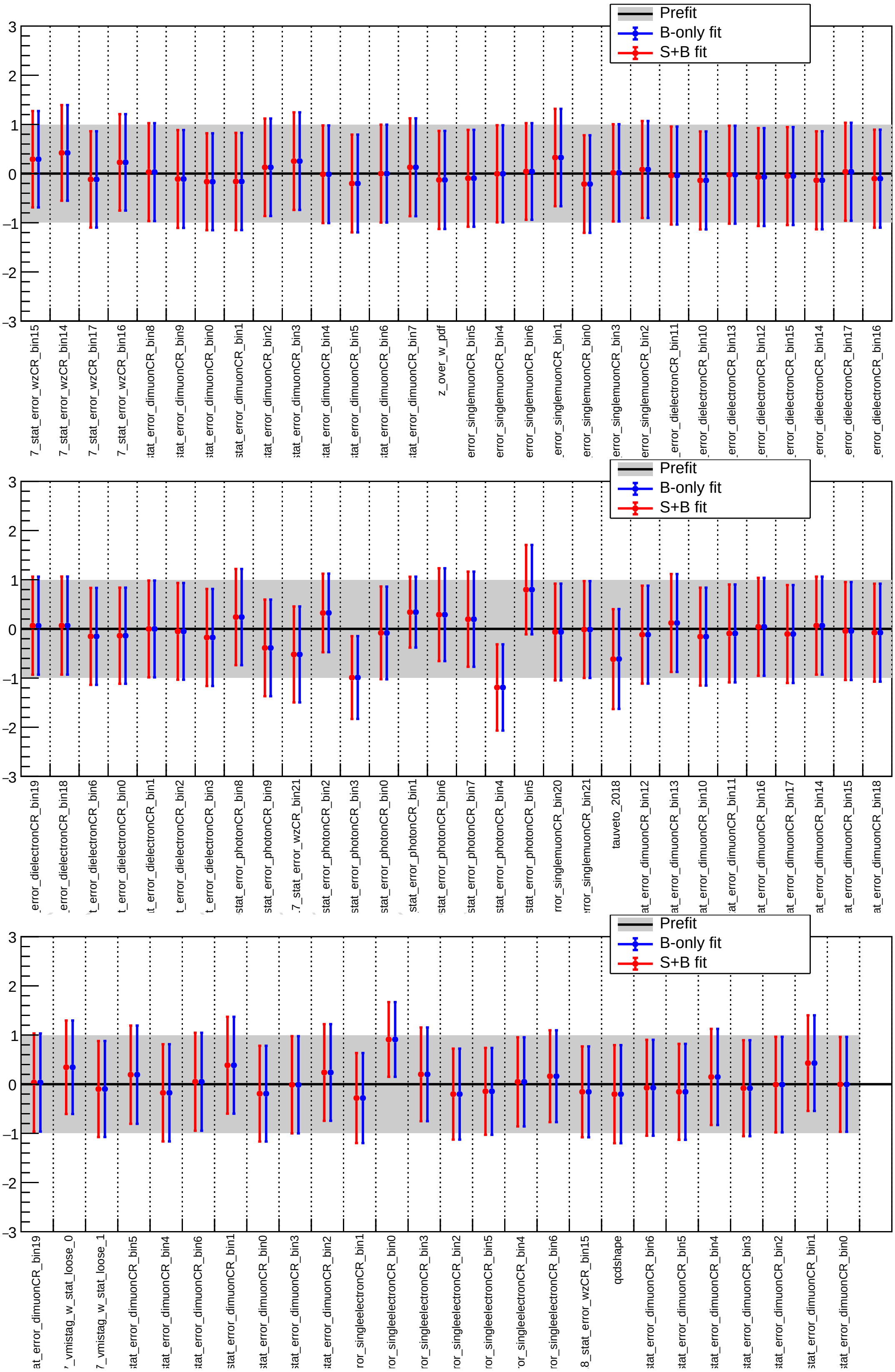

Figure 221: Continuation of Fig. 220

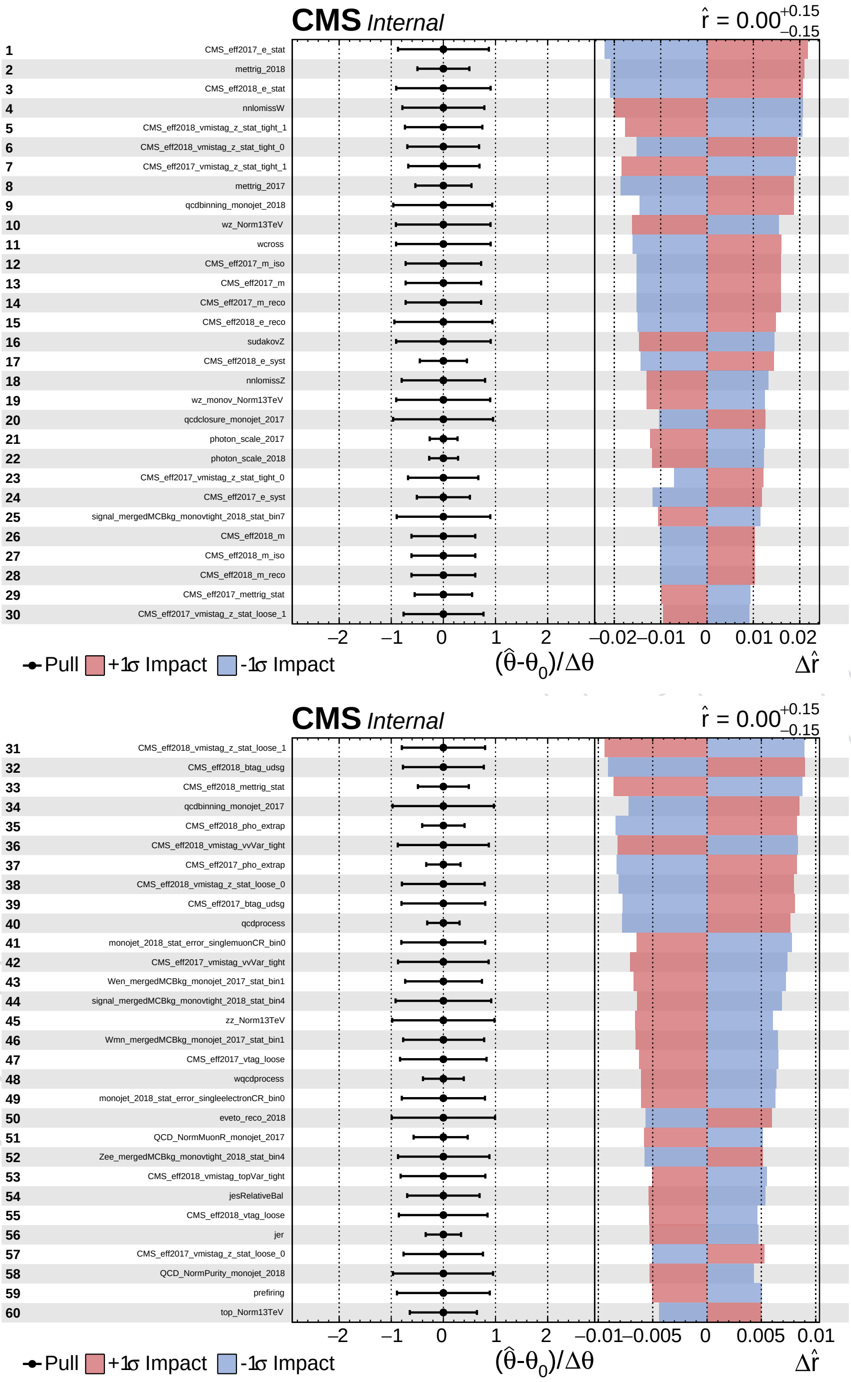

Figure 222: Nuisance parameter impacts for fit on the combined 2017+2018 mono-V+monojet Asimov dataset. The signal hypothesis is the invisible Higgs scenario with signal strength $\mu = 0$

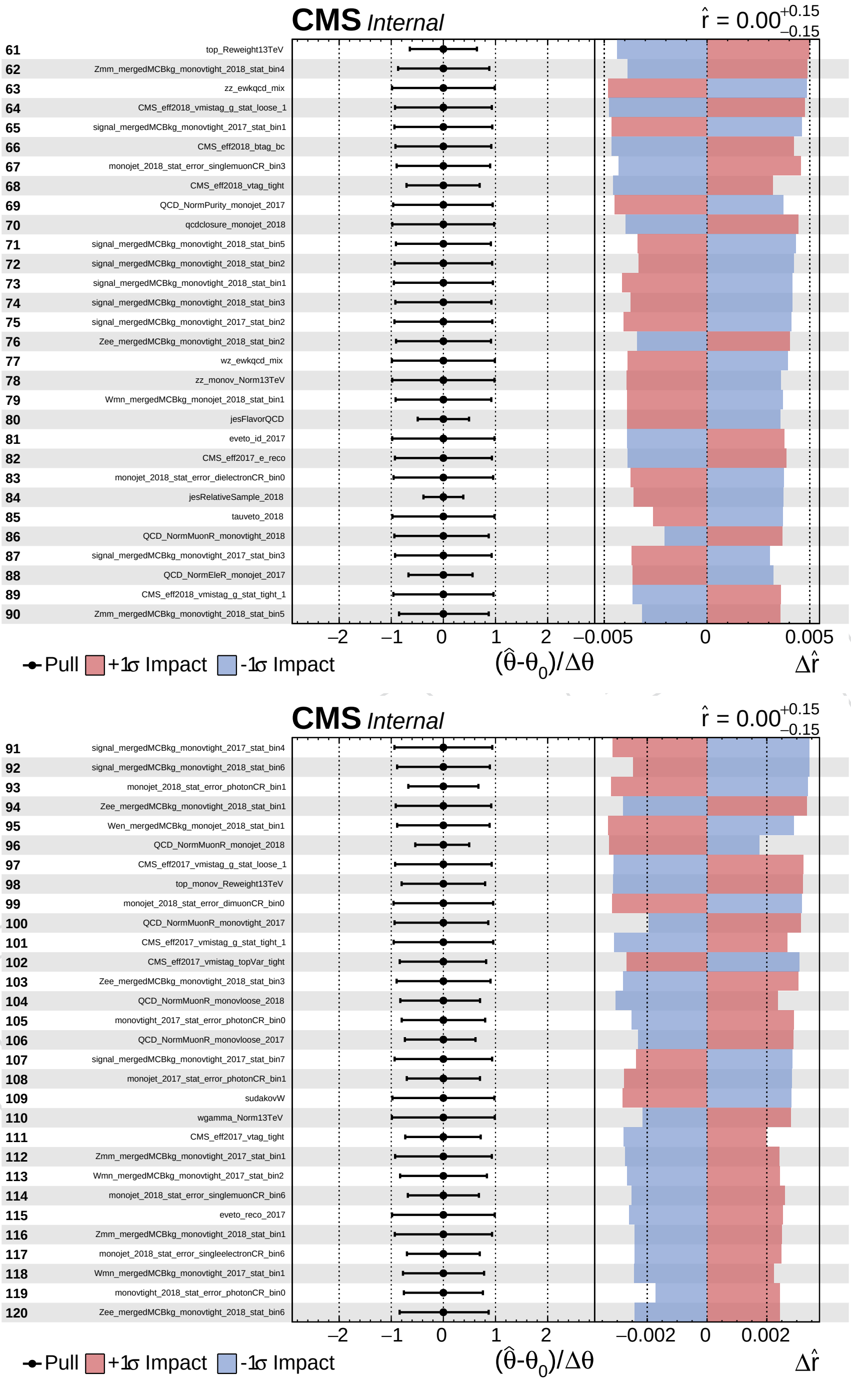

Figure 223: Continuation of Fig. 222.

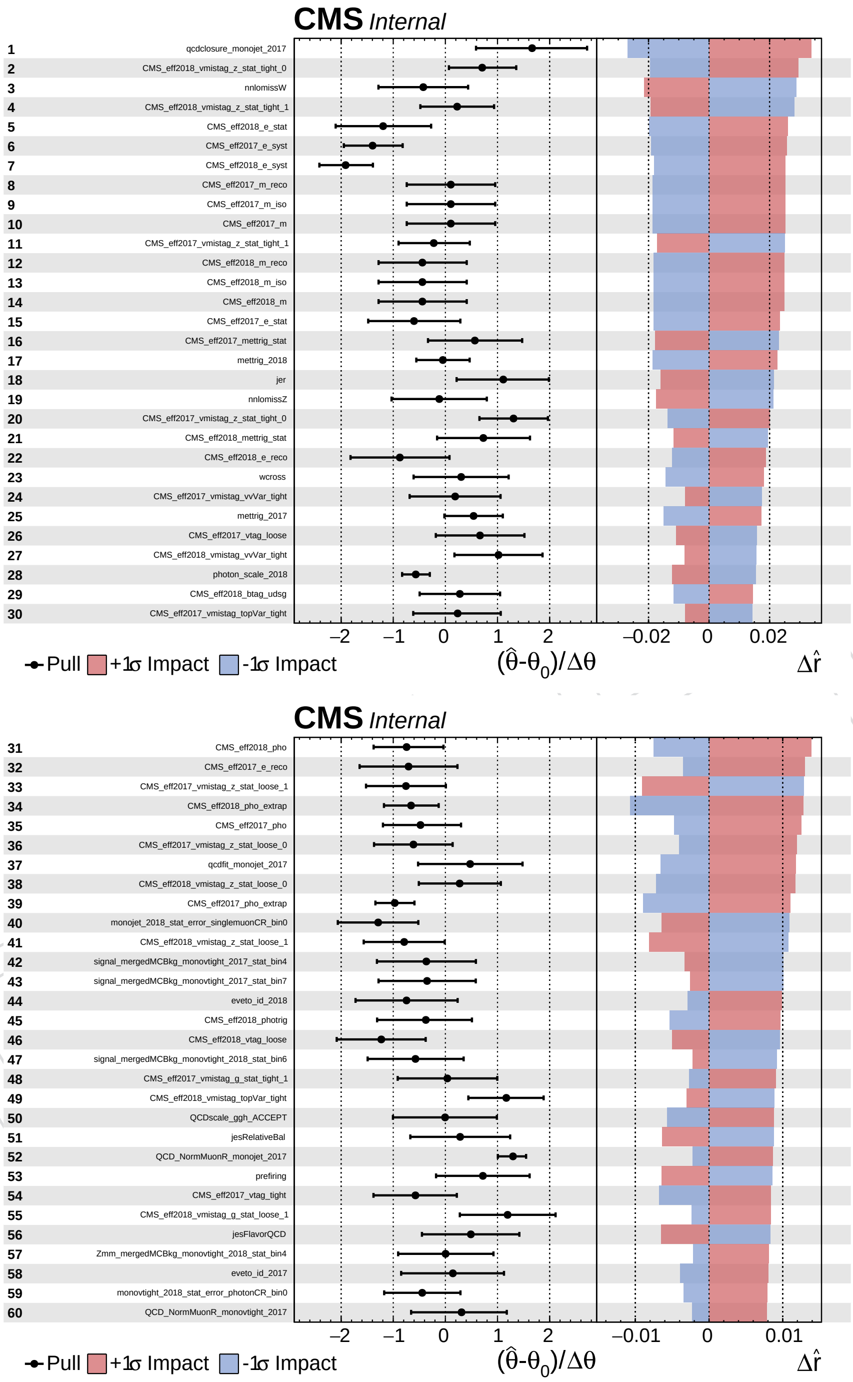

Figure 224: Nuisance parameter impacts for fit on the combined 2017+2018 mono-V+monojet dataset. The signal hypothesis is the invisible Higgs scenario.

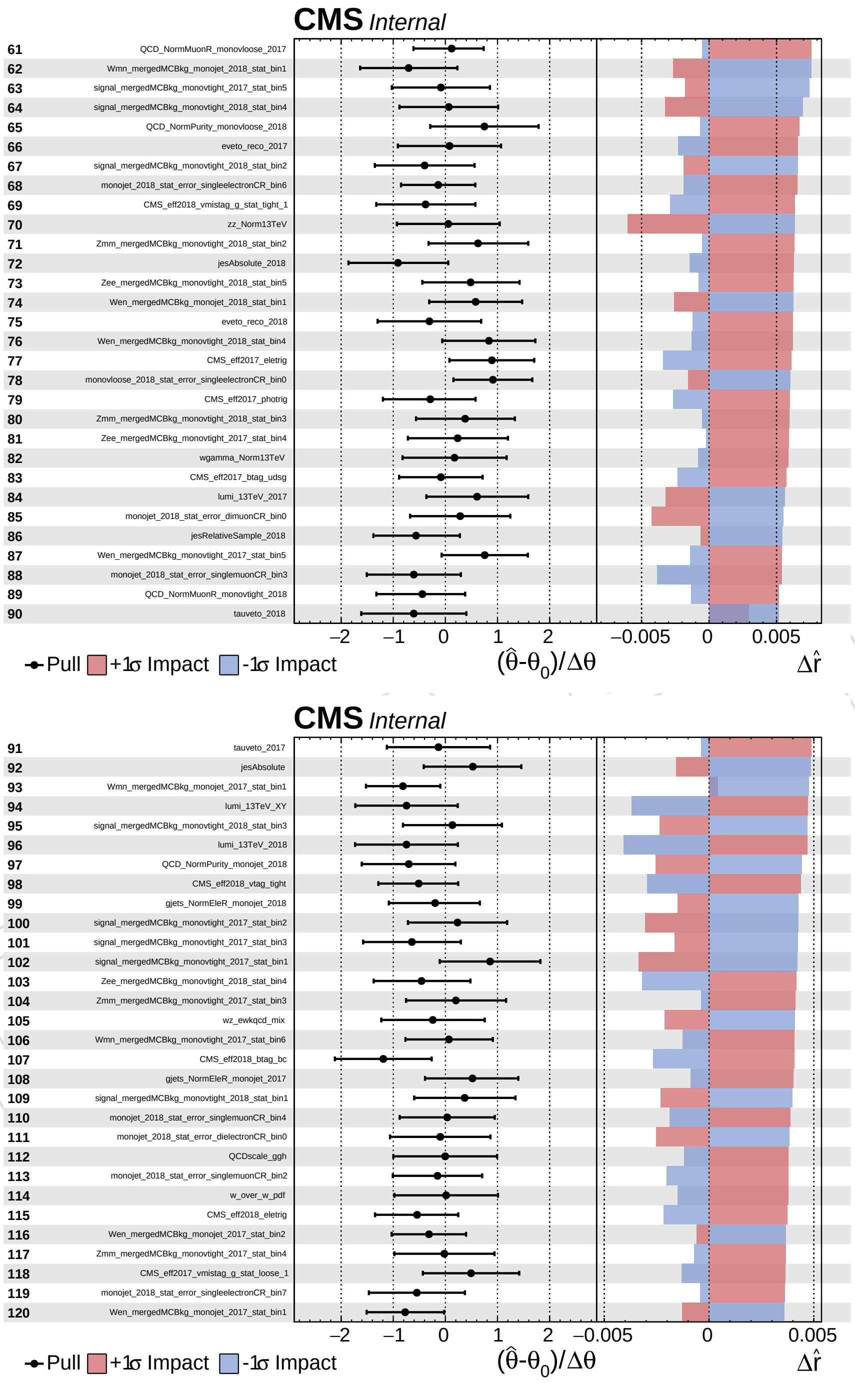

Figure 225: Continuation of Fig. 224.

G Signal samples

Data set name	Cross section (pb)	Order in QCD
ScalarFirstGenLeptoquarkToQNu_Mlq-1000_Ylq-0p1_TuneCP5_madgraph-pythia8	0.003673	LO
ScalarFirstGenLeptoquarkToQNu_Mlq-1000_Ylq-0p25_TuneCP5_madgraph-pythia8	0.007515	LO
ScalarFirstGenLeptoquarkToQNu_Mlq-1000_Ylq-0p5_TuneCP5_madgraph-pythia8	0.02173	LO
ScalarFirstGenLeptoquarkToQNu_Mlq-1250_Ylq-0p25_TuneCP5_madgraph-pythia8	0.001871	LO
ScalarFirstGenLeptoquarkToQNu_Mlq-1250_Ylq-0p5_TuneCP5_madgraph-pythia8	0.006132	LO
ScalarFirstGenLeptoquarkToQNu_Mlq-1250_Ylq-0p7_TuneCP5_madgraph-pythia8	0.01188	LO
ScalarFirstGenLeptoquarkToQNu_Mlq-1500_Ylq-0p5_TuneCP5_madgraph-pythia8	0.002064	LO
ScalarFirstGenLeptoquarkToQNu_Mlq-1500_Ylq-0p7_TuneCP5_madgraph-pythia8	0.004088	LO
ScalarFirstGenLeptoquarkToQNu_Mlq-1500_Ylq-1_TuneCP5_madgraph-pythia8	0.008728	LO
ScalarFirstGenLeptoquarkToQNu_Mlq-1750_Ylq-0p7_TuneCP5_madgraph-pythia8	0.001568	LO
ScalarFirstGenLeptoquarkToQNu_Mlq-1750_Ylq-1_TuneCP5_madgraph-pythia8	0.003424	LO
ScalarFirstGenLeptoquarkToQNu_Mlq-1750_Ylq-1p25_TuneCP5_madgraph-pythia8	0.005757	LO
ScalarFirstGenLeptoquarkToQNu_Mlq-2000_Ylq-1_TuneCP5_madgraph-pythia8	0.00148	LO
ScalarFirstGenLeptoquarkToQNu_Mlq-2000_Ylq-1p25_TuneCP5_madgraph-pythia8	0.00252	LO
ScalarFirstGenLeptoquarkToQNu_Mlq-2000_Ylq-1p5_TuneCP5_madgraph-pythia8	0.00406	LO
ScalarFirstGenLeptoquarkToQNu_Mlq-2250_Ylq-1p25_TuneCP5_madgraph-pythia8	0.00122	LO
ScalarFirstGenLeptoquarkToQNu_Mlq-2250_Ylq-1p5_TuneCP5_madgraph-pythia8	0.00202	LO
ScalarFirstGenLeptoquarkToQNu_Mlq-2500_Ylq-1p5_TuneCP5_madgraph-pythia8	0.00107	LO
ScalarFirstGenLeptoquarkToQNu_Mlq-500_Ylq-0p01_TuneCP5_madgraph-pythia8	0.2776	LO
ScalarFirstGenLeptoquarkToQNu_Mlq-500_Ylq-0p05_TuneCP5_madgraph-pythia8	0.2817	LO
ScalarFirstGenLeptoquarkToQNu_Mlq-750_Ylq-0p05_TuneCP5_madgraph-pythia8	0.02314	LO
ScalarFirstGenLeptoquarkToQNu_Mlq-750_Ylq-0p1_TuneCP5_madgraph-pythia8	0.02541	LO
ScalarFirstGenLeptoquarkToQNu_Mlq-750_Ylq-0p25_TuneCP5_madgraph-pythia8	0.04152	LO

Table 28: Signal samples used to model the leptoquark scenario.

Data set name	Cross section (pb)	Order in QCD
DMsimp_t-S3D_uR_JChiChi_Mphi-1000_Mchi-1_Lambda-1p0_TuneCUETP8M1_13TeV-madgraph_pythia8	0.08845	LO
DMsimp_t-S3D_uR_JChiChi_Mphi-1000_Mchi-200_Lambda-1p0_TuneCUETP8M1_13TeV-madgraph_pythia8	0.07656	LO
DMsimp_t-S3D_uR_JChiChi_Mphi-1000_Mchi-400_Lambda-1p0_TuneCUETP8M1_13TeV-madgraph_pythia8	0.04771	LO
DMsimp_t-S3D_uR_JChiChi_Mphi-1000_Mchi-600_Lambda-1p0_TuneCUETP8M1_13TeV-madgraph_pythia8	0.02813	LO
DMsimp_t-S3D_uR_JChiChi_Mphi-1000_Mchi-750_Lambda-1p0_TuneCUETP8M1_13TeV-madgraph_pythia8	0.01809	LO
DMsimp_t-S3D_uR_JChiChi_Mphi-1000_Mchi-900_Lambda-1p0_TuneCUETP8M1_13TeV-madgraph_pythia8	0.005617	LO
DMsimp_t-S3D_uR_JChiChi_Mphi-100_Mchi-1_Lambda-1p0_TuneCUETP8M1_13TeV-madgraph_pythia8	354.7	LO
DMsimp_t-S3D_uR_JChiChi_Mphi-1200_Mchi-1_Lambda-1p0_TuneCUETP8M1_13TeV-madgraph_pythia8	0.03858	LO
DMsimp_t-S3D_uR_JChiChi_Mphi-1200_Mchi-200_Lambda-1p0_TuneCUETP8M1_13TeV-madgraph_pythia8	0.03347	LO
DMsimp_t-S3D_uR_JChiChi_Mphi-1200_Mchi-400_Lambda-1p0_TuneCUETP8M1_13TeV-madgraph_pythia8	0.02149	LO
DMsimp_t-S3D_uR_JChiChi_Mphi-1200_Mchi-600_Lambda-1p0_TuneCUETP8M1_13TeV-madgraph_pythia8	0.01323	LO
DMsimp_t-S3D_uR_JChiChi_Mphi-1400_Mchi-1_Lambda-1p0_TuneCUETP8M1_13TeV-madgraph_pythia8	0.01703	LO
DMsimp_t-S3D_uR_JChiChi_Mphi-1400_Mchi-200_Lambda-1p0_TuneCUETP8M1_13TeV-madgraph_pythia8	0.0163	LO
DMsimp_t-S3D_uR_JChiChi_Mphi-1400_Mchi-350_Lambda-1p0_TuneCUETP8M1_13TeV-madgraph_pythia8	0.01184	LO
DMsimp_t-S3D_uR_JChiChi_Mphi-1400_Mchi-500_Lambda-1p0_TuneCUETP8M1_13TeV-madgraph_pythia8	0.008361	LO
DMsimp_t-S3D_uR_JChiChi_Mphi-1400_Mchi-650_Lambda-1p0_TuneCUETP8M1_13TeV-madgraph_pythia8	0.005887	LO
DMsimp_t-S3D_uR_JChiChi_Mphi-1400_Mchi-800_Lambda-1p0_TuneCUETP8M1_13TeV-madgraph_pythia8	0.004101	LO
DMsimp_t-S3D_uR_JChiChi_Mphi-1600_Mchi-1_Lambda-1p0_TuneCUETP8M1_13TeV-madgraph_pythia8	0.008651	LO
DMsimp_t-S3D_uR_JChiChi_Mphi-1600_Mchi-200_Lambda-1p0_TuneCUETP8M1_13TeV-madgraph_pythia8	0.008674	LO
DMsimp_t-S3D_uR_JChiChi_Mphi-1600_Mchi-350_Lambda-1p0_TuneCUETP8M1_13TeV-madgraph_pythia8	0.006336	LO
DMsimp_t-S3D_uR_JChiChi_Mphi-1600_Mchi-500_Lambda-1p0_TuneCUETP8M1_13TeV-madgraph_pythia8	0.004501	LO
DMsimp_t-S3D_uR_JChiChi_Mphi-1600_Mchi-650_Lambda-1p0_TuneCUETP8M1_13TeV-madgraph_pythia8	0.006586	LO
DMsimp_t-S3D_uR_JChiChi_Mphi-1600_Mchi-800_Lambda-1p0_TuneCUETP8M1_13TeV-madgraph_pythia8	0.00221	LO
DMsimp_t-S3D_uR_JChiChi_Mphi-1800_Mchi-1_Lambda-1p0_TuneCUETP8M1_13TeV-madgraph_pythia8	0.005062	LO
DMsimp_t-S3D_uR_JChiChi_Mphi-1800_Mchi-200_Lambda-1p0_TuneCUETP8M1_13TeV-madgraph_pythia8	0.005013	LO
DMsimp_t-S3D_uR_JChiChi_Mphi-1800_Mchi-350_Lambda-1p0_TuneCUETP8M1_13TeV-madgraph_pythia8	0.003646	LO
DMsimp_t-S3D_uR_JChiChi_Mphi-1800_Mchi-500_Lambda-1p0_TuneCUETP8M1_13TeV-madgraph_pythia8	0.002565	LO
DMsimp_t-S3D_uR_JChiChi_Mphi-1800_Mchi-650_Lambda-1p0_TuneCUETP8M1_13TeV-madgraph_pythia8	0.001792	LO
DMsimp_t-S3D_uR_JChiChi_Mphi-2000_Mchi-1_Lambda-1p0_TuneCUETP8M1_13TeV-madgraph_pythia8	0.002823	LO
DMsimp_t-S3D_uR_JChiChi_Mphi-2000_Mchi-200_Lambda-1p0_TuneCUETP8M1_13TeV-madgraph_pythia8	0.003096	LO
DMsimp_t-S3D_uR_JChiChi_Mphi-2000_Mchi-350_Lambda-1p0_TuneCUETP8M1_13TeV-madgraph_pythia8	0.002218	LO
DMsimp_t-S3D_uR_JChiChi_Mphi-2000_Mchi-500_Lambda-1p0_TuneCUETP8M1_13TeV-madgraph_pythia8	0.001543	LO
DMsimp_t-S3D_uR_JChiChi_Mphi-2200_Mchi-1_Lambda-1p0_TuneCUETP8M1_13TeV-madgraph_pythia8	0.001719	LO
DMsimp_t-S3D_uR_JChiChi_Mphi-2200_Mchi-200_Lambda-1p0_TuneCUETP8M1_13TeV-madgraph_pythia8	0.002019	LO
DMsimp_t-S3D_uR_JChiChi_Mphi-2200_Mchi-350_Lambda-1p0_TuneCUETP8M1_13TeV-madgraph_pythia8	0.001435	LO
DMsimp_t-S3D_uR_JChiChi_Mphi-300_Mchi-1_Lambda-1p0_TuneCUETP8M1_13TeV-madgraph_pythia8	12.07	LO
DMsimp_t-S3D_uR_JChiChi_Mphi-300_Mchi-200_Lambda-1p0_TuneCUETP8M1_13TeV-madgraph_pythia8	2.55	LO
DMsimp_t-S3D_uR_JChiChi_Mphi-500_Mchi-1_Lambda-1p0_TuneCUETP8M1_13TeV-madgraph_pythia8	1.89	LO
DMsimp_t-S3D_uR_JChiChi_Mphi-500_Mchi-200_Lambda-1p0_TuneCUETP8M1_13TeV-madgraph_pythia8	1.214	LO
DMsimp_t-S3D_uR_JChiChi_Mphi-500_Mchi-400_Lambda-1p0_TuneCUETP8M1_13TeV-madgraph_pythia8	0.2628	LO
DMsimp_t-S3D_uR_JChiChi_Mphi-750_Mchi-1_Lambda-1p0_TuneCUETP8M1_13TeV-madgraph_pythia8	0.3372	LO
DMsimp_t-S3D_uR_JChiChi_Mphi-750_Mchi-200_Lambda-1p0_TuneCUETP8M1_13TeV-madgraph_pythia8	0.2633	LO
DMsimp_t-S3D_uR_JChiChi_Mphi-750_Mchi-400_Lambda-1p0_TuneCUETP8M1_13TeV-madgraph_pythia8	0.149	LO
DMsimp_t-S3D_uR_JChiChi_Mphi-750_Mchi-550_Lambda-1p0_TuneCUETP8M1_13TeV-madgraph_pythia8	0.08558	LO
DMsimp_t-S3D_uR_JChiChi_Mphi-750_Mchi-700_Lambda-1p0_TuneCUETP8M1_13TeV-madgraph_pythia8	0.03231	LO

Table 29: Signal sampels used to model the t-channel scenario. These samples include production mechanisms with zero or one on-shell mediators.

Data set name	Cross section (pb)	Orde
DMsimp_t-S3D_uR_PhiPhiToJJChiChi_Mphi-1000_Mchi-1_Lambda-1p0_TuneCUETP8M1_13TeV-madgraph_pythia8	0.007799	
DMsimp_t-S3D_uR_PhiPhiToJJChiChi_Mphi-1000_Mchi-200_Lambda-1p0_TuneCUETP8M1_13TeV-madgraph_pythia8	0.007163	
DMsimp_t-S3D_uR_PhiPhiToJJChiChi_Mphi-1000_Mchi-400_Lambda-1p0_TuneCUETP8M1_13TeV-madgraph_pythia8	0.005943	
DMsimp_t-S3D_uR_PhiPhiToJJChiChi_Mphi-1000_Mchi-600_Lambda-1p0_TuneCUETP8M1_13TeV-madgraph_pythia8	0.004816	
DMsimp_t-S3D_uR_PhiPhiToJJChiChi_Mphi-1000_Mchi-750_Lambda-1p0_TuneCUETP8M1_13TeV-madgraph_pythia8	0.003998	
DMsimp_t-S3D_uR_PhiPhiToJJChiChi_Mphi-1000_Mchi-900_Lambda-1p0_TuneCUETP8M1_13TeV-madgraph_pythia8	0.002277	
DMsimp_t-S3D_uR_PhiPhiToJJChiChi_Mphi-100_Mchi-1_Lambda-1p0_TuneCUETP8M1_13TeV-madgraph_pythia8	539.9	
DMsimp_t-S3D_uR_PhiPhiToJJChiChi_Mphi-100_Mchi-75_Lambda-1p0_TuneCUETP8M1_13TeV-madgraph_pythia8	34.56	
DMsimp_t-S3D_uR_PhiPhiToJJChiChi_Mphi-1200_Mchi-1_Lambda-1p0_TuneCUETP8M1_13TeV-madgraph_pythia8	0.002139	
DMsimp_t-S3D_uR_PhiPhiToJJChiChi_Mphi-1200_Mchi-200_Lambda-1p0_TuneCUETP8M1_13TeV-madgraph_pythia8	0.002006	
DMsimp_t-S3D_uR_PhiPhiToJJChiChi_Mphi-1200_Mchi-400_Lambda-1p0_TuneCUETP8M1_13TeV-madgraph_pythia8	0.001724	
DMsimp_t-S3D_uR_PhiPhiToJJChiChi_Mphi-1200_Mchi-600_Lambda-1p0_TuneCUETP8M1_13TeV-madgraph_pythia8	0.001432	
DMsimp_t-S3D_uR_PhiPhiToJJChiChi_Mphi-1200_Mchi-750_Lambda-1p0_TuneCUETP8M1_13TeV-madgraph_pythia8	0.001239	
DMsimp_t-S3D_uR_PhiPhiToJJChiChi_Mphi-1200_Mchi-900_Lambda-1p0_TuneCUETP8M1_13TeV-madgraph_pythia8	0.001062	
DMsimp_t-S3D_uR_PhiPhiToJJChiChi_Mphi-1400_Mchi-1_Lambda-1p0_TuneCUETP8M1_13TeV-madgraph_pythia8	0.0006457	
DMsimp_t-S3D_uR_PhiPhiToJJChiChi_Mphi-1400_Mchi-200_Lambda-1p0_TuneCUETP8M1_13TeV-madgraph_pythia8	0.000615	
DMsimp_t-S3D_uR_PhiPhiToJJChiChi_Mphi-1400_Mchi-350_Lambda-1p0_TuneCUETP8M1_13TeV-madgraph_pythia8	0.0005629	
DMsimp_t-S3D_uR_PhiPhiToJJChiChi_Mphi-1400_Mchi-500_Lambda-1p0_TuneCUETP8M1_13TeV-madgraph_pythia8	0.0005018	
DMsimp_t-S3D_uR_PhiPhiToJJChiChi_Mphi-1400_Mchi-650_Lambda-1p0_TuneCUETP8M1_13TeV-madgraph_pythia8	0.0004413	
DMsimp_t-S3D_uR_PhiPhiToJJChiChi_Mphi-1400_Mchi-800_Lambda-1p0_TuneCUETP8M1_13TeV-madgraph_pythia8	0.0003876	
DMsimp_t-S3D_uR_PhiPhiToJJChiChi_Mphi-1600_Mchi-1_Lambda-1p0_TuneCUETP8M1_13TeV-madgraph_pythia8	0.000209	
DMsimp_t-S3D_uR_PhiPhiToJJChiChi_Mphi-1600_Mchi-200_Lambda-1p0_TuneCUETP8M1_13TeV-madgraph_pythia8	0.0002013	
DMsimp_t-S3D_uR_PhiPhiToJJChiChi_Mphi-1600_Mchi-350_Lambda-1p0_TuneCUETP8M1_13TeV-madgraph_pythia8	0.000187	
DMsimp_t-S3D_uR_PhiPhiToJJChiChi_Mphi-1600_Mchi-500_Lambda-1p0_TuneCUETP8M1_13TeV-madgraph_pythia8	0.0001692	
DMsimp_t-S3D_uR_PhiPhiToJJChiChi_Mphi-1600_Mchi-650_Lambda-1p0_TuneCUETP8M1_13TeV-madgraph_pythia8	0.0001513	
DMsimp_t-S3D_uR_PhiPhiToJJChiChi_Mphi-1600_Mchi-800_Lambda-1p0_TuneCUETP8M1_13TeV-madgraph_pythia8	0.000134	
DMsimp_t-S3D_uR_PhiPhiToJJChiChi_Mphi-1800_Mchi-1_Lambda-1p0_TuneCUETP8M1_13TeV-madgraph_pythia8	7.129e-05	
DMsimp_t-S3D_uR_PhiPhiToJJChiChi_Mphi-1800_Mchi-200_Lambda-1p0_TuneCUETP8M1_13TeV-madgraph_pythia8	6.898e-05	
DMsimp_t-S3D_uR_PhiPhiToJJChiChi_Mphi-1800_Mchi-350_Lambda-1p0_TuneCUETP8M1_13TeV-madgraph_pythia8	6.496e-05	
DMsimp_t-S3D_uR_PhiPhiToJJChiChi_Mphi-1800_Mchi-500_Lambda-1p0_TuneCUETP8M1_13TeV-madgraph_pythia8	5.963e-05	
DMsimp_t-S3D_uR_PhiPhiToJJChiChi_Mphi-1800_Mchi-650_Lambda-1p0_TuneCUETP8M1_13TeV-madgraph_pythia8	5.388e-05	
DMsimp_t-S3D_uR_PhiPhiToJJChiChi_Mphi-2000_Mchi-1_Lambda-1p0_TuneCUETP8M1_13TeV-madgraph_pythia8	2.523e-05	
DMsimp_t-S3D_uR_PhiPhiToJJChiChi_Mphi-2000_Mchi-200_Lambda-1p0_TuneCUETP8M1_13TeV-madgraph_pythia8	2.457e-05	
DMsimp_t-S3D_uR_PhiPhiToJJChiChi_Mphi-2000_Mchi-350_Lambda-1p0_TuneCUETP8M1_13TeV-madgraph_pythia8	2.33e-05	
DMsimp_t-S3D_uR_PhiPhiToJJChiChi_Mphi-2000_Mchi-500_Lambda-1p0_TuneCUETP8M1_13TeV-madgraph_pythia8	2.164e-05	
DMsimp_t-S3D_uR_PhiPhiToJJChiChi_Mphi-2200_Mchi-1_Lambda-1p0_TuneCUETP8M1_13TeV-madgraph_pythia8	9.246e-06	
DMsimp_t-S3D_uR_PhiPhiToJJChiChi_Mphi-2200_Mchi-200_Lambda-1p0_TuneCUETP8M1_13TeV-madgraph_pythia8	9.025e-06	
DMsimp_t-S3D_uR_PhiPhiToJJChiChi_Mphi-2200_Mchi-350_Lambda-1p0_TuneCUETP8M1_13TeV-madgraph_pythia8	8.635e-06	
DMsimp_t-S3D_uR_PhiPhiToJJChiChi_Mphi-300_Mchi-1_Lambda-1p0_TuneCUETP8M1_13TeV-madgraph_pythia8	5.411	
DMsimp_t-S3D_uR_PhiPhiToJJChiChi_Mphi-300_Mchi-200_Lambda-1p0_TuneCUETP8M1_13TeV-madgraph_pythia8	2.668	
DMsimp_t-S3D_uR_PhiPhiToJJChiChi_Mphi-500_Mchi-1_Lambda-1p0_TuneCUETP8M1_13TeV-madgraph_pythia8	0.4683	
DMsimp_t-S3D_uR_PhiPhiToJJChiChi_Mphi-500_Mchi-200_Lambda-1p0_TuneCUETP8M1_13TeV-madgraph_pythia8	0.3763	
DMsimp_t-S3D_uR_PhiPhiToJJChiChi_Mphi-500_Mchi-400_Lambda-1p0_TuneCUETP8M1_13TeV-madgraph_pythia8	0.1863	
DMsimp_t-S3D_uR_PhiPhiToJJChiChi_Mphi-750_Mchi-1_Lambda-1p0_TuneCUETP8M1_13TeV-madgraph_pythia8	0.04884	
DMsimp_t-S3D_uR_PhiPhiToJJChiChi_Mphi-750_Mchi-200_Lambda-1p0_TuneCUETP8M1_13TeV-madgraph_pythia8	0.04277	
DMsimp_t-S3D_uR_PhiPhiToJJChiChi_Mphi-750_Mchi-400_Lambda-1p0_TuneCUETP8M1_13TeV-madgraph_pythia8	0.03356	
DMsimp_t-S3D_uR_PhiPhiToJJChiChi_Mphi-750_Mchi-550_Lambda-1p0_TuneCUETP8M1_13TeV-madgraph_pythia8	0.02651	
DMsimp_t-S3D_uR_PhiPhiToJJChiChi_Mphi-750_Mchi-700_Lambda-1p0_TuneCUETP8M1_13TeV-madgraph_pythia8	0.01642	

Table 30: Signal sampels used to model the t-channel scenario. These samples include production mechanisms with two on-shell mediators.

Data set name	Cross section (pb)	Order in QCD
Scalar_MonoJ_LO_Mphi-10_Mchi-1_gSM-1p0_gDM-1p0_TuneCP5-madgraph-pythia8	2.183	LO
Scalar_MonoJ_LO_Mphi-10_Mchi-4_gSM-1p0_gDM-1p0_TuneCP5-madgraph-pythia8	2.205	LO
Scalar_MonoJ_LO_Mphi-10_Mchi-6_gSM-1p0_gDM-1p0_TuneCP5-madgraph-pythia8	0.1283	LO
Scalar_MonoJ_LO_Mphi-50_Mchi-1_gSM-1p0_gDM-1p0_TuneCP5-madgraph-pythia8	1.901	LO
Scalar_MonoJ_LO_Mphi-50_Mchi-20_gSM-1p0_gDM-1p0_TuneCP5-madgraph-pythia8	1.939	LO
Scalar_MonoJ_LO_Mphi-50_Mchi-22_gSM-1p0_gDM-1p0_TuneCP5-madgraph-pythia8	1.944	LO
Scalar_MonoJ_LO_Mphi-50_Mchi-28_gSM-1p0_gDM-1p0_TuneCP5-madgraph-pythia8	0.05681	LO
Scalar_MonoJ_LO_Mphi-100_Mchi-1_gSM-1p0_gDM-1p0_TuneCP5-madgraph-pythia8	1.464	LO
Scalar_MonoJ_LO_Mphi-100_Mchi-40_gSM-1p0_gDM-1p0_TuneCP5-madgraph-pythia8	1.494	LO
Scalar_MonoJ_LO_Mphi-100_Mchi-45_gSM-1p0_gDM-1p0_TuneCP5-madgraph-pythia8	1.503	LO
Scalar_MonoJ_LO_Mphi-100_Mchi-55_gSM-1p0_gDM-1p0_TuneCP5-madgraph-pythia8	0.03114	LO
Scalar_MonoJ_LO_Mphi-200_Mchi-1_gSM-1p0_gDM-1p0_TuneCP5-madgraph-pythia8	0.8415	LO
Scalar_MonoJ_LO_Mphi-300_Mchi-1_gSM-1p0_gDM-1p0_TuneCP5-madgraph-pythia8	0.5766	LO
Scalar_MonoJ_LO_Mphi-350_Mchi-1_gSM-1p0_gDM-1p0_TuneCP5-madgraph-pythia8	0.5731	LO
Scalar_MonoJ_LO_Mphi-400_Mchi-1_gSM-1p0_gDM-1p0_TuneCP5-madgraph-pythia8	0.4599	LO
Scalar_MonoJ_LO_Mphi-450_Mchi-1_gSM-1p0_gDM-1p0_TuneCP5-madgraph-pythia8	0.3114	LO
Scalar_MonoJ_LO_Mphi-500_Mchi-150_gSM-1p0_gDM-1p0_TuneCP5-madgraph-pythia8	0.1543	LO
Scalar_MonoJ_LO_Mphi-500_Mchi-1_gSM-1p0_gDM-1p0_TuneCP5-madgraph-pythia8	0.2064	LO
Scalar_MonoJ_LO_Mphi-500_Mchi-200_gSM-1p0_gDM-1p0_TuneCP5-madgraph-pythia8	0.09118	LO
Scalar_MonoJ_LO_Mphi-500_Mchi-225_gSM-1p0_gDM-1p0_TuneCP5-madgraph-pythia8	0.04418	LO
Scalar_MonoJ_LO_Mphi-500_Mchi-275_gSM-1p0_gDM-1p0_TuneCP5-madgraph-pythia8	0.001084	LO
Scalar_MonoJ_LO_Mphi-500_Mchi-50_gSM-1p0_gDM-1p0_TuneCP5-madgraph-pythia8	0.2016	LO
Scalar_MonoJ_LO_Mphi-600_Mchi-1_gSM-1p0_gDM-1p0_TuneCP5-madgraph-pythia8	0.09364	LO
Scalar_MonoJ_LO_Mphi-700_Mchi-1_gSM-1p0_gDM-1p0_TuneCP5-madgraph-pythia8	0.04571	LO
Scalar_MonoJ_LO_Mphi-800_Mchi-1_gSM-1p0_gDM-1p0_TuneCP5-madgraph-pythia8	0.02372	LO
Pseudoscalar_MonoJ_LO_Mphi-10_Mchi-1_gSM-1p0_gDM-1p0_TuneCP5-madgraph-pythia8	4.941	LO
Pseudoscalar_MonoJ_LO_Mphi-10_Mchi-4_gSM-1p0_gDM-1p0_TuneCP5-madgraph-pythia8	4.94	LO
Pseudoscalar_MonoJ_LO_Mphi-10_Mchi-6_gSM-1p0_gDM-1p0_TuneCP5-madgraph-pythia8	0.3936	LO
Pseudoscalar_MonoJ_LO_Mphi-50_Mchi-1_gSM-1p0_gDM-1p0_TuneCP5-madgraph-pythia8	4.316	LO
Pseudoscalar_MonoJ_LO_Mphi-50_Mchi-20_gSM-1p0_gDM-1p0_TuneCP5-madgraph-pythia8	4.322	LO
Pseudoscalar_MonoJ_LO_Mphi-50_Mchi-22_gSM-1p0_gDM-1p0_TuneCP5-madgraph-pythia8	4.308	LO
Pseudoscalar_MonoJ_LO_Mphi-50_Mchi-28_gSM-1p0_gDM-1p0_TuneCP5-madgraph-pythia8	0.2407	LO
Pseudoscalar_MonoJ_LO_Mphi-100_Mchi-1_gSM-1p0_gDM-1p0_TuneCP5-madgraph-pythia8	3.366	LO
Pseudoscalar_MonoJ_LO_Mphi-100_Mchi-40_gSM-1p0_gDM-1p0_TuneCP5-madgraph-pythia8	3.369	LO
Pseudoscalar_MonoJ_LO_Mphi-100_Mchi-45_gSM-1p0_gDM-1p0_TuneCP5-madgraph-pythia8	3.362	LO
Pseudoscalar_MonoJ_LO_Mphi-100_Mchi-55_gSM-1p0_gDM-1p0_TuneCP5-madgraph-pythia8	0.1616	LO
Pseudoscalar_MonoJ_LO_Mphi-200_Mchi-1_gSM-1p0_gDM-1p0_TuneCP5-madgraph-pythia8	2.062	LO
Pseudoscalar_MonoJ_LO_Mphi-300_Mchi-1_gSM-1p0_gDM-1p0_TuneCP5-madgraph-pythia8	1.721	LO
Pseudoscalar_MonoJ_LO_Mphi-350_Mchi-1_gSM-1p0_gDM-1p0_TuneCP5-madgraph-pythia8	1.932	LO
Pseudoscalar_MonoJ_LO_Mphi-400_Mchi-1_gSM-1p0_gDM-1p0_TuneCP5-madgraph-pythia8	0.9317	LO
Pseudoscalar_MonoJ_LO_Mphi-450_Mchi-1_gSM-1p0_gDM-1p0_TuneCP5-madgraph-pythia8	0.5286	LO
Pseudoscalar_MonoJ_LO_Mphi-500_Mchi-150_gSM-1p0_gDM-1p0_TuneCP5-madgraph-pythia8	0.2764	LO
Pseudoscalar_MonoJ_LO_Mphi-500_Mchi-1_gSM-1p0_gDM-1p0_TuneCP5-madgraph-pythia8	0.3205	LO
Pseudoscalar_MonoJ_LO_Mphi-500_Mchi-200_gSM-1p0_gDM-1p0_TuneCP5-madgraph-pythia8	0.2214	LO
Pseudoscalar_MonoJ_LO_Mphi-500_Mchi-225_gSM-1p0_gDM-1p0_TuneCP5-madgraph-pythia8	0.1709	LO
Pseudoscalar_MonoJ_LO_Mphi-500_Mchi-275_gSM-1p0_gDM-1p0_TuneCP5-madgraph-pythia8	0.007509	LO
Pseudoscalar_MonoJ_LO_Mphi-500_Mchi-50_gSM-1p0_gDM-1p0_TuneCP5-madgraph-pythia8	0.3159	LO
Pseudoscalar_MonoJ_LO_Mphi-600_Mchi-1_gSM-1p0_gDM-1p0_TuneCP5-madgraph-pythia8	0.1338	LO
Pseudoscalar_MonoJ_LO_Mphi-700_Mchi-1_gSM-1p0_gDM-1p0_TuneCP5-madgraph-pythia8	0.06279	LO
Pseudoscalar_MonoJ_LO_Mphi-800_Mchi-1_gSM-1p0_gDM-1p0_TuneCP5-madgraph-pythia8	0.03192	LO

Table 31: Signal samples used to model the scenario with a color-neutral spin-0 mediator in the monojet topology.

Data set name	Cross section (pb)	Order in QCD
Scalar_MonoV_LO_Mphi-10_Mchi-1_gSM-1p0_gDM-1p0_TuneCP5-madgraph-pythia8	0.02423	LO
Scalar_MonoV_LO_Mphi-10_Mchi-6_gSM-1p0_gDM-1p0_TuneCP5-madgraph-pythia8	0.001724	LO
Scalar_MonoV_LO_Mphi-50_Mchi-1_gSM-1p0_gDM-1p0_TuneCP5-madgraph-pythia8	0.02391	LO
Scalar_MonoV_LO_Mphi-50_Mchi-20_gSM-1p0_gDM-1p0_TuneCP5-madgraph-pythia8	0.02428	LO
Scalar_MonoV_LO_Mphi-50_Mchi-22_gSM-1p0_gDM-1p0_TuneCP5-madgraph-pythia8	0.02441	LO
Scalar_MonoV_LO_Mphi-50_Mchi-28_gSM-1p0_gDM-1p0_TuneCP5-madgraph-pythia8	0.0008642	LO
Scalar_MonoV_LO_Mphi-100_Mchi-1_gSM-1p0_gDM-1p0_TuneCP5-madgraph-pythia8	0.02196	LO
Scalar_MonoV_LO_Mphi-100_Mchi-40_gSM-1p0_gDM-1p0_TuneCP5-madgraph-pythia8	0.02251	LO
Scalar_MonoV_LO_Mphi-100_Mchi-45_gSM-1p0_gDM-1p0_TuneCP5-madgraph-pythia8	0.0227	LO
Scalar_MonoV_LO_Mphi-100_Mchi-55_gSM-1p0_gDM-1p0_TuneCP5-madgraph-pythia8	0.0005077	LO
Scalar_MonoV_LO_Mphi-200_Mchi-1_gSM-1p0_gDM-1p0_TuneCP5-madgraph-pythia8	0.01593	LO
Scalar_MonoV_LO_Mphi-300_Mchi-1_gSM-1p0_gDM-1p0_TuneCP5-madgraph-pythia8	0.009997	LO
Scalar_MonoV_LO_Mphi-350_Mchi-1_gSM-1p0_gDM-1p0_TuneCP5-madgraph-pythia8	0.007678	LO
Scalar_MonoV_LO_Mphi-400_Mchi-1_gSM-1p0_gDM-1p0_TuneCP5-madgraph-pythia8	0.004824	LO
Scalar_MonoV_LO_Mphi-450_Mchi-1_gSM-1p0_gDM-1p0_TuneCP5-madgraph-pythia8	0.003063	LO
Scalar_MonoV_LO_Mphi-500_Mchi-150_gSM-1p0_gDM-1p0_TuneCP5-madgraph-pythia8	0.00151	LO
Scalar_MonoV_LO_Mphi-500_Mchi-1_gSM-1p0_gDM-1p0_TuneCP5-madgraph-pythia8	0.002041	LO
Scalar_MonoV_LO_Mphi-500_Mchi-200_gSM-1p0_gDM-1p0_TuneCP5-madgraph-pythia8	0.0008999	LO
Scalar_MonoV_LO_Mphi-500_Mchi-225_gSM-1p0_gDM-1p0_TuneCP5-madgraph-pythia8	0.0004438	LO
Scalar_MonoV_LO_Mphi-500_Mchi-275_gSM-1p0_gDM-1p0_TuneCP5-madgraph-pythia8	1.379e-05	LO
Scalar_MonoV_LO_Mphi-500_Mchi-50_gSM-1p0_gDM-1p0_TuneCP5-madgraph-pythia8	0.001995	LO
Scalar_MonoV_LO_Mphi-600_Mchi-1_gSM-1p0_gDM-1p0_TuneCP5-madgraph-pythia8	0.001002	LO
Scalar_MonoV_LO_Mphi-700_Mchi-1_gSM-1p0_gDM-1p0_TuneCP5-madgraph-pythia8	0.0005454	LO
Scalar_MonoV_LO_Mphi-800_Mchi-1_gSM-1p0_gDM-1p0_TuneCP5-madgraph-pythia8	0.0003139	LO
Pseudoscalar_MonoV_LO_Mphi-10_Mchi-1_gSM-1p0_gDM-1p0_TuneCP5-madgraph-pythia8	0.0275	LO
Pseudoscalar_MonoV_LO_Mphi-10_Mchi-4_gSM-1p0_gDM-1p0_TuneCP5-madgraph-pythia8	0.02173	LO
Pseudoscalar_MonoV_LO_Mphi-10_Mchi-6_gSM-1p0_gDM-1p0_TuneCP5-madgraph-pythia8	0.001938	LO
Pseudoscalar_MonoV_LO_Mphi-50_Mchi-1_gSM-1p0_gDM-1p0_TuneCP5-madgraph-pythia8	0.02713	LO
Pseudoscalar_MonoV_LO_Mphi-50_Mchi-20_gSM-1p0_gDM-1p0_TuneCP5-madgraph-pythia8	0.02748	LO
Pseudoscalar_MonoV_LO_Mphi-50_Mchi-22_gSM-1p0_gDM-1p0_TuneCP5-madgraph-pythia8	0.02766	LO
Pseudoscalar_MonoV_LO_Mphi-50_Mchi-28_gSM-1p0_gDM-1p0_TuneCP5-madgraph-pythia8	0.0009662	LO
Pseudoscalar_MonoV_LO_Mphi-100_Mchi-1_gSM-1p0_gDM-1p0_TuneCP5-madgraph-pythia8	0.02475	LO
Pseudoscalar_MonoV_LO_Mphi-100_Mchi-40_gSM-1p0_gDM-1p0_TuneCP5-madgraph-pythia8	0.02547	LO
Pseudoscalar_MonoV_LO_Mphi-100_Mchi-45_gSM-1p0_gDM-1p0_TuneCP5-madgraph-pythia8	0.02559	LO
Pseudoscalar_MonoV_LO_Mphi-100_Mchi-55_gSM-1p0_gDM-1p0_TuneCP5-madgraph-pythia8	0.0005582	LO
Pseudoscalar_MonoV_LO_Mphi-200_Mchi-1_gSM-1p0_gDM-1p0_TuneCP5-madgraph-pythia8	0.01771	LO
Pseudoscalar_MonoV_LO_Mphi-300_Mchi-1_gSM-1p0_gDM-1p0_TuneCP5-madgraph-pythia8	0.01101	LO
Pseudoscalar_MonoV_LO_Mphi-350_Mchi-1_gSM-1p0_gDM-1p0_TuneCP5-madgraph-pythia8	0.00658	LO
Pseudoscalar_MonoV_LO_Mphi-400_Mchi-1_gSM-1p0_gDM-1p0_TuneCP5-madgraph-pythia8	0.00343	LO
Pseudoscalar_MonoV_LO_Mphi-450_Mchi-1_gSM-1p0_gDM-1p0_TuneCP5-madgraph-pythia8	0.00227	LO
Pseudoscalar_MonoV_LO_Mphi-500_Mchi-150_gSM-1p0_gDM-1p0_TuneCP5-madgraph-pythia8	0.001049	LO
Pseudoscalar_MonoV_LO_Mphi-500_Mchi-1_gSM-1p0_gDM-1p0_TuneCP5-madgraph-pythia8	0.001594	LO
Pseudoscalar_MonoV_LO_Mphi-500_Mchi-200_gSM-1p0_gDM-1p0_TuneCP5-madgraph-pythia8	0.0005519	LO
Pseudoscalar_MonoV_LO_Mphi-500_Mchi-225_gSM-1p0_gDM-1p0_TuneCP5-madgraph-pythia8	0.0002595	LO
Pseudoscalar_MonoV_LO_Mphi-500_Mchi-275_gSM-1p0_gDM-1p0_TuneCP5-madgraph-pythia8	1.398e-05	LO
Pseudoscalar_MonoV_LO_Mphi-500_Mchi-50_gSM-1p0_gDM-1p0_TuneCP5-madgraph-pythia8	0.001531	LO
Pseudoscalar_MonoV_LO_Mphi-600_Mchi-1_gSM-1p0_gDM-1p0_TuneCP5-madgraph-pythia8	0.0008496	LO
Pseudoscalar_MonoV_LO_Mphi-700_Mchi-1_gSM-1p0_gDM-1p0_TuneCP5-madgraph-pythia8	0.0004829	LO
Pseudoscalar_MonoV_LO_Mphi-800_Mchi-1_gSM-1p0_gDM-1p0_TuneCP5-madgraph-pythia8	0.0002875	LO

Table 32: Signal samples used to model the scenario with a color-neutral spin-0 mediator in the mono-V topology.

Data set name	Cross section (pb)	Order in QCD
ADDMonoJet_MD_4_d_7_TuneCUETP8M1_13TeV_pythia8	0.9125	LO
ADDMonoJet_MD_5_d_4_TuneCUETP8M1_13TeV_pythia8	0.653	LO
ADDMonoJet_MD_5_d_5_TuneCUETP8M1_13TeV_pythia8	0.3679	LO
ADDMonoJet_MD_5_d_6_TuneCUETP8M1_13TeV_pythia8	0.2331	LO
ADDMonoJet_MD_5_d_7_TuneCUETP8M1_13TeV_pythia8	0.1569	LO
ADDMonoJet_MD_6_d_3_TuneCUETP8M1_13TeV_pythia8	0.577	LO
ADDMonoJet_MD_6_d_4_TuneCUETP8M1_13TeV_pythia8	0.2226	LO
ADDMonoJet_MD_6_d_5_TuneCUETP8M1_13TeV_pythia8	0.1055	LO
ADDMonoJet_MD_6_d_6_TuneCUETP8M1_13TeV_pythia8	0.05733	LO
ADDMonoJet_MD_6_d_7_TuneCUETP8M1_13TeV_pythia8	0.03357	LO
ADDMonoJet_MD_7_d_2_TuneCUETP8M1_13TeV_pythia8	1.161	LO
ADDMonoJet_MD_7_d_3_TuneCUETP8M1_13TeV_pythia8	0.2675	LO
ADDMonoJet_MD_7_d_4_TuneCUETP8M1_13TeV_pythia8	0.08856	LO
ADDMonoJet_MD_7_d_5_TuneCUETP8M1_13TeV_pythia8	0.03633	LO
ADDMonoJet_MD_7_d_6_TuneCUETP8M1_13TeV_pythia8	0.017	LO
ADDMonoJet_MD_7_d_7_TuneCUETP8M1_13TeV_pythia8	0.008616	LO
ADDMonoJet_MD_8_d_2_TuneCUETP8M1_13TeV_pythia8	0.6768	LO
ADDMonoJet_MD_8_d_3_TuneCUETP8M1_13TeV_pythia8	0.137	LO
ADDMonoJet_MD_8_d_4_TuneCUETP8M1_13TeV_pythia8	0.03959	LO
ADDMonoJet_MD_8_d_5_TuneCUETP8M1_13TeV_pythia8	0.0143	LO
ADDMonoJet_MD_8_d_6_TuneCUETP8M1_13TeV_pythia8	0.005902	LO
ADDMonoJet_MD_8_d_7_TuneCUETP8M1_13TeV_pythia8	0.002644	LO
ADDMonoJet_MD_9_d_2_TuneCUETP8M1_13TeV_pythia8	0.4226	LO
ADDMonoJet_MD_9_d_3_TuneCUETP8M1_13TeV_pythia8	0.07592	LO
ADDMonoJet_MD_9_d_4_TuneCUETP8M1_13TeV_pythia8	0.0197	LO
ADDMonoJet_MD_9_d_5_TuneCUETP8M1_13TeV_pythia8	0.006278	LO
ADDMonoJet_MD_9_d_6_TuneCUETP8M1_13TeV_pythia8	0.002282	LO
ADDMonoJet_MD_9_d_7_TuneCUETP8M1_13TeV_pythia8	0.0009088	LO
ADDMonoJet_MD_10_d_2_TuneCUETP8M1_13TeV_pythia8	0.2785	LO
ADDMonoJet_MD_10_d_3_TuneCUETP8M1_13TeV_pythia8	0.04484	LO
ADDMonoJet_MD_10_d_4_TuneCUETP8M1_13TeV_pythia8	0.01038	LO
ADDMonoJet_MD_11_d_2_TuneCUETP8M1_13TeV_pythia8	0.1896	LO
ADDMonoJet_MD_11_d_3_TuneCUETP8M1_13TeV_pythia8	0.02784	LO
ADDMonoJet_MD_11_d_4_TuneCUETP8M1_13TeV_pythia8	0.005886	LO
ADDMonoJet_MD_12_d_2_TuneCUETP8M1_13TeV_pythia8	0.1337	LO
ADDMonoJet_MD_12_d_3_TuneCUETP8M1_13TeV_pythia8	0.01801	LO
ADDMonoJet_MD_13_d_2_TuneCUETP8M1_13TeV_pythia8	0.09772	LO
ADDMonoJet_MD_13_d_3_TuneCUETP8M1_13TeV_pythia8	0.01203	LO
ADDMonoJet_MD_14_d_2_TuneCUETP8M1_13TeV_pythia8	0.0726	LO
ADDMonoJet_MD_15_d_2_TuneCUETP8M1_13TeV_pythia8	0.05483	LO

Table 33: Signal samples used to model the ADD scenario

H Signal template generation for 2016 cards

In order to harmonize the theoretical signal modeling between the data sets in te full Run-2 combination, the original signal templates from EXO-16-048 are replaced. The signal region selection from that analysis, which was based on RunIISummer16 MC in the 80X reconstruction, is reproduced as closely as possible based on RunIISummer16 MC in the 94X reconstruction, delivered via 102X NanoAOD v7. One pertinent difference between the analyses is the reconstruction of AK8 jets. In 2016, CHS jets were used, and the jet mass is evaluated with the "pruned mass" definition. In 2017 and 2018, PUPPI jets are used, and the mass is evaluated via the softdrop method. It is found that the 2016 selection, which identifies V candidates via a criterion based on the n-subjettiness ratio τ_{21}, can be reproduced with PUUPI jets by slightly modifying the applied criteria. The following changes are made:

- The τ_{21} threshold is changed from 0.6 to 0.55 (on average, PUPPI jets have lower τ_{21}.).
- The jet mass window is altered from $65 - -105\,\text{GeV}$ to $65 - -120\,\text{GeV}$ (on average, the corrected soft drop mass is higher than the pruned mass).
- The jet pt scale is modified by 3% (on average, CHS jets have lower reponse than PUPPI jets)

The procedure is validated on SM $Z+$jets events simulated at LO in RunIISummer16, which are part of the SM BG estimate in the original 2016 cards. A comparison of the original and new templates is shown in Fig. 226, and good agreement is observed. The replaced H(inv) signal templates are compared in Fig. **??** and Fig. **??**.

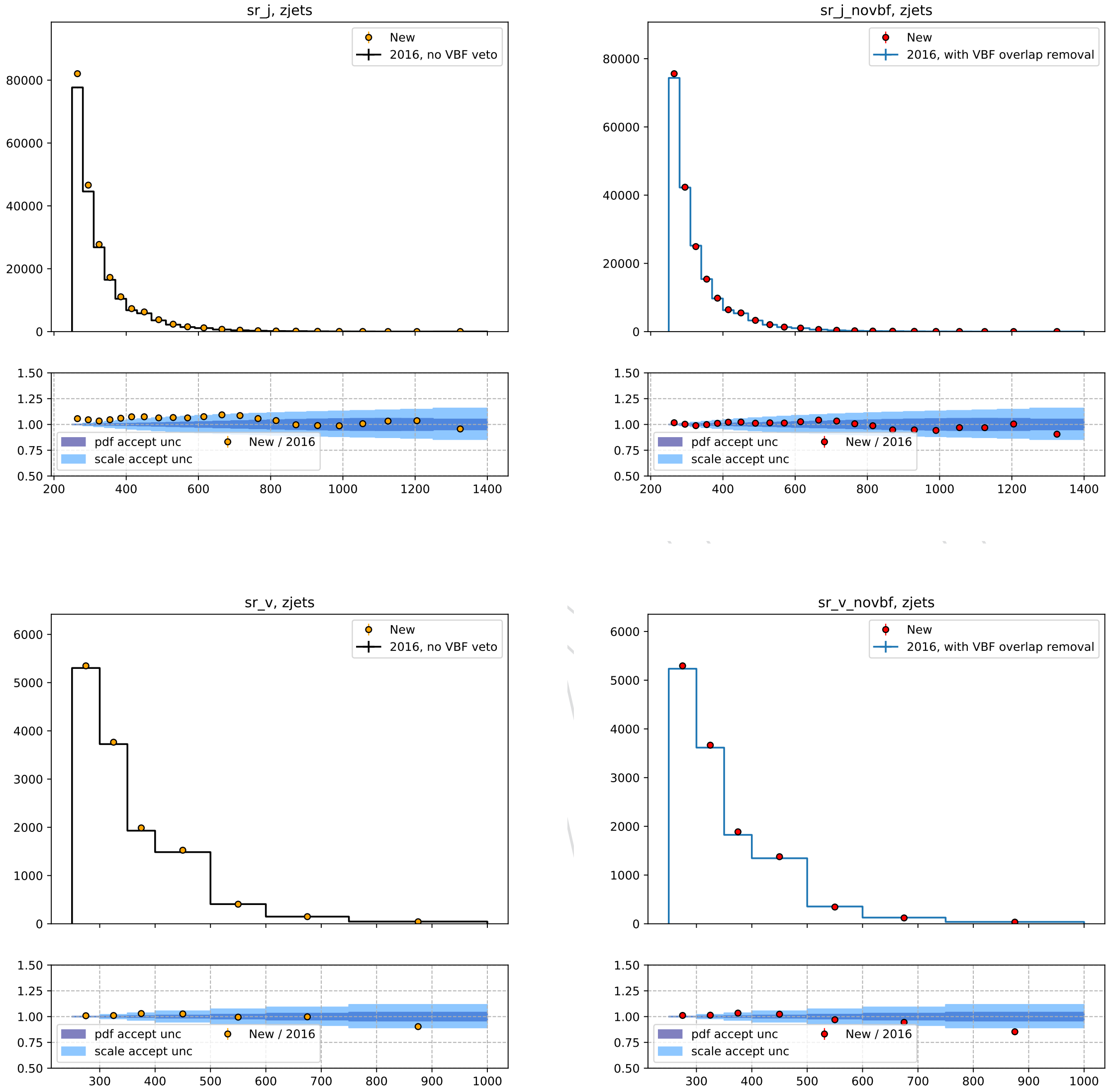

Figure 226: Comparison of original and re-derived Z + jets templates in 2016. The monojet selection is shown in the upper row, and the mono-V selection is shown in the lower row. The left and right columns represent the selection with and without VBF overlap removal, respectively. The VBF overlap removal is used for the H(inv) interpretation, while the version without this overlap removal is used in all other interpretations.

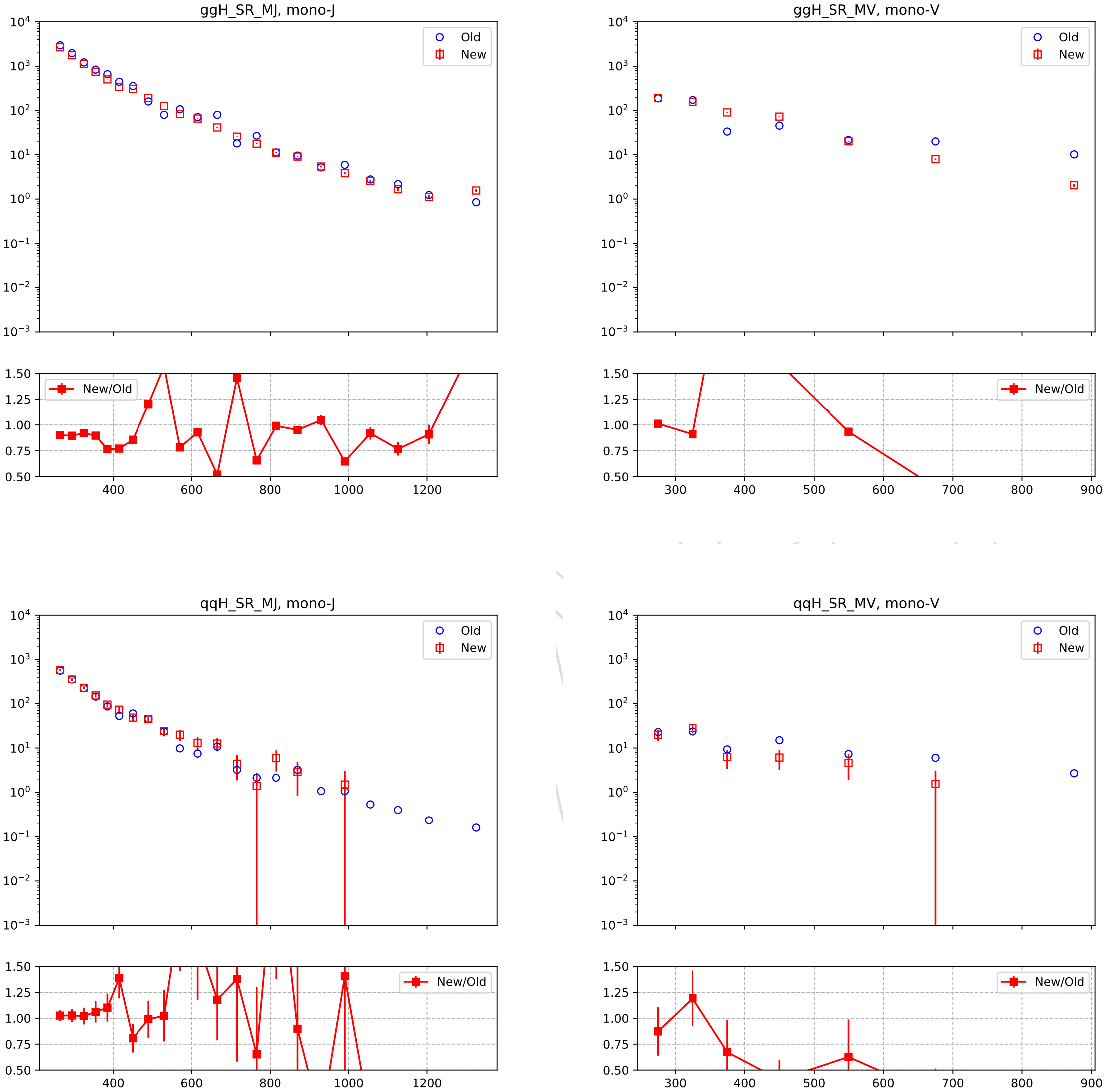

Figure 227: Comparison of original and re-derived H(inv) signal templates in 2016. From top to bottom, the rows represent gluon fusion and VBF production. The left and right columns represent the monojet and mono-V categories, respectively.

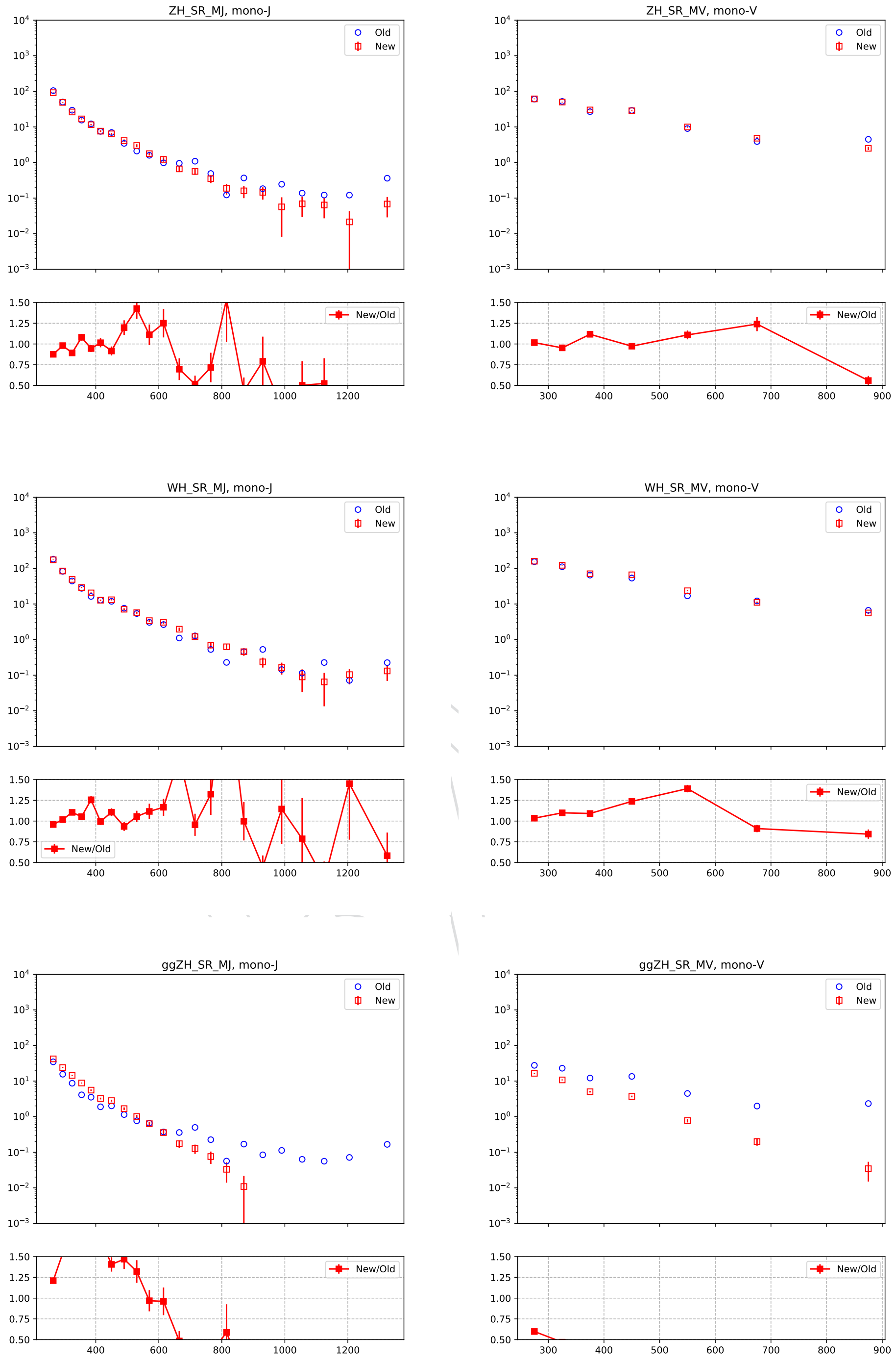

Figure 228: Comparison of original and re-derived H(inv) signal templates in 2016. From top to bottom, the rows represent WH, ZH and ggZH production. The left and right columns represent the monojet and mono-V categories, respectively.

I Mono-V H(inv) comparison to 2016

2125

Mono-V update

November 24, 2020

Andreas Albert,
on behalf of the monojet group

BOSTON UNIVERSITY

EXO-20-004 CADI

Introduction

- **EXO-20-004 = 2017/18 monojet + mono-V analysis, to be combined with 2016 result (EXO-16-048)**
- **Topic at hand: mono-V sensitivity comparison between EXO-16-048 and EXO-20-004**
  - Basic observation: with nominally same V-tag definition ($\tau_{21} < 0.6$), 2017/18 gives worse sensitivity:
    - 2016: BR(H→ inv) < 45%
    - 2017: BR(H→ inv) < 67%
- **Previous presentations:**
  - Initial presentation: October 16th
  - Followup: November 6th
- **Initial hypotheses (details next slide):**
  - Difference in VH signal model between years
  - Difference in jet definition (CHS / PUPPI) between years

Recap: Previous findings

Details in talk from November 6th

VH signal model differences
VH modeled by JHU in ‘16, powheg in ‘17/’18

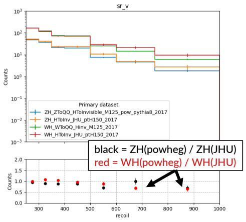

black = ZH(powheg) / ZH(JHU)
red = WH(powheg) / WH(JHU)

JHU predicts harder H boost == higher MET
→ 10-15% effect on sensitivity

Tagging performance between years
CHS + mass pruning used in ‘16
PUPPI + softdrop mass used in ‘17/’18

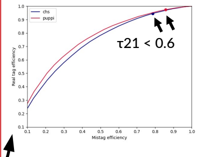

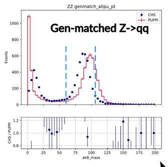

No real difference in τ_{21} performance
just need to tighten numerical cut value for PUPPI ✓
→ Does not suffice to reproduce 2016 templates, though

Nominal mass window (65-105) significantly cuts into signal → reoptimize!

Today’s talk

- **2016 vs 17/18 comparison:**
  - **Optimization of the jet mass window and tagger working point**
  - **A closer look at the non-VH signal model**
  - **Further plan**
- **Lessons for the 2017/18 DeepAK8-based analysis**

Reproducing 2016: Mass window and τ_{21} optimization

Optimization introduction

- **Method: pragmatically scan τ_{21} cuts and mass window definitions**
  - generate templates & data cards for ≈ 300 combinations
- **Optimize for two different targets:**
  - **1. Optimize for best sensitivity**
  - **2. Optimize to replicate 2016 templates**
- **Setup:**
  - Out-of-the-box 2017 setup
  - Performed optimization with VH signal samples from powheg as well as JHU
  - No special scaling applied
  - No accounting for τ21 SF + uncertainty evolution

Approach 1: Sensitivity scan

(This slide == plot explanation, Result discussion on next slide)

colors = jet mass windows
entries ordered by their most sensitive point

y axis == limit
→ smaller is better

x axis == τ21 cut
jets are accepted if they have a value smaller than x

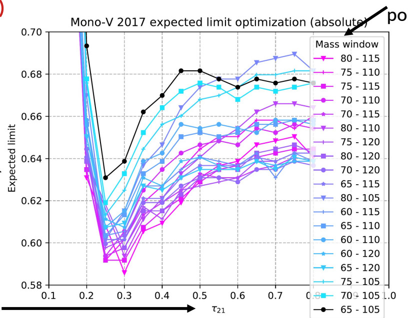

Approach 1: Sensitivity scan

Best limits here (powheg): 59% / 63%

General Observations:
- **For nominal window (65-105):**
  - sensitivity is flat as a function of τ21 in ~0.45-0.8
    → This is why our previous attempts
    at varying τ21 alone showed little effect
- **Sensitivity slope in τ21 varies with the mass window**
- **Sensitivity generally improves with**
  - upward shift of mass window
  - Smaller (=tigther) τ21 cut

Overall best sensitivity:
- τ21 < 0.3 & mass in [80,115]
- Improves ≈ 12% relative to nominal

→ Good but much tighter than than 2016!

Best sensitivity with τ21<0.5:
- Similarly tight to 2016
- Mass in [75,120]
- ≈7% better than nominal

→ 2016 not really optimal either

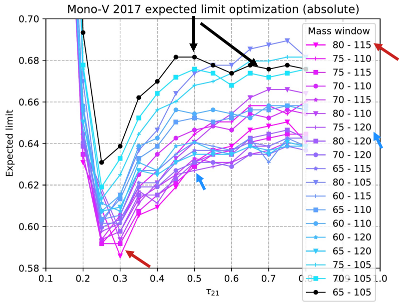

→ Tagging optimization yields improvement, but does not close gap to 2016

Best limits here (JHU): 53% / 57%

Optimization with JHU VH instead of powheg

2126

If we use **JHU VH**, the result is **qualitatively the same**

Sensitivity is **overall improved,** but still does not reach 2016:

53 – 57% here vs 45% in ‘16

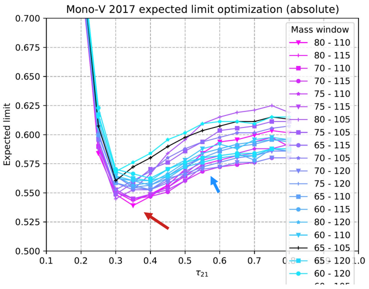

Approach 2: Optimizing for similarity to 2016

- **Want to find parameter combination that reproduces 2016 templates**
  - We need to get real and fake V(qq) tags right at the same time
  - Attempt to simultaneously reproduce the Z+jets BG (fake tags) and the JHU WH signal (real tags)
- **Figure of merit: χ_2 of signal template shapes**
  - Single-process $\chi^2 = \sum_{\text{bins}} [(\text{xs } 2017 - \text{xs } 2016) / (\text{xs } 2017 + \text{xs } 2016)]^2$
    (xs = bin content of template divided by luminosity of given year)
  - Total $\chi^2 = \chi^2(\text{wh}) + \chi^2(\text{zjets})$

Best limits here (JHU): 57%

Approach 2: Result

```
Parameter combos with best total chi2

Tag               chi2 WH       chi2 zjet     chi2 total
m75to120_tau0.55  6.43937e-07   0.000108723   0.000109367
m70to110_tau0.55  9.55023e-05   2.77215e-05   0.000123224
m60to110_tau0.50  0.000194412   0.000353031   0.000547444
m75to110_tau0.65  9.62977e-05   0.00048808    0.000584378
m75to110_tau0.60  0.000297197   0.000423324   0.000720521
m80to120_tau0.60  0.000688737   4.11272e-05   0.000729864
m75to115_tau0.60  1.21083e-06   0.000791634   0.000792845
m80to115_tau0.70  0.000935965   7.56962e-05   0.00101166
m75to115_tau0.55  0.0001504     0.000938966   0.00108937
m80to115_tau0.75  0.000817354   0.000398855   0.00121621
```

2016 best reproduced with:
- τ21 around 0.5 – 0.7 ✓
- mass window upper boundary 110-120 ✓
  → These values are completely consistent with our expectation from the tagging study

Best combination:

- **reproduces 2016** Z(vv), W+Jets and W(qq)H(inv)✓
- **Gives limit of** only 57% compared to 45% in ‘16. **Why?**

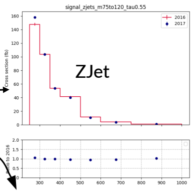

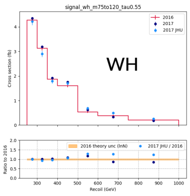

Left-over sensitivity disagreement

Our optimized templates match the 2016 background and VH signals well, but limit disagrees
We already know that
- nuisance and fit definitions are not a driver of difference between years
- VH signals make up ≈ half of the total signal

→ What do the other signals look like?

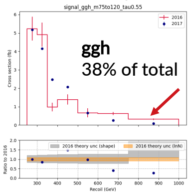

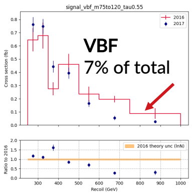

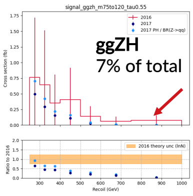

2016 templates severely stat limited + partially unphysical shapes + very large tails
Given that Z+jets, WH, ZH agree, there is no tagging reason for this difference
→ Once again differences in signal model?

---

full study in backup

Investigation of 2016 ggH (== largest non-VH signal)

Compared 2016 and 2017 powheg ggH(inv) samples at gen and reco levels
comparison also includes our recent requests with pt(H)>190 cut

Findings:
1. 2016 ggH has fixed scale setting $\mu = m_{H,}$
while newer samples have running scale

2. Original sample **too small** to populate high MET
→ not clear if scale diff is relevant

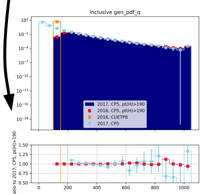

Factorization scale (GeV)

Not clear what was done to get around stat limitation in ‘16
→ 2016 analyzers are following up, will provide details

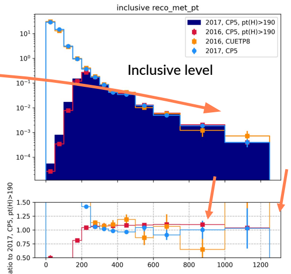

PF MET (GeV)

What about VBF, ggZH?

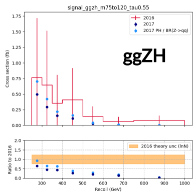

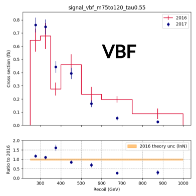

ggZH:
- 2016 cards have much harder tail than 2017/2018
- Have found that wrong XS was used in 2016 (missing factor of BR(Z→qq) = 0.7)
- 2016 did not have central prod sample.
  → template derived from qqZH by reweighting

VBF:
- Same tail difference
- 2016 likely used central prod sample, to be confirmed

2016 analyzers are following up, will provide details

Possible explanation: Scale settings?

2017 / 2018 powheg signal samples have running scales → scale depends on boost

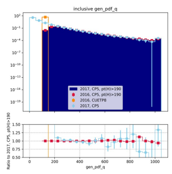

‘16 ggH
scale fixed
@ m_H

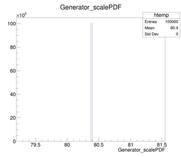

‘16 VBF
scale fixed
@ 80 GeV
≈ m_W?

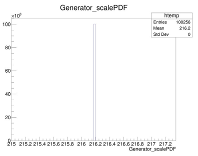

‘16 ggZH
scale fixed
@ m_H+m_Z

Is the scale scheme choice (fixed vs running scale) responsible for the difference?
→ Checking now by generating high-pt GEN samples with either setting

---

Back to the sensitivity question: Replacing signal templates

Can we attribute the sensitivity difference to the difference in signal shapes?

We can test this:

- Take our optimized 2017 cards reproduce 2016 WH and BG
- replace signal templates by the ones from the 2016 cards
- Quantify sensitivity difference

Result: Difference in signal shapes can account for sensitivity difference

	Limit
2017 optimized to match '16	0.57
replace ggh	0.48
replace ggh+ggzh	0.45
replace ggh+ggzh+vbf	0.40
replace ggh+ggzh+vbf+zh+wh	0.43
2016 target	0.45

ggH is biggest driver (≈15%)
but ggzh and VBF contribute

can reproduce 2016 to ≈ 10% now
residual differences in BG templates + nuisances OK ✓

→ This is the final piece we have been looking for!

Summary of comparison to 2016

Sensitivity differences to 2016 now fully understood

- No problems have been found with 2017/18 analysis

Largest part of sensitivity driven by signal modeling
- JHU VH
- ggZH XS
- ggH / ggZH / VBF tail model

Small additional effect from τ21 WP, mass window definition

Point-by-point sensitivity changes:

2017 tau21 starting point	0.67
→ Switch to JHU VH	0.61
→ Optimize mass & tau21 to match '16	0.57
→ replace ggh	0.48
→ replace ggh+ggzh	0.45
→ replace ggh+ggzh+vbf	0.40
→ replace ggh+ggzh+vbf+zh+wh	0.43
2016 target	0.45

How to proceed

Propose the following steps:

1) **Nominal model choice:**

   as the nominal signal model, use the nominal conventions from the HIG group

2) **Combination treatment:**

   Replace the signal templates in the 2016 cards with the nominal model from 1).

   Discuss the effect of this update explicitly in the publication.

3) **Quantifying the differences:**

   If there are several similarly valid models, also quote the sensitivity with one or two alternative models.

Change of topic: Can we also further optimize the DeepAK8 analysis?

DeepAK8 optimization (I)

Performed τ21 optimizatoin for sync with 2016, but actual analysis is DeepAK8-based
→ Can perform same type of optimization here

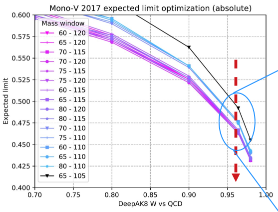

```
Mlow mhigh tagger limit
65   120   0.96   0.4629
70   120   0.96   0.4629
75   120   0.96   0.4629
80   120   0.96   0.4629
60   120   0.96   0.4648
70   115   0.96   0.4648
75   115   0.96   0.4648
60   115   0.96   0.4668
65   115   0.96   0.4668
80   115   0.96   0.4668
65   110   0.96   0.4746
70   110   0.96   0.4746
75   110   0.96   0.4746
80   110   0.96   0.4746
60   110   0.96   0.4766
70   105   0.96   0.4902
75   105   0.96   0.4902
65   105   0.96   0.4922
80   105   0.96   0.4922
60   105   0.96   0.4941
```

Current DeepAK8 WP close to optimal ✓
Cannot go tighter without losing stats

For fixed WP, can still optimize mass window
larger mass window is preferred
→ Consistent with previous observation ✓
→ Effect enhanced bc tagger really shapes mass distribution of passing jets

Exact boundaries of window make little diff as long as mhigh > 110 GeV

NB: absolute limit values not reliable here bc no tagging SF is applied for optimization
→ Trust the ratios!

DeepAK8 optimization (II)

Optimization on last slide was done without tagging SF → Absolute values not reliable.

What are the absolute limit values with tagging SF taken into account?
Compare nominal mass window (65-105) to best one from last slide (65-120)

Depending on year and category (loose / tight), gain ranges from 5 to 15 %

2017+2018 combined mono-V improves by 10%

NB: Still have to propagate mass cut to
1. data-driven QCD estimate
2. mistag SF measurement

→ Straightforward adjustments

		Expected limit		
Year	**Category**	**mass 65 - 105**	**mass 65 - 120**	**ratio**
2017	Loose	1.01	0.91	90%
	tight	0.59	0.52	88%
	combined	0.48	0.41	85%
2018	Loose	1.05	0.94	89%
	tight	0.57	0.55	96%
	combined	0.45	0.43	96%
2017 + 2018	combined	0.34	0.31	90%

Summary and plan

2016 sensitivity comparison has been understood
- most of the apparent difference was driven by signal modeling
- For combination: update 2016 result with latest signal model + quantify differences
- 2016 analyzers are following up on EXO-16-048 / HIG-17-023

Ported insights to DeepAK8 analysis:
- adopting extended mass window 65-120 into the nominal analysis ✓
- Now propagating to auxilliary meaurements:
  - data-driven QCD estimate for mono-V
  - mistag scale factors

  → Straightforward to propagate

Will update the documentation with full results this week

After this update, propose to proceed to EXO-20-004 ARC review

---

Backup: EXO-16-048

EXO-16-048: H(inv) results and composition

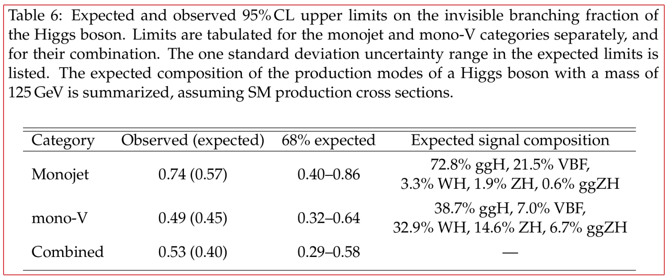

Table 6: Expected and observed 95% CL upper limits on the invisible branching fraction of the Higgs boson. Limits are tabulated for the monojet and mono-V categories separately, and for their combination. The one standard deviation uncertainty range in the expected limits is listed. The expected composition of the production modes of a Higgs boson with a mass of 125 GeV is summarized, assuming SM production cross sections.

Category	Observed (expected)	68% expected	Expected signal composition
Monojet	0.74 (0.57)	0.40–0.86	72.8% ggH, 21.5% VBF, 3.3% WH, 1.9% ZH, 0.6% ggZH
mono-V	0.49 (0.45)	0.32–0.64	38.7% ggH, 7.0% VBF, 32.9% WH, 14.6% ZH, 6.7% ggZH
Combined	0.53 (0.40)	0.29–0.58	—

2016 signal uncertainties

2128

Most signal uncertainty is normalization only

Process	total lnN
ggh	8.6 %
ggzh	23.6 %
vbf	3.0 %
wh	3.0 %
zh	4.4 %

Total is geometric sum of QCD scale, PDF components

Additionally, ggH has shape variation

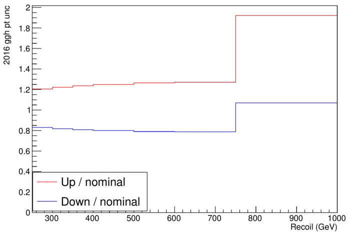

Overall 20-30%, but last bin is likely pathological (stats?)

Important: Signal uncs have almost no effect on median expected sensitivity

What is the effect of signal uncertainties on sensitivity?

Simple case study: 20% flat uncertainty on ggH

- based on 2016 mono-V card
- disable all other theory uncertainties on ggH (==clean slate)
- Add new dummy lnN 1.2 nuisance for demonstration

Observations:

- Uncertainty has almost no effect on median expected sensitivity
- Effect of rescaling signal is much larger than effect of uncertainty

	Median exp.	Ratio to baseline	16% quantile	84% quantile
Baseline	0.45	100%	0.32	0.63
Add new 20% ggH unc	0.45	101%	0.32	0.64
Scale ggH down by 20%	0.49	109%	0.35	0.69
Scale ggH up by 20%	0.42	93%	0.30	0.59

→ Quoting separate limit numbers for different theory choices is better representation

Backup: Optimization

Optimization: JHU vs Powheg (I)

Note: Colors and markers are different between plots!

Powheg

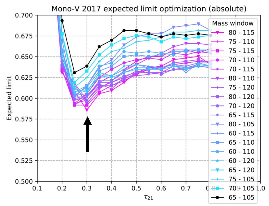

Optimal at ≈ 0.3, 80-115

JHU

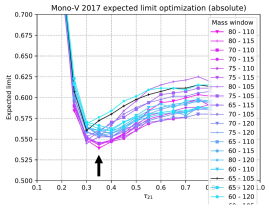

Optimal at ≈ 0.35, 80-110

JHU VH gives overall better limit (we knew that)

Optimization results qualitatively similar, though

Optimization: JHU vs Powheg (II)

For most of the points, the JHU sensitivity is ~(10±3)% better than powheg

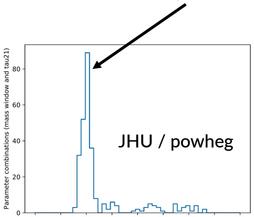

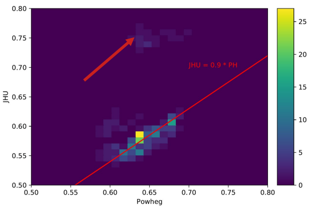

However, there is a tail where the difference is larger and JHU is worse

These are mostly points with very tight tau21 cut ~ 0.2 (→ not really what we care about)

Optimization: JHU vs Powheg (III)

Full data here

When we optimize mass window and τ21, JHU and powheg have different tradeoff
JHU: tighter mass, looser τ21
Powheg: looseer mass, tighter τ21

Description	Tag	Powheg	JHU	JHU/PH
Nominal setup	m65to105_tau0.60	0.674	0.607	90%
Globally optimal based on JHU	m80to110_tau0.35	0.611	0.539	88%
Globally optimal based on powheg	m80to115_tau0.30	0.586	0.551	94%
Optimal tau0.5 based on JHU	m70to115_tau0.50	0.633	0.561	89%
Optimal tau0.5 based on powheg	m75to120_tau0.50	0.627	0.566	90%

Ratio varies significantly

When we fix τ21<0.5 and only optimize the mass window, outcome is similar
JHU prefers 5 GeV loser window (same width), but sensitivity effect is only ~1%

Backup: Comparison of ggH 2016 vs 2017

Why look at ggH?

From optimization studies, we know:

1. can reproduce 2016 wh, zjets, wjets with optimized working points

2. Main remaining difference seems driven by ggH and VBF

Specifically, ggH has significantly different shape in '16: factor ≈2 in tail

Where does this difference come from?

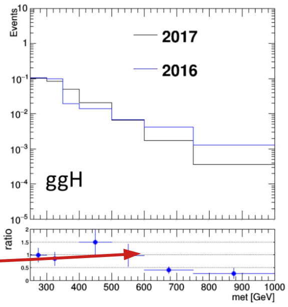

GgH datasets for comparison

Ggh datasets exist in two variations:

1. inclusive

2129

→ this type of sample has been around a long time

→ used in 2016

→ previously used in 2017 until we realized stats were bad

2. with gen pt(H) cut > 190 GeV

→ Recently requested by us

→ We requested 2016 as well because it's good to have

Inclusive 2016

```
/GluGlu_HToInvisible_M125_13TeV_powheg_pythia8/RunIISummer16NanoAODv7-PUMoriond17_Nano02Apr2020_102X_mcRun2_asymptotic_v8-v1/NANOAODSIM
```

2016 pth190

```
/GluGlu_HToInvisible_M125_TuneCP5_13TeV_powheg_pythia8/RunIISummer16NanoAODv7-PUMoriond17_Nano02Apr2020_102X_mcRun2_asymptotic_v8-v1/NANOAODSIM
```

Note: Name accidentally does not include the pt cut, but its included in the GEN settings!

Inclusive 2017

```
/GluGlu_HToInvisible_M125_TuneCP5_13TeV_powheg_pythia8/RunIIFall17NanoAODv7-PU2017_12Apr2018_Nano02Apr2020_102X_mc2017_realistic_v8-v1/NANOAODSIM
```

2017 pth190

```
/GluGlu_HToInvisible_M125_HiggspTgt190_TuneCP5_13TeV_powheg_pythia8/RunIIFall17NanoAODv7-PU2017_12Apr2018_Nano02Apr2020_102X_mc2017_realistic_v8-v1/NANOAODSIM
```

What are the sample sizes?

The inclusive samples differ
by a factor 5 in size between years

Effective lumi not great in either case

	Events	xs	Effective lumi (fb)
Inclusive 2016	200000	48.58	4
2016 pth190	2544338	0.772	3296
Inclusive 2017	994000	48.58	20
2017 pth190	2473983	0.772	3205

For the high-pt samples
Stats are effectively
Infinite in the analysis
Phase space ✓

To put that in perspective: How many events
Does each sample have above a given met cut?

No other selection applied, no fat jets, no tagging, etc

```
Dataset           > 250    > 500    > 750
--------------  -------  -------  -------
2016 high-pt    1224542    70371     8073
2016 inclusive     1580       74        8
2017 high-pt    1108877    62601     7216
2017 inclusive     7199      397       46
```

Signal region binning is:
[250,300,350,400,500,600,750,1000]

Statistics comparison to 2016 data cards

2016 data cards contain stat uncertainties for the signals

Signal region binning is:
[250,300,350,400,500,600,750,1000]

Process	Bin	Up / nom	Down / nom
---------	-----	----------	-----------
ggH	1	1.12	0.88
ggH	2	1.13	0.87
ggH	3	1.24	0.76
ggH	4	1.2	0.8
ggH	5	1.37	0.63
ggH	6	1.13	0.88
ggH	7	1.12	0.87

12-13% in the highest bins

→ Trend as function of MET does not make sense

→ overall values not possible with what we saw on last slide!

Is this really the sample that was used in '16?

No bigger samples exist in 2016 central prod., also not in 80x

Was some gen-reweighting used?

TOP=/cvmfs/cms.cern.ch/phys_generator/gridpacks/

Gen settings

- **Two sets of GEN information to consider:**
  - Powheg gridpack content = defines ME-level prediction
  - Shower fragment= defines pythia settings + gen filters
- **Two gridpacks are used:**
  - **"GP1" is used in inclusive 2016, nowhere else:**

    ```
    ${TOP}/slc6_amd64_gcc481/13TeV/powheg/V2/gg_H_quark-mass-effects_NNPDF30_13TeV_M125/v2/gg_H_quark-mass-
    effects_NNPDF30_13TeV_M125_tarball.tar.gz
    ```
  - **"GP2" is used in the three other cases:**

    ```
    ${TOP}/2017/13TeV/powheg/V2/gg_H_quark-mass-effects_NNPDF31_13TeV_M125/v1/gg_H_quark-mass-
    effects_NNPDF31_13TeV_M125_slc6_amd64_gcc630_CMSSW_9_3_0.tgz
    ```
  - **Differences:**
    - Powheg version (not clear how to quantify tbh)
    - PDF: NNPDF30_nlo_as_0118 vs NNPDF31_nnlo_hessian_pdfas
    - Powheg scale settings: GP1 has fixed scale == 125 GeV, GP2 has running scale → Will come back to this
    - Possibly other powheg settings that I do not understand
- **No surprise differences in shower settings:**
  - No dipole recoil setting difference!
  - Tune: 2016 inclusive has CUETp8, all others have CP5
  - Only diff is presence or absence of gen filters for pt(H) cut ✓

Technical setup for sample comparison

- **All plots based on central NanoAOD v7**
  - latest JECs are already applied in this release
  - No JER, JMR, JMS, softdrop mass corrections applied anywhere
  - No scale factors applied for anything, events weighted with gen weight and XS only

---

Inclusive comparison of samples: PDF event properties

Factorization scale in PDF

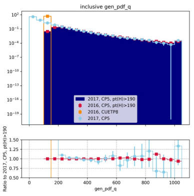

2016 inclusive has fixed scale
== peak at 120

other samples agree modulo
low-scale cutoff due to pt(H) cut

PDF weight xf

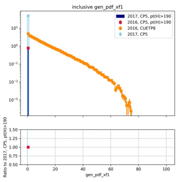

The PDF weight xf for the incoming
partons differs significantly:
long tail in inclusive '16

→ Not obvious if this means anything

Inclusive comparison of pt(H) (== main boost indicator)

LHE level

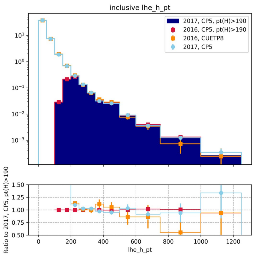

GEN level

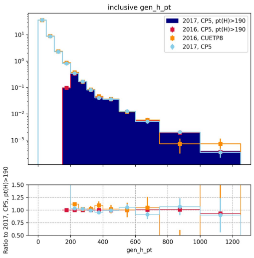

No gross discrepancies, but high-pt stats also obscure a lot

Comparison of MET

Inclusive spectra:

GEN

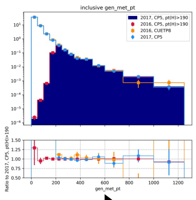

Reco

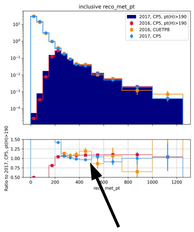

Gen matches well,
Reco MET has offset between '16 and '17 (orange ratio)

(note: 2017 low-pt diff with/without pt(H) cut not present in SR)

reco/gen -1 for gen > 250

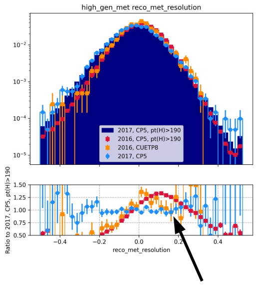

→ Difference in
Met response /resolution
(latest JECs applied in each case)

MET response / resolution as function of PU

Gen MET > 250

Is PU responsible for 16/17 shift in response?

2130

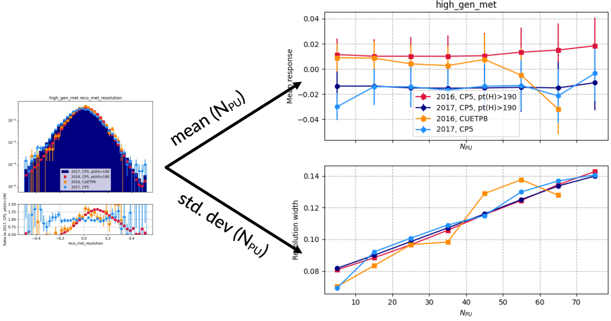

systematic difference in response (≈constant in PU)

resolution agrees well between years

Comparison of reco-level leading PUPPI AK8 jet pt

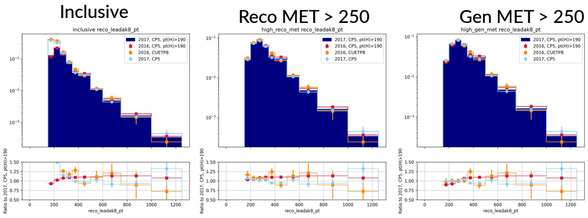

Inclusive 2016 agrees well with 2017 samples within stats
High-pt 2016 sample deviates from others → Why?
(not necessarily relevant for understanding of EXO-16-048, though)

Same effect as previously seen in MET response?

PFMET > 250 && (Ak8 pt > 250) && (Ak8 |η| < 2.4)

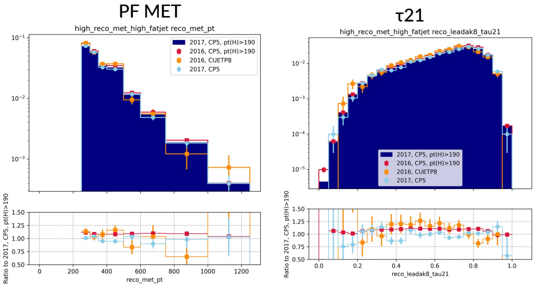

Acceptance difference 16 vs 17 in more signal-like selection as result of previously observed reco boost diff
→ Inclusive 2016 could go either way, so nothing's certain

Summary

- **Multiple differences between samples & years**
  - PDF, tune, stats, scale setting
- **Main take-away:** central prod sample with 200k events cannot have been the only input for EXO-16-048: stats not consistent

  → It's not clear we are really looking at the right sample here!
- **Ignoring that, the face value comparison shows:**
  - 2016 vs 17 differs in MET response/resolution
    - NB: have not used '17 MET v2 recipe here

      → ≈ 10% acceptance difference
  - No immediate hints for shape difference

    we see in the cards

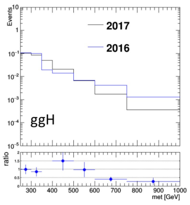

Backup: Misc

What JECs are in the 2016 userFloats?

- **Dataset we are interested in :**
  - `/WW_TuneCUETP8M1_13TeV-pythia8/RunIISummer16NanoAODv7-PUMoriond17_Nano02Apr2020_102X_mcRun2_asymptotic_v8-v1/NANOAODSIM`
- Chain in MCM

Miniaod request, runs on top of AOD

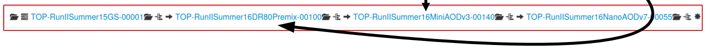

TOP-RunIISummer15GS-00001 → TOP-RunIISummer16DR80Premix-00100 → TOP-RunIISummer16MiniAODv3-00140 → TOP-RunIISummer16NanoAODv7-00055

- setup + cmsDriver for MiniAOD step:

```
cmsDriver.py \

--filein "dbs:/WW_TuneCUETP8M1_13TeV-pythia8/RunIISummer16DR80Premix-
PUMoriond17_80X_mcRun2_asymptotic_2016_TrancheIV_v6-v1/AODSIM" \

--step PAT \

--conditions 94X_mcRun2_asymptotic_v3 \

(…)
```

- `CondDB:  94X_mcRun2_asymptotic_v3`

AK8PFPuppi	JetCorrectorParametersCollection_Summer16_07Aug2017_V11_MC_AK8PFPuppi
AK8PFchs	JetCorrectorParametersCollection_Summer16_07Aug2017_V11_MC_AK8PFchs

- `JEC twiki`

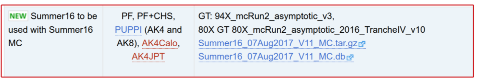

NEW Summer16 to be used with Summer16 MC	PF, PF+CHS, PUPPI (AK4 and AK8), AK4Calo, AK4JPT	GT: 94X_mcRun2_asymptotic_v3, 80X GT 80X_mcRun2_asymptotic_2016_TrancheIV_v10 Summer16_07Aug2017_V11_MC.tar.gz Summer16_07Aug2017_V11_MC.db

→ userFloats have latest JEC ✓

How different is the b tagging between years?

CSVv2 medium WP in 2016
→ (63%, 1%)

DeepCSV medium in 2017
→ (68%, 1%)

Slight diff in real tags, but
Same fake tags

Checked that we see ≈ 10%
Veto inefficiency in either year

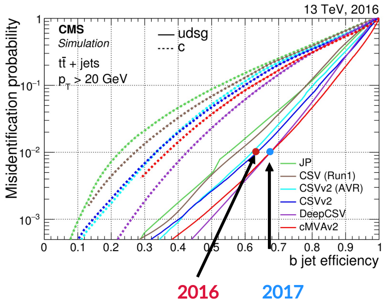

Acknowledgments

References

[1] G. Bertone, D. Hooper, and J. Silk, “Particle dark matter: Evidence, candidates and constraints”, *Phys. Rept.* **405** (2005) 279–390, `doi:10.1016/j.physrep.2004.08.031`, `arXiv:hep-ph/0404175`.

[2] J. L. Feng, “Dark Matter Candidates from Particle Physics and Methods of Detection”, *Ann. Rev. Astron. Astrophys.* **48** (2010) 495, `doi:10.1146/annurev-astro-082708-101659`, `arXiv:1003.0904`.

[3] T. A. Porter, R. P. Johnson, and P. W. Graham, “Dark Matter Searches with Astroparticle Data”, *Ann. Rev. Astron. Astrophys.* **49** (2011) 155, `doi:10.1146/annurev-astro-081710-102528`, `arXiv:1104.2836`.

[4] N. Arkani-Hamed, S. Dimopoulos, and G. Dvali, “The hierarchy problem and new dimensions at a millimeter”, *Phys. Lett. B* **429** (1998) 263, `doi:10.1016/S0370-2693(98)00466-3`, `arXiv:hep-ph/9803315`.

[5] N. Arkani-Hamed, S. Dimopoulos, and G. R. Dvali, “Phenomenology, astrophysics and cosmology of theories with submillimeter dimensions and TeV scale quantum gravity”, *Phys. Rev. D* **59** (1999) 086004, `doi:10.1103/PhysRevD.59.086004`, `arXiv:hep-ph/9807344`.

[6] I. Antoniadis, K. Benakli, and M. Quiros, “Direct collider signatures of large extra dimensions”, *Phys. Lett. B* **460** (1999) 176, `doi:10.1016/S0370-2693(99)00764-9`, `arXiv:hep-ph/9905311`.

[7] G. Giudice, R. Rattazzi, and J. Wells, “Quantum gravity and extra dimensions at high-energy colliders”, *Nucl. Phys. B* **544** (1999) 3, `doi:10.1016/S0550-3213(99)00044-9`, `arXiv:hep-ph/9811291`.

[8] E. Mirabelli, M. Perelstein, and M. Peskin, “Collider signatures of new large space dimensions”, *Phys. Rev. Lett.* **82** (1999) 2236, `doi:10.1103/PhysRevLett.82.2236`, `arXiv:hep-ph/9811337`.

[9] ATLAS Collaboration, “Search for dark matter in events with a hadronically decaying W or Z boson and missing transverse momentum in pp collisions at $\sqrt{s} = 8$ TeV with the ATLAS detector”, *Phys. Rev. Lett.* **112** (2014) 041802, `doi:10.1103/PhysRevLett.112.041802`, `arXiv:1309.4017`.

[10] CMS Collaboration, “Search for dark matter, extra dimensions, and unparticles in monojet events in proto-proton collisions at $\sqrt{s} = 8$ TeV”, *Eur. Phys. J. C* **75** (2015) 235, `doi:10.1140/epjc/s10052-015-3451-4`, `arXiv:1408.3583`.

[11] ATLAS Collaboration, “Search for new phenomena in final states with an energetic jet and large missing transverse momentum in pp collisions at $\sqrt{s}$ =8 TeV with the ATLAS detector”, *Eur. Phys. J. C* **75** (2015) 299, `doi:10.1140/epjc/s10052-015-3517-3`, `10.1140/epjc/s10052-015-3639-7`, `arXiv:1502.01518`. [Erratum: *Eur. Phys. J. C* **75** (2015) 408].

[12] CMS Collaboration, “Search for dark matter in proton-proton collisions at 8 TeV with missing transverse momentum and vector boson tagged jets”, `arXiv:1607.05764`.

[13] ATLAS Collaboration, “Search for new phenomena in final states with an energetic jet and large missing transverse momentum in pp collisions at $\sqrt{s} = 13$ TeV using the ATLAS detector”, `arXiv:1604.07773`.

[14] CMS Collaboration, "Search for dark matter produced with an energetic jet or a hadronically decaying W or Z boson at $\sqrt{s}$ = 13 TeV", arXiv:1703.01651.

[15] ATLAS Collaboration, "Search for dark matter and other new phenomena in events with an energetic jet and large missing transverse momentum using the ATLAS detector", *JHEP* **01** (2018) 126, doi:/10.1007/JHEP01(2018)126, arXiv:1711.03301.

[16] CMS Collaboration, "Search for new physics in final states with an energetic jet or a hadronically decaying W or Z boson and transverse momentum imbalance at $\sqrt{s} = 13$ TeV", *Phys. Rev.* **D97** (2018), no. 9, 092005, doi:10.1103/PhysRevD.97.092005, arXiv:1712.02345.

[17] J. M. Lindert et al., "Precise predictions for $V+$ jets dark matter backgrounds", *Eur. Phys. J.* **C77** (2017), no. 12, 829, doi:10.1140/epjc/s10052-017-5389-1, arXiv:1705.04664.

[18] CMS EGamma POG, "EgHLTRunIISummary". https://twiki.cern.ch/twiki/bin/view/CMS/EgHLTRunIISummary.

[19] CMS Collaboration, "Extraction and validation of a new set of CMS PYTHIA8 tunes from underlying-event measurements", arXiv:1903.12179.

[20] M. L. Mangano, M. Moretti, F. Piccinini, and M. Treccani, "Matching matrix elements and shower evolution for top-quark production in hadronic collisions", *JHEP* **01** (2007) 013, doi:10.1088/1126-6708/2007/01/013, arXiv:hep-ph/0611129.

[21] R. Frederix and S. Frixione, "Merging meets matching in MC@NLO", *JHEP* **12** (2012) 061, doi:10.1007/JHEP12(2012)061, arXiv:1209.6215.

[22] NNPDF Collaboration, "Parton distributions from high-precision collider data", *Eur. Phys. J.* **C77** (2017), no. 10, 663, doi:10.1140/epjc/s10052-017-5199-5, arXiv:1706.00428.

[23] GEANT4 Collaboration, "GEANT4: A Simulation toolkit", *Nucl. Instrum. Meth. A* **506** (2003) 250, doi:10.1016/S0168-9002(03)01368-8.

[24] CMS Collaboration, "Search for invisible decays of a Higgs boson produced through vector boson fusion in proton-proton collisions at $\sqrt{s} = 13$ TeV", *Phys. Lett.* **B793** (2019) 520–551, doi:10.1016/j.physletb.2019.04.025, arXiv:1809.05937.

[25] A. Albert, "Search for new invisible particles in events with a Z boson at CMS". PhD thesis, RWTH Aachen University, Aachen, 2019. doi:10.18154/RWTH-2019-05664.

[26] LHC New Physics Working Group Collaboration, "Simplified models for LHC new physics searches", *J. Phys. G* **39** (2012) 105005, doi:10.1088/0954-3899/39/10/105005, arXiv:1105.2838.

[27] J. Abdallah et al., "Simplified models for dark matter searches at the LHC", *Phys. Dark Univ.* **9-10** (2015) 8, doi:10.1016/j.dark.2015.08.001, arXiv:1506.03116.

[28] O. Mattelaer and E. Vryonidou, "Dark matter production through loop-induced processes at the LHC: the s-channel mediator case", *Eur. Phys. J. C* **75** (2015) 436, doi:10.1140/epjc/s10052-015-3665-5, arXiv:1508.00564.

[29] M. Backovi et al., "Higher-order QCD predictions for dark matter production at the lhc in simplified models with s-channel mediators", *Eur. Phys. J. C* **75** (2015) 482, doi:10.1140/epjc/s10052-015-3700-6, arXiv:1508.05327.

[30] M. Neubert, J. Wang, and C. Zhang, "Higher-order QCD predictions for dark matter production in mono-z searches at the lhc", *JHEP* **02** (2016) 082, doi:10.1007/JHEP02(2016)082, arXiv:1509.05785.

[31] G. Busoni et al., “Recommendations on presenting LHC searches for missing transverse energy signals using simplified s-channel models of dark matter”, arXiv:1603.04156.

[32] T. C. monojet group, “Search for dark matter produced with an energetic jet, or a hadronically decaying w or z boson, at sqrt(s) = 13 tev with the full 2016 dataset”, CMS Note 2016/473, 2016.

[33] C. Arina, B. Fuks, and L. Mantani, “A universal framework for t-channel dark matter models”, *Eur. Phys. J. C* **80** (2020), no. 5, 409, doi:10.1140/epjc/s10052-020-7933-7, arXiv:2001.05024.

[34] Z. Diaz, Schmaltz, “The leptoquark hunter’s guide: Pair production”, doi:10.1007/JHEP10(2017)097.

[35] M. Cacciari, G. P. Salam, and G. Soyez, “The anti-k_t jet clustering algorithm”, *JHEP* **04** (2008) 063, doi:10.1088/1126-6708/2008/04/063, arXiv:0802.1189.

[36] M. Cacciari, G. P. Salam, and G. Soyez, “FastJet user manual”, *Eur. Phys. J. C* **72** (2012) 1896, doi:10.1140/epjc/s10052-012-1896-2, arXiv:1111.6097.

[37] CMS Collaboration, “Jet energy scale and resolution in the CMS experiment in pp collisions at 8 TeV”, *JINST* **12** (2017) P02014, doi:10.1088/1748-0221/12/02/P02014, arXiv:1607.03663.

[38] CMS JME POG, “Jet Identification for the 13 TeV data Run2017”. https://twiki.cern.ch/twiki/bin/view/CMS/JetID13TeVRun2017.

[39] CMS JME POG, “Jet Identification for the 13 TeV data Run2018”. https://twiki.cern.ch/twiki/bin/view/CMS/JetID13TeVRun2018.

[40] CMS Collaboration, “Identification of heavy-flavour jets with the CMS detector in pp collisions at 13 TeV”, *JINST* **13** (2018), no. 05, P05011, doi:10.1088/1748-0221/13/05/P05011, arXiv:1712.07158.

[41] CMS JMAR POG, “Boosted Jet Tagging using Deep Neural Networks and low level variables: DeepAK(X)”. https://twiki.cern.ch/twiki/bin/viewauth/CMS/DeepAKXTagging#DeepAK8_V2_Working_Points_and_Sc.

[42] CMS JME POG. https://twiki.cern.ch/twiki/bin/view/CMS/MissingETOptionalFiltersRun2.

[43] CMS JME POG, “2017 MET recipe v2”. https://hypernews.cern.ch/HyperNews/CMS/get/JetMET/1865.html.

[44] CMS Collaboration, “Performance of electron reconstruction and selection with the CMS detector in proton-proton collisions at $\sqrt{s} = 8\,\mathrm{TeV}$”, *JINST* **10** (2015) P06005, doi:10.1088/1748-0221/10/06/P06005, arXiv:1502.02701.

[45] CMS Collaboration, “Description and performance of track and primary-vertex reconstruction with the CMS tracker”, *JINST* **9** (2014) P10009, doi:10.1088/1748-0221/9/10/P10009, arXiv:1405.6569.

[46] CMS EGamma POG. https://twiki.cern.ch/twiki/bin/viewauth/CMS/CutBasedElectronIdentificationRun2#Spring15_selection_25ns.

[47] CMS Collaboration Collaboration, “Performance of CMS muon reconstruction in pp collision events at $\sqrt{s} = 7\,\mathrm{TeV}$”, *JINST* **7** (2012) P10002, doi:10.1088/1748-0221/7/10/P10002, arXiv:1206.4071.

[48] CMS Muon POG. https://twiki.cern.ch/twiki/bin/view/CMS/SWGuideMuonIdRun2#Loose_Muon.

[49] CMS Muon POG. https://twiki.cern.ch/twiki/bin/view/CMS/SWGuideMuonIdRun2#Tight_Muon.

[50] CMS Collaboration, "Reconstruction and identification of τ lepton decays to hadrons and ν_τ at CMS", *JINST* **11** (2016) P01019, doi:10.1088/1748-0221/11/01/P01019, arXiv:1510.07488.

[51] CMS TAU POG. https://twiki.cern.ch/twiki/bin/viewauth/CMS/TauIDRecommendationForRun2#Corrections_to_be_applied_to_AN3.

[52] CMS Collaboration, "Performance of photon reconstruction and identification with the CMS detector in proton-proton collisions at $\sqrt{s} = 8$ TeV", *JINST* **10** (2015) P08010, doi:10.1088/1748-0221/10/08/P08010, arXiv:1502.02702.

[53] CMS EGamma POG. https://twiki.cern.ch/twiki/bin/viewauth/CMS/CutBasedPhotonIdentificationRun2#SPRING15_selections_bunch_crossi.

[54] CMS Lumi POG. https://twiki.cern.ch/twiki/bin/view/CMS/PileupJSONFileforData#Pileup_JSON_Files_For_Run_II.

[55] Reweighting recipe to emulate Level 1 ECAL prefiring. https://twiki.cern.ch/twiki/bin/viewauth/CMS/L1ECALPrefiringWeightRecipe.

[56] Prefiring correction implementation in nanoaod-tools. https://github.com/cms-nanoAOD/nanoAOD-tools/blob/master/python/postprocessing/modules/common/PrefireCorr.py.

[57] CMS Muon POG. https://twiki.cern.ch/twiki/bin/view/CMS/MuonReferenceSelectionAndCalibrationsRun2.

[58] S. Yuan, "Measurement of cut-basedID SF medium WP for high p_T photons for EXO-20-004". https://indico.cern.ch/event/879924/contributions/3872624/attachments/2042983/3422039/Photon_ID_EGamma_meeting0521.pdf.

[59] CMS BTV POG, "Heavy flavour tagging for 13 TeV data in 2017 and 94X MC". https://twiki.cern.ch/twiki/bin/viewauth/CMS/BtagRecommendation94X.

[60] CMS BTV POG, "Heavy flavour tagging for 13 TeV data in 2018 and 10_2_X MC". https://twiki.cern.ch/twiki/bin/viewauth/CMS/BtagRecommendation102X.

[61] J. Baglio, L. D. Ninh, and M. M. Weber, "Massive gauge boson pair production at the LHC: a next-to-leading order story", *Phys. Rev. D* **88** (2013) 113005, doi:10.1103/PhysRevD.94.099902, arXiv:1307.4331. [Erratum: Phys.Rev.D 94, 099902 (2016)].

[62] A. Denner, S. Dittmaier, M. Hecht, and C. Pasold, "NLO QCD and electroweak corrections to W+γ production with leptonic W-boson decays", *JHEP* **04** (2015) 018, doi:10.1007/JHEP04(2015)018, arXiv:1412.7421.

[63] A. Denner, S. Dittmaier, M. Hecht, and C. Pasold, "NLO QCD and electroweak corrections to Z+γ production with leptonic Z-boson decays", *JHEP* **02** (2016) 057, doi:10.1007/JHEP02(2016)057, arXiv:1510.08742.

[64] CMS Collaboration, "Performance of missing transverse momentum reconstruction in proton-proton collisions at $\sqrt{s} = 13$ TeV using the CMS detector", *Submitted to: JINST* (2019) arXiv:1903.06078.

[65] P. Lenzi, C. A. Palmer, J. Thomas-Wilsker et al., "Performance of flavour tagging algorithms at 13 tev with 2018 data", CMS Note 2018/323, 2019.

[66] CMS Collaboration, "Jet algorithms performance in 13 TeV data", CMS Physics Analysis Summary CMS-PAS-JME-16-003.

[67] A. J. Larkoski, S. Marzani, G. Soyez, and J. Thaler, "Soft drop", *JHEP* **05** (2014) 146, doi:10.1007/JHEP05(2014)146, arXiv:1402.2657.

[68] A. Denner, S. Dittmaier, T. Kasprzik, and A. Muck, "Electroweak corrections to W + jet hadroproduction including leptonic W-boson decays", *JHEP* **08** (2009) 075, doi:10.1088/1126-6708/2009/08/075, arXiv:0906.1656.

[69] A. Denner, S. Dittmaier, T. Kasprzik, and A. Muck, "Electroweak corrections to dilepton + jet production at hadron colliders", *JHEP* **06** (2011) 069, doi:10.1007/JHEP06(2011)069, arXiv:1103.0914.

[70] A. Denner, S. Dittmaier, T. Kasprzik, and A. Mck, "Electroweak corrections to monojet production at the LHC", *Eur. Phys. J. C* **73** (2013) 2297, doi:10.1140/epjc/s10052-013-2297-x, arXiv:1211.5078.

[71] J. H. Kuhn, A. Kulesza, S. Pozzorini, and M. Schulze, "Electroweak corrections to hadronic photon production at large transverse momenta", *JHEP* **03** (2006) 059, doi:10.1088/1126-6708/2006/03/059, arXiv:hep-ph/0508253.

[72] S. Kallweit et al., "NLO electroweak automation and precise predictions for W+multijet production at the LHC", *JHEP* **04** (2015) 012, doi:10.1007/JHEP04(2015)012, arXiv:1412.5157.

[73] S. Kallweit et al., "NLO QCD+EW predictions for V + jets including off-shell vector-boson decays and multijet merging", *JHEP* **04** (2016) 021, doi:10.1007/JHEP04(2016)021, arXiv:1511.08692.

[74] CMS Collaboration, "Search for New Physics with Jets and Missing Transverse Momentum in pp collisions at $\sqrt{s} = 7$ TeV", *JHEP* **08** (2011) 155, doi:10.1007/JHEP08(2011)155, arXiv:1106.4503.

[75] J. H. Kuhn, A. Kulesza, S. Pozzorini, and M. Schulze, "Logarithmic electroweak corrections to hadronic Z+1 jet production at large transverse momentum", *Phys. Lett. B* **609** (2005) 277, doi:10.1016/j.physletb.2005.01.059, arXiv:hep-ph/0408308.

[76] J. H. Kuhn, A. Kulesza, S. Pozzorini, and M. Schulze, "One-loop weak corrections to hadronic production of Z bosons at large transverse momenta", *Nucl. Phys. B* **727** (2005) 368, doi:10.1016/j.nuclphysb.2005.08.019, arXiv:hep-ph/0507178.

[77] J. H. Kuhn, A. Kulesza, S. Pozzorini, and M. Schulze, "Electroweak corrections to hadronic production of W bosons at large transverse momenta", *Nucl. Phys. B* **797** (2008) 27, doi:10.1016/j.nuclphysb.2007.12.029, arXiv:0708.0476.

[78] CMS Collaboration, "Performance of the CMS missing transverse momentum reconstruction in pp data at $\sqrt{s}$ = 8 TeV", *JINST* **10** (2015) P02006, doi:10.1088/1748-0221/10/02/P02006, arXiv:1411.0511.

[79] CMS JME. https://twiki.cern.ch/twiki/bin/view/CMS/JECUncertaintySources#Run_2_reduced_set_of_uncertainty.

[80] CMS Collaboration, "Measurement of the top quark pair production cross section in proton-proton collisions at $\sqrt{s} = 13$ TeV", *Phys. Rev. Lett.* **116** (2016) 052002, doi:10.1103/PhysRevLett.116.052002, arXiv:1510.05302.

[81] LHC Dark Matter Working Group, "Recommendations of the LHC dark matter working group: Comparing LHC searches for heavy mediators of dark matter production in visible and invisible decay channels", (2017). arXiv:1703.05703.

[82] Planck Collaboration, “Planck 2018 results. VI. Cosmological parameters”, `arXiv:1807.06209`.

[83] R. Cousins, “Generalization of chisquare goodness-of-fit testfor binned data using saturated models, with application to histograms”, (2010).